DISSERTATION

SYNTHESIS AND EVALUATION OF FLUOROUS POLYCYCLIC AROMATIC HYDROCARBON DERIVATIVES FOR ORGANIC ELECTRONICS

Submitted by

Kerry C. Rippy

Department of Chemistry

In partial fulfillment of the requirements

For the Degree of Doctor of Philosophy

Colorado State University

Fort Collins, Colorado

Summer 2019

Doctoral Committee:

Advisor: Steven H. Strauss

Amy L. Prieto
James R. Sites
Grzegorz Szamel

ABSTRACT

SYNTHESIS AND EVALUATION OF FLUOROUS POLYCYCLIC AROMATIC HYDROCARBON DERIVATIVES FOR ORGANIC ELECTRONICS

Advances in the performance of electron acceptor materials for organic electronics critically depend on the efficiency of synthetic routes for new materials and fundamental understanding of the correlation between molecular structure and electronic and solid-state properties. The research presented here endeavors to address both of these needs, by developing original methods for synthesis of new organic electron acceptor materials, and by characterizing relevant properties of the resulting materials. In total, synthesis and analysis of more than 60 new molecules is presented in this work.

These molecules are derivatives of polycyclic aromatic hydrocarbons (PAHs) and hetero-PAHs functionalized with fluorous moieties, synthesized via development of substrate-specific efficient, single-step direct-substitution methods. Investigation of solid-state and electronic properties focused upon effects of structural motifs including (i) the type, number, and position of electron withdrawing fluorous substituents (ii) the size and shape of aromatic π systems, and (iii) presence of hetero atoms within the aromatic core.

The first chapter of this work details the development and optimization of a gas-phase radical reaction between the perfluoroalkyl diiodide 1,4-$C_4F_8I_2$ and the PAH triphenylene (TRPH). The perfluoroalkyl diiodide, with two C–I bonds, one at either end, has the unique ability to bind to vicinal C atoms, forming a 6-membered ring. A family of TRPH derivatives functionalized with such rings was synthesized, and the reaction was optimized. Additionally, reductive partial defluorination of the perfluoroalkyl ring was achieved, leading to aromatization of the fluorous substituent (RD/A). The extension of the π-system, as well as the effect of fluorine atoms bound

directly to the aromatic system, was examined with respect to solid-state packing and electronic levels.

In Chapter 2, results of screening of 13 new PAH and *n*-hetero PAH substrates with respect to their reactivity towards 1,4-$C_4F_8I_2$ are described. Pure compounds derived from these reactions are presented, adding several new families to the library of fluorous PAH derivatives. Unique reactivities and interesting potential applications are discussed for several of these families. Solid-state packing and electronic properties are analyzed for selected derivatives.

A particularly promising family of fluorous acceptors is presented and analyzed in greater depth in Chapter 3. It is based on the substrate phenazine (PHNZ). This family of molecules is notable because several derivatives exhibit enhanced acceptor strength and linearly-fused molecular structures resembling the acene class of PAHs, a high performing class of materials widely used in organic electronics. Results suggest that the molecules investigated in this chapter would be suitable for applications as air-stable *n*-type semiconductors in electronic devices.

Finally, in Chapter 4, the characterization of a family of trifluromethylated acridine (ACRD) derivates is described. This investigation yields new insights into the reactivity of ACRD. Furthermore, detailed structural, spectroscopic and electronic property analysis combined with computational data revealed that not only the number of substituents, but also the position of substituents affects electronic energy levels. This finding not only expands basic understanding of how molecular structure affects electronic properties of PAHs, but also provides a valuable new tool for molecular design of acceptors with desirable properties.

ACKNOWLEDGMENTS

Thank you to my family and friends, who have provided incalculable (dare I say infinite?) support throughout my life, and who fostered in me the curiosity and academic interest that led me to pursue this research.

Thank you to my advisors, Steven H. Strauss and Olga V. Boltalina. I respect and admire both of you, perhaps more than you know. You have taught me innumerable lessons as, in Steve's words, I worked to evolve from a student of science to a Scientist. Thank you to all the past and present members of the Strauss-Boltalina Research Group. My work would not have been possible without your insights, assistance, and mentorship. In particular, I owe a great deal to Dr. Igor V. Kuvychko, who laid the foundations of my research, and who inspired me greatly.

Thank you to all the colleagues who allowed me to visit their labs, patiently introduced me to their laboratory techniques, and above and beyond this, acted as wonderful hosts. They assisted me with many needs outside of lab, and invited me along on incredible outings. I would particularly like to thank Dr. Alexey Popov, Dr. Koen Vandewal, Dr. Xue-Bin Wang, Dr. Nikos Kopidakis, Frank Ziegs, Bernhard Nell, Marc Zeplichal, and Sebastian Balser in this respect.

Finally, although he fits into more than one of the categories listed above, I must extend individual thanks to Nicholas J. DeWeerd. Nick, you have supported me both academically and personally to such an extent that this achievement is yours as much as it is mine. I look forward to celebrating your graduation soon!

I also thank the National Science Foundation (grant NSF/CHE- 1362302 (S.H.S. and O.V.B.), the DAAD German Academic Exchange Program, and the Endeavour Fellowship program of the Australian government. Use of the Advanced Photon Source (APS) was supported by the U.S. Department of Energy, Office of Science, Office of Basic Energy Sciences, under Contract No. DE-AC02- 06CH11357. APS Chem-MatCARS Sector 15 is principally supported by the NSF/DOE under grant NSF/CHE-1316572.

TABLE OF CONTENTS

INTRODUCTION

I.1. BACKGROUND AND MOTIVATION

Organic electronic materials have unique properties, including flexibility and tunable absorption/emission, allowing them to be used for unprecedented applications. Despite recent commercial success of organic semiconductor-based electronics, development of *n*-type (electron transporting) organic semiconductor materials continues to lag well behind development of *p*-type materials.[1-4] Rectifying this imbalance would have profound impacts on the performance of organic electronic devices, including organic light emitting diodes (OLEDs), organic photovoltaic (OPVs) devices, and organic field effect transistors (OFETs). Given the wide array of applications for such devices, their facile, energy efficient, inexpensive processing, and their unique material properties, the potential impact of improvement of n-type organic semiconductors is far-reaching.[1] (see appx D.i.1 for examples of uses of electron acceptor materials in these technologies) However, before these impacts can be realized, synthetic routes must be opened up for new materials, and

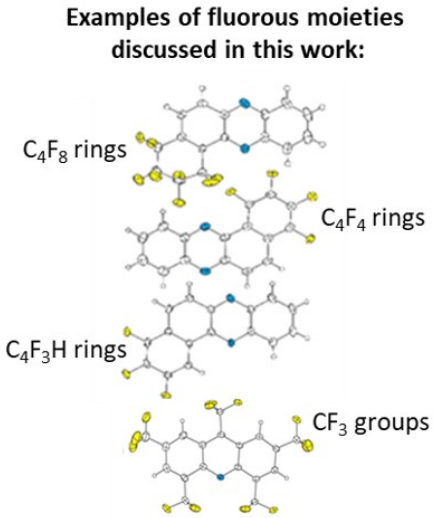

Figure i-1. This work focuses on synthesis and evaluation families of PAH and hetero-PAH derivatives, primarily functionalized the four types of fluorous moieties shown above. The hetero-PAHs phenazine (PHNZ) and acridine (ACRD) are used as arbitrary example substrates for the purpose of this illustration. Not pictured are C_4F_8H, C_4F_8I, and C_2F_5 moieties, fluorous alkyl chain substituents which were also observed in the course of this work. In total, over 60 new molecules functionalized with these groups are presented.

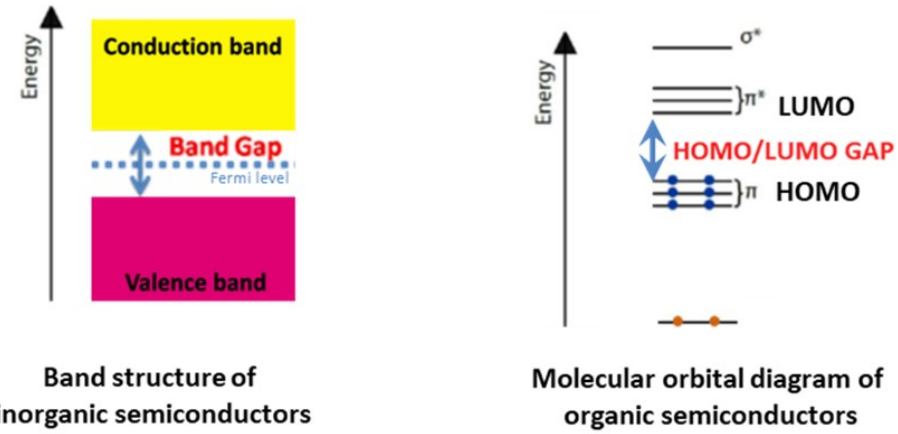

Figure i-2. Simplified energy diagrams illustrating the relationship between the band structure of inorganic semiconductors and the molecular orbitals of organic semiconductors. In a general sense, the band gap of an inorganic semiconductor and the HOMO/LUMO gap of an inorganic semiconductor are analogous. Notably, the HOMO and LUMO levels of organic materials can be tuned synthetically, using method such as substitution with electron withdrawing groups. This is an important advantage of organic semiconductors, and a focus of this work.

fundamental research into the correlation between molecular structure and physiochemical properties must be conducted. This work endeavors to address both of these needs, by developing methodologies for synthesis of new organic electron acceptor materials and by characterizing relevant material properties of families of these molecules.

Functionalization of aromatic systems with electron withdrawing groups has emerged as the most viable route toward creating n-type semiconductors.[5-9] In light of this, the molecules targeted by this research are all derivatives of polycyclic aromatic hydrocarbons (PAHs) or hetero-PAHs (PAHs contain hetero-atoms in their aromatic core) functionalized with fluorine or fluorinated substituents. Several such molecules are shown in Figure i-1, exemplifying the types of molecules that will be discussed in this work.

The rationale behind the focus on PAHs and hetero-PAHs functionalized with electron withdrawing groups is twofold. The first reason is best understood through examination of the basic physical principles underlying the function of organic semiconductors. In the more familiar case of inorganic semiconductors, a valence band and a conduction band are separated by a band gap, within which falls the Fermi level. The analogous situation in organic electronic materials

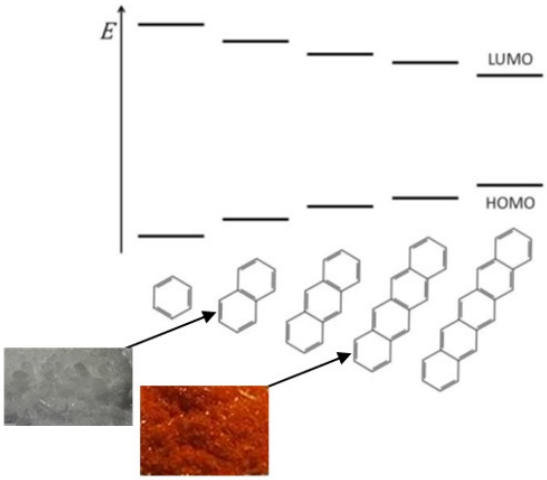

Figure i-3. There exists a correlation between the size of the π system of a PAH and the HOMO/LUMO gap. Shown above is a qualitative series of HOMO/LUMO gaps for PAHs with very similar shapes and peripheries to illustrate the shrinking HOMO/LUMO gap for larger PAHs, and the effect of this change upon PAH color (absorption in the visible spectrum).

involves the molecular orbitals of aromatic systems. The highest occupied molecular orbitals (HOMOs), which are the π orbitals, are analogous to the valence band. The lowest unoccupied molecular orbitals (LUMOs), which are π* orbitals, are analogous to the conduction band. The gap between these so-called frontier orbitals may be thought of as similar to the band gap. See Figure i-2 for an illustration of this analogy.

Of course, the analogy is not perfect. Inorganic bands, containing a continuum and multiplicity of states, are quite distinct from molecular orbitals, which are localized on single molecules. Although this distinction presents challenges, one of which is discussed below, it also endows organic electronic materials with uniquely tunable properties unrivaled by inorganic semiconductors.

This is because energy levels of organic electronic materials can be tuned incrementally through strategic molecular design. Features that can be manipulated include (i) the size and shape of the aromatic π system, (ii) the presence or absence of hetero atoms in the aromatic ring, and (iii) the presence or absence of electron withdrawing substituents all affect the energy levels of frontier orbitals. An example (i) is shown in Figure i-3, illustrating that larger aromatic systems tend to have smaller HOMO/LUMO gaps.[10] As a general trend, larger π systems have the ability to

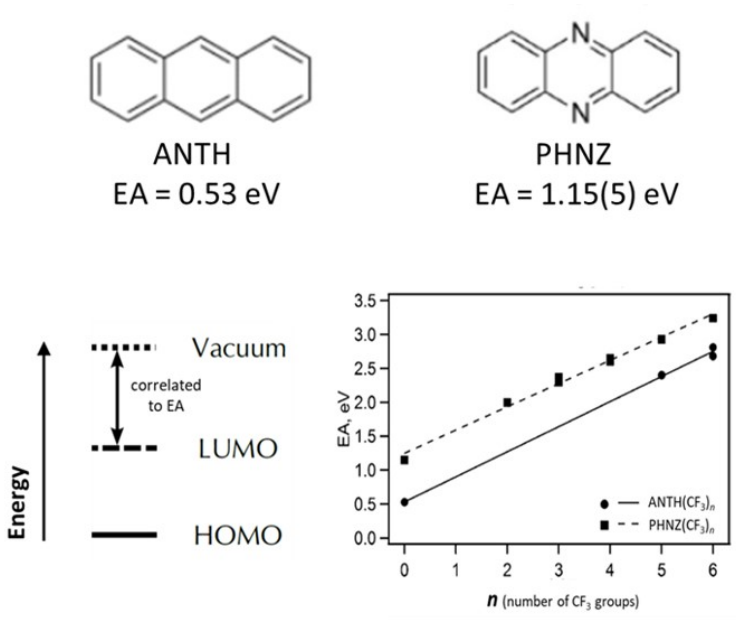

Figure i-4. The PAH anthracene (ANTH) and the hetero-PAH phenazine (PHNZ) both have aromatic systems composed of three linearly fused benzenoid rings. However, they have substantially different energy levels, as illustrate by their EA values. The presence of a hetero atom increases the EA. Also shown here, the EA of these substrates can be tuned in a linear, incremental fashion by addition of trifluoromethyl groups. Values from reference 11.

delocalize electron density across a greater number of C atoms, and therefore have lower HOMO/LUMO gaps, though other factors, such as the shape and periphery of the π system also have an effect on energy levels.[10] This shrinking gap is evidenced by the fact that naphthene, the second PAH in this series which has a relatively large HOMO/LUMO gap, is white, while tetracene, the fourth PAH in this series with a smaller HOMO/LUMO gap, absorbs within the visible range of light, is highly therefore colored. Examples of (ii) and (iii) are shown in Figure i-4, illustrating that electron affinity values (EA), which are correlated to frontier energy levels as shown, are altered by hetero atoms and substituents.[11-15] This phenomenon results from the removal of electron density from the aromatic system, tuning energy levels to more readily accept electrons. In addition to improving electron acceptor performance, higher EA values have been correlated to higher air-stability in devices.[16]

A second important justification for the focus on PAHs and hetero-PAHs functionalized with electron withdrawing groups is their unique packing in the solid state. In the case of inorganic

semiconductors, free carriers move with very high mobility through the crystalline or semi-crystalline lattices of the extended solids. However, in organic materials, the charge carriers must move from molecule to molecule. The exact mechanism of charge transport in organic semiconductors is a subject of intensive research.[14, 17, 18] However, it is agreed upon that the overlap of the aromatic systems favors better charge transport.[14] It has also been shown that fluoroalkylation of PAHs improves their π–π interactions and often causes them to transition from a herringbone stacking configuration, with little π-overlap, to columns of π-stacked molecules,[19, 20] These stacks have great promise as high-mobility materials for organic electronics.

Therefore, the primary motivation for the studies presented here are to tune electronic and solid-state packing properties of PAHs via substitution with fluorous groups.

I.2. OVERVIEW OF RESEARCH PRESENTED HERE

As motivated by the discussion above, the work presented here explores the effects of hetero-atoms, fluorous substituents, and alteration of π-system size and shape on electronic properties and solid-state packing of PAHs. It builds on synthetic work conducted by previous Strauss-Boltalina Research Group members, especially Dr. Igor V. Kuvychko and Dr. Karlee P. Castro, who developed a single-step gas-phase reaction of PAHs with R_F• radicals, produced by thermal decomposition of perfluoroalkyl iodides.[21-25] This method allows for synthesis of families of molecules of the formula PAH$(CF_3)_n$, which can be separated by high pressure liquid chromatography (HPLC).[26]

The first goal of this work, presented in Chapter 1, was to develop a synthetic method utilizing the perfluoroalkyl iodide $C_4F_8I_2$ and the highly symmetric PAH triphenylene (TRPH). This PAH was chosen as a model system due in part to the many applications of TRPH, especially in liquid crystalline devices,[27-31] but also due to the fact that high symmetry precludes formation of an abundance of isomers. The perfluoroalkyl iodide was chosen because its two C-I bonds, one at either end, gives this reagent the unique ability to bind to vicinal C atoms, forming a 6-membered ring.[22] A family of TRPH derivatives functionalized with such rings was synthesized, and the

reaction was optimized. Additionally, reductive partial defluorination of the perfluoroalkyl ring was achieved, leading to aromatization of the substituent (RD/A). The extension of the π-system, as well as the effect of fluorine atoms bound directly to the aromatic system as opposed to perfluoroalkyl substituents, was examined particularly with respect to electronic levels and packing behavior.

In Chapter 2, the synthetic method developed in chapter 1 is employed using a number of different PAH and hetero-PAH substrates. In total, the results of screening 12 additional substrates are presented. Pure compounds derived from these substrates are presented, adding several new families to the library of fluorous PAH derivatives. Unique reactivities and interesting potential applications are discussed for several of these families. For a selection of molecules, packing and electronic levels are analyzed.

A particularly promising family of compounds is presented and analyzed in greater depth in Chapter 3, based on the substrate phenazine (PHNZ). This family of molecules is notable because several derivatives have promising electronic properties, indicating that they could function as electron acceptor materials in devices. Additionally, the linear PHNZ π-system is similar to the linearly fused π-system of the acene family of PAHs, which are champion performers among p-type organic semiconductors.[32]

Finally, in Chapter 4, a family of trifluoromethylated acridine (ACRD) derivates is presented. In the case of this unique hetero-PAH, it is found that not only number of substituents, but position of substituents affects energy levels. This is the first report of such a finding, expands understanding of how structure affects electronic properties of PAHs. Additionally, an understanding of the reactivity of ACRD is useful for applications extending beyond organic electronics, including medicinal applications.[33, 34]

I.3. METHODS COMMONLY UTILIZED IN THIS WORK

For most compounds presented in the work, purification was achieved by HPLC using a specialized COSMOSIL Buckyprep column with a variety of different eluents. Structural

characterization was primarily accomplished via ^{1}H and ^{19}F NMR spectroscopy. In certain cases, the single crystal X-ray structure was required to resolve ambiguities in the NMR assignments.

As discussed above, a major motivation for this work is to create a library of compounds with incrementally tuned electron acceptor properties. Therefore, methodologies for assessment of electron acceptor properties were necessary. In this work, this is most commonly accomplished via assessment of gas phase electron affinity (EA), and electrochemical reduction potential in solution ($E_{1/2}$). These parameters yield insight into the energy levels of frontier orbitals, which, as discussed above, are of paramount importance for organic electronic materials. Values of EA correlate to LUMO energies, as shown in Figure I-4. Values of EA were obtained at Pacific Northwest National Lab, utilizing low temperature photoelectron spectroscopy (PES, appx *A.4.8.*), under the supervision of Dr. Xue-Bin Wang with assistance from Dr. Gao-Lei Hou.[35] The PES samples were solutions of the one-electron-reduced anions. Values of $E_{1/2}$ were obtained by the author at Colorado State University (CSU), or by the author with assistance from Dr. Peter Machata and Ilka Vincon at IFW (Leibniz Institute for Solid State and Materials Research), utilizing a three-electrode electrochemical cell (appx *A.4.4.*).

In some cases, supplementary methods were used to further investigate electronic levels. In chapters 3 and 4, spectroelectrochemical experiments, conducted with Dr. Machata and Ms. Vincon at IFW, allowed for simultaneous monitoring of electron spin resonance (ESR) spectra and vis-NIR absorption spectra during electrochemical reduction allowed study of reduced species. In chapter 3, the complementary techniques of photoluminescence (PL) and time-resolved microwave conductivity (TRMC), conducted at Macquarie University under the supervision of Dr. Nikos Kopidakis, were employed to confirm that molecules behave as electron acceptors in thin films with Poly(3-hexylthiophene-2,5-diyl)(P3HT) as a donor. In chapters 1 and 4, computationally predicted relative stabilities were used to analyze reaction characteristics. In chapter 4, additional calculation including DFT-predicted EA and $E_{1/2}$ values, and frontier orbital levels were obtained to address questions concerning substitution-pattern related variance in

experimentally measured physiochemical properties.[7, 36-38] Computations were performed by Dr. Alexey Popov and Ms. Vincon at IFW.

In all chapters, solid state properties including stacking and planarity were investigated through analysis of single crystal X-ray structures, primarily obtained at Argonne National Laboratory at the Advanced Photon Source, sector 15 ChemMatCARS, with Dr. Yu-Sheng Chen. In most cases, structures were solved by Nicholas J. DeWeerd.

REFERENCES

1. Anthony, J. E.; Facchetti, A.; Heeney, M.; Marder, S. R.; Zhan, X., n-Type Organic Semiconductors in Organic Electronics. *Adv. Mater.* **2010,** *22* (34), 3876-3892.
2. Gao, X.; Hu, Y., Development of n-type organic semiconductors for thin film transistors: a viewpoint of molecular design. *J. Mat. Chem. C* **2014,** *2* (17), 3099-3117.
3. Wang, C.; Dong, H.; Hu, W.; Liu, Y.; Zhu, D., Semiconducting π-Conjugated Systems in Field-Effect Transistors: A Material Odyssey of Organic Electronics. *Chem. Rev.* **2012,** *112* (4), 2208-2267.
4. Newman, C. R.; Frisbie, C. D.; da Silva Filho, D. A.; Brédas, J.-L.; Ewbank, P. C.; Mann, K. R., Introduction to Organic Thin Film Transistors and Design of n-Channel Organic Semiconductors. *Chem. Mater.* **2004,** *16* (23), 4436-4451.
5. Tang, M. L.; Bao, Z., Halogenated Materials as Organic Semiconductors. *Chem. Mater.* **2011,** *23* (3), 446-455.
6. Babudri, F.; Farinola, G. M.; Naso, F.; Ragni, R., Fluorinated organic materials for electronic and optoelectronic applications: the role of the fluorine atom. *Chem. Comm.* **2007,** (10), 1003-1022.
7. Sun, H.; Putta, A.; Billion, M., Arene Trifluoromethylation: An Effective Strategy to Obtain Air-Stable n-Type Organic Semiconductors with Tunable Optoelectronic and Electron Transfer Properties. *J. Phys. Chem. A* **2012,** *116* (30), 8015-8022.
8. Yoon, M.-H.; Facchetti, A.; Stern, C. E.; Marks, T. J., Fluorocarbon-Modified Organic Semiconductors: Molecular Architecture, Electronic, and Crystal Structure Tuning of Arene- versus Fluoroarene-Thiophene Oligomer Thin-Film Properties. *J. Am. Chem. Soc.* **2006,** *128* (17), 5792-5801.
9. Usta, H.; Facchetti, A.; Marks, T. J., n-Channel Semiconductor Materials Design for Organic Complementary Circuits. *Acc. Chem. Res.* **2011,** *44* (7), 501-510.
10. Watson, M. D.; Fechtenkötter, A.; Müllen, K., Big Is Beautiful−"Aromaticity" Revisited from the Viewpoint of Macromolecular and Supramolecular Benzene Chemistry. *Chem. Rev.* **2001,** *101* (5), 1267-1300.
11. Castro, K. P.; Clikeman, T. T.; DeWeerd, N. J.; Bukovsky, E. V.; Rippy, K. C.; Kuvychko, I. V.; Hou, G.-L.; Chen, Y.-S.; Wang, X.-B.; Strauss, S. H.; Boltalina, O. V., Incremental Tuning Up of Fluorous Phenazine Acceptors. *Chem.-Eur. J.* **2016,** *22* (12), 3930-3936.
12. Schlosser, M., CF3-Bearing Aromatic and Heterocyclic Building Blocks. *Angew. Chem.-Int. Edit.* **2006,** *45* (33), 5432-5446.
13. Schmidt, B. M.; Lentz, D., Syntheses and Properties of Buckybowls Bearing Electron-withdrawing Groups. *Chem. Lett.* **2014,** *43* (2), 171-177.
14. Feng, X.; Marcon, V.; Pisula, W.; Hansen, M. R.; Kirkpatrick, J.; Grozema, F.; Andrienko, D.; Kremer, K.; Müllen, K., Towards high charge-carrier mobilities by rational design of the shape and periphery of discotics. *Nature Mater.* **2009,** *8* (5), 421.
15. Geib, S.; Martens, S. C.; Zschieschang, U.; Lombeck, F.; Wadepohl, H.; Klauk, H.; Gade, L. H., 1,3,6,8-Tetraazapyrenes: Synthesis, Solid-State Structures, and Properties as Redox-Active Materials. *J. Org. Chem. Soc.* **2012,** *77* (14), 6107-6116.
16. Chang, Y. C.; Kuo, M. Y.; Chen, C. P.; Lu, H. F.; Chao, I., On the Air Stability of n-Channel Organic Field-Effect Transistors: A Theoretical Study of Adiabatic Electron Affinities of Organic Semiconductors. *J. Phys. Chem. C* **2010,** *114* (26), 11595-11601.
17. Radke, K. S.; Scholz, R.; Ortmann, F.; Leo, K.; Cuniberti, G., Dynamic Effects on the Charge Transport in an Organic Near-Infrared Absorber Material. *J. Phys. Chem. C* **2014,** *118* (13), 6537-6547.
18. Coropceanu, V.; Cornil, J.; da Silva Filho, D. A.; Olivier, Y.; Silbey, R.; Brédas, J.-L., Charge Transport in Organic Semiconductors. *Chem. Rev.* **2007,** *107* (4), 926-952.
19. Sun, H.; Tottempudi, U. K.; Mottishaw, J. D.; Basa, P. N.; Putta, A.; Sykes, A. G., Strengthening π–π Interactions While Suppressing Csp2–H···π (T-Shaped) Interactions via Perfluoroalkylation: A

Crystallographic and Computational Study That Supports the Beneficial Formation of 1-D π–π Stacked Aromatic Materials. *Cryst. Growth. Des.* **2012,** *12* (11), 5655-5662.
20. Główka, M. L.; Martynowski, D.; Kozłowska, K., Stacking of six-membered aromatic rings in crystals. *J. Mol. Struct.* **1999,** *474*, 81–89.
21. Kuvychko, I. V.; Castro, K. P.; Deng, S. H. M.; Wang, X.-B.; Strauss, S. H.; Boltalina, O. V., Taming Hot CF3 Radicals: Incrementally Tuned Families of Polyarene Electron Acceptors for Air-Stable Molecular Optoelectronics. *Angew. Chem.-Int. Edit.* **2013,** *52* (18), 4871-4874.
22. Kuvychko, I. V.; Dubceac, C.; Deng, S. H. M.; Wang, X.-B.; Granovsky, A. A.; Popov, A. A.; Petrukhina, M. A.; Strauss, S. H.; Boltalina, O. V., C20H4(C4F8)3: A Fluorine-Containing Annulated Corannulene that Is a Better Electron Acceptor Than C60. *Angew. Chem.-Int. Edit.* **2013,** *52* (29), 7505-7508.
23. Kuvychko, I. V.; Spisak, S. N.; Chen, Y.-S.; Popov, A. A.; Petrukhina, M. A.; Strauss, S. H.; Boltalina, O. V., A Buckybowl with a Lot of Potential: C5-C20H5(CF3)5. *Angew. Chem.-Int. Edit.* **2012,** *51* (20), 4939-4942.
24. San, L. K.; Bukovsky, E. V.; Kuvychko, I. V.; Popov, A. A.; Strauss, S. H.; Boltalina, O. V., Single-Step Gas-Phase Polyperfluoroalkylation of Naphthalene Leads to Thermodynamic Products. *Chem.-Eur. J.* **2014,** *20* (15), 4373-4379.
25. Boltalina, O. V.; Popov, A. A.; Kuvychko, I. V.; Shustova, N. B.; Strauss, S. H., Perfluoroalkylfullerenes. *Chem. Rev.* **2015,** *115* (2), 1051-1105.
26. Jinno, K.; Nagoshi, T.; Tanaka, N.; Okamoto, M.; Fetzer, J. C.; Biggs, W. R., Elution Behaviour of Planar and Non-Planar Polycyclic Aromatic Hydrocarbons on Various Chemically Bonded Stationary Phases in Liquid Chromatography. *J. Chromatog.* **1987,** *392*, 75–82.
27. Adam, D.; Schuhmacher, P.; Simmerer, J.; Häussling, L.; Siemensmeyer, K.; Etzbachi, K.; Ringsdorf, H.; Haarer, D., Fast photoconduction in the highly ordered columnar phase of a discotic liquid crystal. *Nature* **1994,** *371* (6493), 141.
28. Hird, M., Fluorinated liquid crystals - properties and applications. *Chem. Soc. Rev.* **2007,** *36* (12), 2070-2095.
29. Pal, S. K.; Setia, S.; Avinash, B. S.; Kumar, S., Triphenylene-based discotic liquid crystals: recent advances. *Liq. Cryst.* **2013,** *40* (12), 1769-1816.
30. Tschierske, C., Fluorinated Liquid Crystals: Design of Soft Nanostructures and Increased Complexity of Self-Assembly by Perfluorinated Segments. In *Liquid Crystals: Materials Design and Self-Assembly*, Tschierske, C., Ed. 2012; Vol. 318, pp 1-108.
31. Wöhrle, T.; Wurzbach, I.; Kirres, J.; Kostidou, A.; Kapernaum, N.; Litterscheidt, J.; Haenle, J. C.; Staffeld, P.; Baro, A.; Giesselmann, F., Discotic liquid crystals. *Chem. Rev.* **2015,** *116* (3), 1139-1241.
32. Ye, Q.; Chi, C., Recent Highlights and Perspectives on Acene Based Molecules and Materials. *Chem. Mater.* **2014,** *26* (14), 4046-4056.
33. Valdés, A. F.-C., Acridine and acridinones: old and new structures with antimalarial activity. *The open medicinal chemistry journal* **2011,** *5*, 11-20.
34. Chiron, J.; Galy, J.-P., *Reactivity of the Acridine Ring: A Review*. 2004; *35*, 313-325.
35. Wang, X.-B.; Wang, L.-S., Development of a low-temperature photoelectron spectroscopy instrument using an electrospray ion source and a cryogenically controlled ion trap. *Rev. Sci. Instrum.* **2008,** *79* (7), 073108.
36. Rippy, K. C.; Bukovsky, E. V.; Clikeman, T. T.; Chen, Y.-S.; Hou, G.-L.; Wang, X.-B.; Popov, A. A.; Boltalina, O. V.; Strauss, S. H., Copper Causes Regiospecific Formation of C_4F_8-Containing Six-Membered Rings and their Defluorination/Aromatization to C_4F_4-Containing Rings in Triphenylene/1,4-$C_4F_8I_2$ Reactions. *Chem.-Eur. J.* **2016,** *22* (3), 874-877.
37. Clikeman, T. T.; Bukovsky, E. V.; Kuvychko, I. V.; San, L. K.; Deng, S. H. M.; Wang, X.-B.; Chen, Y.-S.; Strauss, S. H.; Boltalina, O. V., Poly(trifluoromethyl)azulenes: structures and acceptor properties. *Chem. Comm.* **2014,** *50* (47), 6263-6266.

38. Sevryugina, Y.; Rogachev, A. Y.; Jackson, E. A.; Scott, L. T.; Petrukhina, M. A., X-ray and Density Functional Theory Structural Study of 1,3,5,7,9-Penta-tert-butylcorannulene, C40H50. *J. Org. Chem.* **2006,** *71* (17), 6615-6618.

CHAPTER 1. SYTHESIS AND ANALYSIS OF FLUOROUS TRIPHENYLENE DERIVATIVES

1.1. CHAPTER 1 INTRODUCTION

Triphenylene (TRPH) is a planar, fully benzenoid polycyclic aromatic hydrocarbon (PAH) with D_{3h} symmetry, shown in Figure 1-1.[1] While TRPH itself crystalizes preferentially in a herringbone configuration, TRPH derivatives have an intrinsic propensity to form columnar stacks in the solid state, with a high degree of π-π interaction between neighboring molecules.[2, 3] These stacks exhibit one-dimensional charge transport and excellent liquid-crystalline properties, first noted in the seminal report of the highly-conductive columnar phase of 2,3,6,7,10,11-hexahexylthiotriphenylene 25 years ago.[4, 5] Since that time, intensive research efforts have been devoted to the discovery of new TRPH derivatives, with hundreds of compounds synthesized to date.[5-7]

In particular, significant focus has been devoted to the synthesis of triphenylenes with fluorous substituents, as they exhibit remarkable improvements in liquid-crystal properties compared to hydrocarbon analogs.[7-9] Replacing hydrogen atoms with highly electronegative fluorine atoms results in dramatic changes in molecular structure and alterations to many physical properties including polarity and thermal stability. Importantly, intermolecular interactions in

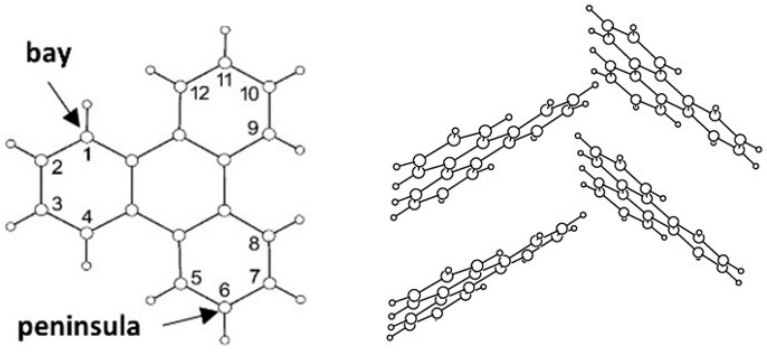

Figure 1-1. Structure of TRPH, with numbering scheme and 'bay' and 'peninsula' position indicated (left), and single crystal x-ray structure of unsubstituted TRPH showing herringbone stacking.[3]

fluorinated materials result in better self-organizing and ordering, and the stability of columnar mesophase is enhanced as a result of these interactions.[6, 10, 11] For example, studies of fluorinated triphenylenes showed improved charge transport characteristics compared to hexa(alkoxy)triphenylenes, presumably due to more cohesive columnar structures.[11] Theoretical studies of fluorinated triphenylenes have substantiated these conclusions and observations.[12]

Therefore, there is great demand for the development of new fluorous TRPH derivatives. Overwhelmingly, the most common method for production of such derivatives in the literature is a 'bottom up' approach, in which building blocks bearing functional groups undergo condensation reactions. These reactions include cyclization of terphenyl, coupling (cycloaddition) of an aromatic precursor linked by a biaryl bond, addition of two peripheral rings to a naphthalene moiety, synthesis from phenanthrene, trimerization of six-membered rings, and one-pot cyclizations of a specific precursors that are themselves made in multiple steps.[13] Utilizing these methods, simple fluorinated derivatives (excluding liquid-crystalline compounds containing fluorous chains) that have been prepare include: TRPH(F)$_n$ (n=1–4, 6, 12),[14-16] 1-TRPH(CF_3), and 2-TRPH(CF_3).[17, 18]

Notwithstanding the prevalence of 'bottom up' synthetic approaches in the literature, TRPH itself is commercially available at a low cost. It was first intentionally synthesized from cyclohexanone, with an 8% yield, over a century ago.[19] Currently, it is produced by one of several 1-3 step reaction pathways with 40-90% yields.[13] Therefore, TRPH is readily available as a substrate for substitution. This possibility was explored by Kuvychko *et al.*, who found that, despite TRPH's relatively low reactivity compared to other PAHs,[20] direct CF_3• radical substitution in a high temperature reaction of TRPH and CF_3I yielded TRPH(CF_3)$_6$.[21] As is usual for R_F• high-temperature radical reactions of PAHs and perfluoroalkyl iodide reagents, this reactions exhibited low selectivity and produced many additional products (which were not isolated).[21-24] Despite this, the success of the reaction and the availability of other perfluoroalkyliodide reagents provided impetus for the work reported here.

In this work, the gas-phase radical reaction of TRPH and 1,4-diiodooctoflurobutane (1,4-$C_4F_8I_2$) was investigated and optimized, and the resulting fluorous TRPH derivatives were

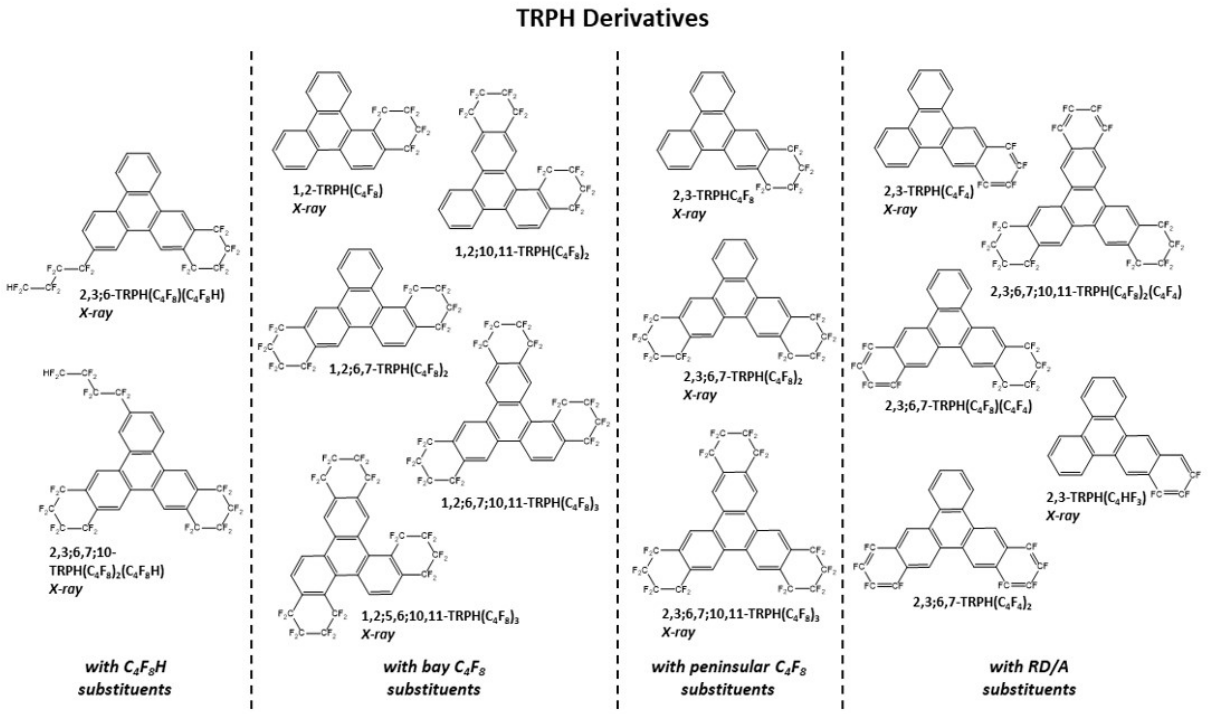

Figure 1-2. Molecular structure of all fluorous triphenylenes prepared in this work. Many have been characterized by single crystal X-ray crystallography, as indicated. For details of synthesis and purification, see sections 1.2.1. and appx. B.1. For details of structural characterization, see section 1.2.2. and appx C.1.

analyzed. Products functionalized with four types of fluorous substituent were identified, including C_4F_8H, C_4F_8, C_4F_4, and C_4F_3H. The latter three moieties substitute for vicinal H-atoms on the TRPH core to form 6-membered rings. In the case of C_4F_4 and C_4F_3H, these rings are aromatic, the result of a novel Cu-promoted reductive defluorination/aromatization (RD/A) of alkyl C_4F_8 moieties.[25] The products resulting from this RD/A are partially fluorinated fully aromatic PAHs, with larger cores than triphenylene. More correctly, they are benzotriphenylenes. However, in this work, for convenience and consistency, these larger PAH molecules are informally referred to as triphenylene derivatives bearing C_4F_4 substituents rather than partially fluorinated benzotriphenylenes. For brevity, compounds are referred to in this work with a 4-letter abbreviation of the PAH substrate name followed by an abbreviation for the fluorous moiety. For example, 10,11,12,13-tetrafluorobenzo[*f*]tetraphene is called 2,3-TRPH(C_4F_4).

While few closely related examples of the Cu-promoted RD/A reaction reported here exist in the literature, precedent for the reaction of 1,4-$C_4F_8I_2$ (without Cu) to form six- and seven-

membered rings includes reactions with the following arenes: benzene,[26] *p*-xylene,[26] tris(perfluorophenyl)corrole,[27] corannulene,[28] and tetraphenylporphyrin.[29, 30] In addition, Vicic and co-workers have reported a series of arene(C_4F_8) derivatives from reactions of *o*-diiodoarenes with organometallic complexes.[31, 32] Concerning RD/A, the most closely related examples in the literature that could be found is the treatment of Zn(TPP(C_4F_8)) with $Na_2S_2O_4$ and $NaHCO_3$ in DMSO/CH_2Cl_2 to form Zn(TPP(C_4F_4)).[29]

In this work, regiospecificity, selectivity, and high yield were achieved for the products 2,3-TRPH(C_4F_8) and 2,3;5,6;11,12-TRPH(C_4F_8)$_3$, a noteworthy improvement over previous work on direct (poly)substitution of perfluoroalkyl (R_F) groups. In total, 15 TRPH derivatives are presented. For 10 of these compounds, single crystal X-ray strictures have been obtained.[25, 33] This family of molecules is illustrated in full in Figure 1-2.

Aside from developing a new synthetic route for TRPH derivatives, this family of molecules afforded a remarkable opportunity to study, with detail and precision, the effects of incremental structural alterations upon packing in the solid state. Theoretical studies have suggested that for TRPH derivatives, even small fluctuations in twist angle, lateral slide, out-of-plane distortion, or increased intermolecular distance between aromatic cores may have significant detrimental effects on charge transport.[34] These fluorinated triphenylenes do not contain long alkyl-(fluoroalkyl) chains in their structures and are not expected to possess liquid-crystalline properties. However, their analysis contributes, at the molecular level, to an understanding of the effects of substituents attached to the aromatic core on columnar self-organization in the solid state, which is important for the rational design of highly conducting materials based on TRPH.

Finally, this family of compounds facilitated study of the impact of the 3 novel types of annulated substituents upon frontier orbital energies. This investigation was conducted primarily through evaluation of gas phase electron affinity (EA). This family of molecules is not anticipated to have exceptional electron acceptor properties due to that fact that, compared to other PAHs, TRPH has an exceptionally large HOMO-LUMO gap and low EA.[20] Despite this, a fundamental

insight into the relationship between substituent structure and its impact of frontier energy levels is very useful for the advancement of organic electronic materials.

1.2. RESULTS AND DISCUSSION

1.2.1. Development of synthetic method and optimization

1.2.1.a. Synthesis, including targeted syntheses for TRPH(C_4F_8)$_n$'s in high yield

Reactions of TRPH and 1,4-$C_4F_8I_2$ were conducted at elevated temperature, resulting in synthesis of products bearing the substituents C_4F_8, C_4F_8H, C_4F_4, and C_4F_3H. Five optimized reactions (1.1-1.5) are reported here, the important features of which are noted in scheme 1-1. Additionally, two reactions (1.6 and 1.7) yielding large distributions of isolable products are

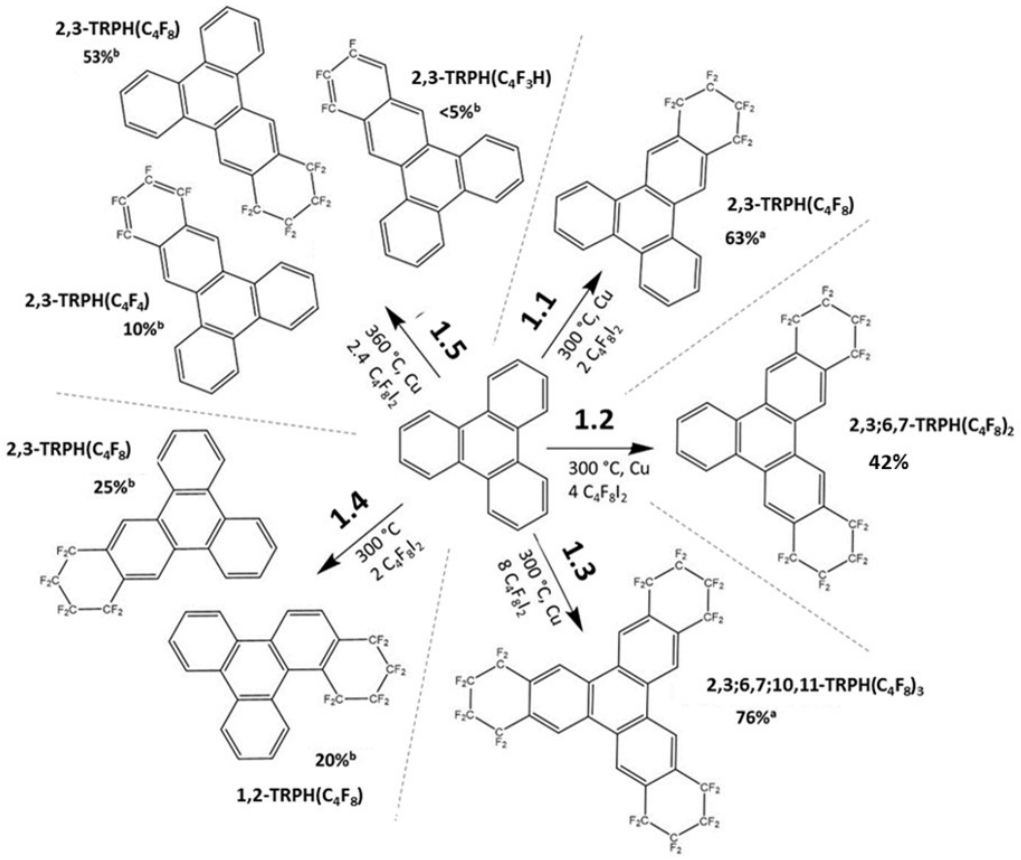

Scheme 1-1. Optimized reactions to produce major products discussed in this chapter. a= isolated mol % yield. b = mol % yield based on integration of ^{1}H NMR spectrum. For discussion of these reactions, see section 1.2.1. For details of reactions, see appx B.1.1-B.1.5.

reported, for the purpose of expanding the library of TRPH derivatives. For generalized experimental procedures, see appx A.1. For details of specific experiments, see appx B.1.1-B.1.7.

Reactions 1.1, 1.2, and 1.3 were conducted to target specific compounds 2,3-C_4F_8, 2,3;6,7-$(C_4F_8)_2$, and 2,3;6,7;10,11-$(C_4F_8)_3$ respectively. They demonstrate unprecedented regioselectivity, as the formation of products with peninsular C_4F_8 moieties is favored. Historically, it has been extremely difficult to target specific products when performing high temperature radical reactions with PAHs.[21] At best, partial thermodynamic control of product distribution achieved. For example, the most thermodynamically stable isomers (predicted by DFT calculations) are isolated in these reaction of CF_3I and CORA.[35] In contrast, "bottom-up" syntheses result in the least stable isomers of CORA$(CF_3)_{2,3,4}$.[35] However, for PAHs with lower molecular symmetry than C_{5v}-corannulene, the number of possible stable isomers of poly(trifluoromethyl) PAHs is far larger, marginalizing the benefit of partial thermodynamic control. For these PAHs, high temperature radical reactions result in a complex product mixture, which requires laborious HPLC separation in order to isolate individual pure PAH$(CF_3)_n$ derivatives.[21] As noted above, Kuvychko *et al.*' previously reported work on the trifluoromethylation, which, in spite of the D_{3h} symmetry of the core, showed low selectivity. Multiple isomers with compositions TRPH$(CF_3)_n$, n=5-7, were formed in the 360 ºC reaction with excess CF_3I, and only one pure compound, an isomer of TRPH$(CF_3)_6$, was isolated.[21]

Through optimization of reaction conditions, this work achieves much higher selectivity. Three primary strategies were identified for control of product distribution. (i) Stoichiometric ratio of TRPH substrate to 1,4-$C_4F_8I_2$ has a dramatic effect upon product distribution. For every C_4F_8 group appended to the TRPH core, two equivalents 1,4-$C_4F_8I_2$ are required, (discussed below in section *1.2.1.c.*) For example, use of two equivalents favors formation of TRPH(C_4F_8)'s, and four equivalents favors TRPH$(C_4F_8)_2$'s. In order to favor the maximum possible number of annulated substations, which is 3, using an even higher ratio of 1:8 yields ideal results. (ii.) Use of Cu-powder, which was intended to promote radical formation through formation of CuI, also precludes formation of bay-substituted products (*i.*e. 1,2-TRPH(C_4F_8), limiting product distribution to

Table 1-1. Optimized reactions of triphenylene and 1,4-$C_4F_8I_2$ at 300 °C.[a]

reaction	equiv. 1,4-$C_4F_8I_2$	crude product recovered, mg [wt % yield based on TRPH]	targeted product	% yield of targeted product
1.1	2	34 [136]	**2,3-TRPH(C_4F_8)**	63
1.2	4	52 [208]	**2,3;6,7-TRPH(C_4F_8)$_2$**	42
1.3	8	55 [220]	**2,3;6,7;10,11-TRPH(C_4F_8)$_3$**	76

a - Experimental conditions: 25 mg TRPH, at 300 °C, 750 mg Cu, ca. 50 mL glass ampoules (or Monel reactors) under vacuum for 2 h. For further details, see appx. A.1.1-A.1.3.

compounds bearing peninsular C_4F_8 groups. For further discussion of this phenomenon, see section *1.2.1.c*. (iii) The moieties C_4F_4 and C_4F_3H, RD/A products, are only observed at higher temperatures, (360 ºC), so limiting reaction temperature to 300 °C limits the total number of possible products.

Table 1-1 lists selected optimized reaction conditions reactions 1.1, 1.2, and 1.3, for the synthesis of the three compounds: **2,3-C_4F_8**, **2,3;6,7-(C_4F_8)$_2$**, and **2,3;6,7;10,11-(C_4F_8)$_3$**. Figure 1-3 shows corresponding ^{19}F NMR spectra. For detailed discussion of NMR chemical shifts of these compounds, see section *1.2.2.b*, below.

The highest selectivity and isolated yield were achieved in reaction 1.3 (appx B.1.3). The recovered product mixture gave **2,3;6,7;10,11-(C_4F_8)$_3$** with 76% isolated yield, the highest value among analogous high-temperature perfluoroalkylations of PAHs reported to date. In the NMR spectra of the product of reaction 1.3, the only significant peaks are due to **2,3;6,7;10,11-(C_4F_8)$_3$**, consistent with the high selectivity of this reaction. Relatively low solubility of **2,3;6,7;10,11-(C_4F_8)$_3$**, likely due to its low polarity (attributed to its high symmetry), made its extraction with dichloromethane more difficult than the other analogs and resulted in some losses of the material. If this problem is overcome, either by finding a better solvent for extraction or an alternative isolation method, the NMR spectra suggests that the isolated yield may improve still further.

Reaction 1.1 (appx B.1.1), utilizing 2 equivalents of 1,4-$C_4F_8I_2$, produced 2,3-C_4F_8 with a 63% isolated yield. In contrast to the spectra for reaction 1.3, several compounds can be clearly identified in the NMR spectra of the product: unreacted TRPH evidenced by multiplets at δ=7.65 and δ=8.6 in the 1H NMR spectrum, and products bearing C_4F_8H moieties. which give four characteristic multiplets in the ^{19}F NMR spectrum. Formation of the latter product may be due to insufficient excess of 1,4-$C_4F_8I_2$, increasing stoichiometry on product distribution. Attempts to increase conversion of starting material and suppress formation of products bearing C_4F_8H moieties through variation of reaction duration and temperature were unsuccessful.

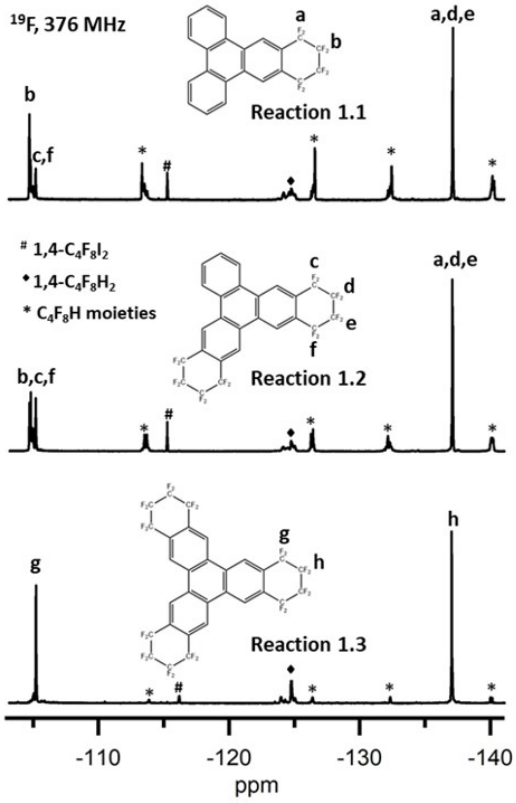

Figure 1-3. ^{19}F NMR spectra of products of optimized reactions 1.1, 1.2, and 1.3. For reaction 1.1, the major product is 2,3-TRPH(C_4F_8), although smaller amounts of 2,3;6,7-TRPH(C_4F_8)$_2$ and products bearing C_4F_8H moieties are also formed. For reaction 2.2, 22,3;6,7-TRPH(C_4F_8)$_2$ forms, but significant amount of 2,3-TRPH(C_4F_8) is are also observed, as well as products bearing C_4F_8H moieties. Reaction 1.3 is the cleanest reaction of the three, producing 2,3;6,7;10,11-TRPH(C_4F_8)$_3$ with only trace amounts of other products. Peaks corresponding to residual 1,4-$C_4F_8I_2$ and 1,4-$C_4F_8H_2$, a byproduct of the reaction, are observed in all spectra. Solvent is $CDCl_3$. Spectra are referenced to hexafluorobenzene (δ -164.9, not shown).

Reaction 1.2 (appx B.1.2), which was designed to produce maximal yield of 2,3;6,7-$(C_4F_8)_2$, showed the lowest selectivity of the three reactions targeting specific C_4F_8-functionalized products. Inevitably, there was appreciable presence of 2,3-(C_4F_8). Although the isolated yield for 2,3;6,7-$(C_4F_8)_2$ is the lowest of the three compounds reported here, it is still higher than in the most reported reactions with PAHs under analogous conditions. It is also worth noting that a similar reaction, reaction 1.9 performed in a Monel reactor and discussed below, produced a 60% yield of 2,3-6,7-TRPH$(C_4F_8)_2$ by integration of NMR spectra.

In contrast to the three reactions discussed above, reaction 1.4 (appx B.1.4) was performed in order to target products substituted at bay positions. Therefore, Cu powder was not used. Both 1,2-TRPH(C_4F_8) and 2,3-TRPH(C_4F_8) were formed in 20% and 25% yield respectively (by ^{1}H NMR integration). This indicates a slight bias for peninsular substitution even without Cu powder. Statistically, if substitution was equally likely at both types of position, a 3:1 ration of 1,2-TRPH(C_4F_8):2,3-TRPH(C_4F_8) would be expected. Initial substitution would occur on bay and peninsular C atoms an equal amount of the time, but bay substitutions would always result in the formation of 1,2-TRPH(C_4F_8) upon annulation, whereas peninsular would produce both products in equal amount.

Reaction 1.5 (appx B.1.5) was conducted in order to target RD/A products. Conditions favoring products bearing only one moiety were selected, to limit the number of products formed. Despite extensive optimization attempts, higher yields have not been achieved for RD/A products. These attempts included (i) modification of Cu powder type, method of Cu powder mixing, and increase of Cu-powered (ii) variation of reaction time and temperature, and (iii) reductive defluorination via a variety of other methods, including use of sodium napthalenide, Birch reduction, or sodium metal (appx D.1.1). Marginal success was achieved in a two-step RD/A procedure, involving RD/A of purified 2,3-TRPH(C_4F_8), which produced a 25% yield of 2,3-TRPH(C_4F_4), illustrated in Figure 1-4. Optimization difficulties notwithstanding, the RD/A process remains an intriguing chemical process, discussed at length in section *1.2.1.c*, below. Additionally, in this reaction, the product 2,3-TRPH(C_4F_3H) was formed.

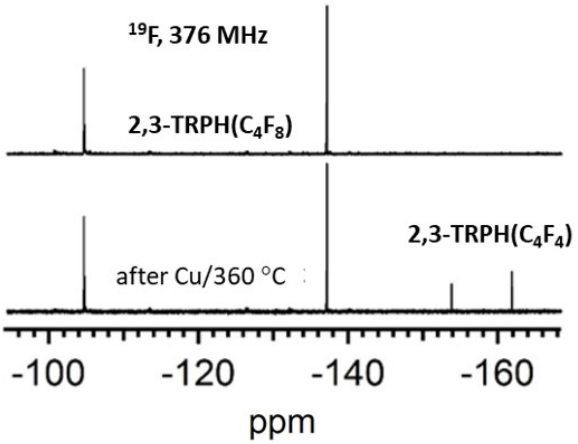

Figure 1-4. ^{19}F NMR spectra of pure 2,3-TRPH(C_4F_8) before (top) and after being heated to 360 ºC in the presence of Cu powder. The formation of the RD/A product 2,3-TRPH(C_4F_4) is observed in 25% yield. Solvent is $CDCl_3$. Spectra are referenced to hexafluorobenzene (δ -164.9, not shown).

Aside from the six products shown in scheme 1-1 and formed as major products of optimized reactions 1.1-1.5, nine additional TRPH derivatives are reported in this chapter. These products were isolated from reaction 1.6 (appx B.1.6.), conducted to obtain products with multiple aliphatic substituents, and reaction 1.7 (appx B.1.7), conducted to obtain RD/A products with multiple substituents. The conditions utilized for these reactions did not favor high selectivity. Rather, they were designed to produce a wide range of new compounds for study.

1.2.1.b. Development of synthetic strategies

Four reactions, 1.8-1.11 (appx D.1.2), were conducted to investigate the possibility of utilizing a novel reaction vessel. As noted above, reaction 1.9 was performed in a Monel reactor under an inert atmosphere of N_2(g). With respect to selectivity and yield, this reaction is comparable to, and, in fact, slightly more efficient than reaction 1.2, performed under similar conditions in a glass ampoule. Comparability between reactions in Monel reactors and in glass ampoules holds true under a variety of conditions. Reactions 1.8-1.11 were similar to reactions 1.1-1.4 except conducted in different vessel types, to show that similar product yields and distributions are possible in flame sealed glass ampoules and Monel vessels. For example,

synthesis of 2,3-TRPH(C_4F_8) in reactions 1.8 and 1.1 yielded 60% and 63% of isolated product in Monel and in a glass ampoule, respectively.

This is the first time this vessel has been utilized for perfluoroalkylation of PAHs. As an alternative reactor type to glass ampoules, it is useful for several reasons. First, flame-sealed glass ampoules present a potential safety concern, especially in the academic lab environment. These ampoules can explode at high temperatures due to the internal pressure build-up if the seal has imperfections. Therefore, preparation and handling of such glassware requires supervision, training and experience. Monel reactors, on the other hand, are robust, safe and are rated to withstand significantly higher pressures than glass vessels. Second, while it is much more challenging to produce large glass ampoules than small glass ampoules, reaction scale-up is straightforward for the Monel vessels, simply requiring selection of a larger vessel. Third, glass ampoules are not reusable, so inevitable variations in glass ampoule volumes may be detrimental to reproducibility of results, whereas Monel reactor is constant from synthesis to synthesis.

One caveat concerning the use of Monel reactors is that only reactions promoted by Cu are possible in them. The Monel alloy itself contains Cu. Even without addition of Cu powder, reactions in Monel reactors would not be truly Cu free, and furthermore, failing to add Cu powder as an I_2 scavenger would result in corrosion of the Monel alloy by I_2 at reaction temperatures.

Aside from the investigation of effects of stoichiometric ratios and reaction vessel type, a number of other parameters were explored in the course of this work. Targeting of specific product distributions was accomplished via variation of reaction parameters reaction duration and the use of Cu powder. Additionally, the effects of temperature were explored extensively. The reported reactions represent the culmination of research efforts exploring the effects of these parameters. Notes on the observed effects of each of these parameters are elaborated upon below.

Reaction temperatures between 280 °C and 420 °C were investigated in increments of 15 °C. Reactions below 300 °C give low conversion. Reductive defluorination products (products bearing C_4F_4 and C_4F_3H moieties) are first observed at 345 °C in low yield (<5% total product based on ^{1}H NMR integration). Maximum yield of reductive defluorination products is observed

at 360 °C. At higher temperatures, both total product recovery and yield of reductive defluorination products decreases. At 420 °C, approximately half as much crude product was recovered as was at 360 °C, and no reductive defluorination products was observed.

With Cu powder (both in Monel reactor and in glass ampoules), 2 h was a sufficient length of time for all starting materials to react. Reactions shorter than 2 h contained unreacted $C_4F_8I_2$ and TRPH. Without Cu (in glass ampoules), 3 h were required for all staring materials to react. However, increasing reaction duration beyond these lengths, up to 48 h, was not found to have a significant impact upon yield or product distribution. Notably, for reactions at higher temperatures, decreasing reaction duration did not mitigate product decomposition. For example, significant product decomposition was observed for a 1 h long reaction at 420 °C.

As discussed above when Cu metal was not used in glass-ampoule reactions, abundant formation of bay-substituted products was observed (*i.e.* in the case of reaction 1.4). For reactions with Cu, a large excess of Cu was always utilized. Variation of the scale of this excess, between 0.5 and 20 g, did not impact product yield or distribution. Different methods of mixing of the Cu powder and TRPH starting material, (including stirring Cu powder and TRPH together prior to reaction, mixing Cu powder with a solution of TRPH in dichloromethane and drying, and mixing TRPH and Cu powder in a small open-ended glass insert within the reaction vessel to ensure contact between TRPH and Cu) did not impact product yield or distribution. Various types of Cu, including Cu filings and Cu mesh, produced results similar to Cu powder. Agitation of reaction vessel during reaction (ca. every 15 min) to expose fresh Cu surface did not impact product yield or distribution. Use of CuI in place of Cu produced results similar to a reaction with no Cu powder.

1.2.1.c. Discussion of plausible reaction pathways

Reaction of TRPH and 1,4-$C_4F_8I_2$ was likely initiated by the homolytic cleavage of C-I bonds to form R_F• radicals. Previous work has shown that formation of radicals occurs rapidly at temperatures of 300 °C and higher.[36-39] Byproducts of this reaction included CuI or I_2, which were formed when the reaction was performed with and without a Cu metal promoter, respectively.

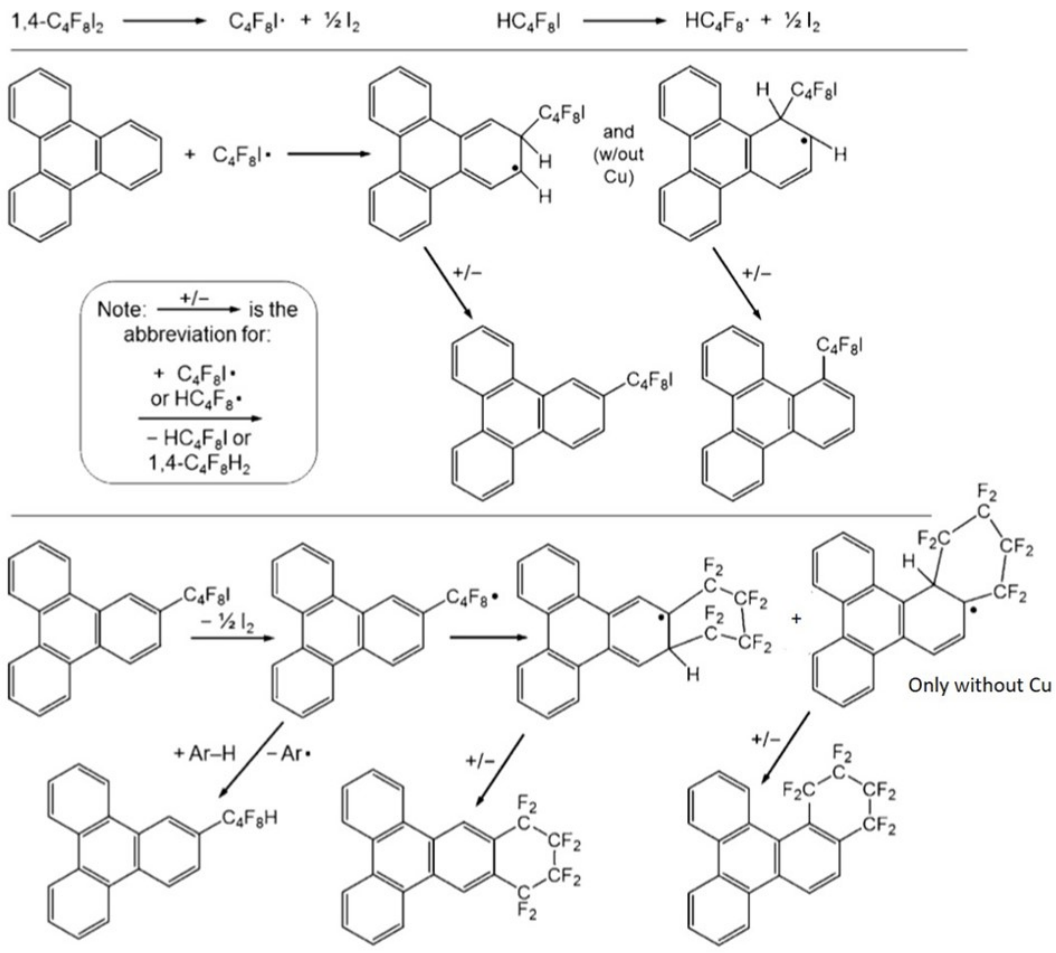

Scheme 1-2. Plausible sequence of steps for reaction of TRPH and 1,4-$C_4F_8I_2$ at 300 ºC.

Without Cu powder, I_2 was observed as a purple gas forming during the reaction, which condensed to dark purple I_2 crystals upon cooling. These crystals dissolved in the dichloromethane used to recover products but were easily removed from the resultant purple solution by washing with saturated sodium thiosulfate, leaving a light-yellow solution of crude TRPH-derivative product mixture. For reactions in which Cu metal was utilized, CuI rather than I_2 was formed. This yellow solid did not dissolve in dichloromethane and was removed via filtration.

Scheme 1-2 shows a likely sequence of steps for the formation of fluoroalkyl species. The R_F• radicals likely played a dual role in this reaction. In some cases, they reacted with TRPH, forming substituents, while in other cases, they acted as acceptors for the H atoms displaced from TRPH upon substitution. In support of this, 1,4-$C_4F_8H_2$ has been identified by NMR as a byproduct

of this reaction. This is analogous to previously reported trifluoromethylation of PAHs, in which CF_3H and I_2 are identified as byproducts. [21] A notable distinction from work with CF_3I is the fact that, in the case of the diiodo compounds used here, it is possible for a single fluoroalkyl moiety to act as both substituent and H atom acceptor. For this reason, stoichiometry is less straightforward here than is the case for trifluromethylation reactions. Rather than ½ of them acting as substituents and the other ½ as acceptors, some fraction of them form C_4F_8H moieties, which have been identified in product mixture as minor side products.

When Cu metal was not used in glass-ampoule reactions, abundant formation of bay-substituted products was observed (reaction 1.4). As far as the observed Cu-promoted regiospecificity is concerned, note that both 1,2-C_4F_8 and 2,3-C_4F_8 can be formed from the common intermediate 2-TRPH(C_4F_8I), whereas the intermediate 1-TRPH(C_4F_8I) can only produce 1,2-C_4F_8. The DFT calculated relative energies for 2,3-C_4F_8 and 1,2-C_4F_8 are 0.0 and 53.3 $kJmol^{-1}$, respectively. Because it is unlikely that Cu isomerizes 1,2-C_4F_8 to 2,3-C_4F_8,the regiospecificity is likely kinetic in origin, and may be related to the high-energy twist of the TRPH core necessary for the formation of 1,2-C_4F ,which is due in part to F···C(sp^2) repulsion. In contrast, the aromatic C(sp2)core of 2,3-C_4F_8 is remarkably planar. Furthermore, the difference in DFT energies for intermediates 2- TRPH-(C_4F_8I) (0.0 $kJmol^{-1}$) and 1-TRPH-(C_4F_8I) (65.4 $kJmol^{-1}$) is even larger. Because PAHs like TRPH are known to be strongly physisorbed to metal surfaces, including Cu,[40, 41] it is possible that TRPH is bound to Cu as it reacts with $IC_4F_8\bullet$ radicals in these reactions. The facile formation of planar-core, Cu-bound 2-C_4F_8 relative to severely-nonplanar-core, Cu-bound 1-C_4F_8I, may preclude the formation of any bay substituted products.

In the reactions performed at 360 °C in the presence of Cu powder, reductive defluorination occurred, leading to the formation of products bearing C_4F_4 moieties (reactions 1.5, 1.7). Interestingly, the compound 2,3-C_4F_3H was also isolated, in which one F atom is substituted for H atom compared to 2,3-C_4F_4. Formation of this compound is indicative of the possibility of complete defluorination of TRPH$(C_4F_8)_x$ molecules, potentially facilitating access to rare partially-

and non-fluorinated PAH structures that are not accessible by other means, if optimal conditions are discovered.

Cu-promoted RD/A of C_4F_8 groups to C_4F_4 groups most likely occurred when the compounds were physisorbed to the Cu surface. This is supported by a direct-conversion control experiment and two literature precedents for C-F activation unambiguously attributable to Cu.[42] In the control experiment, an HPLC-purified sample of 2,3-C_4F_8 was cleanly converted to 2,3-C_4F_4 by exposure to Cu at 360 °C under vacuum for 1 h. See Figure 1-4. The conversion was 25 mol % under these conditions. Similar reductive defluorination reactions with purified 2,3;6,7-$(C_4F_8)_2$ and 2,3;6,7;10,11-$(C_4F_8)_3$ were less productive. Only 5% conversion was achieved.

In literature precedents, defluorination occurred while the species were surface bound. Specifically, perfluoropentacene was absorbed to, and defluorinated by, Cu(111),[43] and surface-bound Cu(111)-CF_3 species (formed by dissociative chemisorption of CF_3I) were shown to readily form surface-bound Cu(111)-CF_2 species.[26] Note that these examples are distinct from the work reported here in that no molecular species were desorbed, let alone isolated, in either case. In both cases carbon films were ultimately formed.

1.2.1.d. Related synthesis with CF_3I and 1,2-$C_2F_4I_2$

Following the significant improvements in the selectivity and regiospecificity of the Cu-promoted perfluoroannulation of TRPH achieved in this work, the possibility of similar positive effects on TRPH trifluoromethylation was investigated. (appx D.1.3, reactions 1R-4R) An initial study of high-temperature trifluoromethylation of TRPH in a glass ampoule in the absence of Cu metal showed low selectivity, and only one compound was isolated in pure form, TRPH$(CF_3)_6$.[21] Its X-ray structure revealed that CF_3 substitutions occurred in both bay and peninsula positions. Here, a new reaction was carried out at 300 °C with Cu powder. However, analysis of the product mixture showed no improvement in the selectivity due to the presence of Cu metal: at least 5 isomers of TRPH$(CF_3)_5$ were identified, and a new isomer of TRPH$(CF_3)_6$ with C_{3h} symmetry was isolated and spectroscopically characterized. In the new molecule, 1,3,5,7,9,11-TRPH$(CF_3)_6$-2,

three CF_3 groups are located in the bay positions and three – in the peninsula positions. Variation of the reaction stoichiometry from 3 to 24 equivalents of CF_3I did not result in the improved selectivity either.

A reaction between TRPH and 18 equivalents of C_2F_5I at 300 °C in the glass ampoule was performed by a lab mate Dr. Kuvychko to determine if increased bulkiness of the R_F moiety would lead to fewer products, each bearing fewer substituents than trifluromethylation reactions. Indeed, a mass spectrometry analysis showed that only species with 4 and 5 C_2F_5 groups formed. The intensity of the latter species is likely over-represented due to a higher ionization efficiency in the negative mode. A major product was isolated, a non-symmetric TRPH$(C_2F_5)_4$, with ca. 30% yield, its structure cannot be definitively elucidated from the NMR data at this time. Because of the steric hindrance, substitutions in ortho-positions are not likely to occur, and therefore improved selectivity is observed in this case. This result shows that this or similar methodologies can be applied to access other highly substituted TRPH$(R_F)_n$, with n = 1-5, using HPLC separation as described in this work for purification. Derivatives with longer-chain R_F groups prepared by this approach may possess interesting liquid-crystal properties.

Perfluoroannulation upon bay positions of TRPH with 1,2-$C_2F_4I_2$ was also attempted (appx D.1.3, reaction 5R) However, the primary products, identified by NMR spectroscopy, appeared to bear C_2F_4H substituents, and no evidence for annulation was observed.

1.2.2. Isolation and structural characterization of pure compounds

1.2.2.a. Development of HPLC separation method

High performance liquid chromatography (HPLC) was utilized to isolate pure molecules. This technique has previously proved extremely useful for purification of otherwise inseparable very similar molecules.[21] The unique ability to separate these similar isomers is attributable to the specialized stationary phase utilized in the work reported here. This stationary phase is composed of silica gel beads with modified surfaces, functionalized with 3-(1-pyrenyl)propyl (appx figure A-3). For separation, a mixture of crude product mixture dissolved in a selected eluent was injected

into the system. For PAH-based analytes, affinity for the stationary phase is likely affected by several factors such as π system shape, degree of planarity, polarity, and the steric bulk of substituents. Separation was achieved with eluents including acetonitrile, toluene, methanol, isopropyl alcohol, and combinations thereof (appx B.1). The HPLC is equipped with a UV-vis detector. The TRPH derivatives discussed here have absorption maxima below 300 nm (appx D.1.4, figure D-14). However, as molar absorption coefficients are not identical, HPLC cannot be utilized for quantitative assessment of product distribution.

1.2.2.b. Structural elucidation via ^{19}F and ^{1}H NMR spectra

The ^{1}H and ^{19}F NMR of the four different types of substituents discussed in this chapter exhibit consistent features and trends which can be reliably utilized to assign molecular structures. Confidence in this method of structural assignment is bolstered by the good agreement between NMR spectroscopy-predicted structures and single crystal X-ray structures.

^{1}H NMR resonances for this family of TRPH derivatives appear in the region between 5.5 and 9.3 ppm. Generally, peaks corresponding to H atoms on bay positions appear further downfield than peaks arising from H atoms on peninsular positions. Furthermore, proximity to the electron-withdrawing fluorous substituents results in peaks that are shifted downfield. The H atoms bound to functionalized TRPH core rings give rise to doublet and singlets, whereas the H atoms bound to unsubstituted TRPH core rings appear as complex multiplets, likely due to long range coupling facilitated by the π system.

As a rule, The F atoms of fluoroalkyl moieties give rise to ^{19}F NMR peaks between −95 and −140 ppm. As distance from the TRPH core increases, F atoms give rise to more negative resonances within this region. For F atoms bound to aromatic rings, resonances appear between −135 and −165 ppm. For ^{19}F peaks, broadening and unresolved coupling are frequently observed, suggesting interactions between neighboring F atoms, but coupling constants could not be obtained. This is attributed to both complex coupling patterns and insufficient spectral resolution.

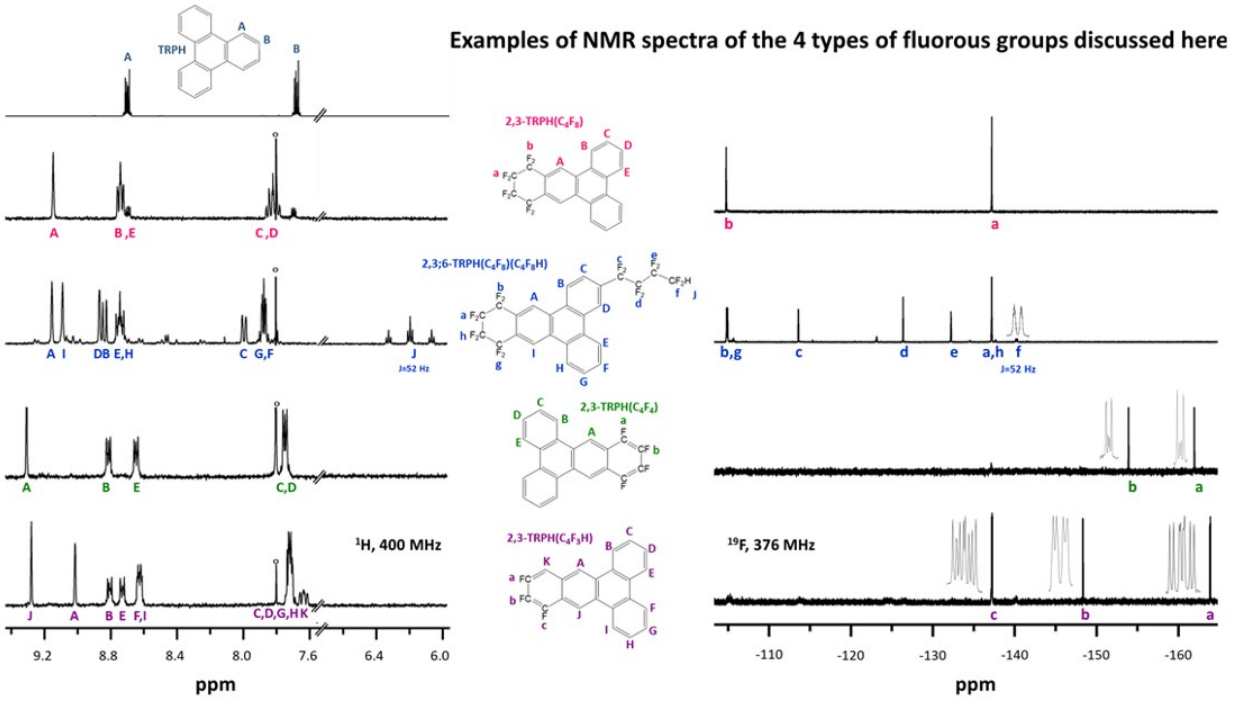

Figure 1-5. ^{1}H and ^{19}F NMR spectra of TRPH derivatives bearing each of the four different substituent types discussed in this work, as well as the ^{1}H NMR spectrum of TRPH. Solvent is $CDCl_3$. Spectra are referenced to bistrifluromethylbenzene (^{1}H, δ -66.4 (◦), ^{19}F, δ -66.4, not shown). Residual unreacted TRPH (*)observed in the ^{1}H NMR spectra of 2,3-TRPH(C_4F_8).

The ^{1}H resonances for TRPH derivatives bearing C_4F_8 moieties appear in the region between 7.60 and 9.15 ppm (Figure 1-5, 2,3-TRPH(C_4F_8), right, second spectrum from top). For comparison, the ^{1}H NMR spectrum of unsubstituted TRPH is composed of two complex multiplets with equal integration intensities (Figure 1-5, right, top). The first peak of the C_4F_8-functionalized derivative appears at 7.66-7.70 ppm and arises from the H atoms on the bay positions of TRPH. The second, at 8.66-8.70 ppm, arises from H atoms on the peninsular positions. The H atoms bonded to unsubstituted benzenoid rings of C_4F_8-bearing TRPH's resemble the peaks of unsubstituted TRPH in that they are complex multiplets, and in that peaks attributed to peninsular H atoms appear further downfield than peaks attributed to H atoms. For example, see peaks B-E n the spectrum of 2,3-TRPH(C_4F_8) in Figure 1-5. In contrast, upon TRPH rings bearing C_4F_8 substituents, the remaining H atoms are shifted further downfield due to their proximity to the electron withdrawing moiety. For peninsular substitutions, broad singlets are from approximately

8.8-9.15 ppm. As an example, see peak A in the spectrum of 2,3-TRPH(C_4F_8) in Figure 1-5. When bay substituted C_4F_8 groups are present, doublets are observed. As may be expected, the bay H atom gives rise to a doublet that is further downfield than the doublet arising from the peninsular H atom. Doublets arising from both bay and peninsular H atoms are shifted further downfield than peaks corresponding to counterpart H atoms upon unsubstituted TRPH rings, again due to proximity to an electron withdrawing moiety.

For C_4F_8 moieties, ^{19}F resonances can be expected in two distinct regions: −100 to −105 ppm and −135 to −140 ppm (see Figure 1-5, 2,3-TRPH(C_4F_8), left, top). For the four F atoms bonded to the C atoms closest to the aromatic TRPH core (C atoms 1 and 4), ^{19}F NMR peaks are observed between −95 and −110 ppm. For the four F atoms bonded to the C atoms further from the aromatic TRPH core (C atoms 2 and 3), ^{19}F NMR peaks appear in the region from −125 to −135 ppm. For example, see peaks a and b in the spectrum of 2,3-TRPH(C_4F_8) in Figure 1-5. Due to the high symmetry of 2,3-TRPH(C_4F_8), only one peak appears in each of these two regions, of equal integration intensity. However, asymmetry arising from substitution at different positions and/or from the presence of multiple substituents can lead to multiple peaks appearing in each region. As an example of the former case, the ^{19}F NMR spectrum of 1,2-TRPH(C_4F_8) displays two peaks in each region, for a total of four peaks of equal integration intensities (appx figure C-3). As an example of the latter case, the ^{19}F NMR spectrum of 1,2;6,7-TRPH(C_4F_8)$_2$ exhibits two peaks in the region from −95 to −110 ppm, each integrating to ½ the area of the single peak appearing at −137.1 ppm (appx figure C-7). The greater sensitivity of the chemical shifts of F atoms bonded directly to the TRPH core to the presence of other substituents on the TRPH core is a consistent trend and is perhaps due to the fact that these F atoms are closer to the TRPH core and to other substituents.

The most recognizable feature of ^1H NMR spectra arising from C_4F_8H substitution is a triplet of multiplets appearing around 6.2 ppm. (Figure 1-5, 2,3;6-TRPH(C_4F_8)(C_4F_8H), right, third spectrum from top). This multiplet arises from the terminal H atom on the fluoroalkyl butane moiety, and therefore integrates to an area corresponding to 1 H atom. It has a characteristic 52

Hz J-value, matching the J-value of a doublet of multiplets appearing in the corresponding ^{19}F spectrum, indicating F-H coupling. As an example, see the peak labeled J in Figure 1-5 in the spectrum of 2,3;6-TRPH(C_4F_8)(C_4F_8H). Other features of these NMR spectra include a singlet and a pair of doublets arising from the H atoms bonded to the substituted TRPH ring, integrating 1:1:1 and all shifted downfield as compared to peaks arising from H atoms on unsubstituted TRPH rings. For example, see the peaks labeled B, C, and Din Figure 1-5 in the spectrum of 2,3;6-TRPH(C_4F_8)(C_4F_8H).

In ^{19}F NMR spectra, C_4F_8H moieties give rise to 4 peaks integrating 1:1:1:1. (Figure 1-5, TRPH(C_4F_8)(C_4F_8H), left, second spectrum from top). Three of these peaks are complex multiplets between −100 and −135 ppm, as exemplified by peaks a, b, and c in Figure 1-5 in the spectrum of 2,3;6-TRPH(C_4F_8)(C_4F_8H). These peaks correspond to F atoms bonded to C atoms 1-3 on the C_4F_8H moiety. The more negative the resonance, the further from the TRPH core the F atoms is, so peak a corresponds to F atoms on the C atom bound directly to the TRPH core. The fourth peak appears around −140 ppm and corresponds to the F atoms bound to C atom 4, the outermost C atom of the C_4F_8H moiety. This C atom also bears an H atom. This peak is a doublet of multiplets, with the characteristic 52 Hz coupling constant seen in peak J in the ^1H NMR spectrum of 2,3;6-TRPH(C_4F_8)(C_4F_8H), indicating F-H coupling.

Effects of C_4F_4 moieties upon ^1H NMR spectra are very similar to the effects of C_4F_8 moieties, with two noteworthy exceptions. (Figure 1-5, 2,3-TRPH(C_4F_4), right, second spectrum from bottom). First, the ^1H peaks arising from H atoms near C_4F_4 moieties are shifted further downfield than those adjacent to C_4F_8 moieties. This is illustrated by comparison of peak A in the spectrum of 2,3-TRPH(C_4F_4) to peak A in the 2,3-TRPH(C_4F_8). Second, differences in chemical shifts of bay H atoms on unsubstituted TRPH rings are impacted more by proximity to TRPH rings functionalized with C_4F_4 moieties than TRPH rings functionalized with C_4F_8 moieties. For example, compare the multiplet labeled B, E in Figure 1-5in the spectrum of 2,3-TRPH(C_4F_8), to the multiplets labeled B and E in the spectrum of 2,3-TRPH(C_4F_4). In the latter case, H atoms have discernably different chemical shifts, whereas in the former case, one multiplet is observed. This

distinction can be attributed to increased sensitivity of H atoms to the electron-withdrawing fluorine atoms when positioned near a C_4F_4 moiety, due to sharing the same delocalized π electrons.

In contrast to the ^1H NMR spectrum, ^{19}F NMR spectra of C_4F_4 moieties are very obviously distinct from the ^{19}F NMR spectra of C_4F_8 moieties. (Figure 1-5, 2,3-TRPH(C_4F_4), left, second spectrum from bottom). It is possible to distinguish these substituents at a glance because peaks arising from C_4F_4 appear in a much more negative region, from −140 to −165 ppm. See peaks a and b in the spectrum of 2,3-TRPH(C_4F_4). These peaks are multiplets. They are better resolved than peaks arising from C_4F_8 moieties, likely due to larger J-values due to coupling through the aromatic system. However, complexity of coupling still precludes elucidation of J-values.

The most immediately discernable hallmark of C_4F_3H substitutions is a triplet of multiplets in the ^1H NMR spectrum with the characteristic shape of peak K in in the spectrum of 2,3-TRPH(C_4F_3H). (Figure 1-5, 2,3-TRPH(C_4F_3H), left, bottom). It arises from the H atom of the C_4F_3H moiety. While the characteristic shape makes it immediately identifiable, its chemical shift varies greatly in the presence of other substituents, such that it can appear almost anywhere in the region associated with this family of molecules. The fact that it is directly bonded to the aromatic core, and therefore can interact with adjacent substituent through the delocalized π system may contribute to this. Additionally, it is possible that the chemical shifts of the H atoms on these substituents varies because the position of the H within the C_4F_3H moiety may vary . The structure in Figure 1-5, with the H atom bonded to a C atom close to the TRPH core, was confirmed by single crystal X-ray crystallography. However, with NMR spectroscopy alone, it would be impossible to determine if the H was bound to this C atom, or to one of the two C atoms further from the TRPH core. For other molecules bearing a C_4F_3H substituent, it is possible that the H atom is in the second type of position. Therefore, while C_4F_3H moieties may be immediately discernable upon analysis by NMR spectroscopy, structures cannot be fully assigned without further investigation.

In the ^{19}F NMR spectra of molecules bearing C_4F_3H moieties, three peaks with integrated areas of intensity 1:1:1 appear between −130 and −165 ppm. (Figure 1-5, 2,3-TRPH(C_4F_3H), right, bottom). These peaks are similar to peaks in the ^{19}F NMR spectrum of C_4F_4 moieties, in that they are complex multiplets suggesting relatively large but not measurable J values. Consistent with trends observed for other groups, F atoms bound to the C atoms further from the TRPH core appear at more negative resonances. However, the regions in which they appear are not sufficiently well defined as to provide a method for determining the position of the H atom. For the example shown, in combination with the X-ray structure, this trend is useful to identify peak c in the spectrum of 2,3-TRPH(C_4F_3H). However, which of the other two peaks arises from which of the two outermost F atoms remains ambiguous.

1.2.3. Effect of fluorous substituents upon solid-state packing

1.2.3.a. General comments on single crystal X-ray structures presented in this work

In the course of this work single-crystal X-ray structures were obtained for the ten compounds 1,2-TRPH(C_4F_8), 2,3-TRPH(C_4F_8), 2,3-TRPH(C_4F_4) 2,3-TRPH(C_4HF_3), 2,3:6-TRPH(C_4F_8)(C_4F_8H), 1,2:10,11-TRPH(C_4F_8)$_2$, 2,3:6,7-TRPH(C_4F_8)$_2$, 1,2:5,6:10-TRPH(C_4F_8)$_2$(C_4F_8H), 1,2:5,6:10,11-TRPH(C_4F_8)$_3$, and 2,3:6,7:10,11-TRPH(C_4F_8)$_3$. Data collection and refinement parameters for these seven structures are listed in appx D.1.5. Thermal ellipsoid drawings of a single molecule in each of the ten structures are shown in Figure 1-6. Discussion of particularly important aspects of these structures is given below, in sections *1.2.3.b* and *1.2.3.c*. For extended analysis beyond this, see appx D.1.6.

Collection of these crystal structure allowed analysis of the effects of fluorous substituents of TRPH induce upon solid-state packing motifs. Such analysis is useful to the field of crystal engineering, providing direction for the strategic incorporation of substituents into structures in order to influence packing, and thereby charge transport or other properties. Here, the effects of substituents are analyzed in terms of motifs such as the polarity of the TRPH core, intermolecular π-π overlap, and the evolution of columnar stacking, including intermolecular distances.

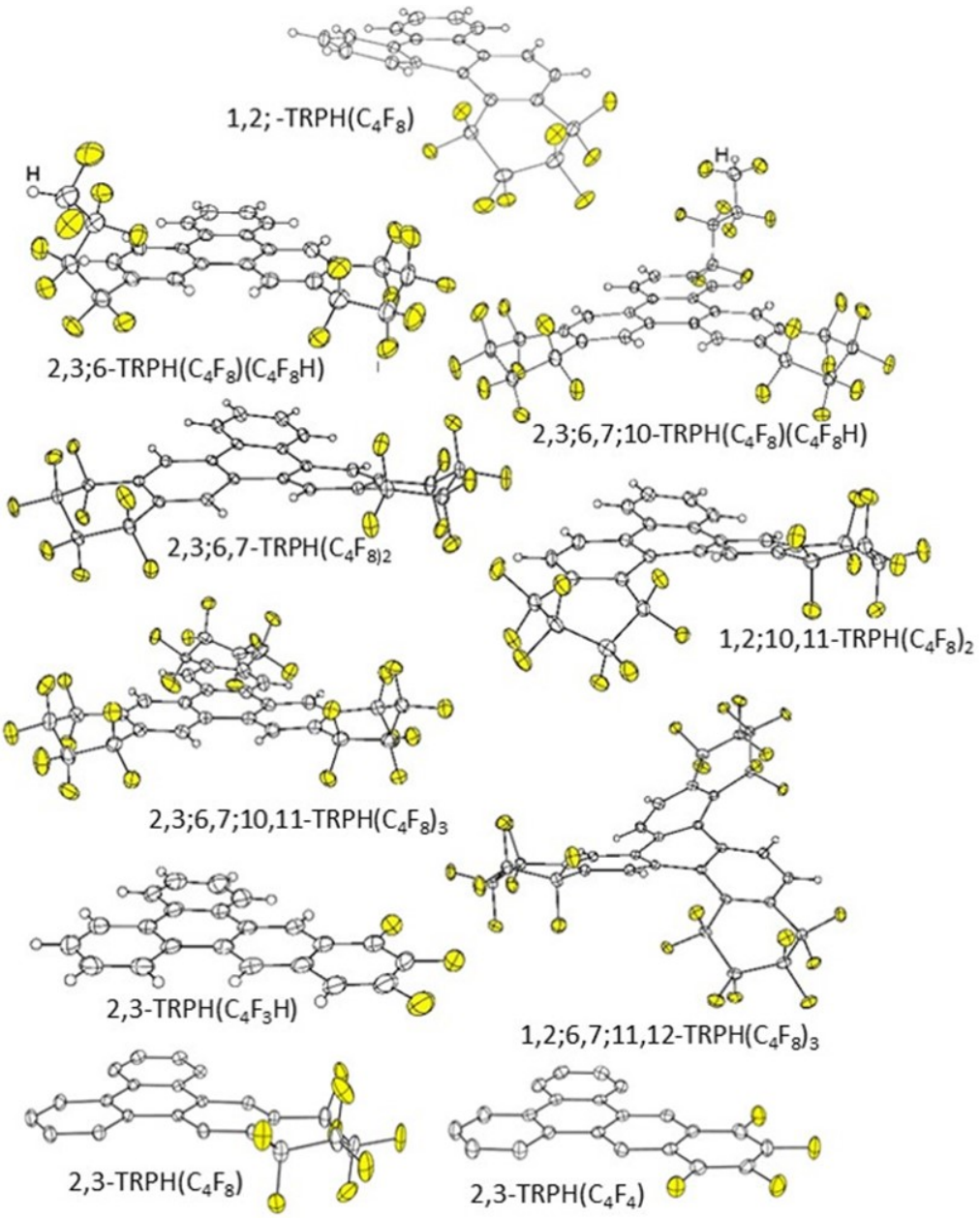

Figure 1-6. Thermal ellipsoid drawings of the ten compounds structurally characterized in this work (50% ellipsoids for nine of the seven structures; 35% ellipsoids for 2,3:6,7:10,11-TRPH(C_4F_8)$_3$; all H atoms shown as spheres of arbitrary size).Compounds with substituents on bay C atoms (i.e., C1, C4, C5, etc.) result in more significant distortions of the TRPH core from planarity than compounds only substituted on peninsular C atoms. Several of the structures exhibited disorder of the C and F atoms in the C_4F_8 moieties. Only the major part of the disordered portion(s) of those molecules are shown.

Pure samples of *ca.* 95% purity by NMR were obtained in 0.5-5 mg quantity by HPLC purification as described above. These samples were dissolved in an excess (0.5-1 mL) of dichloromethane, which was allowed to slowly evaporate through a pinhole over the course of several days. During evaporation, the compounds discussed here formed small, colorless, needle-like crystals. The shape of these crystals likely reflects the underlying columnar crystal structure. The diameter of single crystal needles was on the order of tens of microns. Therefore, the advanced photon source (APS) at Argonne national lab was utilized to collect single crystal X-ray data sets. Use of a synchrotron source was necessitated by the small size of the crystals (appx D.1.6, figure D-25) Data sets were collected by the author and colleagues under the supervision of Dr. Yu-Sheng Chen. See appendix A.2.3 and A.4.9. for details of data collection.

1.2.3.b. Planarity of TRPH core and relative stability

The degree of PAH planarity can greatly influence solid-state stacking and packing, π–π overlap, chromatographic retention times on various stationary phases, and the degree to which various PAH environmental contaminants can be extracted. The compounds with substituents on bay region C atoms display more significant distortions of the TRPH core from planarity than TRPH itself or the compounds without substituents on bay-region C(sp^2) atoms. This is also true for the compounds 2,3:6,7:10,11-TRPH$(OH)_6$,[44] 1-TRPH(CH_3),[45] 1,3,6,7,10,11-TRPH$(CF_3)_6$,[21] 1,4,5,8,9,12-TRPH$(CH_3)_6$,[46] TRPH$(F)_{12}$,[46] and TRPH$(Cl)_{12}$.[47]

Distortion from planarity parameters for the fluorous TRPH derivatives discussed here are listed in Table 1-2, including (i) the average displacement and (ii) the sum of the maximum displacements of the TRPH core C(sp_2) atoms from their least-squares plane (OOP_{av} and ΣOOP_{max}, respectively) and (iii) the "thickness" of the TRPH core,[48, 49] which can be defined as the sum of the maximum out-of-plane displacements (OOPs) plus twice the van der Waals radius of a C atom, 3.60 Å.[50] The eight compounds with no substituents on bay C(sp^2) atoms, with up to six substituents on the other TRPH C(sp^2) atoms, have OOPav and OOPmax values with ranges of 0.02–0.08 Å and 0.07–0.29 Å, respectively. The four compounds with one substituent on a bay

Table 1-2. Distortion from planarity parameters for TRPH(X)$_n$ compounds[a]

compd	# bay C(sp^2)–X substitutions[b]	av. OOP displacement, Å[c]	Σ max. OOP displacements, Å[c]	thickness of core, Å[d]
TRPH[e]	0	0.03	0.12	3.72
2,3-TRPH(C_4F_4)[f]	0	0.02	0.07	3.67
2,3-TRPH(C_4F_3H)	0	0.04	0.15	3.75
2,3-TRPH(C_4F_8)[f]	0	0.03	0.15	3.75
1,2:6-TRPH(C_4F_8)(C_4F_8H)	0	0.03	0.11	3.71
2,3:6,7-TRPH(C_4F_8)$_2$	0	0.08[g]	0.29[g]	3.89[g]
2,3:6,7:10,11-TRPH(C_4F_8)$_3$	0	0.07	0.28	3.88
1,2:6,7:10-TRPH(C_4F_8)$_2$(C_4F_8H)	0	0.06	0.27	3.87
2,3:6,7:10,11-TRPH(OH)$_6$[h]	0	0.05[h]	0.25[h]	3.85[h]
1-TRPH(CH_3)[i]	1	0.16	0.58	4.18
1,2-TRPH(C_4F_8)[f]	1	0.17[j]	0.73[j]	4.33[j]
1,2:10,11-TRPH(C_4F_8)$_2$	1	0.14	0.56	4.16
1,3,6,7,10,11-TRPH(CF_3)$_6$[k]	1	0.18	0.85	4.45
1,2:5,6:10,11-TRPH(C_4F_8)$_3$	2	0.31	1.37	4.97
1,4,5,8,9,12-TRPH(CH_3)$_6$[l]	6	0.40	2.06	5.66
TRPH(F)$_{12}$[m]	6	0.33	1.58	5.18
TRPH(Cl)$_{12}$[n]	6	0.42	2.08	5.68

[a] All results from this work unless otherwise indicated. [b] The bay C(sp^2) atoms of TRPH are C1, C4, C5, C8, C9, and C12. [c] OOP = out-of-plane. [d] The thickness is given by the sum of maximum OOP displacements plus 3.60 Å, which is two times the van der Waals radius of a C(sp^2) atom (see Ref. 50). [e] Ref.52. [f] Ref.25. [g] These are the lowest values for the four independent molecules. The average values for all four molecules are 0.14, 0.37, and 3.97. [h] Ref.44; average values for two similar structures. [i] Ref.45. [j] Average values for the two independent molecules. [k] Ref.21. [l] Ref.70. [m] Ref.46. [n] Ref.47.

C(sp2) atom, with up to five substituents on the other C(sp2) atoms, have OOP_{av} and OOP_{max} values with ranges of 0.14–0.18 Å and 0.56–0.85 Å, respectively. The compound with substituents on two bay C(sp^2) atoms (1,2:5,6:10,11-TRPH(C_4F_8)$_3$) has OOP_{av} and OOP_{max} values of 0.31 and 1.37 Å, respectively. Finally, the three compounds with substituents on all six of the bay C(sp^2) atoms have OOP_{av} and OOP_{max} values with ranges of 0.33–0.42 Å and 1.58–2.08 Å, respectively. Given the different types, sizes, and shapes of the substituents on the compounds listed in table 1-2 (e.g., OH, F, CH_3, CF_3, C_4F_4, C_4F_8, Cl), it is significant that the ranges of the distortion-from-planarity figures of merit do not overlap.

There are three pairs of TRPH(C_4F_8)$_n$ isomers, with significant differences in their degree of TRPH core planarity, for which we can compare relative energies. For n = 1, the DFT-predicted relative energies of planar-core 2,3-TRPH(C_4F_8) (OOP_{av} 0.03 Å) and 1,2-TRPH(C_4F_8) (OOP_{av} 0.17 Å) are 0 and 54.1 kJ mol^{-1}. For n = 2, the relative energies of 2,3:6,7-TRPH(C_4F_8)$_2$ (OOP_{av} 0.08 Å) and 1,2:10,11-TRPH(C_4F_8)$_2$ (OOP_{av} 0.14 Å) are 0 and 51.6 kJ mol^{-1}. For n = 3, the relative

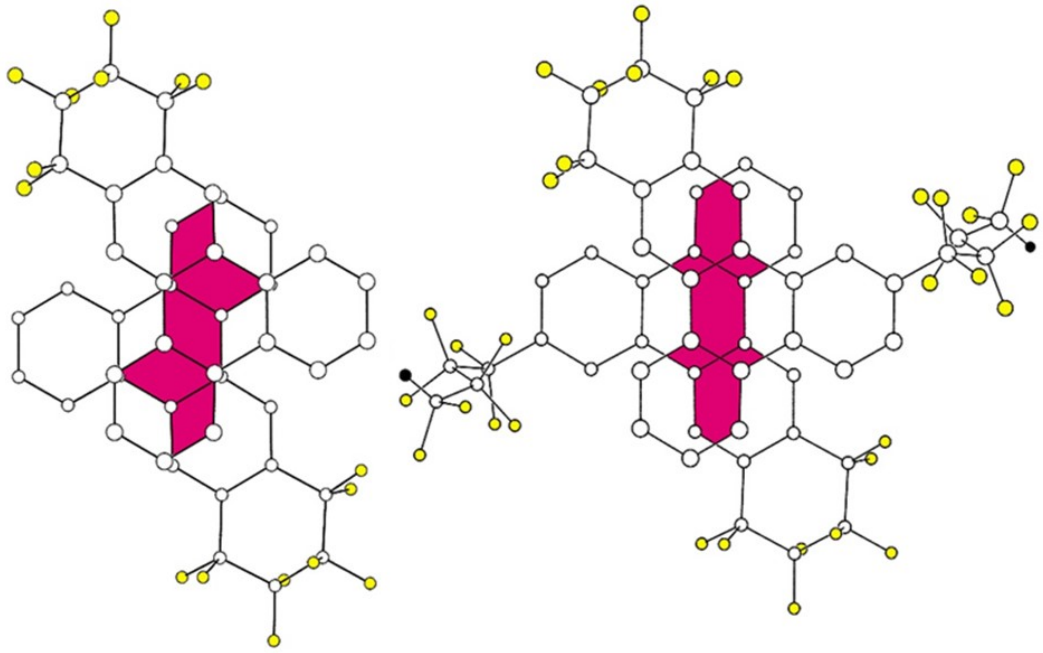

Figure 1-7. Parallel projections of neighboring molecules stacked together in the structures of 2,3:6-TRPH(C_4F_8)(C_4F_8H) (right) and 2,3- TRPH(C_4F_8) (left). The amount of π–π overlap is similar in the two structures, but the perpendicular distances to the least-squares planes of neighboring molecules are shorter in 2,3-TRPH(C_4F_8) (3.30–3.40 Å; av. 3.34 Å) than in 2,3:6-TRPH(C_4F_8)(ω-C_4F_8H) (3.37 to 3.44 Å; av. 3.40 Å).

energies of 2,3:6,7:10,11-TRPH(C_4F_8)$_3$ (OOP_{av} 0.07 Å) and 1,2:5,6:10,11-TRPH(C_4F_8)$_3$ (OOP_{av} 0.31 Å) are 0 and 98.6 kJ mol^{-1}. Note that a single bay substitution, in either 1,2-TRPH(C_4F_8) or 1,2:10,11-TRPH(C_4F_8)$_2$, raises the energy of each compound relative to its corresponding no-bay isomer by the same amount, *ca.* 50 kJ mol^{-1}, and two bay substitutions, as in 1,2:5,6:10,11-TRPH(C_4F_8)$_3$ raises the energy relative to the no-bay isomer by twice this amount, ca. 100 kJ mol^{-1}.

The degree of planarity also affected the distances between the π clouds of neighboring molecules, although it did not significantly affect the amount of π–π overlap of neighboring molecules. Eight C(sp^2) atoms of each planar 2,3-TRPH(C_4F_8) molecule overlap the π systems of neighboring molecules in infinite stacks of parallel molecules, with perpendicular distances to the least-squares planes of neighboring molecules that range from 3.30 to 3.40 Å and average 3.34 Å. For non-planar 1,2-TRPH(C_4F_8), the perpendicular distances to the least-squares planes of neighboring molecules range from 3.37 to 3.63 Å and average 3.55 Å. For planar 2,3:6,7-

TRPH(C_4F_8)$_2$, the perpendicular distances to the least-squares planes of neighboring molecules range from 3.38 to 3.62 Å and average 3.51 Å. Finally, for non-planar 1,2:10,11-TRPH(C_4F_8)$_2$, the perpendicular distances to the least-squares planes of neighboring molecules range from 3.48 to 3.74 Å and average 3.62 Å. Significantly, for these two pairs of isomers, and for relatively planar 2,3:6,7:10,11-TRPH(C_4F_8)$_3$ and distinctly non-planar 1,2:5,6:10,11-TRPH(C_4F_8)$_3$, the more planar isomer had an HPLC retention time longer than for the non-planar isomer. This is consistent with the chromatographic behavior of other planar vs. non-planar PAHs.[49, 51]

The TRPH C(sp^2) core of 2,3:6-TRPH(C_4F_8)(C_4F_8H), like that of 2,3-TRPH(C_4F_8), is relatively planar. The perpendicular distances to the least-squares planes of neighboring 2,3:6-TRPH(C_4F_8)(C_4F_8H) molecules range from 3.37 to 3.44 Å and average 3.40 Å. The degree of π–π overlap is similar in the two structures, as shown in Figure 1-7, although the molecules are closer together in 2,3-TRPH(C_4F_8) (3.30–3.40 Å; av. 3.34 Å) than in 2,3:6-TRPH(C_4F_8)(C_4F_8H).

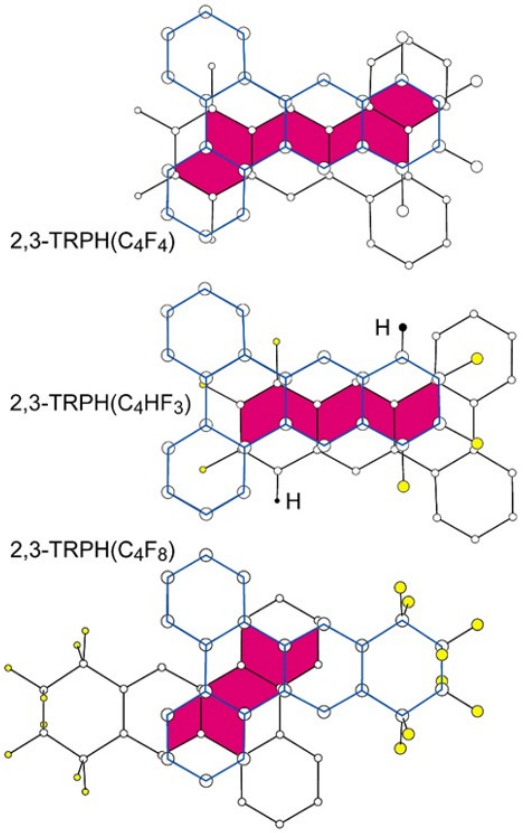

Figure 1-8. Comparison of the amounts of π–π overlap between neighboring parallel molecules in stacks in the structures of 2,3-TRPH(C_4F_4), 2,3-TRPH(C_4F_3H), and 2,3-TRPH(C_4F_8).

1.2.3.c. Trends in π-π overlap and intermolecular distance

The influences on PAH derivative crystal packing and π–π overlap by fluorinated substituents, which are generally attributed to a combination of steric effects, dipole-dipole orientations, and C–F···H, C–F···π, and F···F interactions, have been widely discussed in the literature.[10, 30, 46, 52-58] Linear *n*-perfluorobutyl groups, which are virtually isostructural to the C_4F_8H substituents in 2,3:6-TRPH(C_4F_8)(C_4F_8H) and 2,3:6,7:10-TRPH(C_4F_8)$_2$(C_4F_8H), have been found to be particularly effective in promoting lamellar stacking with short π–π distances in structures of PAH(n-C_4F_9)$_x$ derivatives.[55, 56]

The π–π overlap in the structures of 2,3-TRPH(C_4F_3H), 2,3-TRPH(C_4F_4), and 2,3-TRPH(C_4F_8)[25] are compared in Figure 1-8. The π–π overlap is extensive and many of the perpendicular distances between overlapped C(sp^2) atoms in one molecule and the least-squares plane of the closest neighboring molecule are less than 3.40 Å. This is expected based on the tendency of arenes and perfluoroarenes, as well as aromatic molecules with arene and perfluoroarene moieties, to form parallel-stacked structures. An earlier example of the latter is the structures of the partially fluorinated PAH 1,2,3,4-tetrafluoroanthracene.[54]

In spite of the similar structures, the amount of π–π overlap is significant greater in 2,3-TRPH(C_4F_4) than in 2,3-TRPH(C_4F_3H). It is not clear at this time why such similar molecules crystallize into hexagonal arrays of stacks of parallel molecules with such different amounts of π–π overlap between neighboring molecules. It may be related to the number and strength of C–H···F–C, C–F···F–C, and C–F···π interactions, the different magnitudes and directions of molecular dipole moments, differences in electrostatic potential distributions, differences in molecular quadrupole interactions, or some combination of these factors.[2, 30, 52, 54, 56, 59-70] Perhaps additional comparisons of PAH(C_4F_4) and PAH(C_4F_3H) structures, when they become available, along with a theoretical study of their solid-state packing, will allow these various factors to be deconvoluted.

Finally, the molecular structure of the symmetric molecule 2,3:6,7:10,11-TRPH(C_4F_8)$_3$ can be compared with the equally-precise 150 K structure of unsubstituted TRPH[71] to demonstrate that the presence of six strong electron withdrawing groups does not affect the core C–C bond distances

to within ±σ,. Our DFT calculations confirm this observation based on the X-ray structures. The TRPH core C–C distances are virtually indistinguishable in 2,3:6,7:10,11-TRPH(C_4F_8)$_3$ and unsubstituted TRPH.

1.2.4. Electronic properties of selected TRPH derivatives

1.2.4.a. TRPH derivative electronic properties compared to literature compounds

Part of the justification for this work is to prepare electron acceptors that are stronger than their underivatized counterparts for various applications in molecular electronics,[72-74] including the formation of donor/acceptor co-crystals[2, 52, 71, 75] possibly with separate donor stacks and acceptor stacks.[55] To gauge the effect that each six membered ring has on the electron affinity (EA) of a planar PAH, the gas-phase EAs of several of the compounds were measured using low-temperature photoelectron spectroscopy.[76] Kuvychko *et al.* previously showed that the (non-regiospecific) addition of three C_4F_8 groups to CORA increased its EA by 2.2 eV (from 0.5(1) eV for CORA to 2.25(2) eV for CORA(C_4F_8)$_3$).[22] Additionally, the electronic properties of TRPH-6-1 have been previously measured.[21]

Comparison of the values associated with these previous molecules and the fluorous TRPH family reported here is interesting for several reasons. First, the impact of an annulated fluoroalkyl group compared to, for example, trifluoromethyl groups and fluoroalkyl groups substituted at single positions on PAHs, has not previously been investigated. Furthermore, the effect of the C_4F_4 groups as compared to the C_4F_8 groups is of interest, as there are competing factors at play. Larger aromatic systems are generally better electron acceptors,[20] but for planar PAHs, perfluoroalkylation generally increases electron acceptor properties more than direct fluorination on the C(sp^2) carbons of the π-system, due to F atom lone pairs donating electron density to the π-system.

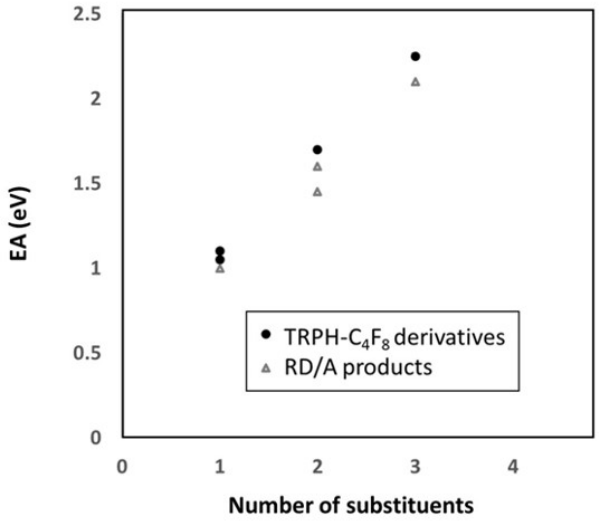

Figure 1-9. Gas phase EA of flurous TRPHs. The C_4F_8 moieties have a consistently larger impact on the EA compared to products of RD/A.

1.2.4.b. Gas phase EA measurements of fluorous TRPHs

The author performed gas phase electron affinity measurements in collaboration with and under the supervision of Xue-Bin Wang at Pacific Northwest National Laboratory. The resulting values are summarized in Figure 1-9. For further details of gas phase EA measurements, see appx *A.4.8.* and appx D.1.7. for selected PES spectra.

As can be seen in Figure 1-9, the effect of addition of C_4F_8 moieties is roughly linear. The perfluoroalkyl C_4F_8 moieties have a larger impact upon EA values than the RD/A products, consistently. This seems to indicate, in terms of creating a better electron acceptor, that the negative effects of F atom lone pair donation of electron density into the π system dominate the positive effect of extending the π-system. As expected, the molecule bearing a C_4F_3H moiety, with one F atom less than its counterpart C_4F_4 substituted product, had the lowest impact upon EA values.

Noteworthy, the bay substituted product 1,2-TRPH(C_4F_8) had a lower EA than the peninsula substituted product 2,3-TRPH(C_4F_8). This suggests that the bending of the TRPH core may reduce electron acceptor ability.

Compared to trifluoromethylation, it seems that the groups reported here, particularly the C_4F_8 groups, have a slightly larger impact upon EA values. Comparing a molecule substituted at

the same number of positions (*i.e.* 6 CF_3 groups compared to 3 C_4F_8 groups), the effect of the C_4F_8 ring is slightly larger than the effect of 2 CF_3 groups (*ca.* 0.6 eV per C_4F_8 group vs. *ca*. 0.25 + 0.25 = 0.5 eV for per 2 CF_3 groups).[21] This could be attributed to the higher number of F-atoms present (8 vs, 6), despite the fact that fewer C atoms (2 rather than 3) are bonded to the C-atom directly substituted on the TRPH core. This result is distinct from previous reports by San *et al.*, in which length of a variety of perfluoroalkyl chains did not substantially alter the incremental effect of their substitution upon the PAH naphthalene.[24]

1.2.4.c. Electrochemical behavior of fluorous TRPHs

Attempts to perform cyclic voltammetry upon fluorous TRPHs did not meet with success. Reversibility was not achieved, (appx. D.1.8) even with scan rates up to 500 V/s, and a white film deposited onto the electrode during every scan, requiring flame-cleaning before the electrode could be used again. Perhaps the tendency of PAHs such as TRPH to physisorb to metal surfaces, noted above in section *1.2.1.c.* has some bearing upon this phenomenon.[40, 41]

1.3. SUMMARY AND CONCLUSIONS

In this work, judicious selection of reaction conditions led to relatively high selectivity and yields in the high-temperature reaction of triphenylene and 1,4-$C_4F_8I_2$. Through modification of reaction conditions, a degree of control over product distribution was achieved. This result demonstrates, for the first time, that direct one-step perfluoroalkylations of PAH substrates can be as effective as the more conventional multistep bottom-up syntheses. It also indicates that, even at the relatively high reaction temperatures, the lowest energy isomers of polysubstituted products form predominantly. Specifically, the lowest energy structures (within 0-15 kJ/mol) are formed as predominant products, as shown in this study and in previous work on CORA$(CF_3)_n$ by Kuvychko *et al.*[25, 35] This provides a clear distinction of these emerging families of polyperfluoroalkylated PAHs as thermodynamically stable compounds (in contrast to kinetic isomers typically formed in bottom-up syntheses).

Cu powder was utilized in perfluoroannulation of TRPH not only due to its already known role as a promoter of R_F radical formation, but also because it helped to significantly improve selectivity of the reaction. When Cu powder was present, no products with bay substitutions were formed, when Cu was absent, the reaction was non-selective and contained products with bay and peninsula substitutions. This approach has not worked, however, for CF_3 substitutions of TRPH, which produced similarly complex mixtures of TRPH$(CF_3)_n$ isomers both with and without Cu powder. Further mechanistic studies are therefore necessary.

Overall, as a result of the studies of structures of ten fluorous TRPH derivatives, it has been demonstrated, in much greater detail than it was possible prior to this work, that fluorination (perfluoroalkylation) of TRPH induces dramatic changes of solid-state packing motifs including planarity of the TRPH core, π–π overlaps and the evolution of columnar stacking. Knowledge of these newly observed trends can be strategically applied to advanced crystal engineering of TRPH-based functional materials.

Finally, preliminary studies of the electronic effect of the three annulated groups discussed here, namely C_4F_8, C_4F_4, and C_4F_3H groups, have been conducted. The substrate TRPH has relatively poor electron accepting properties, but introduction of the above fluorous groups results in incremental increase in EA, up to 2.3 eV, in the case TRPH$(C_4F_8)_3$

REFERENCES

1. Rieger, R.; Müllen, K., Forever young: polycyclic aromatic hydrocarbons as model cases for structural and optical studies. *J. Phys. Org. Chem.* **2010,** *23* (4), 315-325.
2. Collings, J. C.; Roscoe, K. P.; Thomas, R. L.; Batsanov, A. S.; Stimson, L. M.; Howard, J. A. K.; Marder, T. B., Arene-Perfluoroarene Interactions in Crystal Engineering. Part 3. Single-Crystal Structures of 1:1 Complexes of Octafluoronaphthalene with Fused-Ring Polyaromatic Hydrocarbons. *New J. Chem.* **2001,** *25* (11), 1410–1417.
3. Ahmed, F. R.; Trotter, J., The Crystal Structure of Triphenylene. *Acta Cryst.* **1963,** *16*, 503-508.
4. Wöhrle, T.; Wurzbach, I.; Kirres, J.; Kostidou, A.; Kapernaum, N.; Litterscheidt, J.; Haenle, J. C.; Staffeld, P.; Baro, A.; Giesselmann, F., Discotic liquid crystals. *Chem. Rev.* **2015,** *116* (3), 1139-1241.
5. Pal, S. K.; Setia, S.; Avinash, B. S.; Kumar, S., Triphenylene-based discotic liquid crystals: recent advances. *Liq. Cryst.* **2013,** *40* (12), 1769-1816.
6. Boden, N.; Bushby, R. J.; Cammidge, A. N.; Duckworth, S.; Headdock, G., α-Halogenation of triphenylene-based discotic liquidcrystals: towards a chiral nucleus. *J. Mater. Chem.* **1997,** *7* (4), 601-605.
7. Umesh, C. P.; Marcelis, A. T. M.; Zuilhof, H., Fluorine-containing triphenylenes. Liquid crystalline properties and surface ordering. *Liq. Cryst.* **2014,** *41* (12), 1911-1922.
8. Tschierske, C., Fluorinated Liquid Crystals: Design of Soft Nanostructures and Increased Complexity of Self-Assembly by Perfluorinated Segments. In *Liquid Crystals: Materials Design and Self-Assembly*, Tschierske, C., Ed. 2012; Vol. 318, pp 1-108.
9. Hird, M., Fluorinated liquid crystals - properties and applications. *Chem. Soc. Rev.* **2007,** *36* (12), 2070-2095.
10. Terasawa, N.; Monobe, H.; Kiyohara, K., Mesomorphic phase transition behavior of novel triphenylene compounds possessing fluoroalkylated side chains. *J. Fluorine Chem.* **2006,** *127*, 954–961.
11. Zhao, K. Q.; Du, J. Q.; Long, X. H.; Jing, M.; Wang, B. Q.; Hu, P.; Monobe, H.; Henrich, B.; Donnio, B., Design of Janus triphenylene mesogens: Facile synthesis, mesomorphism, photoluminescence, and semiconductivity. *Dyes and Pigments* **2017,** *143*, 252-260.
12. Dong, R. Y.; Boden, N.; Bushby, R. J.; Martin, P. S., Deuteron NMR study of dynamics and order in the columnar phase of a fluorinated discotic liquid crystal. *Mol. Phys.* **1999,** *97* (11), 1165-1171.
13. Pérez, D.; Guitián, E., Selected strategies for the synthesis of triphenylenes. *Chem. Soc. Rev.* **2004,** *33* (5), 274-283.
14. Peña, D.; Escudero, S.; Pérez, D.; Guitián, E.; Castedo, L., Efficient Palladium-Catalyzed Cyclotrimerization of Arynes: Synthesis of Triphenylenes. *Angew. Chem. Int. Ed.* **1998,** *37* (19), 2659-2661.
15. King, P. F.; O'Malley, R. F., Fluorination of polycyclic aromatic hydrocarbons: charge vs. frontier orbital control in substitution reactions of radical cations. *J. Org. Chem.* **1984,** *49* (15), 2803-2807.
16. Mathew, B. P.; Yang, H. J.; Kim, J.; Lee, J. B.; Kim, Y.-T.; Lee, S.; Lee, C. Y.; Choe, W.; Myung, K.; Park, J.-U.; Hong, S. Y., An Annulative Synthetic Strategy for Building Triphenylene Frameworks by Multiple C−H Bond Activations. *Angew. Chem.* **2017,** *129* (18), 5089-5093.
17. Wu, X.; Han, J.; Wang, L., Palladium Catalyzed C–I and Vicinal C–H Dual Activation of Diaryliodonium Salts for Diarylations: Synthesis of Triphenylenes. *J. Org. Chem.* **2017,** *83* (1), 49-56.
18. Iwasaki, M.; Araki, Y.; Iino, S.; Nishihara, Y., Synthesis of Multisubstituted Triphenylenes and Phenanthrenes by Cascade Reaction of o-Iodobiphenyls or (Z)-β-Halostyrenes with o-Bromobenzyl Alcohols through Two Sequential C–C Bond Formations Catalyzed by a Palladium Complex. *J. Org. Chem.* **2015,** *80* (18), 9247-9263.
19. Mannich, C., Über die Kondensation des Cyclohexanons. *Ber. Dtsch. Chem. Ges.* **1907,** *40* (1), 153-158.

20. Watson, M. D.; Fechtenkötter, A.; Müllen, K., Big Is Beautiful−"Aromaticity" Revisited from the Viewpoint of Macromolecular and Supramolecular Benzene Chemistry. *Chem. Rev.* **2001,** *101* (5), 1267-1300.
21. Kuvychko, I. V.; Castro, K. P.; Deng, S. H. M.; Wang, X.-B.; Strauss, S. H.; Boltalina, O. V., Taming Hot CF_3 Radicals: Incrementally Tuned Families of Polyarene Electron Acceptors for Air-Stable Molecular Optoelectronics. *Angew. Chem. Int. Ed.* **2013,** *52*, 4871-4874.
22. Kuvychko, I. V.; Dubceac, C.; Deng, S. H. M.; Wang, X.-B.; Granovsky, A. A.; Popov, A. A.; Petrukhina, M. A.; Strauss, S. H.; Boltalina, O. V., C20H4(C4F8)3: A Fluorine-Containing Annulated Corannulene that Is a Better Electron Acceptor Than C60. *Angew. Chem. Int. Ed.* **2013,** *52* (29), 7505-7508.
23. Clikeman, T. T.; Bukovsky, E. V.; Kuvychko, I. V.; San, L. K.; Deng, S. H. M.; Wang, X.-B.; Chen, Y.-S.; Strauss, S. H.; Boltalina, O. V., Poly(trifluoromethyl) azulenes: structures and acceptor properties. *Chem. Commun.* **2014,** *50*, 6263-6266.
24. San, L. K.; Bukovsky, E. V.; Kuvychko, I. V.; Popov, A. A.; Strauss, S. H.; Boltalina, O. V., Single-Step Gas-Phase Polyperfluoroalkylation of Naphthalene Leads to Thermodynamic Products. *Chem. Eur. J.* **2014,** *20*, 4373-4379.
25. Rippy, K. C.; Bukovsky, E. V.; Clikeman, T. T.; Chen, Y.-S.; Hou, G.-L.; Wang, X.-B.; Popov, A. A.; Boltalina, O. V.; Strauss, S. H., Copper Causes Regiospecific Formation of C_4F_8-Containing Six-Membered Rings and their Defluorination/Aromatization to C_4F_4-Containing Rings in Triphenylene/1,4-$C_4F_8I_2$ Reactions. *Chem. Eur. J.* **2016,** *22*, 874–877.
26. Hou, Y.-C.; Chiang, C.-M., Selective and Facile C-F Bond Activation of Trifluoromethyl Groups on Cu(111). *J. Am. Chem. Soc.* **1999,** *121*, 8116-8117.
27. Du, R.-B.; Liu, C.; Shen, D.-M.; Chen, Q.-Y., Partial Bromination and Fluoroalkylation of 5,10,15-Tris(pentafluorophenyl)corrole. *Synlett* **2009**, 2701-2705.
28. Kuvychko, I. V.; Dubceac, C.; Deng, S. H. M.; Wang, X.-B.; Granovsky, A. A.; Popov, A. A.; Petrukhina, M. A.; Strauss, S. H.; Boltalina, O. V., C20H4(C4F8)3. *Angew. Chem. Int. Ed.* **2013,** *52*, 7505-7508.
29. Zeng, Z.; Liu, C.; Jin, L.-M.; Guo, C.-C.; Chen, Q.-Y., Unexpected Intramolecular Cyclization of 2-(Perfluoroalkyl)tetraarylporphyrin Radicals: Approaches for the Intramolecular Cyclization of 2-(Perfluoroalkyl)tetraarylporphyrin Radicals. *Eur. J. Org. Chem.* **2005**, 306-316.
30. Liu, L.; Yang, G.; Duan, Y.; Geng, Y.; Wu, Y.; Su, Z., The relationship between intermolecular interactions and charge transport properties of trifluoromethylated polycyclic aromatic hydrocarbons. *Org. Electronics* **2014,** *15*, 1896–1905.
31. Kaplan, P. T.; Chen, B.; Vicic, D. A., Synthetic utility of dizinc reagents derived from 1,4-diiodo- and 1,4-dibromooctafluorobutane. *J. Fluorine Chem.* **2015,** *168*, 158-162.
32. Kaplan, P. T.; Xu, L.; Chen, B.; McGarry, K. R.; Yu, S.; Wang, H.; Vicic, D. A., Mild, Safe, and Versatile Reagents for (CF2)n Transfer and the Construction of Fluoroalkyl-Containing Rings. *Organometallics* **2013,** *32*, 7552-7558.
33. Rippy, K. C.; DeWeerd, N. J.; Kuvychko, I. V.; Chen, Y.-S.; Strauss, S. H.; Boltalina, O. V., Fluorination-Induced Evolution of Columnar Packing in Fluorous Triphenylenes and Benzotriphenylenes. *ChemPlusChem* **2018,** *83* (12), 1067-1077.
34. Grozema, F. C.; Siebbeles, L. D., Mechanism of charge transport in self-organizing organic materials. *Int. Rev. Phys. Chem.* **2008,** *27* (1), 87-138.
35. Kuvychko, I. V.; C., C. T.; Dubceac, C.; Yu.-S., C.; Petrukhina, M. A.; Strauss, S. H.; Popov, A. A.; Boltalina, O. V., Understanding Polyarene Trifluoromethylation with Hot CF_3 Radicals Using Corannulene. *Eur. J. Org. Chem.* **2018,** *on line*, 7505-7508.
36. Kareev, I. E.; Kuvychko, I. V.; Lebedkin, S. F.; Miller, S. M.; Anderson, O. P.; Strauss, S. H.; Boltalina, O. V., Synthesis and structures of poly (perfluoroethyl) 60 fullerenes: 1,7,16,36,46,49-C-60(C2F5)(6) and 1,6,11,18,24,27,32,35-C-60(C2F5)(8). *Chem. Commun.* **2006,** (3), 308-310.
37. Shustova, N. B.; Kareev, I. E.; Kuvychko, I. V.; Whitaker, J. B.; Lebedkin, S. F.; Popov, A. A.; Dunsch, L.; Chen, Y. S.; Seppelt, K.; Strauss, S. H.; Boltalina, O. V., High-temperature and

photochemical syntheses of C-60 and C-70 fullerene derivatives with linear perfluoroalkyl chains. *J. Fluorine Chem.* **2010,** *131* (11), 1198-1212.
38. Shustova, N. B.; Kuvychko, I. V.; Peryshkov, D. V.; Whitaker, J. B.; Larson, B. W.; Chen, Y. S.; Dunsch, L.; Seppelt, K.; Popov, A. A.; Strauss, S. H.; Boltalina, O. V., Chemical tailoring of fullerene acceptors: synthesis, structures and electrochemical properties of perfluoroisopropylfullerenes. *Chem. Commun.* **2011,** *47* (3), 875-877.
39. San, L. K.; Clikeman, T. T.; Dubceac, C.; Popov, A. A.; Chen, Y.-S.; Petrukhina, M. A.; Strauss, S. H.; Boltalina, O. V., Corannulene Molecular Rotor with Flexible Perfluoro-benzyl Blades: Synthesis, Structure and Properties. *Chem. Eur. J.* **2015**, in press (doi 10.1002/chem.201500465).
40. Söhnchen, S.; Hänel, K.; Birkner, A.; Witte, G.; Wöll, C. H., Molecular Beam Deposition of Perylene on Copper: Formation of Ordered Phases. *Chem. Mater.* **2005,** *17*, 5297-5304.
41. Manandhar, K.; Parkinson, B. A., Photoemission and STM Study of the Morphology and Electronic Structure of Benz[a]anthracene on Cu(111) on Mica and on HOPG. *J. Phys. Chem. C* **2011,** *115*, 5910-5918.
42. Amli, H.; Uneyama, K., C-F Bond Activation in Organic Synthesis. *Chem. Rev.* **2009,** *109*, 2119-2183.
43. Schmidt, C.; Breuer, T.; Wippermann, S.; Schmidt, W. G.; Witte, G., Substrate Induced Thermal Decomposition of Perfluoropentacene Thin Films on the Coinage Metals. *J. Phys. Chem. C* **2012,** *116*, 24098-24106.
44. Toda, F.; Tanaka, K.; Matsumoto, T.; Nakai, T.; Miyahara, I.; Hirotsu, K., A new host 2,3,6,7,10,11-hexahydroxy triphenylene which forms chiral inclusion crystalline lattice: X-ray structural study of the chiral crystalline lattice. *J. Phys. Org. Chem.* **2000,** *13*, 39–45.
45. Jones, D. W.; Sowden, J. M.; Yerkess, J.; Hazell, A. C.; Hazell, R. G., The crystal structure of 1-methyltriphenylene. *Z. Krist.* **1990,** *191*, 59–66.
46. Hursthouse, M. B.; Smith, V. B., The crystal and molecular structure of dodecafluorotriphenylene, $C_{18}F_{12}$. *J. Fluorine Chem.* **1977,** *10*, 145–155.
47. Shibata, K.; Kulkarni, A. A.; Ho, D. M.; Pascal Jr., R. A., Perchlorotriphenylene. *J. Am. Chem. Soc.* **1994,** *116*, 5983–5984.
48. Sander, L. C.; Wise, S. A., Polycyclic Aromatic Hydrocarbon Structure Index (NIST Special Publication 922; https://www.nist.gov/mml/csd/special-publication-922-polycyclic-aromatichydrocarbon-structure-index). Natl. Inst. of Standards and Technology: Gaithersburg, MD, 2011; pp 1-103.
49. Wilson, W. B.; Hayes, H. V.; Sander, L. C.; Campiglia, A. D.; Wise, S. A., Normal-phase liquid chromatography retention behavior of polycyclic aromatic hydrocarbon and their methyl-substituted derivatives on an aminopropyl stationary phase. *Anal. Bioanal. Chem.* **2017,** *409*, 5291–5305.
50. Bondi, A., van der Waals Volumes and Radii. *J. Phys. Chem.* **1964,** *68*, 441–451.
51. Jinno, K.; Nagoshi, T.; Tanaka, N.; Okamoto, M.; Fetzer, J. C.; Biggs, W. R., Elution Behaviour of Planar and Non-Planar Polycyclic Aromatic Hydrocarbons on Various Chemically Bonded Stationary Phases in Liquid Chromatography. *J. Chromatog.* **1987,** *392*, 75–82.
52. Collings, J. C.; Batsanov, A. S.; Howard, J. A. K.; Marder, T. B., Arene–perfluoroarene interactions in crystal engineering. Part 14. 1:1 Complexes of octafluoronaphthalene with fluorene and 9,10-dihydrophenanthrene. *Can. J. Chem.* **2006,** *84*, 238–242.
53. Weck, M.; Dunn, A. R.; Matsumoto, K.; Coates, G. W.; Lobkovsky, E. B.; Grubbs, R. H., Influence of Perfluoroarene–Arene Interactions on the Phase Behavior of Liquid Crystalline and Polymeric Materials. *Angew. Chem. Int. Ed.* **1999,** *38*, 2741–2745.
54. Cozzi, F.; Bacchi, S.; Filippini, G.; Pilati, T.; Gavezzotti, A., Synthesis, X-ray Diffraction and Computational Study of the Crystal Packing of Polycyclic Hydrocarbons Featuring Aromatic and Perfluoroaromatic Rings Condensed in the Same Molecule: 1,2,3,4-Tetrafluoronaphthalene, -anthracene and -phenanthrene. *Chem. Eur. J.* **2007,** *13*, 7177–7184.
55. Putta, A.; Mottishaw, J. D.; Wang, Z.-H.; Sun, H., Rational Design of Lamellar π–π Stacked Organic Crystalline Materials with Short Interplanar Distance. *Cryst. Growth Des.* **2014,** *14*, 350-356.

56. BaniKhalid, M. O.; Mottishaw, J. D.; Sun, H., Steering Power of Perfluoroalkyl Substituents in Crystal Engineering: Tuning the π–π Distance While Maintaining the Lamellar Packing Motif for Aromatics with Various Sizes of π-Conjugation. *Cryst. Growth Des.* **2015,** *15*, 2235–2242.
57. Hiszpanski, A. M.; Woll, A. R.; Kim, B.; Nuckolls, C.; Loo, Y.-L., Altering the Polymorphic Accessibility of Polycyclic Aromatic Hydrocarbons with Fluorination. *Chem. Mater.* **2017,** *29*, 4311–4316.
58. Yao, Z.-F.; Wang, J.-Y.; Pei, J., Control of π–π Stacking via Crystal Engineering in Organic Conjugated Small Molecule Crystals. *Cryst. Growth Des.* **2018,** *18*, 7–15, and references therein.
59. Wheeler, S. E., Local Nature of Substituent Effects in Stacking Interactions. *J. Am. Chem. Soc.* **2011,** *133* (26), 10262–10274.
60. Schatschneider, B.; Phelps, J.; Jezowski, S., A new parameter for classification of polycyclic aromatic hydrocarbon crystalline motifs: a Hirshfeld surface investigation. *CrystEngComm* **2011,** *13*, 7216–7223, and references therein.
61. Desiraju, G. R.; Gevezzotti, A., Crystal Structures of Polynuclear Aromatic Hydrocarbons. Classification, Rationalization and Prediction from Molecular Structure. *Acta Crystallogr., Sect. B: Struct. Sci.* **1989,** *B45*, 473–482.
62. Raju, R. K.; Bloom, J. W. G.; Wheeler, S. E., Broad Transferability of Substituent Effects in π-Stacking Interactions Provides New Insights into Their Origin. *J. Chem. Theory Comput.* **2013,** *9*, 3479–3490, and references therein.
63. Wheeler, S. E., Controlling the local arrangements of π-stacked polycyclic aromatic hydrocarbons through substituent effects{. *CrystEngComm* **2012,** *14*, 6140–6145.
64. Cho, D. M.; Parkin, S. R.; Watson, M. D., Partial Fluorination Overcomes Herringbone Crystal Packing in Small Polycyclic Aromatics. *Org. Lett.* **2005,** *7*, 1067–1068.
65. Reichenbacher, K.; Suss, H. I.; Hulliger, J., Fluorine in crystal engineering - "the little atom that could". *Chemical Society Reviews* **2005,** *34* (1), 22-30.
66. Chopra, D.; Guru Row, T. N., Role of organic fluorine in crystal engineering. *CrystEngComm* **2011,** *13*, 2175–2186.
67. Oosterwijk, M. A.; Saunders, G. C.; Zou, W., Polyfluoroarene–arene π–π stacking in three directions to provide crystal polarity. *J. Fluorine Chem.* **2016,** *188*, 80–84.
68. Althagbi, H. I.; Bernstein, D. R.; Crombie, W. C.; Lane, J. R.; McQuiston, D. K.; Oosterwijk, M. A.; Saunders, G. C.; Zou, W., The crystal structures of 1-(4-halo-2,3,5,6-tetrafluorophenyl)-3-benzylimidazolium bromides: The relative importance of anion–π, lone pair–π, π–π stacking and halogen bonding interactions. *J. Fluor. Chem.* **2018,** *206*, 61–71.
69. Spackman, M. A.; Jayatilaka, D., Hirshfeld surface analysis. *CrystEngComm* **2009,** *11*, 19–32.
70. Wang, Y.; Stretton, A. D.; McConnell, M. C.; Wood, P. A.; Parsons, S.; Henry, J. B.; Mount, A. R.; Galow, T. H., 1,4,5,8,9,12-Hexamethyltriphenylene. A Molecule with a Flipping Twist. *J. Am. Chem. Soc.* **2007,** *129*, 13193–13200.
71. Collings, J. C.; Roscoe, K. P.; Robins, E. G.; Batsanov, A. S.; Stimson, L. M.; Howard, J. A. K.; Clark, S. J.; Marder, T. B., Arene-perfluoroarene interactions in crystal engineering 8: structures of 1 : 1 complexes of hexafluorobenzene with fused-ring polyaromatic hydrocarbons. *New J. Chem.* **2002,** *26* (12), 1740–1746.
72. Usta, H.; Facchetti, A.; Marks, T. J., n-Channel Semiconductor Materials Design for Organic Complementary Circuits. *Acc. Chem. Res.* **2011,** *44* (7), 501-510.
73. Mishra, A.; Bauerle, P., Small Molecule Organic Semiconductors on the Move: Promises for Future Solar Energy Technology. *Angew. Chem. Int. Ed.* **2012,** *51* (9), 2020-2067.
74. Wang, C. L.; Dong, H. L.; Hu, W. P.; Liu, Y. Q.; Zhu, D. B., Semiconducting pi-Conjugated Systems in Field-Effect Transistors: A Material Odyssey of Organic Electronics. *Chem. Rev.* **2012,** *112* (4), 2208-2267.
75. Collings, J. C.; Roscoe, K. P.; Thomas, R. L.; Batsanov, A. S.; Stimson, L. M.; Howard, J. A. K.; Marder, T. B., Arene-perfluoroarene interactions in crystal engineering. Part 3. Single-crystal

structures of 1 : 1 complexes of octafluoronaphthalene with fused-ring polyaromatic hydrocarbons. *New J. Chem.* **2001,** *25* (11), 1410-1417.
76. Wang, X. B.; Wang, L. S., Development of a Low-Temperature Photoelectron Spectroscopy Instrument Using an Electrospray Ion Source and a Cryogenically Controlled Ion Trap. *Rev. Sci. Instrum.* **2008,** *79* (7), 073108.

CHAPTER 2. APPLICATION OF PERFLUROANNULATION AND RD/A SYNTHETIC TECHNIQUE TO A BROAD RANGE OF PAH AND HETERO-PAH SUBSTRATES

2.1. INTRODUCTION

The properties of PAH and hetero-PAHs vary substantially based upon their size, shape, and atomic composition.[1-4,] This is particularly true with respect to their electronic properties, as illustrated in Figure 2-1 using EA as a metric. Of particular interest, the inclusion of an N-atom in an aromatic system substantially increases its EA, as has been demonstrated both experimentally and through computational studies.[5-10] This increase makes this class of materials particularly promising as electron acceptors in organic electronics, the primary application targeted by the research reported here.[11, 12] Functionalized PAHs and hetero-PAHs have additional applications as components in organic electronics, including as ligands for emitters in OLEDs and as dyes for LCD-based devices.[13-24] Additionally, they are useful in other fields such as medicine,[25-27] spectroscopy,[28] astrophysics,[29, 30] as ligands for organometallic complexes with a wide variety of applications,[15, 31] and for organic synthesis.[32] In particular, fluorous derivatives of PAHs are in demand.[23] Further details of uses of individual substrates are discussed below in section 2.2.1.

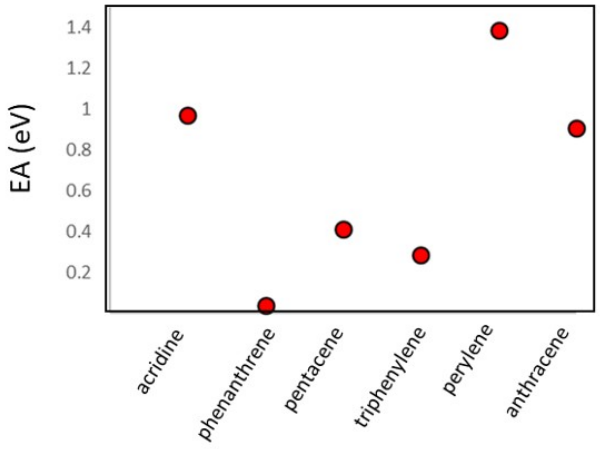

Figure 2-1. Electronic properties of different PAHs and hetero-PAHs vary substantially based on size, shape, and atom type, as illustrated here by a series of gas phase EAs.[1,2,3] Of particular note here is the gas phase EA of acridine(ACRD), the hetero-atom containing analog of anthracene. Note that the presence of a single N atom dramatically increases EA, by almost 0.5 eV.

In the work reported in this chapter, reactions of 13 different substrates with 1,4-$C_4F_8I_2$ were investigated , utilizing the synthetic method developed by the author and described in chapter 1. These substrates are shown in Figure 2-2. For seven of the substrates (Figure 2-2 top), reactions led to the fluorous products from which six new compounds were isolable by HPLC. These products were functionalized with three fluorous moieties , namely C_4F_8, C_4F_4, C_4F_3H. Notably, the conditions under which the latter two RD/A moieties formed were found to be substrate

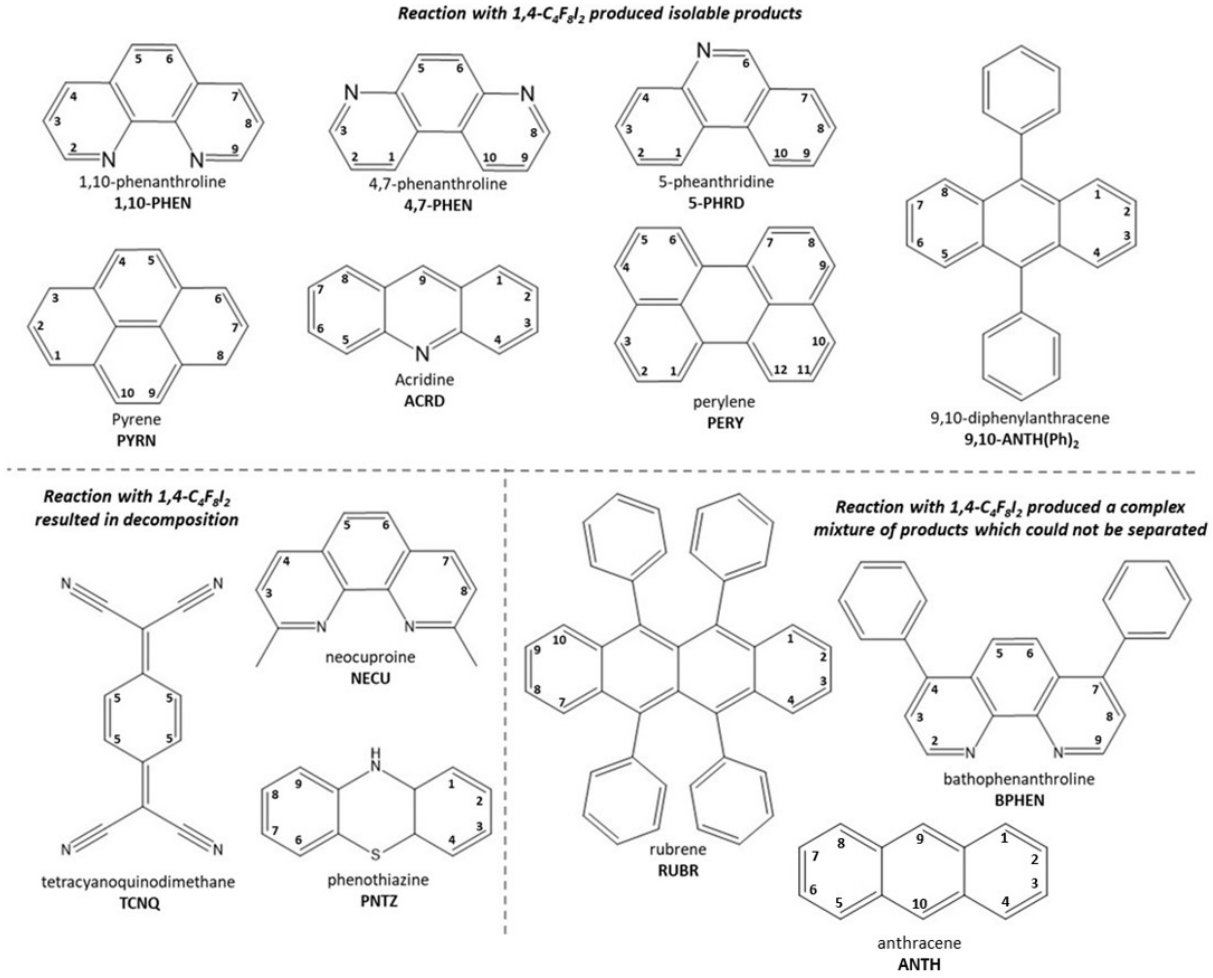

Figure 2-2. The thirteen substrates above were reacted with 1,4-$C_4F_8I_2$ using the synthetic method discussed in chapter 1 (appx A.1). For seven substrates, (top) these reactions produced isolable compounds bearing C_4F_8 substituents, and in some cases, RD/A products. For details of these reactions, see section 2.2.1 and appx B.2. For three substrates, (bottom right) NMR spectroscopy of crude product mixtures indicated that reaction had produced mixtures of derivatized compounds, but attempts to develop purification methods were unsuccessful (appx D.2.1). Finally, for two substrates (bottom right), reaction produced no soluble, material that gave rise to a signal by ^{19}F NMR spectroscopy, indicating that no products formed. (appx D.2.1) In both cases, significant amounts of char were observed.

dependent. Analysis of NMR spectra of crude product mixtures indicates that products bearing the fourth type of moiety, C_4F_8H, also formed. However, these compounds tended to elute from the HPLC column very quickly with poor separation. Therefore, no pure products bearing C_4F_8H were isolated. Additionally, a new type of substituent, C_4F_7H, was observed, contributing new insight to RD/A reaction steps.

For three additional substrates (Figure 2-2 bottom right), crude product mixture was recovered that, by NMR spectroscopy, appeared to contain products functionalized with the four target groups. However, suitable purification methods were not discovered.

For the final three substrates, reaction resulted in decomposition (Figure 2-2 bottom left). However, this result may be explained by structural features of these three substrates (discussed in section *2.2.1.h*). With the exception of these substrates, this reaction method appears to be applicable for many PAHs and hetero-PAHs containing N atoms.

With one exception, optimization of reactions conditions with respect to overall yield or product selectivity has not been carried out for the substrates shown in Figure 2-2. The goal of the work reported in this chapter was rather to demonstrate that the functionalization method discussed in chapter 1 is suitable for a wide range of substrates, particularly with regard to the novel RD/A process, and to isolate a limited number of pure fluorous PAH and hetero-PAH derivatives for analysis of solid-state packing and electronic properties. To this end, ten compounds were analyzed by single crystal X-ray crystallography, yielding eight structures and two preliminary structures.

2.2. RESULTS AND DISCUSSION

2.2.1. Synthesis, isolation, and structural characterization of pure compounds

2.2.1.a. General comments on syntheses

A general scheme for synthesis of the products discussed in this chapter is shown in scheme 2-1. The experimental procedure was analogous to the procedure reported in chapter 1 and discussed generally in appx A.1.[33-35] In this method, the PAH or hetero-PAH substrate was heated with 1,4-$C_4F_8I_2$, and the gas-phase radical reaction resulted in the formation of products bearing

C_4F_8, C_4F_4, or C_4F_3H rings. NMR spectra indicate that products bearing C_4F_8H moieties were also formed, but none were isolated in high purity.

For 4,7-PHEN, PYRN, and PERY, Cu powder was used as a promoter, forming CuI. However, for the reaction of 9,10-ANTH$(Ph)_2$ and reactions of hetero-PAHs at the temperature of 350 °C, Cu powder was not used because Cu powder caused substrate decomposition. In general, glass ampoule or Monel reaction vessels were used interchangeably, the notable exception being reactions for which Cu could not be used. All reactions were conducted at a temperature of 350 °C in order to favor formation of RD/A products, except in the case of 4,7-PHEN. For 4,7-PHEN, the reported reactions were conducted at 200 °C, due to the unusual selectivity observed at this temperature. For details of specific reactions, see appx B.2. For characterization of pure isolated products, see appx C.2.

2.2.1.b. Compounds derived from 4,7-PHEN

The hetero-PAH 4,7-Phenanthroline (4,7-PHEN) was prepared in 1947 by Haskelberg *et al.*[36] Its original synthesis by a double Skraup reaction has been modified such that yields of up to 75% are readily achievable.[37] Although less widely utilized than 1,10-phenathroline, there is interest in its derivatives, particularly with respect to medicinal and biological chemistry, as well as chromatography.[38, 39] Despite its more limited range of applications, 4,7-phenanthroline is

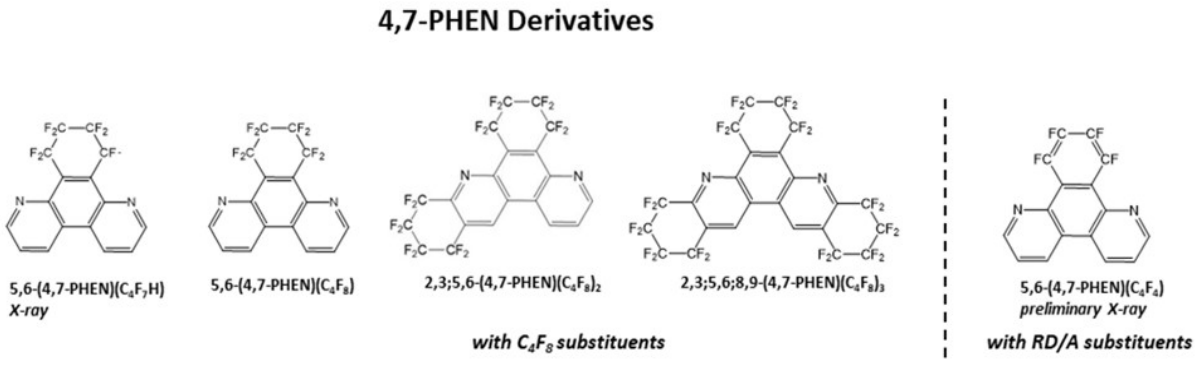

Figure 2-3. All 4,7-PHEN derivatives isolated in this work. For details of synthesis, see section 2.2.1.b. and appx B.2.1. and B.2.2. For full structural characterization of molecules, see appx. *C.2.1-C.2.5.*

interesting due to the fact that its reactivity is distinct from 1,10-phenanthroline. For example, 1,10-PHEN is subject to reduction preferentially upon the rings containing N atoms, reduction of 4,7-PHEN proceeds equally at all positions.[37] In the work reported here, the unique reactivity of 4,7-PHEN proved to be of great interest. Despite the relatively low symmetry of the molecule allowing for the possibility of three distinct isomers of 4,7-PHEN(C_4F_8), the reaction appears to be selective for substitution at the 5,6-position.

The 4,7-PHEN derivatives reported here were isolated from two reactions, reactions 2.1 and 2.2. They are shown in Figure 2-3. For details of these reactions, see appx B.2.1 and B.2.2. For full characterization of compounds, see appx *C.2.1-C.2.5*. These reactions were conducted at 200 °C, near the lower limit of homolytic cleavage of the C-I bond to form radicals, because it was noted that the unusually high selectivity was observed preferentially at these temperatures. Reaction 2.1 was conducted on a larger scale for isolation of a greater number of products. Interestingly, products bearing multiple substituents were prevalent despite the use of only 2 equiv. 1,4-$C_4F_8I_2$. It is possible that this resulted from partial decomposition of the starting material (resulting in an actual ratio of 1,4-$C_4F_8I_2$:4,7-PHEN greater than 2:1). This is consistent with the recovery of only 64 mg soluble product, despite using 100 mg 4,7-PHEN starting material. Reaction 2.2 was conducted on a smaller scale for isolated yield of 5,6-(4,7-PHEN)(C_4F_8), with only one equiv. 1,4-$C_4F_8I_2$. Nearly half (45%) of the recovered product was 5,6-(4,7-PHEN)(C_4F_8). The second most abundant product, 2,3;5,6-(4,7-PHEN)(C_4F_8)$_2$, is apparently a product of further reaction of 5,6-(4,7-PHEN)(C_4F_8). Notably, monosubstituted product 2,3-(4,7-PHEN)(C_4F_8) was not formed. The NMR spectra of the crude product mixture of reaction 2.2 is shown in Figure 2-4.

The observed selectivity is not consistent with the product distribution that would result from each C-H bond being equally likely to undergo radical substitution. Indeed, the 1,2 and 2,3 positions would statistically dominate in this case. Substitution at the 5 or 6 position would occur ¼ of the time. Initial substitution at the 1,2 and 2,3 positions would occur ¾ of the time. However, not only do these substation positions not dominate, but the products 2,3-(4,7-PHEN)(C_4F_8) and

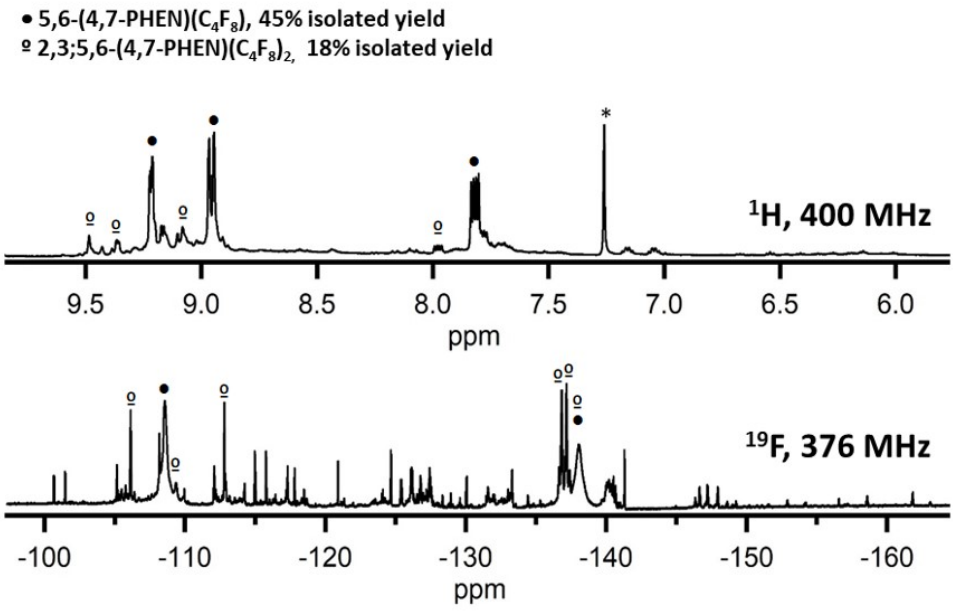

Figure 2-4. NMR spectra of product mixture resulting from reaction 2.2. ^{1}H NMR spectrum (top) referenced to $CHCl_3$ (δ = 7.26, denoted *). ^{19}F NMR spectrum (bottom) referenced to perfluorobenzene (δ = –164.9, not shown).

1,2-(4,7-PHEN)(C_4F_8) have not been observed at all. Therefore, it is likely that there is a directing effect toward substitution on the 5,6-positon.

Notably, it is not a directing effect caused by the lack of a heteroatom in the benzenoid ring. If the presence of an N atom disfavored substitution, the same trend toward substitution on the 5,6 position would hold for 1,10-PHEN, and it does not, as is shown below in section *2.2.1.c*. Therefore, it is likely that there is a specific preference for radical substitution upon C atoms across a fissure from N atoms. This is consistent with trends observed for the trifluoromethylation of PHNZ, in which the 1, 4, 6, and 9 positions, those across a fissure from an N atom are the most reactive.[5, 40]

At present, a satisfactory explanation for this phenomenon is not forthcoming. Reactivities of various positions on PAHs and hetero-PAHs are the subject of intensive study.[41] Often, reactivity is highly nuanced based on structure. For example, susceptibility toward various different types of reactions (*i.e.* nucleophilic vs. electrophilic) has been shown to be extremely positionally dependent in the case of some hetero-PAHs.[42-45] Generally, radicals of organic species

bearing strongly electron withdrawing groups are electrophilic in nature (although not to the extent that, for example, an F• would be.) It is therefore likely that radical addition occurs preferentially at sites more prone to electrophilic substitution.[5, 41, 46-49] In keeping with this, there is evidence in the literature to suggest that positions across a fissure from an N atom are active toward such electrophilic substitution.[43, 50] However, this explanation is not definitive, as fluoroalkyl radicals are not exclusively electrophilic. For example, perfluorobenzyl and trifluoromethyl radicals have both electrophilic and nucleophilic indices that fall in the mid-range compared to other radical species.[47] Further studies, such as computational studies of relative stabilities of different isomers, could help elucidate underlying reasons for the observed selectivity.

Another interesting facet of this reaction is the observation of a product functionalized with a C_4F_7H moiety. This is possibly a first reductive defluorination step in the process that would eventually lead to aromatization. The possibility that this moiety could result from a 1,4-$C_4F_7HI_2$ impurity in the starting material was considered. However, NMR spectra of the starting material did not indicate the presence of such an impurity (appx D.2.1).

In accordance with the prevalence of 5,6-(4,7-PHEN)(C_4F_8), the only RD/A product present in a large enough amount to isolate was 5,6-(4,7-PHEN)(C_4F_4). Attempts to optimize yields of this product through modification of reaction time, temperature, and amount of Cu powder were unsuccessful. However, it is noteworthy that RD/A occurred at the low temperature of 200 °C in the presence of Cu powder, much lower than RD/A was observed for TRPH. This is possibly due to the ease of reduction of this hetero-PAH, attributable to the presence of N-atoms.[10]

For reactions 2.1 and 2.2, acetonitrile was a suitable eluent for purification of crude material on a Cosmosil Buckyprep column. Although methanol results in greater product separation for hetero-PAHs,(albeit with longer retention times) the selectivity of this reaction resulted in only a few products, so that the somewhat smaller degree of separation afforded by acetonitrile was sufficient for purification.

General NMR spectroscopic trends for the different types of fluorous groups, discussed in chapter 1 hold true for most 4,7-PHEN derivatives with respect to chemical shifts and coupling.

The spectrum of 5,6-(4,7-PHEN)(C_4F_7H) is notable for the interesting 'peak doubling' observed, as a result of broken symmetry. Also, for this compound, a peak is present in the ^{19}F spectrum that is far more shielded than any peaks observed previously, likely due to the fact that is bound to a C atom which is neither part of an aromatic system, nor bound to other F atoms. (appx *C.2.5*).

Additionally, a unique feature of hetero-PAH ^{19}F NMR spectra of some compounds, including several of the 4,7-PHEN derivatives, is that when F atoms are attached to C atoms vicinal to N atoms, broad signals are observed. An example is shown in Figure 2-5, for the compound 2,3;5,6-(4,7-PHEN)(C_4F_8)$_2$. It is possible that the peak broadening is due to indirect quadripolar scalar relaxation between the ^{19}F and ^{14}N nuclei, analogous to quadripolar ^{13}C and ^{14}N coupling,[51, 52] but no reports of such were found in the literature. Another possibility is that it is simply broad unresolved coupling. Further spectroscopic studies could resolve this question.

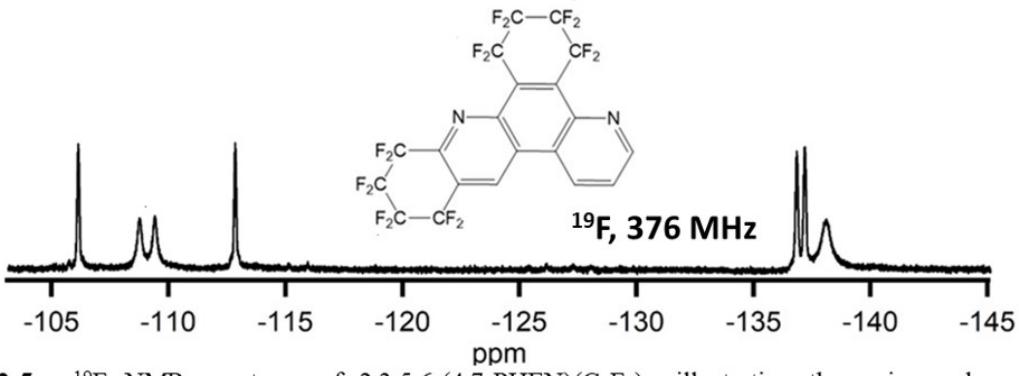

Figure 2-5. ^{19}F NMR spectrum of 2,3;5,6-(4,7-PHEN)(C_4F_8)$_2$, illustrating the unique observed peak broadening for substituents at the 5,6 position.

2.2.1.c. Compounds derived from 1,10-PHEN

1,10-Phenananthroline (1,10-PHEN), is a classic ligand in coordination chemistry, with a broad range of applications due to the versatility of its metal ion binding and interesting properties, of its complexes.[15, 37] With regard to organic electronic applications, it has luminescent properties, making it interesting for development of OLED materials.[19, 20, 22, 24] Similar to 4,7-PHEN, it is synthesized by heating *o*-phenylenediamine or 8-aminoquinoline with glycerol, H_2SO_4, and nitrobenzene, and is readily commercially available.[37]

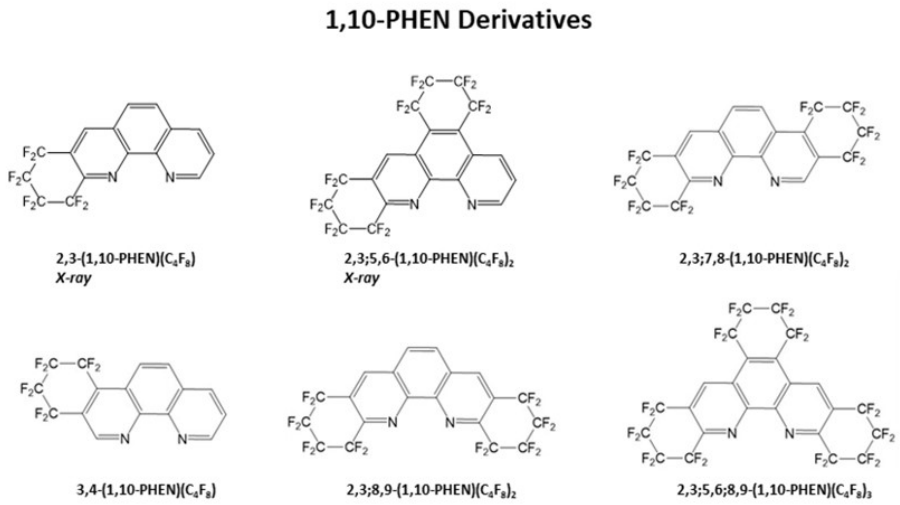

Figure 2-6. All 1,10-PHEN derivatives isolated in this work. For details of synthesis, see section 2.2.1.c. and appx B.2.3. For full structural characterization of molecules, see appx. *C.2.6-C.2.11*.

The reaction to generate 1,10-PHEN derivatives, reaction 2.3, did not display a similarly high selectivity to the 4,7-PHEN reaction, despite the similarities in their structures and use of similar conditions. Therefore, a larger number of products were identified and isolated in lower yield. They are shown in Figure 2-6. For full characterization, see appx C.2.6-C.2.11.

Possibly due to the large number of products and low yield of each product, no pure RD/A products could be isolated from this reaction. Assuming a low yield of RD/A from every C_4F_8 compound formed compounding the already low yields, it is reasonable to expect that amounts of any given RD/A product would be only trace amounts, and therefore not isolable. Additionally, the presence of many products complicated HPLC separation, such that even if RD/A products were formed, they may not be readily isolated in pure form. Were such products desired, it would perhaps be advisable to synthesize and purify multi-milligram quantities of pure C_4F_8 products and heat them, causing them to undergo RD/A in a second step.

Due to the larger number of products produced by this reaction, using acetonitrile as an eluent alone was not sufficient for separation of pure compounds. methanol:acetonitrile mixtures worked well. A 1:2 methanol:acetonitrile mixed eluent increased retention times sufficiently to

allow isolation of most compounds. A 1:1 mixture of methanol:toluene also gave good separation but did not yield as many pure products as the methanol-acetonitrile mixture. It did, however, allow isolation of one product that the primary method did not, namely 2,3;8,9-(1,10-PHEN)(C_4F_8)$_2$.

Similar to the 4,7-PHEN derivatives, ^{19}F NMR spectra showed peak broadening in some cases. However, the phenomenon was not consistent. For example, 2,3;5,6-(1,10-PHEN)(C_4F_8)$_2$ gives broad ^{19}F peaks, but 2,3-(1,10-PHEN)(C_4F_8) does not.

Due to the large body of literature concerning the use of 1,10-PHEN as a ligand in coordination chemistry, particularly in OLED devices,[19-22, 53] preliminary attempts were made to synthesize Cu-metal based complexes with the pure 1,10-PHEN derivatives isolated in this research via ligand exchange. A color change was observed from yellow to strawberry pink, and a weak absorption band at *ca.* 500 nm (appx D.2.2). indicated at least partial formation of compound. However, analysis by NMR was inconclusive due to low amounts of material. Additionally, for asymmetric substrates such as 2,3;5,6-(4,7-PHEN)(C_4F_8)$_2$, multiple stereoisomers are possible, further complicating analysis. However, if reaction conditions were optimized and compounds became available in larger amounts, preliminary results indicate that complex formation could be an interesting topic for further study.

2.2.1.d. Compounds derived from for 5-PHRD

The compound 5-phenanthridine (5-PHRD) is synthesized through a variety of cyclization-based methods.[54] It is most widely utilized in biological applications, for its ability to intercalate

into DNA.[55] Reaction 2.4, the reaction of 5-PHRD and 1,4-$C_4F_8I_2$ produced, as expected based on the low symmetry of the substrate, a large number of products.[56] Due to the complex product mixture, yields of purified compounds were low and separation was difficult. However, moderate

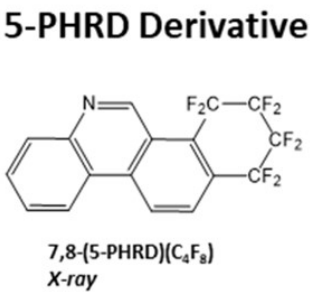

Figure 2-7. One 5-PHRD derivative was isolated and definitively structurally characterized in this work. A second isomer was also isolated in high purity but its structure could not be definitively elucidated. For details of synthesis, see section 2.2.1.d. and appx B.2.4. For full structural characterization of 5-PHRD derivatives, see appx. *C.2.12-C.2.13*.

separation was achieved in acetonitrile. An alternative eluent, methanol was tested also, and a peak resolution was achieved, but at the expense of longer retention times. However, this would be a viable method to explore further if particular derivatives from the crude product are desired in pure form.

Given the limitations of purification, only two pure products were identified. One is shown in Figure 2-7, which was confirmed by single crystal X-ray crystallography. For the other pure compound, a structure could not be definitively assigned by on NMR spectra alone.

2.2.1.e. Compounds derived from ACRD

Acridine is a linear fused N-hetero-PAH. It is analogous to the PAH anthracene (ANTH) with an N-atom in the 10 position. It is commonly synthesized through a number of convenient coupling reactions, and as a substrate, its reactivity has been widely explored.[57, 58] ACRD is used for a variety of applications including dyes and as an antiseptic.[27, 43, 50, 57-60] Among the substrates investigated in this chapter, ACRD was one of three compounds for which EA studies could be found in the literature (the other two being pyrene, *2.2.1.g*, and perylene, *2.2.1.h*). According to

these studies ACRD has an EA of 0.91 eV.[61] The presence of single heteroatom therefore gives the EA of ACRD a substantial increase over the EA of ANTH, 0.53 eV, making it of interest for the electron accepting applications targeted in this work.[62]

Given the observed propensity of PHNZ[40] and 4,7-PHEN (*2.2.1.a*) to undergo radical substitution on the position across a fissure from an N atom it was predicted that the reaction of ACRD and 1,4-$C_4F_8I_2$ would show some selectivity for substitution at the 3,4 and 5,6 positions. However, the reaction, reaction 2.5, was not selective. By NMR spectroscopy it appeared that the crude product mixture contained only a few isomers. (appx figure B-23). However, upon HPLC separation using and eluent of 2:1 methanol:acetonitrile, six different pure ACRD derivatives were isolated, and other fractions containing mixtures of many other ACRD derivatives were observed. It is likely that substantial peak overlap and poor baseline resolution of the NMR spectra precluded observation of the true number of products in the NMR spectra of the crude product mixture.

Of the six pure ACRD derivatives isolated, the structures of only three of them were definitively elucidated, shown in Figure 2-9. Interestingly, the RD/A moiety is present upon two pure compounds, 1,2-ACRD(C_4F_3H) and ACRD(C_4F_3H)-B, despite the fact that no C_4F_4 moieties are observed. As product distribution of high temperature reaction is often thermodynamic, it is

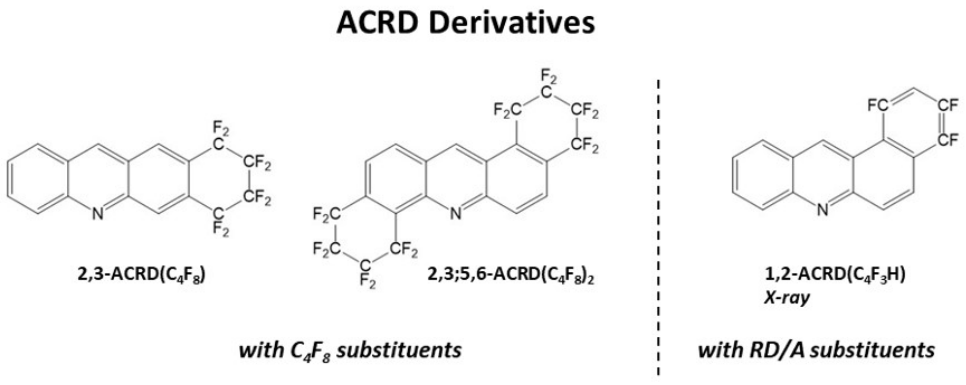

Figure 2-9. All ACRD derivatives isolated in this work that could be definitively structurally characterized. For details of synthesis, see section 2.2.1.e and appx B.2.5. For full structural characterization of these molecules, as well as other compounds for which definitive structures have not been assigned, see appx. *C.2.14-C.2.19*.

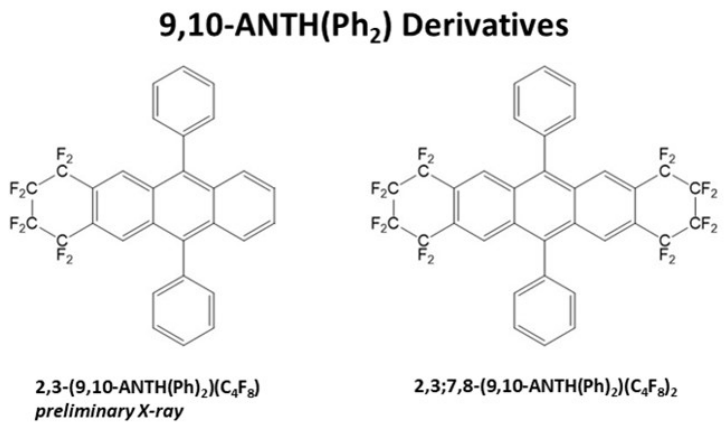

Figure 2-10. All 9,10-ANTH(Ph)$_2$ derivatives isolated in this work. For details of synthesis, see section 2.2.1.f and appx B.2.6. For full structural characterization of these molecules, see appx. *C.2.20-C.2.21*.

possible based on this result that the C_4F_3H moiety is particularly stable, although DFT studies would be necessary to further investigate this possibility. [56]

Also noteworthy among the products in this family is 2,3-ACRD(C_4F_8). Substitution at this position is particularly interesting, because the RD/A product substituted at this position, (which could presumably be obtained by treatment of pure 2,3-ACRD(C_4F_8) with Cu powder at high temperature despite the fact that it was not itself isolated in this reaction) would be a N-heteroacene, partially fluorinated tetracene analog. Tetracene is a champion p-type material for organic electronics.[8, 63, 64] These modifications would make it an n-type material, while still likely exhibiting favorable properties such as good charge transport.[8]

2.2.1.f. Compounds derived from 9,10-ANTH(Ph)$_2$

The compound 9,10-diphenylantrhacene (9,10-ANTH(Ph)$_2$), which can be readily synthesized from anthraquinone, demonstrates high electron (ca. 13 $cm^2\ Vs^{-1}$) and hole transport (ca. 3.7 $cm^2\ Vs^{-1}$) in organic semiconductor crystals, and has photophysical properties that make it a promising building block for fluorescent applications in organic electronics.[65-68] However, it is generally regarded as an electron donor, so modifying its properties to make it electron accepting could lead to the n-type semiconducting material.[67]

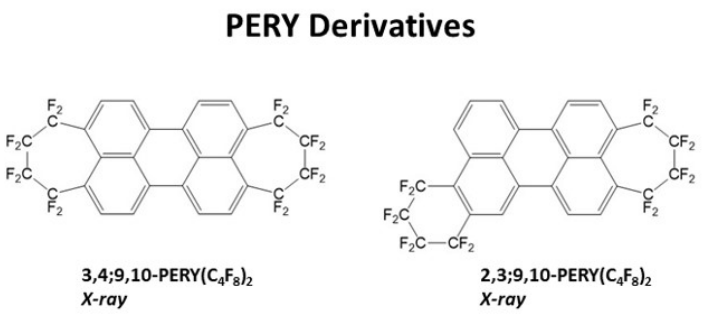

Figure 2-11. All PERY derivatives isolated in this work. For details of synthesis, see section 2.2.1.g and appx B.2.7. For full structural characterization of these molecules, see appx. *C.2.22-C.2.23*.

As a substrate for the reaction of interest here, 9,10-ANTH(Ph)$_2$ was unique due to its two phenyl rings on the 9 and 10 positions. It was predicted that (i) the phenyl rings would be bulky enough to preclude substitution at the 1,4,5, and 8 positions, and (ii) substitution would occur preferentially upon the ANTH core rather than on the phenyl group themselves, due to their smaller conjugated systems.[4] These predictions were validated by the experimental results. The ^{19}F NMR spectrum of the crude product mixture (appx figure B-25) of reaction 2.6, the reaction of 9,10-ANTH(Ph)$_2$ and 1,4-$C_4F_8I_2$ shows that a limited number of cyclic products formed, though it also shows evidence of additional products bearing C_4F_8H functionalized species. However, products bearing C_4F_8H compounds have sufficiently distinct properties to be readily separated from cyclic products by HPLC, and separation of these species proved readily achievable using an eluent of 2:1 methanol:acetonitrile. The resulting two products, shown in Figure 2-10, are the products predicted based upon (i) and (ii). No products of RD/A were identified. It is possible that the use of Cu powder would promote formation of RD/A products, although it was avoided in reaction 2.6 due to stability concerns.[69]

2.2.1.g. Compounds derived from PERY

The PAH perylene (PERY), which demonstrates excellent fluorescent properties, has a wide range of applications in organic electronics.[70] It is particularly useful as a dye and a photoconductor.[13, 14, 70-76] It has an EA of 0.97, which is high for an all-C atom PAH.[74]

Reaction of this substrate with 1,4-$C_4F_8I_2$, reaction 2.8 (appx B.2.8) appeared to yield two main products based on NMR spectroscopy of the crude reaction product. Indeed, upon separation by HPLC in 2:1 methanol:acetonitrile, two pure products were identified, shown in Figure 2-11. These products both demonstrated strong orange/yellow fluorescence, even fluorescing visibly in direct sunlight, which is promising for fluorescence-based applications. Isolated yields were not obtained, as separation focused on purity rather than maximum product recovered. When half of the crude product mixture (half of 65 mg, *ca.* 32 mg) was separated, the products were each obtained in mutlimilligram amounts (5 and 8 mg). Therefore, it seems that obtaining these products in relatively large amounts would be facile.

The NMR spectra of these products were difficult to interpret until single crystal X-ray structure were obtained, revealing that for the first time on a planar PAH substrate, 7-membered rings had formed. Seven-membered ring formation by substitution of C_4F_8 across a fissure on corannulene, a bowl shaped PAH, was previously reported by Kuvychko *et al*.[35] . Due to the bond angle associated with this bowl shape, 7-membered rings do not induce as much strain on corannulene as they would on a planar system. In the case of PERY derivatives, this strain can induce a twist to the PERY core, which is evident in the crystal structure of 3,4-9,10-PERY$(C_4F_8)_2$, analyzed below in section 2.2.2.

Aside from the surprising formation of 7-membered rings on a planar PAH, the predominance of these two reaction products is not surprising. The 3, 4, 9, and 10 positions are known to the be most reactive positions, and must be functionalized to create sufficiently stable materials for commercial applications, as exemplified by the widespread use of perylene diimides.[77] Functionalization of these reactive positions with fluorous groups not only increases stability, but has the additional advantage of altering the electronic properties of the substrate, making the compounds reported promising for a wide variety of applications.

PYRN Derivative

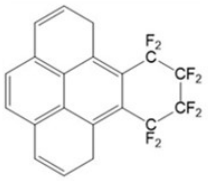

4,5-PYRN(C_4F_8)
X-ray

Figure 2-12. One PYRN derivative was isolated in this work. For details of synthesis, see section 2.2.1.h and appx B.2.8. For structural characterization, see appx. *C.2.24*

2.2.1.h. Compound derived from PYRN

The compound pyrene (PYRN) has an EA of 0.46, and is therefore not a particularly promising candidate as an electron acceptor material.[78] Due to its photophysical and electronic properties, this PAH substrate is useful for electronic applications such as OFETs, OLED, and supramolecular photosensors.[79] It is also valuable for biological chemistry.[12, 79] However, its applications have historically been limited by the relatively narrow range of methods and outcomes for methods for direct substitution and complexity of indirect methods for substitution.[6, 72, 78-82]

The reaction 4.7 (appx B.2.7) with the substrate PYRN produced, many compounds substituted with C_4F_8H moieties, as

well as other products, based on NMR spectroscopy of the crude product mixture. However, a suitable HPLC method was not found to give products of high purity. This difficulty notwithstanding, a pure single crystal crystallized out of an impure solution, and therefore one PYRN derivative, shown in Figure 2-12, was isolated.

2.2.1.i. Substrates which yielded no isolable products

Three additional substrates were investigated which yielded soluble crude product that, when analyzed by NMR spectroscopy, appeared to contain products functionalized with fluorous moieties. These results are shown in appx. D.2.3. For anthracene (ANTH), C_4F_8H moieties appeared to dominate, consistent with reaction primarily at the 9 and 10 positions, which cannot

annulate to form 6 membered rings. For rubrene (RUBR) and bathophenanthroline, despite the apparent formation of a relatively small number of products which appeared to bear C_4F_8 rings, HPLC separation was unsuccessful due to excessive streaking of products on the column.

For the final three substrates evaluated in this work, decompositions occurred. In the case of neocuprouine (NECU), this decomposition is likely due to the sp^3 hybridized C atoms on the methyl groups decomposing under reaction conditions. For phenothiazine (PTNZ), the unique nature of the central ring, bearing an S atom and a protonated N atom is the likely reason for decomposition. After reaction, a char that smelled strongly of sulfur was observed. The final substrate, TCNQ, is not technically polycyclic, although it has a widely delocalized π-system. However, it is likely that, like phenyl groups, it is not prone to radical substitution.

2.2.2. Single crystal X-ray structures

2.2.2.a. General comments on single crystal X-ray structures.

In the course of this work, 8 new crystal structures were obtained, shown in Figure 2-13. Details of these structures can be found in appx D.2.4. Additionally, two preliminary structures, pictured in Figure 2-14, were obtained.

Analysis of these crystal structures yielded several interesting insights. Most compounds crystallized into stacks demonstrate increased π overlap as compared to the herringbone pattern of unfunctionalized PAHs. These stacks were generally arranged in a hexagonal array, with the molecules of adjacent stacks usually tilted with respect to one another, sometimes by more than 70 º, but also sometimes coplanar. The intermolecular for molecules within the same stack (OOP_{av}) ranged from an average of 3.37 in the case of the fully aromatic 1,2-ACRD(C_4F_3H) to over 4 Å in the case of 2,3;6,7-ANTH$(Ph)_2(C_4F_8)$ with its bulky phenyl groups.

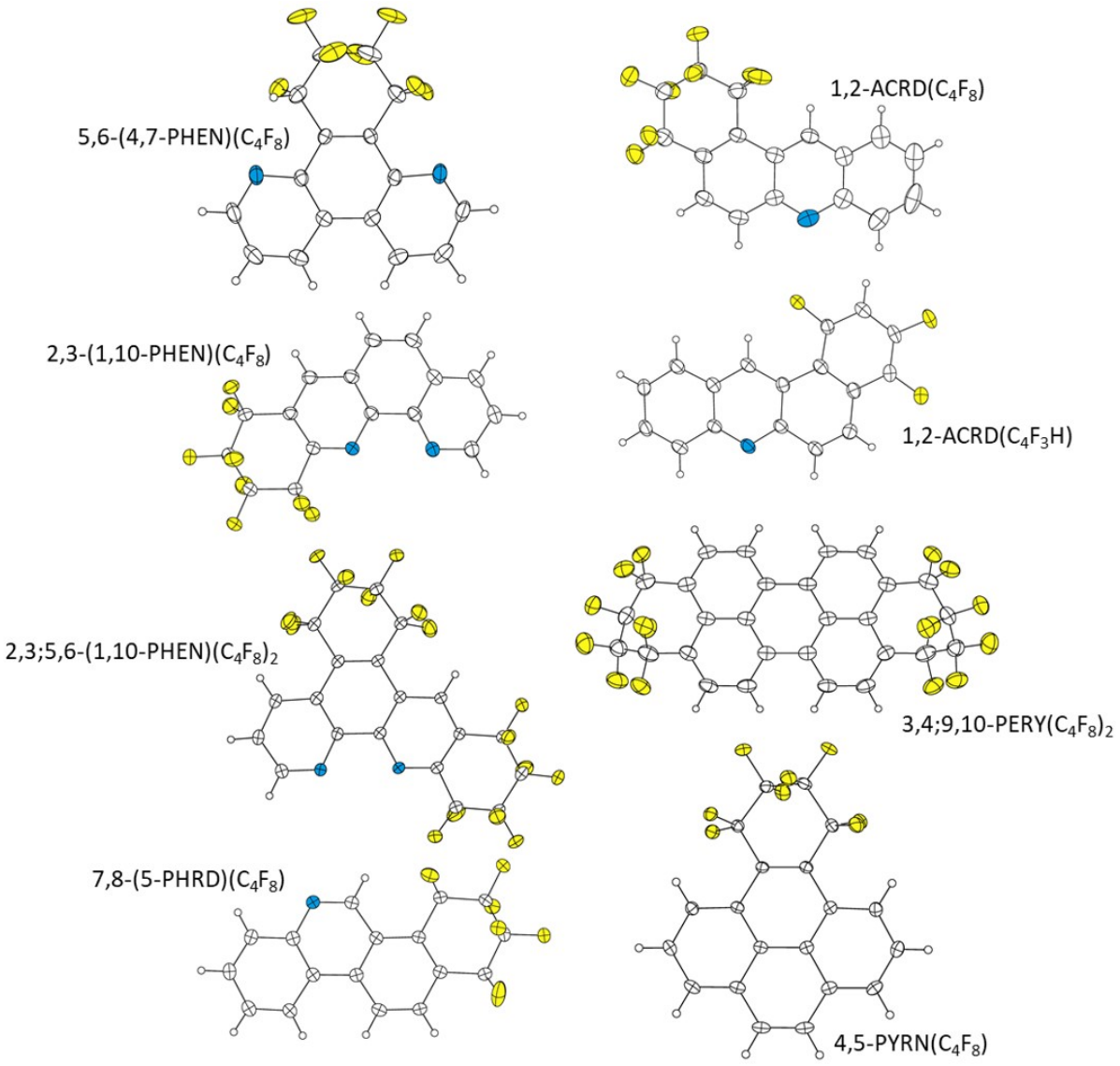

Figure 2-13. Thermal ellipsoid drawings of the eight single crystal x-ray structures obtained in the course ofthis work (thermal ellipsoids shown at the 50% probability level; all H atoms shown as spheres of arbitrary size).

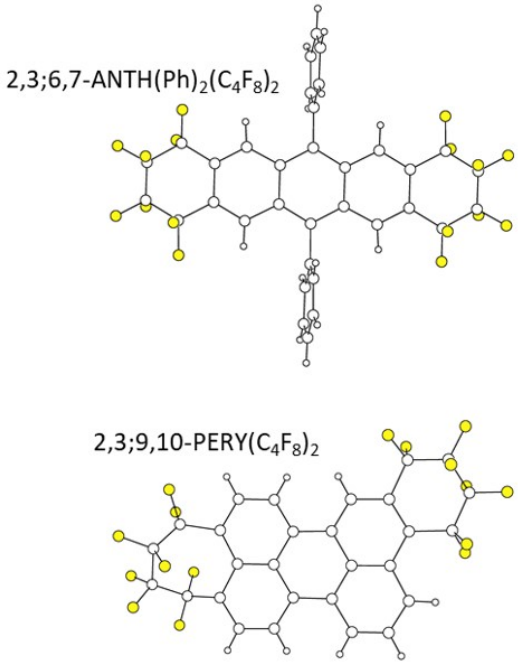

Figure 2-14. Drawings of the two compounds reported in this work for which preliminary single crystal X-ray structures were obtained.

An interesting comparison may be drawn between the behavior of TRPH derivatives functionalized with C_4F_8 vs C_4F_3H moieties, reported in the last chapter, and ACRD derivatives functionalized with these same substituents. As can be observed in Figure 2.15, the same patterns are observed. Overlap of the fluorous moiety is observed in the fully aromatic case, whereas in the case of C_4F_8 groups, only the substrate cores overlap.

Analysis of the 9,10-ANTH$(Ph)_2$ derivative is also interesting, as it manages to pack with good alignment of the aromatic core despite large intermolecular distances necessitated by the bulky substituents. The quality of the structure is not sufficient to establish packing distances to a high degree of accuracy, but it is clear the distances are over 4 Å, so it is surprising that the interaction was still sufficient to result in columnar, rather than herringbone stacking.

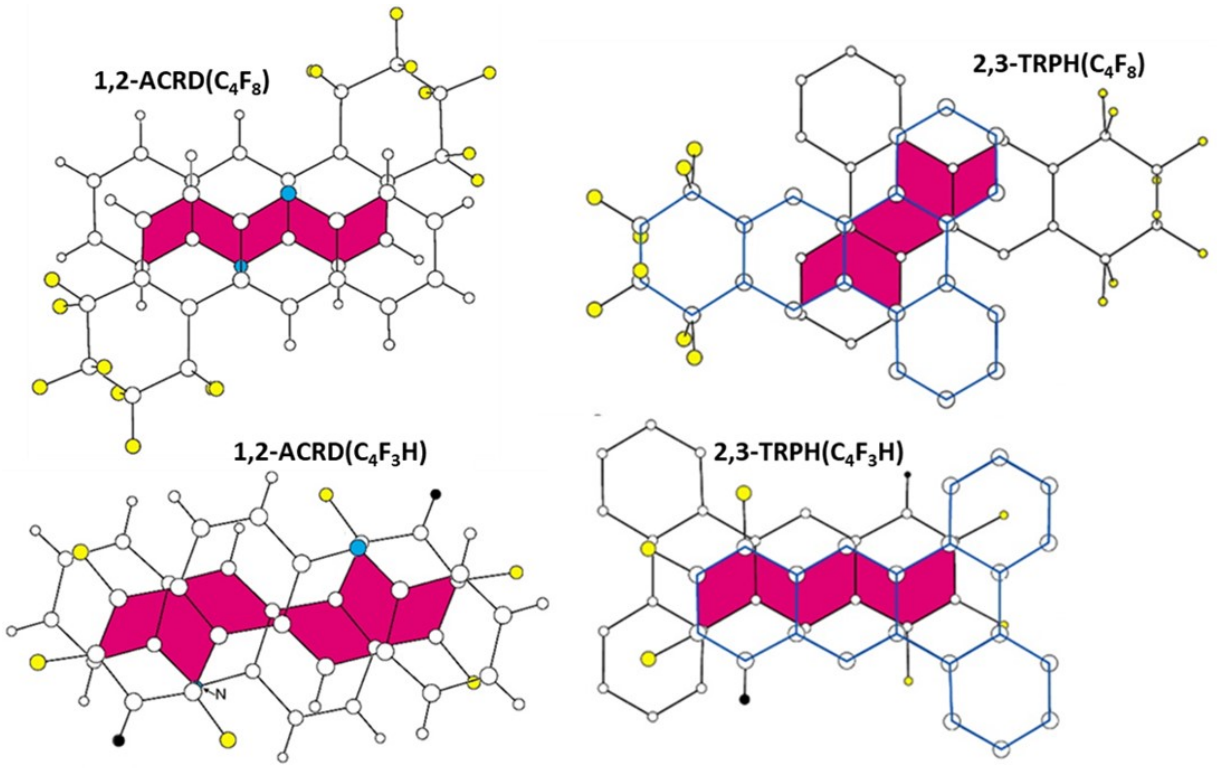

Figure 2-15. Drawings of the overlap of the π systems (overlap highlighted) of both TRPH and ACRD derivatives bearing C_4F_8 and C_4F_3H moieties. Note that in both cases, C_4F_8 moieties do not overlap the π systems of adjacent molecules, but C_4F_3H moieties do.

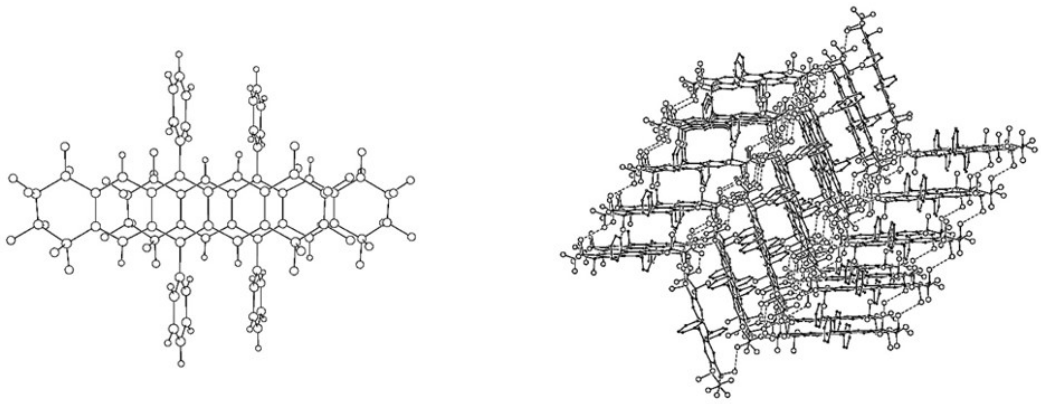

Figure 2-16. Despite the bulky phenyl groups on the 9,10-ANTH($Ph)_2$ derivative, it still stacks in columns with ANTH aromatic cores aligned with one another (left). However, intermolecular distances are large (well over 4 Å), and columns are tilted with respect to one another (right).

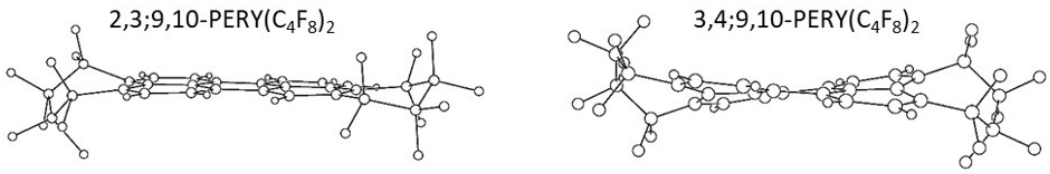

Figure 2-17. Upon substitution at the 3,4 and 9,10 positions of PERY, significant twisting of the aromatic core is observed (right). This is not the case for substitution at the 2,3 and 9,10 positions, as the aromatic core remains planar.

Finally, analysis of the single crystal X-ray structures of PERY derivatives is interesting, primarily in terms of core planarity. Figure 2-17 depicts a side-on view of the 2 single crystal structures of PERY derivatives. It clearly illustrates that in the case of 2,4;9,10-PERY(C_4F_8)$_2$, which has two 7-membered rings formed by the C_4F_8 substitutions across fissures, a substantial bend to the PAH core is necessitated. This does not hold true in the case of 2,3;9,10-PERY(c_4F_8)$_2$, despite the fact that it also bears a 7 membered ring.

2.2.3. Gas phase EA of selected compounds

2.2.3.a. General comments EA values

In order to probe the effect of these substituents on the electronic levels of a variety of substrates, gas phase EA studies were carried out on a selection of the compounds here, as they were for TRPH derivatives in chapter 1.

Measurements were performed by Dr. Xue-Bin Wang at Pacific Northwest National Laboratory. An illustration of the PES spectra obtained for one family of compounds, 1,10-PHEN derivatives, is shown in Figure 2-18. The values for all compounds studied are summarized in Figure 2-19. For further details of gas phase EA measurements, see appx *A.4.8.* and appx D.2.5 for additional PES spectra.

As can be seen in Figure 2-18 and 2-19, the effect of addition of C_4F_8 moieties is roughly linear and incremental. Interestingly, the perfluoroalkyl C_4F_8 moieties have a larger impact upon EA values of these substrates than they did upon TRPH derivatives reported in chapter 1.

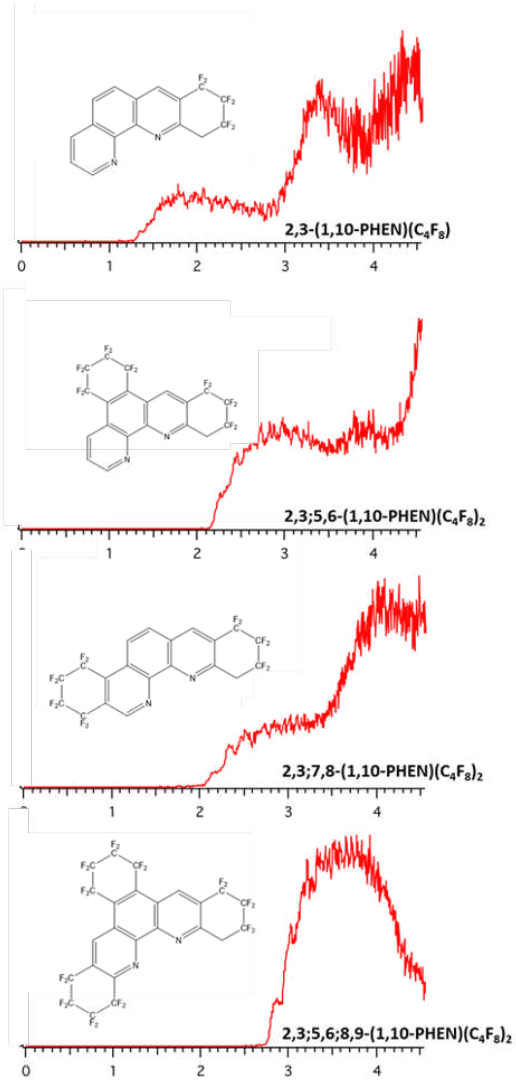

Figure 2-18. Low-temperature photoelectron spectra (20 K, 266 nm) for a series of 1,10-PHEN derivatives. A substantial shift of *c.a.* 0.75 eV per C_4F_8 moiety is observed.

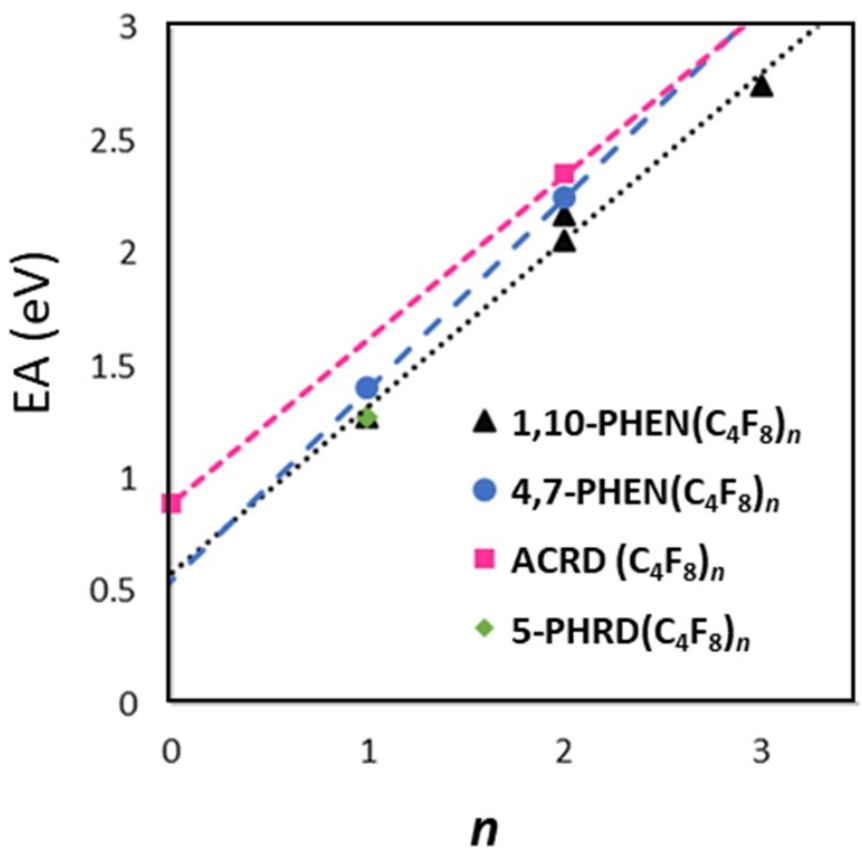

Figure 2-19. Gas phase EA data for selected compounds reported in this work. Interestingly, the effect of each C_4F_8 moiety appears to be greater for these substrates (0.73 eV per group for ACRD to 0.85 eV per group for 4,7-PHEN) than for TRPH. ACRD EA from ref [1].

Therefore, for the substrates reported here, there is an even more substantial increase per fluorous substituent as compared to trifluoromethyl groups reported in the literature.[83] In fact, a single substituent seems to have the impact of three to four trifluoromethyl groups.

Figure 2-19 additionally illustrates that the incremental effect of each C_4F_8 substituent is somewhat substrate dependent for the compound investigated here For example, the incremental increase per C_4F_8 group is significantly greater for 4,7-PHEN derivatives, which exhibit an average increase of 0.85 eV per additional group, than for ACRD and 1,10-PHEN derivatives, for which the average incremental increases are 0.73 eV and 0.74 eV, respectively.

2.3. SUMMARY AND CONCLUSIONS

The results described here demonstrate the synthetic method developed in this work (see chapter 1), coupled with individualized HPLC purification methods, can be used with a wide variety of PAH and N-hetero-PAH substrates. These compounds demonstrate interesting physical properties and are useful in fundamental studies of the correlations between molecular composition/structure and physicochemical properties. Many of these reactions could be further optimized to generate sufficient material for a wide variety of organic electronic applications not limited to organic electron acceptor materials. For example, 1,10-PHEN derivatives have been shown through preliminary studies to have potential as air stable emitters for OLED devices,[15-21, 31] and PERY derivatives could be used to make highly stable fluorescent dyes and dyes for LCD based electronics[14].[13] Other compounds discussed here also have potential applications in the fields of biology, medicine, and organic synthesis.[15, 31, 43, 55]

REFERENCES

1. Dillow, G. W.; Kebarle, P., Electron affinities of aza-substituted polycyclic aromatic hydrocarbons. *Can. J. Chem.* **1989,** *67* (10), 1628-1631.
2. Ando, N.; Mitsui, M.; Nakajima, A., Comprehensive photoelectron spectroscopic study of anionic clusters of anthracene and its alkyl derivatives: Electronic structures bridging molecules to bulk. *Can. J. Chem.* **2007,** *127* (23), 234305.
3. Kuvychko, I. V.; Castro, K. P.; Deng, S. H. M.; Wang, X.-B.; Strauss, S. H.; Boltalina, O. V., Taming Hot CF3 Radicals: Incrementally Tuned Families of Polyarene Electron Acceptors for Air-Stable Molecular Optoelectronics. *Angew. Chem.* **2013,** *52* (18), 4871-4874.
4. Watson, M. D.; Fechtenkötter, A.; Müllen, K., Big Is Beautiful−"Aromaticity" Revisited from the Viewpoint of Macromolecular and Supramolecular Benzene Chemistry. *Chem. Rev.* **2001,** *101* (5), 1267-1300.
5. Robins, K. A.; Jang, K.; Cao, B.; Lee, D.-C., Tuning the electronic properties of phenazine and bisphenazine derivatives: a theoretical and experimental investigation. *Phys. Chem. Chem. Phys.* **2010,** *12* (39), 12727-12733.
6. Hu, B.-L.; Zhang, K.; An, C.; Schollmeyer, D.; Pisula, W.; Baumgarten, M., Layered Thiadiazoloquinoxaline-Containing Long Pyrene-Fused N-Heteroacenes. **2018,** *57* (38), 12375-12379.
7. Kabanda, M.; Murulana, L.; Ebenso, E., *Theoretical Studies on Phenazine and Related Compounds as Corrosion Inhibitors for Mild Steel in Sulphuric Acid Medium*. 2012; Vol. 7, p 7179–7205.
8. Lehnherr, D.; Alzola, J. M.; Mulzer, C. R.; Hein, S. J.; Dichtel, W. R., Diazatetracenes Derived from the Benzannulation of Acetylenes: Electronic Tuning via Substituent Effects and External Stimuli. *J. Org. Chem.* **2017,** *82* (4), 2004-2010.
9. Bunz, U. H. F., The Larger Linear N-Heteroacenes. *Acc. Chem. Res.* **2015,** *48* (6), 1676-1686.
10. Appleton, A. L.; Brombosz, S. M.; Barlow, S.; Sears, J. S.; Bredas, J.-L.; Marder, S. R.; Bunz, U. H. F., Effects of electronegative substitution on the optical and electronic properties of acenes and diazaacenes. *Nat Commun.* **2010,** *1*, 91.
11. Anthony, J. E., Functionalized Acenes and Heteroacenes for Organic Electronics. *Chem. Rev.* **2006,** *106* (12), 5028-5048.
12. Alves, C. A.; Vicente, A. M.; Custódio, D.; Cerqueira, M.; Nunes, T.; Pio, C.; Lucarelli, F.; Calzolai, G.; Nava, S.; Diapouli, E.; Eleftheriadis, K.; Querol, X.; Musa Bandowe, B. A., Polycyclic aromatic hydrocarbons and their derivatives (nitro-PAHs, oxygenated PAHs, and azaarenes) in PM2.5 from Southern European cities. *Science of The Total Environment* **2017,** *595*, 494-504.
13. Choi, J.; Sakong, C.; Choi, J.-H.; Yoon, C.; Kim, J. P., Synthesis and characterization of some perylene dyes for dye-based LCD color filters. *Dyes and Pigments* **2011,** *90* (1), 82-88.
14. Nowak-Król, A.; Würthner, F., Progress in the synthesis of perylene bisimide dyes. *Org. Chem. Front.* **2019,** *6* (8), 1272-1318.
15. Bencini, A.; Lippolis, V., 1,10-Phenanthroline: A versatile building block for the construction of ligands for various purposes. *Coord. Chem. Rev.* **2010,** *254* (17), 2096-2180.
16. Collings, J. C.; Batsanov, A. S.; Howard, J. A. K.; Marder, T. B., Arene–perfluoroarene interactions in crystal engineering. Part 14. 1:1 Complexes of octafluoronaphthalene with fluorene and 9,10-dihydrophenanthrene. *Can. J. Chem.* **2006,** *84*, 238–242.
17. Collings, J. C.; Roscoe, K. P.; Robins, E. G.; Batsanov, A. S.; Stimson, L. M.; Howard, J. A. K.; Clark, S. J.; Marder, T. B., Arene-perfluoroarene interactions in crystal engineering 8: structures of 1 : 1 complexes of hexafluorobenzene with fused-ring polyaromatic hydrocarbons. *New J. Chem.* **2002,** *26* (12), 1740–1746.
18. Collings, J. C.; Roscoe, K. P.; Thomas, R. L.; Batsanov, A. S.; Stimson, L. M.; Howard, J. A. K.; Marder, T. B., Arene-Perfluoroarene Interactions in Crystal Engineering. Part 3. Single-Crystal

Structures of 1:1 Complexes of Octafluoronaphthalene with Fused-Ring Polyaromatic Hydrocarbons. *New J. Chem.* **2001,** *25* (11), 1410–1417.
19. Elie, M.; Sguerra, F.; Di Meo, F.; Weber, M. D.; Marion, R.; Grimault, A.; Lohier, J.-F.; Stallivieri, A.; Brosseau, A.; Pansu, R. B.; Renaud, J.-L.; Linares, M.; Hamel, M.; Costa, R. D.; Gaillard, S., Designing NHC–Copper(I) Dipyridylamine Complexes for Blue Light-Emitting Electrochemical Cells. *ACS Appl. Mat. & Interfac.* **2016,** *8* (23), 14678-14691.
20. Hashimoto, M.; Igawa, S.; Yashima, M.; Kawata, I.; Hoshino, M.; Osawa, M., Highly Efficient Green Organic Light-Emitting Diodes Containing Luminescent Three-Coordinate Copper(I) Complexes. *J. Am. Chem. Soc.* **2011,** *133* (27), 10348-10351.
21. Igawa, S.; Hashimoto, M.; Kawata, I.; Yashima, M.; Hoshino, M.; Osawa, M., Highly efficient green organic light-emitting diodes containing luminescent tetrahedral copper(i) complexes. *J. Mat. Chem. C* **2013,** *1* (3), 542-551.
22. Lin, S.; Fan, W.; Wang, G.; Cui, Y.; Liu, J.; Shi, L.; Li, Z.; Jin, Q.; Yang, Y.; Zhang, Z.; Liu, Y., Structures and photophysical properties of copper(I) complexes bearing 1,10-phenanthroline and 1,3-bis(diphenylphosphino)propane. **2017,** *47* (1674-7224), 757.
23. Liu, H.; Yang, W.; Zhou, W.; Xu, Y.; Xie, J.; Li, M., Crystal structures and antimicrobial activities of copper(II) complexes of fluorine-containing thioureido ligands. *Inorg. Chim. Acta.* **2013,** *405*, 387-394.
24. Skórka, Ł.; Filapek, M.; Zur, L.; Małecki, J. G.; Pisarski, W.; Olejnik, M.; Danikiewicz, W.; Krompiec, S., Highly Phosphorescent Cyclometalated Iridium(III) Complexes for Optoelectronic Applications: Fine Tuning of the Emission Wavelength through Ancillary Ligands. *J. Phys. Chem. C* **2016,** *120* (13), 7284-7294.
25. Shi, Y.-M.; Brachmann, A. O.; Westphalen, M. A.; Neubacher, N.; Tobias, N. J.; Bode, H. B., Dual phenazine gene clusters enable diversification during biosynthesis. *Nature Chem. Bio.* **2019,** *15* (4), 331-339.
26. Laursen, J. B.; Nielsen, J., Phenazine Natural Products: Biosynthesis, Synthetic Analogues, and Biological Activity. *Chem. Rev.* **2004,** *104* (3), 1663-1686.
27. MARTIN, G. J., ACRIDINE ANTISEPTICS: A REVIEW. *Medicine* **1944,** *23* (1), 79-103.
28. Tommasini, M.; Lucotti, A.; Alfè, M.; Ciajolo, A.; Zerbi, G., Fingerprints of polycyclic aromatic hydrocarbons (PAHs) in infrared absorption spectroscopy. *Spectrochim. Acta. A.* **2016,** *152*, 134-148.
29. *Polycyclic Aromatic Hydrocarbons and Astrophysics*. Springer Netherlands 1987; Vol. 191.
30. Tielens, A. G. G. M., Interstellar Polycyclic Aromatic Hydrocarbon Molecules. *Ann. Rev.* **2008,** *46* (1), 289-337.
31. Chandraleka, S.; Ramya, K.; Chandramohan, G.; Dhanasekaran, D.; Priyadharshini, A.; Panneerselvam, A., Antimicrobial mechanism of copper (II) 1,10-phenanthroline and 2,2′-bipyridyl complex on bacterial and fungal pathogens. *J. Saudi. Chem. Soc.* **2014,** *18* (6), 953-962.
32. Studer, A.; Hadida, S.; Ferritto, R.; Kim, S.-Y.; Jeger, P.; Wipf, P.; Curran, D. P., Fluorous Synthesis: A Fluorous-Phase Strategy for Improving Separation Efficiency in Organic Synthesis. *Science* **1997,** *275* (5301), 823-826.
33. Rippy, K. C.; DeWeerd, N. J.; Kuvychko, I. V.; Chen, Y.-S.; Strauss, S. H.; Boltalina, O. V., Fluorination-Induced Evolution of Columnar Packing in Fluorous Triphenylenes and Benzotriphenylenes. *ChemPlusChem* **2018,** *83* (12), 1067-1077.
34. Rippy, K. C.; Bukovsky, E. V.; Clikeman, T. T.; Chen, Y.-S.; Hou, G.-L.; Wang, X.-B.; Popov, A. A.; Boltalina, O. V.; Strauss, S. H., Copper Causes Regiospecific Formation of C4F8-Containing Six-Membered Rings and their Defluorination/Aromatization to C4F4-Containing Rings in Triphenylene/1,4-C4F8I2 Reactions. *Chem. Eur. J.* **2016,** *22* (3), 874-877.
35. Kuvychko, I. V.; Dubceac, C.; Deng, S. H. M.; Wang, X.-B.; Granovsky, A. A.; Popov, A. A.; Petrukhina, M. A.; Strauss, S. H.; Boltalina, O. V., C20H4(C4F8)3: A Fluorine-Containing Annulated Corannulene that Is a Better Electron Acceptor Than C60. *Angew. Chem. Int. Ed.* **2013,** *52* (29), 7505-7508.

36. Haskelberg, L., 4,7-Phenanthroline. *Journal of the American Chemical Society* **1947,** *69* (6), 1538-1539.
37. Summers, L. A., The Phenanthrolines. In *Advances in Heterocyclic Chemistry*, Katritzky, A. R.; Boulton, A. J., Eds. Academic Press: 1978; Vol. 22, pp 1-69.
38. N. Gusak, K.; Tereshko, A. B.; G. Kozlov, N., *Synthesis of 4,7-Phenanthroline Methyl Derivatives*. 2004; Vol. 40, p 1662-1668.
39. Tahghighi, A.; Karimi, S.; Parhizgar, A. R.; Zakeri, S., Synthesis and antiplasmodial activity of novel phenanthroline derivatives: An in vivo study. *Iranian journal of basic medical sciences* **2018,** *21* (2), 202-211.
40. Castro, K. P.; Clikeman, T. T.; DeWeerd, N. J.; Bukovsky, E. V.; Rippy, K. C.; Kuvychko, I. V.; Hou, G.-L.; Chen, Y.-S.; Wang, X.-B.; Strauss, S. H.; Boltalina, O. V., Incremental Tuning Up of Fluorous Phenazine Acceptors. *Chem.-Eur. J.* **2016,** *22* (12), 3930-3936.
41. Kromann, J. C.; Jensen, J. H.; Kruszyk, M.; Jessing, M.; Jørgensen, M., Fast and accurate prediction of the regioselectivity of electrophilic aromatic substitution reactions. *Chem. Sci.* **2017,** *9* (3), 660-665.
42. Schmidt, A.; Liu, M., Chapter Four - Recent Advances in the Chemistry of Acridines. In *Advances in Heterocyclic Chemistry*, Scriven, E. F. V.; Ramsden, C. A., Eds. Academic Press: 2015; Vol. 115, pp 287-353.
43. Schmidt, A.; Liu, M., Recent advances in the chemistry of acridines. *Advances in Heterocyclic Chemistry* **2015,** *2015*, 287.
44. Schmidt , B. M.; Topolinski , B.; Yamada , M.; Higashibayashi, S.; Shionoya, M.; Sakurai, H.; Lentz, D., Fluorinated and Trifluoromethylated Corannulenes. *Chem.-Eur. J.,* **2013,** *19* (41), 13872-13880.
45. Aitken, R. A.; Boubalouta, Y., Chapter Two - Recent Advances in the Synthesis of Heterocyclic Compounds Using Flash Vacuum PyrolysisaaDedicated to the memory of two major figures in this field of research: Gloria Inés Yranzo (1957–2008) and Hamish McNab (1949–2010). In *Advances in Heterocyclic Chemistry*, Scriven, E. F. V.; Ramsden, C. A., Eds. Academic Press: 2015; Vol. 115, pp 93-150.
46. Parr, R. G.; Szentpály, L. v.; Liu, S., Electrophilicity Index. *J. Am. Chem. Soc.* **1999,** *121* (9), 1922-1924.
47. De Vleeschouwer, F.; Van Speybroeck, V.; Waroquier, M.; Geerlings, P.; De Proft, F., Electrophilicity and Nucleophilicity Index for Radicals. *Org. Lett.* **2007,** *9* (14), 2721-2724.
48. Roberts, J. D.; Streitwieser, A., Quantum Mechanical Calculations of Orientation in Aromatic Substitution1. *J. Am. Chem. Soc.* **1952,** *74* (18), 4723-4725.
49. Ni, C.; Hu, J., The unique fluorine effects in organic reactions: recent facts and insights into fluoroalkylations. *Chemical Society Reviews* **2016,** *45* (20), 5441-5454.
50. Chiron, J.; Galy, J.-P., *Reactivity of the Acridine Ring: A Review*. 2004; Vol. 35.
51. Wasylishen, R., Spin—Spin Coupling Between Carbon-13 and the First Row Nuclei. 1978; Vol. 7, pp 245-291.
52. Eichele, K.; Wasylishen, R., Observation of nitrogen-14, carbon-13 indirect spin-spin coupling in high-resolution 13C CPMAS spectra of solids. *Solid State Nuclear Magnetic Resonance* **1992,** *1*, 159-163.
53. Iwasaki, M.; Araki, Y.; Iino, S.; Nishihara, Y., Synthesis of Multisubstituted Triphenylenes and Phenanthrenes by Cascade Reaction of o-Iodobiphenyls or (Z)-β-Halostyrenes with o-Bromobenzyl Alcohols through Two Sequential C–C Bond Formations Catalyzed by a Palladium Complex. *J. Org. Chem.* **2015,** *80* (18), 9247-9263.
54. Katritzky, A. R.; Ramsden, C. A.; Joule, J. A.; Zhdankin, V. V., 4.5 - Synthesis of Tri- and Polycyclic Ring Systems Without Ring Junction Heteroatoms. In *Handbook of Heterocyclic Chemistry (Third Edition)*, Katritzky, A. R.; Ramsden, C. A.; Joule, J. A.; Zhdankin, V. V., Eds. Elsevier: Amsterdam, 2010; pp 872-888.

55. Tumir, L.-M.; Radić Stojković, M.; Piantanida, I., Come-back of phenanthridine and phenanthridinium derivatives in the 21st century. *Beilstein journal of organic chemistry* **2014,** *10*, 2930-2954.
56. Kuvychko, I. V.; C., C. T.; Dubceac, C.; Yu.-S., C.; Petrukhina, M. A.; Strauss, S. H.; Popov, A. A.; Boltalina, O. V., Understanding Polyarene Trifluoromethylation with Hot CF_3 Radicals Using Corannulene. *Eur. J. Org. Chem.* **2018,** *on line*, 7505-7508.
57. Das, S.; Thakur, A. J., A green development of Bernthsen 9-substituted acridine synthesis in the absence of solvent catalyzed by p-toluenesulphonic acid (p-TSA). *Green Chem. Lett. and Rev.* **2011,** *4* (2), 131-135.
58. Chiron, J.; Galy, J.-P., *Synthesis and Crystallographic Studies of New Acridinic Esters and Amides: An Efficient Synthetic Route to 4Methyl Functionalized Acridines*. 2003; Vol. 60.
59. Chiron, J.; Galy, J.-P., *Synthesis and Crystallographic Studies of New Acridinic Esters and Amides: An Efficient Synthetic Route to 4Methyl Functionalized Acridines*. 2003; Vol. 60.
60. Schmidt, A.; Liu, M., Chapter Four - Recent Advances in the Chemistry of Acridines. In *Adv. Heterocycl. Chem.*, Scriven, E. F. V.; Ramsden, C. A., Eds. Academic Press: 2015; Vol. 115, pp 287-353.
61. Kokubo, S.; Ando, N.; Koyasu, K.; Mitsui, M.; Nakajima, A., Negative ion photoelectron spectroscopy of acridine molecular anion and its monohydrate. *J. Chem. Phys.* **2004,** *121* (22), 11112-11117.
62. Kuvychko, I. V.; Castro, K. P.; Deng, S. H. M.; Wang, X.-B.; Strauss, S. H.; Boltalina, O. V., Taming Hot CF_3 Radicals: Incrementally Tuned Families of Polyarene Electron Acceptors for Air-Stable Molecular Optoelectronics. *Angew. Chem. Int. Ed.* **2013,** *52*, 4871-4874.
63. Abthagir, P. S.; Ha, Y.-G.; You, E.-A.; Jeong, S.-H.; Seo, H.-S.; Choi, J.-H., Studies of Tetracene- and Pentacene-Based Organic Thin-Film Transistors Fabricated by the Neutral Cluster Beam Deposition Method. *J. Phys. Chem. B* **2005,** *109* (50), 23918-23924.
64. Campione, M.; Sassella, A., Tetracene thin films grown by organic molecular beam deposition under a static magnetic field. *J. Chem. Phys.* **2006,** *124* (22), 224705.
65. Kim, S. O.; Jung, H. C.; Lee, M.-J.; Jun, C.; Kim, Y.-H.; Kwon, S.-K., Synthesis and characterization of 9,10-diphenylanthracene-based blue light emitting materials. *J. Polym. Sci. A Polym. Chem.* **2009,** *47* (21), 5908-5916.
66. Ting, C.-H., Electronic structure and intersystem crossing in 9,10-diphenylanthracene. *Phys. Chem. Lett.* **1967,** *1* (8), 335-336.
67. Tripathi, A. K.; Heinrich, M.; Siegrist, T.; Pflaum, J., Growth and Electronic Transport in 9,10-Diphenylanthracene Single Crystals—An Organic Semiconductor of High Electron and Hole Mobility. *Adv. Mater.* **2007,** *19* (16), 2097-2101.
68. Zhi, Z.; Yang, X.; Lu, L.; Wang, X. J. T. C. E., Synthesis and Verification of 9,10-Diphenylanthracene and Its Utility as a Fluorescer in a Peroxyoxalate Chemiluminescence System. An Organic Laboratory Project Integrating Synthesis with Fluorescence and Chemiluminescence. *The Chem. Educ.* **2000,** *5* (4), 187-189.
69. Tsuneyasu, S.; Ichikawa, T.; Nakamura, K.; Kobayashi, N., Electrochemical Stability of Diphenylanthracene and Its Effect on Alternating-Current-Driven Blue-Light Electrochemiluminescence Properties. *ChemElectroChem* **2017,** *4* (7), 1731-1735.
70. Clikeman, T. T.; Bukovsky, E. V.; Wang, X.-B.; Chen, Y.-S.; Rumbles, G.; Strauss, S. H.; Boltalina, O. V., Core Perylene Diimide Designs via Direct Bay- and ortho-(Poly)trifluoromethylation: Synthesis, Isolation, X-ray Structures, Optical and Electronic Properties. *Eur. J. Org. Chem.* **2015,** *2015* (30), 6641-6654.
71. Avlasevich, Y.; Li, C.; Müllen, K., Synthesis and applications of core-enlarged perylene dyes. *J. Mater. Chem.* **2010,** *20* (19), 3814-3826.
72. Bhowmick, D. K.; Stegemann, L.; Bartsch, M.; Strassert, C. A.; Zacharias, H., Fluorescence Properties of Perylene and Pyrene Dyes Covalently Linked to 6H-SiC(0001) and Silicate Surfaces. *J. Phys. Chem. C* **2016,** *120* (6), 3275-3288.

73. Kim, J. Y.; Sakong, C.; Choi, S.-a.; Jang, H.; Kim, S. H.; Chang, K. S.; Han, M. S.; Lee, J. S.; Kim, J. P., The effect of fluorescence of perylene red dyes on the contrast ratio of LCD color filters. *Dyes and Pigments* **2016,** *131*, 293-300.
74. Schiedt, J.; Weinkauf, R., Photodetachment photoelectron spectroscopy of perylene and CS2: two extreme cases. *Chem. Phys. Lett.* **1997,** *274* (1), 18-22.
75. Söhnchen, S.; Hänel, K.; Birkner, A.; Witte, G.; Wöll, C. H., Molecular Beam Deposition of Perylene on Copper: Formation of Ordered Phases. *Chem. Mater.* **2005,** *17*, 5297-5304.
76. Türkmen, G.; Erten-Ela, S.; Icli, S., Highly soluble perylene dyes: Synthesis, photophysical and electrochemical characterizations. *Dyes and Pigments* **2009,** *83* (3), 297-303.
77. Zhang, F.; Ma, Y.; Chi, Y.; Yu, H.; Li, Y.; Jiang, T.; Wei, X.; Shi, J., Self-assembly, optical and electrical properties of perylene diimide dyes bearing unsymmetrical substituents at bay position. *Scientific Reports* **2018,** *8* (1), 8208.
78. Ando, N.; Kokubo, S.; Mitsui, M.; Nakajima, A., Photoelectron spectroscopy of pyrene cluster anions, (pyrene)n− (n=1–20). *Chem. Phys. Lett.* **2004,** *389* (4), 279-283.
79. Casas-Solvas, J. M.; Howgego, J. D.; Davis, A. P., Synthesis of substituted pyrenes by indirect methods. *Org. Biomol. Chem,* **2014,** *12* (2), 212-232.
80. Clikeman, T. T.; Bukovsky, E. V.; Kuvychko, I. V.; San, L. K.; Deng, S. H. M.; Wang, X.-B.; Chen, Y.-S.; Strauss, S. H.; Boltalina, O. V., Poly(trifluoromethyl)azulenes: structures and acceptor properties. *Chem. Comm.* **2014,** *50* (47), 6263-6266.
81. de Halleux, V.; Mamdouh, W.; De Feyter, S.; De Schryver, F.; Levin, J.; Geerts, Y. H., Emission properties of a highly fluorescent pyrene dye in solution and in the liquid state. *J. Photochem & Photobio. A* **2006,** *178* (2), 251-257.
82. Niko, Y.; Didier, P.; Mely, Y.; Konishi, G.-i.; Klymchenko, A. S., Bright and photostable push-pull pyrene dye visualizes lipid order variation between plasma and intracellular membranes. *Scientific Reports* **2016,** *6*, 18870.
83. Kuvychko, I. V.; Castro, K. P.; Deng, S. H. M.; Wang, X. B.; Strauss, S. H.; Boltalina, O. V., Taming Hot CF_3 Radicals: Incrementally Tuned Families of Polyarene Electron Acceptors for Air-Stable Molecular Optoelectronics. *Angew. Chem., Int. Ed.* **2013,** *52* (18), 4871-4874.

CHAPTER 3. STUDY OF THE PHYSICAL PROPERTIES OF FLUOROUS PHENAZINE DERIATIVES WITH PROMISE AS ELECTRON ACCEPTOR MATERIALS

3.1. CHAPTER 3 INTRODUCTION

Phenazine (PHNZ) is an N-hetero-PAH analogous to anthracene (ANTH), shown in Figure 3-1. Many PHNZ derivatives have been identified as natural products.[1] Commercially, PHNZ is commonly used for pharmaceuticals, dyes, sensors, light emitting diodes.[1-6] However, it is particularly promising as an organic semiconductor, an application for which it has been under-exploited.[7-13] The presence of the two N atoms result in PHNZ having an EA of 1.3+/- 0.1 eV, more than twice the EA of ANTH.[14, 15] With the addition of electron withdrawing groups to the core, its EA has been shown to surpass that of commonly used electron acceptor materials C_{60} and F4-TCNQ.[16-19] Additionally, it has a linear structure, making it analogous to the high-performance acene family of PAHs (anthracene, tetracene, pentacene, etc.). Such linear materials generally demonstrate high mobilities and good device performance.[7-10, 12, 20-22] For this work, it is a particularly promising substrate, as RD/A moieties (C_4F_4 and C_4F_3H) bound to the peninsular positions would create fluorous, N-hetero tetracene and pentacene derivatives.

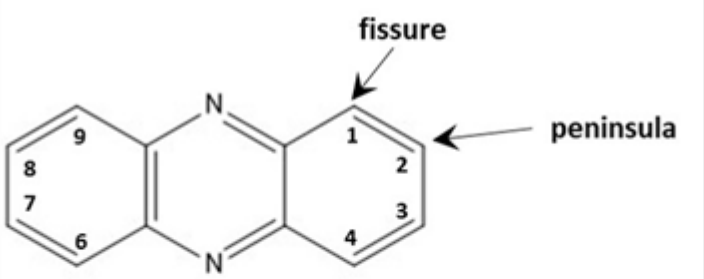

Figure 3-1. Molecular structure of PHNZ. Numbering is indicated, as are positions referred to as 'fissure,' (C atoms 1, 4, 6, and 9) and 'peninsula' (C atoms 2, 3, 7, and 8). For simplicity, annulations occurring across a fissure and a peninsular C atom (ie. in the 1,2 position) will be referred to as annulations in the fissure position. Annulations occurring solely upon peninsular C atoms (ie. in the 2,3 position) will be referred to as peninsular.

Previously, a variety of fluorous PHNZ derivatives have been reported. [23-32] However, only one example of synthesis of fluorous PHNZ derivatives by direct substitution is known: the synthesis of family of trifluoromethyl derivatives by the author's lab mate Dr. Karlee Castro,[14] work with which the author assisted. In the work reported here, a family of PHNZ derivatives bearing C_4F_8, C_4F_4, and C_4F_3H was synthesized via the gas-phase radical reaction developed in the previous chapters. Additionally, new experimental conditions are reported, involving a reaction of 1,4-$C_4F_8I_2$ and PHNZ in *ortho*-dichlorobenzene (*o*-DCB). In addition to producing products bearing $C4F_8$ moieties, the milder conditions of this solution-based reaction allowed isolation, for the first time, of compounds bearing C_4F_8I moieties. These molecules are not only of interest as they assist in understanding reaction pathways, but also as precursors for new chemical syntheses. In total, eleven fluorous PHNZ derivatives are reported, ten of which have been definitively structurally characterized. These are shown in Figure 3-2.

Isolation and purification of these molecules was achieved via HPLC. Single crystal X-ray structures were obtained for five compounds. Additionally, preliminary X-ray structures were obtained for two more. This allowed analysis of solid-state packing of these derivatives.

Similar to work reported in preceding chapters, the EA of a selection of these compounds was obtained through low-temperature PES at PNNL, by Dr. Xue-Bin Wang. The results indicate that compounds bearing two substituents, especially substituted in the peninsular position, do indeed surpass 2.8 eV, which has been established as a threshold for air stable electron acceptor materials. [19] Additionally, unlike TRPH derivatives reported in the previous chapter, a number of these molecules yielded quasi-reversible cyclic voltammograms (CVs). Therefore, a variety of electrochemical and spectroelectrochemical techniques were employed to complement EA studies.

Finally, photoluminescence measurements (PL) and preliminary time resolved microwave conductivity (TRMC) studies were performed on donor/acceptor blends of a selection of PHNZ derivatives with the donor P3HT. These measurements were conducted at Macquarie University, with the instruction of Dr. Nikos Kopidakis. The results confirm that these molecules act as electron acceptors.

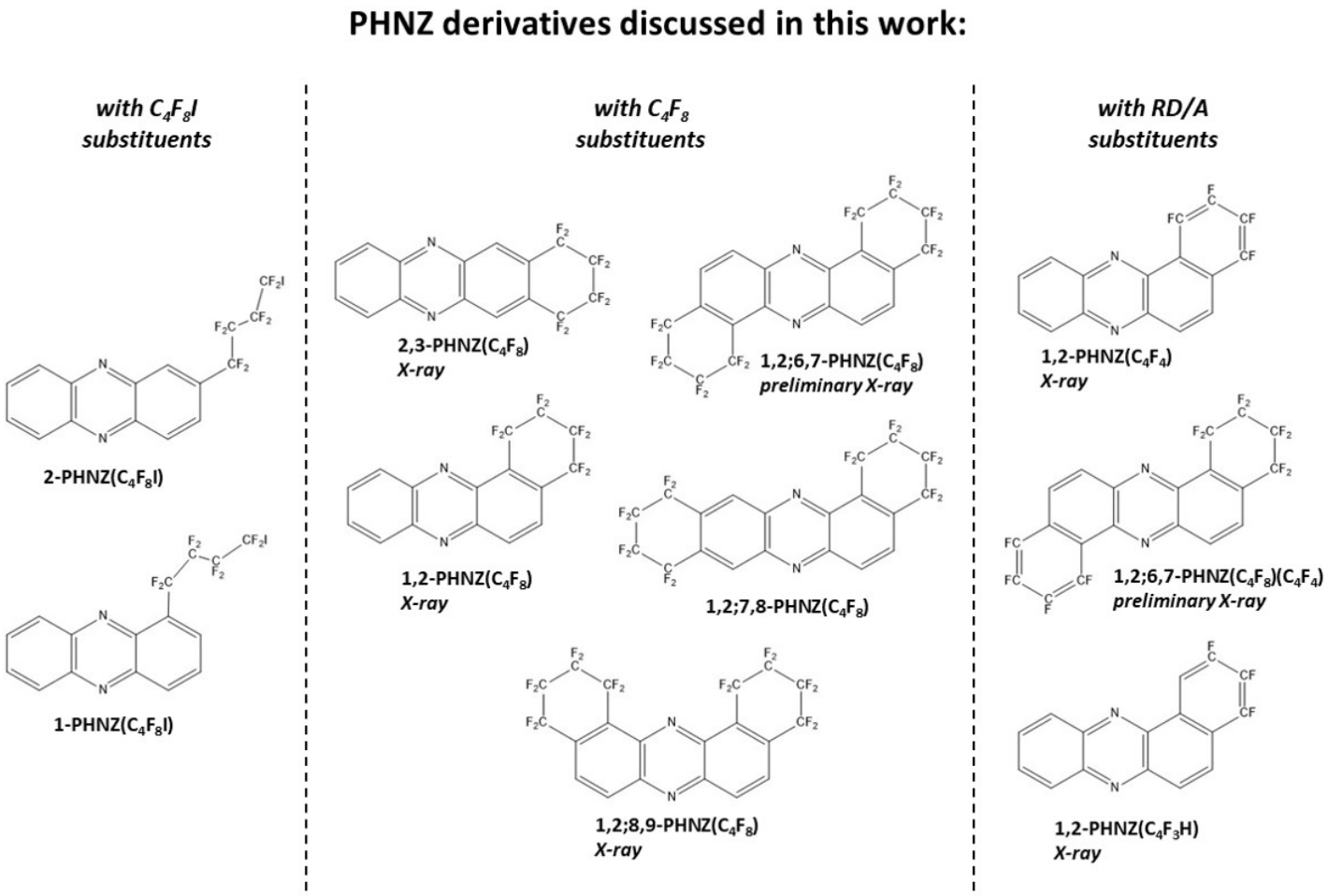

Figure 3-2. Molecular structures of all fluorous PHNZs prepared in this work. Many have been characterized by single crystal x-ray crystallography, as indicated. For the remaining molecules, structural assignment was accomplished via analysis of ^{1}H and ^{19}F NMR spectra. For full characterization of each molecule, see appx C.3.1-C.3.11.

3.2. RESULTS AND DISCUSSION

3.2.1. Synthesis of pure compounds

3.2.1.a. General comments on PHNZ derivative synthesis

In the course of the work reported here, ten fluorous PHNZ derivatives have been synthesized, purified, and definitively structurally characterized. These molecules, all shown in Figure 3-2, were isolated from a series of gas-phase radical reactions, illustrated in scheme 3-1 and discussed in sections *3.2.1a.* and *3.2.1.b*, and from a liquid-phase radical reaction carried out in *o*-DCB. shown in scheme 3-3 and discussed in section *3.2.1.c*. Purification was achieved by HPLC (discussed in *3.2.2a*.) For further details of syntheses, see appx B.3.1-B.3.5.

3.2.1.b. Reactions for PHNZ(C_4F_8)$_n$ products

Gas-phase radical reactions were conducted utilizing a methodology analogous to gas-phase radical reaction method developed by Kuvychko et al., [33] which are also discussed for TRPH and other PAH and hetero-PAH substrates in chapters 1 and 2. For the reactions reported here, the substrate PHNZ and 1,4-$C_4F_8I_2$ were placed together in either a flame-sealed glass ampoule or a Monel reactor. They were then heated until homolytic cleavage of the C-I bond initiated radical reaction. Substitution of I-R_f• radicals upon PHNZ substrates followed by homolytic cleavage of the remaining C-I bond which produced annulated PHNZ(C_4F_8)$_n$ products. This process is outlined in Scheme 3-2. Parameters such as reaction temperature, duration, stoichiometric ratios of starting materials, and the use of a Cu promoter varied for each reaction, as specified in appx B.3.

In total, five products bearing only C_4F_8 moieties were synthesized. Two of these, 1,2-PHNZ(C_4F_8) and 2,3-PHNZ(C_4F_8) bear only one substituent, while the remaining three, 1,2;6,7-PHNZ(C_4F_8)$_2$, 1,2;7,8-PHNZ(C_4F_8)$_2$, and 1,2;8,9-PHNZ(C_4F_8)$_2$ bear two substituents. As shown in scheme 3-1, these products were isolated from reactions 3.1 and 3.2. They were also produced by reactions 3.3-3.5, though they were not the targeted products of these reactions.

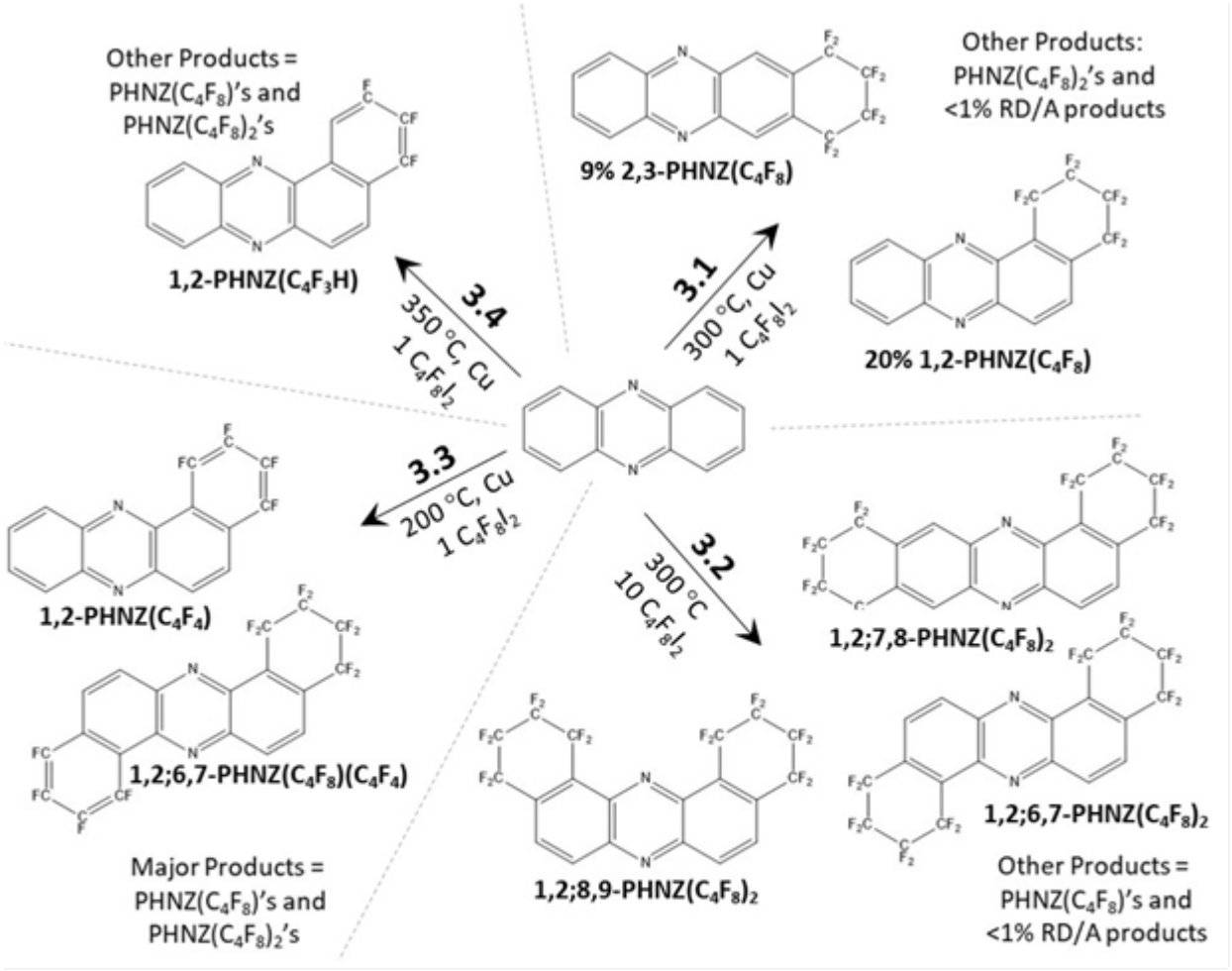

Scheme 3-1. Gas-phase radical reactions to produce major products discussed in this chapter. Products shown in this scheme are not the only products produced by a reaction but are the targeted products. For reaction 3.1, yields given in the scheme are isolated yields. For complete details of reactions, see appendix B.3, reactions 3.1-3.4.

In agreement with the work discussed in chapters 1 and 2, stoichiometric ratios of starting materials had the largest effect upon product distribution of any parameter investigated. Reaction 3.1 utilizes a 1:1 ratio of 1,4-$C_4F_8I_2$ to PHNZ, resulting in a 20% isolated yield of 1,2-PHNZ(C_4F_8) and a 9% isolated yield of 2,3-PHNZ(C_4F_8).

One reason that these yields could not be increased lies in the fact that substitution does not seem to occur preferentially upon unreacted PHNZ substrate over PHNZ substrates already bearing a fluorous substituent. Even with the low amount of perfluoroalkyl iodide present in reaction 3.1, a 15% isolated yield of 1,2;6,7-PHNZ(C_4F_8)$_2$ was recovered. Analysis of the NMR spectra of the crude product indicates that other two PHNZ(C_4F_8)$_2$ products are also present in relatively high yield. As would be expected given that much of the perfluoroalkyl iodide reagent was consumed producing PHNZ(C_4F_8)$_2$ products, a 22% isolated yield of PHNZ starting material was also recovered for reaction 3.1.

Utilization of high stoichiometric ratios of 1,4-$C_4F_8I_2$ to PHNZ resulted in PHNZ(C_4F_8)$_2$ products being favored. In reaction 3.2, the ratio was 10:1. No PHNZ(C_4F_8) products were isolated from this reaction. However, yields of the three PHNZ(C_4F_8)$_2$ products remained relatively low (a maximum of 5-15% by NMR spectrum integration). This is likely attributable to formation of products bearing C_4F_8H moieties similar to those discussed in preceding chapters. Although no such compounds were isolated in high purity, there is evidence for them in the NMR spectra, particularly in the form of peaks between -105 and -135 ppm in the ^{19}F spectra.

Interestingly, products bearing peninsular annulations are produced in much lower quantity than products bearing fissure annulations for all reactions. Indeed, 2,3-PHNZ(C_4F_8) and 1,2;7,8-PHNZ(C_4F_8)$_2$ are produced in much lower yield than the other three products bearing C_4F_8 moieties, and 2,3;7,8-PHNZ(C_4F_8)$_2$ was never isolated despite numerous attempts.

The reason for this is likely twofold. First, even if initial substitution of the I-R_F• radical is equally likely upon both the fissure and peninsular positions, those that add to fissure positions must always form fissure annulations, whereas those that initially add to peninsular positions would give fissure annulations half of the time, and peninsular substitution the other half. This is

illustrated in scheme 3-2. It would result in a 3:1 ratio of fissure annulations over peninsular annulations.

Additionally, there is likely some directing effect toward the fissure positions, similar to the phenomenon observed for 4,7-PHEN in chapter 2. This effect is likely due to the common structural motif of and N atom across a fissure from a substation position. Such enhanced reactivity also agrees with work on the trifluoromethylation of PHNZ, which was primarily conducted by Dr. Karlee Castro, with assistance from the author of this work. Trifluoromethyl derivatives substituted at the fissure positions were most frequently observed.[14]

Reaction duration did not observably affect distribution of products bearing C_4F_8 moieties. However, longer reaction duration did result in decomposition. Reactions of up to 24 h were attempted, at which point no soluble fluorous product was recovered. Shorter reaction times generally yielded higher product recovery. However, reactions shorter than 2 h generally yielded incomplete reaction of perfluoroalkyl iodide reagents.

Similar to the work reported in previous chapters, there was no discernable difference in product distribution resulting from the use of a Monel reactor or flame-sealed glass ampoule for reactions utilizing Cu powder under the same conditions. Reactions in the Monel reactor were slightly favorable due to its more consistent size, ability to be reused, and higher degree of safety.

3.2.1.c. Reactions for PHNZ RD/A products

Reactions 3.3 and 3.4 were undertaken to target RD/A products. Notably, RD/A products were observed under relatively mild reaction conditions for PHNZ substrate. In contrast, for TRPH, temperature of at least 345 °C and Cu powder were required for RD/A. For PHNZ, RD/A was seen at a temperature as low as 200 °C in the presence of Cu powder (reaction 3.3). Even without Cu powder, product of reaction 3.2 contained trace amounts of RD/A products, as evidenced by the ^{19}F NMR spectrum, although the amounts were so slight, they could not be

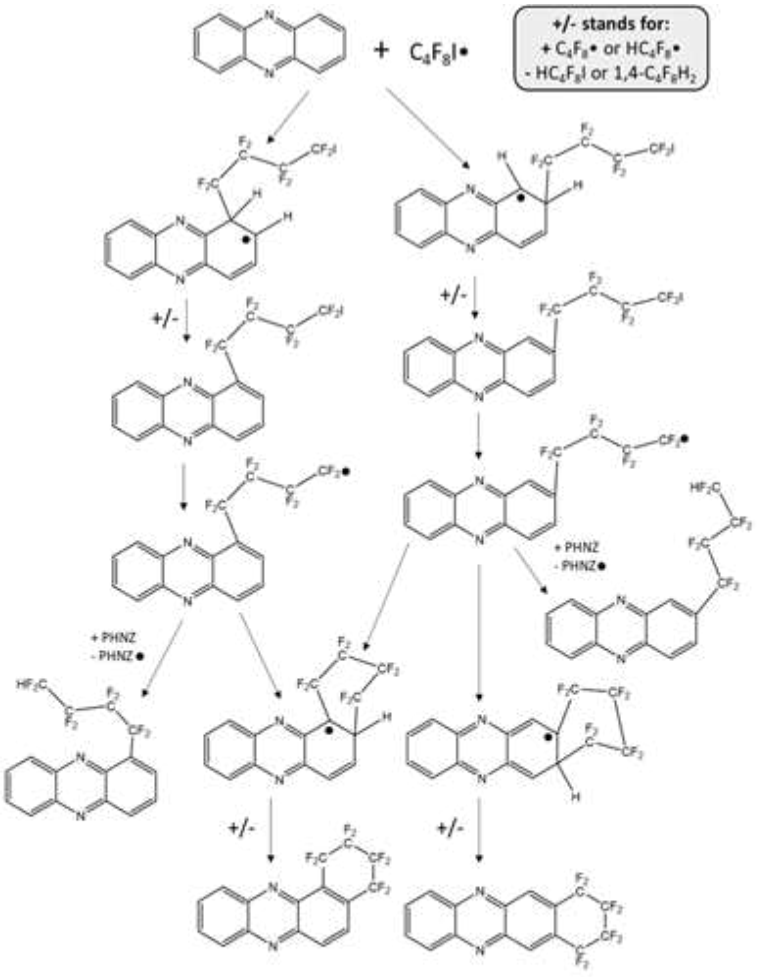

Scheme 3-2. Plausible sequence of steps for formation of PHNZ derivatives bearing single C_4F_8 moieties. Substitution at fissure position is observed more often than at peninsular positions. If both positions are equally reactive, this substitution would be observed 75% of the time, as 100% of additions to fissure C atoms would result in fissure annulations, as would 50% of additions to peninsular C atoms.

isolated. The mild conditions under which RD/A is observed for PHNZ are likely correlated to the lower reduction potential of PHNZ (i.e., PHNZ is much more readily reduced that TRPH, and has a much higher EA due to the presence of a heteroatom).

Attempts to substantially increase yields of RD/A products were unsuccessful. Reactions at low temperatures, such as reaction 3.3, yielded the greatest amount of the product bearing C_4F_4 groups, but even in this case, the amount of the product bearing C_4F_8 moieties was far higher.

This is possibly attributable to RD/A being followed by further rapid reductive defluorination to C_4F_3H moieties and then to fully defluorinated products . Evidence in support of this comes from the analysis of reaction 3.4. This reaction was conducted at a relatively high temperature, 350 °C, and in the presence of Cu. It yielded a far higher percentage of RD/A product than any other reaction, but interestingly, most of this product was 2,3-PHNZ(C_4F_3H). Also, the overall amount of soluble product recovered was extremely low compared to reactions performed at lower temperatures. Achieving a balance of conditions to favor RD/A while maintaining high product yield appeared to be non-trivial.

3.2.1.d. Reaction in o-DCB

In addition to the gas-phase radical reactions that were similar to reactions reported in previous chapters, reaction 3.5, the reaction of PHNZ and 1,4-$C_4F_8I_2$ in *o*-DCB proved possible. This reaction is shown in scheme 3-3. The solvent *o*-DCB was selected as its high dipole moment could help stabilize radicals in solution and it has high boiling point.

For reaction 3.5, PHNZ, Cu powder, and 1,4-C_4F_8 were loaded with a minimal volume (*ca.* 5 mL) of dry, distilled *o*-DCB into a Schenck flask within a dinitrogen glovebox. The flask was then closed, removed from the glovebox, and freeze-pump-thawed to removed dinitrogen. It was then submersed in a constant temperature hot oil bath to the solvent level for the duration of the reaction. Following the reaction, diethyl ether was added in order to form an azeotrope with *o*-DCB which was removed by rotary evaporation.

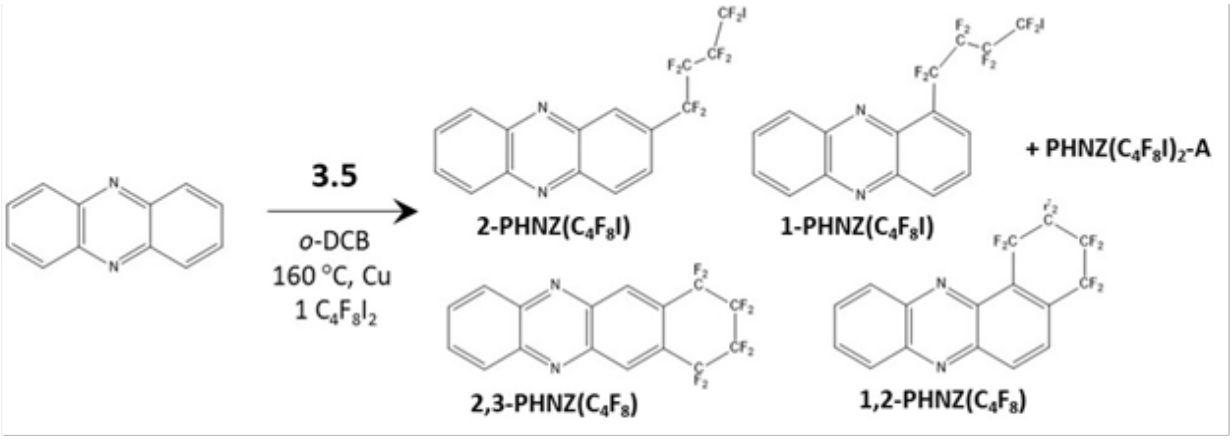

Scheme 3-3. Reaction of PHNZ and 1,4-$C_4F_8I_2$ in *o*-DCB with Cu promoter. Unlike gas phase radical reactions, under these conditions, intermediate products bearing C_4F_8I groups are isolable.

Notably, products bearing C_4F_8I groups were observed, along with the products bearing C_4F_8 moieties. Overall, this reaction in the oDCB solution produced fewer compounds, with higher yields and nearly quantitative conversion of PHNZ substrate. Notably, no decomposition was observed either, making these reaction conditions advantageous for the reactive PAH substrates.

3.2.2. Isolation and structural characterization of pure compounds

3.2.2.a. HPLC separation

Separation of PHNZ products bearing C_4F_8 groups was achieved on a Buckyprep Semipreparative column at a flow rate of 5 ml/min utilizing acetonitrile and methanol as eluents. In both eluents, a complex mixture of products that appeared by NMR spectroscopy to bear C_4F_8H moieties eluted first, followed by products bearing one C_4F_8 moieties. Retention times were longer in methanol, giving more separation between products. Acetonitrile gave sufficient separation for reaction 3.1, in which products bearing only one C_4F_8 moiety were the primary target. However, to separate the products bearing two C_4F_8 moieties, it was necessary to add 50% methanol. HPLC separations can be seen in appx B.3.1.-B.3.5.

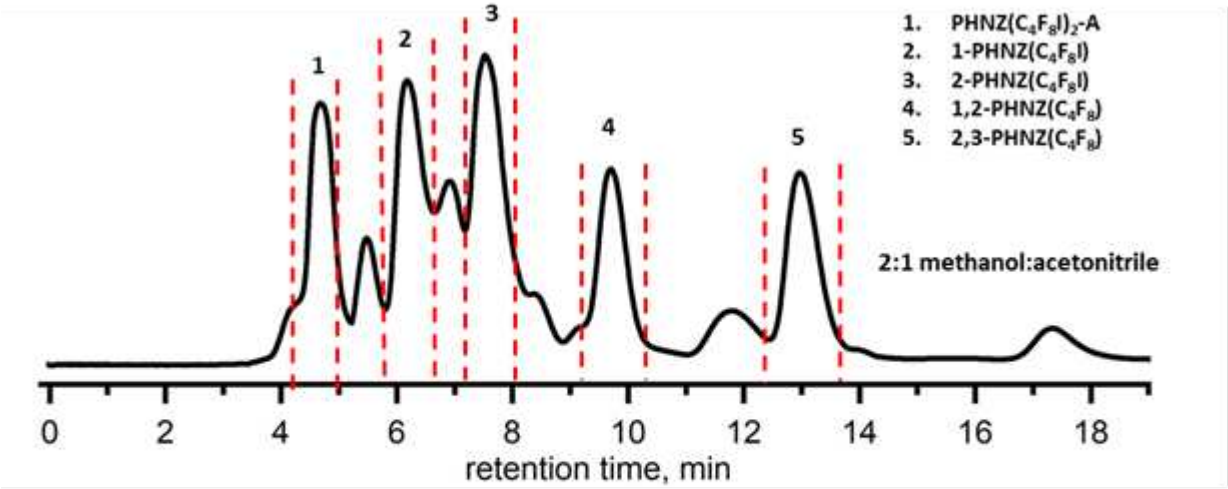

Figure 3-3. HPLC trace of reaction 3.5, the reaction of PHNZ and 1,4-$C_4F_8I_2$ in *o*-DCB with a Cu promoter.

Crude product mixtures were separated on a Cosmosil Buckyprep Semipreparative column with a flow rate of 5 ml/min. Both acetonitrile and a mixture of toluene and isopropyl alcohol were suitable eluents for separation of RD/A products. RD/A products have longer retention times than other products, likely due to the extended π system's increased interaction with the pyrene-derivatized Buckyprep stationary phase. Therefore, these eluents were suitable, whereas methanol, gave unreasonably long retention times and resulted in product smearing on the column and broadening of the peaks.

Separation of products from reaction 3.5 was achieved on a Cosmosil Buckyprep semipreparative column using a 2:1 mixture of methanol to acetonitrile. This eluent was necessary in order to separate the C_4F_8I products, which all have relatively short retention times. This reaction produced fewer unidentified decomposition products that gas-phase radical reactions, as is evidenced by the HPLC trace shown in Figure 3-3. All major peaks are identified, in contrast to the HPLC traces shown in appx B for reactions 3.1-3.4.

3.2.2.b. Structural elucidation via ^{19}F and ^{1}H NMR spectra of PHNZ(C_4F_8)$_n$ compounds

Generally speaking, chemical shifts of C_4F_8 and RD/A products follow the trends discussed in chapter 1 for substitution of these moieties on TRPH substrates. Notably, they do not show significant peak broadening in the ^{19}F NMR spectra, unlike some of the hetero-PAHs discussed in chapter 2.

Compounds with C_4F_8I substituents have distinctive ^{19}F NMR spectra. The ^{19}F NMR muliplet signal arising from the terminal F atoms, on the C atom bearing an I atom, appear at around -65 ppm, similar to the F atoms bonded to the 1 and 4 C atoms of 1,4-$C_4F_8I_2$. In addition to this peak, three multiplets appear in the region where C_4F_8 shifts are expected, i.e., in the region between -95 and -145 ppm.

3.2.2.c. Structural elucidation via single crystal x-ray crystallography

Five single crystal X-ray structure have been deposited with the CCDC as a part of this work. They include 1,2-PHNZ(C_4F_3H), 1,2-PHNZ(C_4F_4), 1,2-PHNZ(C_4F_8), 2,3-PHNZ(C_4F_8), and a cocrystal of 1,2:8,9-PHNZ(C_4F_8)$_2$ and ANTH in a 2:1 ratio. These are shown in Figure 3-4. Additionally, three preliminary structures, sufficient for structural characterization but of insufficient quality for depositing with the CCDC, have been obtained. They are 1,2:6,7-PHNZ(C_4F_8)$_2$, 1,2:6,7-PHNZ(C_4F_4)(C_4F_8), illustrated in Figure 3-5, as well as an additional cocrystal of 1,2:8,9-PHNZ(C_4F_8)$_2$ and ANTH, this time in a 1:1 ratio. In four cases, the X-ray structures simply confirm the structures predicted by NMR spectroscopy. These are those 1,2-PHNZ(C_4F_4), 1,2-PHNZ(C_4F_8), 2,3-PHNZ(C_4F_8), and 1,2:6,7-PHNZ(C_4F_4)(C_4F_8). However, for 1,2-PHNZ(C_4F_3H), 1,2:6,7-PHNZ(C_4F_8)$_2$, 1,2:8,9-PHNZ(C_4F_8)$_2$, definitive structural characterization by NMR spectroscopy was not possible, so the single crystal structures were necessary for structural characterization. For 1,2-PHNZ(C_4F_3H), the position of the H atom in the CF_3H group could not be determined by NMR spectroscopy. The single crystal structure confirm that it is on the C atom bonded to C1 of the PHNZ core. In the case of 1,2:6,7-PHNZ(C_4F_8)$_2$, 1,2:8,9-PHNZ(C_4F_8)$_2$, symmetry precludes differentiation by NMR, as is evidenced by

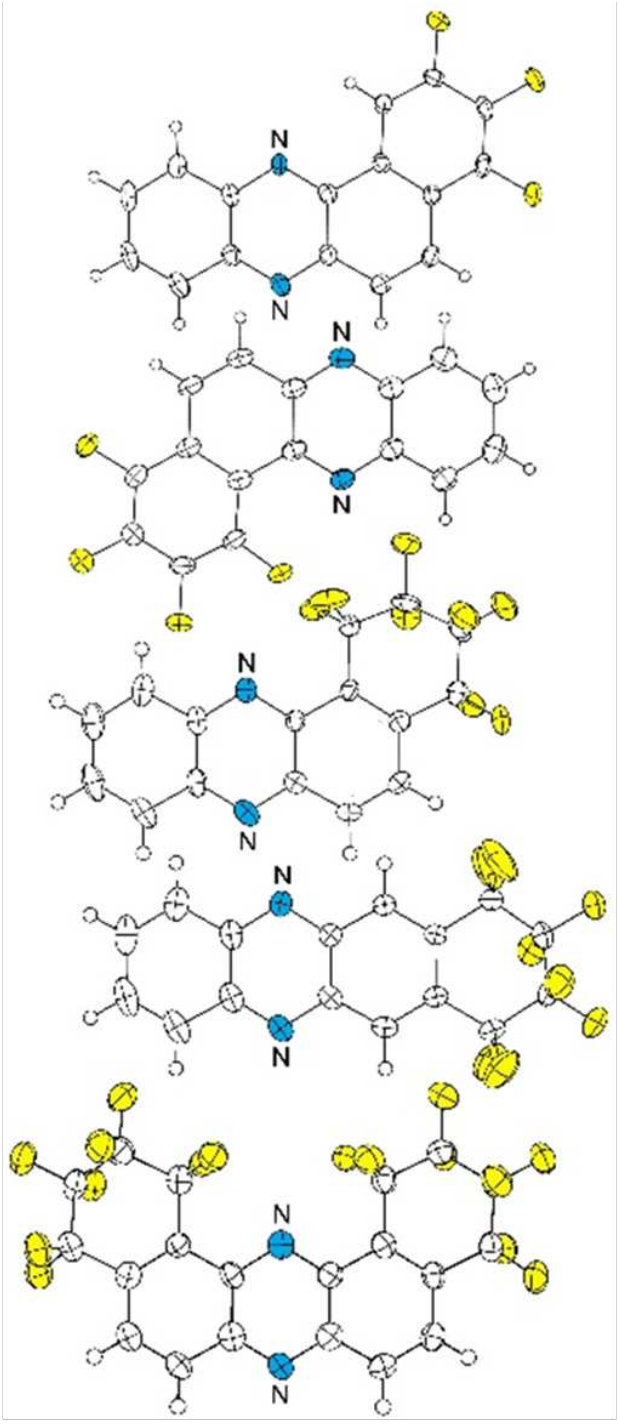

Figure 3-4. Drawings of the single crystal X-ray structures obtained in this work. (50% thermal ellipsoids except for H atoms which are shown as spheres of arbitrary size).

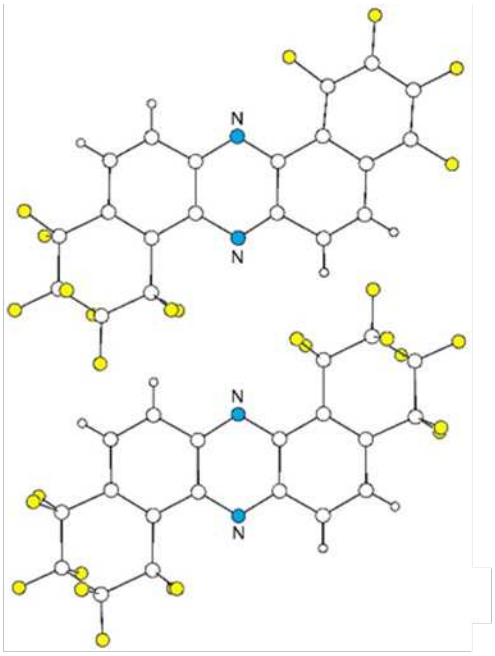

Figure 3-5. Drawings of the preliminary structures of the compounds 1,2:6,7-PHNZ(C_4F_8)$_2$ and 1,2:6,7-PHNZ(C_4F_4)(C_4F_8).

their extremely similar NMR spectra, shown in Figure 3-6. This is also the case for PHNZ(C_4F_8I)$_2$-A, for which a definitive structure cannot be assigned, since no X-ray structure was obtained.

3.2.3. Single crystal X-ray analysis

3.2.2.a. General comments single crystal structures

The compounds discussed here formed small needle-like crystals. The elongated shape of these crystals reflects the underlying columnar crystal structure. The diameter of single crystal needles was on the order of tens of microns. Therefore, the advanced photon source (APS) at Argonne national lab was utilized to collect single crystal x-ray data sets. Data sets were collected by the author and colleagues under the supervision of Dr. Yu-Sheng Chen and solved with assistance from Nicholas DeWeerd. See data collection and refinement parameters listed in appx D.3.1 for details of collection and D.3.2 for additional analysis of structures.

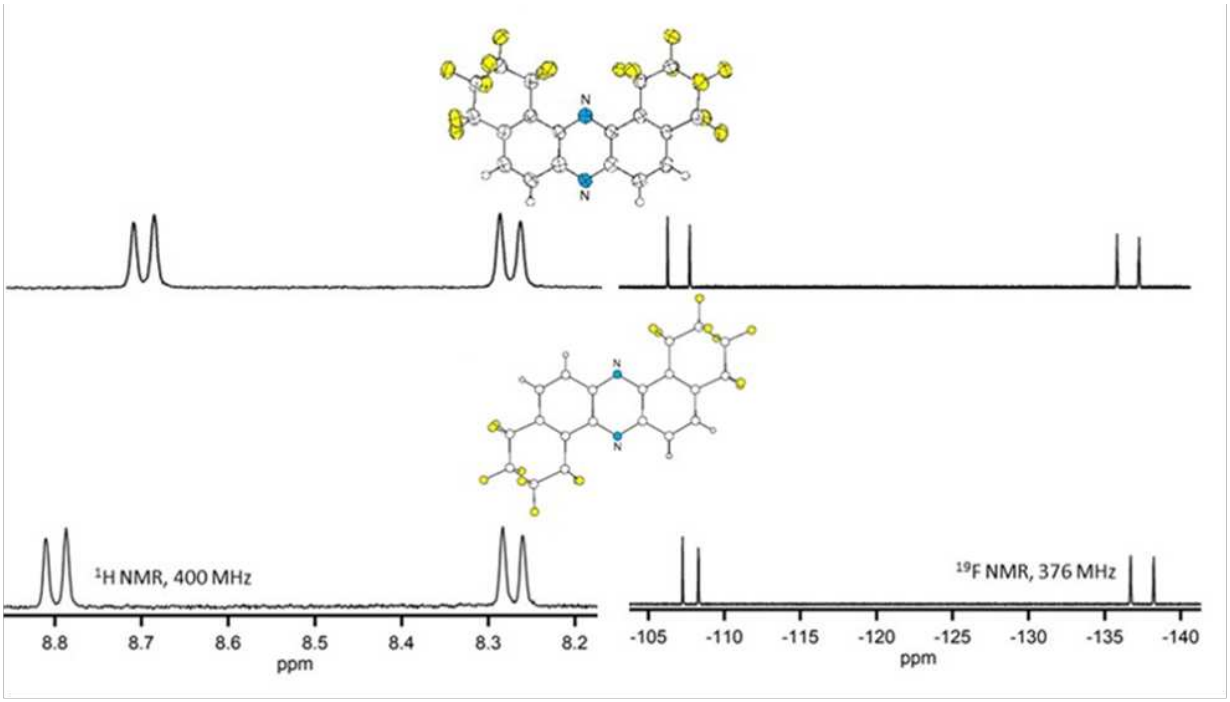

Figure 3-6. It is not possible to distinguish between 1,2:6,7-PHNZ(C_4F_8)$_2$ and 1,2:8,9-PHNZ(C_4F_8)$_2$ by NMR spectroscopy alone, due to the similar spectra resulting from symmetry. Therefore, single crystal X-ray structures were necessary.

The compounds 1,2-PHNZ(C_4F_8) and 2,3-PHNZ(C_4F_8) have the same molecular formula and nearly the same crystal density (the density of 2,3-PHNZ(C_4F_8) is 1.4° higher). Both form hexagonal arrays of infinite head-to-tail stacks of parallel molecules with significant π–π overlap, as shown in Figures 3-7 and D-1. The central hexagon centroids are aligned along the crystallographic a and b axes, respectively, for 1,2-PHNZ(C_4F_8) and 2,3-PHNZ(C_4F_8). In both structures the least-squares planes of adjacent molecules in a stack are rigorously parallel. The

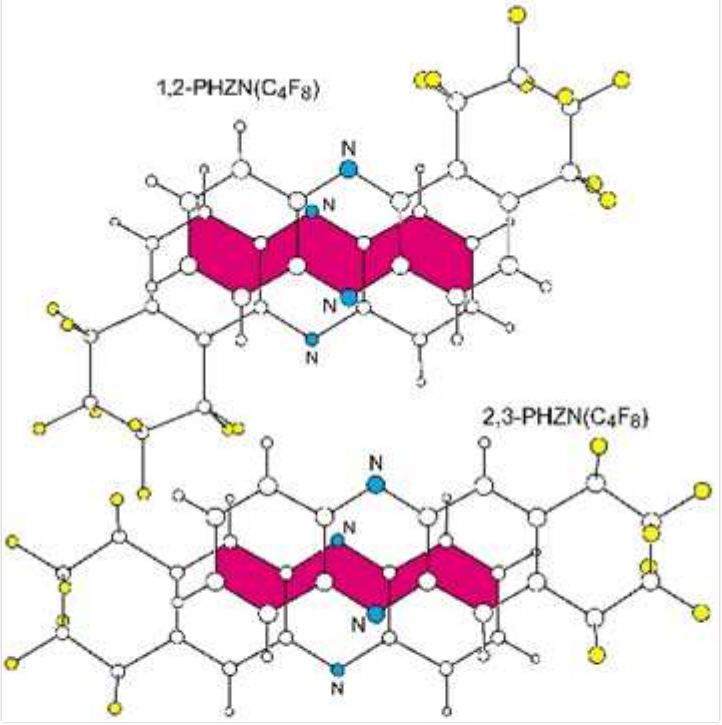

Figure 3-7. Overlap drawings of adjacent molecules in stacks in the structures of 1,2-PHNZ(C_4F_8) (top) and 1,2-PHNZ(C_4F_8) (bottom; N and F atoms shaded blue and yellow, respectively).

perpendicular distances of N and C(sp^2) atoms of one molecule that overlap the π system of adjacent molecules in the stacks 3.37–3.46 Å (six overlaps; ave. 3.41 Å) for 1,2-PHNZ(C_4F_8) and 3.92 Å (six overlaps) for 2,3-PHNZ(C_4F_8).

The compounds 1,2-PHNZ(C_4F_3H) and 1,2-PHNZ(C_4F_4) formally tri- and tetrafluoro derivatives of benzo[a]phenazine, are essentially planar. The deviations from the least squares plane of all non-hydrogen atoms for the trifluoro derivative range from −0.091 to 0.093 Å and average 0.038 Å; for the tetrafluoro compound the deviations range from −0.078 to 0.047 Å and average 0.022 Å. The molecules in both structures are arranged in stacks of parallel molecules with significant π–π overlap, as shown in Figure 3-8. The head-to-tail alignment of adjacent molecules in each stack allows for overlap of the aromatic ring containing the F atoms with the other end of alternate molecule. This was not the case in any of the aforementioned structures in which the F atoms were attached to rings of C(sp^3) atoms.

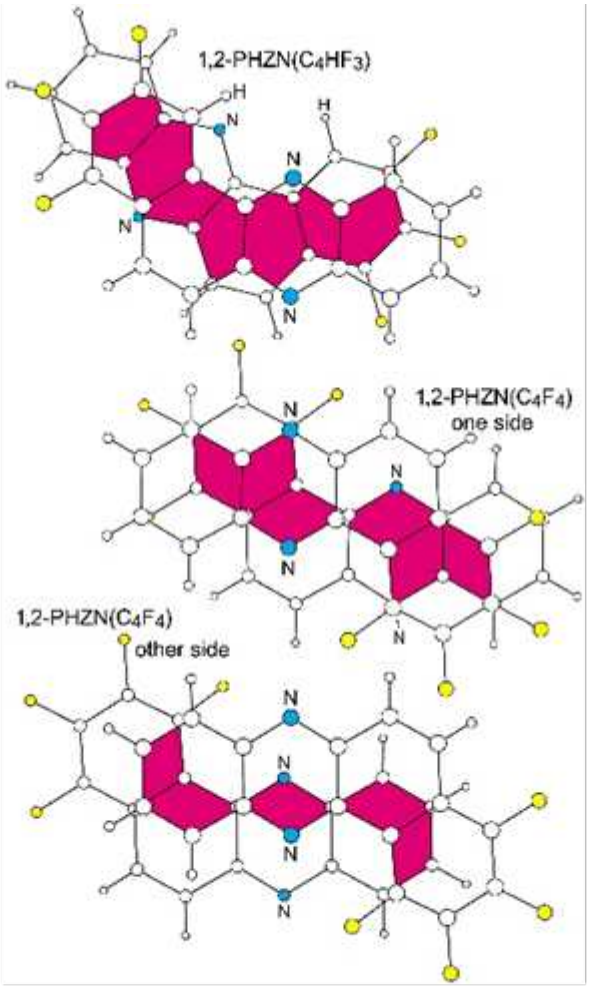

Figure 3-8. Overlap drawings of adjacent molecules in stacks in structures of products bearing RD/A substituents.

The range perpendicular π–π overlap distances in stacks of 1,2-PHNZ(C_4F_3H) is 3.31–3.46 Å (eight overlap atoms, including two C–F C(sp^2) atoms; ave. 3.40 Å; the π–π overlaps on both sides of the molecule are the same). The ranges for the different sides of each 1,2-PHNZ(C_4F_4) molecule in the stack are 3.26–3.35 Å (eight overlap atoms; ave. 3.30 Å) and 3.36–3.40 Å (eight overlap atoms; ave. 3.39 Å). The structure of 1,2,3,4-ANTH$(F)_4$ also exhibits parallel head-to-tail stacks with average perpendicular π–π overlap distances of 3.37 and 3.43 Å.[21] The π–π overlaps in 1,2-PHNZ(C_4F_4) and ANTH$(F)_4$ are shown in figure D.3-2. The hexagonal arrays of stacks in 1,2-PHNZ(C_4HF_3), 1,2-PHNZ(C_4F_4), and ANTH$(F)_4$ are shown in Figure D.3-3.

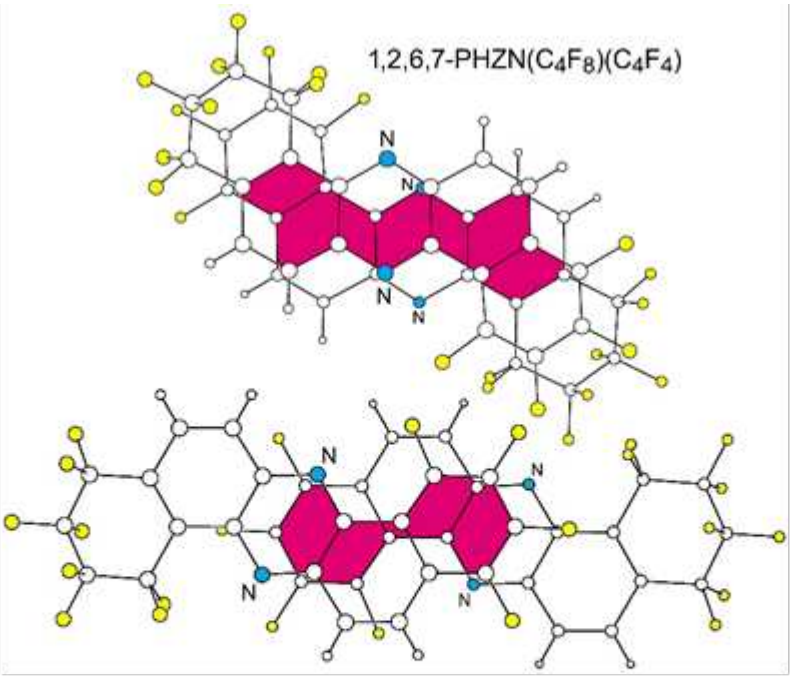

Figure 3-9. Overlap drawings of adjacent molecules in stacks of parallel head-to-tail molecules in the structure of 1,2:6,7-PHNZ(C_4F_8)(C_4F_4) (N and F atoms shaded blue and yellow, respectively). The average perpendicular distances of N and C(sp^2) atoms from the least-squares planes of the aromatic core of neighboring molecules in the stack are 3.47 Å (upper drawing) and 3.42 Å (lower drawing).

In the preliminary structure of 1,2:6,7-PHNZ(C_4F_8)(C_4F_4), the fact that the C_4F_4 substituent is co-planar with the PHNZ core also results in substantial π–π overlap, although the perpendicular distances are greater than in 1,2-PHNZ(C_4F_3H) and 1,2-PHNZ(C_4F_4), as shown in Figure 3-9. The ranges for the different sides of each 1,2:6,7-PHNZ(C_4F_8)(C_4F_4) molecule in the stacks of head-to-tail parallel molecules are 3.42–3.52 Å (seven overlap atoms; ave. 3.47 Å) and 3.24–3.52 Å (six overlap atoms; ave. 3.42 Å). Drawings of the stacks of head-to-tail parallel molecules and the hexagonal array of stacks in the structure of 1,2:6,7-PHNZ(C_4F_8)(C_4F_4) are shown in figure D.3.4.

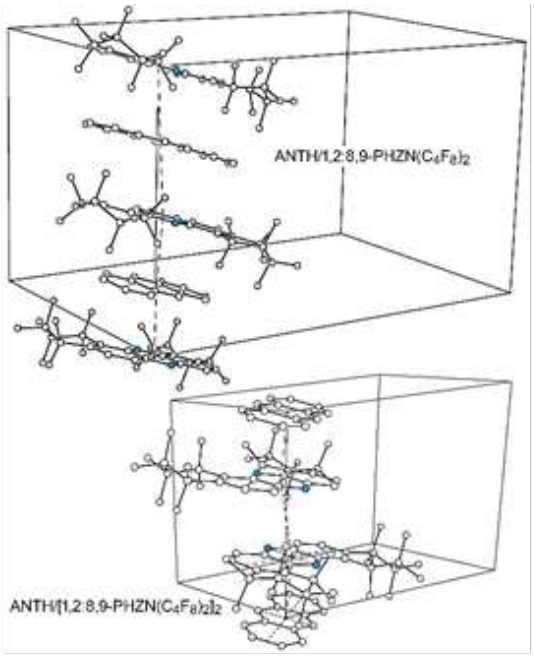

Figure 3-10. Stacking of ANTH donors and 1,2:8,9-PHNZ$(C_4F_8)_2$ acceptors along the crystallographic *b* axes in the co-crystal structures of ANTH/1,2:8,9-PHNZ$(C_4F_8)_2$ (top; b = 14.70 Å) and ANTH/[1,2:8,9-PHNZ$(C_4F_8)_2]_2$ (bottom; b = 10.50 Å; N atoms shaded and H atoms omitted for clarity). The dashed lines connect the centroids of the central hexagon of each molecule. The drawings are to scale.

3.2.2.b. D/A cocrystals

The structures of ANTH/1,2:8,9-PHNZ$(C_4F_8)_2$ and ANTH/[1,2:8,9-PHNZ$(C_4F_8)_2]_2$ consist of infinite A/D/A/D and D/A/A/D/A/A stacks of ANTH donors and ANTH/1,2:8,9-PHNZ$(C_4F_8)_2$ and ANTH/[1,2:8,9-PHNZ$(C_4F_8)_2]_2$ acceptors (A), respectively, aligned along the respective crystallographic b axes, as shown in Figure 3-10. In addition to the difference in donor/acceptor stoichiometry, an important difference is that the perpendicular distances of N and/or C(sp^2) atoms of the acceptor that overlap the least-square plane of the π system of the donor are 3.44–3.58 Å for ANTH/1,2:8,9-PHNZ$(C_4F_8)_2$ (five overlaps; ave. 3.52 Å) but are significantly shorter, 3.27–3.42 Å (five overlaps; ave. 3.34 Å), for ANTH/[1,2:8,9-PHNZ$(C_4F_8)_2]_2$. Drawings showing the D/A and A/A overlap in ANTH/[1,2:8,9-PHNZ$(C_4F_8)_2]_2$ are shown in Figure 3-11 (the A/A perpendicular π–π overlaps, at 3.41–3.45 Å (six overlaps; ave. 3.43 Å), are ca. 0.1 Å larger than

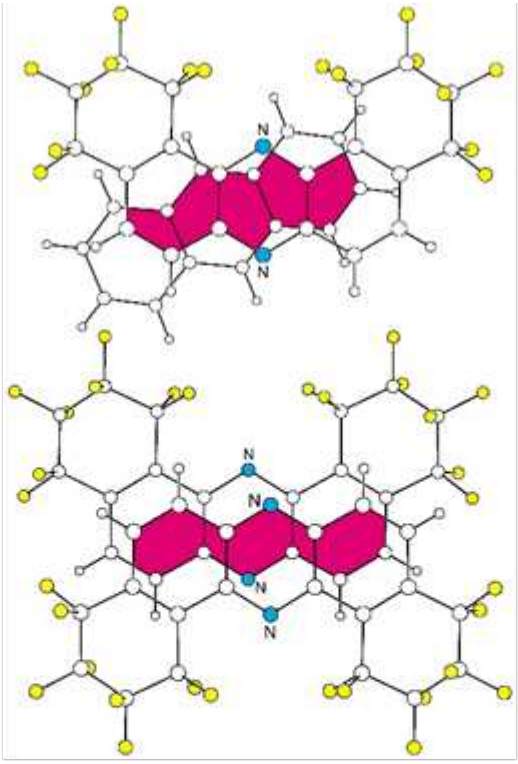

Figure 3-11. Overlap drawings of the ANTH donor and 1,2:8,9-PHNZ(C_4F_8)$_2$ acceptors in the structure of ANTH/[1,2:8,9-PHNZ(C_4F_8)$_2$]$_2$ (N and F atoms shaded blue and yellow, respectively). In both drawings the least-squares planes of the N and C(sp^2) atoms in the upper molecules are in the plane of the page. The ANTH major axis is rotated 23.2° from the 1,2:8,9-PHNZ(C_4F_8)$_2$ major axis. The least-squares plane of the ANTH donor is tilted 3.4° from the plane of the acceptor. In the lower drawing, the least-squares planes of the two acceptors are rigorously parallel.

the D/A overlaps in this compound). The D/A overlap drawings for ANTH/1,2:8,9-PHNZ(C_4F_8)$_2$ are shown in figure D.3-5. Except for the nearly 0.2 Å difference in D/A π–π separation, they are similar in appearance to the D/A overlap drawing for ANTH/[1,2:8,9-PHNZ(C_4F_8)$_2$]$_2$ in Figure 3-11 (i.e., similar regions of overlap, similar D/A major axis rotation). The distorted hexagonal array of stacks in ANTH/[1,2:8,9-PHNZ(C_4F_8)$_2$]$_2$ is shown in figure D.3-6.

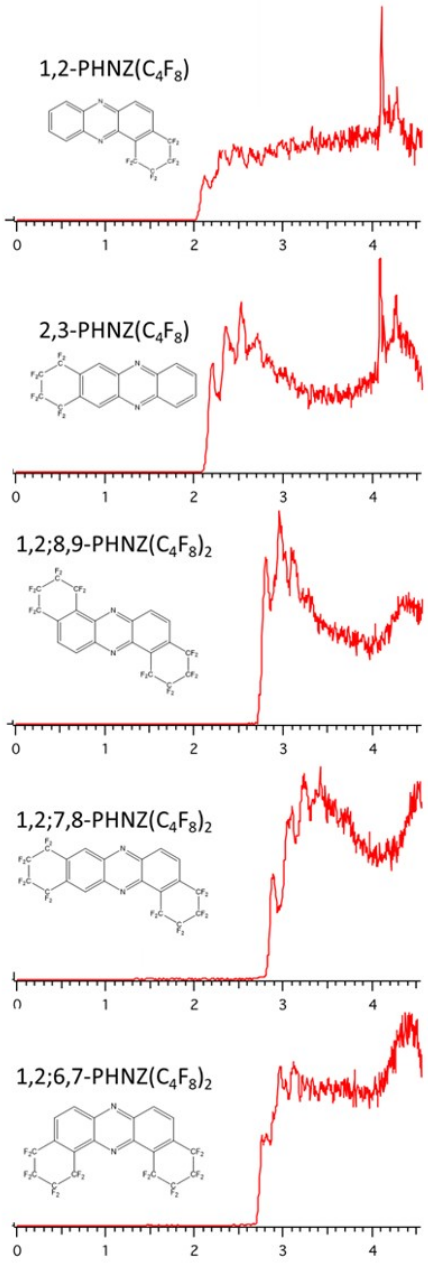

Figure 3-12. Low-temperature photoelectron spectra (20 K, 266 nm) for a series of PHNZ$(C_4F_8)_n$ derivatives. Compounds bearing 2 groups approach, and, in the case of 1,2;7,8-PHNZ$(C_4F_8)_2$, surpass, the 2.8 eV threshold for air stable electron acceptor materials.

Table 3-1. $E_{1/2}(0/-)$ values and electron affinities (*EA*s) for PHNZ$(C_4F_8)_n$ compounds

compound	$E_{1/2}$, V vs. $Fe(Cp)_2^{+/0}$	gas-phase *EA*, eV
1,2-PHNZ(C_4F_8)	-1.17(1)	2.12(2)
2,3-PHNZ(C_4F_8)	-1.12(1)	2.21(1)
1,2;6,7-PHNZ$(C_4F_8)_2$	-0.81(1)	2.81(1)
1,2;7,8-PHNZ$(C_4F_8)_2$	-0.73(1)	2.89(1)
1,2;8,9-PHNZ$(C_4F_8)_2$	-0.80(1)	2.77(1)

3.2.4. PHNZ derivatives as electron acceptor materials

3.2.3.a. Gas phase EA

Low temperature PES of the five PHNZ$(C_4F_8)_n$ compounds were recorded, shown in Figure 3-12. The $E_{1/2}(0/-)$ values and electron-affinities (*EA*s) derived from the LT-PES of all five PHNZ$(C_4F_8)_{1,2}$ compounds are listed in table 3-1. As in previous chapters, this data was collected at PNNL by Dr. Xue-Bin Wang using the method described in appx A.4.8.[18]

Analysis of the values of EA for these five compounds reveals that for compounds bearing two C_4F_8 substituents, the threshold for air stable electron acceptor materials, of *c.a.* 2.8 eV,[8] is met, and, in the case of the compound bearing a peninsular substitution, 1,2;7,8-PHNZ$(C_4F_8)_2$, is exceeded.

The average incremental increase in EA value per C_4F_8 group, calculated using the literature value of 1.3 eV for unsubstituted PHNZ,[14] is 0.84 eV. This value is similar to the large incremental increase observed for the various PAH and hetero-PAH substrates reported in chapter 2. Again, the increase is much larger than would be expected for 2 fluoroalkyl substituents, which each increase EA by *c.a.* 0.25 eV, depending upon the PAH substrate.

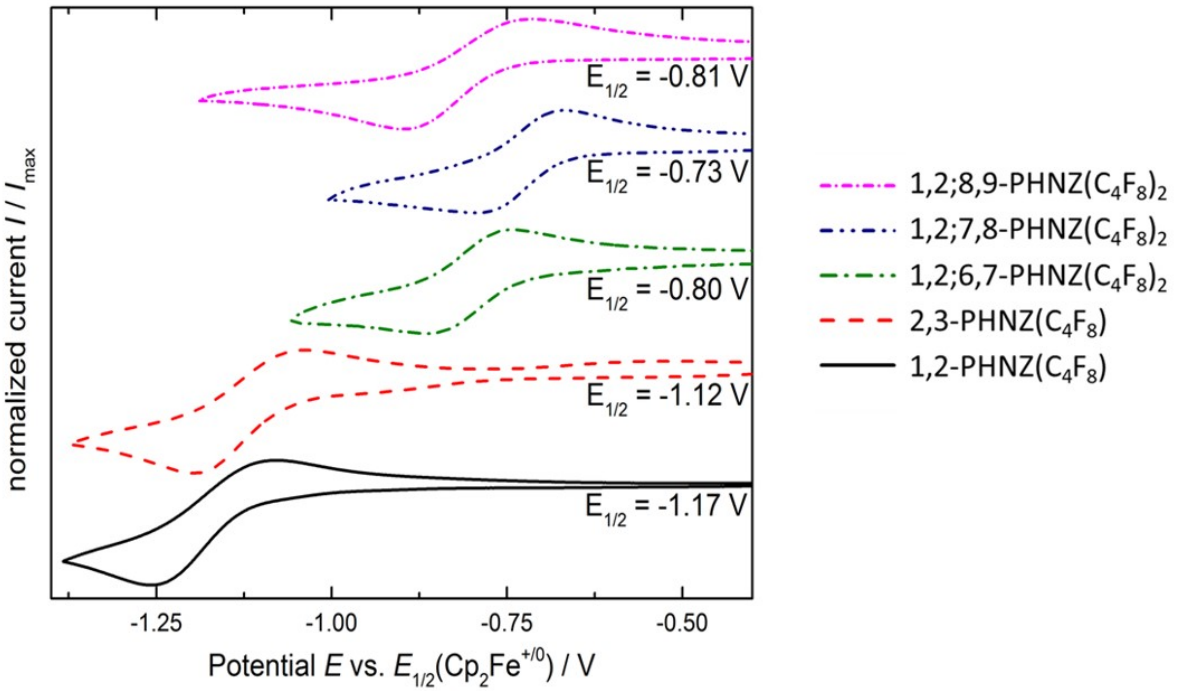

Figure 3-13. Cyclic voltammograms of a series of $PHNZ(C_4F_8)_n$ derivatives, illustrating the substantial shift in $E_{1/2}$ as induced by C_4F_8 groups. Measured vs $Fe(Cp)_2^{+/-}$, 0.1 M $TBAPF_6$ solution in acetonitrile, 100 mV sec^{-1}. Normalized to maximum current value.

3.2.3.b. Cyclic voltammetry

In contrast to the irreversible behavior of $TRPH(C_4F_8)_n$ derivatives, $PHNZ(C_4F_8)_n$ derivatives showed unexpected quasi-reversible CVs, shown in Figure 3-13. A plot of the $E_{1/2}(0/-)$ vs gas-phase *EA*s for PHNZ,[34] seven $PHNZ(CF_3)_n$ compounds (n = 2–6),[35] and the five $PHNZ(C_4F_8)_{1,2}$ compounds studied in this work is shown in Figure 3-14. The plot shows a linear correlation with a slope of 0.62(3) V/eV, showing that differences in the gas-phase energy changes upon reduction are attenuation in solution. This appears to be a general phenomenon, at least for PAHs and PAH derivatives with perfluorocarbyl substituents. A similar linear plot for pyrene (PYRN) and three $PYRN(CF_3)_{5,6}$ derivatives, shown in figure D.3-11, has a slope of 0.70(2) V/eV.

This experimental evidence is particularly significant as it is rare to find experimental *EA*s and the corresponding experimental $E_{1/2}(0/-)$ values for the same set of PAHs and/or PAH

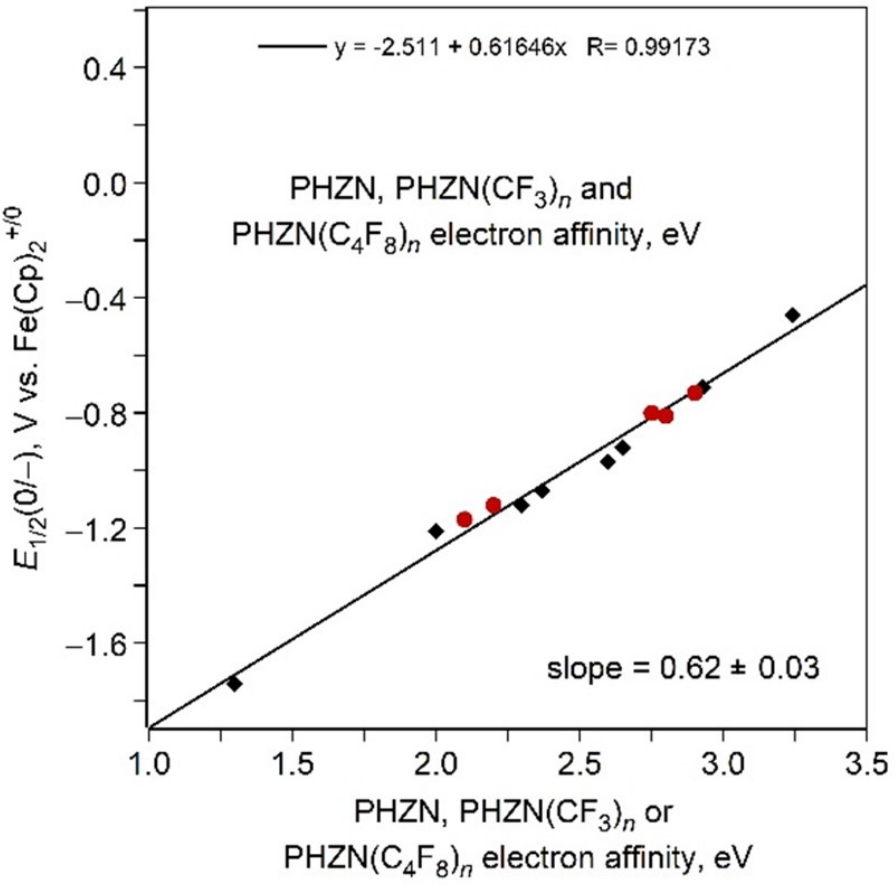

Figure 3-14. Plot of $E_{1/2}(0/-)$ values vs electron affinities for phenazine (PHNZ), seven PHNZ$(CF_3)_n$ derivatives (n = 2-6), and the five PHNZ$(C_4F_8)_{1,2}$ compounds (red circles) studied in this work. Note that the lengths and ranges of values on both axes are equal (i.e., these are square plots), to show unambiguously that the slope of the linear least-squares fit to the data is significantly less than unity.

derivatives, and it is rarer still to find sets of data that were measured with the same instrumentation and under the same conditions in the same laboratories. Therefore, calculated *EA*s and either calculated or "corrected" experimental $E_{1/2}(0/-)$ values are often used to make $E_{1/2}(0/-)$ vs *EA* plots, and it is not uncommon to find plots with slopes of 0.9–1.0 V/eV.[36-41] However, a recent paper by Calbo, Aragó, et al. reported calculated *EA*s for a variety of aromatic molecules and strong electron acceptors, and a plot (prepared for this work) of their G3(MP2) *EA*s vs. experimental $E_{1/2}(0/-)$ values has a slope of 0.75(4) V/eV, as shown in appx. D.3.3., although neither the plot nor the magnitude of the slope of the linear correlation was included or discussed in their paper.[42]

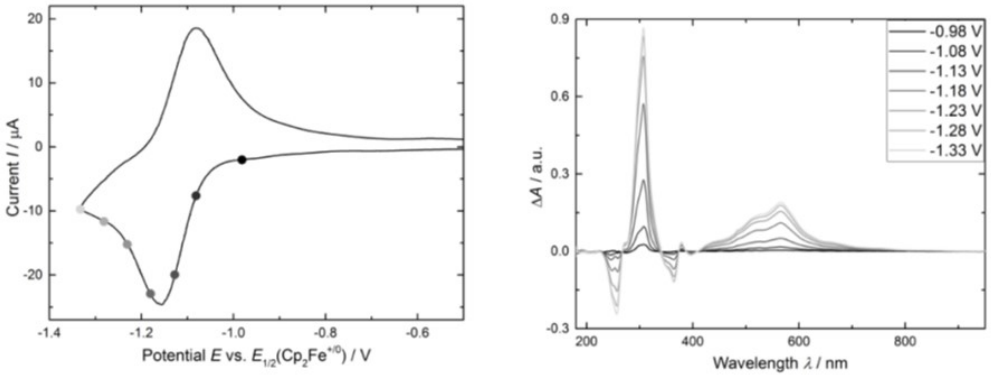

Figure 3-15. Example of the spectroelectrochemical study of 2,3-PHNZ(C_4F_8). Absorption spectra (right) monitored during reduction (left) for spectroelectrochemical experiments.

3.2.3.c. Spectroelectrochemical studies

The author performed spectroelectrochemical experiments with Dr. Peter Machata and Ilka Vincon at the Leibnitz Institute (IFW) Dresden, under the supervision of Dr. Alexey Popov. Optical and electrochemical properties of were investigated by in-situ ESR and UV-Vis spectroscopy while reversibly reducing and oxidizing the sample via cyclic voltammetry, A sweep is illustrated in Figure 3-15(a). The changes in absorbance and the ESR-response have been measured at 0.05 V intervals. Studies were performed on the five PHNZ(C_4F_8)$_n$ compounds for which EA and $E_{1/2}$ values were obtained. For clarity, the discussion in this section pertains to a single compound, 2,3-PHNZ(C_4F_8), but the finding was also observed for the other four compounds. Difference absorption spectra obtained at the marked potentials are shown in Figure 3-15.

At approximately -0.98 V vs. $E_{1/2}(Fc^{+/0})$, the reduction of the neutral compound sets in with an increase in the absorption signal until the switch potential of -1.33 V is reached. The formed anionic species is characterized by a strong absorbance band in the UV-range at about 300 nm and a broad absorption in the visible range. The absorption in the visible region causes a color shift from a yellow-brown solution for the neutral compound to an intensely reddish color after reduction to the anion. The intensity of the optical signal is directly proportional to the

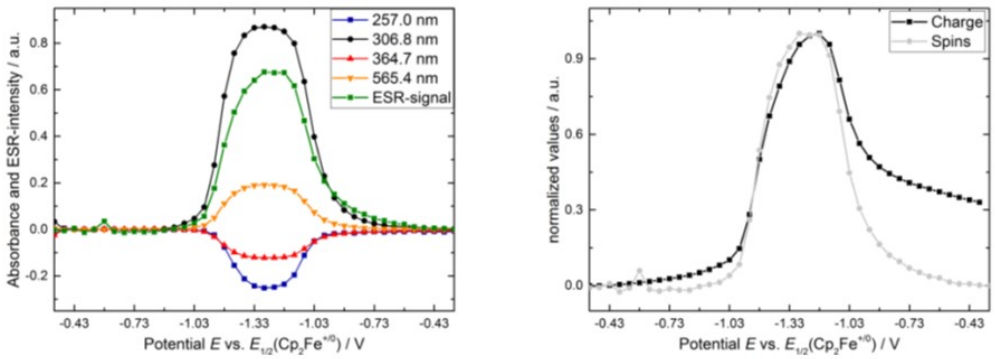

Figure 3-16. Example of the spectroelectrochemical study of 2,3-PHNZ(C_4F_8). ESR signal and absorption monitored during reduction (right), and charge and spin number during reduction (left).

concentration of the anionic species. Thus, the growth in signal intensity in Figure 3-15 implies an increase in concentration until a maximum is reached at the switch potential. A similar behavior is found for the simultaneously monitored ESR-signal, shown in Figure 3-16, green trace. The integrated intensity of the EPR signal is directly proportional to the number of spins generated in solution.

An identical signal evolution for several absorption bands and the ESR-response suggest that no follow-up processes occur, and the paramagnetic species formed by reduction is identical to the one monitored by the optical changes. The chemical reversibility of the reduction is confirmed by the return of the signal intensities to zero after completion of the sweep.

For further confirmation, the charge transferred during the potential sweep has been compared to the number of spins produced, as seen in Figure 3-16. The potential dependency during the forward scan is identical. The ratio between the difference in number of charges and number of spins at adjacent potential values is close to one. This implies that for each transferred charge, one radical is formed which confirms that the radical is stable on the time-scale of the scan.

Such behavior was observed for all PHNZ derivatives investigated. The deviation at the beginning of the scan can be attributed to non-faradaic currents when recharging the diffusion layer. During the backward scan, the spin number decreases more rapidly. In a simple picture, this implies that a larger number of electrons is released by oxidation of the anionic radicals than

transferred to the electrode. However, such a behavior is generally indicative for unstable radicals and the forward scan showed no signs for side reactions.

A possible explanation is partial diffusion of radical molecules out of the sensitive ESR-region in front of the electrode during the scan conducted at a low scan rate of only 2.5mV/s. Since only a part of the radical formed in the beginning can be reduced again, the charge signal does not fully return but converges to a non-zero value. Such a trend depending on the applied scan rate has been observed by Dunsch et al.[43] with an opposing deviation noticed for large scan rates. Thus, by choice of a faster scan rate, the deviation could be diminished.

In summary, a spectroelectrochemical analysis revealed that compounds are reduced by a single electron transfer to a paramagnetic, anionic species which is stable on the time scale of the experiment and can be reversibly oxidized. The anionic form is characterized by a strong absorption in the UV-range at approximately 300 nm and a broad absorption in the visible range inducing a color change from a yellowish to a red solution.

All reduced species show a major absorbance in the UV-range at about 300nm and broad absorption signal in the visible range with a maximum at about 600 nm. However, slightly different were observed for each reduced species. (appx D.3.4). These slight differences mirror the differences in reduction potential and EA, in that molecules containing peninsular substitutions are slightly different than those that do not.

3.2.3.d. ESR hyperfine structure and DFT computational studies

In order to explore the positional effects of C_4F_8 substituents on the PHNZ core, ESR hyperfine structure was both stimulated and investigated experimentally, and spin density distributions were calculated.

In order to obtain high resolution ESR signals for analysis of hyperfine structure, a large amount of radical was generated at a fixed potential (appx A.4.5). Since light elements like carbon and nitrogen only possess small spin orbit couplings [44] the deviation from the g-factor of the free electron is generally small and comparable for different aromatic systems. However, in this case,

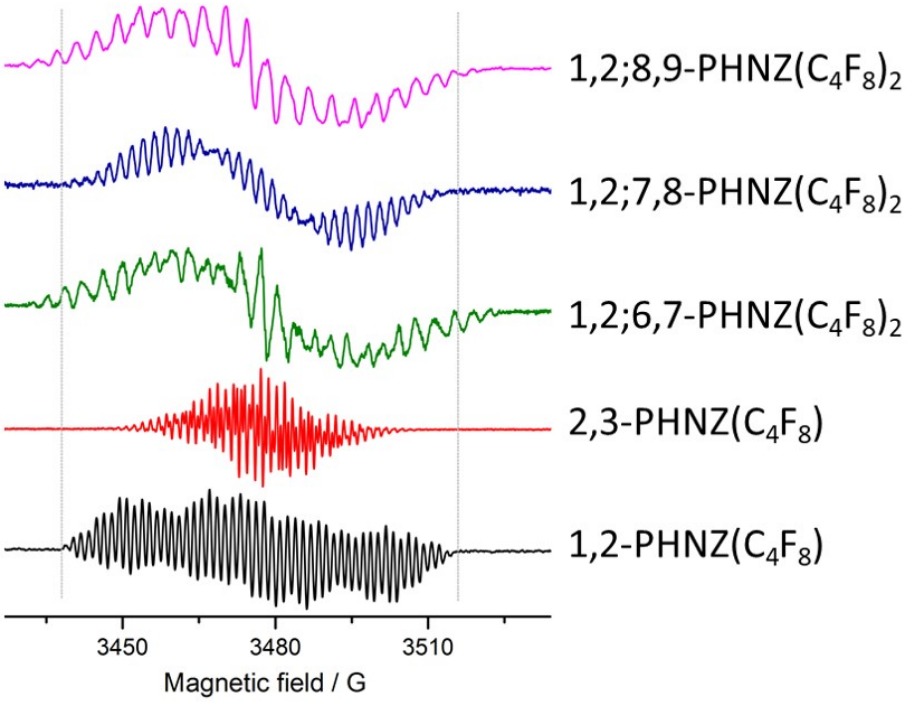

Figure 3-17. ESR signals with resolved hyper-fine splitting for a series of PHNZ$(C_4F_8)_n$ derivatives.

the spectra, shown in Figure 3-17, are significantly broader than expected compared to comparable systems, and the width of the spectra vary greatly between different PHNZ derivatives.[45] Of particular note, the width of the spectrum of 2,3-PHNZ(C_4F_8) is almost half that of the other compounds. This implies that the radical electron in the PHNZ core interacts strongly with some nuclei, most likely the fluorine atoms in the substituents, and that the interaction is different for substituents at different positions

This assumption is confirmed by theoretical determination of ESR-coupling constants for the energetically most favorable structure, which predicts by far the largest values for the fluorine nuclei with coupling constants in the range of 20-80 MHz, while coupling constants for N and H nuclei are only between 2-10 MHz . Especially large values are predicted for fluorine atoms attached to fissure-position C-atoms. This explains the fact that the narrowest spectrum is that obtained for the single compound investigated here which did not bear a fissure-position substituent.

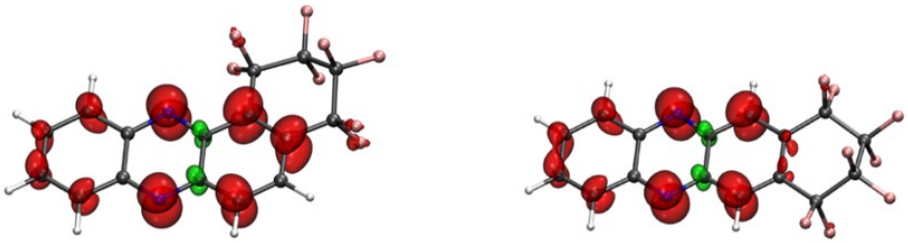

Figure 3-18. Spin density distribution for 1,2-PHNZ(C_4F_8) (right) and 2,3-PHNZ(C_4F_8) (left), showing that in the former case, more spin density is localized on the C atoms bearing the C_4F_8 substituent.

Study of the spin density distribution further clarified this trend. Figure 2-18 shows the spin density distribution associated with substitution at fissure vs peninsular positions. As can be seen, there is much more density on C atoms bearing a fluorous substituent in the case of fissure substitution.

As a final confirmation ESR spectra were simulated and compared to experimental results. These results are shown in Figure 3-19. However, the match was not good using a theoretically predicted geometry. However, upon assuming a flexible C_4F_8 ring, and therefore treating the two different F atoms on each C atom as chemically equivalent, the match improved. This meant that

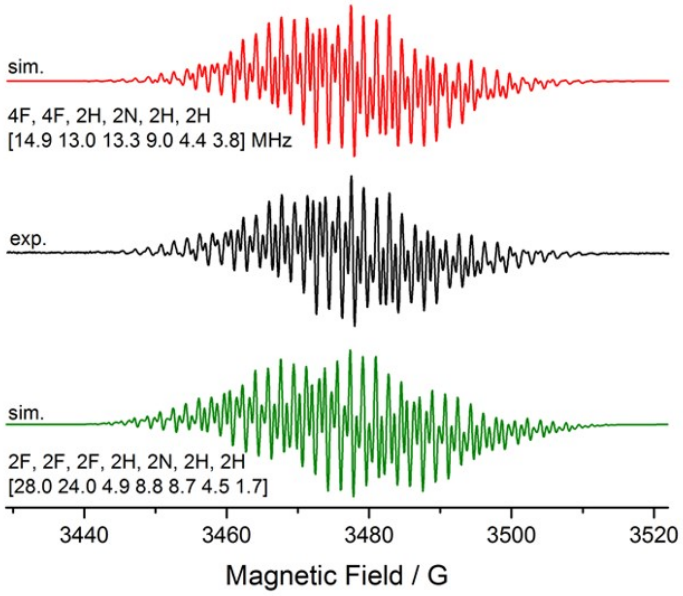

Figure 3-19. Experimental (black, middle) and simulated ESR spectra of 2,3-PHNZ(C_4F_8) assuming fixed ring configuration (green, bottom), and flexible ring (red, top). Better agreement is seen between the experimental spectrum and the simulated spectrum assuming a flexible ring.

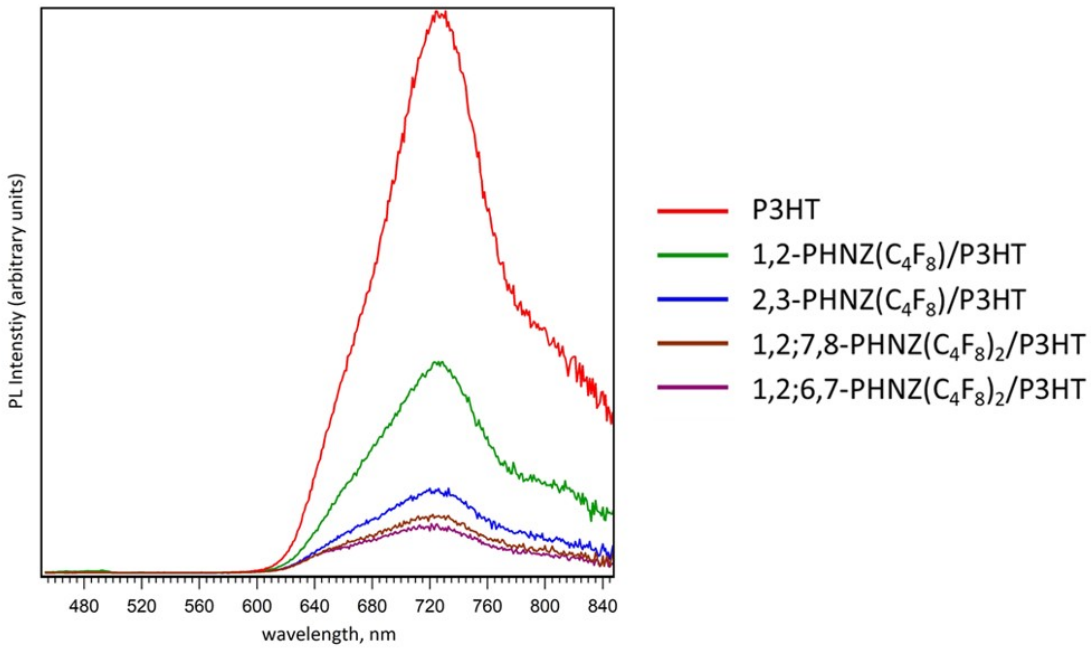

Figure 3-20. PL spectra films of P3HT (red, highest PL intensity) and films of P3HT/PHNZ derivative blends. PL in blended films, indicating PHNZ derivatives are behaving as acceptors. 1,2-PHNZ(C_4F_8) blend has the second highest PL, followed by 2,3-PHNZ(C_4F_8) blend, then the two bends containing PHNZ(C_4F_8)$_2$ isomers. Therefore, PL decreases for films with compounds with higher EAs, as expected.

for the peninsular substation, the molecule was modeled as having quasi-C_{2v} symmetry containing only 2 distinct types of F atom. With this approach, good agreement between simulated and experimental results was obtained.

3.2.3.e. PL spectra

Having confirmed the electronic properties of PHNZ derivatives made them good candidates for electron acceptor materials, thin films were prepared with the donor polymer P3HT, and evaluated by photoluminescence spectroscopy. The donor P3HT was chosen due to its good energy alignment with the HOMO/LUMO levels of the PHNZ derivatives, estimated from the EA and CV data discussed above.[46] Films were prepared by the author in the laboratory of Dr. Nikos Kopidakis at Macquarie university, and experiments were performed by the author in the laboratory of Dr. Koushik Venkatesan at Macquarie University. (appx A.4.6) Films were *ca.* 10

wt % PHNZ derivative, 90 wt % P3HT (for details see table D.3.x), and PL spectra were collected by the author in the laboratory of Dr. Koushik Venkatesan at Macquarie University in Sydney, Australia.

For neat films of P3HT, signal was observed, which was significantly quenched for donor/acceptor (D/A) blend films. The degree of quenching conforms to trends based on analysis above. For the compounds with two C_4F_8 groups and consequently higher EA values, the most quenching is observed as shown in Figure 3-20. For the compounds bearing only one C_4F_8 group, better quenching is observed for peninsular substitution over bay substitution.

3.2.3.f. Microwave conductivity measurements

Microwave conductivity measurements were made by the author in the laboratory of Dr. Nikos Kopidakis at Macquarie University in Sydney, Australia. The same films were used as used for photoluminescence measurements.

This technique allows ns-μs timescale measurements of dynamics of photo-induced charge-carriers.[47] Free charge carriers are generated by laser illumination, in a microwave chamber. The free charge carriers absorb microwave energy, allowing the quantum yield of charge carriers and the sum of their mobilities to be calculated.

Figure 3-21 shows the $\Phi\Sigma\mu$ figure of merit for the thin film samples. High values indicate efficient free-charge carrier generation, which is expected to be much higher in the presence of an electron acceptor than in a neat P3Ht film. (Intensity is $\Phi\Sigma\mu = \Delta G/\beta q_e F_A I_0$ where βis the ratio of the waveguide cross section dimensions (2.2 for the instrument used), q_e is the charge of an electron, I_0 is the incident photon flux, and F_A is. the fraction absorbed by the sample (1 for the samples here). Specific photon flux for each film is listed in appx D.3.5)

Based on these results, it can be concluded that PHNZ derivatives studied in these chapters function as electron acceptors. The films doped with PHNZ derivatives show evidence of

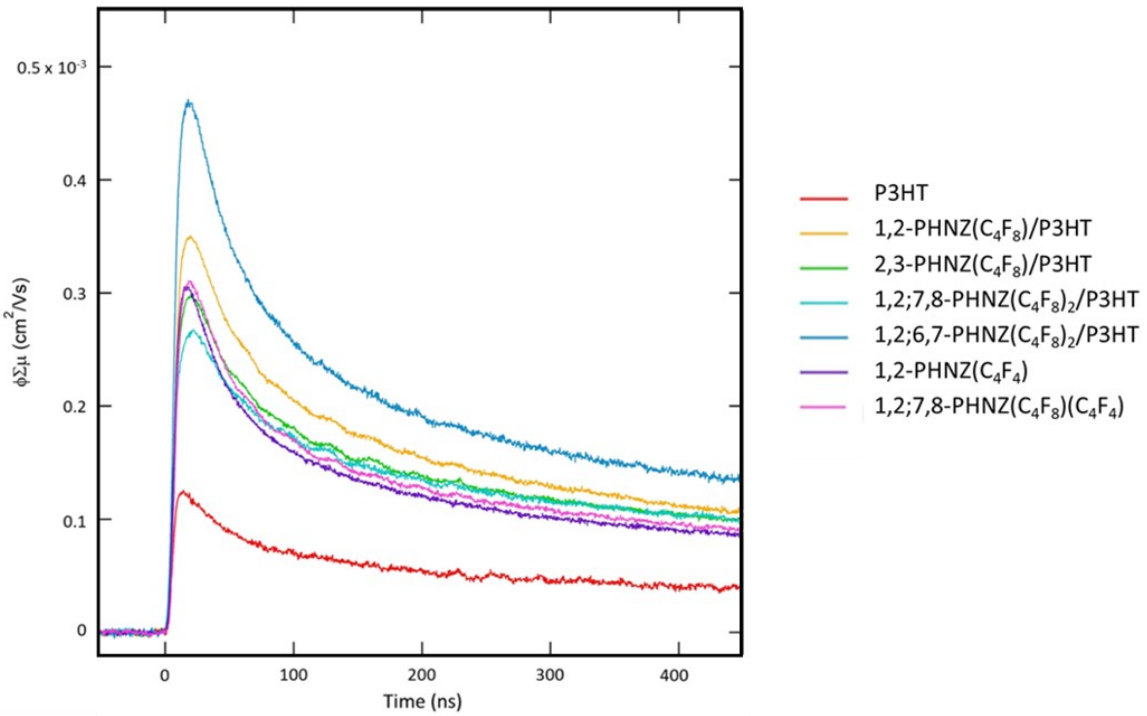

Figure 3-21. Transient profile decay curves over 450 ns for neat P3HT film and films with 7-9 wt % PHNZ derivatives/P3HT blends. All blends behave as acceptors, with higher ΦΣμ values, corresponding to higher ΔG values than the P3HT reference film (red trace, bottom).

significantly more free charge carrier generation than neat P3HT. However, no strong correlations between microwave conductivity and structure are apparent.

At higher optical density (i.e. lower photon flux) no signal was observed. Material limitations prevented films of over 10 wt % from being made. However, TRMC is relatively insensitive to concentration, as charges need not migrate to electrodes. Therefore, it is not likely that much improvement would be seen with more material.

3.3. SUMMARY AND CONCLUSIONS

In summary, a family of PHNZ derivatives has been synthesized and investigated as electron acceptor materials. A family of molecules was synthesized utilizing the gas-phase radical reaction developed in the preceding chapters of this work. A new, solution-based synthetic technique allowed isolation of hitherto-unobserved C_4F_8I moieties bound to the hetero-PAH core.

A number of single crystal X-ray structures, including donor/acceptor complexes, were obtained. The formation of D/A complexes shows promise that these materials function as electron acceptor materials.

Extensive analysis of electronic properties of PHNZ$(C_4F_8)_n$'s by low temperature PES, electrochemistry, spectroelectrochemistry, and computational results was carried out. As a result, it was determined that compounds bearing at least two C_4F_8 groups have suitable properties to function as electron acceptors. Properties were found to be dependent upon substitution position. For fissure substitutions, spin-density of the reduced species was located much nearer to the fluorous substituent, resulting in a reduced effect upon electron acceptor properties. Peninsular substitution is therefore preferred.

The predictions of these studies were validated by PL spectroscopy and TRMC measurements, confirming that PHNZ$(C_4F_8)_n$'s function as electron acceptors. In particular, PL spectroscopy revealed trends aligning with expected results. Compounds with peninsular substitutions are better electron acceptors than compounds with fissure substitutions.

Further studies of electronic properties of RD/A products would be revealing, as the fully aromatic systems, especially those with acene-like character resulting from RD/A of peninsular substituents, are expected to be excellent acceptors. However, further synthetic optimization to yield higher amounts of RD/A product would be necessary to generate sufficient amounts of materials for these studies.

REFERENCES

1. Turner, J. M.; Messenger, A. J., Occurrence, Biochemistry and Physiology of Phenazine Pigment Production. *Adv. Microb. Physiol.* **1986,** *27*, 211-275.
2. Laursen, J. B.; Nielsen, J., Phenazine Natural Products: Biosynthesis, Synthetic Analogues, and Biological Activity. *Chem. Rev.* **2004,** *104* (3), 1663-1686.
3. Singh, M. K.; Pal, H.; Bhasikuttan, A. C.; Sapre, A. V., Dual solvatochromism of neutral red. *Photochem. Photobiol.* **1998,** *68* (1), 32-38.
4. Swan, G. A.; Felton, D. G. I., Phenazines. In *The Chemistry of Heterocyclic Compounds*, Weissberger, A., Ed. Interscience: London, 1957; Vol. XI.
5. Pauliukaite, R.; Ghica, M. E.; Barsan, M. M.; Brett, C. M. A., Phenazines and Polyphenazines In Electrochemical Sensors and Biosensors. *Anal. Lett.* **2010,** *43* (10-11), 1588-1608.
6. Gu, P.-Y.; Zhao, Y.; He, J.-H.; Zhang, J.; Wang, C.; Xu, Q.-F.; Lu, J.-M.; Sun, X. W.; Zhang, Q., Synthesis, Physical Properties, and Light-Emitting Diode Performance of Phenazine-Based Derivatives with Three, Five, and Nine Fused Six-Membered Rings. *J. Org. Chem.* **2015,** *80* (6), 3030-3035.
7. He, Z.; Liu, D.; Mao, R.; Tang, Q.; Miao, Q., Hydrogen-Bonded Dihydrotetraazapentacenes. *Org. Lett.* **2012,** *14* (4), 1050-1053.
8. Liang, Z.; Tang, Q.; Xu, J.; Miao, Q., Soluble and Stable N-Heteropentacenes with High Field-Effect Mobility. *Adv. Mater.* **2011,** *23* (13), 1535-1539.
9. Miao, S.; Brombosz, S. M.; Schleyer, P. V.; Wu, J. I.; Barlow, S.; Marder, S. R.; Hardcastle, K. I.; Bunz, U. H. F., Are N,N-dihydrodiazatetracene derivatives antiaromatic? *J. Am. Chem. Soc.* **2008,** *130* (23), 7339-7344.
10. Bunz, U. H. F., N-Heteroacenes. *Chem. Eur. J.* **2009,** *15* (28), 6780-6789.
11. Winkler, M.; Houk, K. N., Nitrogen-rich oligoacenes: Candidates for n-channel organic semiconductors. *J. Am. Chem. Soc.* **2007,** *129* (6), 1805-1815.
12. Li, J.; Zhang, Q., Linearly Fused Azaacenes: Novel Approaches and New Applications Beyond Field-Effect Transistors (FETs). *ACS Appl. Mater. Interfaces* **2015**.
13. Song, C.-L.; Ma, C.-B.; Yang, F.; Zeng, W.-J.; Zhang, H.-L.; Gong, X., Synthesis of tetrachloro-azapentacene as an ambipolar organic semiconductor with high and balanced carrier mobilities. *Org. Lett.* **2011,** *13* (11), 2880-2883.
14. Castro, K. P.; Clikeman, T. T.; DeWeerd, N. J.; Bukovsky, E. V.; Rippy, K. C.; Kuvychko, I. V.; Hou, G.-L.; Chen, Y.-S.; Wang, X.-B.; Strauss, S. H.; Boltalina, O. V., Incremental Tuning Up of Fluorous Phenazine Acceptors. *Chem.-Eur. J.* **2016,** *22* (12), 3930-3936.
15. Schiedt, J.; Weinkauf, R., Photodetachment photoelectron spectroscopy of mass selected anions: anthracene and the anthracene-H_2O cluster. *Chem. Phys. Lett.* **1997,** *266* (1-2), 201-205.
16. Kuvychko, I. V.; Castro, K. P.; Deng, S. H. M.; Wang, X. B.; Strauss, S. H.; Boltalina, O. V., Taming Hot CF_3 Radicals: Incrementally Tuned Families of Polyarene Electron Acceptors for Air-Stable Molecular Optoelectronics. *Angew. Chem., Int. Ed.* **2013,** *52* (18), 4871-4874.
17. Chen, E. C. M.; Wentworth, W. E., A comparison of experimental determinations of electron affinities of pi charge transfer complex acceptors. *J. Chem. Phys.* **1975,** *63* (8), 3183-3191.
18. Wang, X. B.; Wang, L. S., Development of a low-temperature photoelectron spectroscopy instrument using an electrospray ion source and a cryogenically controlled ion trap. *Rev. Sci. Instrum.* **2008,** *79* (7).
19. Chang, Y. C.; Kuo, M. Y.; Chen, C. P.; Lu, H. F.; Chao, I., On the Air Stability of n-Channel Organic Field-Effect Transistors: A Theoretical Study of Adiabatic Electron Affinities of Organic Semiconductors. *J. Phys. Chem. C* **2010,** *114* (26), 11595-11601.

20. Ando, N.; Mitsui, M.; Nakajima, A., Comprehensive photoelectron spectroscopic study of anionic clusters of anthracene and its alkyl derivatives: Electronic structures bridging molecules to bulk. *J. Chem. Phys.* **2007,** *127* (23).
21. Cozzi, F.; Bacchi, S.; Filippini, G.; Pilati, T.; Gavezzotti, A., Synthesis, X-ray Diffraction and Computational Study of the Crystal Packing of Polycyclic Hydrocarbons Featuring Aromatic and Perfluoroaromatic Rings Condensed in the Same Molecule: 1,2,3,4-Tetrafluoronaphthalene, -anthracene and -phenanthrene. *Chem. Eur. J.* **2007,** *13*, 7177–7184.
22. Anthony, J. E., Functionalized Acenes and Heteroacenes for Organic Electronics. *Chem. Rev.* **2006,** *106* (12), 5028-5048.
23. Birchall, J. M.; Haszeldine, R. N.; Kemp, J. E. G., Polyfluoroarenes. Part X. Polyfluoroaromatic azo-compounds. *J. Chem. Soc. C* **1970,** (3), 449-455.
24. Matsui, M.; Ikeda, R.; Kubota, Y.; Funabiki, K., Red solid-state fluorescent aminoperfluorophenazines. *Tetrahedron Lett.* **2009,** *50* (35), 5047-5049.
25. Matsui, M.; Suzuki, M.; Nunome, I.; Kubota, Y.; Funabiki, K.; Shiro, M.; Matsumoto, S.; Shiozaki, H., Reaction, identification, and fluorescence of aminoperfluorophenazines. *Tetrahedron* **2008,** *64* (37), 8830-8836.
26. Horiuchi, S.; Ishii, F.; Kumai, R.; Okimoto, Y.; Tachibana, H.; Nagaosa, N.; Tokura, Y., Ferroelectricity near room temperature in co-crystals of nonpolar organic molecules. *Nature Mater.* **2005,** *4* (2), 163-U57.
27. Hudson, A. G.; Pedler, A. E.; Tatlow, J. C., Electrochemical Oxidation of Polyfluoroaromatic Amines 1. Synthesis of Fluorophenazines. *Tetrahedron* **1970,** *26* (15), 3791-&.
28. Leyva, E.; Medina, C.; Moctezuma, E.; Leyva, S., Chemical oxidation of fluoroanilines to fluoroazobenzenes and fluorophenazines with potassium ferricyanide and potassium hydroxide. *Can. J. Chem.* **2004,** *82* (12), 1712-1715.
29. Khusniyarov, M. M.; Harms, K.; Sundermeyer, J., New highly fluorinated phenazine derivatives: Correlation between crystal structure and NMR spectroscopy. *J. Fluorine Chem.* **2006,** *127* (2), 200-204.
30. Banks, R. E.; Madany, I. M.; Pritchard, R. G., 1,2,4-Trifluoro-6,8-dimethyl-3-trifluromethylphenazine, $C_{15}H_8F_6N_2$, produced via thermolysys of perfluoro-4-azidotoluene in the presence of 2,4,6-trimethylaniline. *Acta Crystallogr., Sect. C: Cryst. Struct. Comm.* **1993,** *49*, 1988-1990.
31. Chernetsky, V.; Yagupolsky, L.; Serebryany, S., Synthesis of Some Fluorine Derivatives of Phenazine, Azobenzene, and Diphenylamine. *Zh. Obschch. Khim.* **1955**, 14.
32. Banks, R. E.; Prakash, A., Studies in Azide Chemistry 6 Some Reactions of Perfluoroazidobenzene and Perfluoro-4-Azidotoluene. *J. Chem. Soc. Perkin Trans. 1* **1974,** (11), 1365-1371.
33. Kuvychko, I. V.; Dubceac, C.; Deng, S. H. M.; Wang, X.-B.; Granovsky, A. A.; Popov, A. A.; Petrukhina, M. A.; Strauss, S. H.; Boltalina, O. V., C20H4(C4F8)3: A Fluorine-Containing Annulated Corannulene that Is a Better Electron Acceptor Than C60. *Angew. Chem. Int. Ed.* **2013,** *52* (29), 7505-7508.
34. Dillow, G. W.; Kebarle, P., Electron Affinities of aza-substituted polycyclic aromatic hydrocarbons. *Can. J. Chem.* **1989,** *67*, 1628–1631.
35. Castro, K. P.; Clikeman, T. T.; DeWeerd, N. J.; Bukovsky, E. V.; Rippy, K. C.; Kuvychko, I. V.; Hou, G. L.; Chen, Y.-S.; Wang, X.-B.; Strauss, S. H.; Boltalina, O. V., Incremental Tuning Up of Fluorous Phenazine Acceptors. *Chem. Eur. J.* **2016,** *22*, 3930–3936.
36. Ruoff, R. S.; Kadish, K. M.; Boulas, P.; Chen, E. C. M., The Relationship between the Electron Affinities and Half-Wave Reduction Potentials of Fullerenes, Aromatic Hydrocarbons, and Metal Complexes. *J. Phys. Chem.* **1995,** *99*, 8843–8850, and references therein.
37. Chen, E. S.; Chen, E. C. M.; Sane, N.; Talley, L.; Kozanecki, N.; Shulze, S., Classification of organic molecules to obtain electron affinities from half wave reduction potentials: The aromatic hydrocarbons. *J. Chem. Phys.* **1999,** *110*, 9319–9329, and references therein.

38. Betowski, L. D.; Enlow, M.; Riddick, L.; Aue, D. H., Calculation of Electron Affinities of Polycyclic Aromatic Hydrocarbons and Solvation Energies of Their Radical Anion. *J. Phys. Chem. A* **2006,** *110*, 12927–12946, and references therein.
39. Modelli, A.; Mussoni, L.; Fabbri, D., Electron Affinities of Polycyclic Aromatic Hydrocarbons by Means of B3LYP/6-31+G* Calculations. *J. Phys. Chem. A* **2006,** *110*, 6482–6486, and references therein.
40. Berionni, G.; Gonçalves, J. M.; Mathieu, C.; Devic, T.; Etchéberry, A.; Goumont, R., Electrochemical and spectrophotometrical investigation of the electron-accepting strength of organic superelectrophiles: X-ray structure of their charge transfer complexes with tetrathiafulvalene. *Phys. Chem. Chem. Phys.* **2011,** *13*, 2857–2869.
41. Méndez-Hernández, D. D.; Tarakeshwar, P.; Gust, D.; Moore, T. A.; Moore, A. L.; Mujica, V., Simple and accurate correlation of experimental redox potentials and DFT-calculated HOMO/LUMO energies of polycyclic aromatic hydrocarbons. *J. Mol. Model* **2013,** *19*, 2845–2848, and references therein.
42. Calbo, J.; Viruela, R.; Ortí, E.; Aragó, J., Relationship between Electron Affinity and Half-Wave Reduction Potential: A Theoretical Study on Cyclic Electron-Acceptor Compounds. *ChemPhysChem* **2016,** *17*, 3881–3890.
43. Petr, A.; Dunsch, L.; Neudeck, A., In situ uv-vis esr spectroelectrochemistry. *Journal of Electroanalytical Chemistry* **1996,** *412* (1), 153-158.
44. Holtzhauer, M., ESR-Spektroskopie — eine Analysenmethode für paramagnetische Zentren in Proteinen. In *Methoden in der Proteinanalytik*, Holtzhauer, M., Ed. Springer Berlin Heidelberg: Berlin, Heidelberg, 1996; pp 202-229.
45. Clikeman, T. T.; Bukovsky, E. V.; Wang, X.-B.; Chen, Y.-S.; Rumbles, G.; Strauss, S. H.; Boltalina, O. V., Core Perylene Diimide Designs via Direct Bay- and ortho-(Poly)trifluoromethylation: Synthesis, Isolation, X-ray Structures, Optical and Electronic Properties. *Eur. J. Org. Chem.* **2015,** *2015* (30), 6641-6654.
46. San, L. K.; Bukovsky, E. V.; Larson, B. W.; Whitaker, J. B.; Deng, S. H. M.; Kopidakis, N.; Rumbles, G.; Popov, A. A.; Chen, Y.-S.; Wang, X.-B.; Boltalina, O. V.; Strauss, S. H., A faux hawk fullerene with PCBM-like properties. *Chem. Sci.* **2015,** *6* (3), 1801-1815.
47. Reid, O. G.; Moore, D. T.; Li, Z.; Zhao, D.; Yan, Y.; Zhu, K.; Rumbles, G., Quantitative analysis of time-resolved microwave conductivity data. *J. Phys. D. Appl. Phys.* **2017,** *50* (49), 493002.

CHAPTER 4. TUNING ELECTRONIC AND OPTICAL PROPERTIES OF ACRIDINE VIA TRIFLUOROMETHYLATION

4.1. CHAPTER 4 INTRODUCTION

In this chapter, the properties of a family of trifluromethylated ACRD derivatives are presented. Similar to the fluorous groups discussed in previous chapters, trifluoromethyl groups dramatically increase the electron accepting properties of PAHs and hetero-PAHs. Previously, Strauss-Boltalina research group members have reported the trifluoromethylation of a large library of PAH substrates[1-4], and Castro *et al.*[5] has reported a family of trifluoromethylated derivatives of the hetero-PAH PHNZ, which is structurally similar to ACRD.

The compound ACRD was first identified in 1870 as an impurity in crude ANTH isolated from coal tar. Its name, which derives from the Latin word for sharp, was chosen due to its irritating effect on skin. It is air stable, basic, hetero-PAH that has a tendency to crystallize in to a variety of polymorphs which have been the subject of extensive study.[6-8] Despite its irritating effect, ACRD is not among the PAHs, which pose acute health or environmental risks, making it a useful PAH for a number of applications including dyes, antiseptics, antimalarials, and antibacterials, fluorescence-based sensors, and more recently, OLED and OPV technologies.[9-13] As a heterocyclic PAH, its interesting physical properties including basicity, its π-system, and its frontier orbital levels have been the subject of numerous calculations.[9]

Acridine and its derivatives are synthetically accessible via several routes, making it a widely available and accessible compound. Bottom-up synthetic pathways generally involve ring closures.[9, 14-16] Substitution reactions are also viable synthetic routes, but often give a mixture of regioisomers.[15] Rearrangements or oxidation and reduction of acridanes or acridones have also been reported.[14]

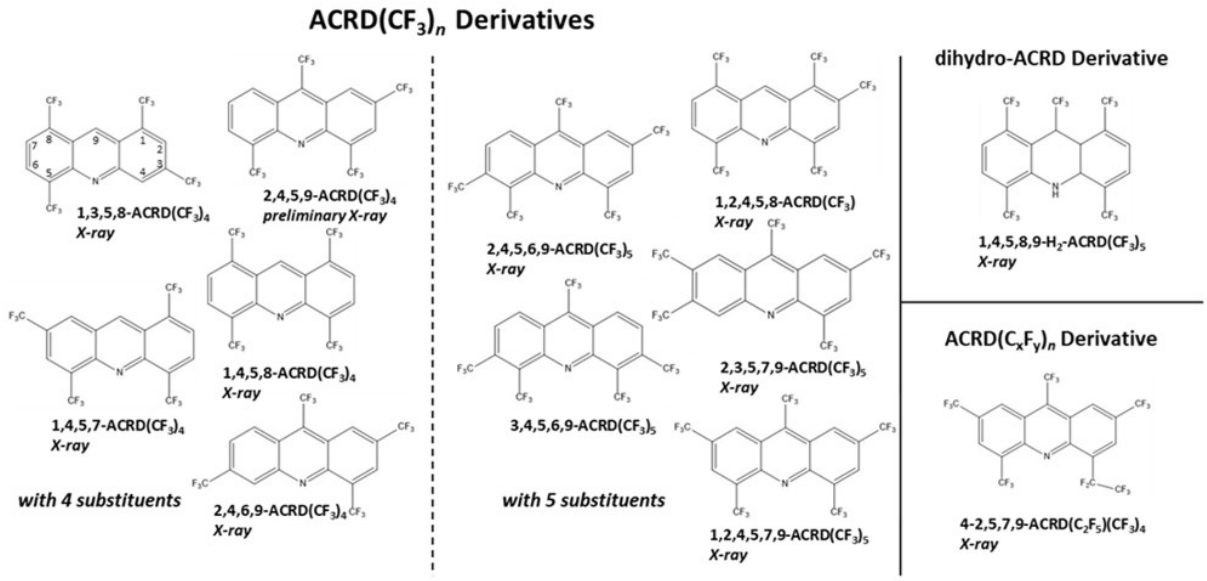

Figure 4-1. Molecular structures of all ACRD derivatives prepared from reaction 4.1. Numbering scheme shown on derivative in upper left. Not pictured is ACRD$(CF_3)_3$-A, a pure compound for which the substitution pattern has not been definitively identified. For the remaining molecules, structural assignment was accomplished via analysis of ^{1}H and ^{19}F NMR spectra. Many of the compounds have also been characterized by single crystal x-ray crystallography, as indicated. For synthesis and purification of these molecules, see sections *4.2.1.a* and *4.2.1.b.* and appx B.4. For structural characterization of molecules, see *4.2.1.c.* and *4.2.1.d.* and appx C.4.

The work reported here employed the synthetic method developed by Kuvychko *et al,.*[17] a route not previously attempted with the substrate ACRD. In this method, , thermal decomposition of CF_3I initiates a gas-phase radical reaction, allowing introduction of CF_3 to the perimeter of PAH cores by substitution of hydrogen atoms. In general, selective formation of specific isomers is not expected for these reactions. Rather, a range of compositions is obtained, with several isomers of each composition. However, as these reactions proceed at high temperatures, the product distribution is close to thermodynamic control.[1, 4] Thus, product distribution is not random, and calculation of relative energies of different isomers allows prediction of possible products.

In this case, the reaction led to isolation of a series of ACRD$(CF_3)_n$ derivatives, with *n* ranging from 3 to 5. The compounds for which definitive structural elucidation was possible are shown in Figure 4-1. An isomer of ACRD$(CF_3)_3$ (ACRD$(CF_3)_3$-A) was also isolated but has not been definitively characterized with respect to substitution pattern. In addition to

triflurомethylated ACRDs, two unusual structures were identified, including a hydroacridine(hydroACRD) derivative resulting from addition, rather than substitution of CF_3 at the 9 position, and a compound bearing a perfluoroethyl group.

Ten single crystal X-ray structures and one preliminary X-ray structure have been obtained, and an analysis of structural properties and solid-state packing is given. Electrochemical, spectroelectrochemical, and computational studies have been carried out on selected compounds. This has led to identification of unique physiochemical trends; of particular interest, a substitution-pattern dependence has been observed for reduction potential and frontier orbital level shifts associated with trifluoromethylation of ACRD. This phenomenon is unprecedented among other triflurомethylated PAHs and hetero-PAHs, even the structurally similar family of triflurомethylated PHNZs. For example, for previously investigated substrates, functionalization induces positive shifts in reduction potential of *ca*. 0.25 V per CF_3 group. The shift is independent of substitution pattern, although its exact increment is dependent on the size, shape, and composition of the PAH core. In the case of ACRD, the reduction potentials of isomers with the same number of substituents but different substitution patterns can vary by as much as 0.20 V, a shift rivaling the incremental effects of substituent number.

4.2. RESULTS AND DISCUSSION

4.2.1. Synthesis and isolation of pure compounds

4.2.1.a. Reaction to produce ACRD(CF_3)$_n$'s

The reaction to produce the material discussed in this chapter was performed by Dr. Igor V. Kuvychko. ACRD (179 mg, 1 mmol) was placed into a 300 mL glass ampoule. The ampoule was evacuated using a vacuum line equipped with a pressure gauge and a calibrated volume (268 mL). Using the calibrated volume and the pressure gauge CF_3Igas was measured (9 mmol, 9.0 equiv). The CF_3I was condensed into the ampoule using liquid nitrogen, and the ampoule was flame-sealed. It was then placed in a furnace and heated to 330 °C. This temperature was held for 8.5 h, at which point the ampoule was removed and cooled to room temperature. It was then

opened, allowing any gaseous contents to evaporate. The ampoule was rinsed with dichloromethane to retrieve soluble products, forming a dark purple solution. The dichloromethane solution was filtered to remove any insoluble material and washed with a saturated sodium thiosulfate solution (aq) to remove I_2. Upon washing, the dichloromethane solution changed from dark purple to yellow. The dichloromethane was allowed to evaporate, leaving 278 mg of crude product, a relatively high recovery for a gas-phase radical reaction with 179 mg of substrate starting material. Details of this reaction are also given in Appx B.4. For ^{1}H and ^{19}F NMR spectroscopic characterization of the crude product mixture see Appx figure B-44.

4.2.1.b. Multi-stage HPLC purification

Although members of our laboratory have recently reported unprecedented success isolating various trifluoromethylated PAHs, separation of multiple isomers with similar properties and structures is often extremely complex.[17] In the case of ACRD$(CF_3)_x$, lowering core symmetry by introducing N atom exacerbates the problem significantly. Separation of the product of reaction 4.1 required a multi-stage separation with up to four HPLC injections to obtain pure compounds. This separation of ACRD$(CF_3)_n$ derivatives was carried out on a COSMOSIL Buckyprep column, eluent flow rate 5 mL min^{-1} (with one exception in the case of 2,4,6,9-ACRD$(CF_3)_4$, noted below). This column was shown to be useful for separation of similar compounds, notably PHNZ$(CF_3)_n$ derivatives, which differ from ACRD by only by one N atom. As in the case of PHNZ$(CF_3)_n$ derivatives, separation was complicated by the similarity of isomers. In this case, separation was further complicated by the lower symmetry of ACRD (PHNZ has a mirror plane along the long axis of the hetero-acene core; ACRD does not), leading to a higher number of isomers.

Despite this, separation was achieved via a complex multi-step process that was conducted by the combined efforts of Dr. Long K. San, and the author of this work. The following description of this separation concerns only the purification routes which ultimately led to pure products. Many

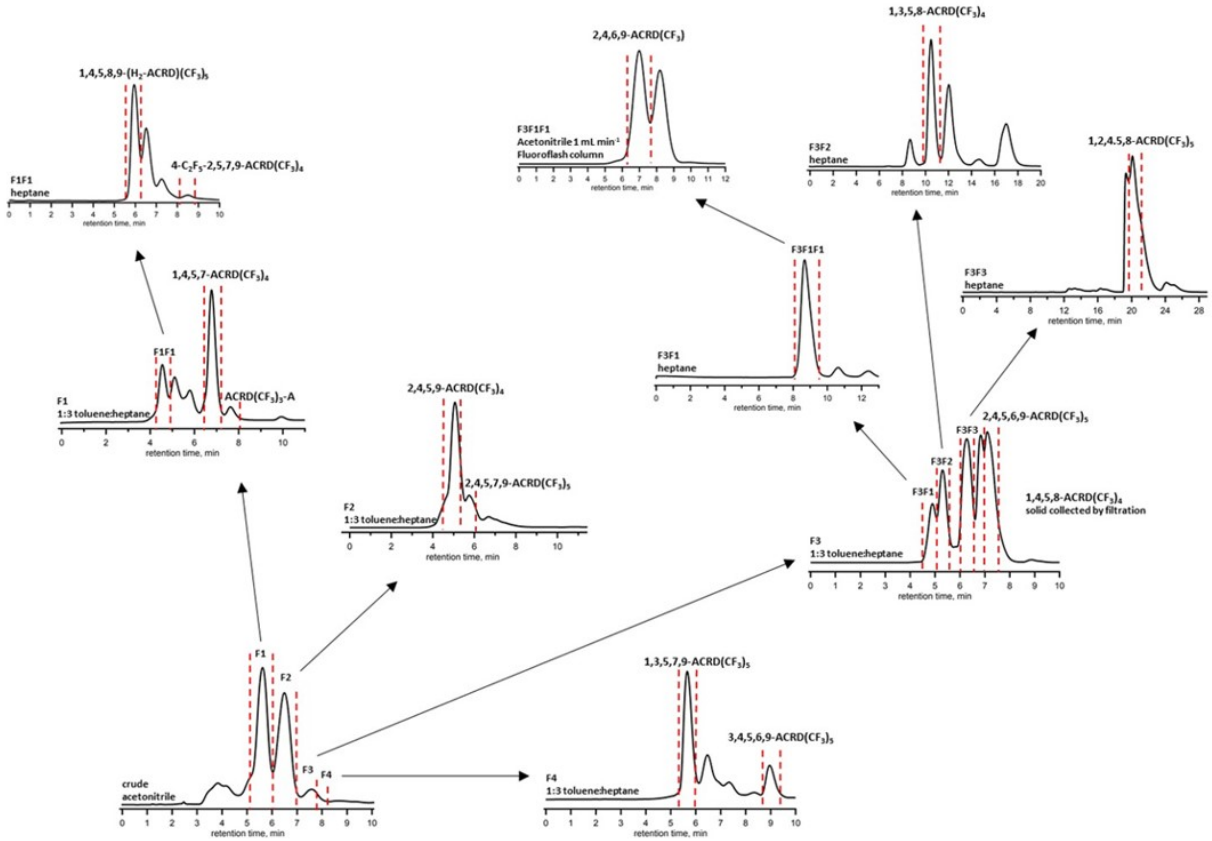

Figure 4-2. HPLC separation of reaction 4.1. Unless otherwise indicated, all separation was conducted on a COSMOSIL Buckyprep semi-preparative column with a flow rate of 5 mL min^{-1}. See section *4.2.1.b.* and Appx B.4. for details of synthesis.

more fractions were isolated, which did not yield pure products. In total, this purification yielded 13 pure products in 1-10 mg amounts from the 278 mg crude product recovered. For details of this separation, see Figure 4-2. (Appx figure B-45).

Stage 1 separation was performed using an acetonitrile eluent. Fractions eluting at 5.0 min (F1), 6.0 min(F2), 7.0 min(F3), and 7.6 min(F4) were collected for further purification.

Fraction F1 was further separated in a second stage, using a 1:3 toluene:heptane eluent. Fractions eluting at 4.3 min(F1F1), 6.2 min, and 7 min were collected. The fraction eluting at 6.2 min was pure 1,4,5,7-ACRD-$(CF_3)_4$ (Appx *C.4.4*). The fraction eluting at 7.0 min was pure ACRD-$(CF_3)_3$-A (Appx *C.4.1*). Fraction F1F1 was further separated in a third stage with a heptane eluent. One fraction, eluting at 5.5 min, was pure 1,4,5,8,9-H_2-ACRD$(CF_3)_5$ (Appx *C.4.12*). Another fraction, eluting at 8.2 min, was pure 4-C_2F_5-2,5,7,9-ACRD$(CF_3)_4$ (Appx *C.4.13*).

Fraction F2 further separated in a second stage, using a 1:3 toluene:heptane eluent. A fraction was collected, eluting at 4.2 minutes, which was pure 2,4,5,9-ACRD(CF_3)$_4$ (Appx *C.4.2*). A fraction eluting at 5.0 minutes was also collected, which was 2,4,5,7,9-ACRD(CF_3)$_5$ (Appx *C.4.7*).

From fraction F3, a solid was observed to precipitate. This solid was obtained by filtration, and was pure 1,4,5,8-ACRD(CF_3)$_4$ (Appx *C.4.5*). The filtrate of F3 was further separated in a second stage HPLC separation, using a 1:3 toluene:heptane eluent. Fractions were collected that eluted at 4.4 min(F3F1), 5.0 min(F3F2), 6.0 min(F3F3), and 7.0 min. The fraction which eluted at 7.0 min was pure 2,4,5,6,9-ACRD(CF_3)$_5$ (Appx *C.4.11.*).

Fraction F3F1 was further purified in a third stage using a heptane eluent. A fraction was collected, at 6.2 min(F3F1F1). This fraction was further purified in a fourth stage separations using the Fluoroflash (Fluorous Technologies Inc. USA) analytical column, acetonitrile at 1.0 mL min^{-1}. This fraction was pure 2,4,6,9-ACRD(CF_3)$_4$ (Appx *C.4.3*).

Fraction F3F2 was further purified in a third stage using a heptane eluent. A fraction was collected at 9.8 minutes which was pure 1,4,6,8-ACRD(CF_3)$_4$ (Appx *C.4.3*).

Fraction F4 was further separated in a second stage using a 1:3 toluene:heptane eluent. A fraction eluting at 5.3 min was pure 1,3,5,7,9-ACRD(CF_3)$_5$(Appx *C.4.8*). A fraction eluting at 8.6 min was pure 3,4,5,6,9-ACRD(CF_3)$_5$(Appx *C.4.9*).

4.2.1.c. DFT-calculated effects of trifluoromethylation at different substitution positions

The product distributions of gas phase radical trifluromethylation of PAHs has been previously shown to be predominantly under thermodynamic control. Therefore, calculations were performed to analyze whether there was any thermodynamic control of product distribution in this case. On the ACRD core, there are nine C-H bonds at which CF_3 radical substitution may occur. A systematic theoretical study of various possible substitution patterns was undertaken by Ilka Vincon, with assistance from the author of this work. The following systematic approach was

Table 4-1. The relative energies of ACRD$(CF_3)_{1,2}$'s.

Theoretical structure	E_{rel} (kJ/mol)
ACRD	-
1-ACRD(CF_3)	8.17
2-ACRD(CF_3)	0.00
3-ACRD(CF_3)	1.11
4-ACRD(CF_3)	11.77
9-ACRD(CF_3)	41.20
2,7-ACRD$(CF_3)_2$	0.0
2,6-ACRD$(CF_3)_2$	1.14
2,5-ACRD$(CF_3)_2$	11.39
4,5-ACRD$(CF_3)_2$	25.95
3,4-ACRD$(CF_3)_2$	60.23
2,4-ACRD$(CF_3)_2$	14.09
1,4-ACRD$(CF_3)_2$	22.89
4,9-ACRD$(CF_3)_2$	54.24
2,9-ACRD$(CF_3)_2$	43.37
1,9-ACRD$(CF_3)_2$	98.33

utilized: A series of theoretical molecules with one CF_3 substituent each was analyzed, such that the energy differences associated with substitution in each possible position was elucidated. Additionally, a series of theoretical compounds bearing two CF_3 substituents each were analyzed, to understand energy differences associated with substituent interactions. From this, relative energies of compounds with higher substitution degree can be predicted using energy increments of structural fragments within ±5 kJ/mol, the relative energies of each fragment are additive.[3]

The results of these calculations are summarized in table 4-1. Substitution at the 2 position is found to be the most thermodynamically favored, taken as the zero-energy isomer for relative comparisons. By far, the highest energy single-substituent isomer is 9-ACRD(CF_3), with an E_{rel} of 41.20 kJ/mol. Taken in isolation, this result seems to be at odds with the observed product distribution of reaction 4.1, as substitution at this position is observed on approximately half of the isolated compounds. However, consideration of the data for isomers bearing two substituents clarifies this point. Mono substitution at the 9 position is more favorable than, for example, placing two groups adjacent to each other at the 3 and 4 positions (60.23 kJ/mol). Therefore, substitution at the 9 position is expected given the excess of trifluoromethyl iodide reagent utilized in this

Table 4-2. Computational results describing the relative energies of a selection of ACRD$(CF_3)_n$'s with n = 4 and 5 as well as 4-(C_2F_5)-2,5,7,9-ACRD$(CF_3)_4$ both calculated for complete molecules and for energetics of structural fragements taken from data in table 4-1.

Structure	$E_{rel.}$ theoretical (kJ/mol)	$E_{rel.\,pred.}$ theoretical (kJ/mol)
1,3,5,8-ACRD$(CF_3)_4$	0.0	0
1,4,5,7-ACRD$(CF_3)_4$	2.7	-3
2,4,5,9-ACRD$(CF_3)_4$	37.7	33
1,2,4,5,8-ACRD$(CF_3)_5$	20.4	20
4-(C_2F_5)-2,5,7,9-ACRD$(CF_3)_4$	--	--
2,4,5,7,9-ACRD$(CF_3)_5$	0.0	0.0
3,4,5,6,9-ACRD$(CF_3)_5$	88.1	92
2,3,5,7,9-ACRD$(CF_3)_5$	--	--
1,3,5,7,9-ACRD$(CF_3)_{5,\,theor.}$	40.1	45

reaction, as trifluoromethyl groups could not indefinitely preferentially add to the lower energy positions 1-8 without eventually incurring unfavorable substituent-substituent interactions to a degree that substitution at the 9 position is no longer less favored.

Additionally, reactivity at this position may be unique compared to the other positions, as it was reported in the literature that addition, rather than substitution, to the ACRD core often occurs at the 9 position, breaking aromaticity. This is usually, but not always, followed by spontaneous re-aromatization.[18] The isolation of 1,4,5,8,9-H_2-ACRD$(CF_3)_5$ from this reaction is evidence in favor of this reaction pathway occurring in this case.

Mono substitution at the remaining 3 positions has a relatively narrow range of E_{rel} values, ranging from 1.11-11.77 kJ/mol. All three of these positions lie on the outermost ring of the ACRD molecule rather than the central ring. Interestingly, of these positions, the position 4 is the least favored, with a relative energy of 11.77 kJ/mol. However, upon the 12 structurally characterized ACRD derivatives presented in this work, substitution has occurred at the positions 4 and symmetrically related 5 twenty-one times. In only 3 cases is this position not substituted, making it the most frequently observed substitution position. Of course, not all synthesized products could be isolated, given limitations of HPLC separation. Therefore, it is possible that the observed prevalence of products substituted at this position is due to a bias for facile isolation of such products. However, if this is not the case, the reactivity of this position may truly be higher for another reason, likely related to the same underlying phenomena that caused the selectivity toward

substitution at a C-H bond across a fissure from an N atom was observed for 4,7-PHEN and PHNZ in chapters 2 and 3 in this work. It has been documented that this position on ACRD is subject to electrophilic substitution.[15] Radicals bearing strongly electron-withdrawing groups tend to be electrophilic. The trifluoromethyl radical has a sufficiently high electrophilicity index that it is possible it favors substation at this position, despite the higher relative energy of substitution at this postion.[18-20]

4.2.2. Structural characterization of pure compounds

4.2.2.a. Structural elucidation via ^{19}F and ^{1}H NMR spectra

In the ^{1}H NMR spectra, of ACRD$(CF_3)_n$ compounds, the chemical shifts appear in the region of 7.5 to 9.7 ppm. The most distinctive feature of the ^{1}H NMR spectra is that when an H atom is present on the 9 position, a very deshielded singlet appears, around 9.5 ppm. As an example, see the spectrum of 1,3,5,8-ACRD$(CF_3)_4$, Figure 4-3.

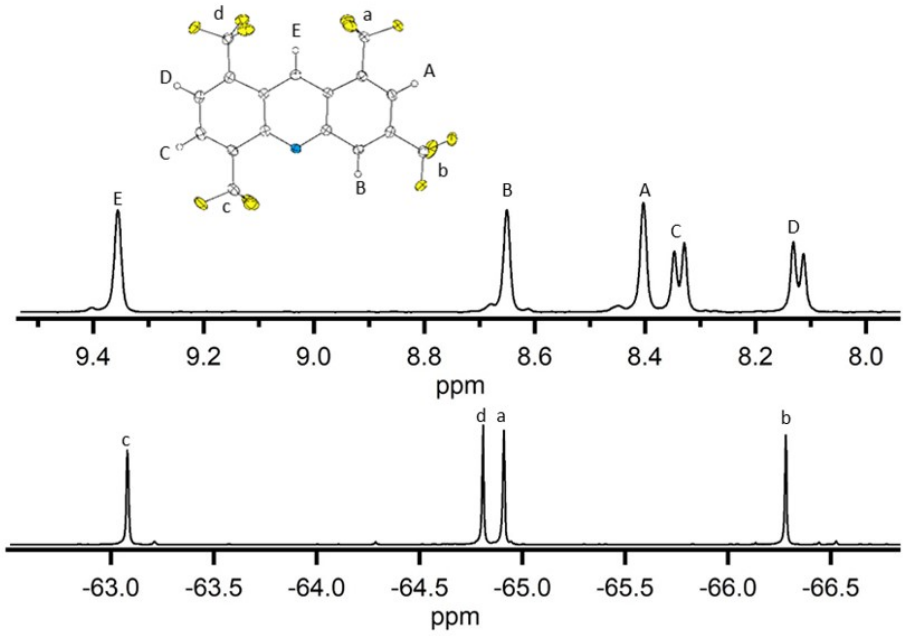

Figure 4-3. Example NMR spectra of 1,3,5,8-ACRD$(CF_3)_4$ with probable peak assignments. The ^{1}H NMR spectrum (top) is referenced to $CHCl_3$ (δ = 7.26). The ^{19}F NMR spectrum (bottom) is referenced to perfluorobenzene (δ = –164.9).

The second most deshielded H atoms are in the 4 and 5 positions, next to an N atom. However, H atoms in these positions are only present upon 3 of the 12 structures for which structures have been definitively assigned.

On positions 1-3 and 6-8, H atoms give rise to resonances in the mid-range of the ^{1}H NMR spectra of these compounds, appearing anywhere from 7.9 to 9.1 ppm. Proximity to CF_3 substituents, rather than position relative to N atom, appears to dominate the trends of chemical shifts of H atoms in these positions. However, it can be generally stated that positions closer to the N atom, that is, for example, in positions 3 and 6, are more deshielded. For example, in the case of 1,3,5,8-ACRD$(CF_3)_4$ shown in Figure 4-3, the peak corresponding to the H atom bound to position 6 is further to the left than the peak arising from the H atom bound to position 7.

An interesting case is the ^{1}H NMR spectrum of hydroACRD 1,4,5,8,9-H_2-ACRD$(CF_3)_5$, (figure C-120), in which the H atom bound to the 9 position is the most shielded, giving rise to a signal at 5.8 ppm. However, this is expected, as this hydrogen is attached to sp3 carbon in this case, and no longer bound directly to the aromatic core. In this compound the H atom bound to N is the most deshielded, appearing as a broad singlet at 8.1 ppm.

Coupling, within the resolution of the NMR spectrometer utilized, appears limited to H atoms bound to vicinal C atoms. When isolated by CF_3 substitution on adjacent C atoms, H atoms give rise to broad singlets. Adjacent H atoms appear as doublets, with J values between 7.0 and 10.5 Hz. Only in the case of 2,4,5,9-ACRD$(CF_3)_4$, in which three consecutive C atoms (positions 6, 7, and 8) bear H atoms, higher order coupling is observed, appearing as a triplet (figure C-99).

In ^{19}FNMR spectra, the chemical shifts appear in the region of -50 to -75 ppm. This is comparable to the regions observed for CF_3 substitution on other PAHs and hetero-PAHs, notable PHNZ$(CF_3)_n$'s. Shifts and peak characteristics are affected by both the position on the core and the proximity of other CF_3 groups. Again, the most immediately recognizable feature is a peak appearing further downfield than any other features, at around -52 to -56 ppm, arising when CF_3 substitutions are present on the 9 position. Trifluoromethyl groups bound to the 4 and 5 positions give rise to peaks that are also relatively deshielded, in the region from -57 to -65. Of

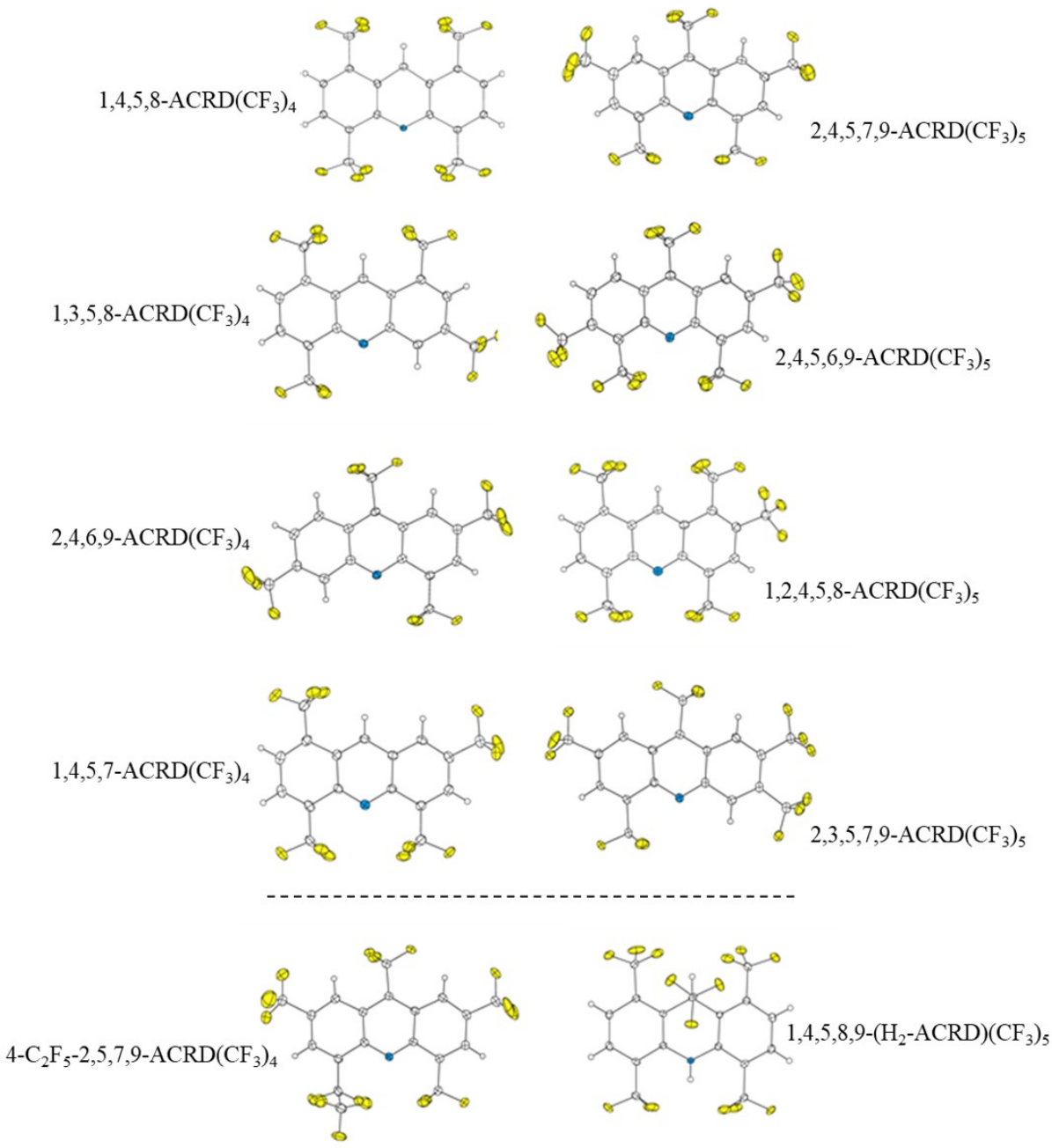

Figure 4-4. Drawings of the structures ACRD derivatives isolated in this work. Thermal ellipsoids shown at the 50% probability level.

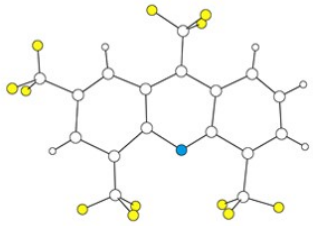

Figure 4-5. Preliminary X-ray structure of 2,4,5,9-ACRD(CF_3)$_4$.

the 1-3 and 6-8 positions, 2 and 7 are generally the most shielded, and 3 and 6 are generally the most deshielded, but, as in the case of H atoms in these positions, proximity to substituents is the dominant effect. When bound to adjacent C atoms, coupling is observed, leading to complex multiplets. In all other cases, singlets are observed.

4.2.3. Single crystal X-ray analysis

4.2.3.a. Structures obtained via crystal X-ray crystallography

Single crystal structures were obtained for ten of the 13 compounds presented in this chapter. (appx D.4.1) These structures are shown in Figure 4-4. Additionally, a preliminary data set, sufficient for structural determination but of insufficient quality to deposit with the CCDC, was obtained for of 2,4,5,9-ACRD(CF_3)$_4$. This is shown in Figure 4-5.

Crystals were grown by Dr. Long K. San by slow evaporation from solvent. Data sets were collected by the author of this work, Tyler Clikeman and Nicholas J. DeWeerd at Advanced Photon Source synchrotron facility at Argonne National Laboratory, Argonne IL, on beamline 15ID-B, employing a diamond 111 monochromator and Bruker D8 goniometer. Crystal structures were solved collaboratively by the author and Nicholas J. DeWeerd. Unit cell parameters were obtained from least-squares fits to the angular coordinates of all reflections, and intensities were integrated from a series of frames (w and f rotation) covering more than a hemisphere of reciprocal space. Absorption and other corrections were applied using SCALE. The structure was solved using direct methods and refined (on F2, using all data) by a full-matrix, weighted least-squares process.

Standard Bruker control and integration software (APEX II) was employed, and Bruker SHELXTL software was used with OLEX structure solution, refinement, and molecular graphics.

Crystals of trifluoromethylated acridine compounds suitable for diffraction were grown by slow evaporation of dichloromethane or methanol solutions. Diffraction data were collected at the Advanced Photon Source at Argonne National Laboratory on beamline 15ID-B, using a diamond 111 monochromator, at X-ray wavelengths of 0.40651 or 0.41328 Å, and a Bruker D8 goniometer, and multiscan absorption corrections. Unit cell parameters were determined by the least squares fit of the angular coordinates of all reflections. Integrations of all frames were performed using APEX III software[21, 22], and the structures were solved using SHELXTL/OLEX 2 software.[23] The structure of 1,4,5,7-ACRD(CF_3)$_4$ has one identifiable twin which modeled using the twin law, -1, 0, 0, 0, 1, 0, 0, 0, -1, with a BASF value of 0.321. The structure of 4-C_2F_5-2,5,7,9-ACRD(CF_3)$_4$ suffers from severe rotational disorder about the CF_3 group at C3 and C23. It has been modeled as a 3-part disorder with fixed occupancies for the three parts. Further there is residual density outside the normal bond length distances for the C-F bond. This density likely represents flexing of the CF_3 group in addition to the rotational disorder resulting in positional disorder as well. However, attempts to model the rotational disorder as a two-part positional disorder were unsuccessful. The three-part rotational disorder appears to be the best fit for the data. Further the thermal ellipsoids on the fluorine atoms associated with the three-part disorders are elongated as a result of the disorder. The structure of 2,4,5,6,9-ACRD(CF_3)$_5$ has a rotationally disordered trifluoromethyl group on the C7 carbon. This disorder was modeled as a three-part rotational disorder with fixed fluorine occupancies.

The structure of 2,4,5,9-ACRD(CF_3) is shown here as a preliminary structure. The data is of enough quality to confidently assign the structure, but the figures of merit are outside publishable standard. Better data sets are being collected on higher quality crystals, and publishable quality structures will be submitted to the CCDC in conjunction with a full paper.

4.2.3.b. Substitution-induced deviations from planarity

A crystallographic steric figure of merit for ACRD derivatives with n-RF and/or CF_3 groups on C9 and C10 is the aromatic core bend angle θ. It is the angle that the two halves of the aromatic core have been bent away from planarity at the ACRD C9···N hinge. A recent review of literature structures by lab mate Nicholas DeWeerd *et al.*[24] literature structures and showed that for ANTH derivatives this angle can vary from 0.0° (e.g., 2,6-bis(4-methoxyphenyl)ethynyl-9,10-ANTH$(CF_3)_2$) to 7.4° (e.g., 2,3,6,7,9,10-ANTH$(CF_3)_6$) to 18.0° (e.g., 9,10-ANTH(n-C_6F_{13})(CF_3)) depending on whether the n-R_F and/or CF_3 groups on C9 and C10 are staggered (θ = 0.0°) or eclipsed (θ = 13.5–18.0°). The ANTH core can be significantly bent even if there is only one bulky tripodal substituent on C9 (e.g., θ = 17.3° for 9-ANTH(t-Bu)).

The θ angle for 2,4,5,7,9-ACRD$(CF_3)_5$ is 3.1°. The θ angles for the two independent molecules in the structure of 4-C_2F_5-2,5,7,9-ACRD$(CF_3)_4$ are 4.2° and 4.3°. For references, the literature compound 1,3,6,8,10-ANTH$(CF_3)_5$ (ANTH-5-1) has the same substitution pattern as 2,4,5,7,9-ACRD$(CF_3)_5$, and the angles for the two independent molecules in the structure of ANTH-5-1 are 4.2° and 6.1°.[24]

In contrast, the aromatic core of 1,4,5,8-ACRD$(CF_3)_4$, with no 9-postion substitution, is planar, with θ constrained to be 0° by the crystallographic symmetry imposed by the N/C9 disorder. Adding a CF_3 group to C9 and an H atom to N results in the dihydroacridine derivative 1,4,5,8,9-(9,10-H_2ACRD)$(CF_3)_5$, in which C9 and N are sp^3 hybridized. The three-ring core of the

Table 4-3. Computational and experimental results describing the EA, $E_{1/2}$, and frontier energy levels of a selection of ACRD$(CF_3)_n$'s with n = 4 and 5 as well as 4-(C_2F_5)-2,5,7,9-ACRD$(CF_3)_4$.

Structure	EA theoretical (eV)	$E_{1/2}$ theoretical (V)	$E_{1/2}$ experimental (V)	Δ HOMO/LUMO theoretical (eV)	Δ HOMO•−/LUMO•− theoretical (eV)	Δ HOMO•−/LUMO+1•− theoretical (eV)
1,3,5,8-ACRD$(CF_3)_4$	2.32	0.05	0.05	3.76	2.52	2.89
1,4,5,7-ACRD$(CF_3)_4$	2.32	0.00	0.00	3.77	2.54	2.87
2,4,5,9-ACRD$(CF_3)_4$	2.44	0.16	0.16	3.62	2.90	3.14
1,2,4,5,8-ACRD$(CF_3)_5$	2.67	0.31	0.27	3.69	2.44	3.00
4-(C_2F_5)-2,5,7,9-ACRD$(CF_3)_4$	--	--	0.37	--	--	--
2,4,5,7,9-ACRD$(CF_3)_5$	2.78	0.38	--	3.66	2.79	3.17
3,4,5,6,9-ACRD$(CF_3)_5$	2.78	0.42	0.37	3.51	2.79	3.17
2,3,5,7,9-ACRD$(CF_3)_5$	--	--	0.37	--	--	--
1,3,5,7,9-ACRD$(CF_3)_{5,\,theor.}$	2.84	0.47	--	3.56	2.91	3.04

dihydro derivative is significantly bent, with θ = 30.2°. This is ca. 6° larger than the 25.3 and 24.5° literature values of θ for 9,10-H_2ACRD and 9-i-Pr-9,10-H_2ACRD, respectively.[6, 7]

4.2.4. Electron acceptor properties of ACRD upon trifluoromethylation

4.2.4.a. Electrochemical analysis

In this work, the most effective and precise way of assessing electron acceptor properties of ACRD$(CF_3)_n$'s is based on the evaluation of EA and $E_{1/2}$ values in. However, for this family of compounds, it was not possible to obtain EA values as decomposition was observed under experimental conditions (appx D.4.2). Despite this, the compounds did prove stable enough upon reduction in solution to obtain $E_{1/2}$ values for all compounds for which sufficient material for analysis by CV was available.

The results of this study proved extremely interesting. In previous cases, $E_{1/2}$ values varied incrementally with number of substituents, but independent of substitution pattern. For examples,

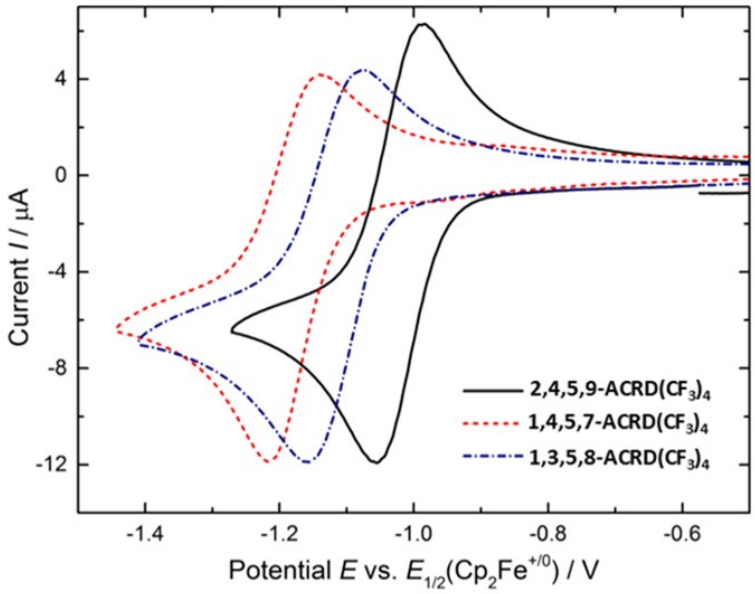

Figure 4-6. Cyclic volatammograms showing different reduction potentials of 3 different isomers of ACRD$(CF_3)_4$;. The difference in the $E_{1/2}$ values are unusually high for derivatives of the same PAH with the same number of functional groups. In particular, the reduction potential of the isomer with a CF_3 at the 9 position, 2,4,5,9-ACRD$(CF_3)_4$, is shifted to a significantly more positive potential compared to the other two, which deviate by a much smaller amount. Measured vs $Fe(Cp)_2^{+/-}$, 0.1 M $TBAPF_6$ solution in acetonitrile, 500 mV sec^{-1}.

in all reported previously studies of PAH$(CF_3)_n$, such as CORA$(CF_3)_n$, PERY$(CF_3)_n$,[3, 19, 24-28] linear incremental increase in $E_{1/2}$ with n(CF_3) was observed, regardless of the substitution patterns in the isomers. For example, for PERY$(CF_3)_5$ isomers, the $E_{1/2}$ values were virtually the same, within experimental uncertainty of 0.01 eV.[25]

For trifluoromethylated ACRD's, this was not the case. As is shown in Figure 4-6 for three representative compounds, $E_{1/2}$ values varied substantially for isomers with the same number of substituents but different substitution patterns.

A complete list of the experimentally obtained $E_{1/2}$ values can be found in table 4-3. Consistently, the $E_{1/2}$ values are substantially more positive for isomers substituted at the 9 position, as illustrated in Figure 4-6 with 2,4,5,9-ACRD$(CF_3)_4$. Overall, the range of $E_{1/2}$ values for isomers of the same chemical composition is so large that it exceeds the incremental change observed upon addition of another trifluoromethyl substituent.

This can be clearly observed when the reduction potential is graphed vs. the number of trifluoromethyl groups, shown in Figure 4-7. Also shown in Figure 4-7 is a similar graph for derivatives of trifluoromethylated PHNZs. PHNZ, as the most structurally similar trifluromethylated substrate previously examined, can be reasonably expected to have similar behavior to ACRD. However, like all other previously examined PAHs, PHNZ(CF3)n has reduction potential that is largely a function of substituent number. While 0.05 mV variations of $E_{1/2}$ values (amongst isomers of the same composition are observed, they are small with respect to the effects of substituent number (i.e., 0.2 mV per CF3 group). This is not the case for ACRD.

4.2.4.b. Spectroelectrochemical analysis

In order to further investigate this trend, spectroelectrochemical studies were performed on compounds available in sufficient quantity, utilizing spectroelectrochemistry techniques utilized by Dr. Popov at IFW (Dresden, Germany) and previously employed by Strauss-Boltalina research group members to study perfluoroalkylated aromatic systems.[29]

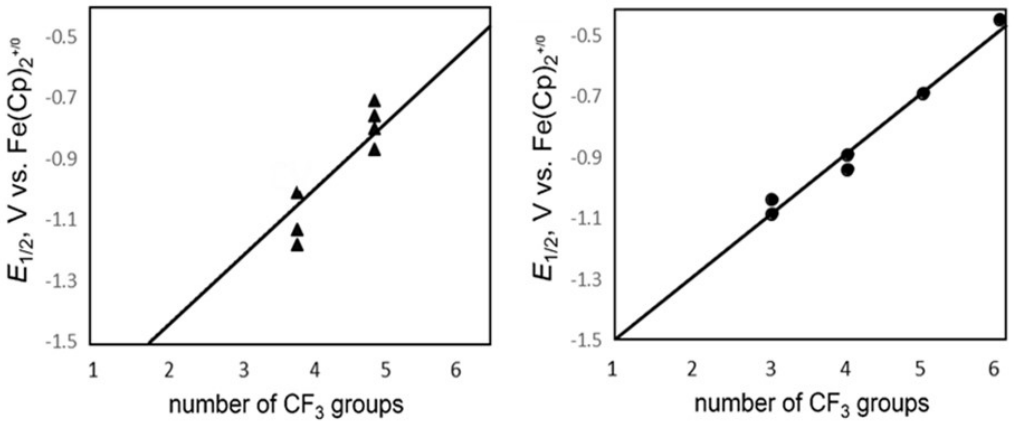

Figure 4-7. $E_{1/2}$ as a function of the number of trifluromethyl groups for ACRD and PHNZ. Trendline is a visual guide for the eye. The values for trifluromethylated ACRDs are spread over a range of nearly 0.2 V. This is comparable to the increase that has been reported per CF_3 group for other trifluromethylated PAHs, but reduction potentials are generally independent of substitution pattern. PHNZ behaves more typically, deviating from the trend line by less than 0.05 V.

. In this technique, a slow CV scan is performed while the ESR signal and vis-NIR absorption are simultaneously monitored in real time. Examples of the data collected during these experiments is shown in Figure 4-8. In the case of this family of ACRD derivatives, at the onset of reduction, the formation of paramagnetic species with complex ESR signals was observed. The appearance of this signal indicates the formation of a relatively stable radical anion. However, ESR spectroscopy detects only paramagnetic species, so any diamagnetic compounds forming upon reduction are not observed. However, these diamagnetic species do give rise to vis-NIR absorptions.

The vis-NIR absorptions of reduced species in this case were particularly interesting. Consistently for isomers substituted at the 9 position, a substantial blue shift of vis-NIR absorption is observed compared to isomers not substituted at this position. This is shown in Figure 4-9 for 2,4,5,9-ACRD$(CF_3)_4$. This shift implies that the π system of the reduced species is greatly altered compared to the neutral species, likely contributing to the notable differences in $E_{1/2}$ values.

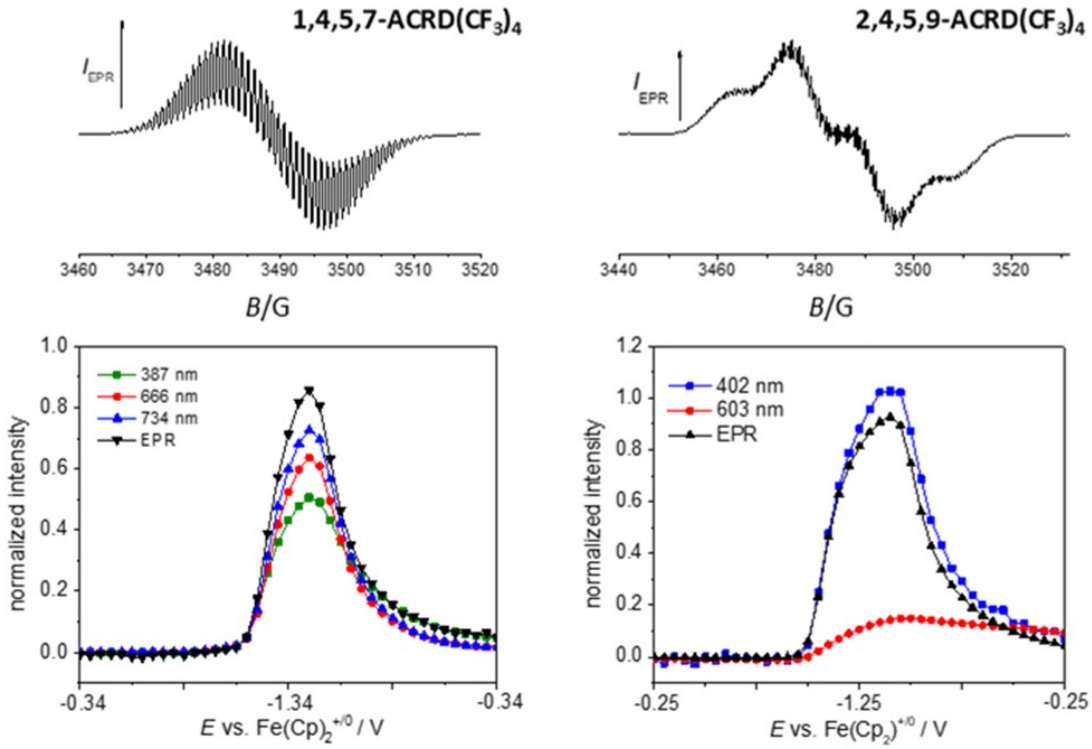

Figure 4-8. Spectroelectrochemical results of two representative compounds with (left) and without (right) substitution at the 9 position. Results indicate formation of a stable, ESR active radical anion in both cases. However, in the case of derivative substituted at the 9 position, the vis-NIR absorption indicates that an ESR silent species with an absorption around 603 nm is growing in and remaining upon the back scan (reoxidization), suggesting a possible chemical change.

A second noteworthy trend in the vis-NIR data associated with substitution at the 9 position was the observation of a feature with an absorption maximum around 603 nm, which grows in upon reduction but does not disappear upon reoxidation. This implies that the species giving rise to this feature is distinct from the reduced species of the molecule, as it would otherwise disappear along with the ESR signal during the back scan. Therefore, it is likely that in the case of the isomers substituted at the 9 position, a chemical change is possible. Though it is not a dominant process, as indicated by the fact that the CVs are quasi-reversible, it implies that the reduced species of molecules substituted at the 9 position do behave distinctly from the reduced species of isomers not substituted at this position.

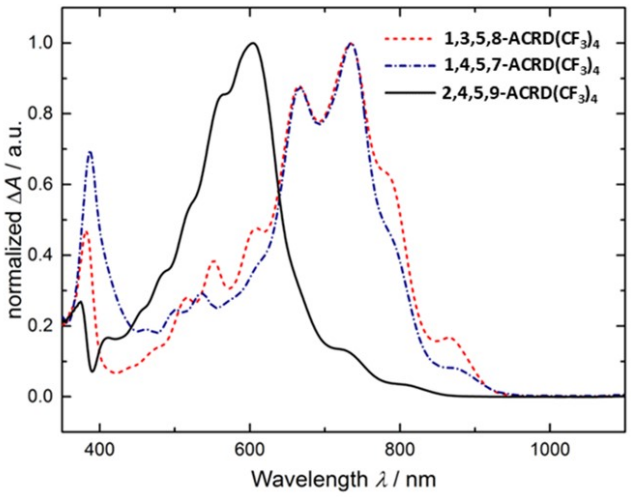

Figure 4-9. There is a significant variation in absorption maxima for the reduced species of trifluromethylated ACRDs. The spectra of the isomer with a substitution at the 9 position, 2,4,5,9-ACRD(CF_3)$_4$, differs much more substantially, with a blue-shift of over 150 nm compared to the other isomers. This trend correlates to the different reductions potentials illustrated in figure 4-x.

4.2.4.c. Computational analysis

Computational data were used to elucidate the distinctions among reduced species of isomers with and without 9 position substitution. Computations undertaken included theoretical $E_{1/2}$ values, EA values, and frontier orbital energy levels. Of these three parameters, the latter are the simplest to obtain computationally from the relaxed structures of the neutral molecules. In this case, due to pertinence of reduction to the trend under investigation, frontier energy calculations were also performed on the compounds in their anionic states. EA values similarly require optimization of the molecule in both the neutral and anionic state. Of the three parameters, $E_{1/2}$ values are the most computationally demanding, as they also require analysis of solvation energies.

The same systematic approach was utilized in this computational analysis as was used above, when studying relative energies of different isomers. First, energies of simplified ACRD(CF_3) and ACRD(CF_3)$_2$ isomers were calculated, to probe effects of position and substituent interactions. The results of these calculations are shown in table 4-4.

Data presented in table 4-4 are visualized graphically in Figure 4-10. Values of HOMO/LUMO gaps are plotted orthogonal to EA values. This highlights the distinct clustering of

Table 4-4. Computational results describing the EA and frontier energy levels of ACRD derivatives.

Theoretical structure	EA (eV)	HOMO (eV)	LUMO (eV)	Δ HOMO/ LUMO (eV)	HOMO•− (eV)	LUMO•− (eV)	Δ HOMO•− /LUMO•− (eV)
ACRD	0.76	-5.93	-2.24	-3.69	0.71	3.50	-2.79
1-ACRD(CF_3)	1.19	-6.30	-2.62	-3.68	0.22	2.97	-2.75
2-ACRD(CF_3)	1.2	-6.34	-2.63	-3.71	0.21	2.79	-2.58
3-ACRD(CF_3)	1.20	-6.33	-2.63	-3.70	0.21	2.80	-2.59
4-ACRD(CF_3)	1.19	-6.30	-2.62	-3.69	0.23	3.02	-2.79
9-ACRD(CF_3)	1.33	-6.27	-2.74	-3.53	0.04	3.10	-3.06
2,7-ACRD(CF_3)$_2$	1.62	-6.74	-2.99	-3.75	-0.29	2.19	-2.48
2,6-ACRD(CF_3)$_2$	1.63	-6.73	-3.00	-3.73	-0.31	2.31	-2.62
2,5-ACRD(CF_3)$_2$	1.60	-6.72	-2.98	-374	-0.24	2.35	-2.59
4,5-ACRD(CF_3)$_2$	1.56	-6.68	-2.95	-3.73	-0.17	2.49	-2.66
3,4-ACRD(CF_3)$_2$	1.64	-6.59	-3.01	-3.58	-0.29	2.42	-2.71
2,4-ACRD(CF_3)$_2$	1.62	-6.67	-3.98	-3.69	-0.29	2.42	-2.71
1,4-ACRD(CF_3)$_2$	1.63	-6.62	-3.00	-3.62	-0.27	2.42	-2.70
4,9-ACRD(CF_3)$_2$	1.72	-6.63	-3.09	-3.54	-0.38	2.72	-3.10
2,9-ACRD(CF_3)$_2$	1.75	-6.66	-3.10	-3.55	-0.42	2.47	-2.90
1,9-ACRD(CF_3)$_2$	1.78	-6.58	-3.14	-3.44	-0.43	2.63	-3.06

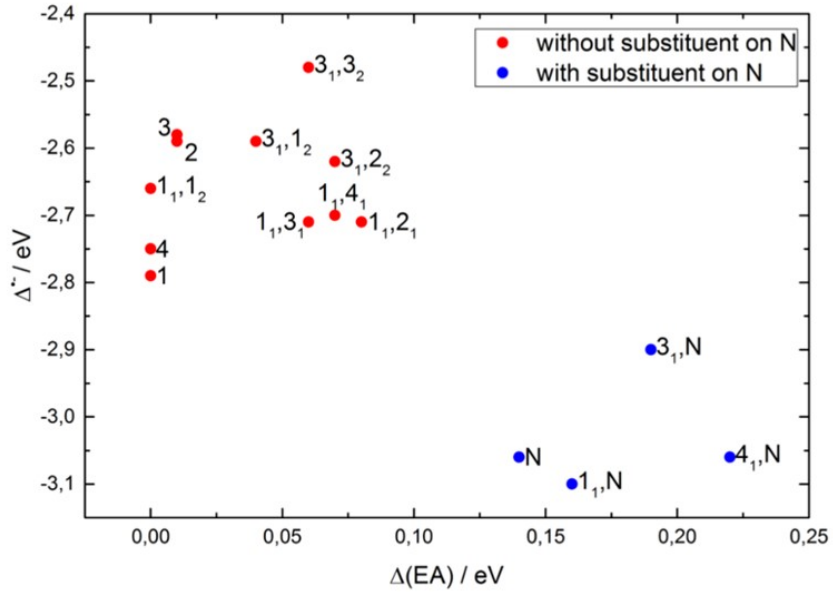

Figure 4-10. Data visualization of values from table 4-4, showing EA and HOMO/LUMO gaps plotted together. When visualized in this way, two distinct clusters can be seen, differentiated by substitution at the 9 position. This illustrates that both properties have consistent trends associated with substitution at the 9 position. EA values are consistently higher upon 9-position substitution, as are HOMO/LUMO gaps

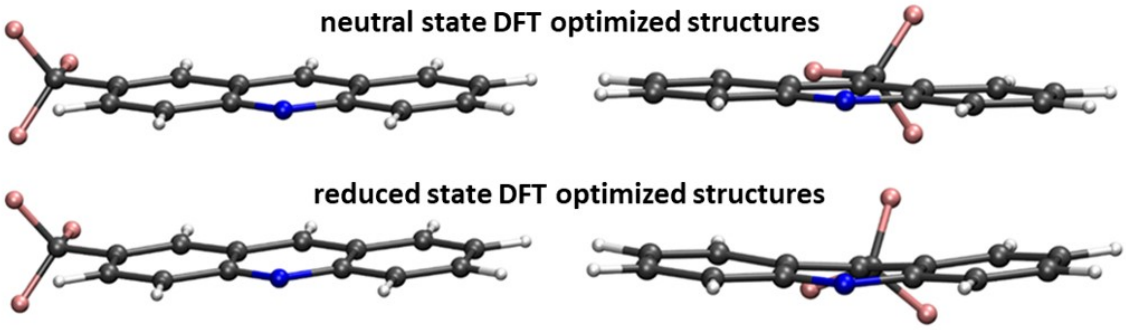

Figure 4-11. DFT optimized relaxed structure show that substitution at the 9 position results in a deviation from planarity in the reduced form (bottom), whereas substitution at other positions (here, position 2), does not.

molecules into two unique groups with respect to both of these two variables. The distinction between these two groups is very whether or not there is substitution at the 9 position, consistent with trends observed in experimental data. Other factors, such as variations in substitution at other positions and, for the ACRD$(CF_3)_2$ isomers, variations in substitution pattern, have a less substantial impact.

The reason for the unique behavior of isomers substituted at the 9 position becomes clear upon analysis of the optimized relaxed structures of the neutral and anionic species of these

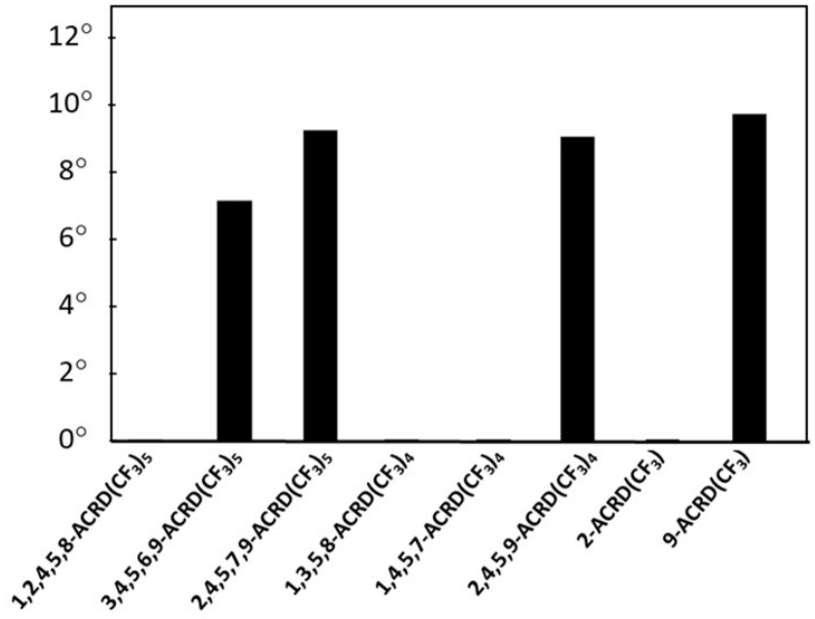

Figure 4-12. Bend angle for reduced form of a selection of experimentally obtained structures as well as theoretical structures with one substituent. Note that only compounds bearing substituents at the 9 position bend upon reduction.

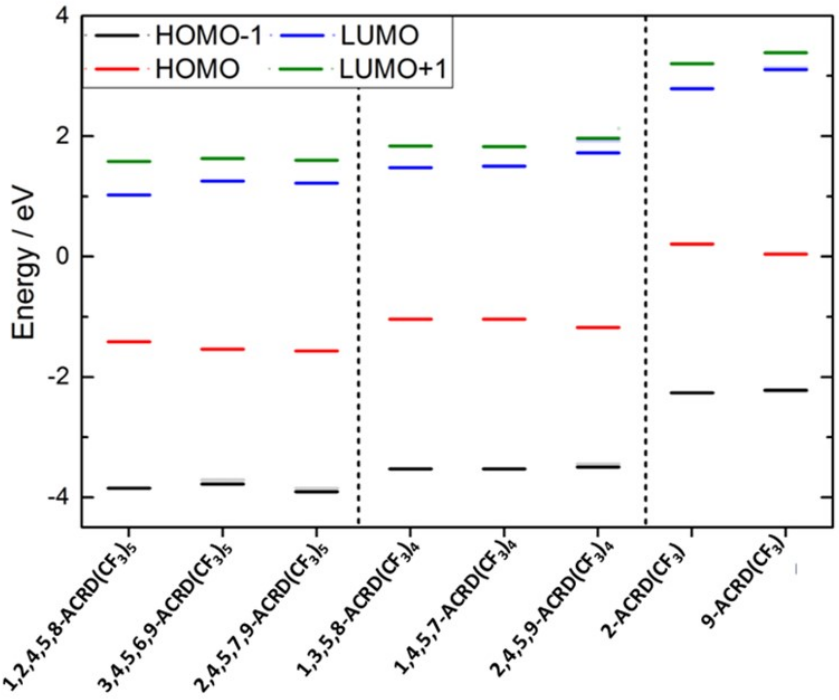

Figure 4-13. Molecular orbitals for the spin-up electron of the relaxed anionic states for selected compounds. Faded lines for compounds with substitution at the 9 position indicate energies calculated using the planar, neutral state rather than the bent reduced species.

simplified ACRD(CF_3) and ACRD(CF_3)$_2$ isomers. As shown in figures 4-11, species substituted at the 9-position bend significantly upon reduction, altering the π-system. Those not substituted at the 9 position remain planar.

To verify that this trend can also be true for compounds with a greater number of species, calculations were undertaken for polysubstituted molecules, which had been experimentally investigated. The results of these calculations are presented in table 4-4. Observed trends agree well with experimental results. As shown in Figure 4-12, a distinct bend is observed upon reduction for isomers substituted at the 9 position. This bend is only observed for the isomers with substitution at the 9 position. This is similar to the trend observed in X-ray structures and correlates with the variation in HOMO/LUMO levels. Figure 4-13 shows a series of computed HOMO and LUMO levels. Clearly, variation is significant for those isomers substituted at the 9 position.

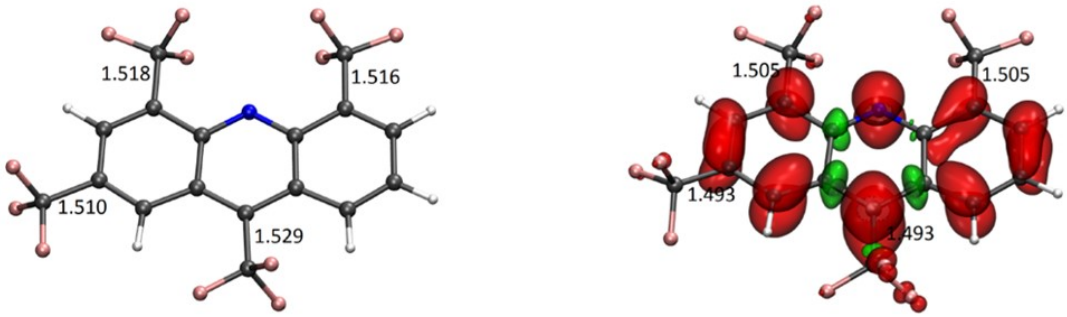

Figure 4-14. Geometry of the relaxed neutral (left) and reduced (right) states of 2,4,5,9-ACRD$(CF_3)_4$, with the spin density distribution of the radical anion shown. Bond lengths are given in angstroms. A clear blend of the ACRD core is observed for the anionic species.

To correlate the bending of the ACRD core to the observed difference in energy levels, calculations were performed for the reduced species using the planar structure resulting from optimization of the neutral species. The resulting energy levels were very similar to the values obtained for species not substituted at the 9 position. This is illustrated in Figure 4-15. Differences

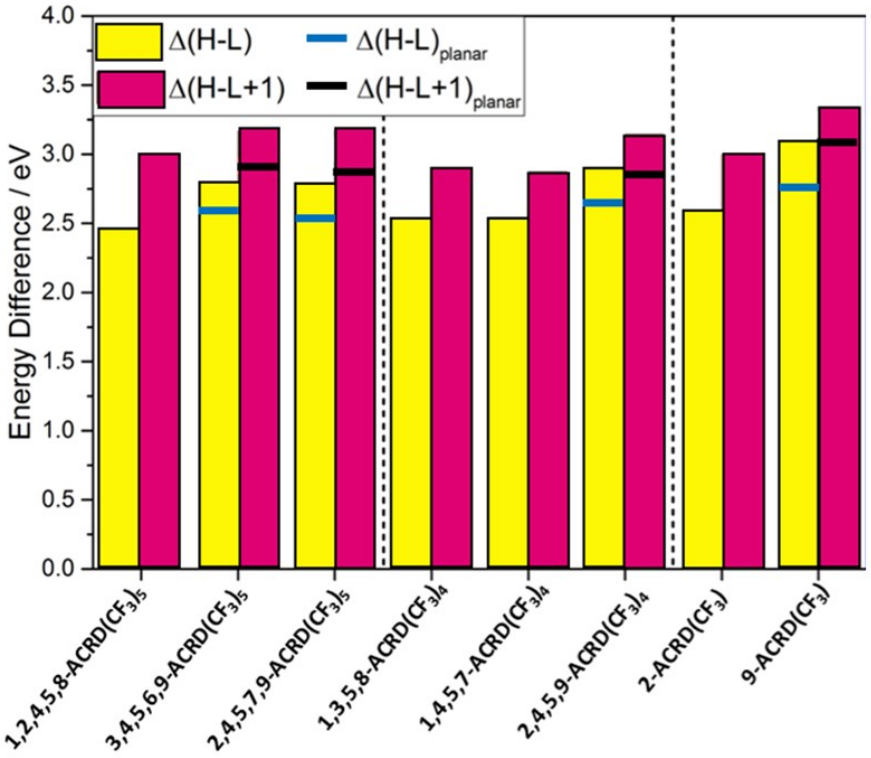

Figure 4-15. HOMO/LUMO and HOMO/LUMO+1 gap for a selection of experimentally obtained compounds as well as the theoretical structures with one substituent. Compounds with bent reduced states have significantly larger gaps. For these compounds, calculations using the planar form of the reduced structure yielded gaps similar to compounds with no substitution at the 9 position.

in frontier energy level gaps for the optimized neutral and anionic species of a range of compounds are shown graphically. However, also indicated on the same graph are the calculated values using planar species in place of bent anionic species, which have approximately the same value as the gaps for the compounds not substituted at the 9 position.

4.3. SUMMARY AND CONCLUSIONS

In this chapter, a family of fluorous ACRD derivatives were synthesized via a gas-phase radical reaction of CF_3I and ACRD and isolated via a multi-step HPLC separation. While this reaction did not demonstrate selectivity or produce thermodynamic products, it yielded a family of compounds for which analysis of solid-state packing and electronic properties proved extremely interesting.

In particular, the effect of substitution at the 9-postion was explored. Analysis of the solid-state structure via single crystal X-ray crystallography was conducted, showing that substitution at this position induced a bending of the aromatic core of several degrees. This effect is analogous to the bending of acenes upon substitution. In the case of acenes, bending was strongly correlated to conformations of CF_3 groups across the PAH core from one another, and serves to lower the overall relative energy of the molecule relative to its hypothetical planar structure.[24] However, in the case of ACRD, the position across the aromatic core is not another C atom available for substitution, but rather, an N atom. Therefore, in this case, the bend is possibly related to interaction of the CF_3 group with N-atom orbitals.

Additionally, substitution at the 9 position was investigated via electrochemical, spectroelectrochemical, and computational methods. Similar to the conclusion reached by analysis of solid-state packing, major changes in electron affinities, $E_{1/2}$ values, frontier orbital energy levels, and absorption spectra for acridines substituted at the 9-position were observed. These methodologies showed that not only was the neutral species bent several degrees, as revealed by the single crystal X-ray structures, but reduced species were substantially bent, by up to almost 10°. This bend was shown to lower the energy of orbitals near the Fermi-level, especially affecting the energy level of the spin-up electron of the HOMO, explaining the altered electronic levels. The altered absorption spectra are explained by the fact that absorption in the

visible range is dominated by transitions between the HOMO orbital and the LUMO and LUMO+1, so upon lowering the HOMO energy, a blue shift is observed.

This work therefore comprises the first known report of substitution patterns significantly affecting the incremental effects of increasing numbers of electron withdrawing substituents upon a PAH core. The incremental effect of trifluoromethyl groups upon PAH EA is usually *c.a.* 0.25 eV, independent of substitution pattern.[3, 27] In this work, incremental increases associated with a higher number of substituents occur similarly, but differences of up to almost 0.20 eV are associated with substitution at the 9 position. Therefore, the effect of the substitution pattern in this case rivals the effect of the number of substituents, opening up a new avenue for synthetic modulation of PAH energy levels.

REFERENCES

1. Clikeman, T. T.; Bukovsky, E. V.; Kuvychko, I. V.; San, L. K.; Deng, S. H. M.; Wang, X.-B.; Chen, Y.-S.; Strauss, S. H.; Boltalina, O. V., Poly(trifluoromethyl)azulenes: structures and acceptor properties. *Chem. Comm.* **2014,** *50* (47), 6263-6266.
2. Clikeman, T. T.; Bukovsky, E. V.; Wang, X.-B.; Chen, Y.-S.; Rumbles, G.; Strauss, S. H.; Boltalina, O. V., Core Perylene Diimide Designs via Direct Bay- and ortho-(Poly)trifluoromethylation: Synthesis, Isolation, X-ray Structures, Optical and Electronic Properties. *Eur. J. Org. Chem.* **2015,** *2015* (30), 6641-6654.
3. Kuvychko, I. V.; Clikeman, T.; Dubceac, C.; Chen, Y.-S.; Petrukhina, M. A.; Strauss, S. H.; Popov, A. A.; Boltalina, O. V., Understanding Polyarene Trifluoromethylation with Hot CF3 Radicals Using Corannulene. *Eur. J. Org. Chem.* **2018,** *2018* (31), 4233-4245.
4. San, L. K.; Bukovsky, E. V.; Kuvychko, I. V.; Popov, A. A.; Strauss, S. H.; Boltalina, O. V., Single-Step Gas-Phase Polyperfluoroalkylation of Naphthalene Leads to Thermodynamic Products. *Chem.-Eur. J.* **2014,** *20* (15), 4373-4379.
5. Castro, K. P.; Clikeman, T. T.; DeWeerd, N. J.; Bukovsky, E. V.; Rippy, K. C.; Kuvychko, I. V.; Hou, G.-L.; Chen, Y.-S.; Wang, X.-B.; Strauss, S. H.; Boltalina, O. V., Incremental Tuning Up of Fluorous Phenazine Acceptors. *Chem.-Eur. J.* **2016,** *22* (12), 3930-3936.
6. Chu, S. S. C.; Rosenstein, R. D.; Napoleone, V., 9-Isopropyl-9,10-dihydroacridine. *Acta Crystallogr. Section B; Struct. Sci., Cryst. Eng., and Material* **1980,** *36*, 2505-2507.
7. Kupka, A.; Schauerte, C.; Merz, K., Isostructural Crystallization Behavior of Dihydroanthracene and Dihydroacridine. *Cryst. Growth Des.* **2014,** *14* (6), 2985-2989.
8. Yoon, M. H.; Facchetti, A.; Stern, C. E.; Marks, T. J., Fluorocarbon-modified organic semiconductors: Molecular architecture, electronic, and crystal structure tuning of arene-versus fluoroarene-thiophene oligomer thin-film properties. *J. Am. Chem. Soc.* **2006,** *128* (17), 5792-5801.

9. Schmidt, A.; Liu, M., Chapter Four - Recent Advances in the Chemistry of Acridines. In *Adv. Heterocycl. Chem.*, Scriven, E. F. V.; Ramsden, C. A., Eds. Academic Press: 2015; Vol. 115, pp 287-353.
10. Valdés, A. F.-C., Acridine and acridinones: old and new structures with antimalarial activity. *The open medicinal chemistry journal* **2011,** *5*, 11-20.
11. Cho, A.-N.; Chakravarthi, N.; Kranthiraja, K.; Reddy, S. S.; Kim, H.-S.; Jin, S.-H.; Park, N.-G., Acridine-based novel hole transporting material for high efficiency perovskite solar cells. *J. Mat. Chem. A* **2017,** *5* (16), 7603-7611.
12. Zhang, M.; Wang, G.; Zhao, D.; Huang, C.; Cao, H.; Chen, M., 3D hole-transporting materials based on coplanar quinolizino acridine for highly efficient perovskite solar cells. *Chem. Sci.* **2017,** *8* (11), 7807-7814.
13. Liu, Y.; Aghdassi, N.; Wang, Q.; Duhm, S.; Zhou, Y.; Song, B., *Solvent-resistant ITO work function tuning by an acridine derivative enables high performance inverted polymer solar cells*. 2016; Vol. 35, p 6-11.
14. Chiron, J.; Galy, J.-P., *Synthesis and Crystallographic Studies of New Acridinic Esters and Amides: An Efficient Synthetic Route to 4Methyl Functionalized Acridines*. 2003; Vol. 60.
15. Schmidt, A.; Liu, M., Recent Advances in the Chemistry of Acridines. In *Adv. Heterocyc. Chem.* , Scriven, E. F. V.; Ramsden., C., Eds. Academic Press Waltham, MA, 2015; Vol. 115, pp 287-353.
16. Skonieczny, S., *Reactions at C-9 of Acridine Derivatives. Part XXV*. 1980; Vol. 14.

17. Kuvychko, I. V.; Castro, K. P.; Deng, S. H. M.; Wang, X.-B.; Strauss, S. H.; Boltalina, O. V., Taming Hot CF3 Radicals: Incrementally Tuned Families of Polyarene Electron Acceptors for Air-Stable Molecular Optoelectronics. *Angew. Chem.-Int. Edit.* **2013,** *52* (18), 4871-4874.
18. Dolbier, W. R.; Chambers, R. D., *Organofluorine Chemistry: Fluroinated Alkenes and Reactive Intermediates* Springer-Verlag: Berlin, 1997; Vol. 192.
19. Schmidt, B. M.; Seki, S.; Topolinski, B.; Ohkubo, K.; Fukuzumi, S.; Sakurai, H.; Lentz, D., Electronic Properties of Trifluoromethylated Corannulenes. *Angew. Chem.-Int. Edit.* **2012,** *51* (45), 11385-11388.
20. Schmidt, A.; Liu, M., Recent advances in the chemistry of acridines. *Advances in Heterocyclic Chemistry* **2015,** *2015*, 287.
21. Sheldrick, G. M. *Crystallography Software Package SHELXTL, v. 6.14 UNIX*, Bruker AXS: Madison, WI, 2001.
22. Sheldrick, G. M. *Crystallography Program APEX2, v. 5-0*, Bruker AXS: Madison,WI, 2014.
23. Dolomanov, O. V.; Bourhis, L. J.; Gildea, R. J.; Howard, J. A.; Puschmann, H., OLEX2: a complete structure solution, refinement and analysis program. *J. Appl. Cryst.* **2009,** *42* (2), 339-341.
24. DeWeerd, N. J.; Bukovsky, E. V.; Castro, K. P.; Kuvychko, I. V.; Popov, A. A.; Strauss, S. H.; Boltalina, O. V., Steric and electronic effects of CF3 conformations in acene(CF3)n derivatives. *J. Fluor. Chem.* **2019,** *221*, 1-7.
25. Kuvychko, I. V.; Castro, K. P.; Deng, S. H. M.; Wang, X. B.; Strauss, S. H.; Boltalina, O. V., Taming Hot CF_3 Radicals: Incrementally Tuned Families of Polyarene Electron Acceptors for Air-Stable Molecular Optoelectronics. *Angew. Chem., Int. Ed.* **2013,** *52* (18), 4871-4874.
26. San, L. K.; Bukovsky, E. V.; Kuvychko, I. V.; Popov, A. A.; Strauss, S. H.; Boltalina, O. V., Single-Step Gas-Phase Polyperfluoroalkylation of Naphthalene Leads to Thermodynamic Products. *Chem. Eur. J.* **2014,** *20* (15), 4373-4379.
27. Kuvychko, I. V.; Spisak, S. N.; Chen, Y.-S.; Popov, A. A.; Petrukhina, M. A.; Strauss, S. H.; Boltalina, O. V., A Buckybowl with a Lot of Potential: C5-C20H5(CF3)5. *Angew. Chem.-Int. Edit.* **2012,** *51* (20), 4939-4942.
28. Seiders, T. J.; Elliott, E. L.; Grube, G. H.; Siegel, J. S., Synthesis of Corannulene and Alkyl Derivatives of Corannulene. *J. Am. Chem. Soc.* **1999,** *121* (34), 7804-7813.
29. Rapta, P.; Popov, A.; Dunsch, L.; Dmitrieva, E., In Situ Spectroelectrochemistry of Organic Compounds. 2015; pp 169-190.

CONCLUSION

c.1. SUMMARY AND REVIEW

c.1.1. Overview of research discussed in this work

The work presented here is a step toward improvement of electron acceptor (*n*-type) materials for organic electronics. The performance of such materials lags behind that of *p*-type materials, even as demand for organic electronic technologies such as OLEDs, OPVs, and OFETs increases.[1, 2] This work took a multi-tiered approach toward rectification of this issue. First, new synthetic techniques were developed (and in some cases optimized), facilitating expansion of the library of available electron acceptor materials. Second, families of these molecules, with incremental structural variations, were studied, in order to better understand correlations between molecular structure, electronic properties, and solid-state properties. Finally, two families of compounds were selected for in-depth studies, including a family of ACRD derivatives exhibiting an unexpected correlation between substitution pattern and reduction potential, and a family of PHNZ derivatives with promisingly high EA values.

c.1.2. Synthetic advances

A gas-phase, radical reaction utilizing 1,4-$C_4F_8I_2$ was developed and shown to be general for a large number of PAH and hetero-PAH substrates. An overview of this reaction is shown in Figure C-1. It allows for addition of novel fluorous moieties to the aromatic core of PAH substrates. First, homolytic cleavage of C–I bonds results in formation of R_F radicals, which substitute for H atoms on substrate cores. This results in the formation of molecules bearing C_4F_8H alkyl chains and/or products bearing annulated C_4F_8 substituents.

While low yields and large product distributions are common for gas-phase radical fluroalkylations,[3, 4] this work reported here is unique in that optimization of reaction conditions facilitated relatively high yields of specific, targeted products. For example, in the most successful case, an isolated yield of 76% 2,3;6,7;10,11-TRPH$(C_4F_8)_3$ was achieved, as shown in Figure C-2.

Product distribution was primarily achieved via manipulation of stochiometric ratios of starting materials. However, parameters such as reaction temperature and the use of Cu powder as a promoter were also investigated. Additionally, the molecular structure of starting materials were found to greatly influence product distribution. Unsurprisingly, high symmetry PAHs such as TRPH gave rise to the fewest number of products. Additionally, the inclusion of hetero-atoms in the PAH core in some cases appeared to have a directing effect. In particular, substitution across a fissure from an N-atom appears to be preferred. This is consistent with previous reports of enhanced reactivity toward electrophilic substitution at such positions.[5]

As is also shown in Figure C-1, under certain conditions (varying by substrate) reductive defluorination/aromatization (RD/A) of C_4F_8 rings to C_4F_4 or C_4F_3H moieties is achieved. This can be achieved in a single reaction producing products with both fluoroalkyl and RD/A products or can be achieved by heating PAH$(C_4F_8)_n$ derivatives to elevated temperatures, especially in the presence of Cu metal. This is a valuable synthetic tool as it provides a viable route to aromatic systems with novel shapes. It also allows for partial fluorination of PAH substrates, which is difficult to achieve selectively via other routes.[1]

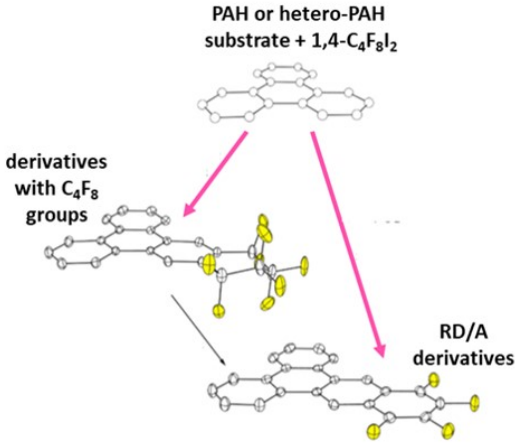

Figure C-1. The synthetic method pioneered in this work involves the reaction of PAH or hetero-PAH substrates with 1,4-$C_4F_8I_2$. Fluoroalkyl radicals, formed via homolytic cleavage of C–I bonds, substitute for H atoms on PAH or hetero-PAH's. This yields products bearing C_4F_8 rings and/or C_4F_8H alkyl chains (not shown). Reductive defluorination/aromatization (RD/A) of C_4F_8 rings (either in a single reaction or in a second reaction utilizing products bearing C_4F_8 groups as starting material) leads to fully aromatic, partially fluorinated products bearing C_4F_4 and/or C_4F_3H moieties (not shown.) Reaction conditions including stoichiometry, temperature, and the use of a Cu powder can be adjusted to target specific products.

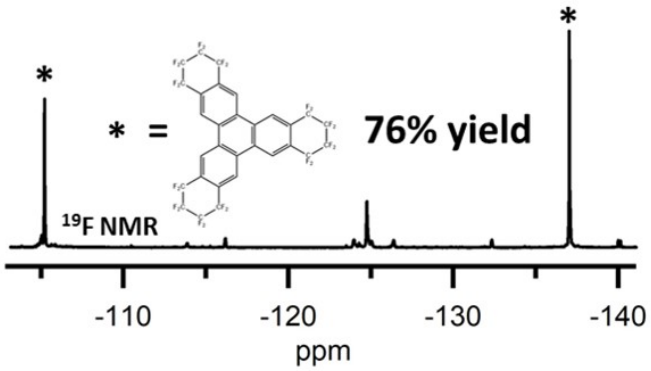

Figure C-2. Optimization of reaction conditions facilitated unusually high yields of specific products as compared to other gas-phase radical fluroalkylation reactions. Shown above, optimization of the reaction of TRPH with 8 equiv. 1,4-$C_4F_8I_2$ gave a 76% isolated yield of 2,3;6,7;10,11-TRPH$(C_4F_8)_3$. This exemplary reaction is reported in chapter 1 (reaction 1.3). ^{19}F NMR referenced to C_6F_6 (δ = -164.9, not shown).

Finally, a reaction solvated in *o*-DCB, rather than in the gas phase, was also successfully developed for the substrate PHNZ. The relatively mild conditions of this reaction allowed isolation of an intermediates bearing C_4F_8I moieties.

c.1.3. Correlations between molecular structure and electronic properties

Creation of so large a library of fluorous aromatic products with incrementally varied structures has given unprecedented opportunity to study the effect of small structural variation upon electronic properties. Thus, the electronic properties of many families of compounds were evaluated, primarily by assessment of EA values via low-temperature PES and/or cyclic voltammetry.

Previously, it was reported that for fluoroalkylated PAHs, electronic acceptor properties varied incrementally with the number of fluoroalkyl substituents. An increase of about 0.25 eV for each H atom substituted by a fluoroalkyl group was reported, and relatively little dependence upon substitution pattern and/or type of fluoroalkyl group was observed.[3, 6] In contrast, notable differences were observed for the compounds studied here. As shown by the slopes of the dotted lines in Figure C-3, the effect of C_4F_8 substitution varies based on PAH substrate. In all cases, it has a slightly greater effect upon EA than two CF_3 groups.

Furthermore, the four different types of fluorous moieties discussed here had distinctly different effects upon reduction potentials, as shown in Figure C-4. The group with the largest number of F-atoms, C_4F_8, yields the largest increase per groups. Note that if a group is appended to a position which causes a twist to the PAH core, it has a slightly smaller effect. The effect of RD/A groups was smaller than C_4F_8 groups, though only slightly. Despite the lower number of electron-withdrawing F-atoms, these compounds have larger aromatic systems, which is correlated to lower HOMO-LUMO gaps, and thus, lower LUMOs and easier reduction.

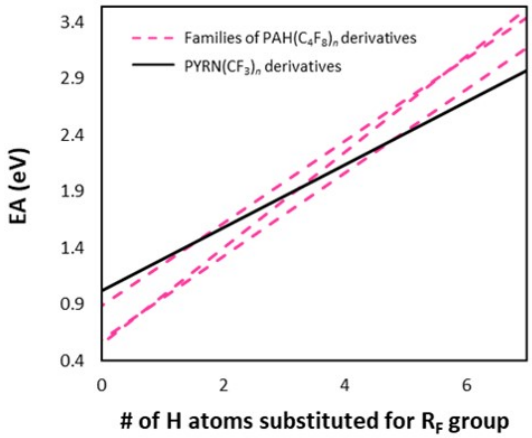

Figure C-3. According to previous reports, the effect of trifluoromethylation upon the EA of PAHs is *ca.* 0.25 eV per CF_3 group, as shown above for PYRN$(CF_3)_n$ derivatives (solid line). Interestingly, the effect of C_4F_8 groups upon EA varies based upon the PAH core, as illustrated by the varying slopes of the dashed lines above (these lines represent families of 1,10-PHEN$(C_4F_8)_n$, 4,7-PHEN$(C_4F_8)_n$ and PYRN$(C_4F_8)_n$ derivatives). However, in all cases, the effect of substitution with a C_4F_8 groups is slightly larger than the effect of two CF_3 groups, as shown by the higher slope of the dashed lines. (For the chart above, each C_4F_8 group is counted as 2 substitutions, as 2 H atoms are displaced to form one C_4F_8 ring. This provides a more direct comparison with trifluoromethylation).

c.1.4. Effects of molecular structure on solid state packing

Fluoalkylation of PAHs is known to induce crystalline packing with a higher degree of π-stacking, which is more favorable for charge transport properties.[7] This is observed in the case of the molecules reported here. In general, PAHs pack in a herringbone motif. However, most of the

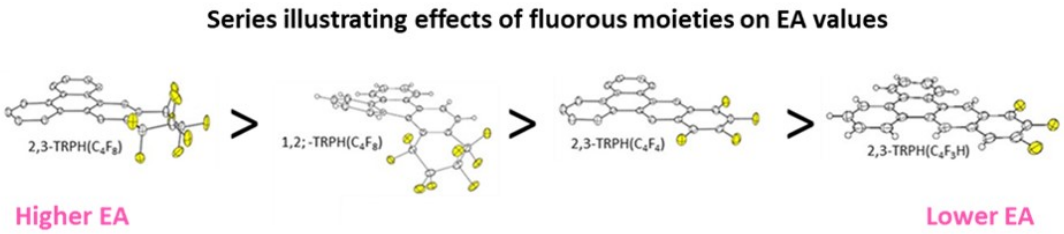

Figure C-4. Electronic properties are affected by not only the number, but also the position and type of fluorous moieties resulting from reaction of 1,4-$C_4F_8I_2$ with PAH and hetero-PAH substrates. This is illustrated above for TRPH derivatives. C_4F_8 groups, with the largest number of F atoms, have the greatest effect upon EA, while RD/A products, despite having larger π systems, result in a smaller increase of EA. Also, substitution patterns that result in bending of the aromatic core have different effects upon EA.

crystalline structures of fluorous PAH and hetero-PAH derivatives reported here packed into hexagonal-close packed columns of π-stacked molecules. This is shown using a derivative of TRPH as an example in figure C-5.

Interestingly, the intermolecular distances within the stacks and the degree of overlap of the π-systems of adjacent molecules varied significantly for different isomers, even those with only small variations in structure. Thus the effect of small variations in structure upon solid state packing have been extensively analyzed, primarily by evaluation of single-crystal X-ray structures. For example, for the series of TRPH derivatives reported here, it was possible to study structures that differed by as little as a single F atom, yet had remarkably different packing in the solid state. As can be clearly seen in Figure C-6, alteration of a single H or F atom can have profound impact

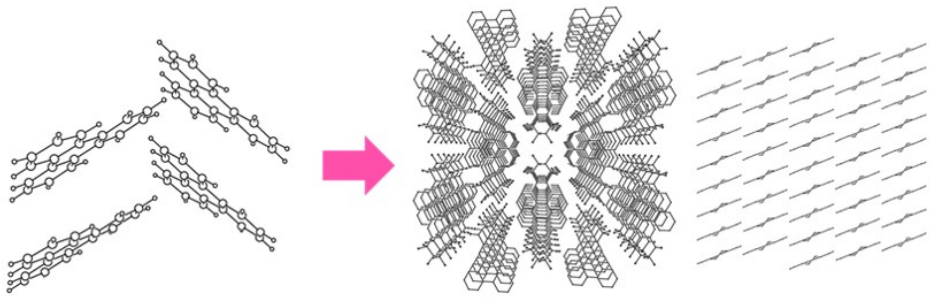

Figure C-5. Substitution of PAH and hetero-PAH substrates with fluorous moieties had a dramatic effect upon solid state packing. As exemplified above in the case of TRPH, above right, unfunctionalized PAHs tend to pack in a herringbone configuration with little π-overlap. However, in most cases, the crystals reported in this work demonstrate columnar stacking in hexagonally packed stacks, with intermolecular distances similar to graphite packing distances in some cases. This type of packing is illustrated above left, with 2,3-TRPH(C_4F_8). Orthogonal renderings of crystalline packing are shown. For simplicity, molecules are rendered as ball and stick drawings.

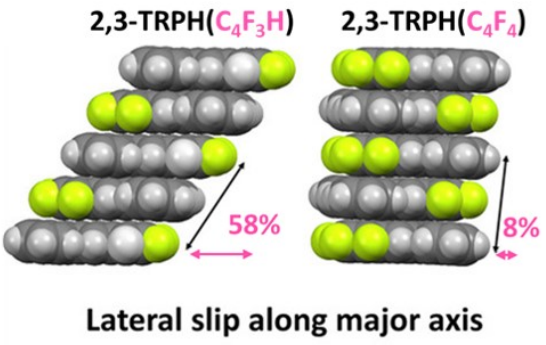

Figure C-6. Properties such as π-system overlap affect charge transport properties, so understanding the effect of structure on solid state packing is important for the development of organic electronics. The large number of compounds isolated in the course of this work allowed analysis the effects of slight and incremental variations in molecular structure upon solid state packing. For example, shown above, substituting a single F atom for an H atom results in a dramatic lateral slip along the major axis of crystalline packing.

upon crystalline packing. An understanding of these dramatic differences is key for crystal engineering, a field which may have a profound impact upon many technologies. It is particularly relevant with respect to charge transfer and charge mobility.

c.1.5. Effects of trifluoromethylation at the 9-position in ACRD$(CF_3)_n$ derivatives

Among the families of compounds investigated in this work, a family of ACRD$(CF_3)_n$ derivatives warranted in-depth analysis due to unique effects of substitution at the 9-postion. As has been mentioned, the reduction potentials of trifluormethylated PAHs generally increase in increments of *ca.*-0.25 V per CF_3 group, independent of substitution pattern. However, ACRD$(CF_3)_n$ derivatives substituted at the 9-position had $E_{1/2}$ values up to 0.16 V more positive than isomers not substituted at the 9 position with the same number of substituents. Spectroelectrochemical studies revealed that absorption maxima of the reduced species of compounds substituted at the 9-position also shifted compared to isomers not substituted at this position.

Examination of the solid-state structures of these compounds via single crystal X-ray crystallography revealed that substitution at this position induced a bending of the aromatic core of several degrees. DFT calculations were used to determine that the reduced species of compounds substituted at the 9 position had a bend even greater than that observed in the crystal

structures of the neutral compounds, of approximately 12°. This resulted in a significantly larger calculated HOMO-LUMO gap for these isomers, explaining the different reduction potentials and absorption maxima.

This effect may be analogous to the previously reported bending of acenes upon trifluoromethylation. In the case of acenes, bending was strongly correlated to conformations of CF_3 groups across the PAH core from one another, and serves to lower the overall relative energy of the molecule relative to its hypothetical planar structure.[8] In the case of ACRD$(CF_3)_n$ derivatives, similar interactions may be occurring, but between a trifluoromethyl group and N atom lone pairs rather than between two trifluoromethyl groups.

c.1.6. Evaluation of PHNZ derivatives with promise as electron acceptors

Among the many compounds synthesized in this work, PHNZ$(C_4F_8)_n$ derivates were identified as particularly promising candidates for use in organic electronic devices. When substituted with 2 C_4F_8 groups, they demonstrated high EA and $E_{1/2}$ values. The values are higher for compounds with substitution at peninsular (rather than fissure) positions of PHNZ. This is consistent with analysis of EPR spectra and DFT calculations, which revealed that in the case of fissure substation, spin density of the reduced species is localized nearer to the fluorous substituent. Therefore, the compound 1,2;7,8-PHNZ$(C_4F_8)_2$, with two C_4F_8 groups and a peninsular substation, had the highest EA, of 2.89 eV. This is significant, as 2.8 eV has been identified as the threshold for application in air-stable devices.[6, 9] One other compound, 1,2;6,7-PHNZ$(C_4F_8)_2$, also demonstrated an EA value exceeding this threshold, of 2.81 eV. Therefore, further analysis was conducted with this family of molecules. Thin films were prepared with P3HT polymer acceptors, chosen due to good alignment of frontier orbital energy levels. Analysis by PL and TRMC confirmed that these compounds act as electron acceptors and may be valuable compounds for work in air-stable devices.

c.2. FUTURE DIRECTIONS

c.2.1. Mechanistic studies and improved optimization

Synthetic optimization leading to an isolated yield of 76% of a targeted single compound was achieved for the substrate TRPH. Extension of optimization work to other substrates could lead to similarly high isolated yields. Not all substrates will yield such results, as substrate symmetry, steric considerations, thermodynamics, and reactivity of various C–H bonds affect product distribution. However, on the basis of the work reported here, several substrates can be identified as promising. These include 4,7-PHEN, PHNZ, 1,10-ANTH($Ph)_2$, and PERY. The first two substrates, 4,7-PHEN and PHNZ, are promising because the results reported here indicate that there may be a directing effect toward substitution across a fissure from an N-atom. The unusually high yield of 5,6-(4,7-PHEN)(C_4F_8) particularly suggests this, as does the prevalence of fissure-substituted PHNZ derivatives. Better understanding of this apparent directing affect could allow manipulation of reaction conditions for high yield reactions. The latter two compounds, 1,10-ANTH($Ph)_2$ and PERY, are promising substrates because it appears that few derivatives were formed. In the case of 1,10-ANTH($Ph)_2$ this is attributed to steric considerations, as all positions except peninsular positions are blocked by the bulky phenyl group. In the case of PERY, this is attributed to the higher reactivity of the 3,4,9, and 10 positions.[10] For these two substrates, optimization of recovery and purification techniques would likely lead to high isolated yields.

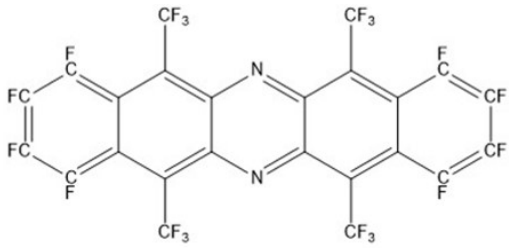

Figure C-7. Drawing of a hypothetical molecule that could be targeted as an result of the methodologies and results reported here. Based upon reported results, synthesis of this molecule would be possible via a two-step method, and it is predicted to have a very high EA and good charge transport properties.

c.2.2. Targeting specific compounds

Correlation of structural motifs with electronic and solid-state properties allows prediction of theoretical molecules which have yet to be isolated, but which would likely have exceptional properties. In particular, synthesis of hetero-acene derivatives is advisable. For example, the work reported here has shown that PHNZ derivatives substituted with two fluorous moieties at peninsular positions, such as 2,3;7,8-PHNZ(C_4F_8)$_2$, 2,3;7,8-PHNZ(C_4F_8)(C_4F_4), and 2,3;7,8-PHNZ(C_4F_4)$_2$ would be exceptionally promising molecules. Not only would these compounds have high EA values, but also, these RD/A products would be n-type analogs of tetracene and pentacene (champion *p*-type materials for organic electronics) and may demonstrate exceptional solid-state packing leading to high mobilities.[1]

Although substitution at peninsular positions is not favored, one proposed method for synthesis of acene analogs based on PHNZ is a two-step reaction, in which a trifluoromethylation is followed by reaction with 1,4-$C_4F_8I_2$. Preliminary research has shown that, using Cu-powder, it is possible to synthesize 1,4,6,9-PHNZ(CF_3)$_4$ in relatively high yield. This material could then be used as a starting material with an excess of 1,4-$C_4F_8I_2$. Due to the placement of the CF_3 groups, C_4F_8 groups could only add at the desired positions, yielding the molecule shown in figure C-7. The CF_3 groups would further increase EA to reach the estimated value of up to 3.9 eV.

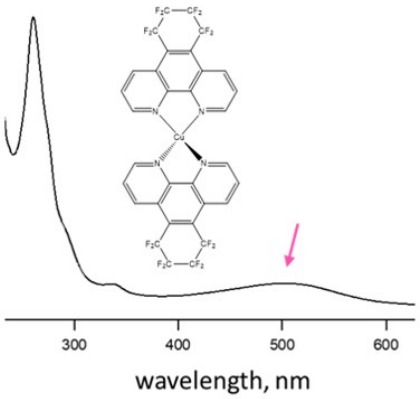

Figure C-8. As an extension of the work reported here, organometallic complexes of 1,10-PHEN derivatives could be synthesized. These compounds would be interesting for a variety of applications, especially OLED devices. Preliminary attempts to form this such complexes show some coordination likely occured, as evidenced by a probable ligand-metal charge transfer band in the UV-Vis spectrum, which is not present in the spectrum of the ligand alone.

The most likely route for synthesis of other *n*-type acene analogs, including those based on anthracene, involves use of bulky groups blocking substitution at fissure positions, as peninsular position substitution of such molecules is generally less favored. The reaction conducted with the substrate 9,10-ANTH$(Ph)_2$ in chapter 2 of this work suggests that this route may be feasible.

Finally, synthesis of fluorous derivatives of phenothiazine, a molecule with a high EA, would likely be valuable. Reaction of phenothiazine and 1,4-$C_4F_8I_2$ in *o*-DCB has shown formation of a low yield of product bearing annulated species, although the data is still preliminary.

C.2.3. Formation of organometallic complexes with n-hetero-PAH derivatives

For OLEDs and other applications, as there is a demand for electron-withdrawing phenanthroline-based ligands.[11] Among the substrates investigated here, 1,10-PHEN derivatives coordinated to Cu(II) may be particularly promising.[12] Preliminary investigation was conducted, in which Cu(I) triflate toluene was used as copper source. Ligand exchange lead to coordination of 1,10-PHEN$(C_4F_8)_n$ derivatives, evidenced by a weak metal-ligand charge transfer band around 500 nm. This is shown in Figure C-8. These complexes were not air-stable, and the exchange did not appear to go to completion, but these preliminary results encourage further investigation.

c.2.4. Scale-up and fabrication of devices

In the research here, it has been demonstrated via testing of thin film donor/acceptor blends that some of the molecules presented here (PHNZ derivatives) function as electron acceptors. A logical next step, therefore, is to fabricate devices, a common method that has been used to evaluate other electron acceptors.[2] A number of different device types and architectures could be analyzed. For example, PHNZ derivatives could be used as electron acceptors in bulk heterojunction OPVs. Not only would this allow direct comparison of PHNZ with other commonly used acceptors, it would yield further information about frontier orbital energies though analysis of open circuit voltage(V_{oc}), and transport via short-circuit current (J_{sc}).

C.2.5. Applications beyond organic electronics

A final avenue for further research is the investigation of the 60+ compounds synthesized here for applications other than organic electron acceptors. As an example, PERY derivatives are often utilized as dyes.[10] These materials demonstrate strong fluorescence, even under ambient light, and therefore could be exceedingly useful as fluorescent dyes. As another example, there is a wide range of possible applications for these molecules in biomedicals fields.[13] In particular, similar ACRD and PHNZ derivatives have been shown to have widespread uses, with applications ranging from antibacterial to antipsychotics.[14]

REFERENCES

1. Anthony, J. E., Functionalized Acenes and Heteroacenes for Organic Electronics. *Chem. Rev.* **2006,** *106* (12), 5028-5048.
2. Anthony, J. E.; Facchetti, A.; Heeney, M.; Marder, S. R.; Zhan, X. W., n-Type Organic Semiconductors in Organic Electronics. *Adv. Mater.* **2010,** *22* (34), 3876-3892.
3. San, L. K.; Bukovsky, E. V.; Kuvychko, I. V.; Popov, A. A.; Strauss, S. H.; Boltalina, O. V., Single-Step Gas-Phase Polyperfluoroalkylation of Naphthalene Leads to Thermodynamic Products. *Chem. Eur. J.* **2014,** *20* (15), 4373-4379.
4. Kuvychko, I. V.; Clikeman, T.; Dubceac, C.; Chen, Y.-S.; Petrukhina, M. A.; Strauss, S. H.; Popov, A. A.; Boltalina, O. V., Understanding Polyarene Trifluoromethylation with Hot CF3 Radicals Using Corannulene. *Eur. J. Org. Chem* **2018,** *2018* (31), 4233-4245.
5. Chiron, J.; Galy, J.-P., *Reactivity of the Acridine Ring: A Review*. 2004; Vol. 35.
6. Kuvychko, I. V.; Castro, K. P.; Deng, S. H. M.; Wang, X. B.; Strauss, S. H.; Boltalina, O. V., Taming Hot CF_3 Radicals: Incrementally Tuned Families of Polyarene Electron Acceptors for Air-Stable Molecular Optoelectronics. *Angew. Chem., Int. Ed.* **2013,** *52* (18), 4871-4874.
7. Sun, H.; Putta, A.; Billion, M., Arene Trifluoromethylation: An Effective Strategy to Obtain Air-Stable n-Type Organic Semiconductors with Tunable Optoelectronic and Electron Transfer Properties. *J. Phys. Chem. A* **2012,** *116* (30), 8015-8022.
8. DeWeerd, N. J.; Bukovsky, E. V.; Castro, K. P.; Kuvychko, I. V.; Popov, A. A.; Strauss, S. H.; Boltalina, O. V., Steric and electronic effects of CF3 conformations in acene(CF3)n derivatives. *J. Fluor. Chem.* **2019,** *221*, 1-7.
9. Chang, Y. C.; Kuo, M. Y.; Chen, C. P.; Lu, H. F.; Chao, I., On the Air Stability of n-Channel Organic Field-Effect Transistors: A Theoretical Study of Adiabatic Electron Affinities of Organic Semiconductors. *J. Phys. Chem. C* **2010,** *114* (26), 11595-11601.
10. Clikeman, T. T.; Bukovsky, E. V.; Wang, X.-B.; Chen, Y.-S.; Rumbles, G.; Strauss, S. H.; Boltalina, O. V., Core Perylene Diimide Designs via Direct Bay- and ortho-(Poly)trifluoromethylation: Synthesis, Isolation, X-ray Structures, Optical and Electronic Properties. *Eur. J. Org. Chem.* **2015,** *2015* (30), 6641-6654.
11. Bencini, A.; Lippolis, V., 1,10-Phenanthroline: A versatile building block for the construction of ligands for various purposes. *Coord. Chem. Rev.* **2010,** *254* (17), 2096-2180.
12. Chandraleka, S.; Ramya, K.; Chandramohan, G.; Dhanasekaran, D.; Priyadharshini, A.; Panneerselvam, A., Antimicrobial mechanism of copper (II) 1,10-phenanthroline and 2,2′-bipyridyl complex on bacterial and fungal pathogens. *J. Saudi. Chem. Soc.* **2014,** *18* (6), 953-962.
13. Alves, C. A.; Vicente, A. M.; Custódio, D.; Cerqueira, M.; Nunes, T.; Pio, C.; Lucarelli, F.; Calzolai, G.; Nava, S.; Diapouli, E.; Eleftheriadis, K.; Querol, X.; Musa Bandowe, B. A., Polycyclic aromatic hydrocarbons and their derivatives (nitro-PAHs, oxygenated PAHs, and azaarenes) in PM2.5 from Southern European cities. *Science of The Total Environment* **2017,** *595*, 494-504.
14. MARTIN, G. J., ACRIDINE ANTISEPTICS: A REVIEW. *Medicine* **1944,** *23* (1), 79-103.

APPENDIX A

GENERALIZED EXPERIMENTAL METHODS

A.1. GENERALIZED SYNTHETIC TECHNIQUES

A.1.1. General method for reactions in Monel vessel

This section broadly describes the method utilized for reactions conducted in a Monel vessel. For experimental details specific to individual reactions, such as amounts of reagents used, temperature, and duration of reaction, refer to appendix B.

For reactions conducted in a Monel vessel, a 300 mL Monel autoclave, shown in figure A-1, and a glass tube (3 inches long, 0.27 inches in diameter 0.27, sealed at one end) was utilized. In the glove box, reagents including PAH substrate, 1,4-$C_4F_8I_2$, and Cu powder (when applicable), were placed in glass tube, which was placed upright within the Monel vessel. The Monel vessel was then closed and removed from the glove box. It was placed in a preheated furnace for the duration of the reaction. Throughout the reaction, the vessel propped upright such that the substrate, which is in the liquid state at reaction temperature under $N_2(g)$, remained in the glass vessel. To stop the reaction, the Monel autoclave was removed from the furnace with tongs and cooled immediately under a flow of water. The Monel autoclave was opened, and the glass tube was removed. Soluble product was retrieved from the glass insert with *ca.* 50 mL of a 1:1 mixture of warm toluene and dichloromethane. This solution was filtered to removed insoluble decomposition product and/or residual Cu powder. The toluene and dichloromethane were evaporated under a stream of N_2, leaving a solid product.

A.1.2. General method for reactions in flame sealed glass ampoules

This section broadly describes the method utilized for reactions conducted in glass ampoules. For experimental details specific to individual reactions, such as amounts of reagent used, ampoule volume, temperature, and duration of reaction, refer to appendix B.

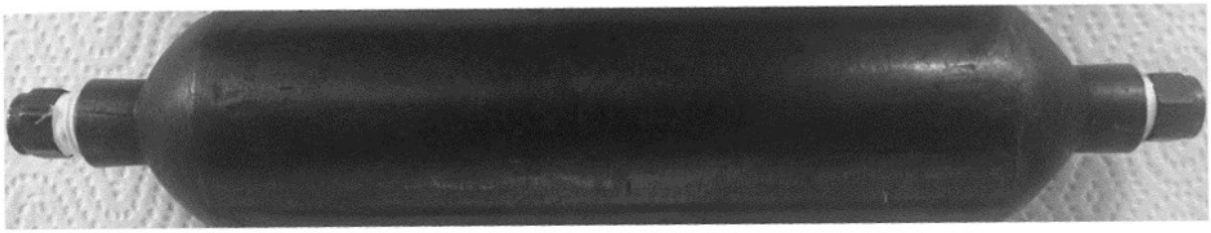

Figure A-1. The 300 mL Monel autoclave utilized in this work. Vessel was closed by tightening screws on either end to hand tight. Teflon tape was utilized to prevent seizing. Subsequent to each reaction, vessel was rinsed with refluxing dichloromethane. It was stored in an oven warmed to 110 ºC to prevent condensation of water. Immediately prior to use, while warm, it was pumped into a dinitrogen filled glovebox.

For reactions conducted in flame sealed glass ampoules, an ampoule was prepared for connection to a Schlenk line by fitting it with either a Cajon fitting, shown in figure A-2(B), or a side arm Teflon valve, shown in figure A-2(B). In a dinitrogen filled glove box, reagents, excluding CF_3I, were placed in the ampoule. The ampoule was then removed from the glove box and attached to a Schlenk line. Contents of the vessel were freeze-pump-thawed three times. For reactions using CF_3I, calibrated volumes filled to specific pressures were utilized to introduce a calculated amount of CF_3I to the vessel, which was condensed with liquid nitrogen. For all reactions in glass ampoules, including using CF_3I or other perfluoroalkyl reagents, the ampoule was then flame sealed under dynamic vacuum while at liquid nitrogen temperature. It was allowed to warm to room temperature, then placed in a preheated furnace for the duration of the reaction.

DANGER! High pressure can be generated within glass ampoules, leading to explosive ampoule failure. The maximum pressure inside the ampoule at high temperature must be calculated using ideal gas law. Depending on the size and wall thickness of the ampoule the maximum allowable pressure changes, so a conservative limit of 2-3 bar must be set. The burst pressure for the glass ampoule is largely determined by the quality of the seal, so care must be taken during the sealing step. Use shields and personal protection at all times. Only experienced personnel must perform these operations.

Figure A-2. The glass ampoules utilized in this work. A) Glass ampoule prepared for attachment to Schlenk line via Cajon fitting. B) Glass ampoule prepared for attachment to Schlenk line via side arm Teflon valve. C) Flame sealed ampoule, containing a reaction with Cu powder, as it appears both before and after reaction. D) Flame sealed ampoule, containing a reaction without Cu powder, as it appears prior to reaction. E) Flame sealed ampoule, containing a reaction without Cu powder, as it appears after reaction, before cooling. Note the presence of purple I_2 (*g*), which condenses into dark crystals upon cooling to room temperature.

The reaction was stopped by removing the ampoule from the furnace and allowing it to cool to room temperature. The seal was then broken, and soluble product was retrieved from the glass insert with *ca.* 50 mL of a 1:1 mixture of warm toluene and dichloromethane. This solution was filtered to remove insoluble decomposed material and/or residual Cu powder. In these cases, the solution was light yellow to orange. When Cu powder was not utilized, the solution was purple,

and a saturated sodium thiosulfate wash was used to extract I_2, resulting in a light yellow to orange solution. The toluene and dichloromethane were then evaporated under a stream of N_2, leaving a while to orange solid product.

A.2. GENERALIZED PURIFICATION AND CHARACTERIZATION

A.2.1. Purification by HPLC

High performance liquid chromatography (HPLC) was utilized to isolate pure molecules. A mobile phase is pumped at high pressure through a column filled with a stationary phase. For information of mobile phase utilized to purify specific reactions, refer to the eluents specified in appendix 2. For all work reported here, the stationary phase was composed of silica gel beads with modified surfaces, functionalized with 3-(1-pyrenyl)propyl groups as shown in figure A-3. For separation, a mixture of analytes is injected into the system. The analytes partition the mobile and stationary phase. With suitable mobile phases, differences in the interaction of the stationary phase with the differently functionalized PAHs results in separation of these PAHs. In a static system, interactions would result in an equilibrium, with some analyte in solution and some interacting with the stationary phase. However, due to the high-pressure flow of the mobile phase, the system is constantly perturbed. The analyte therefore moves along the length of the column. Compounds

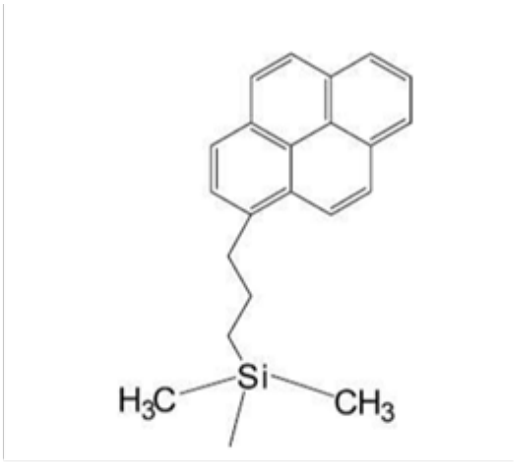

Figure A-3. The stationary phase of Buckyprep is silica functionalized with 3-(1-pyrenyl)propyl groups.

with a higher affinity for the stationary phase are retained on the column longer. For the analytes discussed here, affinity for the stationary phase is likely affected by several factors such as π system shape and size, degree of planarity, polarity, and the steric bulk of substituents.

A.2.2. Characterization by NMR spectroscopy

Structural characterization was achieved, when possible, by ^{1}H (400 MHz) and ^{19}F (376 MHz) NMR spectroscopy. For details of characterization and NMR trends, see NMR spectroscopy sections of chapters 1, 2, 3, and 4.

A.2.3. Characterization by single crystal X-ray structures

Single crystal x-ray structures were obtained in all cases where pure materials yielded single crystals of sufficient quality. Due to the small size and relatively low atomic scattering factor of F and C atoms, structures were primarily collected at sector 15 of APS at Argonne National Labs. Structures were collected by the author and other group members during their visits toChemMatCARS of the University of Chicago in collaboration with and under the supervision of Dr. Yu-Sheng Chen. Single crystal x-ray structures were used to confirm/elucidate molecular structures, as well as analyze relevant solid-state properties such as planarity of molecules, interatomic distances, π-overlap, and packing.

A.2.4. Characterization by mass spectrometry

In some cases, characterization by mass spectrometry was possible. It was primarily utilized as a tool for analysis of crude reaction mixtures, as other techniques such as NMR spectroscopy and single crystal x-ray structures yielded more structural information (number and position of substituents) for pure compounds that mass spectrometry (only number of substituents). This technique was of limited use for characterization of compounds with weak acceptor properties, e.g., TRPH derivatives. Only TRPH derivatives with 3 annulated substituents were observed by MS, possibly due to ion suppression effects.

A.3. REAGENTS AND SOLVENTS

A.3.1. Reagents

Acridine (Aldrich, 97%), anthracene (TCI, 94%), bathophenanthroline (Alfa Aesar 98+%), calcium hydride (Sigma Aldrich, 95%), naphthalene (Acros Organics, 99%) neocuproine (Acros Organics, 99%), perylene (Alfa Aesar, 98+%), phenazine (Aldrich, 98%), phenothiazine (Aldrich, 98%), pyrene (Alfa Aesar, 98%), rubrene (Acros Organics 99%), sodium thiosulfate (Fisher Scientific, >98%) tetracyanoquinodimethane (Aldrich, 98%), triphenylene (Acros Organics, 98%), 1,10-phenanthroline (Acros Organics, 98%), 4,7-phenanthroline (Acros Organics, 98%), 5-phenanthridine (Aldrich, 99%), and 9,10-diphenylanthracene (Aldrich, 97%) were used as received. 1,2-diiodotetrafluoroethane (Fisher Scientific 98%), 1,3-diiodohexafluoropropane (Fisher Scientific, 98%, stabilized with Cu), 1,4-diiodooctafluorobutane ($C_4F_8I_2$, Fisher Scientific, 98%) was freeze-pump-thawed and stored in a purified dinitrogen-filled glovebox prior to use. Copper powder (Alfa Aesar) was heated in a glass tube to ca. 250 °C under a flow of dihydrogen to remove any oxide coating, evacuated to remove all traces of H_2O, and stored in a purified dinitrogen-filled glovebox. Sodium metal was stored in mineral oil and was sliced to expose fresh surface immediately prior to use. Distilled deionized water had a resistance of 18 MΩ or higher.

A.3.2. Solvents and standards

Acetonitrile (Fisher Scientific, ACS grade), chloroform-d (Cambridge Isotope Laboratories, IMC., 99.8%), dichloromethane (DCM, Fisher Scientific, ACS grade), heptane (Fisher Scientific, ACS grade), hexafluorobenzene (Oakwood Products, Inc.), isopropyl alcohol (Fisher Scientific, ACS grade), methanol (Fisher Scientific, ACS grade), toluene (Fisher Scientific, ACS grade), and 1,4-bis-(trifluoromethyl)benzene (Central Glass Co., LTD., 99%) were used as received.

A.4. INSTRUMENTATION

A.4.1. HPLC

HPLC separations were performed with a Cosmosil Buckyprep (Nacalai Tesque) semi-preparative column (250 × 10 mm i.d.) on an HPLC Prominence system (Shimadzu) comprised of LC-6AD pump, 2 mL sample loop, equipped with SPD-20A UV-vis detector, SPD-M20A diode array detector, and CBM-20A communications bus module.

A.4.2. NMR spectroscopy

NMR spectra were recorded in $CDCl_3$ using a Varian INOVA 400 NMR spectrometer. The ^{1}H and ^{19}F frequencies were 400 and 376 MHz, respectively. The ^{19}F chemical shifts were determined using either hexafluorobenzene or 1,4-bis-(trifluoromethyl) benzene as an internal standard (δ −164.9 or δ −66.4, respectively). The ^{1}H chemical shifts were determined using the resonance for the residual $CHCl_3$ in $CDCl_3$ as an internal standard (δ 7.26).

A.4.3. UV/vis spectrometry

UV/vis spectra were collected using a UV-Vis-NIR - Shimadzu UV 3101PC instrument with UVProbe 2.33 software.

A.4.4. Cyclic voltammetry

Cyclic voltammetry measurements were performed in a dinitrogen filled glovebox, in a cell with a volume of *ca*. 0.1 mL. A three-electrode set up was utilized, shown in figure A-4. The working electrode and counter electrodes were platinum wire. Isolation of the electrodes was achieved by fusing the platinum wires into glass capillaries. The reference electrode was an Ag/Ag+ pseudo reference electrode. It was prepared by stripping the end of a Teflon-coated silver

wire to expose Au surface then dipping it into a solution of 3M KCl saturated with silver chloride while applying a short positive voltage pulse, forming coating of AgCl. As the potential of the pseudo reference electrode is unknown, ferrocene was added as an internal standard, and potentials have been referenced to the ferrocene/ferrocenium couple. Electrolyte solutions was 0.1 M tetrabutylammonium hexafluorophosphate solution. Electrolyte concentration was several orders of magnitude higher than the concentration of analyte to ensure that diffusion was the only observed transport process. A PARSTAT 4000 (Princeton Applied Research, AMETEK) potentiostat operated via VersaStudio software was utilized.

A.4.5. EPR hyperfine structure

For measurement of EPR hyperfine structure, the same cell was used that was used for spectroelectrochemistry, described below (appx *A.4.10.*) and in figure A-4. However, it was used with a two-electrode set-up comprised of a platinum mesh with a larger surface exposed (to increase the active area for reduction) and a platinum wire counter electrode. A higher concentration of electrolyte was utilized (to facilitate current flow). The production of radical species was monitored by simultaneous UV-Vis spectroscopic measurements. In some cases, chemical reduction with cobaltocene was utilized in place of electrochemical reduction,

Figure A-4. Electrode for cyclic voltammetry (left) and spectroelectrochemical cell (right), both with working(W), counter(C), and reference(R) electrodes indicated.

particularly in the cases where available analyte quantity was low. In these cases, an NMR tube was utilized as a cell for EPR.

A.4.6. Photoluminescence spectra

PL spectra were recorded on an Edinburgh FLS920 spectrophotometer using a 450 W xenon lamp by exciting at the longest-wavelength absorption maxima with an excitation slit width of 3–5 nm and an emission slit width of 5–10 nm.

A.4.7. Mass spectrometry

The electrospray ionization mass spectrum was recorded on a 2000 Finnigan LC-DUO mass spectrometer (acetonitrile carrier solvent, 0.3 mL min−1 flow rate, samples injected as solutions in acetonitrile).

A.4.8. Photoelectron spectroscopy (PES)

PES experiments were performed with a low-temperature apparatus that couples an electrospray ionization source and a temperature-controlled ion trap to a magnetic-bottle time-of-flight photoelectron spectrometer previously described in detail. The electron affinity of each compound was directly measured from the 0–0 transition in the corresponding photoelectron spectrum. See figure A-5.

A.4.9. Single crystal X-ray structures

Crystals were grown by slow evaporation of a solution of dichloromethane. Data sets were obtained at the Advanced Photon Source synchrotron instrument on beamline 15ID-B at Argonne National Laboratory, a diamond 111 monochromator, and a Bruker D8 goniometer. Unit cell parameters were obtained from a least-squares fit to the angular coordinates of all reflections. Intensities were integrated from a series of frames from ω and ϕ rotation scans. Absorption and

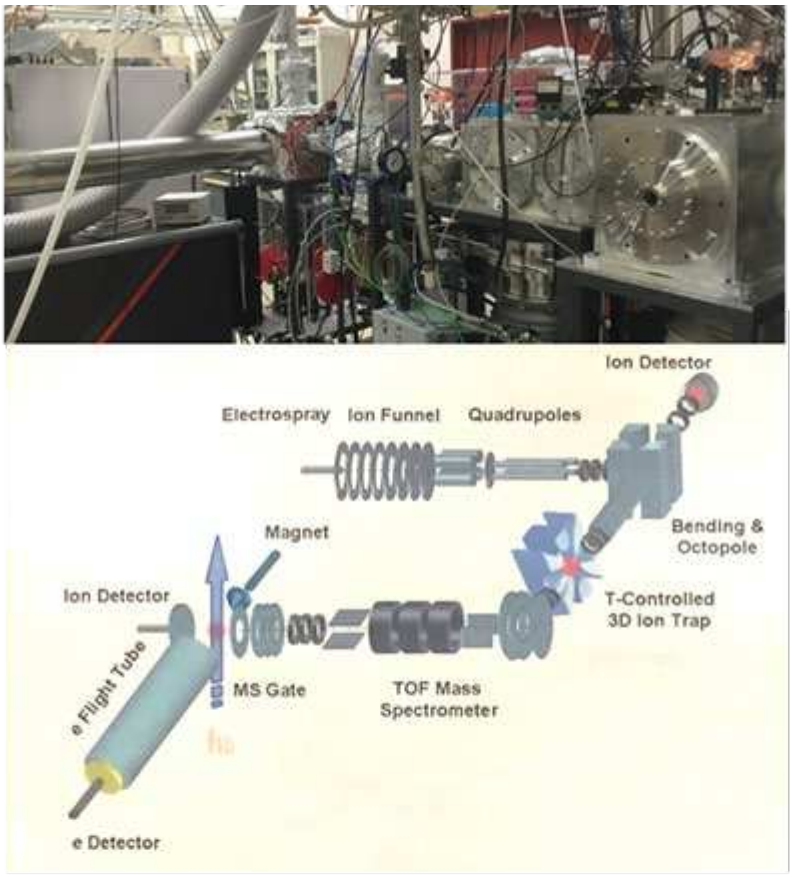

Figure A-5. Photograph of instrument used for low temperature PES (top), and schematic of instrumentation (bottom).

other corrections were applied using TWINABS. Standard Bruker control and integration software (APEX II) was employed, and Bruker SHELXTL software was used with Olex 2 for the structure solution, refinement, and molecular graphics.

A.4.10. Spectroelectrochemistry

A flat cell (0.6 mm^3 × 8 mm^3 × 50 mm^3) with a three-electrode set up was utilized. See figure A-4. A platinum and a silver wire were utilized as the counter and reference electrodes as described above. A fine platinum mesh (wire 60µm diameter, pore size 0.25mm) was utilized as the working electrode. This mesh was laminated such that only a circle (diameter *ca.* 0.5 cm) was

exposed. Working and counter electrodes were positioned with at least 1 cm of space between them to prevent products of the counter electrode from disturbing measurements. The reference electrode was positioned close to working electrode to reduce the influence of non-faradaic currents.

Sample solutions were degassed using a flow of dinitrogen gas, and samples were prepared in a dinitrogen filled glovebox and sealed with Teflon tape to exclude oxygen. To avoid line broadening by spin-spin interactions, analyte concentration was in the range of 10^{-3}–10^{-5} mol/L. Electrolyte solutions was 0.1 M tetrabutylammonium hexafluorophosphate. ESR/UV-Vis-NIR spectroelectrochemical measurements were conducted using a Bruker ER 4104OR optical ESR cavity.

The ESR-signal was measured with a Bruker EMXmicroTM CW spectrometer or an EMXplusTM CW-spectrometer with a X-band microwave bridge (EMXpremiumX) to excite the sample. The magnetic field scale was calibrated utilizing a Bruker NMR ER036TM teslameter and data were processed with the Xenon-software. The power of the microwave bridge and receiver gain have been tuned until an optimal signal has been obtained with a sufficient signal-to-noise ratio, without reaching the saturation limit. In order to detect small changes in the amount of the paramagnetic species, the ESR-signal has been over-modulated with modulation amplitudes between (5-8)G, and therefore the hyperfine structure has not been resolved.

An AVALight-HAL-S or AVALight-DH-S-BAL lamp (Avantes, Netherlands) coupled to the cavity via a FC-UV/IR600-2-SR lightguide (Avantes) was used for UVVis-NIR spectrometry. UVVis-NIR spectra were recorded with an AVS-Rackmount-USB2-unit by Avantes containing two spectrometers: an AvaSpec-2048x14-USB2 spectrometer with a CCD-detector for the UV and Vis region ((200-1160)nm) and an AvaSpec-NIR256-2.2 spectrometer with an InGaAs detector for the NIR-light ((1150-2130)nm). Data were processed with the AvaSoft 7.7 software package.

Voltage was applied using a Heka PG390 potentiostat, connected to the UV-Vis-NIR and ESR spectrometer. This facilitated triggering via the software package PotMaster v2x80 (HEKA

Electronic). Triggering was tuned such that UV-Vis-measurement (several milliseconds) took place at the center of each magnetic field sweep of an ESR-measurement (several seconds).

A.4.11. Time Resolved Microwave Conductivity (TRMC)

Samples for TRMC were blended films of analyte and rr-P3HT, prepared by drop casting from chloroform solutions onto 1 × 2 cm quartz substrates. Neat P3HT films were prepared in the same way. The samples were placed in the resonance cavity at one end of a ca. 9 GHz X-band microwave waveguide. The films were exposed through the quartz substrate to 5 ns pulses of 500 nm photons using a Continuum Panther optical parametric oscillator pumped by the 355 nm harmonic of a Continuum Powerlite Q-switched Nd:YAG laser. The transient change in photoconductance ($\Delta G(t)$) was measured by monitoring changes in the microwave power in the cavity ($\Delta P(t)$) due to absorption of microwave photons by photogenerated electrons and holes in the thin film according to the equation: $\Delta G(t) = -(K(\Delta P(t)/P)^{-1}$ where K is a experimentally-determined calibration factor that depends on the microwave cavity resonance characteristics and the dielectric properties of the sample. The peak photoconductance, ΔG_{peak}, is used to determine the yield of free carriers (i.e., electron and holes), φ, times the sum of the free carrier mobilities, $\sum\mu$, according to the equation: $\Delta G_{peak} = \beta q_e I_0 F_A \varphi \sum\mu$ where β is the ratio of the dimensions of the cross-section of the waveguide (2.2 in this instrument), q_e is the charge on an electron, I_0 is the incident photon flux, and F_A is the fraction of laser pump photons absorbed by the sample.

A.5. COMPUTATIONAL DETAILS

A.5.1. ORCA

For precise calculations, ORCA was used. Electron and exchange correlation were modeled by the hybrid functional B3LYP [42–45] with an unrestricted Kohn-Sham DFT-approach. For the numerical integration, tight options (Grid 5: Lebedev-434, Integration Accuracy 7.0 , no Final Grid) were used during geometry optimization and even more refined (Grid 6: Lebedev-590, Integration Accuracy 8.0 , no Final Grid) for calculations of ESR-parameters. An Ahlrichs-TZVP basis set was used for geometry optimization. Optimizations were performed using the quasi-newton method until energy changes were smaller than $1 \cdot 10^{-6}$ Eh and the maximum gradient smaller than $1 \cdot 10^{-4}$ Eh/bohr. Within each SCF-cycle, energies were converged up to $1 \cdot 10^{-8}$ Eh. To account for solvent effects and estimate halfwave potentials, COSMO solvation model has been applied. Calculations of ESR-parameters were performed with a def2-TZVP basis set for atoms without any coupling to the radical electron (C, O). The EPR-III basis set with extended core region was applied for all other atoms (H, F, N), for which the isotropic part of the coupling tensor was subsequently calculated. Absorption spectra were calculated using time dependent (TD) DFT. The functional was changed to CAM-B3LYP[48] and the level of basis set was reduced to the Ahlrichs-VDZ basis set. The computational effort was further reduced using the RJCOSX approximation.

A.5.2. Priroda Structures

Simulations with Priroda Structures were pre-optimized with Priroda using density functional theory (DFT). A PBE functional with a TZVP basis set was used. For the energy optimization run, the cutoff was set to $4 \cdot 10^{-8}$ Eh and optimizations were performed with a tolerance level of $4 \cdot 10^{-6}$ Eh.

A.5.3. Simulation of EPR spectra

EPR spectra were simulated and fit to experimental data using EasySpin. DFT-computed coupling constants were used as starting parameters for the fitting procedure.

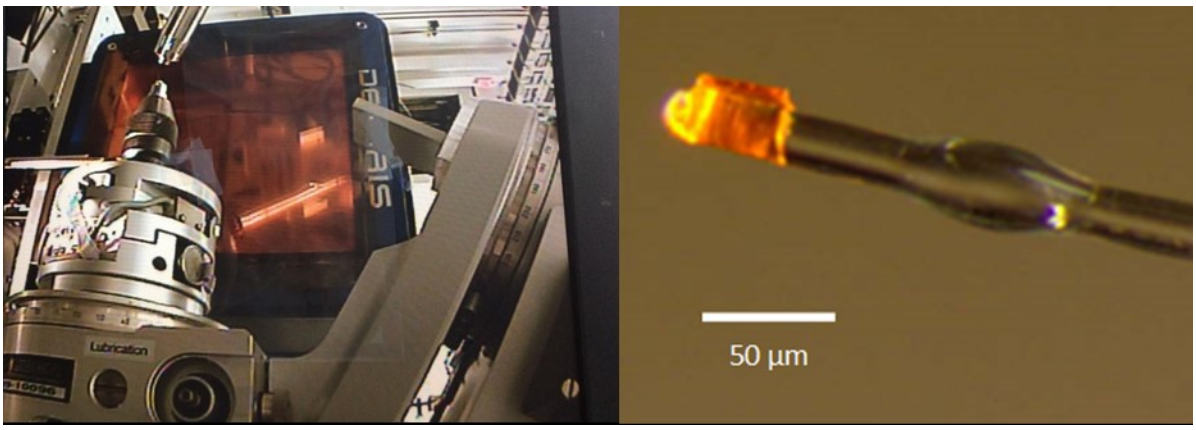

Figure A-6. Goniometer head and image of single crystal illustrating instrumentation used at APS (A.4.9.).

A.6. CRYSTALLOGRAPHIC DETAILS

Crystallographic data for structures have been deposited with the Cambridge Crystallographic Data Centre as supplementary publications. Copies of the data can be obtained free of charge on application to CCDC, 12 Union Road, Cambridge CB2 1EZ, UK, fax: +441223 336033 or e-mail: deposit@ccdc.cam.ac.uk.

APPENDIX B

DETAILS OF REACTIONS FROM WHICH PURE COPOUNDS WERE ISOLATED

B.1.1. Reaction 1.1 optimized for 2,3-TRPH(C_4F_8)

Table B-1. Synthetic details for reaction 1.1.

Reactants	Vessel Type	T	time	Crude Product Recovered	Products Isolated
-25 mg (0.11 mmol) TRPH -40 μL (0.22 mmol) 1,4-$C_4F_8I_2$ -750 mg (excess) Cu powder	flame-sealed glass ampoule, *ca.* 60 mL	300 °C	2 h	34 mg	63% 2,3-TRPH(C_4F_8)

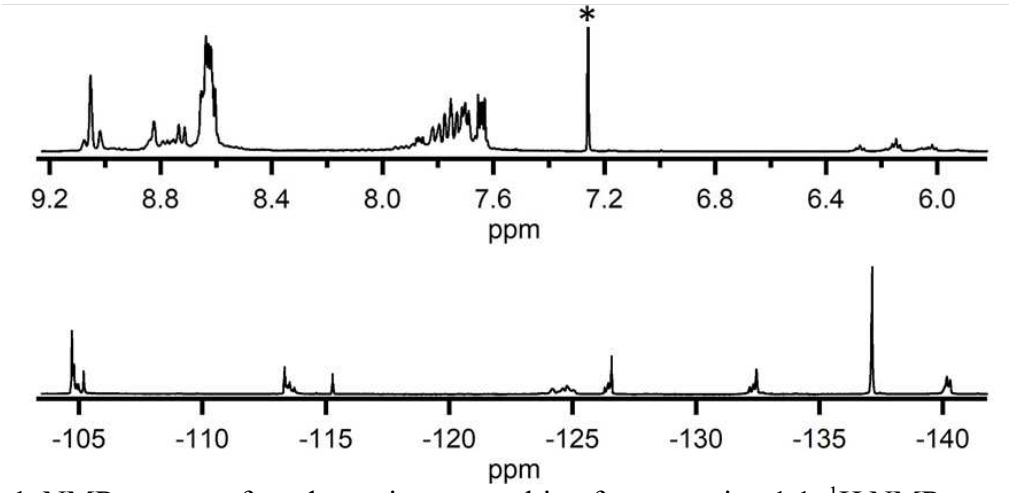

Figure B-1. NMR spectra of product mixture resulting from reaction 1.1. ^{1}H NMR spectrum (top) referenced to $CHCl_3$ (δ = 7.26, denoted *). ^{19}F NMR spectrum (bottom) referenced to perfluorobenzene (δ = −164.9, not shown).

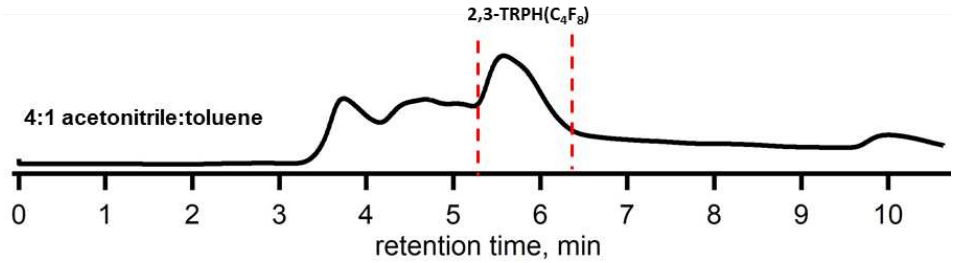

Figure B-2. HPLC separation of reaction 1.1. Detection wavelength 300 nm. Molar absorbances for different compounds at this wavelength vary, and therefore the trace is not representative of product distribution. Due to column condition at time of separation, peak shape is not sharp, but separation was nonetheless good.

B.1.2. Reaction 1.2 optimized for 2,3;6,7-TRPH(C_4F_8)$_2$

Table B-2. Synthetic details for reaction 1.2.

Reactants	Vessel Type	T	time	Crude Product Recovered	Products Isolated
-25 mg (0.11 mmol) TRPH -80 μL (0.44 mmol) 1,4-$C_4F_8I_2$ -750 mg (excess) Cu powder	flame-sealed glass ampoule, *ca.* 60 mL	300 ºC	2 h	52 mg	42% 2,3;6,7-TRPH(C_4F_8)$_2$

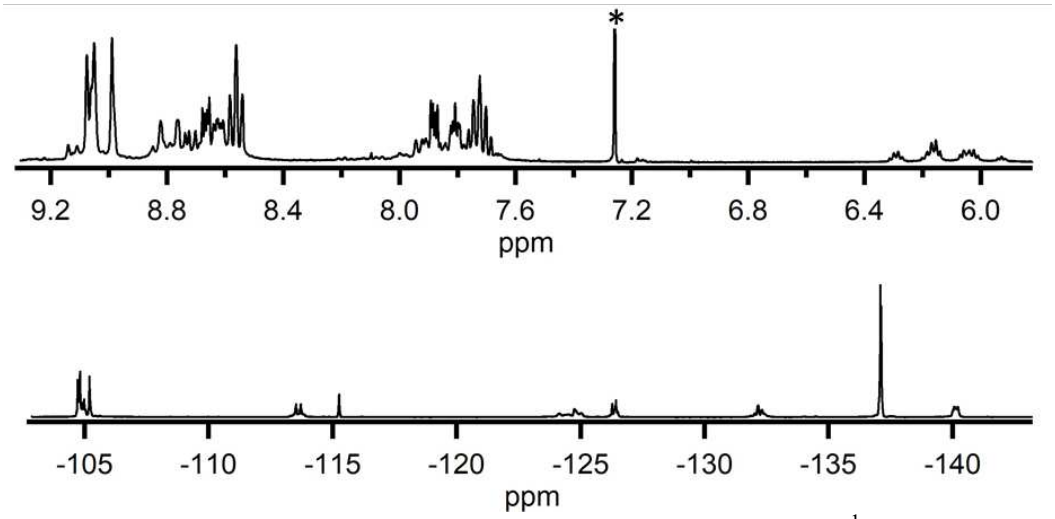

Figure B-3. NMR spectra of product mixture resulting from reaction 1.2. ^{1}H NMR spectrum (top) referenced to $CHCl_3$ (δ = 7.26, denoted *). ^{19}F NMR spectrum (bottom) referenced to perfluorobenzene (δ = −164.9, not shown).

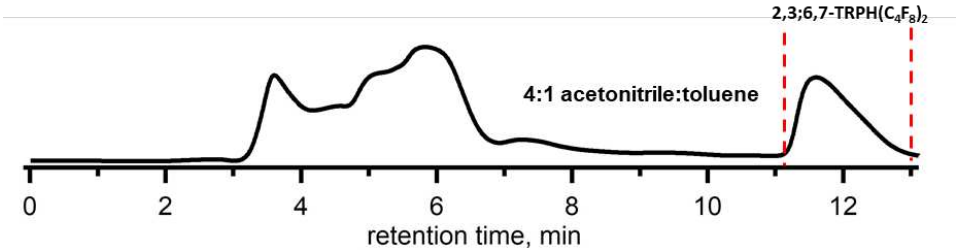

Figure B-4. HPLC separation of reaction 1.2. Detection wavelength 300 nm. Molar absorbances for different compounds at this wavelength vary, and therefore the trace is not representative of product distribution. Due to column condition at time of separation, peak shape is not sharp, but separation was nonetheless good.

B.1.3. Reaction 1.3 optimized for 2,3;6,7;10,11-TRPH(C_4F_8)$_3$

Table B-3. Synthetic details for reaction 1.3.

Reactants	Vessel Type	T	time	Crude Product Recovered	Products Isolated
-25 mg (0.11 mmol) TRPH -161 μL (0.88 mmol) 1,4-$C_4F_8I_2$ -750 mg (excess) Cu powder	flame-sealed glass ampoule, *ca.* 60 mL	300 ºC	2 h	55 mg	76% 2,3;6,7;10,11-TRPH(C_4F_8)$_3$

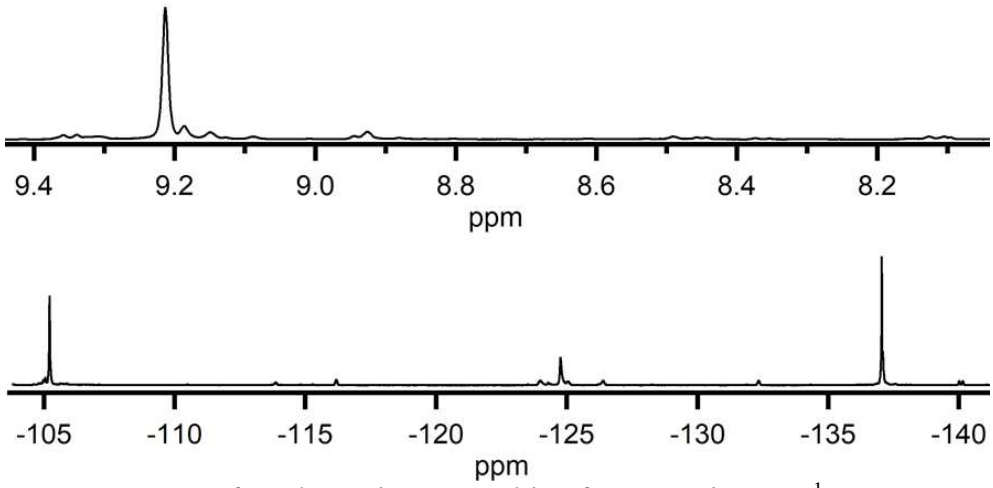

Figure B-5. NMR spectra of product mixture resulting from reaction 1.3. ^{1}H NMR spectrum (top) referenced to $CHCl_3$ (δ = 7.26, not shown). ^{19}F NMR spectrum (bottom) referenced to perfluorobenzene (δ = –164.9, not shown).

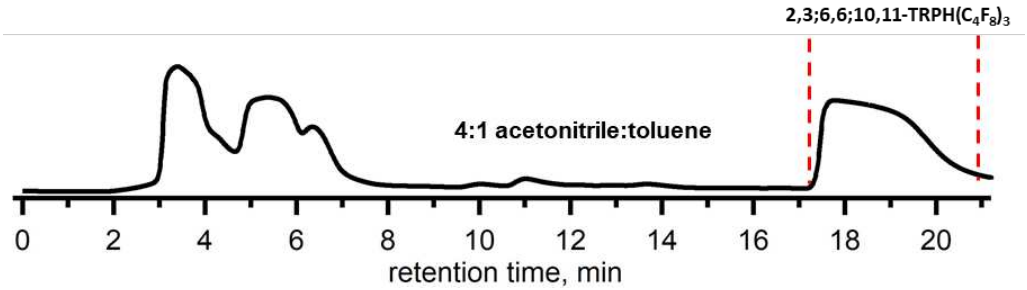

Figure B-6. HPLC separation of reaction 1.3. Detection wavelength 300 nm. Molar absorbances for different compounds at this wavelength vary, and therefore the trace is not representative of product distribution. Due to column condition at time of separation and tendancy of compound to streak on column, peak shape is not sharp, but separation was nonetheless good.

B.1.4. Reaction 1.4 for 1,2-TRPH(C_4F_8) and 2,3-TRPH(C_4F_8)

Table B-4. Synthetic details for reaction 1.4.

Reactants	Vessel Type	T	time	Crude Product Recovered	Products Isolated
-50 mg (0.22 mmol) TRPH -80 µL (0.44 mmol) 1,4-$C_4F_8I_2$	flame-sealed glass ampoule, *ca.* 60 mL	300 ºC	2 h	25 mg	25% 2,3- TRPH(C_4F_8) 20% 1,2- TRPH(C_4F_8)

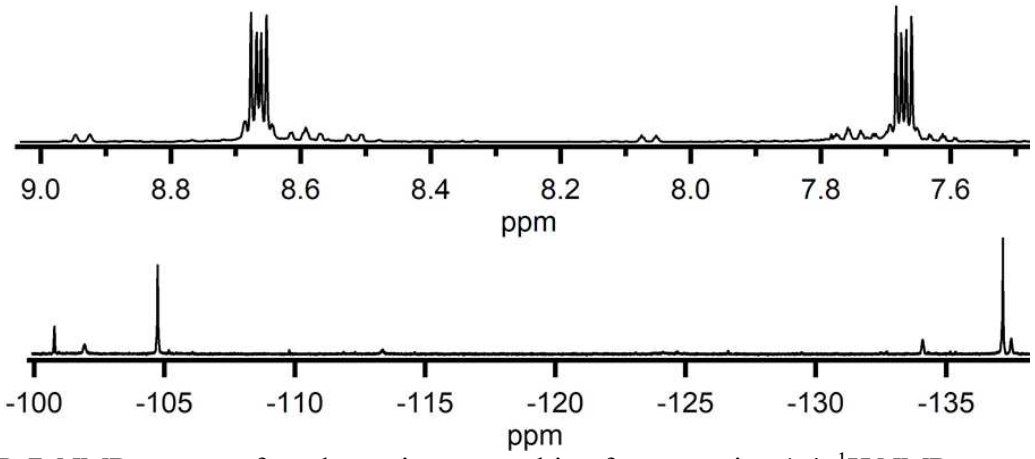

Figure B-7. NMR spectra of product mixture resulting from reaction 1.4. ^{1}H NMR spectrum (top) referenced to $CHCl_3$ (δ = 7.26, not shown). ^{19}F NMR spectrum (bottom) referenced to perfluorobenzene (δ = –164.9, not shown).

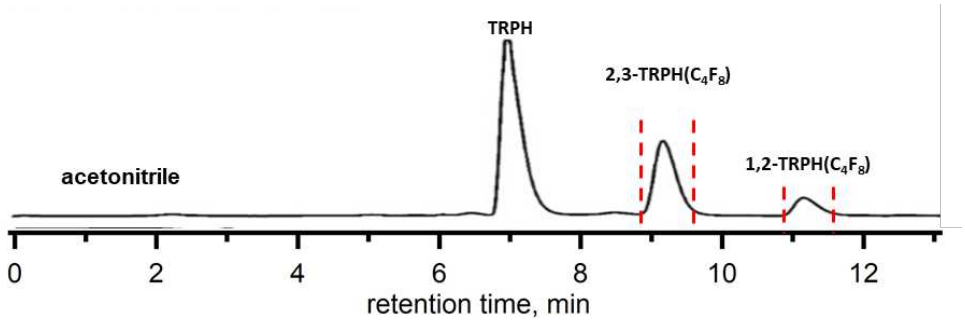

Figure B-8. HPLC separation of reaction 1.4. Detection wavelength 300 nm. Molar absorbances for different compounds at this wavelength vary, and therefore the trace is not representative of product distribution.

B.1.5. Reaction 1.5 for RD/A products

Table B-5. Synthetic details for reaction 1.5.

Reactants	Vessel Type	T	time	Crude Product Recovered	Products Isolated
-50 mg (0.22 mmol) TRPH -97 μL (0.53 mmol) 1,4-$C_4F_8I_2$ - 5000 mg Cu powder	flame-sealed glass ampoule, *ca.* 60 mL	360 ºC	4 h	110 mg	53% 2,3- TRPH(C_4F_8) 10% 2,3-TRPH(C_4F_4) 26% 2,3;6,7- TRPH(C_4F_8)$_2$ <5% 2,3- TRPH(C_4F_3H)

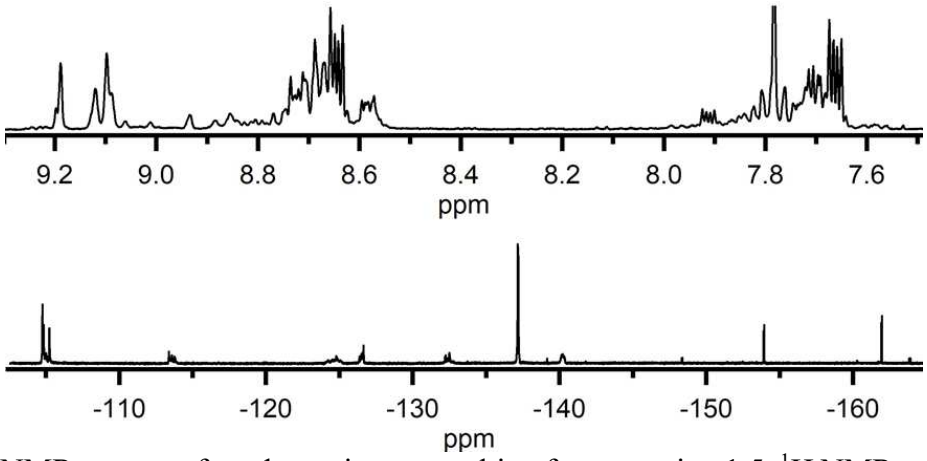

Figure B-9. NMR spectra of product mixture resulting from reaction 1.5. ^{1}H NMR spectrum (top) referenced to $CHCl_3$ (δ = 7.26, not shown). ^{19}F NMR spectrum (bottom) referenced to perfluorobenzene (δ = –164.9, not shown).

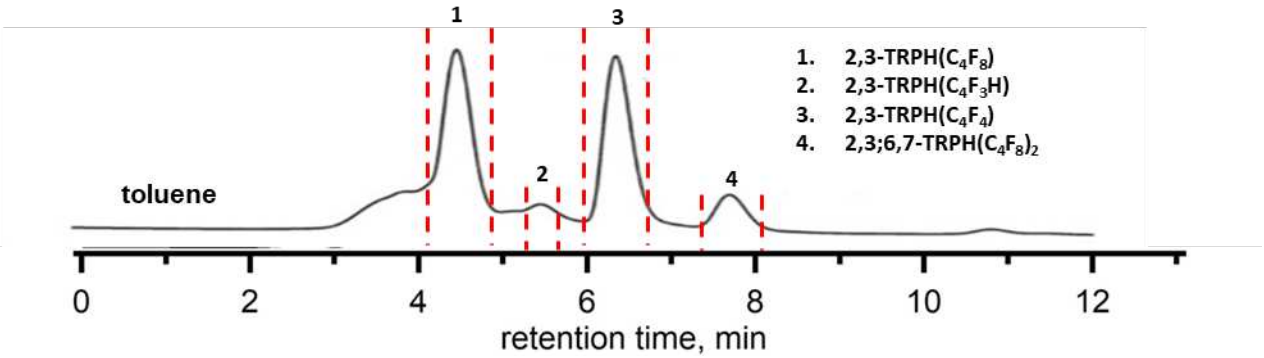

Figure B-10. HPLC separation of reaction 1.5. Detection wavelength 300 nm. Molar absorbances for different compounds at this wavelength vary, and therefore the trace is not representative of product distribution. . 2,3:5,6;10- TRPH(C_4F_8)$_2$(C_4F_8H)

B.1.6. Reaction 1.6 for minor products bearing C_4F_8 moieties

Table B-6. Synthetic details for reaction 1.6.

Reactants	Vessel Type	T	time	Crude Product Recovered	Products Isolated
-50 mg (0.22 mmol) TRPH -80 µL (0.44 mmol) 1,4-$C_4F_8I_2$	flame-sealed glass ampoule, *ca.* 60 mL	300 ºC	2 h	25 mg	<5% 2,3:6- TRPH(C_4F_8)(C_4F_8H) <5% 1,2;6,7- TRPH(C_4F_8)$_2$ <5% 1,2;10,11- TRPH(C_4F_8)$_2$ <5% 1,2;6,7;10,11- TRPH(C_4F_8)$_3$ <5% 1,2;5,6;10,11- TRPH(C_4F_8)$_3$

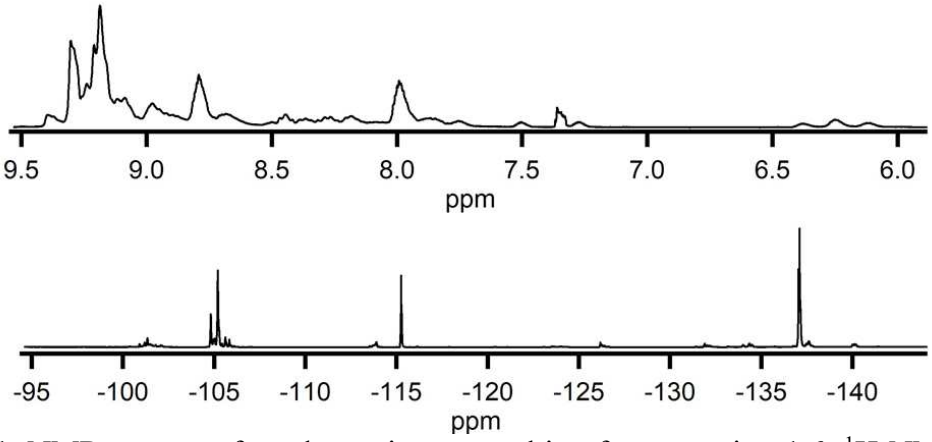

Figure B-11. NMR spectra of product mixture resulting from reaction 1.6. ^{1}H NMR spectrum (top) referenced to $CHCl_3$ ($\delta = 7.26$). ^{19}F NMR spectrum (bottom) referenced to perfluorobenzene ($\delta = -164.9$, not shown).

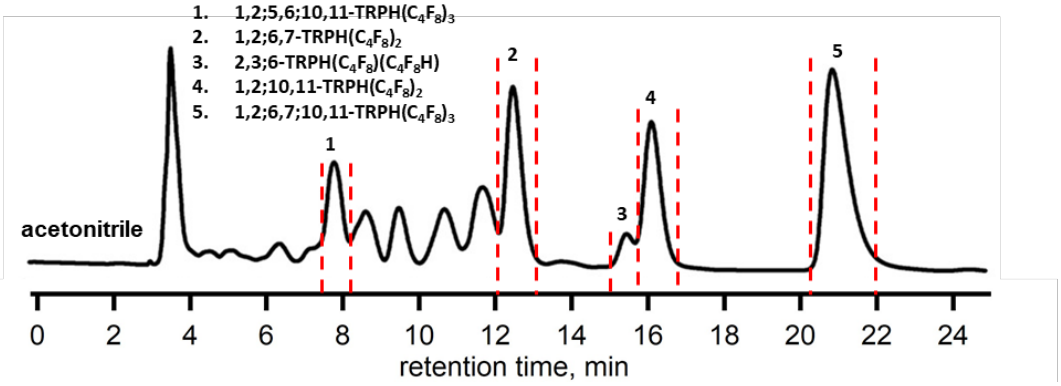

Figure B-12. HPLC separation of reaction 1.6. Detection wavelength 300 nm. Molar absorbances for different compounds at this wavelength vary, and therefore the trace is not representative of product distribution.

B.1.7. Reaction 1.7 for minor RD/A products

Table B-7. Synthetic details for reaction 1.7.

Reactants	Vessel Type	T	time	Crude Product Recovered	Products Isolated
-50 mg (0.22 mmol) TRPH -80 μL (0.44 mmol) 1,4-$C_4F_8I_2$	flame-sealed glass ampoule, *ca.* 60 mL	300 ºC	2 h	25 mg	<5% 2,3;6,7- TRPH(C_4F_4)$_2$ <5% 2,3;6,7;10,11- TRPH(C_4F_8)$_2$(C_4F_4) <5% 2,3- TRPH(C_4F_4) <5% 2,3:5,6;10- TRPH(C_4F_8)$_2$(C_4F_8H)

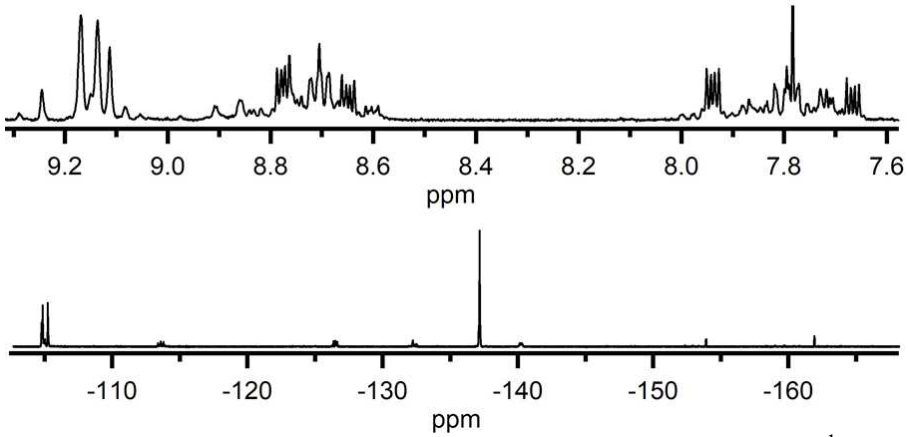

Figure B-13. NMR spectra of product mixture resulting from reaction 1.7. ^{1}H NMR spectrum (top) referenced to $CHCl_3$ (δ = 7.26, not shown). ^{19}F NMR spectrum (bottom) referenced to perfluorobenzene (δ = –164.9, not shown).

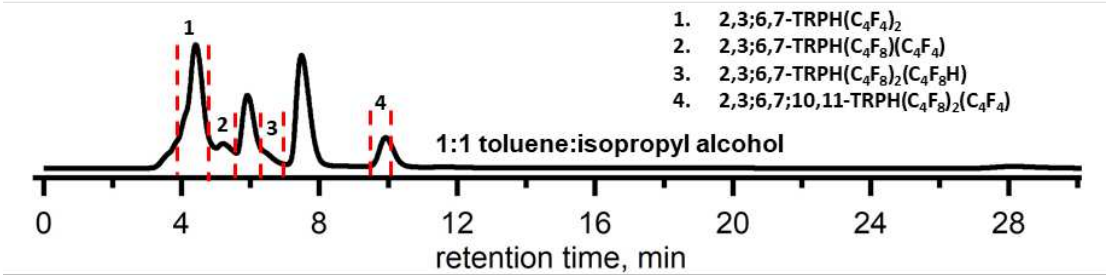

Figure B-14. HPLC separation of reaction 1.7. Detection wavelength 300 nm. Molar absorbances for different compounds at this wavelength vary, and therefore the trace is not representative of product distribution.

B.2. CHAPTER 2 REACTIONS

B.2.1. Reaction 2.1 for 4,7-PHEN derivatives

Table B-8. Synthetic details for reaction 2.1.

Reactants	Vessel Type	T	time	Crude Product Recovered	Products Isolated
-100 mg (0.55 mmol) 4,7-PHEN -200 μL (1.1 mmol) 1,4-$C_4F_8I_2$ -250 mg (excess) Cu powder	flame-sealed glass ampoule, *ca.* 60 mL	200 ºC	2 h	64 mg	5,6-(4,7-PHEN)(C_4F_8) 2,3;5,7-(4,7-PHEN)(C_4F_8)$_2$ 2,3;5,6;8,9-(4,7-PHEN)(C_4F_8)$_3$ 5,6-(4,7-PHEN)(C_4F_4) 5,6-(4,7-PHEN)(C_4F_8)(C_4F_4)

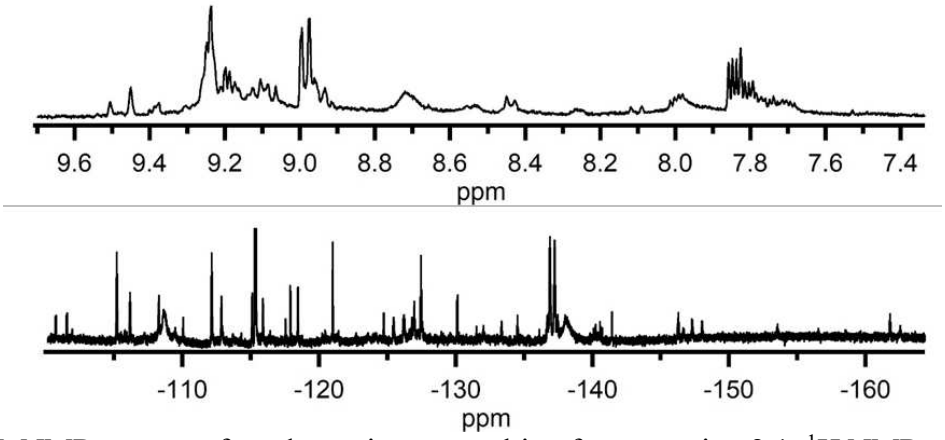

Figure B-15. NMR spectra of product mixture resulting from reaction 2.1. ^{1}H NMR spectrum (top) referenced to $CHCl_3$ (δ = 7.26, not shown). ^{19}F NMR spectrum (bottom) referenced to perfluorobenzene (δ = −164.9, not shown).

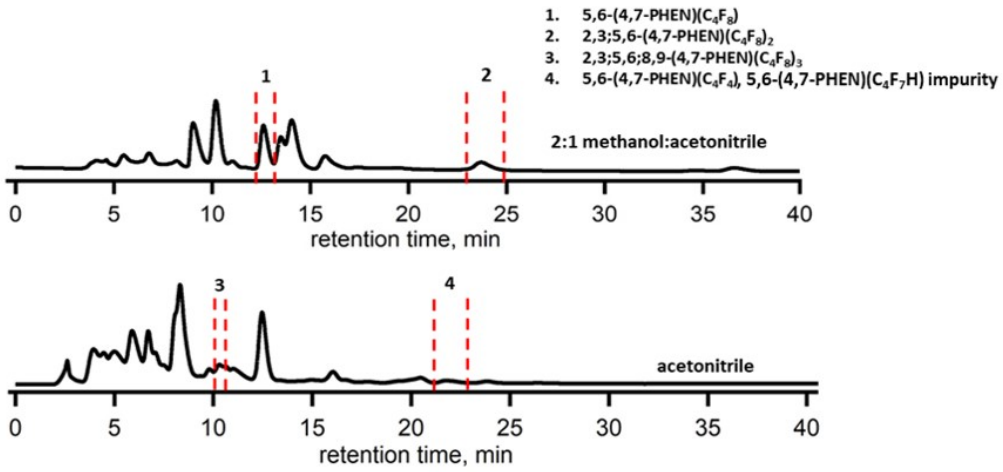

Figure B-16. HPLC separation of reaction 2.1. Detection wavelength 300 nm. Molar absorbances for different compounds at this wavelength vary, and therefore the trace is not representative of product distribution. Other peaks were complex mixtures of impure products.

B.2.2. Reaction 2.2 optimized for 5,6-(4,7-PHEN)(C_4F_8)

Table B-9. Synthetic details for reaction 2.2.

Reactants	Vessel Type	T	time	Crude Product Recovered	Products Isolated
-25 mg (0.14 mmol) 4,7-PHEN -25 µL (0.14 mmol) 1,4-$C_4F_8I_2$ -250 mg (excess) Cu powder	flame-sealed glass ampoule, *ca.* 60 mL	200 ºC	4 h	19 mg	45% 5,6-(4,7-PHEN)(C_4F_8) 18% 2,3;5,7-(4,7-PHEN)(C_4F_8)$_2$

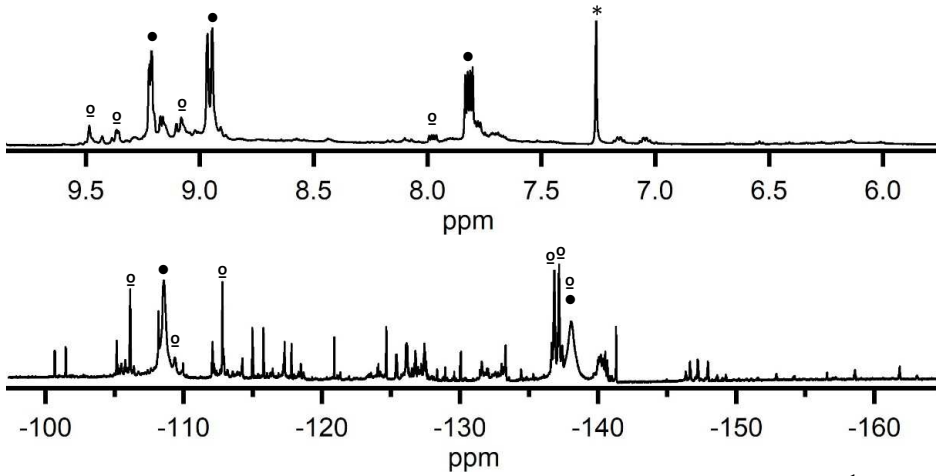

Figure B-17. NMR spectra of product mixture resulting from reaction 2.2. ^{1}H NMR spectrum (top) referenced to $CHCl_3$ (δ = 7.26, denoted *). ^{19}F NMR spectrum (bottom) referenced to perfluorobenzene (δ = –164.9, not shown). Major products of this reaction are 5,6-(4,7-PHNZ)(C_4F_8), denoted • and 2,3;5,6-(4,7-PHNZ)(C_4F_8)$_2$, denoted º.

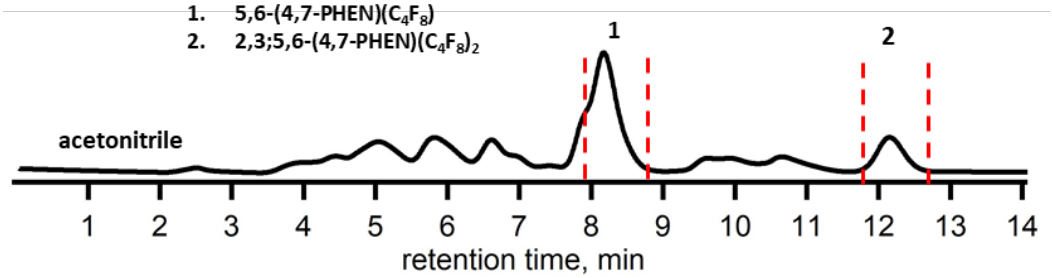

Figure B-18. HPLC separation of reaction 2.2. Detection wavelength 300 nm. Molar absorbances for different compounds at this wavelength vary, and therefore the trace is not representative of product distribution. Other peaks were complex mixtures of impure products.

B.2.3. Reaction 2.3 for 1,10-PHEN derivatives

Table B-10. Synthetic details for reaction 2.3.

Reactants	Vessel Type	T	time	Crude Product Recovered	Products Isolated
-100 mg (0.55 mmol) 1,10-PHEN -200 μL (1.1 mmol) 1,4-$C_4F_8I_2$	flame-sealed glass ampoule, *ca.* 60 mL	350 ºC	1 h	95 mg	2,3-(1,10-PHEN)(C_4F_8) 3,4-(1,10-PHEN)(C_4F_8) 2,3;5,6-(1,10-PHEN)(C_4F_8)$_2$ 2,3;7,8-(1,10-PHEN)(C_4F_8)$_2$ 2,3;8,9(1,10-(PHEN)(C_4F_8)$_2$ 2,3;5,6;8,9(1,10-PHEN)(C_4F_8)$_3$

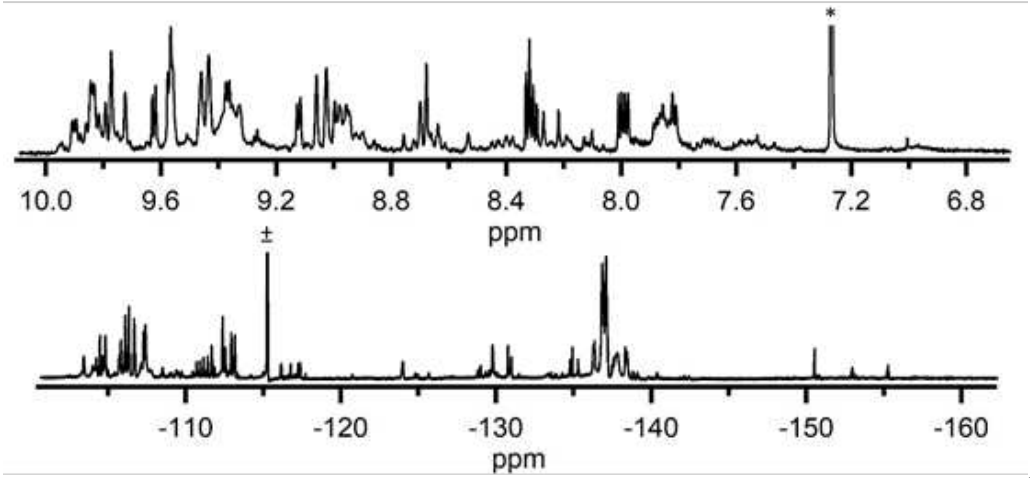

Figure B-19. NMR spectra of crude product mixture recovered from reaction 2.3. ^{1}H NMR spectrum (top) referenced to $CHCl_3$ (δ = 7.26, denoted *). ^{19}F NMR spectrum (bottom) referenced to perfluorobenzene (δ = –164.9, not shown). Residual unreacted $C_4F_8I_2$ present, denoted ±.

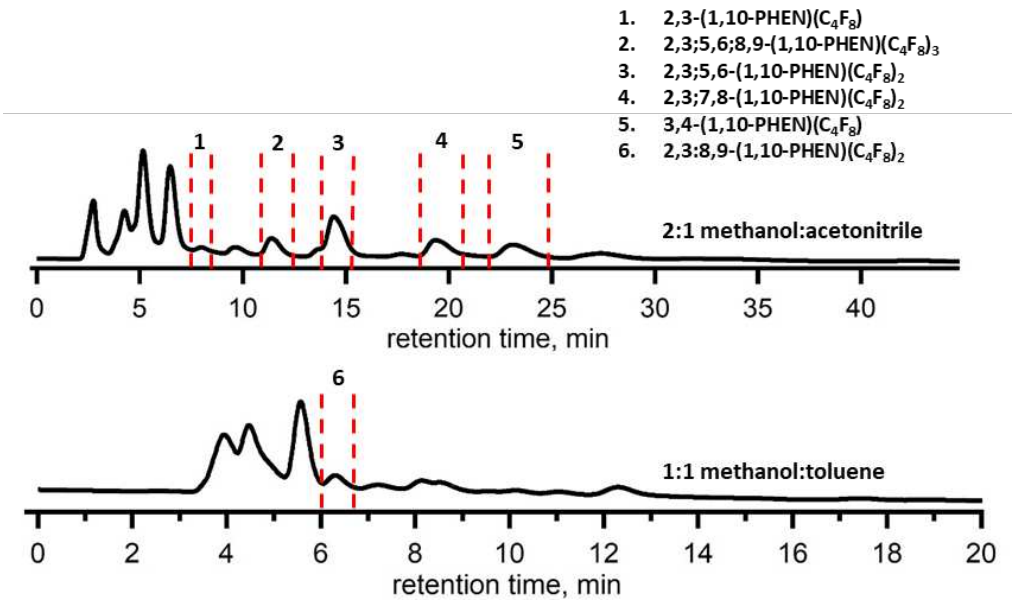

Figure B-20. HPLC separation of reaction 2.3. Detection wavelength 300 nm. Molar absorbances for different compounds at this wavelength vary, and therefore the trace is not representative of product distribution. Other peaks were complex mixtures of impure products. For the 1:1 methanol:toluene was a less effective method than 2:1 methanol:acetonitrile, but yielded one compound that was not isolated in the 2:1 methanol:acetonitrile separation.

B.2.4. Reaction 2.4 for 5-PHRD derivatives

Table B-11. Synthetic details for reaction 2.4.

Reactants	Vessel Type	T	time	Products Isolated
-100 mg (0.55 mmol) 5-PHRD -100 µL (0.55 mmol) 1,4-$C_4F_8I_2$	flame-sealed glass ampoule, *ca.* 60 mL	350 ºC	2 h	7,8-(5-PHRD)(C_4F_8)$^{x\text{-ray}}$ 5-PHRD(C_4F_8)-B

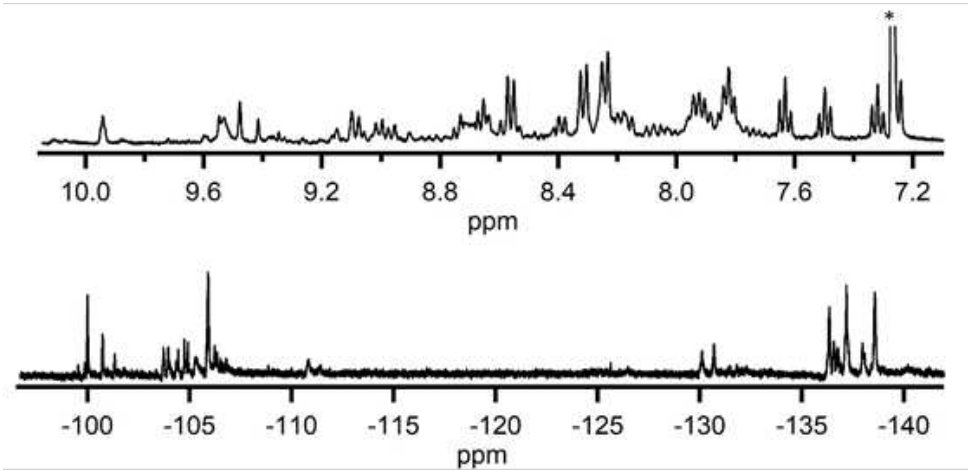

Figure B-21. NMR spectra of product mixture resulting from reaction 2.4. ^{1}H NMR spectrum (top) referenced to $CHCl_3$ (δ = 7.26, denoted *). ^{19}F NMR spectrum (bottom) referenced to perfluorobenzene (δ = −164.9, not shown).

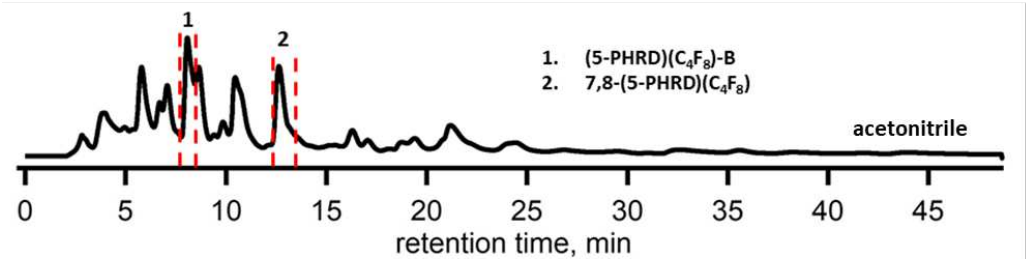

Figure B-22. HPLC separation of reaction 2.4. Detection wavelength 300 nm. Molar absorbances for different compounds at this wavelength vary, and therefore the trace is not representative of product distribution. Other peaks were complex mixtures of impure products.

B.2.5. Reaction 2.5 for ACRD derivatives

Table B-12. Synthetic details for reaction 2.5.

Reactants	Vessel Type	T	time	Products Isolated
-100 mg (0.30 mmol) ACRD -111 μL (0.6 mmol) 1,4-$C_4F_8I_2$	flame-sealed glass ampoule, *ca.* 60 mL	350 °C	2 h	2,3-ACRD(C_4F_8) ACRD(C_4F_8)$_2$-A ACRD(C_4F_8)$_2$-B ACRD(C_4F_8)$_2$-C 1,2-ACRD(C_4HF_3) ACRD(C_4HF_3)-B

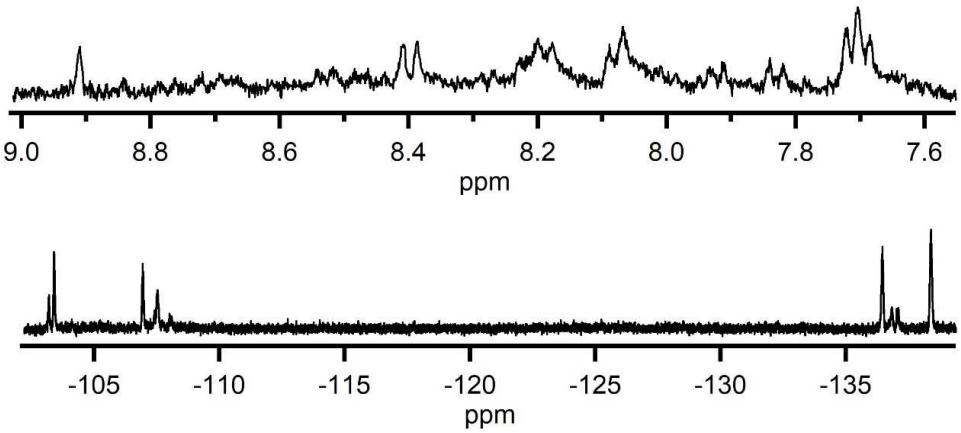

Figure B-23. NMR spectra of product mixture resulting from reaction 2.5. ^{1}H NMR spectrum (top) referenced to $CHCl_3$ (δ = 7.26, not shown). ^{19}F NMR spectrum (bottom) referenced to perfluorobenzene (δ = −164.9, not shown).

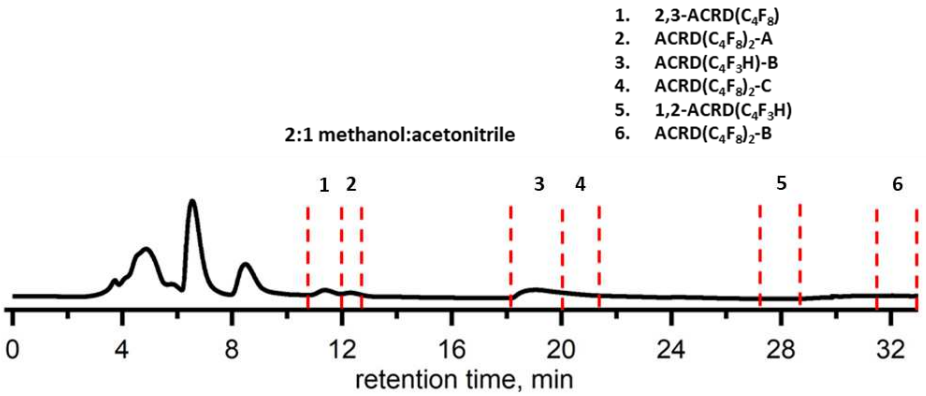

Figure B-24. HPLC separation of reaction 2.5. Detection wavelength 300 nm. Molar absorbances for different compounds at this wavelength vary, and therefore the trace is not representative of product distribution. Other peaks were complex mixtures of impure products.

B.2.6. Reaction 2.6 for 9,10-ANTH(Ph)$_2$ derivatives

Table B-13. Synthetic details for reaction 2.6.

Reactants	Vessel Type	T	time	Crude Product Recovered	Products Isolated
-50 mg (0.20 mmol) 9,10-ANTH(Ph)$_2$ -72 µL (1.1 mmol) 1,4-$C_4F_8I_2$	flame-sealed glass ampoule, *ca.* 60 mL	350 ºC	2 h	81 mg	2,3-(9,10-ANTH(Ph)$_2$)(C_4F_8) 2,3;6,7-(9,10-ANTH(Ph)$_2$)-(C_4F_8)$_2$

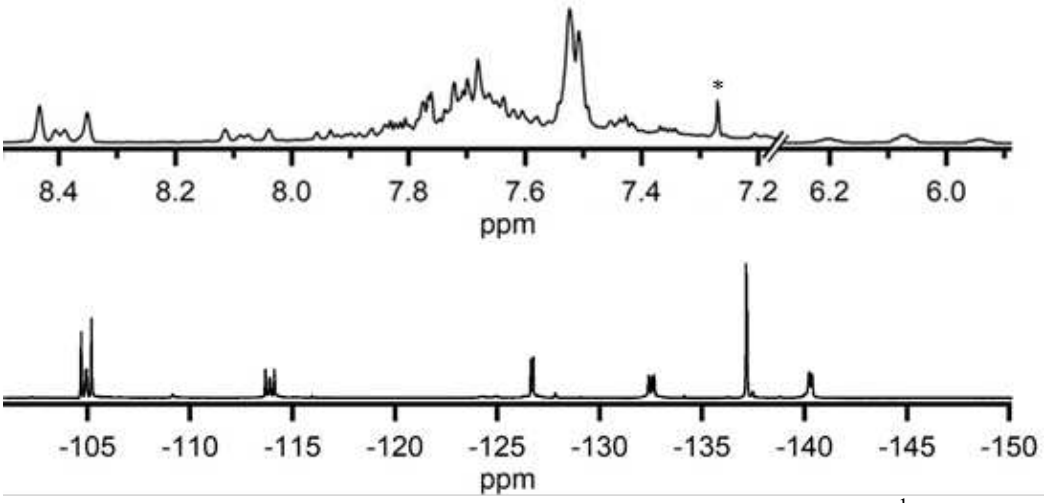

Figure B-25. NMR spectra of product mixture resulting from reaction 2.6. ^{1}H NMR spectrum (top) referenced to $CHCl_3$ (δ = 7.26, denoted *). ^{19}F NMR spectrum (bottom) referenced to perfluorobenzene (δ = −164.9, not shown).

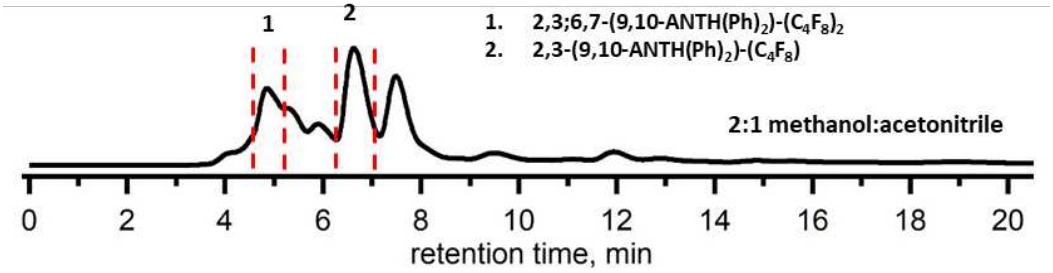

Figure B-26. HPLC separation of reaction 2.6. Detection wavelength 300 nm. Molar absorbances for different compounds at this wavelength vary, and therefore the trace is not representative of product distribution. Other peaks were complex mixtures of impure products.

B.2.7. Reaction 2.7 for PERY derivatives

Table B-14. Synthetic details for reaction 2.7.

Reactants	Vessel Type	T	time	Crude Product Recovered	Products Isolated
-50 mg (0.20 mmol) PERY -72 µL (0.40 mmol) 1,4-$C_4F_8I_2$ -2000 mg (excess) Cu powder	Glass insert in Monel autoclave, N_2(g)	350 ºC	5	65 mg	2,3;9,10-PERY(C_4F_8)$_2$ 3,4;9,10-PERY(C_4F_8)$_2$

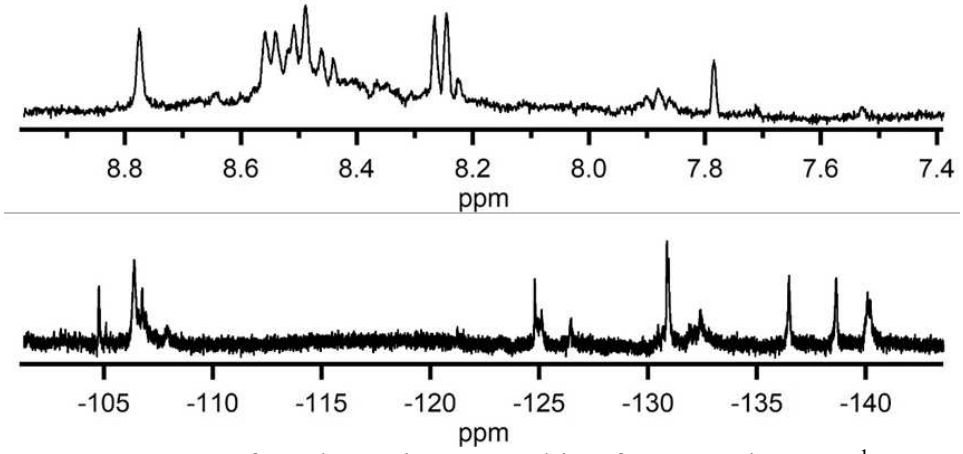

Figure B-27. NMR spectra of product mixture resulting from reaction 2.7. ^{1}H NMR spectrum (top) referenced to $CHCl_3$ (δ = 7.26, not shown). ^{19}F NMR spectrum (bottom) referenced to perfluorobenzene (δ = –164.9, not shown).

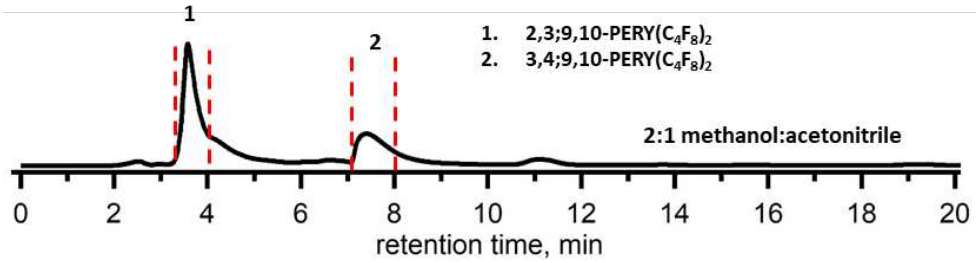

Figure B-28. HPLC separation of reaction 2.7. Detection wavelength 300 nm. Molar absorbances for different compounds at this wavelength vary, and therefore the trace is not representative of product distribution. Other peaks were complex mixtures of impure products.

B.2.8. Reaction 2.8 for PYRN derivatives

Table B-15. Synthetic details for reaction 2.8.

Reactants	Vessel Type	T	time	Crude Product Recovered	Product Isolated
-50 mg (0.25 mmol) PYRN -45 µL (0.25 mmol) 1,4-$C_4F_8I_2$ -2000 mg (excess) Cu powder	Glass insert in Monel autoclave, N_2(g)	350 ºC	5 h	81 mg	4,5-PYRN(C_4F_8)

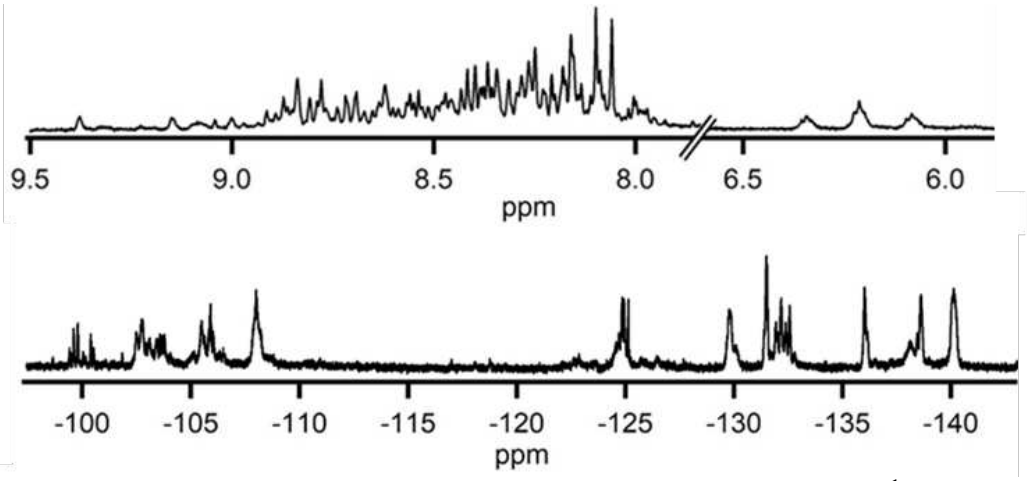

Figure B-29. NMR spectra of product mixture resulting from reaction 2.8. ^{1}H NMR spectrum (top) referenced to $CHCl_3$ (δ = 7.26, not shown). ^{19}F NMR spectrum (bottom) referenced to perfluorobenzene (δ = –164.9, not shown).

B.3. CHAPTER 3 REACTIONS

B.3.1. Reaction 3.1 for PHNZ(C_4F_8)'s

Table B-16. Synthetic details for reaction 3.1.

Reactants	Vessel Type	T	time	Crude Product Recovered	Product Isolated
-50 mg (0.27 mmol) PHNZ -50 μL (0.27 mmol) 1,4-$C_4F_8I_2$ -2000 mg (excess) Cu powder	Glass insert in Monel autoclave, N_2(g)	300 ºC	2 h	45 mg	20% 1,2-PHNZ(C_4F_8) 9% 2,3-PHNZ(C_4F_8) 15% 1,2;6,7-PHNZ(C_4F_8)

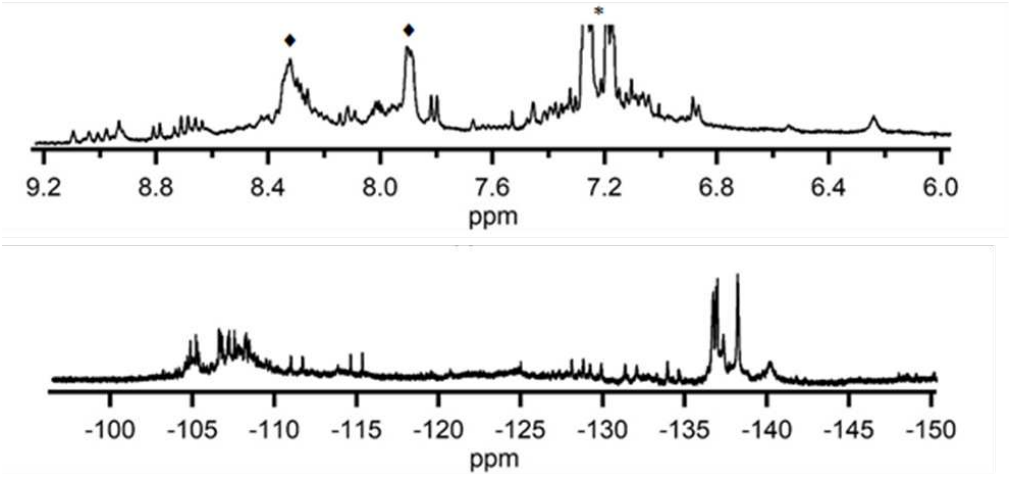

Figure B-30. NMR spectra of product mixture resulting from reaction 3.1. ^{1}H NMR spectrum (top) referenced to $CHCl_3$ (δ = 7.26). Residual toluene from workup present, denoted *. The peaks denoted ♦ primarily arise from unreacted PHNZ, although chemical shifts of desired products overlap this region. ^{19}F NMR spectrum (bottom) referenced to perfluorobenzene (δ = –164.9 not shown).

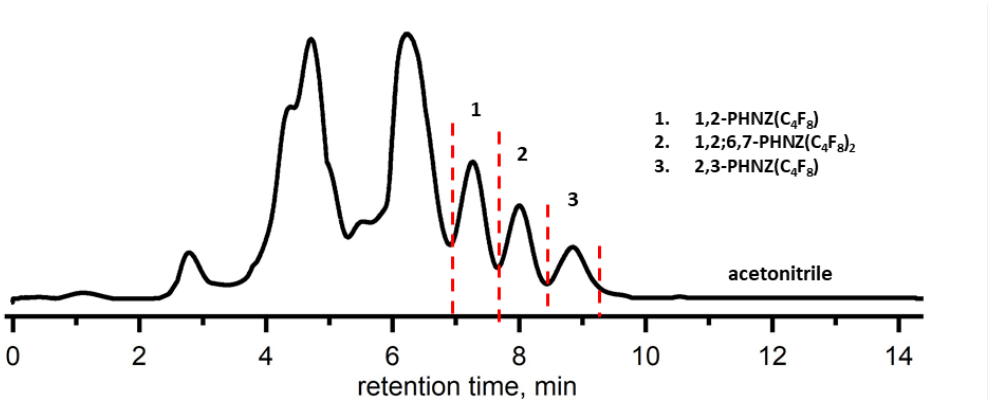

Figure B-31. HPLC separation of reaction 3.1. Detection wavelength 300 nm. Molar absorbances for different compounds at this wavelength vary, and therefore the trace is not representative of product distribution. Other peaks were complex mixtures of impure products. The large peak at 5.7 minutes primarily contains unreacted PHNZ, and accounts for 22% of total recovered mass.

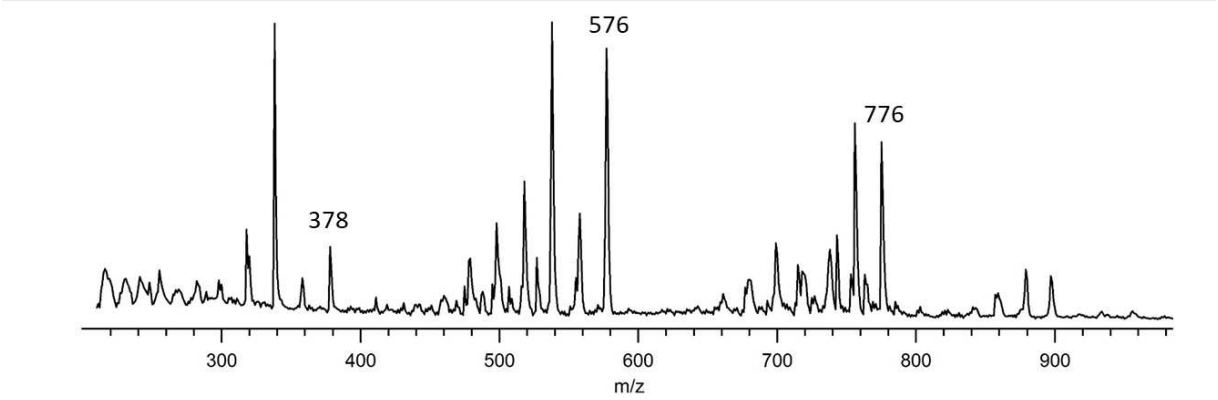

Figure B-32. Analysis of crude product mixture of Reaction 3.1 by mass spectrometry.

B.3.2. Reaction 3.2 for PHNZ(C_4F_8)$_2$'s

Table B-17. Synthetic details for reaction 3.2.

Reactants	Vessel Type	T	time	Crude Product Recovered	Product Isolated
-50 mg (0.27 mmol) PHNZ -495 µL (2.7 mmol) 1,4-$C_4F_8I_2$	sealed glass ampoule, *ca.* 60 mL, under vacuum	300 °C	2 h	45 mg	1,2;6,7-PHNZ(C_4F_8) 1,2;7,8-PHNZ(C_4F_8) 1,2;8,9-PHNZ(C_4F_8)

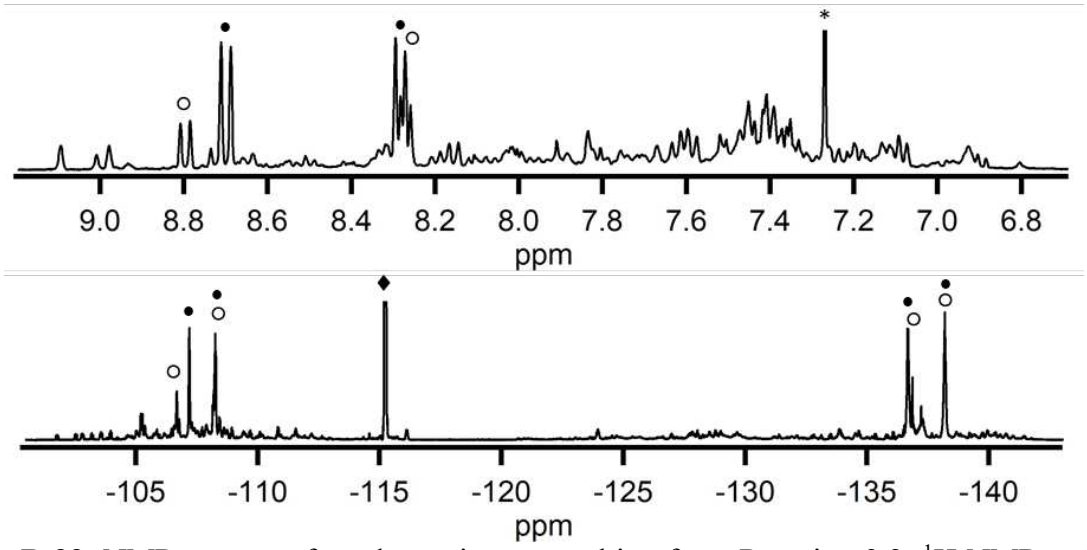

Figure B-33. NMR spectra of product mixture resulting from Reaction 3.2. ^{1}H NMR spectrum (top) referenced to $CHCl_3$ (δ = 7.26, denoted *). ^{19}F NMR spectrum (bottom) referenced to perfluorobenzene (δ = −164.9, not shown). Chemical shifts of major products 1,2;6,7-PHNZ(C_4F_8)$_2$ and 1,2;8,9-PHNZ(C_4F_8) denoted • and °, respectively. Also present is residual 1,4-$C_4F_8I_2$, denoted ♦.

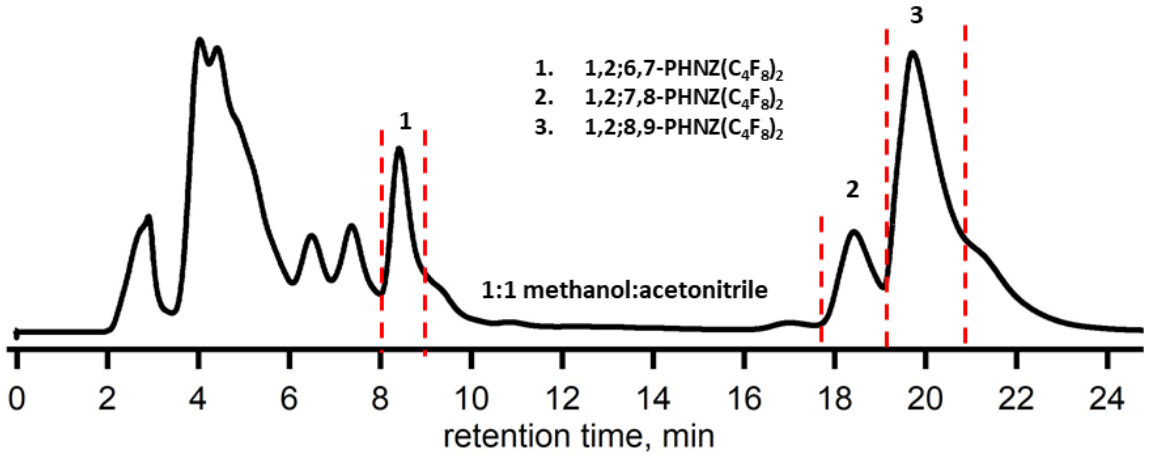

Figure B-34. HPLC separation of reaction 3.2. Detection wavelength 300 nm. Molar absorbances for different compounds at this wavelength vary, and therefore the trace is not representative of product distribution. Other peaks were complex mixtures of impure products. The peak eluting at 7 minutes was not pure but primarily contained 1,2-PHNZ(C_4F_8). The shoulder at 9 minutes was also impure but primarily contained 2,3-PHNZ(C_4F_8). Peaks eluting before 7 minutes were complex mixtures of products but contained many products with C_4F_8H substituents.

B.3.3. Reaction 3.3 200 °C reaction for PHNZ RD/A products

Table B-18. Synthetic details for reaction 3.3.

Reactants	Vessel Type	T	time	Crude Product Recovered	Product Isolated
-50 mg (0.27 mmol) PHNZ -50 µL (0.27 mmol) 1,4-$C_4F_8I_2$ - 250 mg (excess) Cu powder	Glass insert in Monel autoclave, N_2(g)	200 ºC	1 h	79 mg	1,2-PHNZ(C_4F_8) 2,3-PHNZ(C_4F_8) 1,2;6,7-PHNZ(C_4F_8) 1,2;7,8-PHNZ(C_4F_8) 1,2;8,9-PHNZ(C_4F_8) 1,2-PHNZ(C_4F_4)

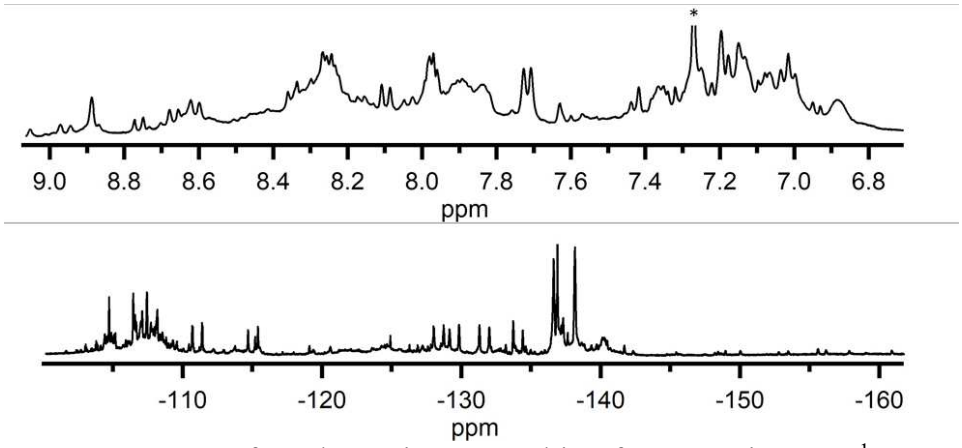

Figure B-35. NMR spectra of product mixture resulting from reaction 3.3. ^{1}H NMR spectrum (top) referenced to $CHCl_3$ (δ = 7.26, denoted *). ^{19}F NMR spectrum (bottom) referenced to perfluorobenzene (δ = –164.9, not shown). Peaks in the region -143 to -164 are indicative of trace products bearing C_4F_4 substituents.

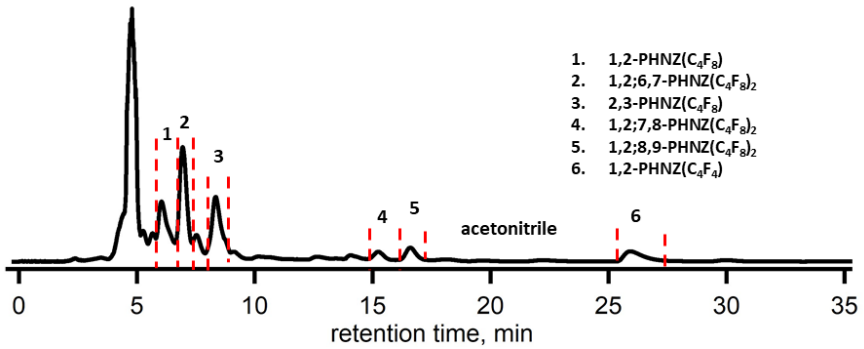

Figure B-36. HPLC separation of reaction 3.3. Detection wavelength 300 nm. Molar absorbances for different compounds at this wavelength vary, and therefore the trace is not representative of product distribution. Other peaks were complex mixtures of impure products. Peaks eluting before 6 minutes were complex mixtures of products but contained many products with C_4F_8H substituents.

B.3.4. Reaction 3.4 350 °C reaction for PHNZ RD/A products

Table B-19. Synthetic details for reaction 3.4.

Reactants	Vessel Type	T	time	Crude Product Recovered	Product Isolated
-50 mg (0.27 mmol) PHNZ -50 µL (0.27 mmol) 1,4-$C_4F_8I_2$ - 2000 mg (excess) Cu powder	Glass insert in Monel autoclave, N_2(g)	350 °C	5 h	4 mg	1,2-PHNZ(C_4F_3H) 1,2;6,7-PHNZ(C_4F_8)(C_4F_4)

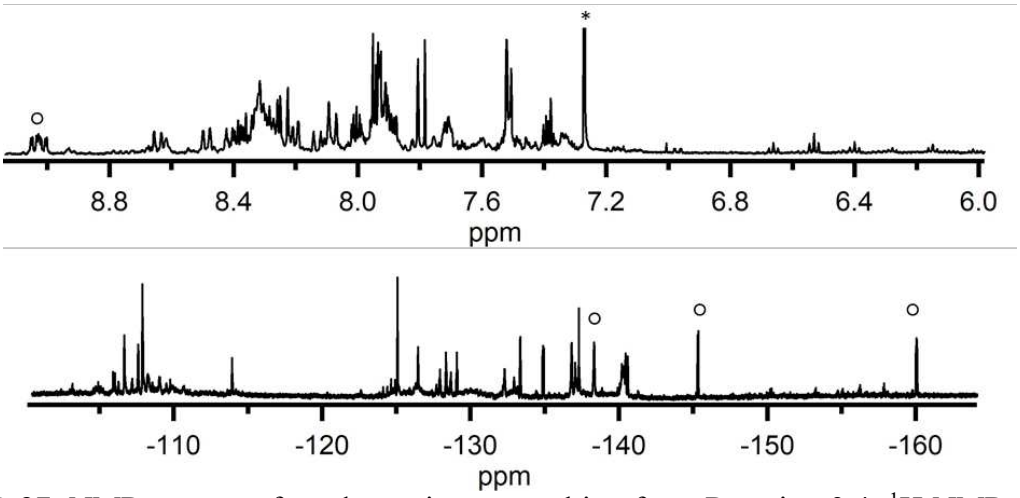

Figure B-37. NMR spectra of product mixture resulting from Reaction 3.4. ^{1}H NMR spectrum (top) referenced to $CHCl_3$ (δ = 7.26, denoted *). ^{19}F NMR spectrum (bottom) referenced to perfluorobenzene (δ = –164.9, not shown). Several peaks characteristic of product 1,2-PHNZ(C_4F_3H) are denoted °.

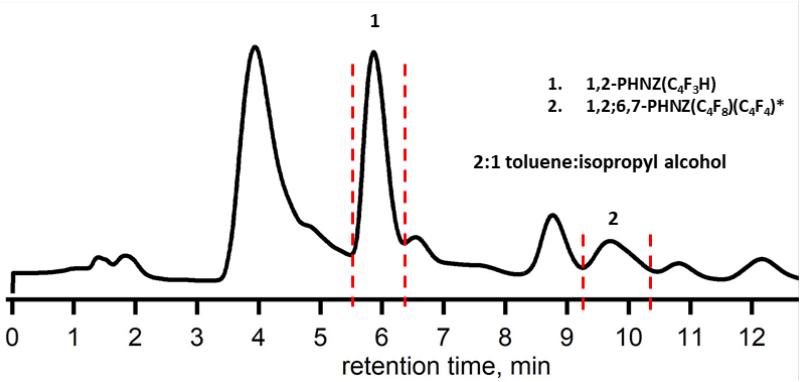

Figure B-38. HPLC separation of reaction 3.4. Detection wavelength 300 nm. Molar absorbances for different compounds at this wavelength vary, and therefore the trace is not representative of product distribution. Other peaks were complex mixtures of impure products. *Peak 2 was an impure fraction from which a pure compound, 1,2;6,7-PHNZ(C_4F_8)(C_4F_4) crystallized.

B.3.5. Reaction 3.5 reaction with PHNZ substrate in *o*-DCB

Table B-20. Synthetic details for reaction 3.5.

Reactants	Vessel Type	T	time	Crude Product Recovered	Product Isolated
-50 mg (0.27 mmol) PHNZ -200 µL (1.09 mmol) 1,4-$C_4F_8I_2$ - 750 mg (excess) Cu powder	Reaction conducted in 5 mL *o*-DCB	160 ºC	6 h	64 mg	1,2-PHNZ(C_4F_8) 2,3-PHNZ(C_4F_8) 1-PHNZ(C_4F_8I) 2-PHNZ(C_4F_8I) PHNZ($C_4F_8I)_2$-A

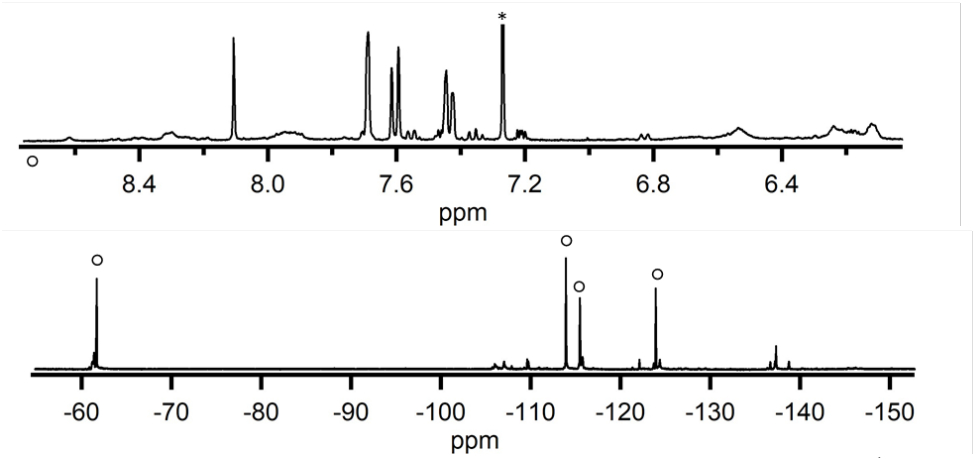

Figure B-39. NMR spectra of product mixture resulting from Reaction 3.5. ^{1}H NMR spectrum (top) referenced to $CHCl_3$ (δ = 7.26, denoted *). ^{19}F NMR spectrum (bottom) referenced to perfluorobenzene (δ = –164.9, not shown). Peaks in ^{19}F NMR spectra arising from C_4F_8I groups denoted º.

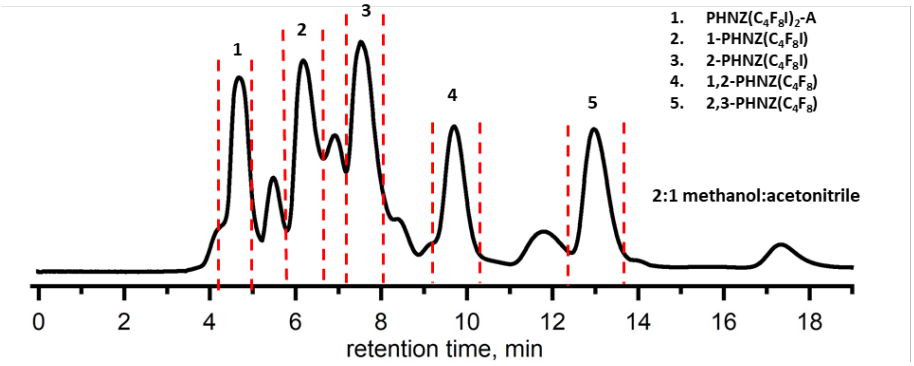

Figure B-40. HPLC separation of reaction 3.5. Detection wavelength 300 nm. Molar absorbances for different compounds at this wavelength vary, and therefore the trace is not representative of product distribution. Other peaks were complex mixtures of impure products.

B.4.1. Reaction 4.1 for ACRD$(CF_3)_n$'s

Table B-21. Synthetic details for reaction 4.1.

Reactants	Vessel Type	T	time	Crude Product Recovered	Product Isolated
-179 mg (1 mmol) ACRD -600 torr CF_3I in 268 mL (9 mmol)	300 mL flame sealed glass ampoule	330 ºC	8.5 h	278 mg	1,3,5,9-ACRD$(CF_3)_4$ 1,3,6,9-ACRD$(CF_3)_4$ 1,4,6,8-ACRD$(CF_3)_4$ 1,4,6,9-ACRD$(CF_3)_4$ 1,3,5,7,9-ACRD$(CF_3)_5$ 1,3,5,6,8-ACRD$(CF_3)_5$ 1,2,5,8,9-ACRD$(CF_3)_5$ 1,3,4,6,9-ACRD$(CF_3)_5$ 1,2,5,7,9-ACRD$(CF_3)_5$ 1,4,5,6,9-ACRD$(CF_3)_5$

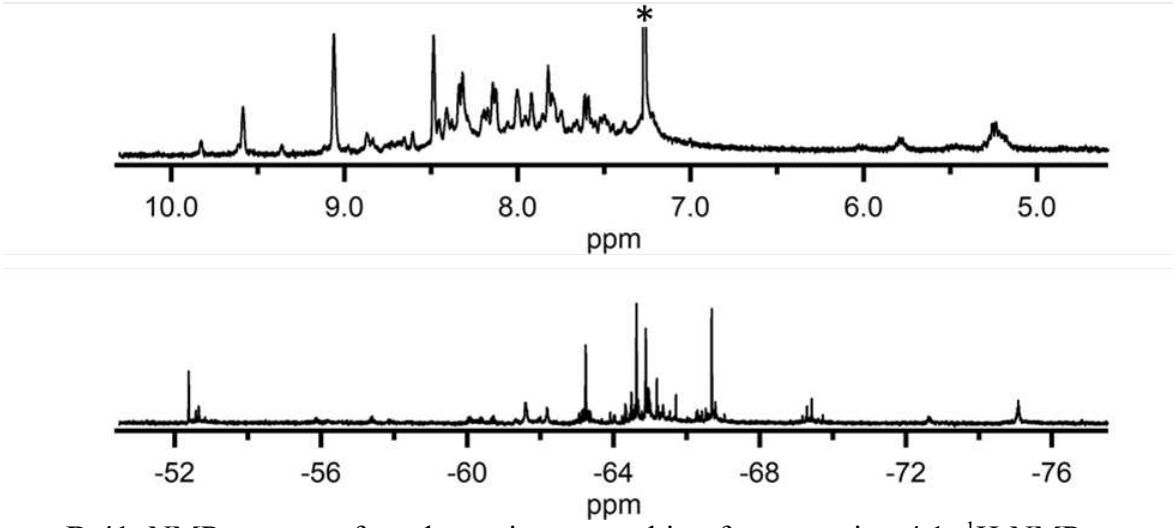

Figure B-41. NMR spectra of product mixture resulting from reaction 4.1. ^{1}H NMR spectrum (top) referenced to $CHCl_3$ (δ = 7.26, denoted *). ^{19}F NMR spectrum (bottom) referenced to perfluorobenzene (δ = −164.9, not shown).

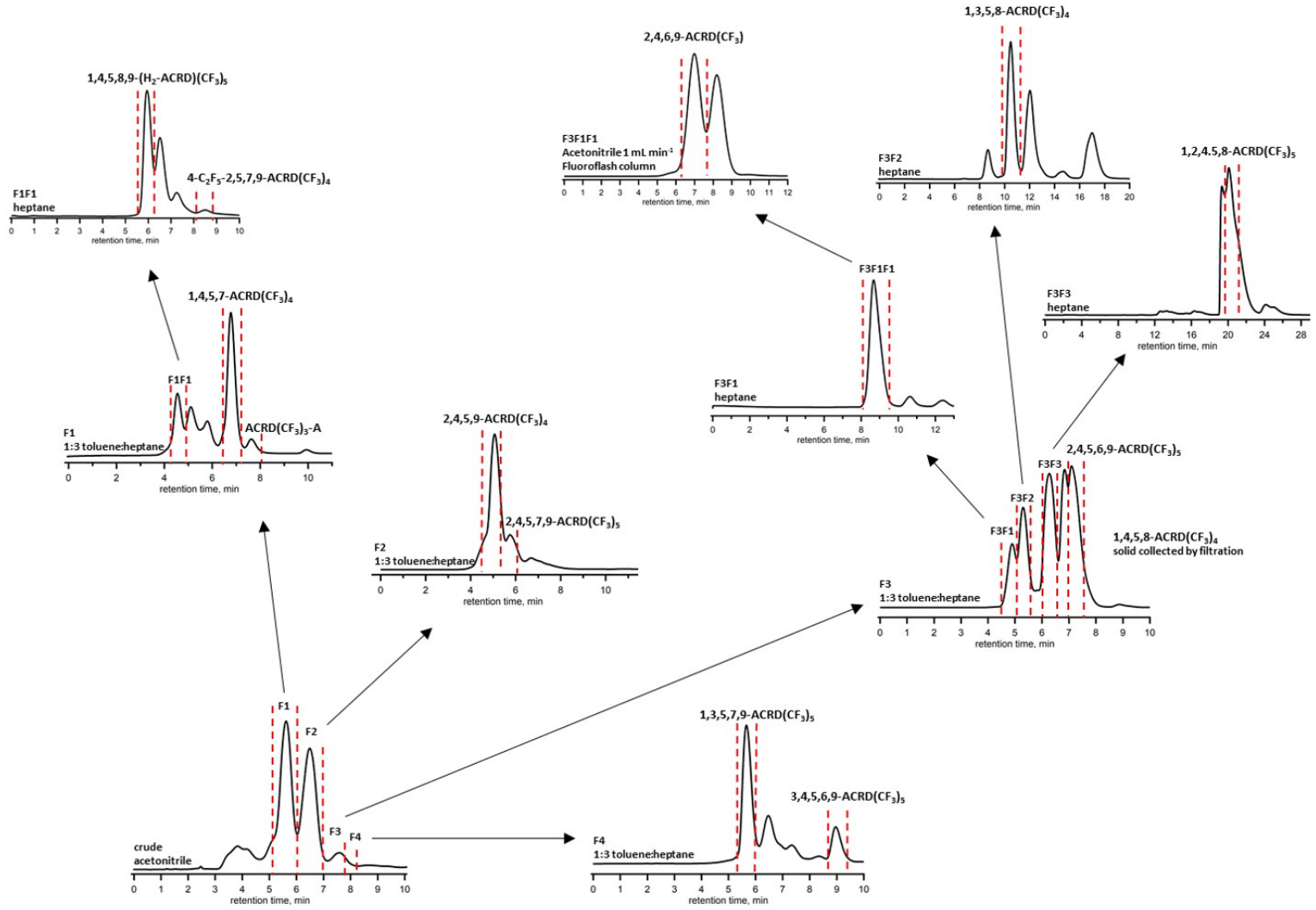

Figure B-42. Multi-stage HPLC separation of reaction 4.1. To obtain traces, samples were dissolved in the indicated eluent and injected onto a semi-preparative Buckyprep Column, 10.0 x 250 mm, using the indicated eluent with a flow rate 5 ml min^{-1}, unless otherwise indicated. Dashed vertical lines mark retention times of the fractions.

APPENDIX C
CHARACTERIZATION OF PURE PRODUCTS

C.1.1. CHARACTERIZATION OF 2,3-TRPH(C_4F_8)

10,10,11,11,12,12,13,13-octafluoro-10,11,12,13-tetrahydrobenzo[*f*]tetraphene

HPLC method: Elutes at 5.2 min in 4:1 acetonitrile:toluene (appx B figure B-2)
Yield information: 63% isolated yield from reaction 1.1 (appx B.1.1)

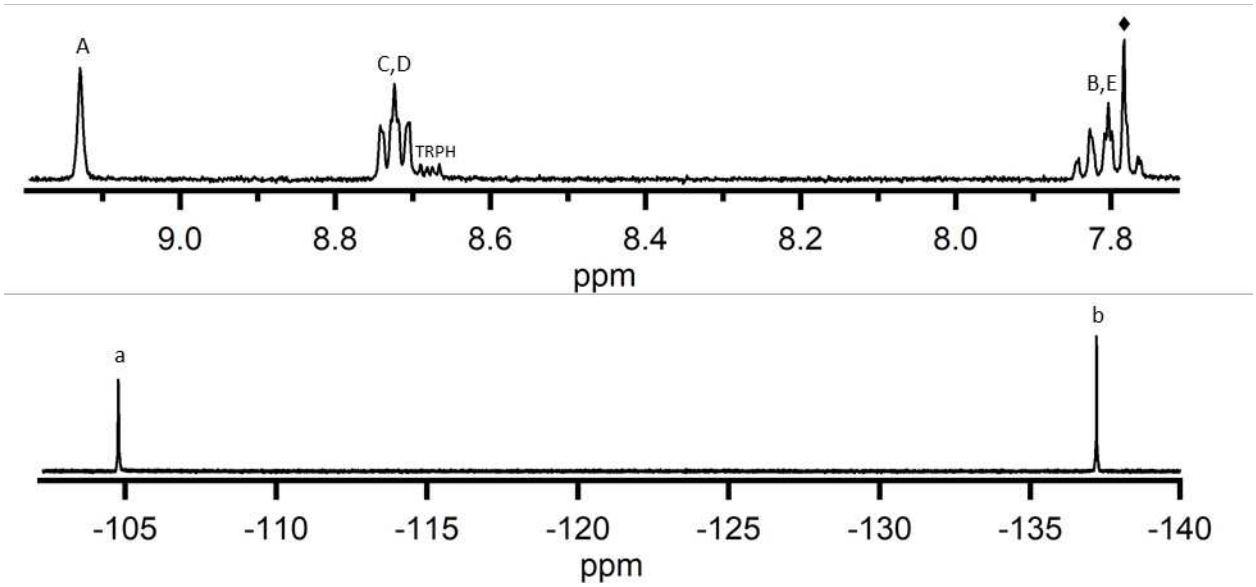

Figure C-1. NMR spectra of 2,3-TRPH(C_4F_8). Product > 90% pure, with TRPH impurity (indicated TRPH). ^{1}H NMR spectrum (top) referenced to $CHCl_3$ (δ = 7.26, not shown). ^{19}F NMR spectrum (bottom) referenced to 1,4-bistrifluromethyl benzene (19F δ = –66.4, not shown, 1H δ = 7.77, denoted♦). See figure below for probable peak assignments.

1H NMR ($CDCl_3$, 400 MHz): δ = 7.80 (m, 4H), 8.72 (m, 4H), 9.13 (s, 2H)
19F NMR ($CDCl_3$ with C_6F_6): δ = -104.7 (m, 4F), -137.1 (m, 4F)

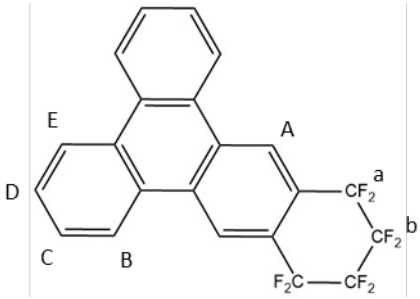

Figure C-2. Drawing of 2,3-TRPH(C_4F_8), elucidated from NMR spectra and confirmed by single crystal X-ray structure.

C.1.2. CHARACTERIZATION OF 1,2-TRPH(C_4F_8)

7,7,8,8,9,9,10,10-octafluoro-7,8,9,10-tetrahydrobenzo[*g*]chrysene

HPLC method: Elutes at 10.9 min in acetonitrile (appx B figure B-8)
Yield information: 20% yield from reaction 1.4 (appx B.1.4)

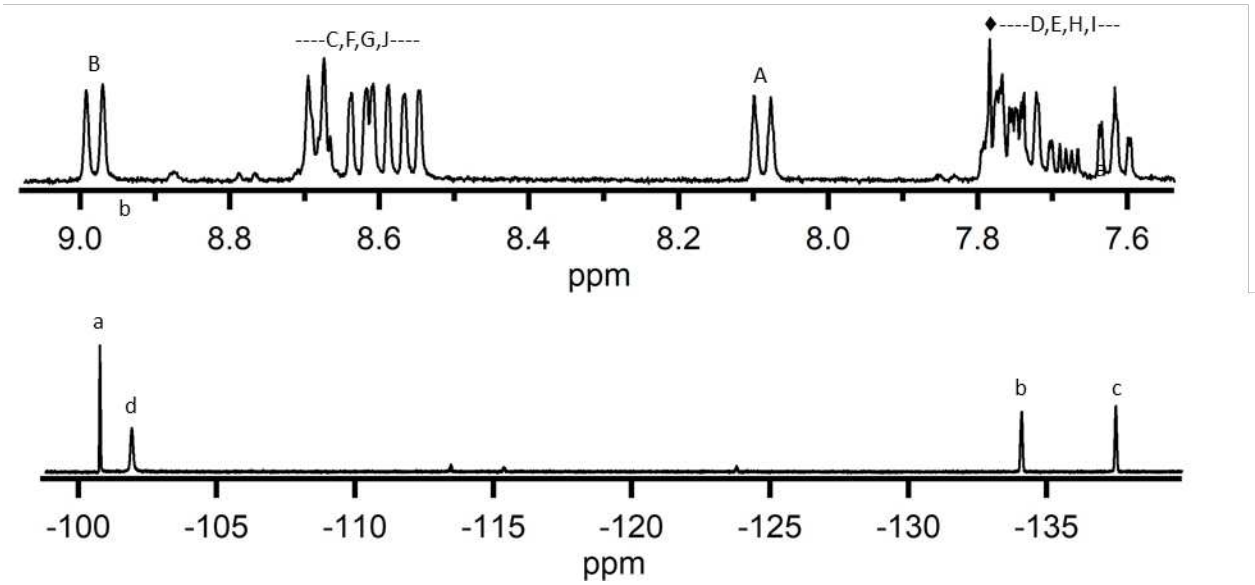

Figure C-3. NMR spectra of 1,2-TRPH(C_4F_8). Product > 95% pure. ^{1}H NMR spectrum (top) referenced to $CHCl_3$ (δ = 7.26, not shown). ^{19}F NMR spectrum (bottom) referenced to 1,4-bistrifluromethyl benzene (19F δ = –66.4, not shown, 1H δ = 7.77, denoted♦). See figure below for probable peak assignments.

1H NMR ($CDCl_3$, 400 MHz): δ = 7.70 (overlapping multiplets, 4H), 8.06 (d, J= 9 Hz, 1H), 8.61 (overlapping multiplets, 4H), 8.98 (d, J=9 Hz, 1H)
19F NMR ($CDCl_3$ with C_6F_6): δ = -100.7 (m, 2F), -101.9 (m, 2F), -134.04 (m, 2F), -137.5 (m, 2F)

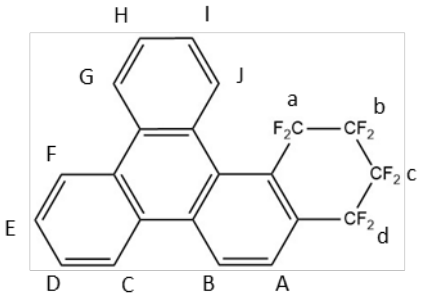

Figure C-4. Drawing of 1,2-TRPH(C_4F_8), elucidated from NMR spectra and confirmed by single crystal X-ray structure.

C.1.3. CHARACTERIZATION OF 2,3;6,7-TRPH(C_4F_8)$_2$

1,1,2,2,3,3,4,4,11,11,12,12,13,13,14,14-hexadecafluoro-1,2,3,4,11,12,13,14-octahydrobenzo[*h*]pentaphene

HPLC method: Elutes at 11.1 min in 4:1 acetonitrile:toluene (appx B figure B-4)
Yield information: 42% isolated yield from reaction 1.2 (appx B.1.2)

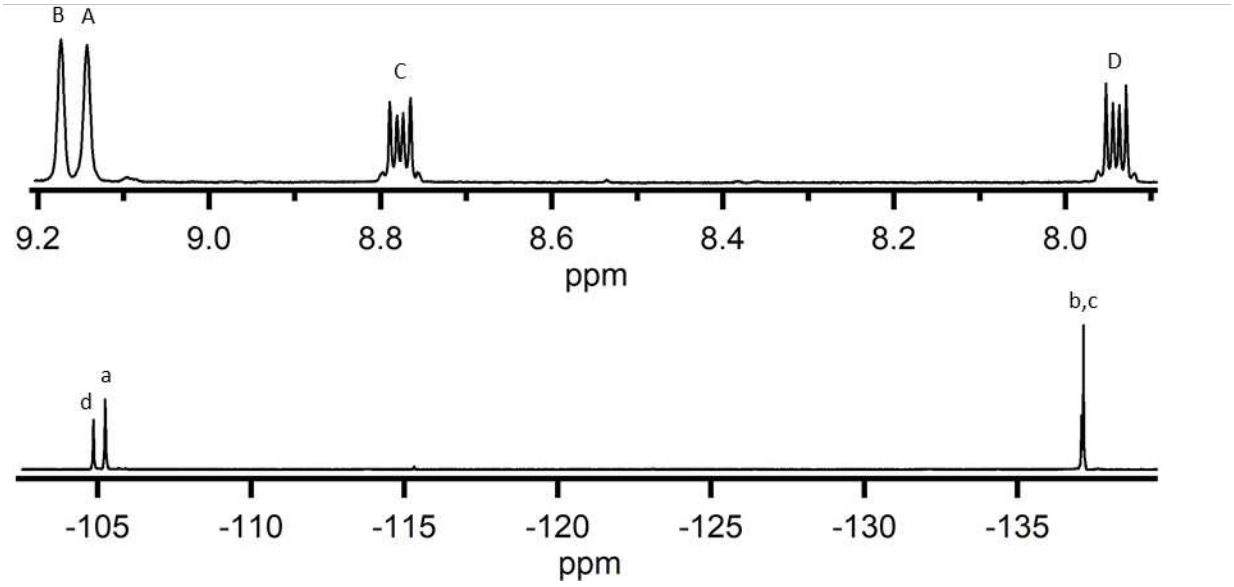

Figure C-5. NMR spectra of 2,3;6,7-TRPH(C_4F_8)$_2$. ^{1}H NMR spectrum (top) referenced to $CHCl_3$ (δ = 7.26, not shown). ^{19}F NMR spectrum (bottom) referenced to 1,4-bistrifluromethyl benzene (19F δ = –66.4, not shown, 1H δ = 7.77, not shown). See figure below for probable peak assignments.

1H NMR ($CDCl_3$, 400 MHz): δ = 7.95 (m, 2H), 8.80 (m, 2H), 9.16 (s, 2H), 9.19 (s, 2H),
19F NMR ($CDCl_3$ with C_6F_6): δ = −104.8 (m, 4F), −105.2 (m, 4F), −137.1 (m, 8F).

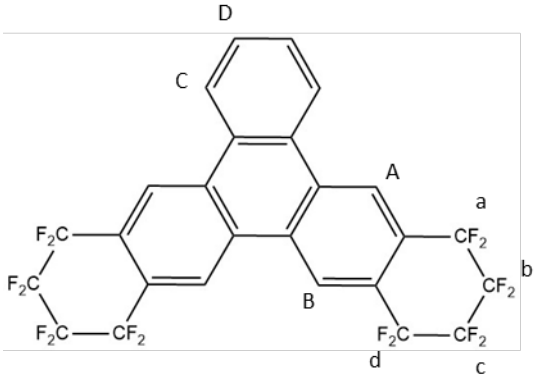

Figure C-6. Drawing of 2,3;6,7-TRPH(C_4F_8)$_2$, elucidated from NMR spectra and confirmed by single crystal X-ray structure.

C.1.4. CHARACTERIZATION OF 1,2;6,7-TRPH(C_4F_8)$_2$

1,1,2,2,3,3,4,4,10,10,11,11,12,12,13,13-hexadecafluoro-1,2,3,4,10,11,12,13-octahydrodibenzo[*c*,*f*]tetraphene

HPLC method: Elutes at 12 min in acetonitrile (appx B figure B-12)
Yield information: <5% yield reaction 1.6 (appx B.1.6)

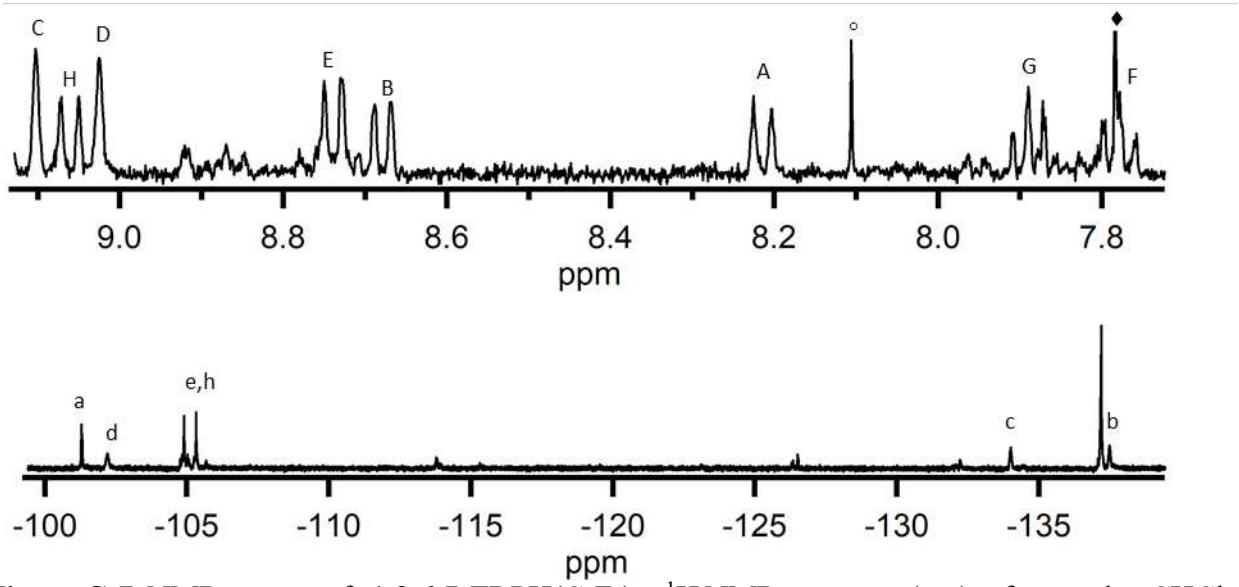

Figure C-7. NMR spectra of 1,2;6,7-TRPH(C_4F_8)$_2$. ^{1}H NMR spectrum (top) referenced to $CHCl_3$ (δ = 7.26, not shown). ^{19}F NMR spectrum (bottom) referenced to 1,4-bistrifluromethyl benzene (19F δ = –66.4, not shown, 1H δ = 7.77, denoted ♦). Impurity present, denoted °. See figure below for probable peak assignments.

1H NMR ($CDCl_3$, 400 MHz): δ = 7.78 (m, 1H), 7.89 (m, 1H), 8.22 (d, J= 9 Hz, 1H), 8.71 (m, 2H), 9.03 (s, 1H), 9.06 (d, J=9 Hz, 1H), 9.10 (s, 1H).
19F NMR ($CDCl_3$ with C_6F_6): δ = −101.2 (m, 2F), −102.2 (m, 2F), −104.9 (m, 2F), −105.3 (m, 2F), −134.0 (m, 2F), −137.2 (m, 4F), −137.4 (m, 2F).

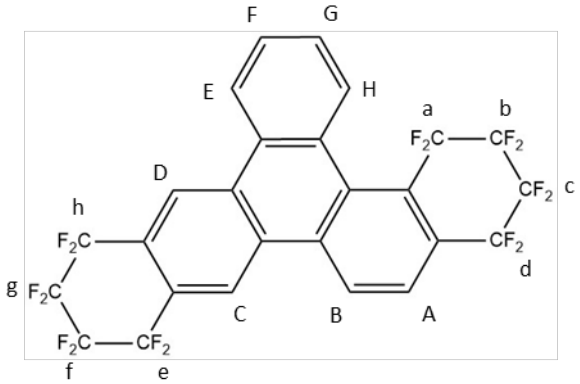

Figure C-8. Drawing of 1,2;6,7-TRPH(C_4F_8)$_2$, elucidated from NMR spectra and confirmed by single crystal X-ray structure.

C.1.5. CHARACTERIZATION OF 1,2;10,11-TRPH(C_4F_8)$_2$

1,1,2,2,3,3,4,4,12,12,13,13,14,14,15,15-hexadecafluoro-1,2,3,4,12,13,14,15-octahydrodibenzo[*a*,*f*]tetraphene

HPLC method: Elutes at 14.9 min in acetonitrile (appx B figure B-12)
Yield information: <5% yield reaction 1.6 (appx B.1.6)

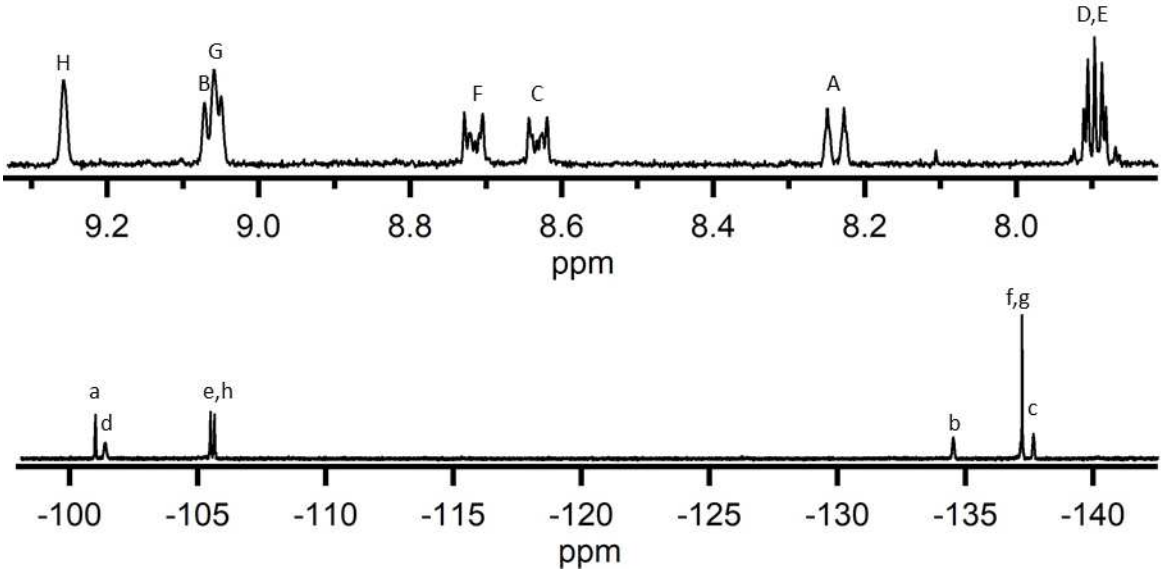

Figure C-9. NMR spectra of 1,2;10,11-TRPH(C_4F_8)$_2$. ^{1}H NMR spectrum (top) referenced to $CHCl_3$ (δ = 7.26, not shown). ^{19}F NMR spectrum (bottom) referenced to hexafluorobenzene (δ = −164.9, not shown). See figure below for probable peak assignments.

1H NMR ($CDCl_3$, 400 MHz): δ = 7.90 (m, 2H), 8.24 (d, J= 9 Hz, 1H), 8.63 (m, 1H), 8.71(m, 1H), 9.04 (d, J=9 Hz, 1H overlapped with s, 1H), 9.23 (s, 1H).
19F NMR ($CDCl_3$ with C_6F_6): δ = −100.9 (m, 2F), −101.3 (m, 2F), −105.5 (m, 2F), −105.6 (m, 2F), −134.5 (m, 2F), −137.1 (m, 4F), −137.6 (m, 2F).

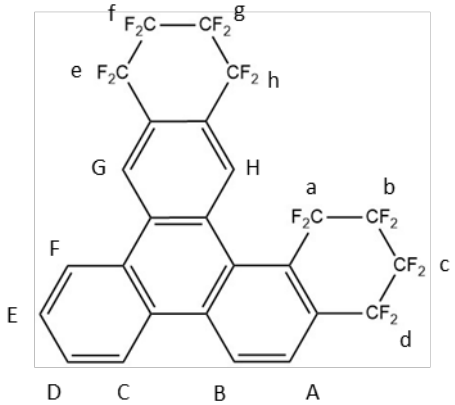

Figure C-10. Drawing of 1,2;10,11-TRPH(C_4F_8)$_2$, elucidated from NMR spectra and confirmed by single crystal X-ray structure.

C.1.6. CHARACTERIZATION OF 2,3;6,7;10,11-TRPH(C_4F_8)$_3$

1,1,2,2,3,3,4,4,7,7,8,8,9,9,10,10,13,13,14,14,15,15,16,16-tetracosafluoro-1,2,3,4,7,8,9,10,13,14,15,16-dodecahydrotrinaphthylene

HPLC method: Elutes at 17.0 min in 4:1 acetonitrile:toluene (appx B figure B-4)
Yield information: 76% isolated yield from reaction 1.3 (appx B.1.3)

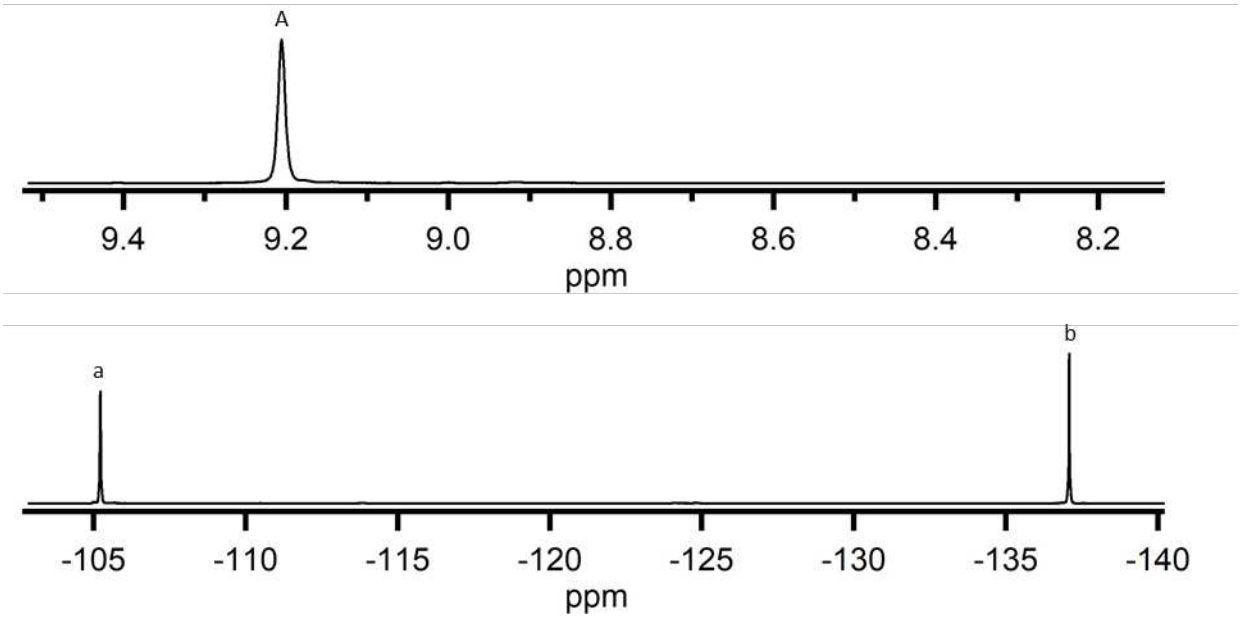

Figure C-11. NMR spectra of 2,3;6,7;10,11-TRPH(C_4F_8)$_3$. ^{1}H NMR spectrum (top) referenced to $CHCl_3$ (δ = 7.26, not shown). ^{19}F NMR spectrum (bottom) referenced to hexafluorobenzene (δ = −164.9, not shown). See figure below for probable peak assignments.

1H NMR ($CDCl_3$, 400 MHz): δ = 9.22 (s, 6H).
19F NMR ($CDCl_3$ with C_6F_6): δ = −105.2 (m, 12F), −137.1 (m, 12F).

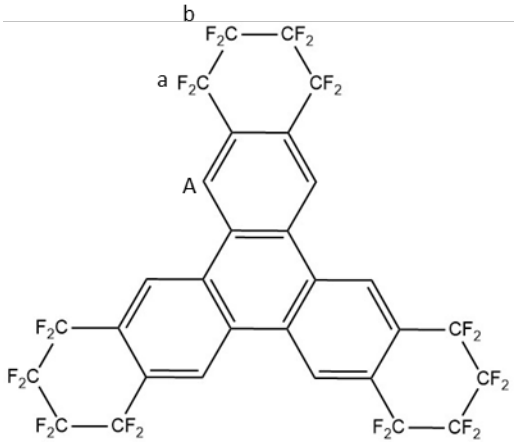

Figure C-12. Drawing of 2,3;6,7;10,11-TRPH(C_4F_8)$_3$, elucidated from NMR spectra and confirmed by single crystal X-ray structure.

.

C.1.7. CHARACTERIZATION OF 1,2;6,7;10,11-TRPH(C_4F_8)$_3$

1,1,2,2,3,3,4,4,6,6,7,7,8,8,9,9,12,12,13,13,14,14,15,15-tetracosafluoro-1,2,3,4,6,7,8,9,12,13,14,15-dodecahydronaphtho[1,2-*h*]pentaphene

HPLC method: Elutes at 20.1 min in acetonitrile (appx B figure B-12).
Yield information: <5% yield reaction 1.6 (appx B.1.6).

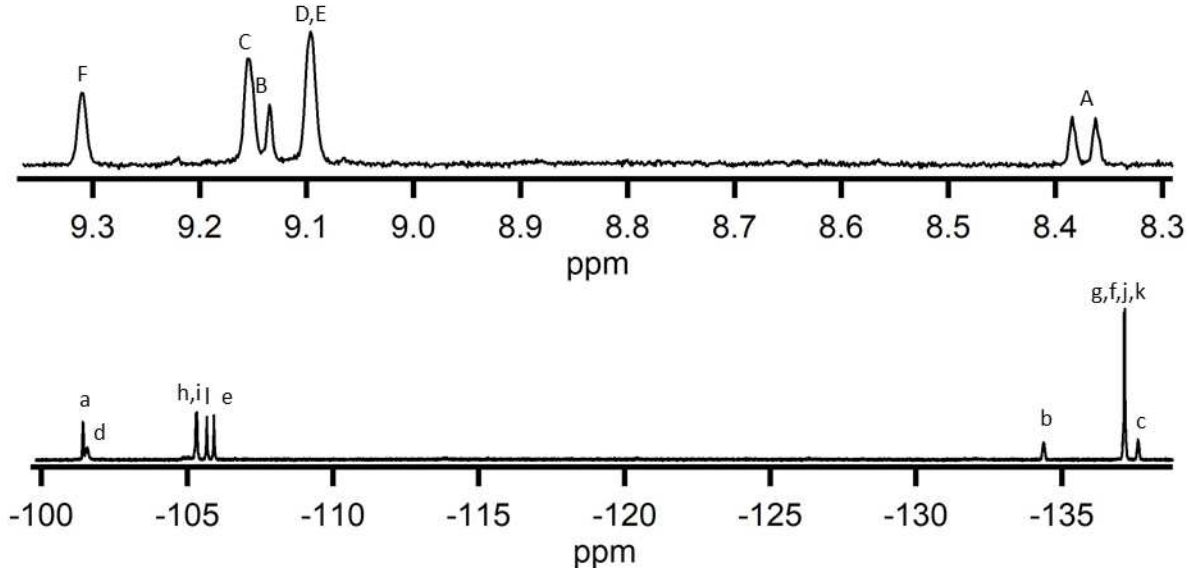

Figure C-13. NMR spectra of 1,2;6,7;10,11-TRPH(C_4F_8)$_3$. ^{1}H NMR spectrum (top) referenced to $CHCl_3$ (δ = 7.26, not shown). ^{19}F NMR spectrum (bottom) referenced to hexafluorobenzene (δ = −164.9, not shown). See figure below for probable peak assignments.

1H NMR ($CDCl_3$, 400 MHz): δ = 8.37 (d, J= 9 Hz, 1H), 9.09 (s, 2H), 9.13 (d, J=9 Hz, 1H), 9.15 (s, 1H), 9.31 (s, 1H).
19F NMR ($CDCl_3$ with C_6F_6): δ = −101.4 (m, 4F), −101.5 (m, 4F), −105.3 (m, 8F), −134.3 (m, 4F),−137.1 (m, 8F),−137.6 (m, 4F).

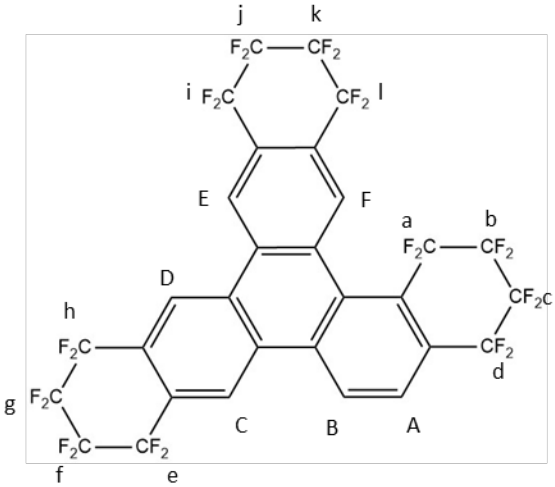

Figure C-14. Drawing of 1,2;6,7;10,11-TRPH(C_4F_8)$_3$, elucidated from NMR spectra and confirmed by single crystal X-ray structure.

C.1.8. CHARACTERIZATION OF 1,2;5,6;10,11-TRPH(C_4F_8)$_3$

1,1,2,2,3,3,4,4,7,7,8,8,9,9,10,10,12,12,13,13,14,14,15,15-tetracosafluoro-1,2,3,4,7,8,9,10,12,13,14,15-dodecahydrobenzo[*a*]naphtho[1,2-*f*]tetraphene

HPLC method: Elutes at 7.5 min in acetonitrile (appx B figure B-12).
Yield information: <5% yield reaction 1.6 (appx B.1.6).

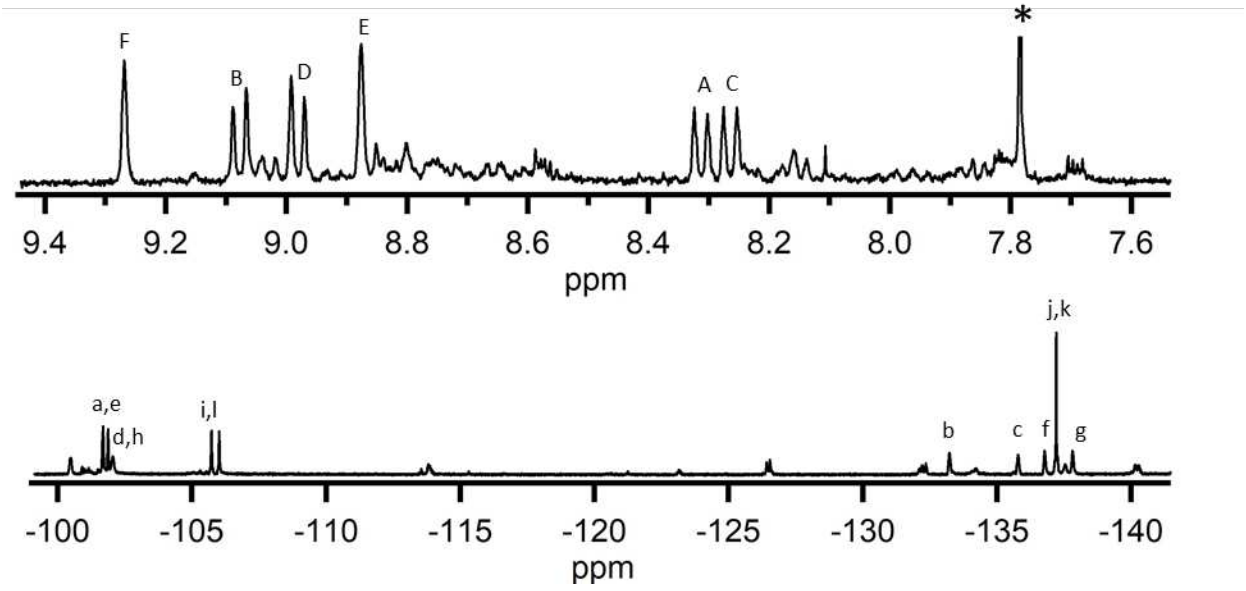

Figure C-15. NMR spectra of 1,2;5,6;10,11-TRPH(C_4F_8)$_3$. ^{1}H NMR spectrum (top) referenced to $CHCl_3$ (δ = 7.26, not shown). ^{19}F NMR spectrum (bottom) referenced to hexafluorobenzene (19F δ = –66.4, not shown, 1H δ = 7.77, denoted♦). See figure below for probable peak assignments.

1H NMR ($CDCl_3$, 400 MHz): δ = 8.27 (d, J= 9 Hz, 1H), 8.31 (d, J=9 Hz, 1H), 8.90 (s, 1H), 8.98 (d, J= 9 Hz, 1H), 9.08 (d, J= 9 Hz, 1H), 9.27 (s, 1H)
19F NMR ($CDCl_3$ with C_6F_6): δ = −100.4 (m, 2F), −101.6 (m, 2F), −101.8 (m, 2F), −102.0 (m, 2F), −105.7 (m, 2F), −108.0 (m, 2F), −133.2 (m, 2F), −135.7 (m, 2F), −136.7 (m, 2F), −137.2 (m, 4F), −137.8 (m, 2F)

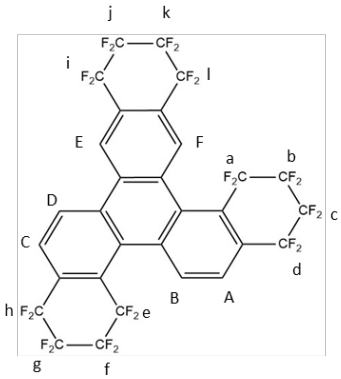

Figure C-16. Drawing of 1,2;5,6;10,11-TRPH(C_4F_8)$_3$, elucidated from NMR spectra and confirmed by single crystal X-ray structure.

C.1.9. CHARACTERIZATION OF 2,3;6-TRPH(C_4F_8)(C_4F_8H)

10,10,11,11,12,12,13,13-octafluoro-2-(1,1,2,2,3,3,4,4-octafluorobutyl)-10,11,12,13-tetrahydrobenzo[*f*]tetraphene

HPLC method: Elutes at 13.0 min in acetonitrile (appx B figure B-12).
Yield information: <5% yield reaction 1.6 (appx B.1.6.).

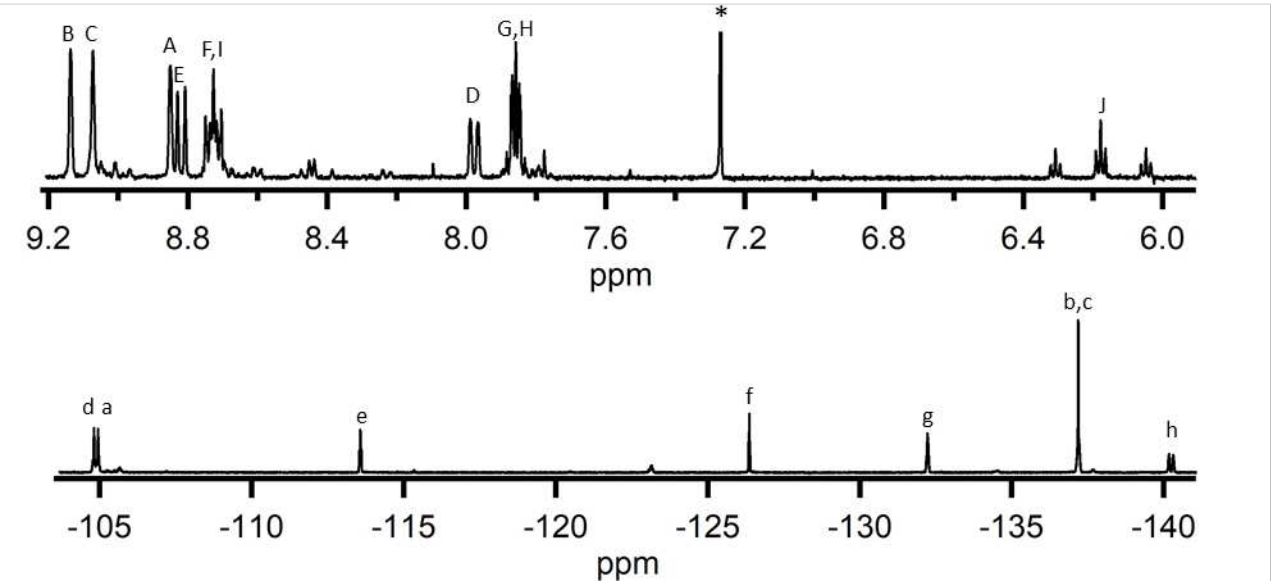

Figure C-17. NMR spectra of 2,3;10-TRPH(C_4F_8)(C_4F_8H). Product > 80% pure. ^{1}H NMR spectrum (top) referenced to $CHCl_3$ (δ = 7.26, denoted *). ^{19}F NMR spectrum (bottom) referenced to perfluorobenzene (δ = –164.9, not shown). See figure below for probable peak assignments.

1H NMR ($CDCl_3$, 400 MHz): δ = 6.17 (m, J=52 Hz, 1H) ,7.85 (m, 2H);), 7.97 (d, J=9 Hz, 1H), 8.72 (m, 2H), 8.81 (d, J=9 Hz, 1H), 8.84 (s, 1H), 9.06 (s, 1H), 9.13 (s, 1H).
19F NMR ($CDCl_3$ with C_6F_6): δ = −104.8 (m, 2F), −104.9 (m, 2F), −113.6 (m, 2F), −128.4 (m, 2F), −132.2 (m, 2F), −137.2 (m, 4F), −140.2 (m, J=52, 2F).

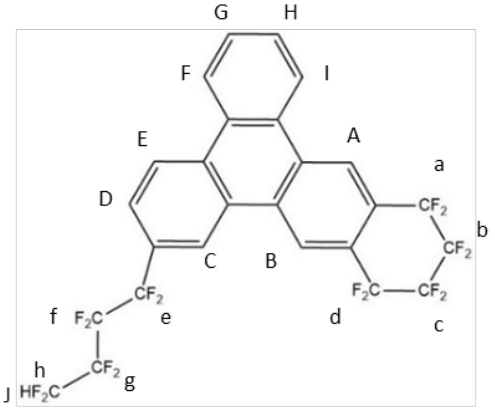

Figure C-18. Drawing of 2,3;10-TRPH(C_4F_8)(C_4F_8H), elucidated from NMR spectra and confirmed by single crystal X-ray structure.

C.1.10. CHARACTERIZATION OF 2,3;6,7;10-TRPH(C_4F_8)$_2$(C_4F_8H)

1,1,2,2,3,3,4,4,11,11,12,12,13,13,14,14-hexadecafluoro-7-(1,1,2,2,3,3,4,4-octafluorobutyl)-1,2,3,4,11,12,13,14-octahydrobenzo[*h*]pentaphene

HPLC method: elutes at 15 minutes in acetonitrile (appx B figure B-12)
Yield information: <5% yield reaction 1.6 (appx B.1.6.).

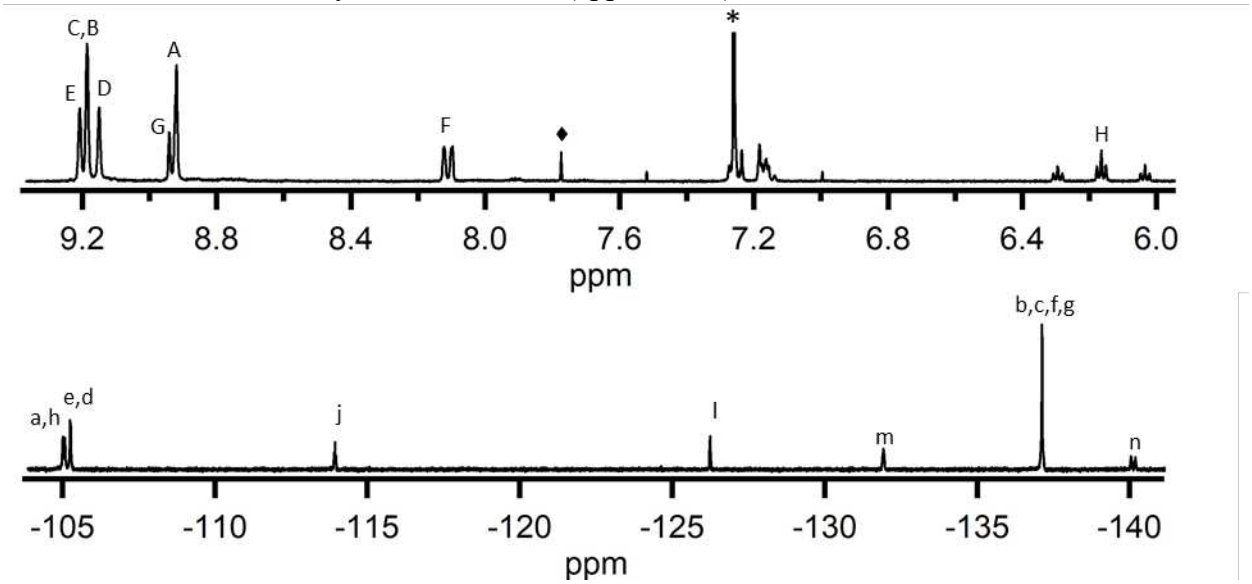

Figure C-19. NMR spectra of 2,3;6,7;10-TRPH(C_4F_8)$_2$(C_4F_8H). Product > 95% pure. ^{1}H NMR spectrum (top) referenced to $CHCl_3$ (δ = 7.26, denoted *) Residual toluene present in ^{1}H NMR spectrum (δ = 7.2 ppm). ^{19}F NMR spectrum (bottom) referenced to 1,4-bistrifluromethyl benzene (19F δ = –66.4, not shown, 1H δ = 7.77, denoted ♦). See figure below for probable peak assignments.

1H NMR ($CDCl_3$, 400 MHz): δ = 6.17 (m, J=52 Hz, 1H), 8.12 (d, J=9 Hz, 1H), 8.93 (s, 1H), 8.94 (d, J=9 Hz, 1H), 9.16 (s, 1H), 9.20 (s, 2H), 9.22 (s, 1H).
19F NMR ($CDCl_3$ with C_6F_6): **:** δ = −104.9 (m, 4F), −105.1 (m, 4F), −113.8 (m, 2F), −126.1 (m, 2F), −131.8 (m, 2F), −137.0 (m, 8F), −139.9 (m, J=52, 2F).

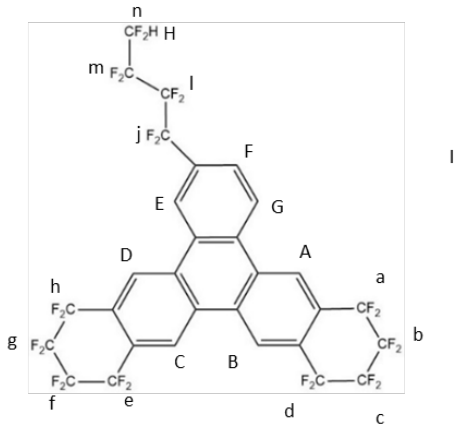

Figure C-20. Drawing of 2,3;6,7;10-TRPH(C_4F_8)$_2$(C_4F_8H), elucidated from NMR spectra and confirmed by single crystal X-ray structure.

C.1.11. CHARACTERIZATION OF 2,3-TRPH(C_4F_4)

10,11,12,13-tetrafluorobenzo[*f*]tetraphene

HPLC method: Elutes at 6.0 min in acetonitrile (appx B figure B-12).
Yield information: <5% yield reaction 1.5 (appx B.1.5.).

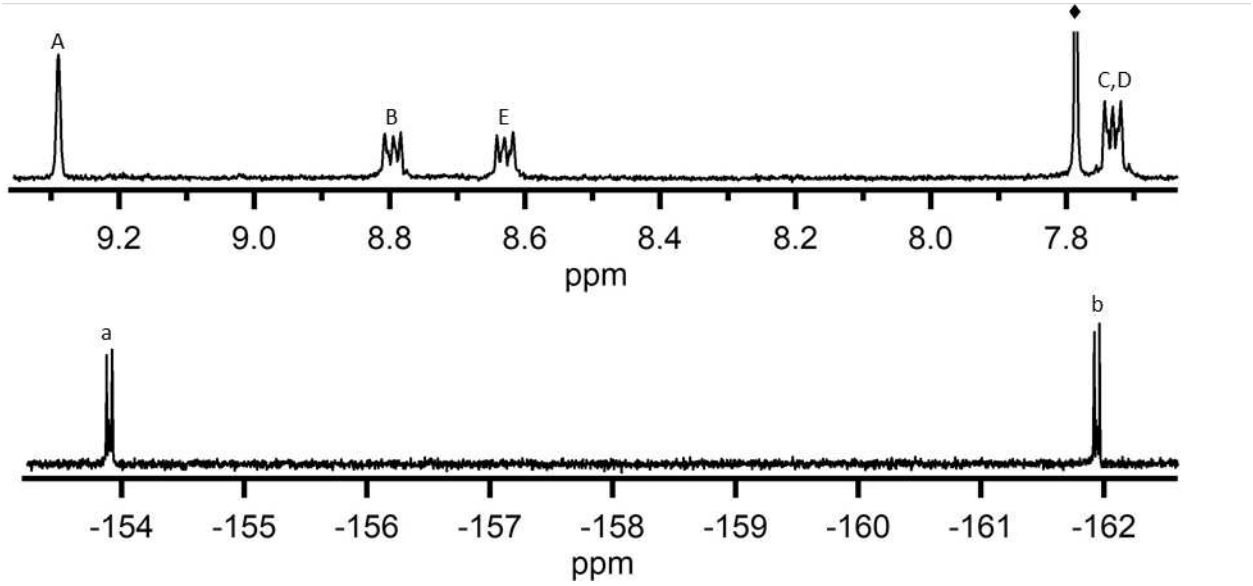

Figure C-21. NMR spectra of 2,3-TRPH(C_4F_4). Product > 98% pure. ^{1}H NMR spectrum (top) referenced to $CHCl_3$ (δ = 7.26, not shown). ^{19}F NMR spectrum (bottom) referenced to 1,4-bistrifluromethyl benzene (19F δ = –66.4, not shown, 1H δ = 7.77, denoted♦). See figure below for probable peak assignments.

1H NMR ($CDCl_3$, 400 MHz): δ = 7.72 (m, 4H), 8.61 (m, 2H), 8.78 (m, 2H), 9.27 (s, 2H).
19F NMR ($CDCl_3$ with C_6F_6): δ = −153.9 (m, 2F), −161.9 (m, 2F).

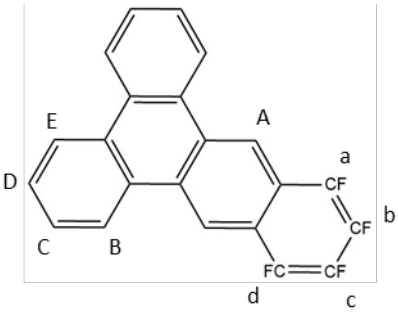

Figure C-22. Drawing of 2,3-TRPH(C_4F_4), elucidated from NMR spectra and confirmed by single crystal X-ray structure.

C.1.12. CHARACTERIZATION OF 2,3-TRPH(C_4F_3H)

10,11,12-trifluorobenzo[*f*]tetraphene

HPLC method: Elutes at 5.5 min in toluene (appx B figure B-10).
Yield information: <5% yield reaction 1.5 (appx B.1.5.).

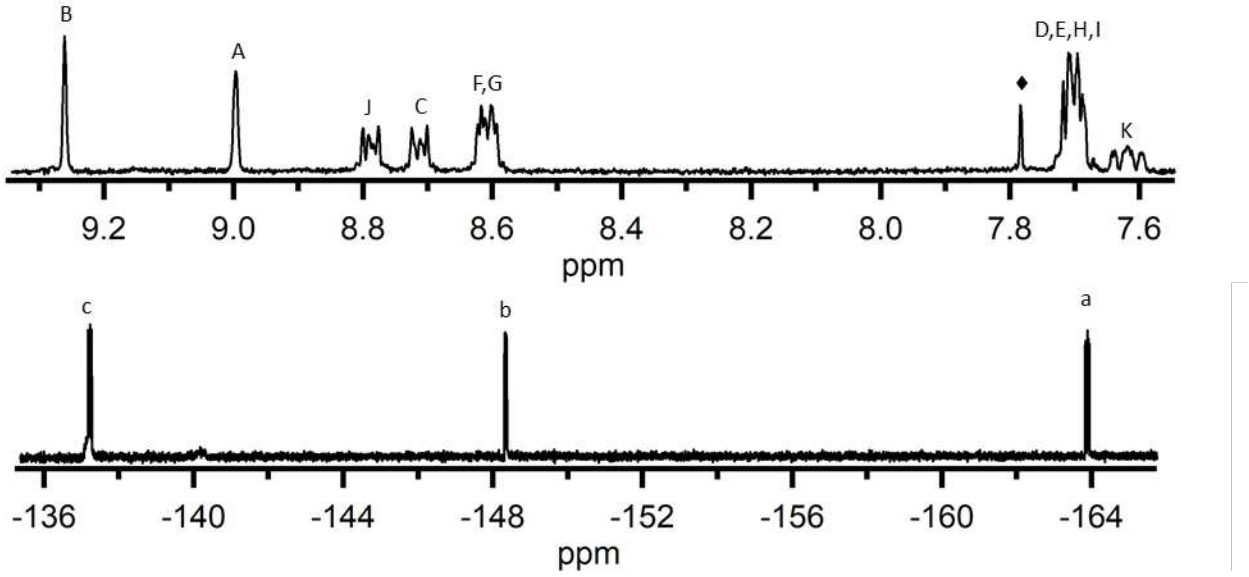

Figure C-23. NMR spectra of 2,3-TRPH(C_4F_3H). Product > 95% pure. ^{1}H NMR spectrum (top) referenced to $CHCl_3$ (δ = 7.26, not shown). ^{19}F NMR spectrum (bottom) referenced to 1,4-bistrifluromethyl benzene (19F δ = –66.4, not shown, 1H δ = 7.77, denoted♦). See figure below for probable peak assignments.

1H NMR ($CDCl_3$, 400 MHz): δ = 7.62 (m, 1H), 7.70 (m, 4H), 8.6 (m, 2H), 8.72 (m, 1H), 8.79 (m, 1H), 9.00 (s, 1H), 9.27 (s, 1H).
19F NMR ($CDCl_3$ with C_6F_6): δ = −137.2 (m, 1F), −148.3 (m, 1F), −163.9 (m, 1F).

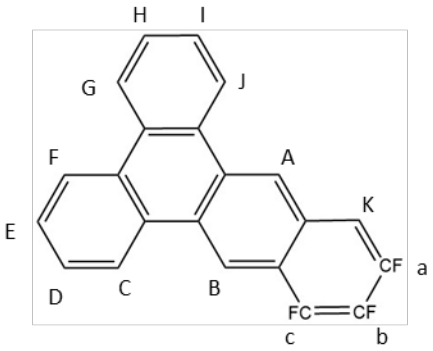

Figure C-24. Drawing of 2,3-TRPH(C_4F_3H), elucidated from NMR spectra and confirmed by single crystal X-ray structure.

C.1.13. CHARACTERIZATION OF 2,3;6,7-TRPH(C_4F_8)(C_4F_4)

1,1,2,2,3,3,4,4,11,12,13,14-dodecafluoro-1,2,3,4-tetrahydrobenzo[*h*]pentaphene

HPLC method: Elutes at 5.0 min in 1:1 toluene:isopropyl alcohol (appx B figure B-14).
Yield information: <5% yield reaction 1.7 (appx B.1.7.).

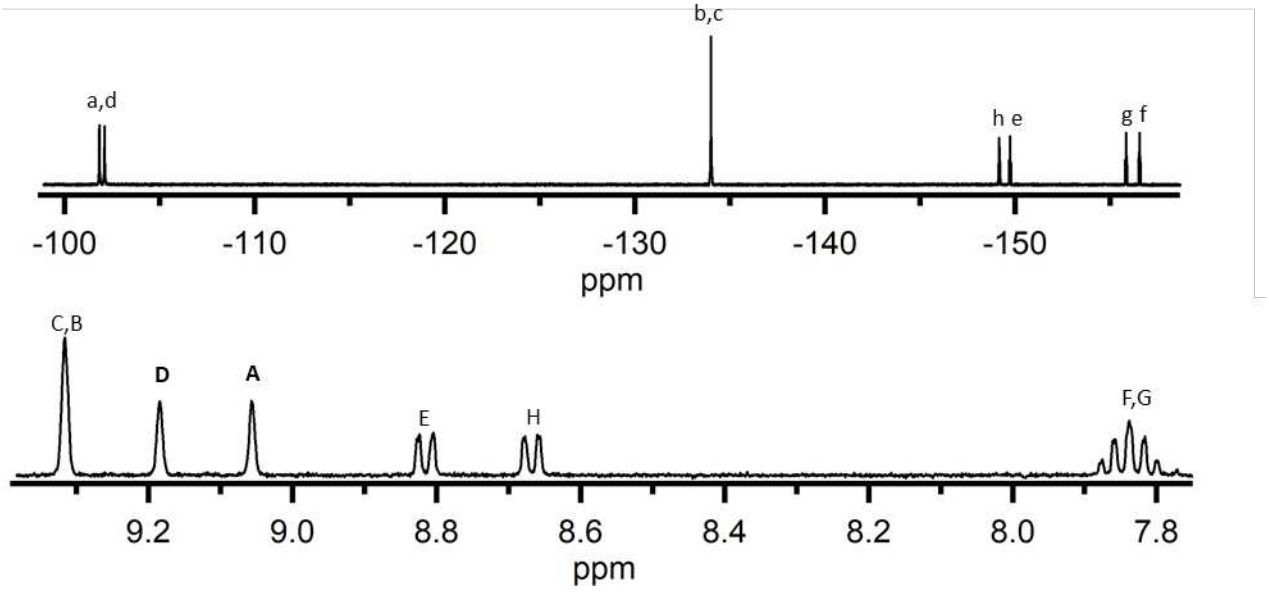

Figure C-25. NMR spectra of 2,3;6,7-TRPH(C_4F_8)(C_4F_4). Product > 98% pure. ^{1}H NMR spectrum (top) referenced to $CHCl_3$ (δ = 7.26, not shown). ^{19}F NMR spectrum (bottom) referenced to perfluorobenzene (δ = −164.9, not shown). See figure below for probable peak assignments.

1H NMR ($CDCl_3$, 400 MHz): δ = 7.84 (m, 2H) ,8.67 (m, 1H), 8.82 (m, 1H), 9.06 (s, 1H), 9.19 (s, 1H), 9.32 (s, 2H).
19F NMR ($CDCl_3$ with C_6F_6): δ = −104.9 (s, 2F), −105.2 (s, 2F), −137.1 (s, 4F), −152.3 (m, 1F), −152.9 (m, 1F), −159.0 (m, 1F), −159.7 (m, 1F).

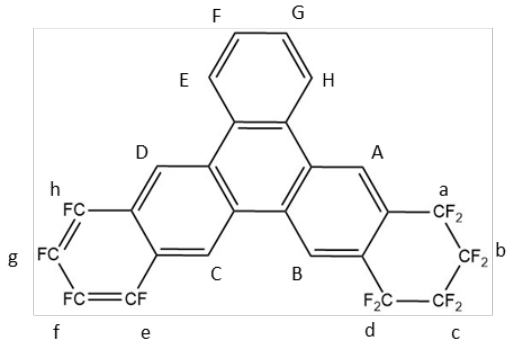

Figure C-26. Drawing of 2,3;6,7-TRPH(C_4F_8)(C_4F_4), elucidated from NMR spectra and confirmed by single crystal X-ray structure.

C.1.14. CHARACTERIZATION OF 2,3;6,7- TRPH(C_4F_8)$_2$

1,2,3,4,11,12,13,14-octafluorobenzo[*h*]pentaphene

HPLC method: Elutes at 4.0 min in 1:1 toluene:isopropyl alcohol (appx B figure B-14).
Yield information: <5% yield reaction 1.7 (appx B.1.7.).

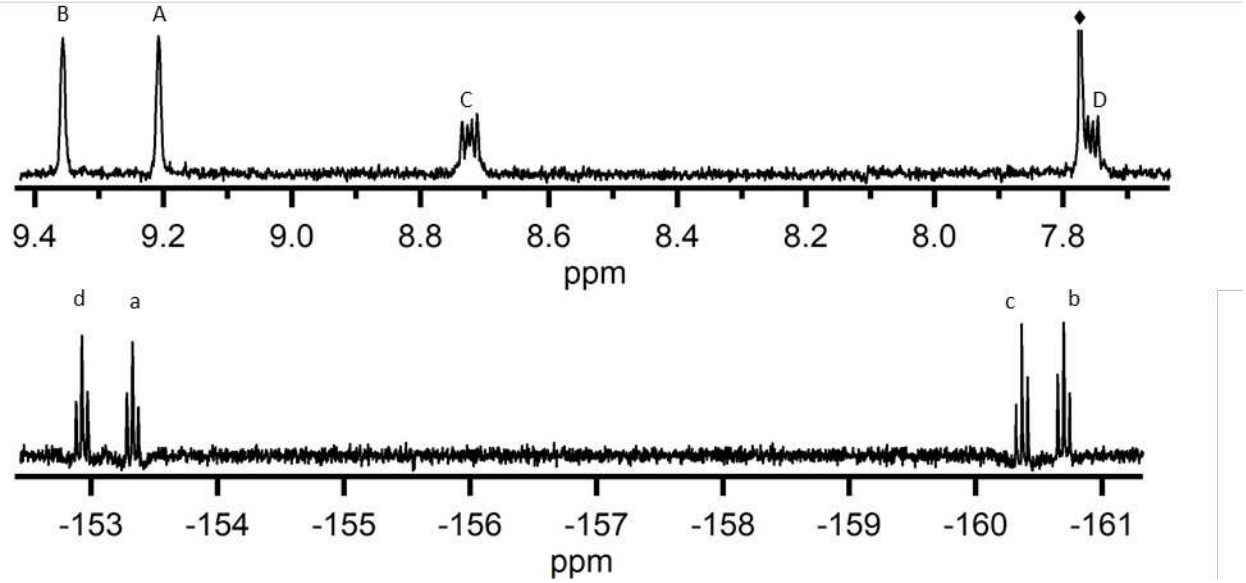

Figure C-27. NMR spectra of 2,3;6,7-TRPH(C_4F_8)$_2$. Product > 95% pure. ^{1}H NMR spectrum (top) referenced to $CHCl_3$ (δ = 7.26, not shown). ^{19}F NMR spectrum (bottom) referenced to 1,4-bistrifluromethyl benzene (19F δ = –66.4, not shown, 1H δ = 7.77, denoted♦). See figure below for probable peak assignments.

1H NMR ($CDCl_3$, 400 MHz): δ = 7.76 (m, 2H), 8.72 (m, 2H), 9.21 (s, 2H), 9.36 (s, 2H).
19F NMR ($CDCl_3$ with C_6F_6): δ = −152.9 (m, 2F), −153.3 (m, 2F), −160.4 (m, 2F), −160.7 (m, 2F).

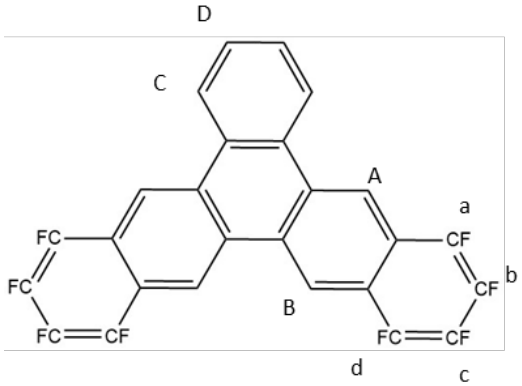

Figure C-28. Drawing of 2,3;6,7-TRPH(C_4F_8)$_2$, elucidated from NMR spectra and confirmed by single crystal X-ray structure.

C.1.15. CHARACTERIZATION OF 2,3;6,7;10,11- TRPH(C_4F_8)$_2$(C_4F_4)

1,1,2,2,3,3,4,4,7,7,8,8,9,9,10,10,13,14,15,16-icosafluoro-1,2,3,4,7,8,9,10-octahydrotrinaphthylene

HPLC method: Elutes at 8.9 min in 1:1 toluene:isopropyl alcohol (appx B figure B-14).
Yield information: <5% yield reaction 1.7 (appx B.1.7.).

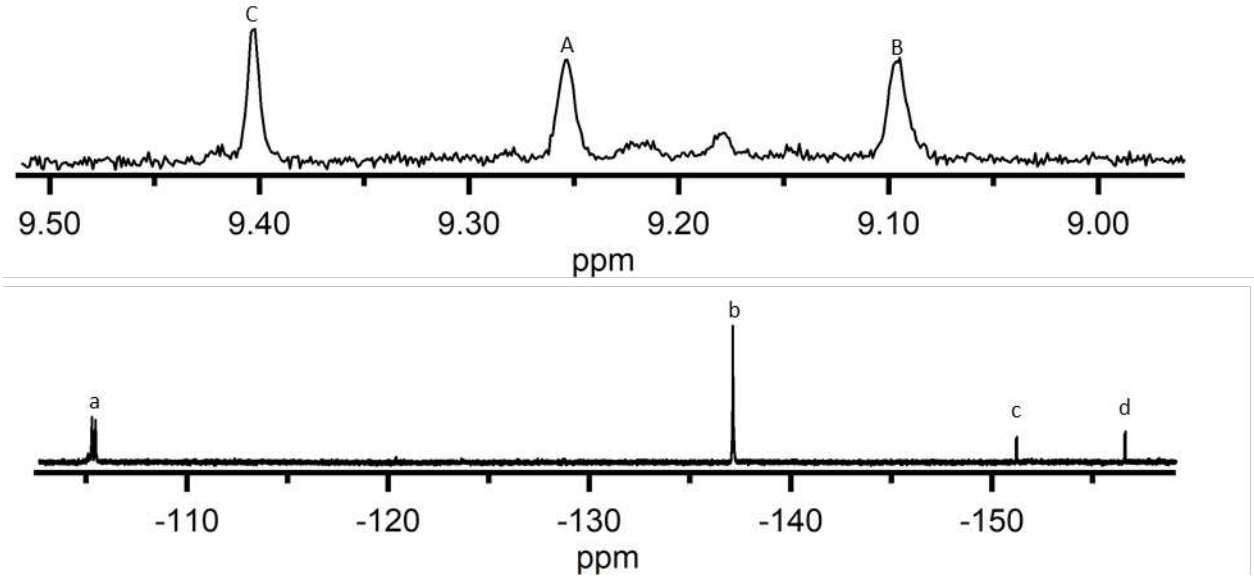

Figure C-29. NMR spectra of 2,3;6,7;10,11-TRPH(C_4F_8)$_3$. Product > 85% pure. ^{1}H NMR spectrum (top) referenced to $CHCl_3$ (δ = 7.26, not shown). ^{19}F NMR spectrum (bottom) referenced to 1,4-bistrifluromethyl benzene (19F δ = –66.4, not shown, 1H δ = 7.77, not shown). See figure below for probable peak assignments.

1H NMR ($CDCl_3$, 400 MHz): δ = 9.09 (s, 2H), 9.24 (s, 2H), 9.39 (s, 2H).
19F NMR ($CDCl_3$ with C_6F_6): δ = −105.3 (m, 8F), −137.1 (m, 8F), −151.2 (m, 2F), −156.5 (m, 2F).

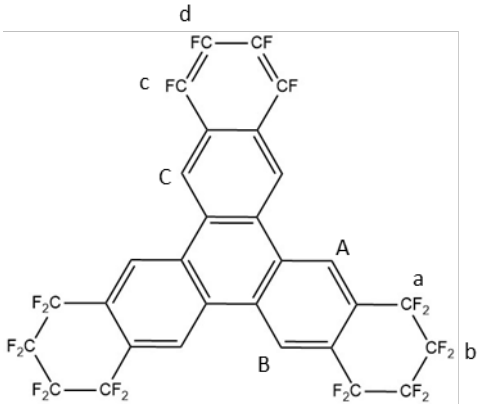

Figure C-30. Drawing of 2,3;6,7;10,11-TRPH(C_4F_8)$_3$, elucidated from NMR spectra and confirmed by single crystal X-ray structure.

C.2.1. CHARACTERIZATION OF 5,6-(4,7-PHEN)(C_4F_8)

9,9,10,10,11,11,12,12-octafluoro-9,10,11,12-tetrahydrobenzo[*f*][4,7]phenanthroline

HPLC method: Elutes at 12.5 minutes in 2:1 methanol:acetonitrile (appx B Figure B-16). Elutes at 7.9 minutes is acetonitrile (appx B Figure B-18).
Yield information: Minor product of reaction 2.1; > 1 mg isolated (appx B.2.1). Major product of reaction 2.2; 45% isolated yield (5 mg of 11 mg sample). (appx B.2.2)

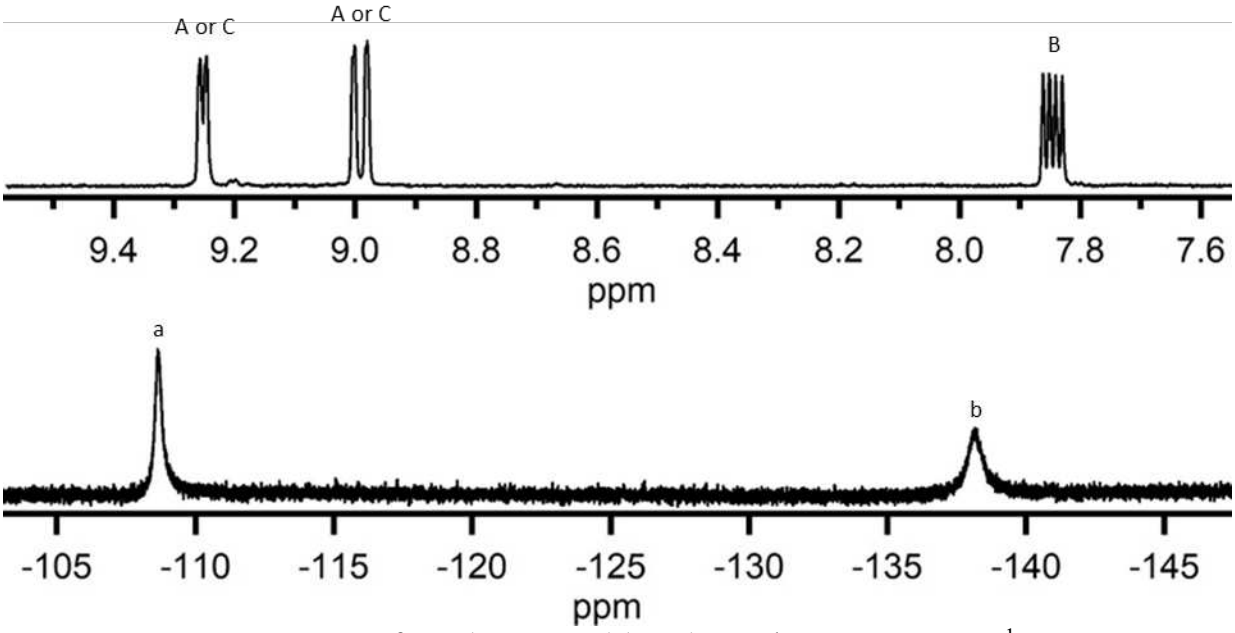

Figure C-31. NMR spectra of 5,6-(4,7-PHEN)(C_4F_8). Product > 95% pure. ^{1}H NMR spectrum (top) referenced to $CHCl_3$ (δ = 7.26, not shown). ^{19}F NMR spectrum (bottom) referenced to perfluorobenzene (δ = −164.9, not shown). See figure below for probable peak assignments.

1H NMR ($CDCl_3$, 400 MHz): δ 9.26 (d, 2H, J = 4.1), 8.99 (d, 2H, J = 8.7), 7.85 (dd, 2H, J_1 = 4.1, J_2 = 8.7).
19F NMR ($CDCl_3$ with C_6F_6): δ −108.6 (br s, 4F), −138.1 (br s, 4F).

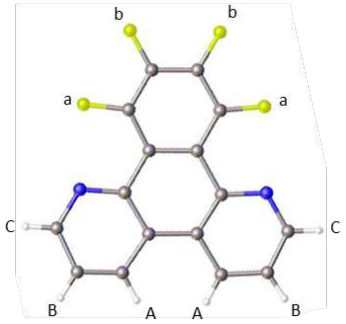

Figure C-32: Single crystal x-ray structure of 5,6-(4,7-PHEN)(C_4F_8). Thermal ellipsoids shown at the 50% probability level.

C.2.2. CHARACTERIZATION OF 2,3;5,6-(4,7-PHEN)(C_4F_8)$_2$

5,5,6,6,7,7,8,8,10,10,11,11,12,12,13,13-hexadecafluoro-5,6,7,8,10,11,12,13-octahydrodibenzo[*b*,*f*][4,7]phenanthroline

HPLC method: Elutes at 23.0 minutes in 2:1 methanol:acetonitrile (appx B Figure B-16). Elutes at 11.9 minutes is acetonitrile (appx B Figure B-18).
Yield information: Minor product of reaction 2.1; > 1 mg isolated (appx B.2.1). Major product of reaction 2.2; 18% isolated yield (2 mg of 11 mg sample) (appx B.2.2).

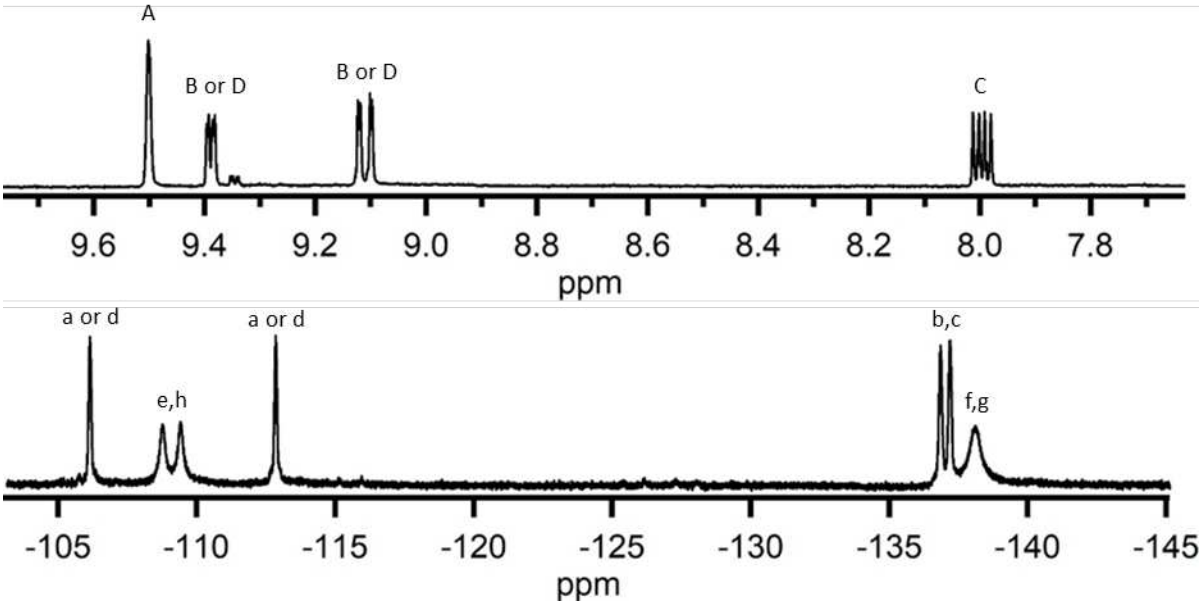

Figure C-33. NMR spectra of 2,3;5,6-(4,7-PHEN)(C_4F_8)$_2$. Product > 95% pure. ^{1}H NMR spectrum (top) referenced to $CHCl_3$ (δ = 7.26, not shown). ^{19}F NMR spectrum (bottom) referenced to perfluorobenzene (δ = −164.9, not shown). See figure below for probable peak assignments.

1H NMR ($CDCl_3$, 400 MHz): δ 9.50 (s, 1H), 8.39 (m, 1H), 9.11 (m, 1H), 7.99 (m, 1 H).
19F NMR ($CDCl_3$ with C_6F_6): δ −106.2 (s, 2F), −108.8 (br s, 2F), −109.5 (br s, 2F), −112.9 (s, 2F), −136.9 (s, 2F), −137.2 (s, 2F), −138.2 (br s, 4F).

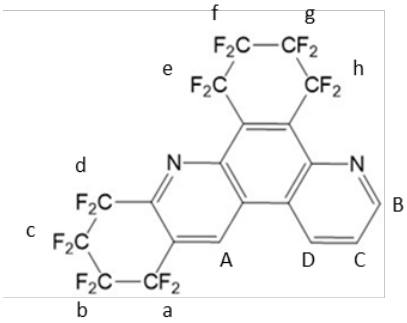

Figure C-34. Drawing of structure of 2,3;5,6-(4,7-PHEN)(C_4F_8)$_2$, elucidated from NMR spectra and comparison to NMR spectra and x-ray structures of other 4,7-PHEN derivatives.

C.2.3. CHARACTERIZATION OF 2,3;5,6;8,9-(4,7-PHEN)(C_4F_8)$_3$

1,1,2,2,3,3,4,4,6,6,7,7,8,8,9,9,11,11,12,12,13,13,14,14-tetracosafluoro-1,2,3,4,6,7,8,9,11,12,13,14-dodecahydrotribenzo[*b*,*f*,*j*][4,7]phenanthroline

HPLC method: Elutes at 10.0 minutes in acetonitrile. (appx B Figure B-16).
Yield information: Minor product of reaction 2.1; > 1 mg isolated (appx B.2.1).

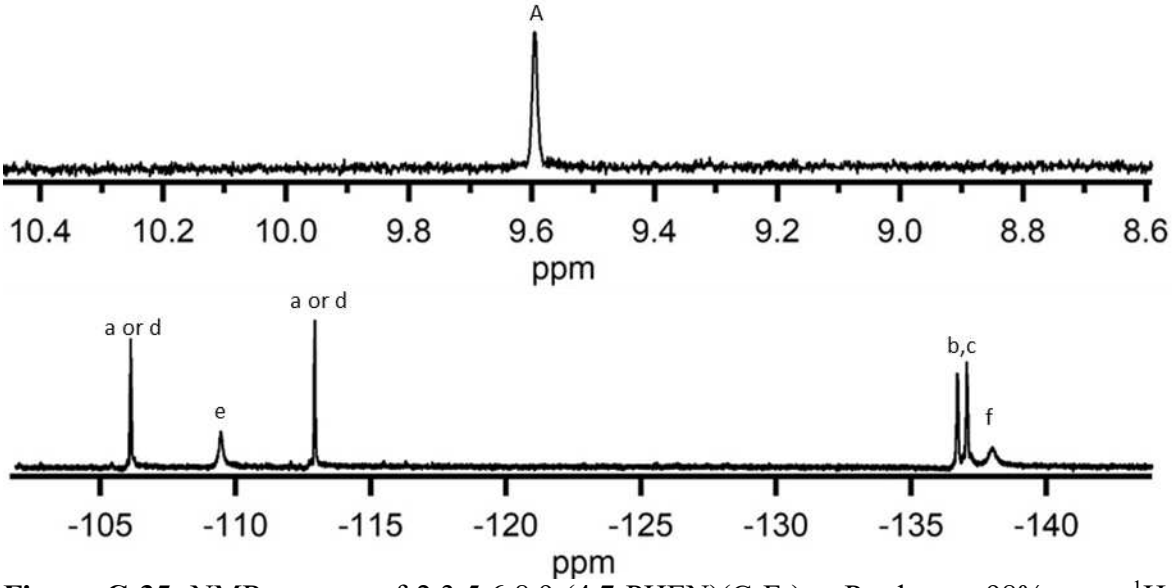

Figure C-35. NMR spectra of 2,3;5,6;8,9-(4,7-PHEN)(C_4F_8)$_3$. Product > 98% pure. ^{1}H NMR spectrum (top) referenced to $CHCl_3$ (δ = 7.26, not shown). ^{19}F NMR spectrum (bottom) referenced to perfluorobenzene (δ = –164.9, not shown). See figure below for probable peak assignments.

1H NMR ($CDCl_3$, 400 MHz): δ 9.59 (s, 2H).
19F NMR ($CDCl_3$ with C_6F_6): δ −106.2 (s, 2F), −108.8 (br s, 2F), −109.5 (br s, 2F), −112.9 (s, 2F), −136.9 (s, 2F), −137.2 (s, 2F), −138.2 (br s, 4F).

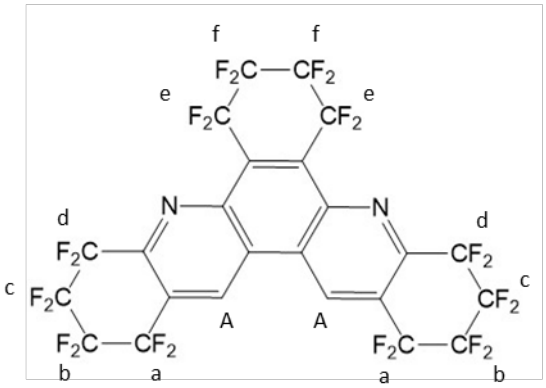

Figure C-36. Drawing of structure of 2,3;5,6;8,9-(4,7-PHEN)(C_4F_8)$_3$, elucidated from NMR spectra, steric considerations, and comparison to NMR spectra and x-ray structures of other 4,7-PHEN derivatives.

C.2.4. CHARACTERIZATION OF 5,6-(4,7-PHEN)(C_4F_4)

9,10,11,12-tetrafluorobenzo[*f*][4,7]phenanthroline

HPLC method: Elutes at 21.0 minutes in acetonitrile. (appx B Figure B-16).
Yield information: Minor product of reaction 2.1; > 1 mg isolated (appx B.2.1).

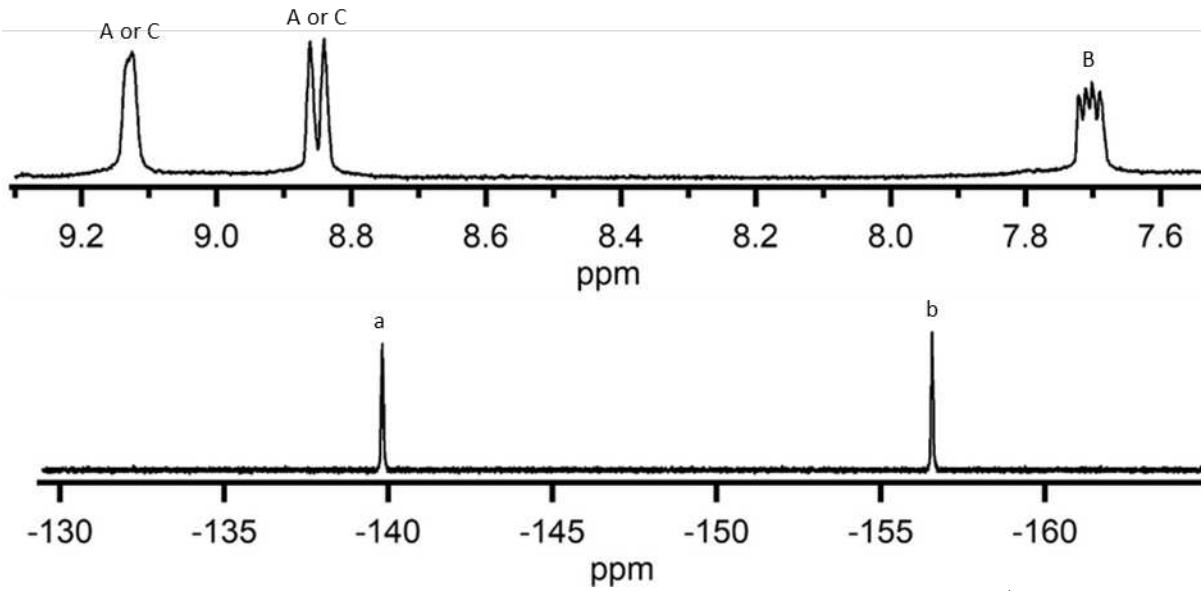

Figure C-37. NMR spectra of 5,6-(4,7-PHEN)(C_4F_4). Product > 98% pure. ^{1}H NMR spectrum (top) referenced to $CHCl_3$ (δ = 7.26, not shown). ^{19}F NMR spectrum (bottom) referenced to perfluorobenzene (δ = −164.9, not shown). See figure below for probable peak assignments.

1H NMR ($CDCl_3$, 400 MHz): δ 9.13 (br s, 2H), 8.85 (d, 2H, J = 8.5), 7.71 (m, 2H).
19F NMR ($CDCl_3$ with C_6F_6): δ −139.8 (m, 2F), −156.6 (m, 2F).

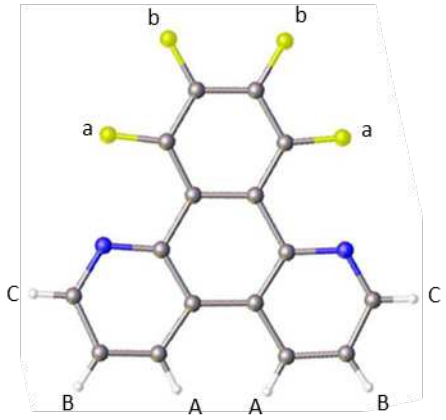

Figure C-38. Single crystal x-ray structure of 5,6-(4,7-PHEN)(C_4F_4). Thermal ellipsoids shown at the 50% probability level.

C.2.4. CHARACTERIZATION OF 5,6-(4,7-PHEN)(C_4F_7H)

9,9,10,10,11,11-hexafluoro-10,11-dihydro-9*H*-12λ^{2-}
benzo[*f*][4,7]phenanthroline hydrofluoride

HPLC method: Elutes at 21.0 minutes in acetonitrile (appx B Figure B-16).
Yield information: Minor product of reaction 2.1; > 1 mg isolated (appx B.2.1).

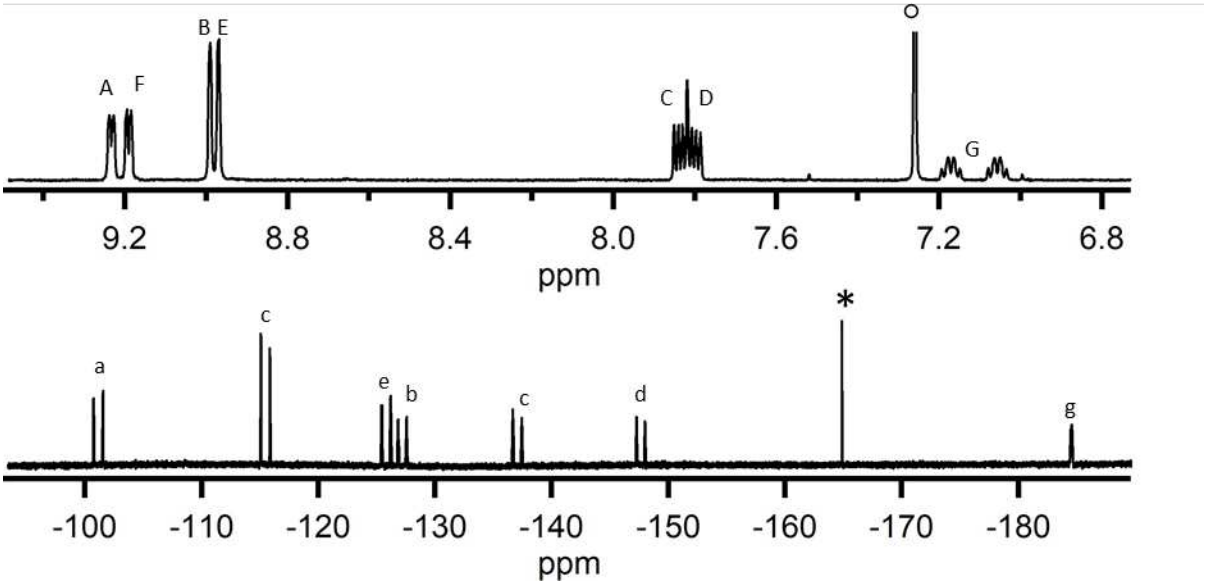

Figure C-39. NMR spectra of 5,6-(4,7-PHEN)(C_4F_7H). Product > 98% pure. ^{1}H NMR spectrum (top) referenced to $CHCl_3$ (δ = 7.26, denoted º). ^{19}F NMR spectrum (bottom) referenced to perfluorobenzene (δ = −164.9, denoted *). See figure below for probable peak assignments.

1H NMR ($CDCl_3$, 400 MHz): δ 9.13 (br s, 2H), 8.85 (d, 2H, J = 8.5), 7.71 (m, 2H).
19F NMR ($CDCl_3$ with C_6F_6): δ −139.8 (m, 2F), −156.6 (m, 2F).

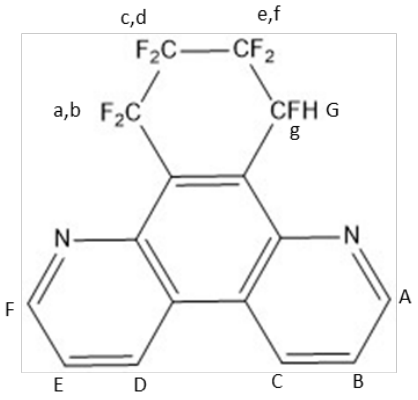

Figure C-40. Drawing of structure of 5,6-(4,7-PHEN)(C_4F_7H), elucidated from NMR spectra and confirmed by single crystal X-ray structure.

C.2.5. CHARACTERIZATION OF 2,3-(1,10-PHEN)(C_4F_8)

8,8,9,9,10,10,11,11-octafluoro-8,9,10,11-tetrahydrobenzo[*b*][1,10]phenanthroline

HPLC method: Eluted at 7.8 minutes in 2:1 methanol:acetonitrile (appx B Figure B-20).
Amount isolated: Minor product of reaction 2.3; 4 mg isolated (appx B.2.3).

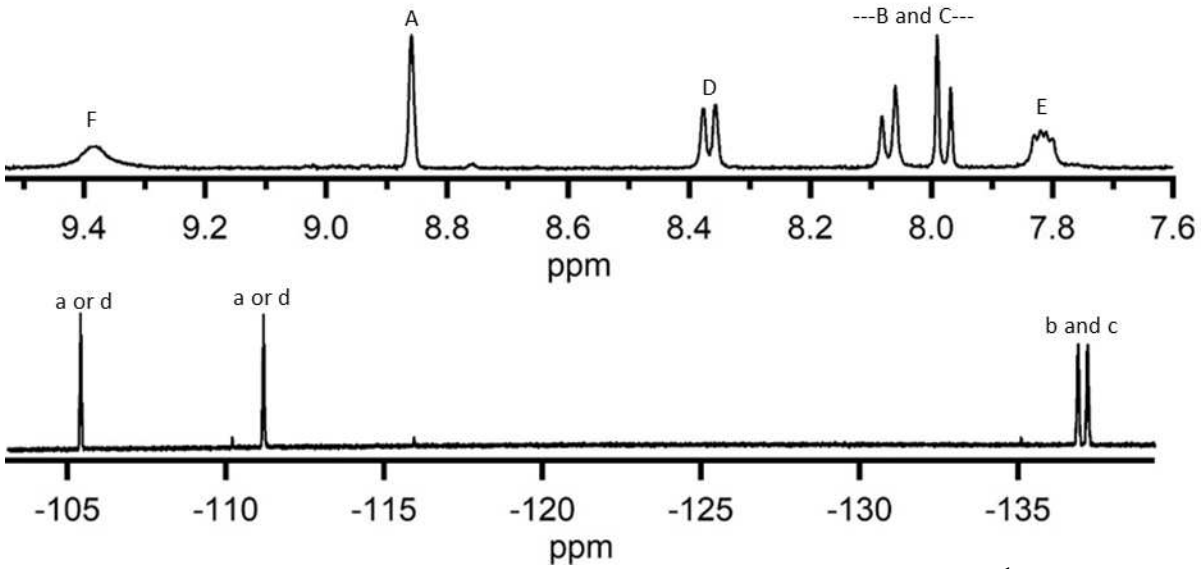

Figure C-41. NMR spectra of 2,3-(1,10-PHEN)(C_4F_8). Product > 95% pure. ^{1}H NMR spectrum (top) referenced to $CHCl_3$ (δ = 7.26, not shown). ^{19}F NMR spectrum (bottom) referenced to perfluorobenzene (δ = −164.9, not shown). See figure below for probable peak assignments.

1H NMR ($CDCl_3$, 400 MHz): δ 9.38 (br s, 1H), 8.86 (s, 1H), 8.37 (d, 1H, J = 8.3 Hz), 8.07 (d, 1H, J = 8.9), 7.98 (d, 1H, J = 8.9), 7.92 (m, 1H).
19F NMR ($CDCl_3$ with C_6F_6, 376 MHz): δ −105.4 (m, 2F), −111.2 (m, 2F), −136.9 (m, 2F), −137.2 (m, 2F).

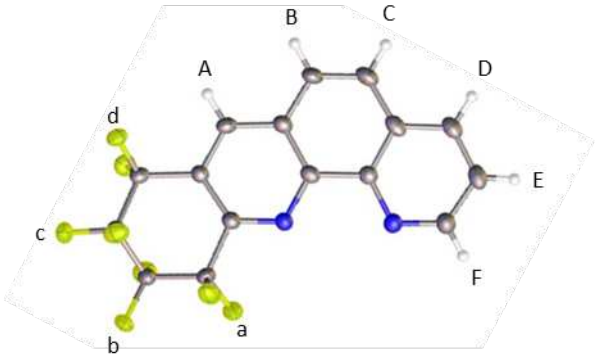

Figure C-42. Single crystal x-ray structure of 2,3-(1,10-PHEN)(C_4F_8). Thermal ellipsoids shown at the 50% probability level.

C.2.6. CHARACTERIZATION OF 3,4-(1,10-PHEN)(C_4F_8)

7,7,8,8,9,9,10,10-octafluoro-7,8,9,10-tetrahydrobenzo[*c*][1,10]phenanthroline

HPLC method: Eluted at 21.8 minutes in 2:1 methanol:acetonitrile(appx B Figure B-20).
Yield information: Minor product of reaction 2.3; 2 mg isolated (appx B.2.3).

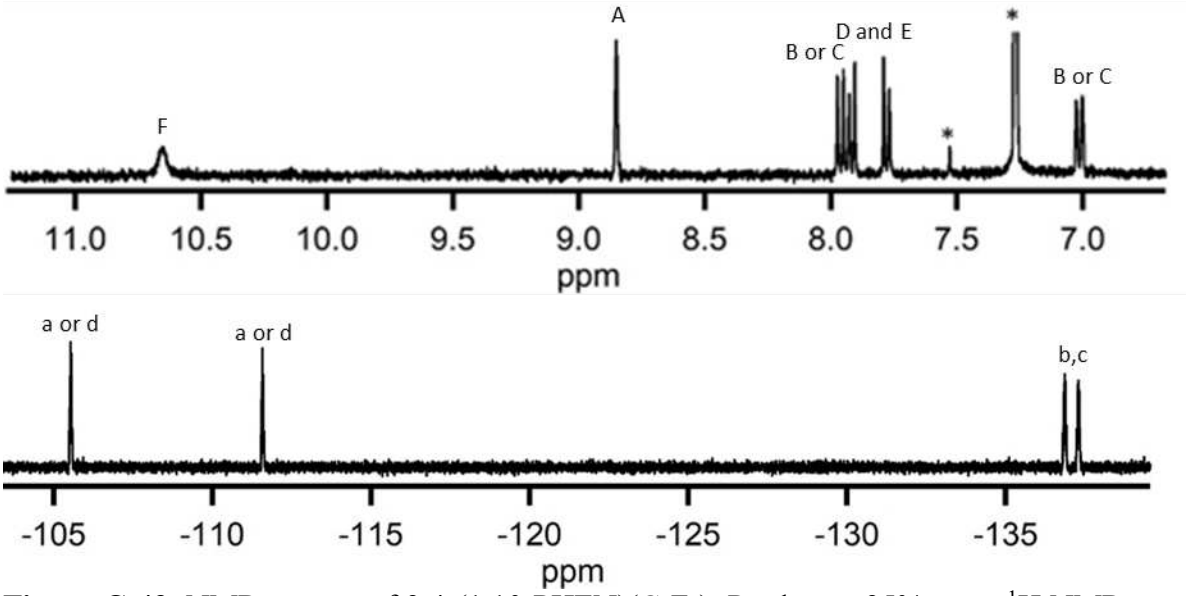

Figure C-43. NMR spectra of 3,4-(1,10-PHEN)(C_4F_8). Product > 95% pure. ^{1}H NMR spectrum (top) referenced to $CHCl_3$ (δ = 7.26, denoted *, ^{13}C satallite peak also present). ^{19}F NMR spectrum (bottom) referenced to perfluorobenzene (δ = –164.9, not shown). See figure below for probable peak assignments.

1H NMR ($CDCl_3$, 400 MHz): δ 10.65 (br s, 1H), 8.85 (s, 1H), 7.96 (d, 1H, J = 9.4), 7.92 (d, 1H, J = 8.9), 7.78 (d, 1H, 8.9), 7.01 (d, 1H, J = 9.4).
19F NMR ($CDCl_3$ with C_6F_6, 376 MHz): δ −105.5 (m, 2F), −111.6 (m, 2F), −136.9 (m, 2F), −137.3 (m, 2F).

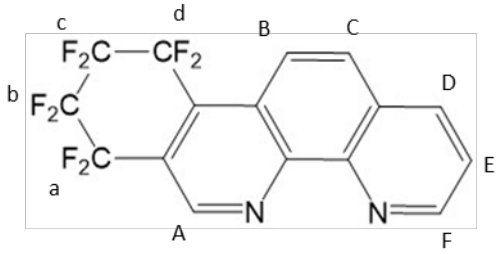

Figure C-44. Drawing of structure of 2,3-(1,10-PHEN)(C_4F_8) elucidated from NMR spectra.

C.2.7. CHARACTERIZATION OF 2,3;5,6-(1,10-PHEN)(C_4F_8)$_2$

5,5,6,6,7,7,8,8,10,10,11,11,12,12,13,13-hexadecafluoro-5,6,7,8,10,11,12,13-octahydrodibenzo[*b*,*f*][1,10]phenanthroline

HPLC method: Eluted at 6.8 minutes in 3:1 methanol:toluene; Eluted at 14.1 minutes in 2:1 methanol:acetonitrile(appx B Figure B-20).
Yield information: Product of reaction 2.3; 7 mg pure compound isolated (appx B.2.3).

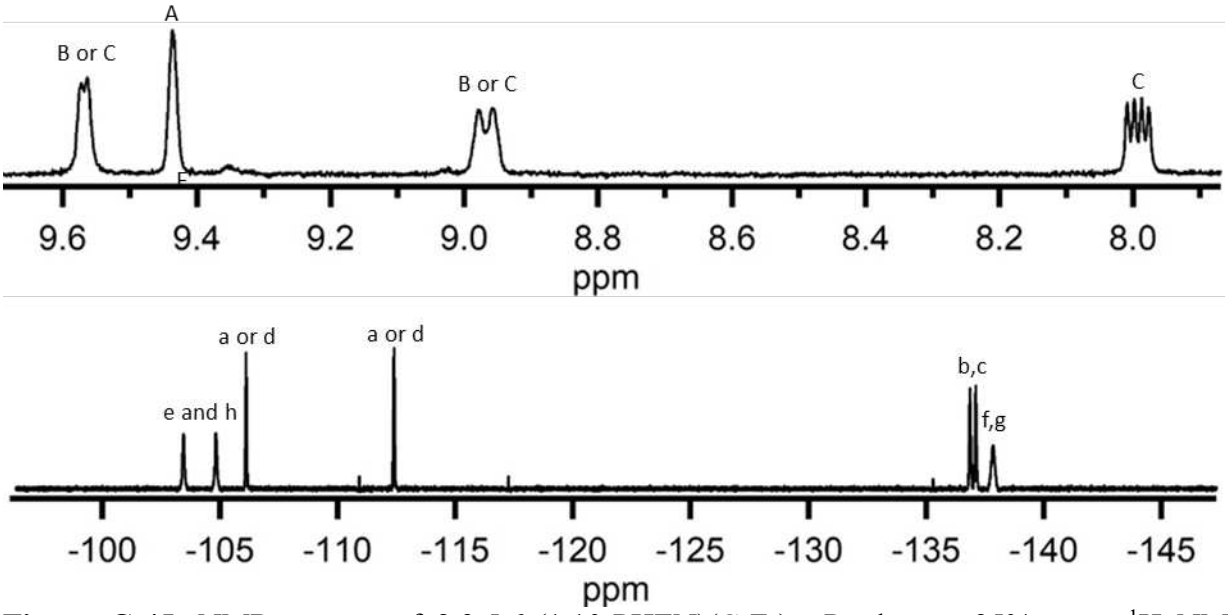

Figure C-45. NMR spectra of 2,3;5,6-(1,10-PHEN)(C_4F_8)$_2$. Product > 95% pure. ^{1}H NMR spectrum (top) referenced to $CHCl_3$ (δ = 7.26, not shown). ^{19}F NMR spectrum (bottom) referenced to perfluorobenzene (δ = –164.9, not shown). See figure below for probable peak assignments.

1H NMR ($CDCl_3$, 400 MHz): δ 9.57 (d, 1H, J = 3.7), 9.44 (s, 1H), 8.97 (d, 1H, J = 9.0), 8.00 (dd, 1 H, J_1 = 3.7, J_2 = 9.0).
19F NMR ($CDCl_3$ with C_6F_6, 376 MHz): δ −103.4 (br s, 2F), −104.8 (br s, 2F), −106.1 (m, 2F), −112.4 (m, 2F), −136.9 (m, 2F), −131.7 (m, 2F), −137.9 (br s, 2F).

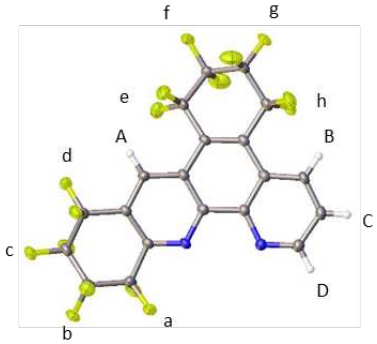

Figure C-46. Single crystal x-ray structure of 2,3;5,6-(1,10-PHEN)(C_4F_8)$_2$. Thermal ellipsoids shown at the 50% probability level.

C.2.8. CHARACTERIZATION OF 2,3;7,8-(1,10-PHEN)(C_4F_8)$_2$

1,1,2,2,3,3,4,4,8,8,9,9,10,10,11,11-hexadecafluoro-1,2,3,4,8,9,10,11-octahydrodibenzo[*b*,*i*][1,10]phenanthroline

HPLC method: Eluted at 18.8 min in 2:1 methanol:acetonitrile(appx B Figure B-20).
Yield information: Minor product of reaction 2.3; <1 mg isolated (appx B.2.3).

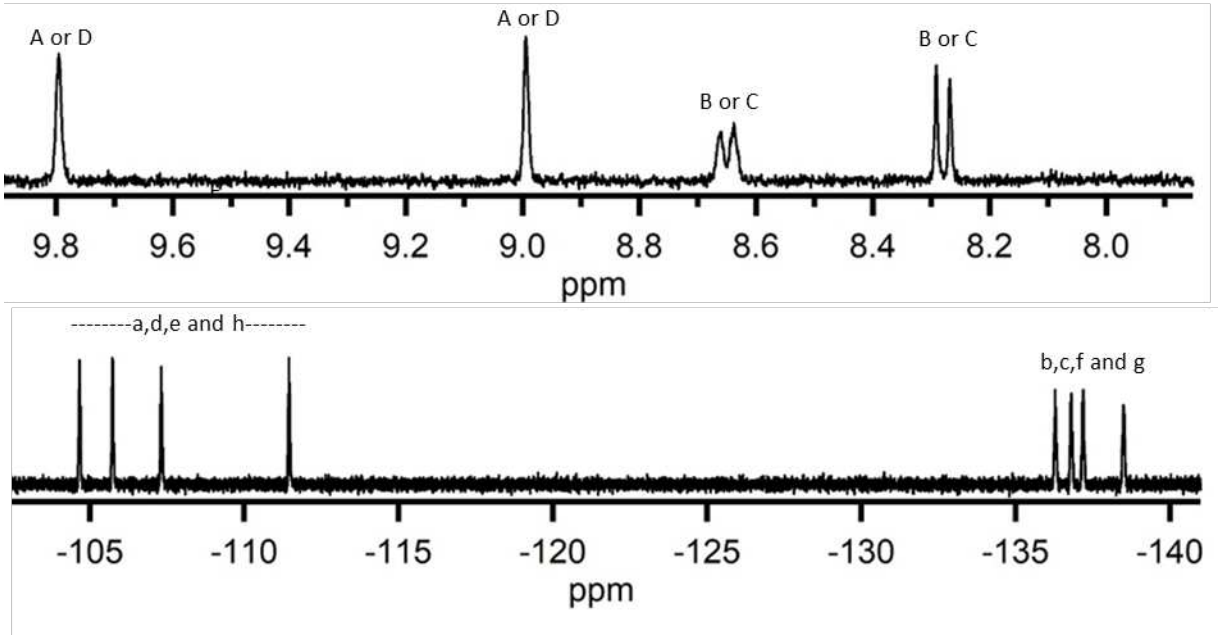

Figure C-47. NMR spectra of 2,3;7.8-(1,10-PHEN)(C_4F_8)$_2$. Product > 95% pure. ^{1}H NMR spectrum (top) referenced to $CHCl_3$ (δ = 7.26, not shown). ^{19}F NMR spectrum (bottom) referenced to perfluorobenzene (δ = –164.9, not shown). See figure below for probable peak assignments.

1H NMR ($CDCl_3$, 400 MHz): δ 9.80 (s, 1H), 8.99 (s, 1H), 8.85 (d, 1H, J = 9.5), 8.28 (d, 1 H, J = 9.5).
19F NMR ($CDCl_3$ with C_6F_6): δ −104.7 (m, 2F), −105.7 (m, 2F), −107.3 (m, 2F), −111.5 (m, 2F), −136.3 (m, 2F), −136.8 (m, 2F), −137.2 (m, 2F), −135.5 (m, 2F).

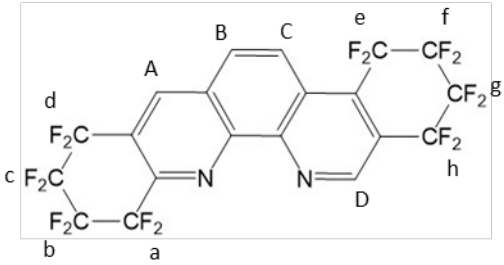

Figure C-48. Drawing of structure of 2,3;7.8-(1,10-PHEN)(C_4F_8)$_2$, elucidated from NMR spectra.

C.2.9. CHARACTERIZATION OF 2,3;8,9-(1,10-PHEN)(C_4F_8)$_2$

1,1,2,2,3,3,4,4,9,9,10,10,11,11,12,12-hexadecafluoro-1,2,3,4,9,10,11,12-octahydrodibenzo[*b*,*j*][1,10]phenanthroline

HPLC method: eluted at 6.0 minutes in 1:1 methanol:toluene (appx B Figure B-20).
Yield information Minor product of reaction 2.3; <1 mg isolated (appx B.2.3).

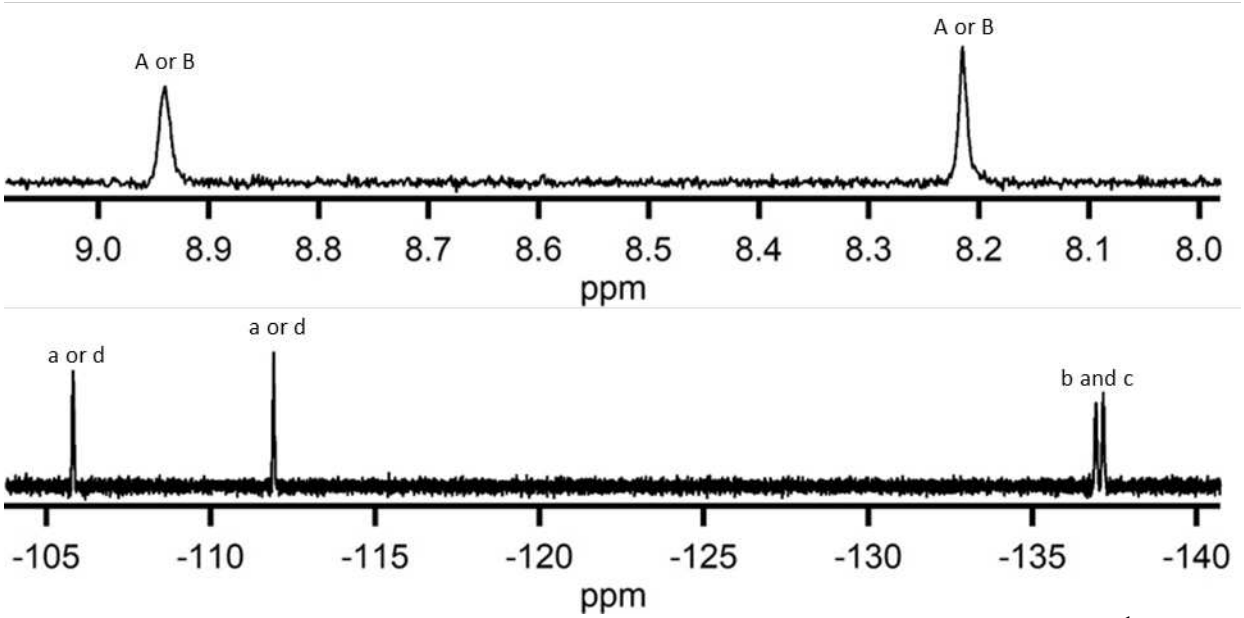

Figure C-49. NMR spectra of 2,3;8,9-(1,10-PHEN)(C_4F_8)$_2$. Product > 95% pure. ^{1}H NMR spectrum (top) referenced to $CHCl_3$ (δ = 7.26, not shown). ^{19}F NMR spectrum (bottom) referenced to perfluorobenzene (δ = –164.9, not shown). See figure below for probable peak assignments.

1H NMR ($CDCl_3$, 400 MHz): δ 8.94 (s, 2H), 8.21 (s, 2H).
19F NMR ($CDCl_3$ with C_6F_6, 376 MHz): δ −105.8 (m, 4F), −111.9 (m, 4F), −136.9 (m, 4F), −137.2 (m, 4F).

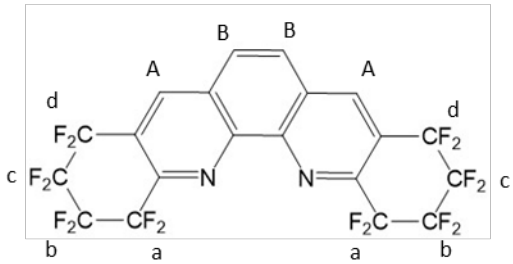

Figure C-50. Drawing of structure of 2,3;8,9-(1,10-PHEN)(C_4F_8)$_2$ elucidated from NMR spectra and comparison to NMR spectra and x-ray structures of other 1,10-PHEN derivatives.

C.2.10. CHARACTERIZATION OF 2,3;5,6;8,9-(1,10-PHEN)(C_4F_8)$_3$

1,1,2,2,3,3,4,4,6,6,7,7,8,8,9,9,11,11,12,12,13,13,14,14-tetracosafluoro-1,2,3,4,6,7,8,9,11,12,13,14-dodecahydrotribenzo[*b*,*f*,*j*][1,10]phenanthroline

HPLC method: eluted at 11.0 minutes in 2:1 methanol:acetonitrile(appx B Figure B-20).
Yield information: Minor product of reaction 2.3; <1 mg isolated (appx B.2.3).

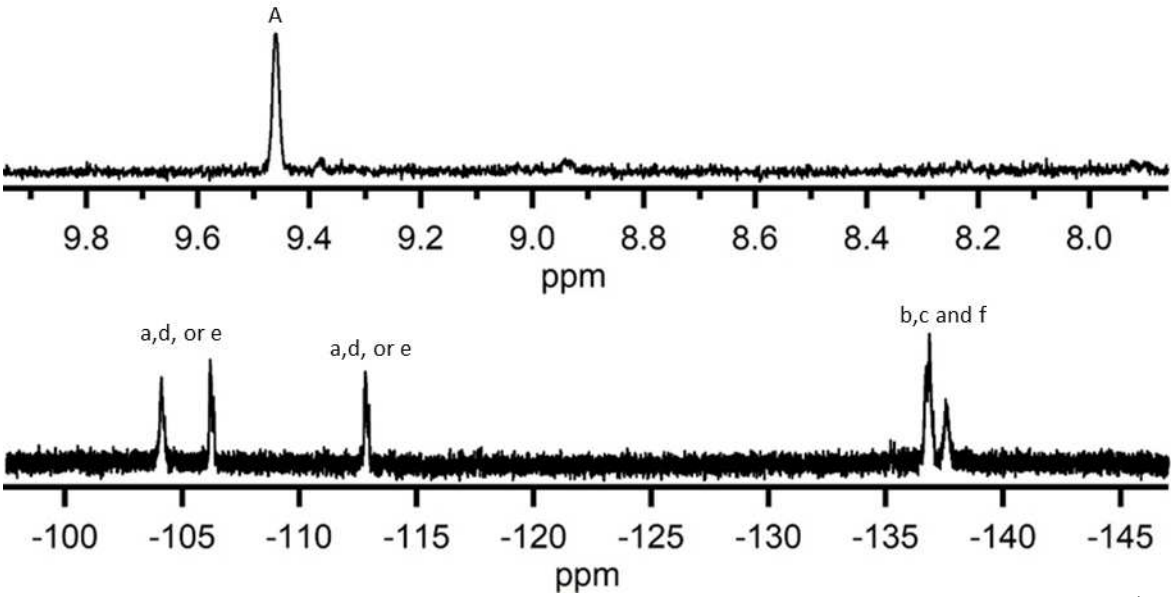

Figure C-51. NMR spectra of 2,3;5,6;8.9-(1,10-PHEN)(C_4F_8)$_3$. Product > 90% pure. ^{1}H NMR spectrum (top) referenced to $CHCl_3$ (δ = 7.26, not shown). ^{19}F NMR spectrum (bottom) referenced to perfluorobenzene (δ = –164.9, not shown). See figure below for probable peak assignments.

1H NMR ($CDCl_3$, 400 MHz): δ 9.46 (s, 2H).
19F NMR ($CDCl_3$ with C_6F_6): δ −104.1 (m, 4F), −106.2 (m, 4F), −112.8 (m, 4F), −136.9 (m, 8F), −137.6 (m, 4F).

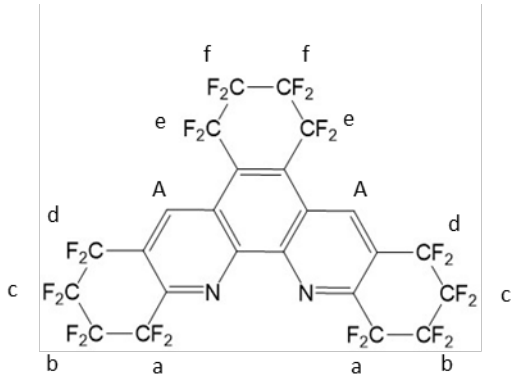

Figure C-52. Drawing of structure of 2,3;5,6;8.9-(1,10-PHEN)(C_4F_8)$_3$, elucidated from NMR spectra, steric considerations, and comparison to NMR spectra and x-ray structures of other 1,10-PHEN derivatives.

C.2.11. CHARACTERIZATION OF 7,8-(5-PHRD)(C_4F_8)

1,1,2,2,3,3,4,4-octafluoro-1,2,3,4-tetrahydrobenzo[*i*]phenanthridine

HPLC method: Elutes at 12.4 minutes in acetonitrile(appx B Figure B-22).
Yield information: Product of reaction 2.4; <1 mg isolated (appx B.2.4).

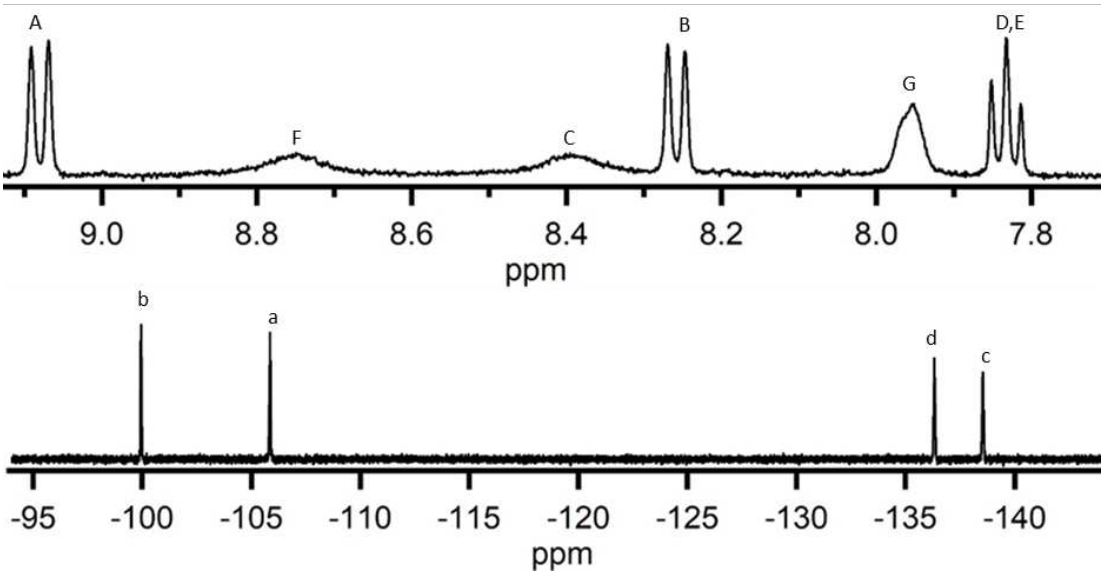

Figure C-53. NMR spectra of 7.8-(5-PHRD)(C_4F_8). Product > 95% pure. ^{1}H NMR spectrum (top) referenced to $CHCl_3$ (δ = 7.26, not shown). ^{19}F NMR spectrum (bottom) referenced to perfluorobenzene (δ = –164.9, not shown). See figure below for probable peak assignments.

1H NMR ($CDCl_3$, 400 MHz): δ 9.08 (d, 1H, J = 8.8), 8.75 (br s, 1H), 8.40 (br s, 1H), 8.26 (d, 1H, J = 8.8), 7.95 (br s, 1H), 7.83 (t, 1H, J = 7.5). (missing proton is broad due to coupling and not seen in spectrum)
19F NMR ($CDCl_3$ with C_6F_6): δ −99.9 (m, 2F), −105.9 (m, 2F), −106.8 (m, 2F), −136.3 (m, 2F), −136.3 (s, 2F), −138.6 (m, 2F).

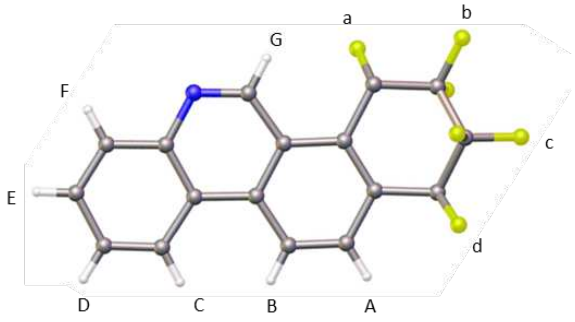

Figure C-54. Single crystal x-ray structure of 5,6-(5-PHRD)(C_4F_8). Thermal ellipsoids shown at the 50% probability level.

C.2.12. CHARACTERIZATION OF 5-PHRD(C_4F_8)-B

HPLC method: Elutes at 8.2 minutes in acetonitrile (appx B Figure B-22).
Yield information: Product of reaction 2.4; <1 mg isolated (appx B.2.4).

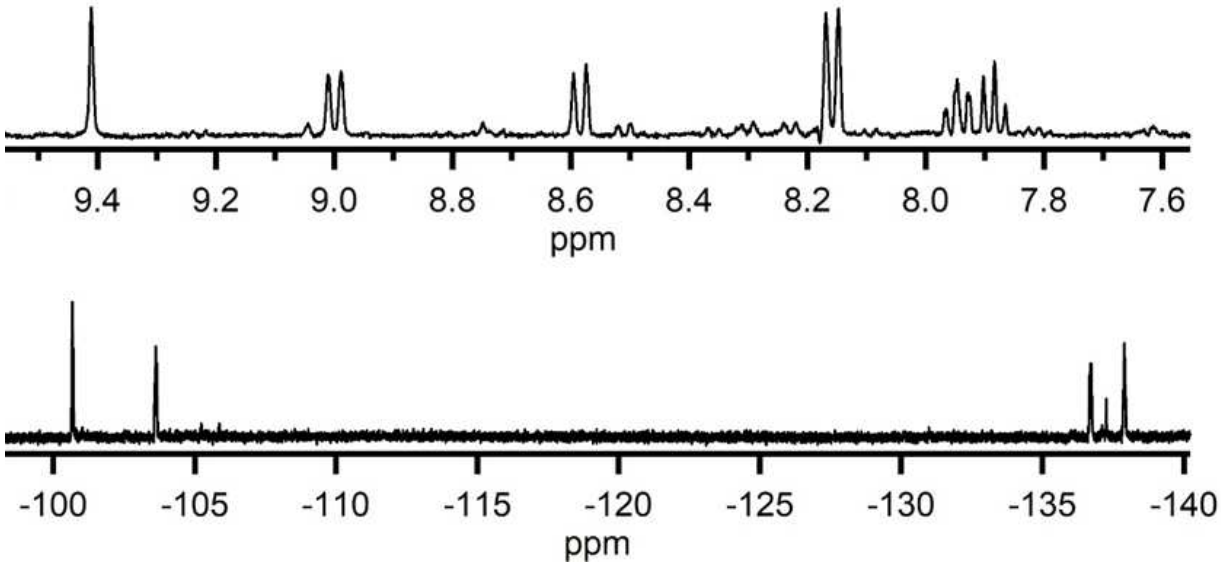

Figure C-55. NMR spectra of(5-PHRD)(C_4F_8)-B. Product > 95% pure. ^{1}H NMR spectrum (top) referenced to $CHCl_3$ (δ = 7.26, not shown). ^{19}F NMR spectrum (bottom) referenced to perfluorobenzene (δ = –164.9, not shown).

1H NMR ($CDCl_3$, 400 MHz): δ 9.41 (s, 1H), 9.00 (d, 1H, J = 8.8), 8.59 (d, 1H, J = 8.8), 8.16 (d, 1H, J = 8.0), 7.95 (m, 1H), 7.88 (m, 1H).
19F NMR ($CDCl_3$ with C_6F_6): δ −100.6 (m, 2F), −103.6 (m, 2F), −136.7 (m, 2F), −137.9 (m, 4F).

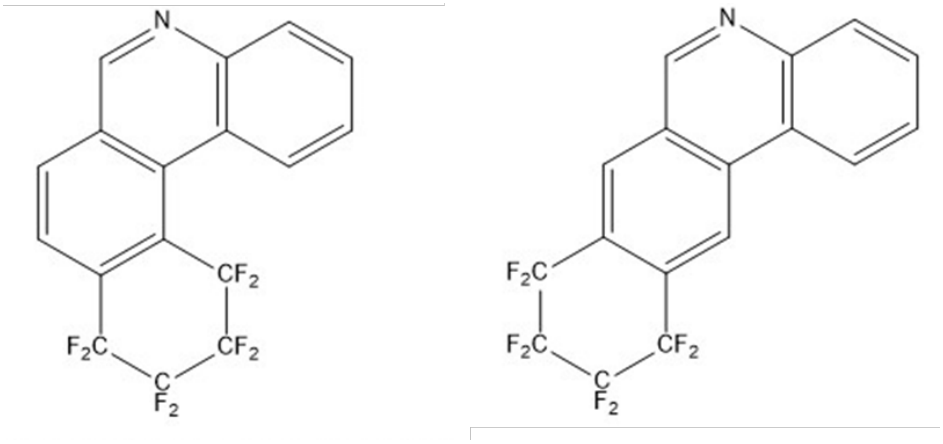

Figure C-56. Drawing of possible structures of 5-PHRD(C_4F_8)-B, elucidated from NMR spectra

C.2.13. CHARACTERIZATION OF 2,3-ACRD(C_4F_8)

7,7,8,8,9,9,10,10-octafluoro-7,8,9,10-tetrahydrobenzo[*b*]acridine

HPLC method: Elutes at 10.5 minutes in 2:1 methanol:acetonitrile(appx B Figure B-24).
Yield information: Minor product of reaction 2.5; <1 mg isolated (appx B.2.5).

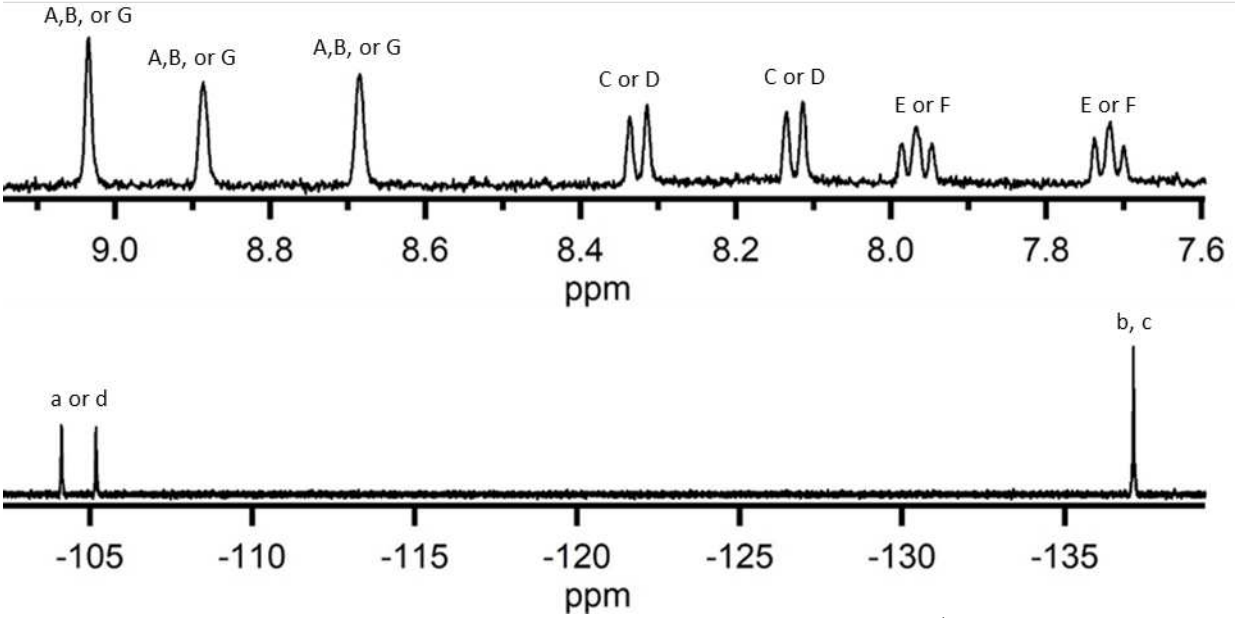

Figure C-57. NMR spectra of 2,3-ACRD(C_4F_8). Product *ca.* 80% pure. ^{1}H NMR spectrum (top) referenced to $CHCl_3$ (δ = 7.26, not shown). ^{19}F NMR spectrum (bottom) referenced to perfluorobenzene (δ = −164.9, not shown). See figure below for probable peak assignments.

1H NMR ($CDCl_3$, 400 MHz): δ 9.03 (s, 1H), 8.89 (s, 1H), 8.68 (s, 1H), 8.33 (d, 1H, J = 8.9), 8.12 (d, 1H, J = 8.9), 7.97 (t, 1H, J = 7.7), 7.72 (t, 1H, J = 7.7).
19F NMR ($CDCl_3$ with C_6F_6): δ −104.1 (m, 2F), −105.2 (m, 2F), −137.1 (m, 4F).

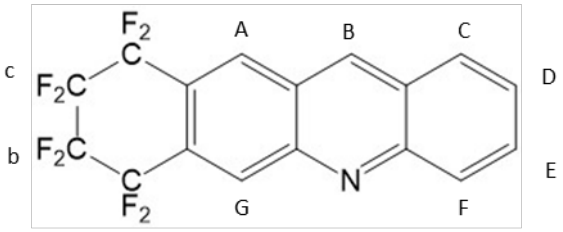

Figure C-58. Drawing of structure of 2,3-ACRD(C_4F_8), elucidated from NMR spectra.

C.2.14. CHARACTERIZATION OF 1,2;5,6-ACRD(C_4F_8)$_2$

7,7,8,8,9,9,10,10-octafluoro-7,8,9,10-tetrahydrobenzo[*b*]acridine

HPLC method: Elutes at 12.0 minutes in 2:1 methanol:acetonitrile (appx B Figure B-24).
Yield information: Minor product of reaction 2.5; <1 mg isolated (appx B.2.5).

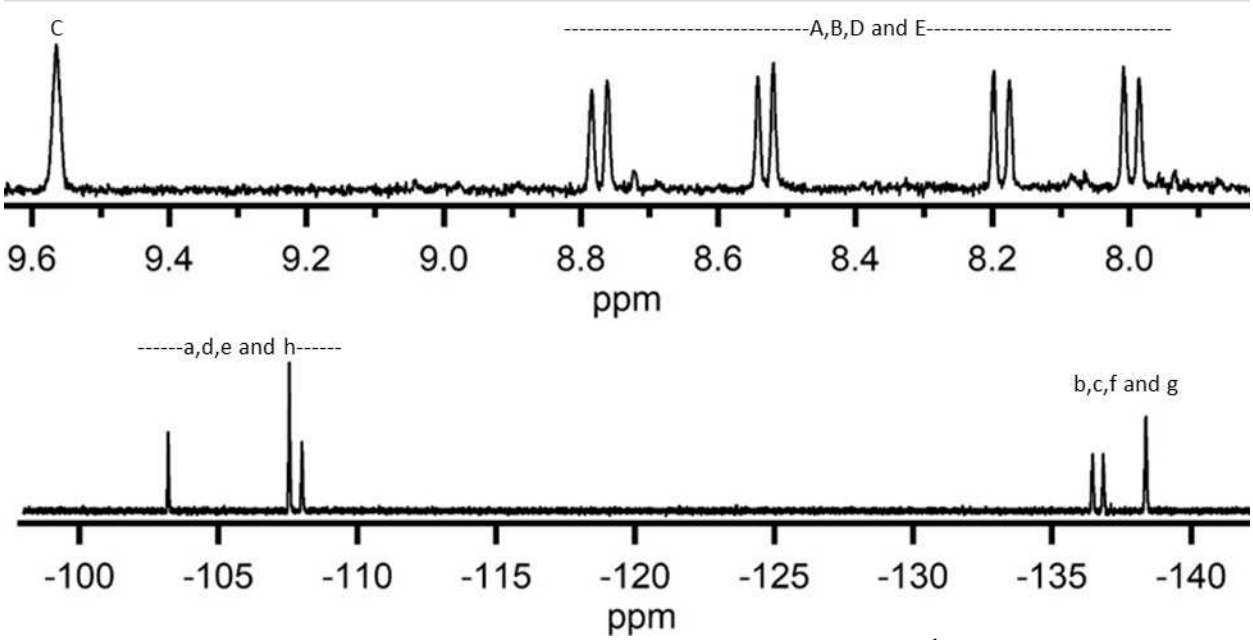

Figure C-59. NMR spectra of ACRD(C_4F_8)$_2$-A. Product > 90% pure. ^{1}H NMR spectrum (top) referenced to $CHCl_3$ (δ = 7.26, not shown). ^{19}F NMR spectrum (bottom) referenced to perfluorobenzene (δ = −164.9, not shown). See figure below for probable peak assignments.

1H NMR ($CDCl_3$, 400 MHz): δ 9.56 (s, 1H), 8.77 (d, 1H J = 9.0), 8.53 (d, 1H, J = 9.0), 8.19 (d, 1H, J = 9.0), 8.00 (d, 1H, J = 9.0).
19F NMR ($CDCl_3$ with C_6F_6): δ −103.2 (m, 2F), −107.6 (m, 4F), −108.2 (m, 2F), −136.5 (m, 2F), −136.8 (m, 2F), −138.4 (m, 4F).

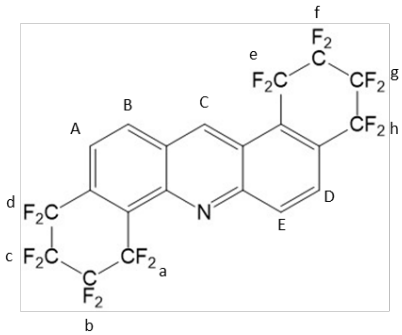

Figure C-60. Drawing of structure of 1,2;5,6-ACRD(C_4F_8)$_2$, elucidated from NMR spectra.

C.2.15. CHARACTERIZATION OF ACRD(C_4F_8)$_2$-B

HPLC method: Elutes at 32.0 minutes in 2:1 methanol:acetonitrile(appx B Figure B-24).
Yield information: Minor product of reaction 2.5; <1 mg isolated (appx B.2.5).

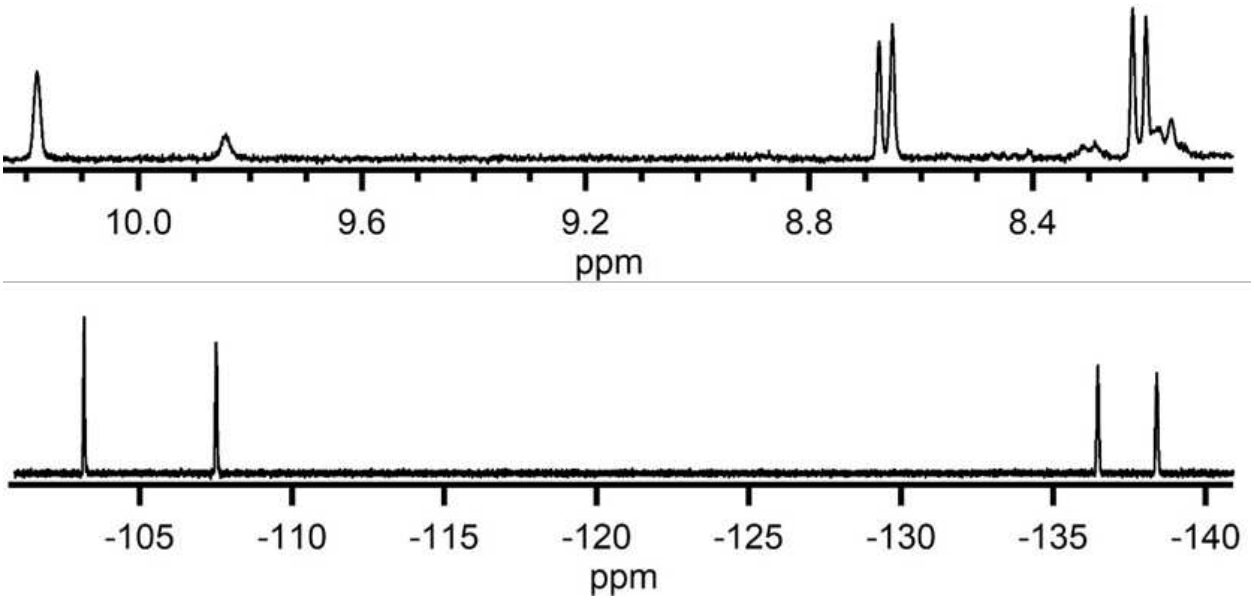

Figure C-61. NMR spectra of ACRD(C_4F_8)$_2$-B. Product *ca.* 80% pure. ^{1}H NMR spectrum (top) referenced to $CHCl_3$ (δ = 7.26, not shown). ^{19}F NMR spectrum (bottom) referenced to perfluorobenzene (δ = −164.9, not shown).

1H NMR ($CDCl_3$, 400 MHz): δ 10.18 (s, 1H), 8.67 (d, 1H J = 9.5), 8.21 (d, 1H, J = 9.5).
19F NMR ($CDCl_3$ with C_6F_6): δ −103.2 (m, 4F), −107.5 (m, 4F), −136.5 (m, 4F), −134.4 (m, 4F).

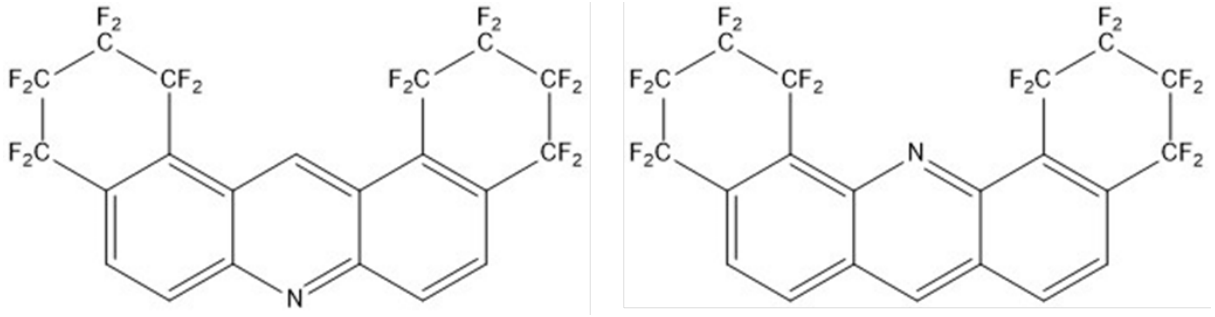

Figure C-62. Drawing of possible structures of 2,3-ACRD(C_4F_8), elucidated from NMR spectra

C.2.16. CHARACTERIZATION OF ACRD-$(C_4F_8)_2$-C

HPLC method: Elutes at 20.0 minutes in 2:1 methanol:acetonitrile(appx B Figure B-24).
Yield information: Minor product of reaction 2.5; <1 mg isolated (appx B.2.5).

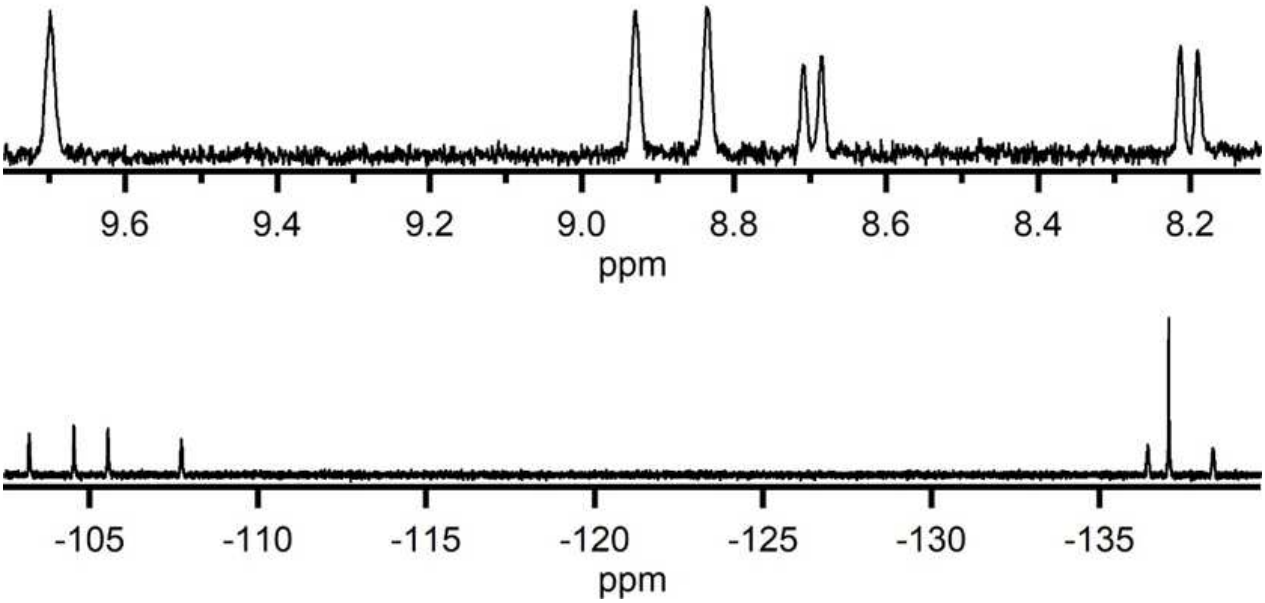

Figure C-63. NMR spectra of ACRD$(C_4F_8)_2$-C. Product *ca.* 80% pure. ^{1}H NMR spectrum (top) referenced to $CHCl_3$ (δ = 7.26, not shown). ^{19}F NMR spectrum (bottom) referenced to perfluorobenzene (δ = −164.9, not shown).

1H NMR ($CDCl_3$, 400 MHz): δ 9.70 (m, 1H), 8.93 (s, 1H), 8.84 (s, 1H), 8.69 (d, 1H, J = 9.2), 8.20 (d, 1H, J = 9.2).
19F NMR ($CDCl_3$ with C_6F_6): δ −103.2 (m, 2F), −104.5 (m, 2F), −105.6 (m, 2F), −107.3 (m, 2F), −136.4 (m, 2F), −137.1 (m, 4F), −138.3 (m, 2F).

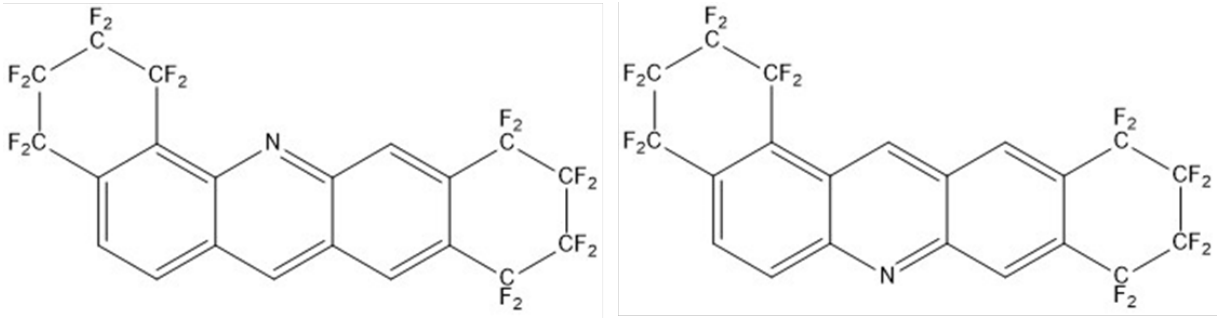

Figure C-64. Drawing of possible structures of 2,3-ACRD(C_4F_8), elucidated from NMR spectra

C.2.17. CHARACTERIZATION OF 1,2-ACRD(C_4HF_3)

2,3,4-trifluorobenzo[*a*]acridine

HPLC method: Elutes at 26.0 minutes in 2:1 methanol:acetonitrile(appx B Figure B-24).
Yield information: Minor product of reaction 2.5; <1 mg isolated (appx B.2.5).

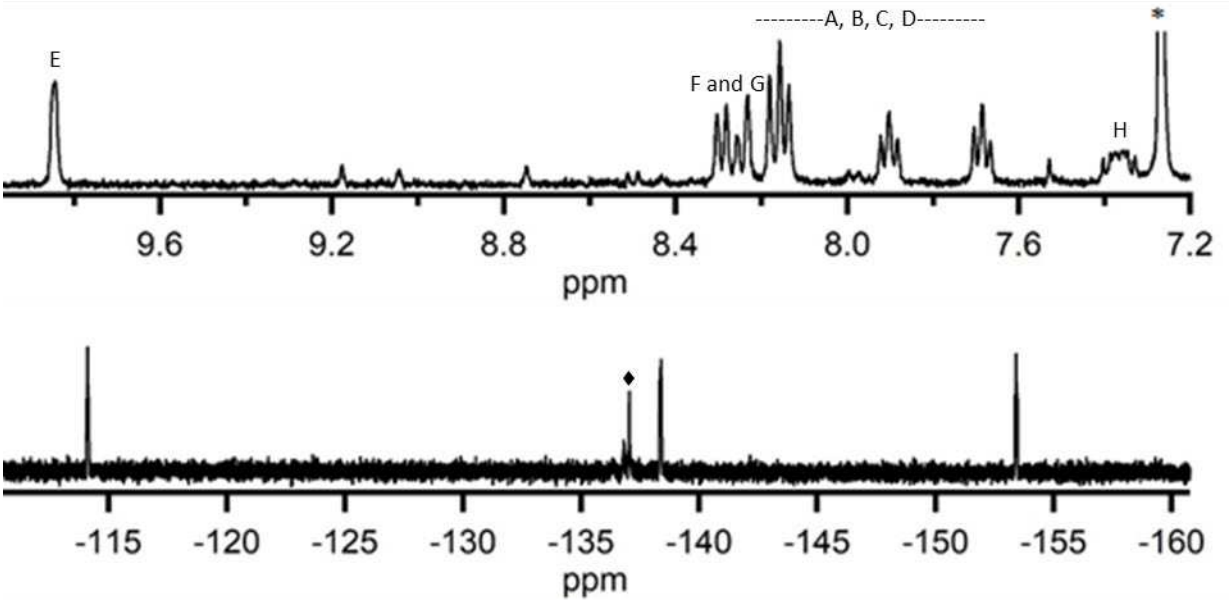

Figure C-65. NMR spectra of 1,2-(ACRD)(C_4F_3H). Product > 90% pure. ^{1}H NMR spectrum (top) referenced to $CHCl_3$ (δ = 7.26, denoted *). ^{19}F NMR spectrum (bottom) referenced to perfluorobenzene (δ = −164.9, not shown). Unidentified impurity denoted ♦. See figure below for probable peak assignments.

1H NMR ($CDCl_3$, 400 MHz): δ 9.84 (s, 1H), 8.26 (m, 2H), 8.16 (t, 2H, J = 9.7), 7.90 (t, 1H, J = 7.5), 7.69 (t, 1H, J = 7.5), 7.69 (t, 1H, J = 7.5), 7.36 (m, 1H).
19F NMR ($CDCl_3$ with C_6F_6): δ −114.2 (m, 1F), −138.4 (m, 1F), −153.4 (m, 1F).

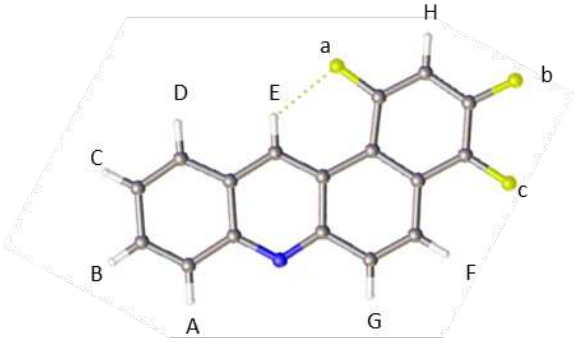

Figure C-66. Single crystal x-ray structure of 1,2-(ACRD)(C_4F_3H). Thermal ellipsoids shown at the 50% probability level.

C.2.18. CHARACTERIZATION OF 3,4-ACRD(C_4HF_3)

HPLC method: Elutes at 17.0 minutes in 2:1 methanol:acetonitrile(appx B Figure B-24).
Yield information: Minor product of reaction 2.5; <1 mg isolated(appx B.2.5).

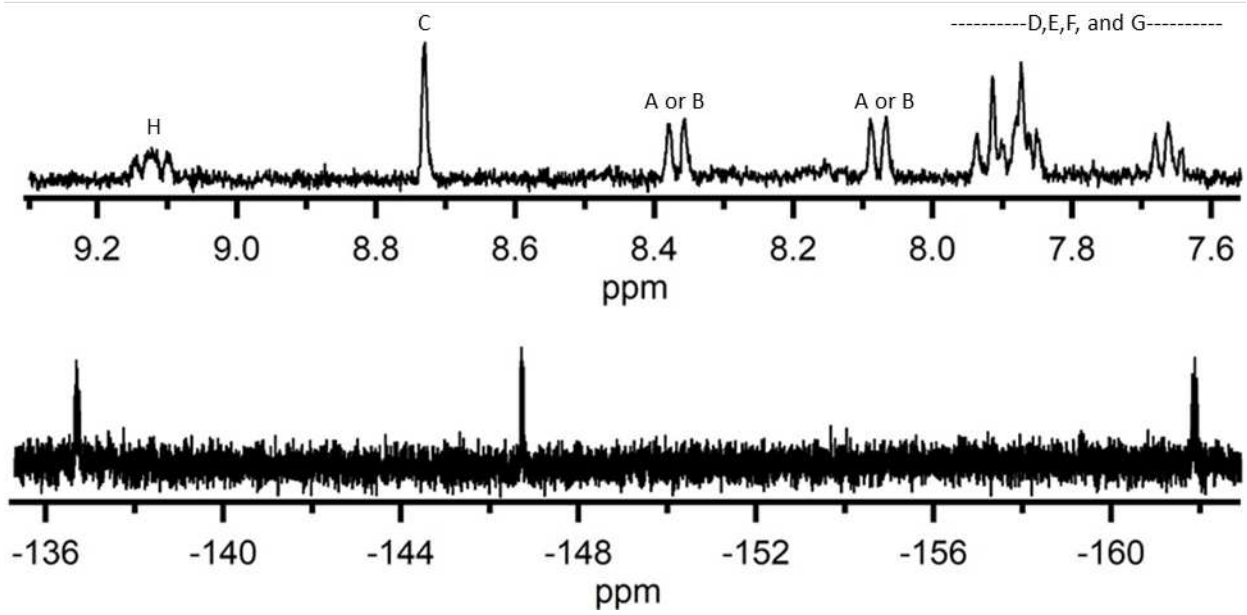

Figure C-67. NMR spectra of ACRD(C_4F_3H)-B. Product > 90% pure. ^{1}H NMR spectrum (top) referenced to $CHCl_3$ (δ = 7.26, not shown). ^{19}F NMR spectrum (bottom) referenced to perfluorobenzene (δ = −164.9, not shown). See figure below for probable peak assignments.

1H NMR ($CDCl_3$, 400 MHz): δ 9.12 (m, 1H), 8.73 (s, 1H), 8.37 (d, 1H, J = 8.4), 8.08 (d, 1H, J = 8.4), 7.89 (m, 3H), 7.66 (m, 1H).
19F NMR ($CDCl_3$ with C_6F_6): δ −136.7 (m, 1F), −146.7 (m, 1F), −161.9 (m, 1F).

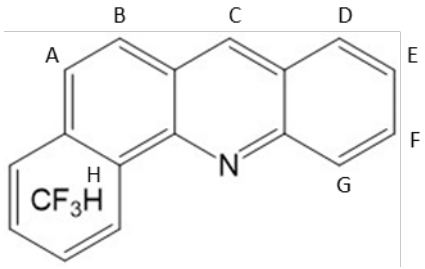

Figure C-68. Drawing of structure of 1,2-ACRD(C_4F_3H), elucidated from NMR spectra. Location of H atom on C_4F_3H moiety not definitively assigned.

C.2.19. CHARACTERIZATION OF 2,3-(9,10-ANTH(Ph)$_2$)(C$_4$F$_8$)

1,1,2,2,3,3,4,4-octafluoro-6,11-diphenyl-1,2,3,4-tetrahydrotetracene

HPLC method: Elutes at 6.2 minutes in 2:1 methanol:acetonitrile(appx B Figure B-26).
Yield information: Product of reaction 2.6; <1 mg isolated (appx B.2.6).

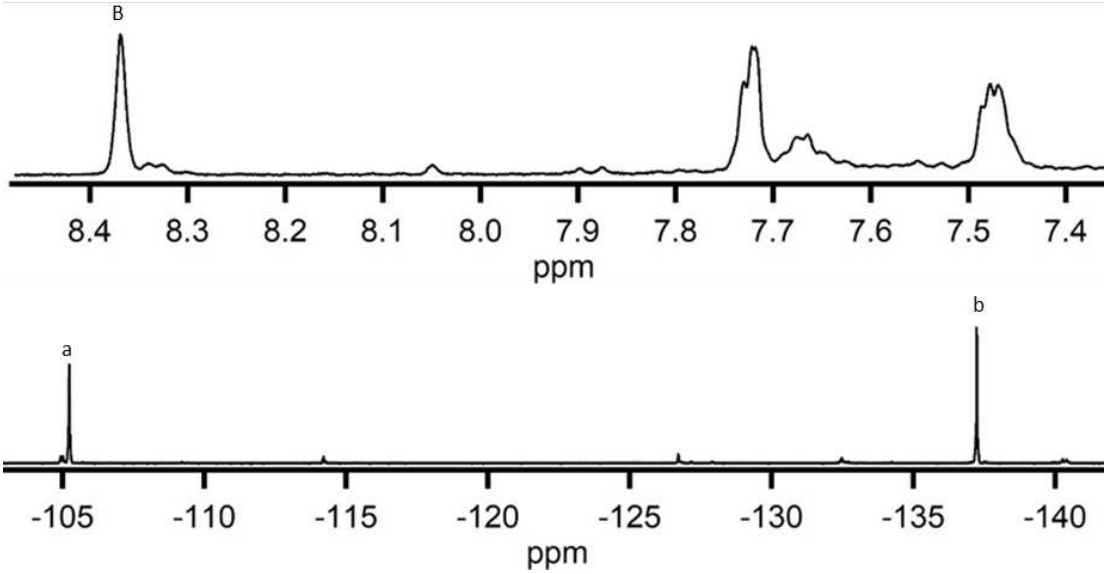

Figure C-69. NMR spectra of 2,3-(9,10-ANTH(Ph)$_2$)(C$_4$F$_8$). Product *ca.* 80% pure. ^{1}H NMR spectrum (top) referenced to $CHCl_3$ (δ = 7.26, not shown). ^{19}F NMR spectrum (bottom) referenced to perfluorobenzene (δ = –164.9, not shown).

1H NMR ($CDCl_3$, 400 MHz): δ 8.31 (s, 2H), 7.79 (m, 2H), 7.66 (m, 6H), 7.48 (m, 6H).
19F NMR ($CDCl_3$ with C_6F_6): δ −104.8 (m, 4H), −137.3 (m, 4F).

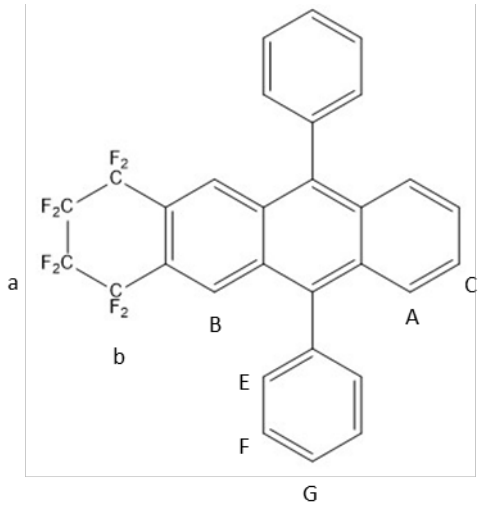

Figure C-70. Drawing of 2,3-(9,10-ANTH(Ph)$_2$)(C$_4$F$_8$), elucidated from NMR spectra.

C.2.20. CHARACTERIZATION OF 2,3;6,7-(9,10-ANTH(Ph)$_2$)(C$_4$F$_8$)$_2$

1,1,2,2,3,3,4,4-octafluoro-6,11-diphenyl-1,2,3,4-tetrahydrotetracene

HPLC method: Elutes at 4.5 minutes in 2:1 methanol:acetonitrile(appx B Figure B-26).
Yield information: Product of reaction 2.6; <1 mg isolated (appx B.2.6).

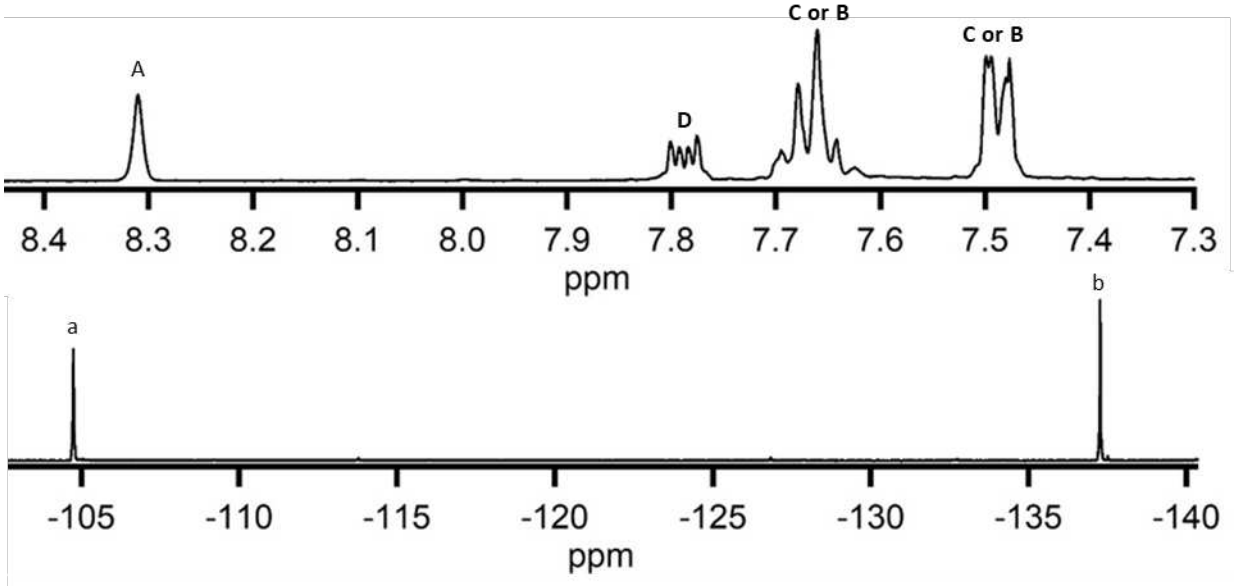

Figure C-71. NMR spectra of 2,3;6,7-(9,10-ANTH(Ph)$_2$)-(C$_4$F$_8$)$_2$ Product *ca.* 80% pure. ^{1}H NMR spectrum (top) referenced to $CHCl_3$ (δ = 7.26, not shown). ^{19}F NMR spectrum (bottom) referenced to perfluorobenzene (δ = –164.9, not shown). See figure below for probable peak assignments.

1H NMR ($CDCl_3$, 400 MHz): δ 8.37 (s, 4H), 7.72 (m, 4H), 7.66 (m, 2H), 7.48 (m, 4H).
19F NMR ($CDCl_3$ with C_6F_6): δ −105.2 (m, 8F), −137.3 (m, 8F).

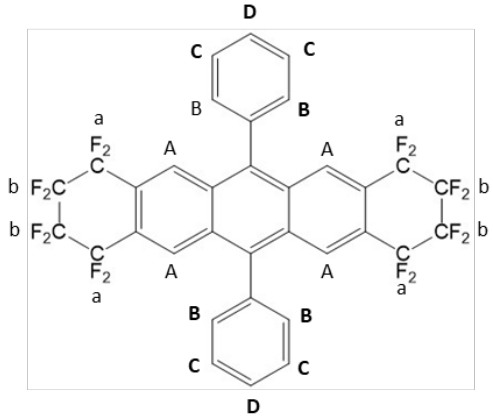

Figure C-72. Drawing of structure of 2,3;6,7-(9,10-PHEN(Ph)$_2$)(C$_4$F$_8$)$_2$, elucidated from NMR spectra. Confirmed by preliminary single crystal X-ray structure.

C.2.21. CHARACTERIZATION OF 2,3;9,10-PERY(C_4F_8)$_2$

1,1,2,2,3,3,4,4,10,10,11,11,12,12,13,13-hexadecafluoro-1,2,3,4,10,11,12,13-octahydrobenzo[*b*]cyclohepta[*lm*]perylene

HPLC method: Elutes at 3.0 minutes in 2:1 methanol:acetonitrile(appx B Figure B-28).
Yield information: Product of reaction 2.7; *ca*. 5 mg isolated (appx B.2.7).

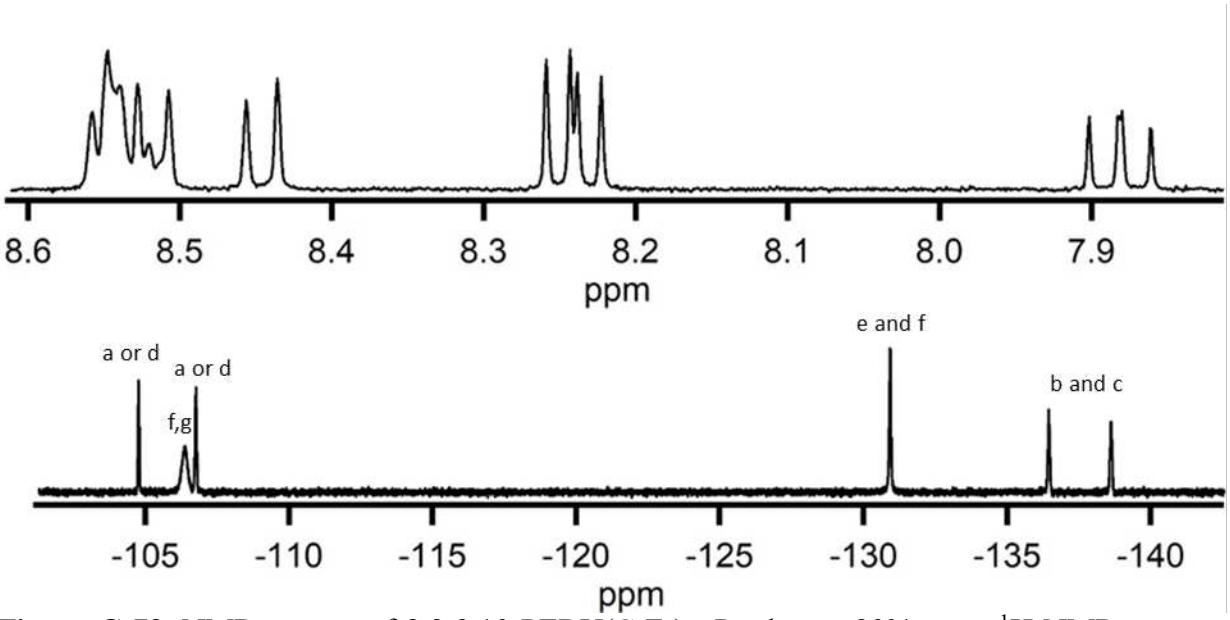

Figure C-73. NMR spectra of 2,3;9,10-PERY(C_4F_8)$_2$. Product > 90% pure. ^{1}H NMR spectrum (top) referenced to $CHCl_3$ (δ = 7.26, not shown). ^{19}F NMR spectrum (bottom) referenced to perfluorobenzene (δ = −164.9, not shown). See figure below for probable peak assignments.

1H NMR ($CDCl_3$, 400 MHz): δ 8.54 (m, 4H), 8.45 (d, 1H, J = 8.0), 8.25 (m, 2H), 7.87 (d, 1H, J = 8.0), 8.25 (m, 2H), 7.87 (m, 1H).
19F NMR ($CDCl_3$ with C_6F_6): δ −104.8 (m, 2F), −106.4 (br s, 4F), −106.8 (m, 2F), −130.9 (m, 4F), −136.5 (s, 2F), −138.6 (m, 2F).

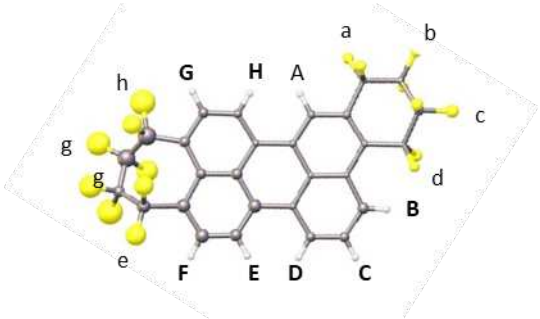

Figure C-74. Single crystal x-ray structure of 2,3;9,10-PERY(C_4F_8)$_2$. Thermal ellipsoids shown at the 50% probability level.

C.2.22. CHARACTERIZATION OF 3,4;9,10-PERY(C_4F_8)$_2$

1,1,2,2,3,3,4,4,9,9,10,10,11,11,12,12-hexadecafluoro-1,2,3,4,9,10,11,12-octahydrodicyclohepta[*cd*,*lm*]perylene

HPLC method: Elutes at 7 minutes in 2:1 methanol:acetonitrile(appx B Figure B-28).
Yield information: Major product of reaction 2.7; *ca*. 8 mg isolated (appx B.2.7).

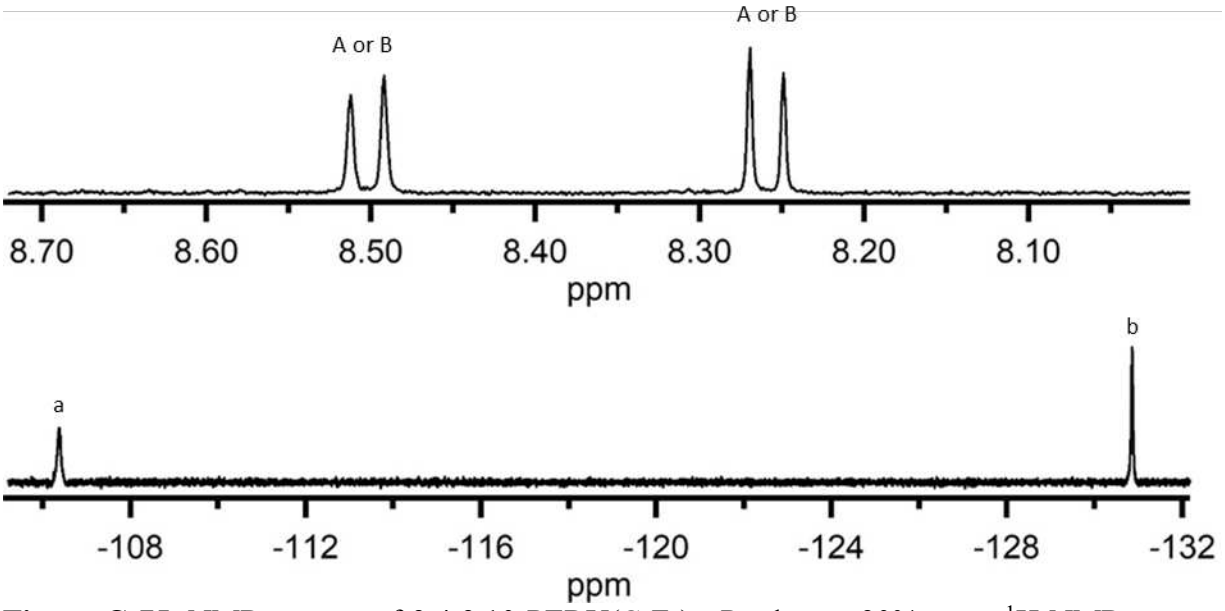

Figure C-75. NMR spectra of 3,4;9,10-PERY(C_4F_8)$_2$. Product > 90% pure. ^{1}H NMR spectrum (top) referenced to $CHCl_3$ (δ = 7.26, not shown). ^{19}F NMR spectrum (bottom) referenced to perfluorobenzene (δ = −164.9, not shown). See figure below for probable peak assignments.

1H NMR ($CDCl_3$, 400 MHz): δ 8.50 (d, 4H, J = 8.1), 8.26 (d, 1H, J = 8.1).
19F NMR ($CDCl_3$ with C_6F_6): δ −106.4 (br s, 8F), −130.9 (br s, 8F).

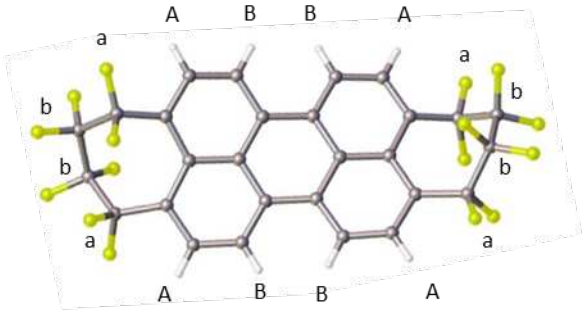

Figure C-76: Single crystal x-ray structure of 3,4;9,10-PERY(C_4F_8)$_2$. Thermal ellipsoids shown at the 50% probability level.

C.2.23. CHARACTERIZATION OF 4,5-PYRN(C_4F_8)

9,9,10,10,11,11,12,12-octafluoro-3,5,9,10,11,12-hexahydrobenzo[*e*]pyrene

crystallized from impure mixture from reaction 2.8.

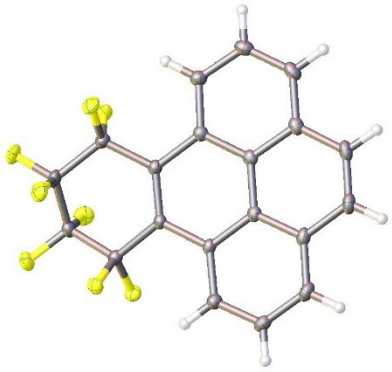

Figure C-77. Single crystal x-ray structure of 4,5-PYRN(C_4F_8). Thermal ellipsoids shown at the 50% probability

C.3.1. CHARACTERIZATION OF 1,2-PHNZ(C_4F_8)

1,1,2,2,3,3,4,4-octafluoro-1,2,3,4-tetrahydrobenzo[*a*]phenazine

HPLC method: Eluted at 6.8 minutes in acetonitrile (appx B Figure B-31).
Yield information: Major product of reactions 3.1 and 3.5. From reaction 1, 9 mg isolated >95% pure by ^{1}H and ^{19}F NMR spectroscopy, for a 20% isolated yield (appx B.3.1 and B.3.5).

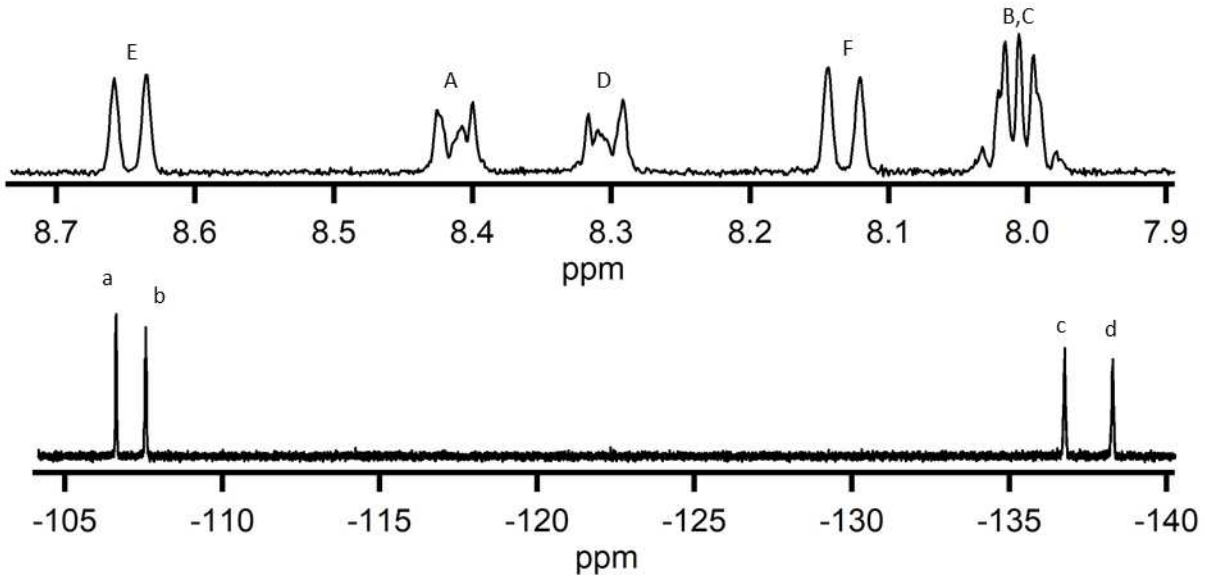

Figure C-78. NMR spectra of 1,2-PHNZ(C_4F_8)**.** Product > 98% pure. ^{1}H NMR spectrum (top) referenced to $CHCl_3$ (δ = 7.26, not shown). ^{19}F NMR spectrum (bottom) referenced to perfluorobenzene (δ = –164.9, not shown). See figure below for probable peak assignments.

1H NMR ($CDCl_3$, 400 MHz): δ 8.64 (d, J=8.5 Hz, 1H), 8.40 (m, 1H), 8.30 (m, 1H), 8.12 (d, J=8.5 Hz, 1H), 8.00 (m, 2H).
19F NMR ($CDCl_3$ with C_6F_6, 376 MHz): δ −106.6 (m, 2F), −107.6 (m, 2F), −136.7 (m, 2F), −138.3 (m, 2F).

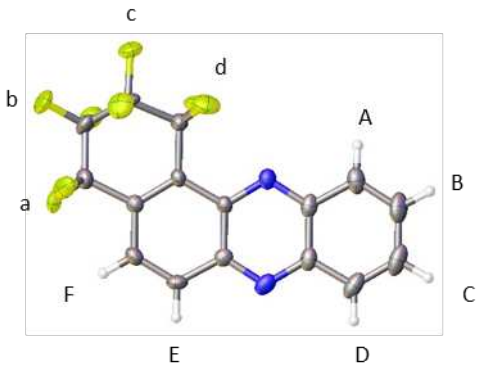

Figure C-79. Single crystal x-ray structure of 1,2-PHNZ(C_4F_8). Thermal ellipsoids shown at the 50% probability level.

C.3.2. CHARACTERIZATION OF 2,3-PHNZ(C_4F_8)

1,1,2,2,3,3,4,4-octafluoro-1,2,3,4-tetrahydrobenzo[*a*]phenazine

HPLC method: Eluted at 8.2 minutes in acetonitrile(appx B Figure B-31).
Yield information: Major product of reactions 3.1 and 3.5. From reaction 1, 4 mg isolated >95% pure by ^{1}H and ^{19}F NMR spectroscopy, for a 9% isolated yield(appx B.3.1 and B.3.5).

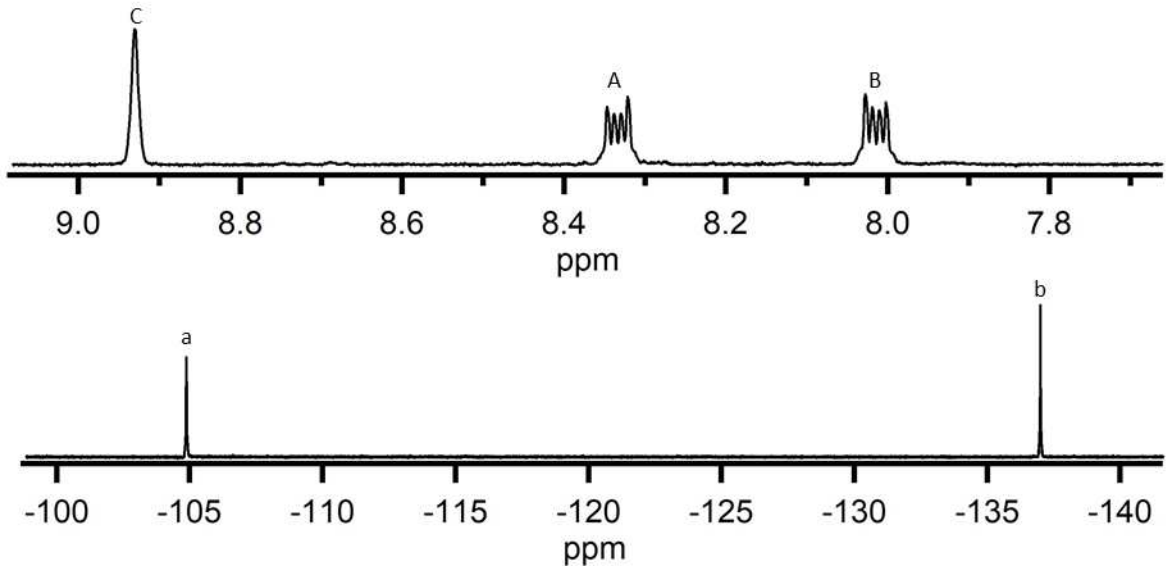

Figure C-80. NMR spectra of 1,2-PHNZ(C_4F_8)**.** Product > 98% pure. ^{1}H NMR spectrum (top) referenced to $CHCl_3$ (δ = 7.26, not shown). ^{19}F NMR spectrum (bottom) referenced to perfluorobenzene (δ = −164.9, not shown). See figure below for probable peak assignments.

1H NMR ($CDCl_3$, 400 MHz): δ 8.92 (s, 2H), 8.33 (m, 2H), 8.01 (m, 2H).
19F NMR ($CDCl_3$ with C_6F_6, 376 MHz): δ −104.9 (m, 4F), −137.0 (m, 4F).

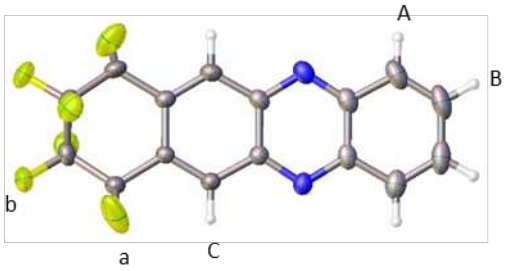

Figure C-81. Single crystal x-ray structure of 2,3-PHNZ(C_4F_8). Thermal ellipsoids shown at the 50% probability level.

C.3.3. CHARACTERIZATION OF 1,2;6,7-PHNZ(C_4F_8)$_2$

1,1,2,2,3,3,4,4,8,8,9,9,10,10,11,11-hexadecafluoro-1,2,3,4,8,9,10,11-octahydrodibenzo[*a*,*h*]phenazine

HPLC method: Eluted at 7.5 minutes in acetonitrile(appx B Figure B-31).
Yield information: Major product of reactions 3.1 and 3.2. From reaction 1, 7 mg isolated >95% pure by ^{1}H and ^{19}F NMR spectroscopy, for a 15% isolated yield(appx B.3.1 and B.3.2).

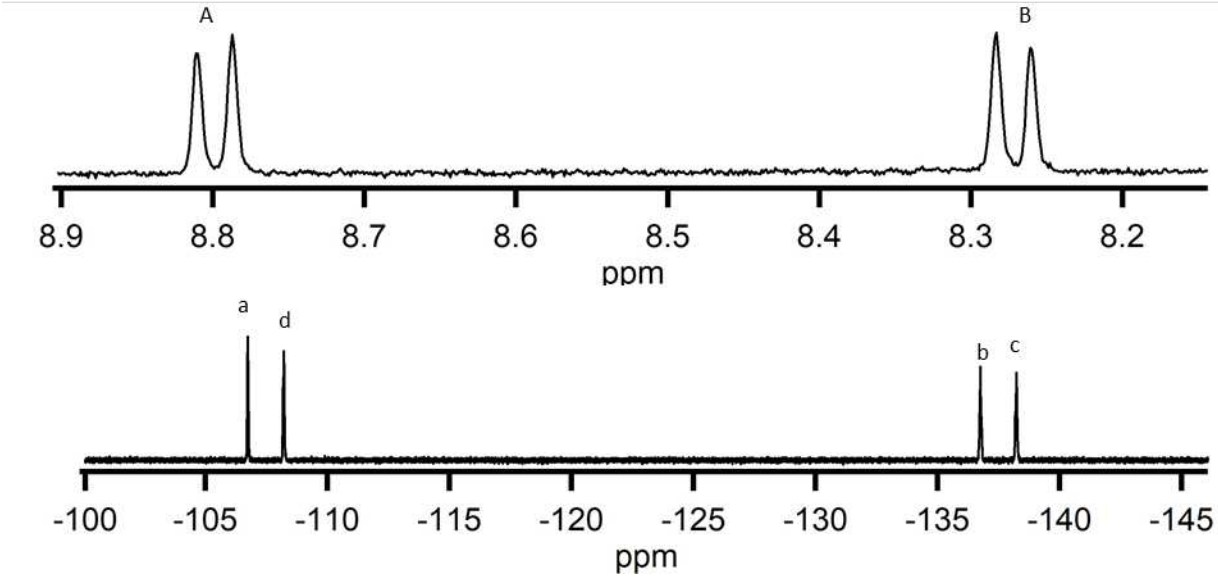

Figure C-82. NMR spectra of 1,2;6,7-PHNZ(C_4F_8)$_2$. Product > 98% pure. ^{1}H NMR spectrum (top) referenced to $CHCl_3$ (δ = 7.26, not shown). ^{19}F NMR spectrum (bottom) referenced to perfluorobenzene (δ = −164.9, not shown). See figure below for probable peak assignments.

1H NMR ($CDCl_3$, 400 MHz): δ 8.79 (d, J=10.0 Hz, 2H), 8.26 (d, J=10.0 Hz, 2H).
19F NMR ($CDCl_3$ with C_6F_6, 376 MHz): δ −106.7 (m, 2F), −108.2 (m, 2F), −136.7 (m, 2F), −138.2 (m, 2F).

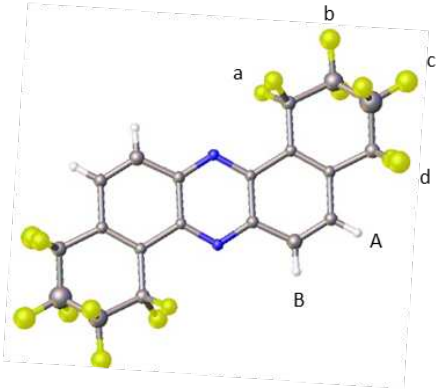

Figure C-83. Single crystal x-ray structure of 1,2;6,7-PHNZ(C_4F_8)$_2$. Thermal ellipsoids shown at the 50% probability level.

C.3.4. CHARACTERIZATION OF 1,2;7,8-PHNZ(C_4F_8)$_2$

1,1,2,2,3,3,4,4,9,9,10,10,11,11,12,12-hexadecafluoro-1,2,3,4,9,10,11,12-octahydrodibenzo[*a*,*i*]phenazine

HPLC method: eluted at 18 minutes in 1:1 methanol:acetonitrile (appx B Figure B-31).
Yield information: Product of reaction 3.2. From a representative sample, *ca*. 5 mg isolated >95% pure by ^{1}H and ^{19}F NMR spectroscopy (appx B.3.2).

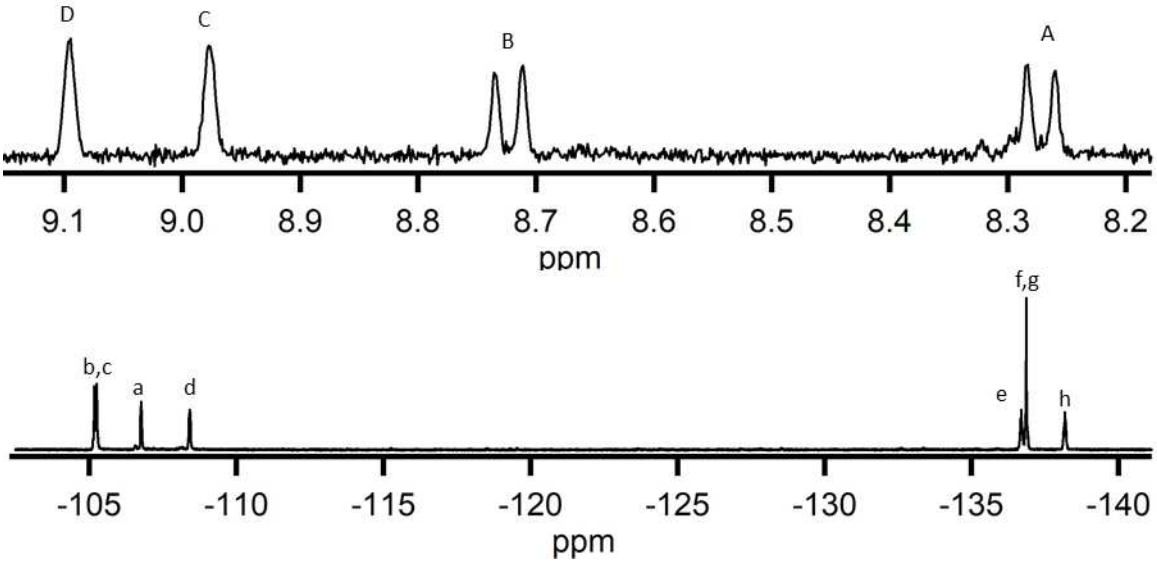

Figure C-84. NMR spectra of 1,2;7,8-PHNZ(C_4F_8)$_2$. Product > 98% pure. ^{1}H NMR spectrum (top) referenced to $CHCl_3$ (δ = 7.26, not shown). ^{19}F NMR spectrum (bottom) referenced to perfluorobenzene (δ = −164.9, not shown). See figure below for probable peak assignments.

1H NMR ($CDCl_3$, 400 MHz): δ 9.07 (s, 1H), 8.96 (s, 1H), 8.71 (d, J=9.0 Hz, 2H), 8.25 (d, J = 9.0, 1H).
19F NMR ($CDCl_3$ with C_6F_6, 376 MHz): δ −105.2 (m, 2F), −105.3 (m, 2F), −106.8 (m, 2F), −106.8 (m, 2F), −108.4 (m, 2F), −136.7 (m, 2F), −136.9 (m, 4F), −138.2 (m, 2F).

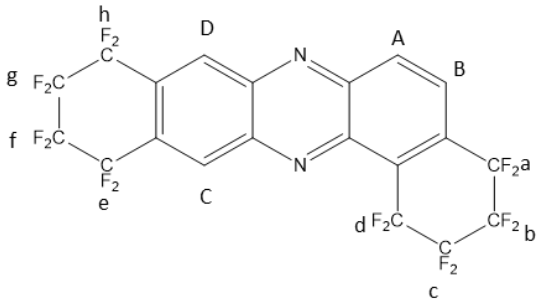

Figure C-85. Drawing of structure of 1,2;7,8-PHNZ(C_4F_8)$_2$, elucidated from NMR spectra.

C.3.5. CHARACTERIZATION OF 1,2;8.9-PHNZ(C_4F_8)$_2$

1,1,2,2,3,3,4,4,10,10,11,11,12,12,13,13-hexadecafluoro-1,2,3,4,10,11,12,13-octahydrodibenzo[*a*,*j*]phenazine

HPLC method: eluted at 19 minutes in 1:1 methanol:acetonitrile (appx B Figure B-34).
Yield information: Major product of reactions 3.2. From reaction 3.1, *ca*. 7 mg isolated >95% pure by ^{1}H and ^{19}F NMR spectroscopy (appx B.3.2).

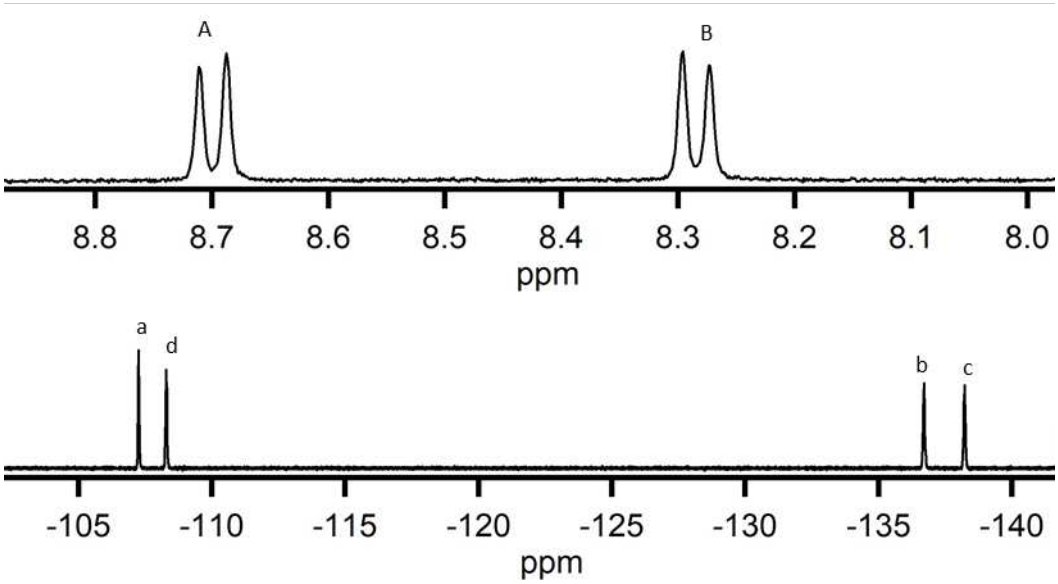

Figure C-86. NMR spectra of 1,2;8,9-PHNZ(C_4F_8)$_2$. Product > 98% pure. ^{1}H NMR spectrum (top) referenced to $CHCl_3$ (δ = 7.26, not shown). ^{19}F NMR spectrum (bottom) referenced to perfluorobenzene (δ = −164.9, not shown). See figure below for probable peak assignments.

1H NMR ($CDCl_3$, 400 MHz): δ 8.69 (d, J=9.5 Hz, 2H), 8.28 (d, J = 9.5, 2H).
19F NMR ($CDCl_3$ with C_6F_6, 376 MHz): δ −107.3 (m, 4F), −108.3 (m, 4F), −136.7 (m, 4F), −138.3 (m, 4F).

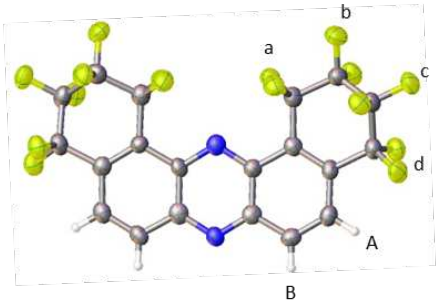

Figure C-87. Single crystal x-ray structure of 1,2;8.9-PHNZ(C_4F_8)$_2$. Thermal ellipsoids shown at the 50% probability level.

C.3.6. CHARACTERIZATION OF 1,2-PHNZ(C_4F_4)

1,2,3,4-tetrafluorobenzo[*a*]phenazine

HPLC method: eluted at 25 minutes in acetonitrile (appx B Figure B-36).
Yield information: Isolated from reaction 3.3. From a representative sample, <1 mg isolated (appx B.3.3).

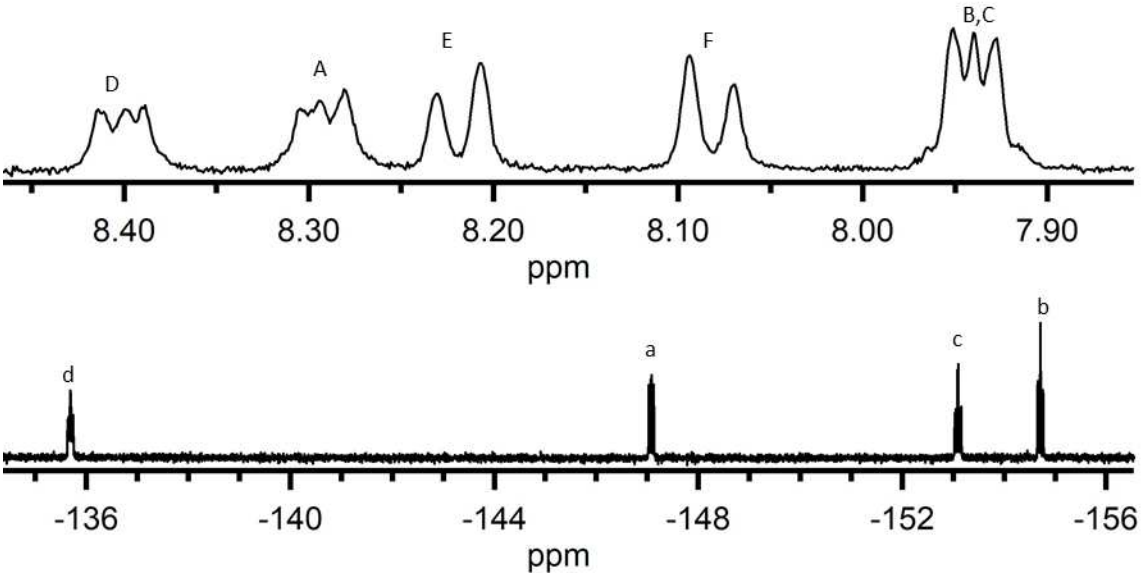

Figure C-88. NMR spectra of 1,2-PHNZ(C_4F_4). Product > 98% pure. ^{1}H NMR spectrum (top) referenced to $CHCl_3$ (δ = 7.26, not shown). ^{19}F NMR spectrum (bottom) referenced to perfluorobenzee (δ = −164.9, not shown). See figure below for probable peak assignments.

1H NMR ($CDCl_3$, 400 MHz): δ 8.42 (m, 1H), 8.31 (m, 1H), 8.24 (d, J=10, 1H), 8.11 (d, J=10, 1H), 7.96 (m, 2H).
19F NMR ($CDCl_3$ with C_6F_6, 376 MHz): δ −138.6 (m, 1F), −150.2 (m, 1F), −156.2 (m, 1F), −154.8 (m, 1F).

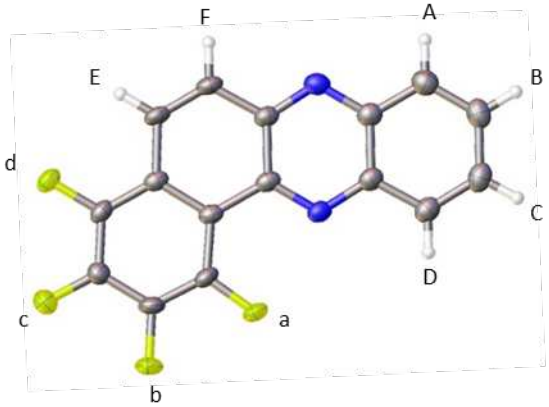

Figure C-89. Single crystal x-ray structure of 1,2-PHNZ(C_4F_4). Thermal ellipsoids shown at the 50% probability level.

C.3.7. CHARACTERIZATION OF 1,2-PHNZ(C_4F_3H)

2,3,4-trifluorobenzo[*a*]phenazine

HPLC method: Eluted at 6 minutes in 2:1 toluene: isopropyl alcohol(appx B Figure B-38).
Yield information: Isolated from reaction 3.4. From this reaction, <1 mg isolated (appx B.3.4).

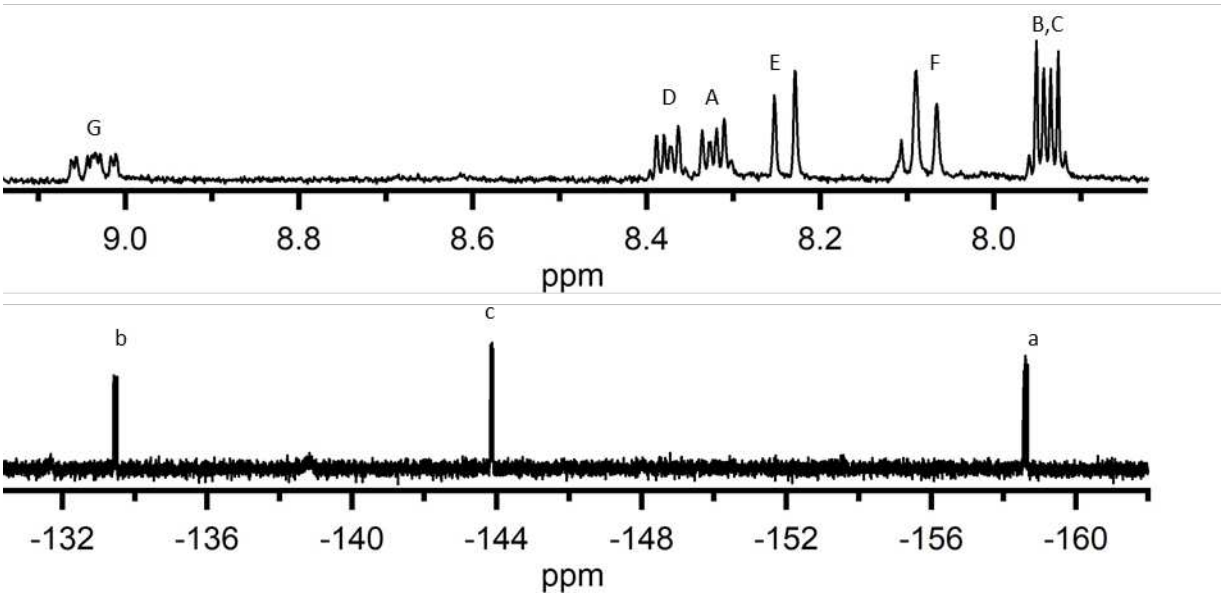

Figure C-90. NMR spectra of 1,2-PHNZ(C_4F_3H). Product > 98% pure. ^{1}H NMR spectrum (top) referenced to $CHCl_3$ (δ = 7.26, not shown). ^{19}F NMR spectrum (bottom) referenced to perfluorobenzene (δ = −164.9, not shown). See figure below for probable peak assignments.

1H NMR ($CDCl_3$, 400 MHz): δ 9.04 (m, 1H), 8.37 (m, 1H), 8.33 (m, 1H), 8.24 (d, J=10, 1H), 8.08 (d, J=10, 1H), 7.94 (m, 2H).
19F NMR ($CDCl_3$ with C_6F_6, 376 MHz): δ −133.4 (m, 1F), −143.9 (m, 1F), −153.6 (m, 1F).

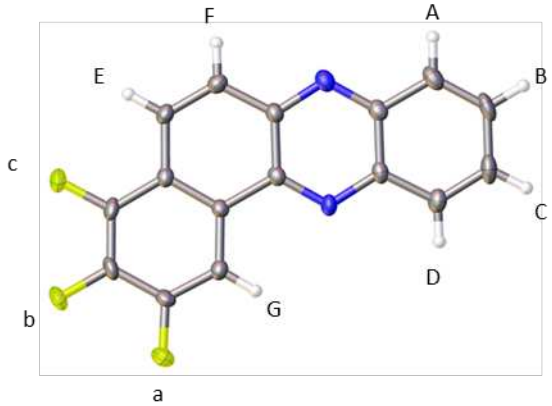

Figure C-91. Single crystal x-ray structure of 1,2-PHNZ(C_4F_3H). Thermal ellipsoids shown at the 50% probability level.

C.3.8. CHARACTERIZATION OF 1,2;7,8-PHNZ(C_4F_8)(C_4F_4)

1,1,2,2,3,3,4,4,9,10,11-undecafluoro-1,2,3,4-tetrahydrodibenzo[*a*,*h*]phenazine

HPLC method: Crystallized from an impure fraction eluting at 9.2 minutes.
Yield information: Isolated from reaction 3.4 (appx B.3.4).

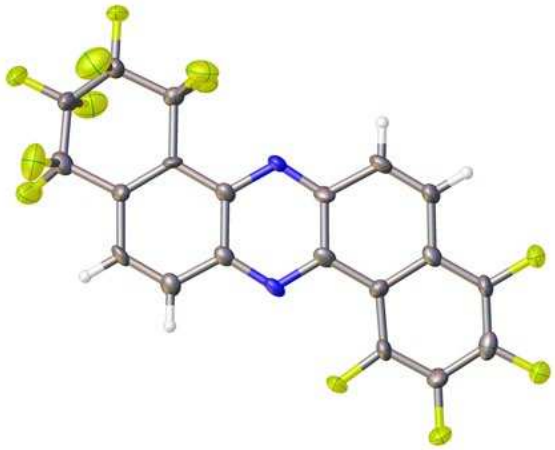

Figure C-92. Single crystal x-ray structure of 1,2-PHNZ(C_4F_3H). Thermal ellipsoids shown at the 50% probability level.

C.3.9. CHARACTERIZATION OF 1-PHNZ(C_4F_8I)

1-(1,1,2,2,3,3,4,4-octafluoro-4-iodobutyl)phenazine

HPLC method: Eluted at 7.1 min in methanol(appx B Figure B-40).
Yield information: From a representative sample of reaction 3.5, <1 mg isolated(appx B.3.5).

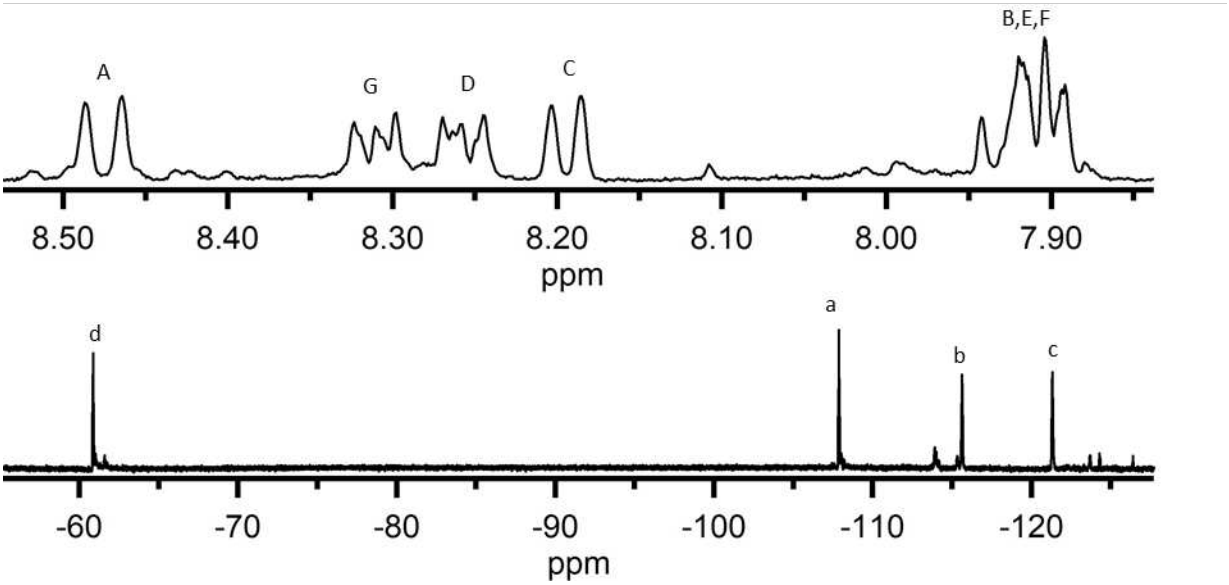

Figure C-93. NMR spectra of 1-PHNZ(C_4F_8I). Product > 98% pure. ^{1}H NMR spectrum (top) referenced to $CHCl_3$ (δ = 7.26, not shown). ^{19}F NMR spectrum (bottom) referenced to perfluorobenzene (δ = −164.9, not shown). See figure below for probable peak assignments.

1H NMR ($CDCl_3$, 400 MHz): δ 8.48 (d, J=10 Hz, 1H), 8.32 (m, 1H), 8.26 (m, 1H), 8.19 (d, J=10, 1H), 7.91 (m, 3H).
19F NMR ($CDCl_3$ with C_6F_6, 376 MHz): δ −60.2 (m, 1F), −107.8 (m, 1F), −115.5 (m, 1F), −121.9 (m, 1F).

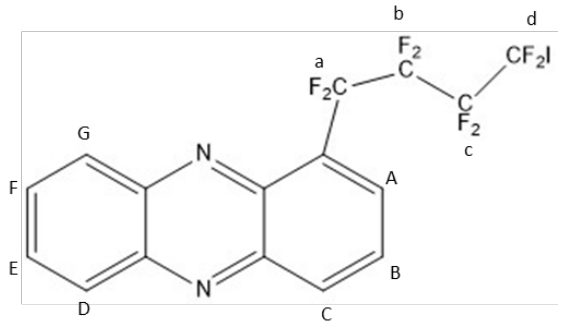

Figure C-94. Drawing of structure of 1-PHNZ(C_4F_8I), elucidated from NMR spectra.

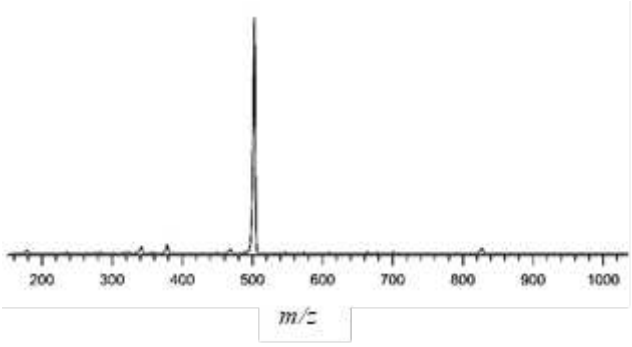

Figure C-95. Mass spectrum of 1-PHNZ(C_4F_8I). Peak at 506 *m/z*.

C.3.10. CHARACTERIZATION OF 2-PHNZ(C_4F_8I)

2-(1,1,2,2,3,3,4,4-octafluoro-4-iodobutyl)phenazine

HPLC method: Eluted at 4.7 min in methanol(appx B Figure B-40).
Yield information: From a representative sample of reaction 3.5, <1 mg isolated(appx B.3.5).

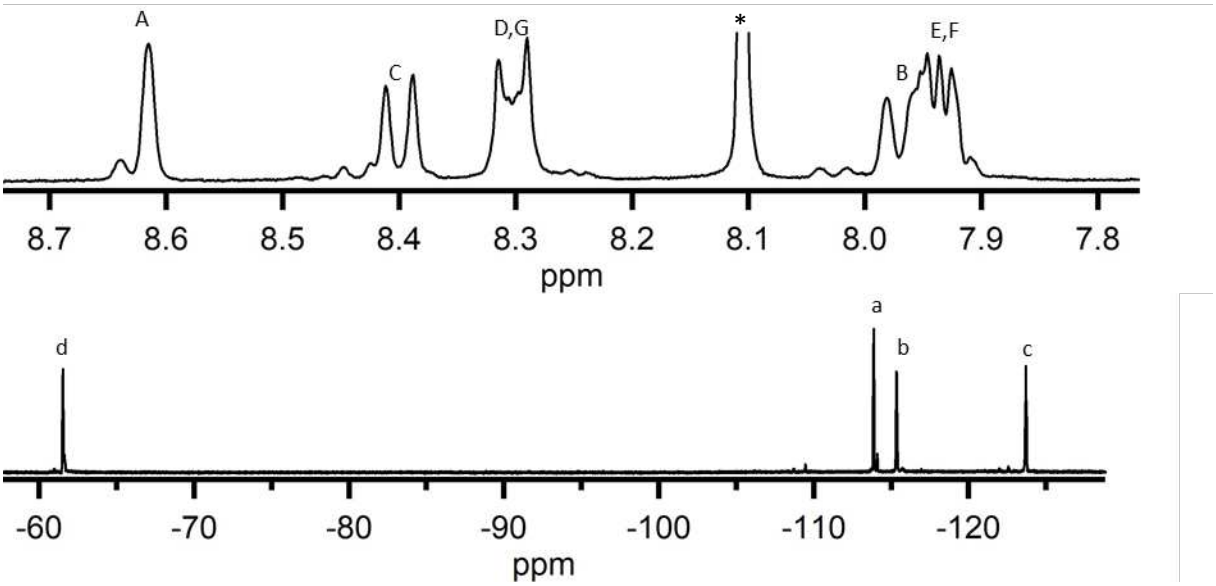

Figure C-96. NMR spectra of 2-PHNZ(C_4F_8I). Product > 98% pure. ^{1}H NMR spectrum (top) referenced to $CHCl_3$ (δ = 7.26, not shown). ^{19}F NMR spectrum (bottom) referenced to perfluorobenzene (δ = −164.9, not shown). Unknown impurity denoted *. See figure below for probable peak assignments.

1H NMR ($CDCl_3$, 400 MHz): δ 8.47 (d, J=8, 1H), 8.31 (m, 1H), 8.19 (d, J=8, 1H), 7.91 (m, 3H).
19F NMR ($CDCl_3$ with C_6F_6, 376 MHz): δ −60.6 (m, 2F), −107.9 (m, 2F), −115.6 (m, 1F), −121.3 (m, 2F).

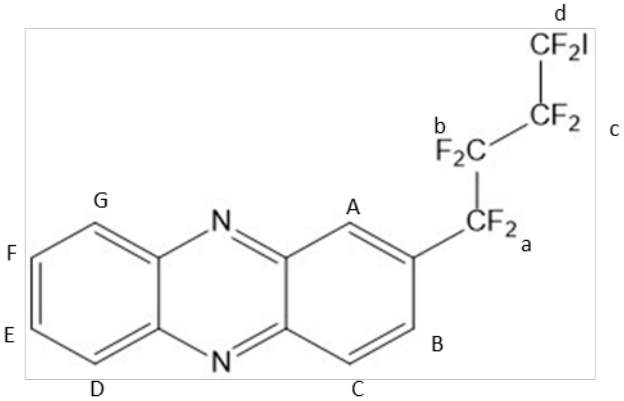

Figure C-97. Drawing of structure of 2-PHNZ(C_4F_8I), elucidated from NMR spectra.

C.3.11. CHARACTERIZATION OF PHNZ($C_4F_8I_2$)-A

HPLC method: Eluted at 4.1 min in methanol(appx B Figure B-40).
Yield information: From a representative sample of reaction 3.5, <1 mg isolated(appx B.3.5).

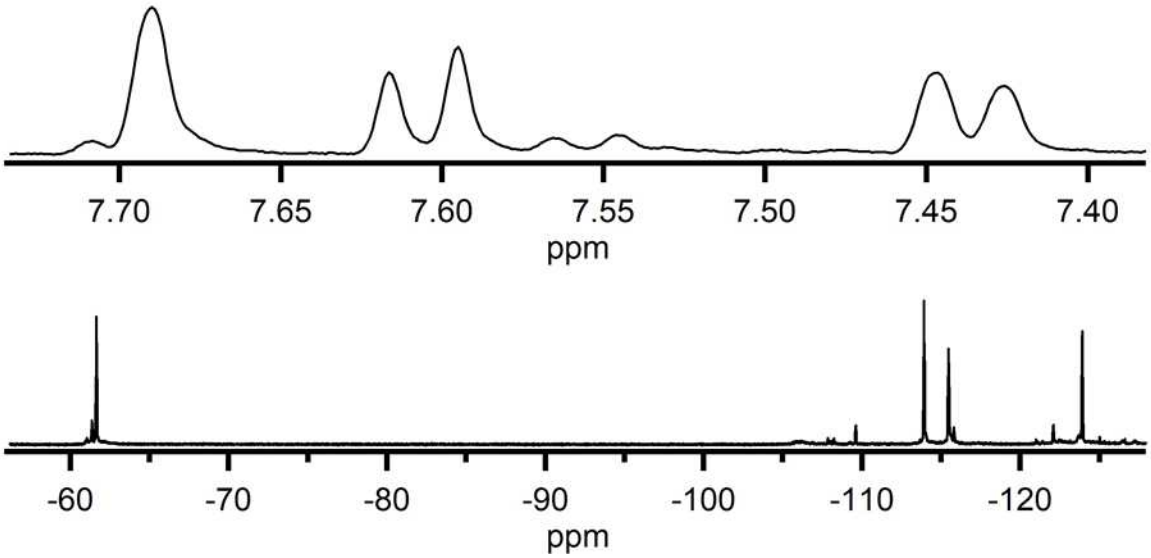

Figure C-98. NMR spectra of PHNZ($C_4F_8I_2$)-A. Product > 98% pure. ^{1}H NMR spectrum (top) referenced to $CHCl_3$ (δ = 7.26, not shown). ^{19}F NMR spectrum (bottom) referenced to perfluorobenzene (δ = −164.9, not shown). See figure below for probable peak assignments.

1H NMR ($CDCl_3$, 400 MHz): δ 7.69 (s, 2H), 7.61 (d J-8, 2H), 7.44 (d, J=8, 2H).
19F NMR ($CDCl_3$ with C_6F_6, 376 MHz): δ −61.7 (m, 4F), −113.9 (m, 4F), −115.5 (m, 4F), −123.9 (m, 4F).

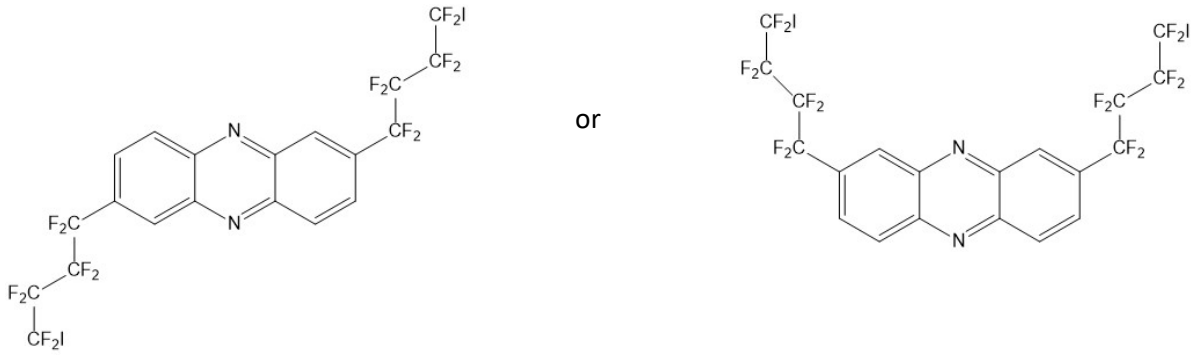

Figure C-99. Possible structures of PHNZ($C_4F_8I_2$)-A elucidated from NMR spectra,

C.4.1. CHARACTERIZATION OF ACRD(CF_3)$_3$-A

HPLC method: Multi-stage isolation on COSMOSIL Buckyprep semi-preparative column (Figure 4-2/B-45). Flow rate 5 mL min^{-1} in indicated eluent. Stage 1: acetonitrile, 5.0 min (F1). Stage 2: 1:3 toluene:heptane, 5.0 min (pure compound), (appx B Figure B-42).
Yield information: Product of reaction 4.1; <5 mg pure compound isolated(appx B.4.1).

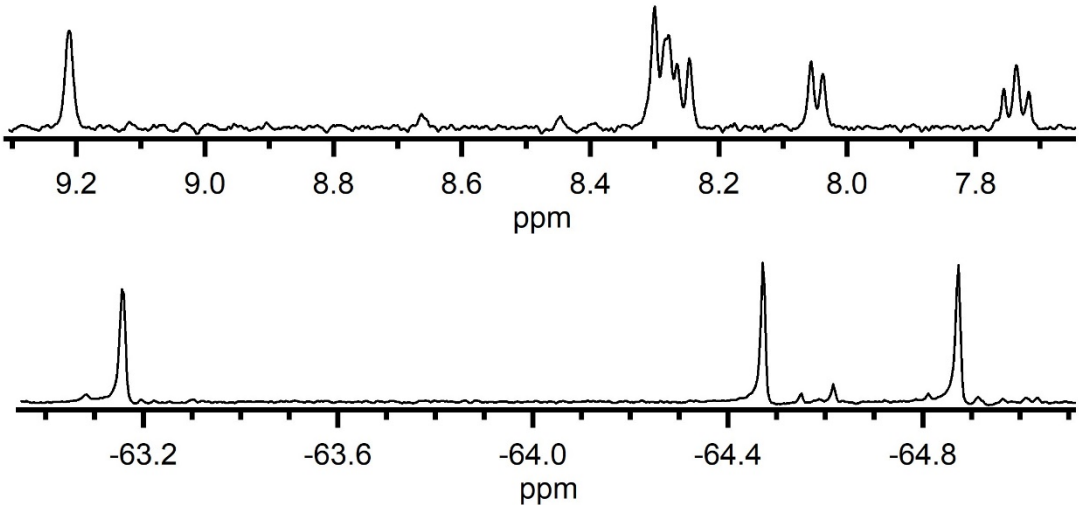

Figure C-100. NMR spectra of ACRD(CF_3)$_4$-A. Product *ca.* 85% pure. ^{1}H NMR spectrum (top) referenced to $CHCl_3$ (δ = 7.26, not shown). ^{19}F NMR spectrum (bottom) referenced to perfluorobenzene (δ = –164.9, not shown). See figure below for possible structural assignments.

1H NMR ($CDCl_3$, 400 MHz): δ 9.21(s, 1H), 8.30(s, 1H), 8.28(s, 1H), 8.27 (d, J=8.1 Hz, 1H), 8.05(d, J=6.2 Hz, 1H), 7.74 (m, 1H).
19F NMR ($CDCl_3$ with C_6F_6, 376 MHz): δ −53.2(s, 1CF_3), −64.5(s, 1CF_3), −64.9(s, 1CF_3).

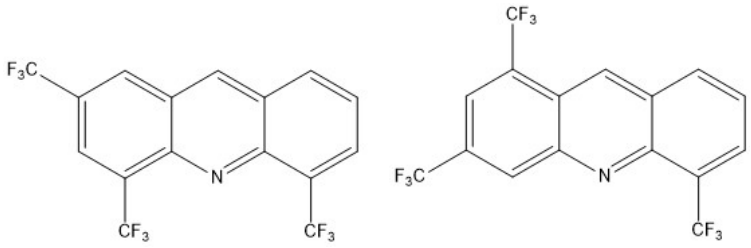

Figure C-101. Drawing of possible structures of ACRD(CF_3)$_4$-A , elucidated from NMR spectra and reaction trends (rare for positions next to N atom not to undergo substitution).

C.4.2. CHARACTERIZATION OF 2,4,5,9-ACRD(CF_3)$_4$

2,4,5,9-tetrakis(trifluoromethyl)acridine

HPLC method: Multi-stage isolation on COSMOSIL Buckyprep semi-preparative column (Figure 4-2/B-45). Flow rate 5 mL min^{-1} in indicated eluent. Stage 1: acetonitrile, 6.0 min (F2). Stage 2: 1:3 toluene:heptane, 4.2 min (pure compound), (appx B Figure B-42).
Yield information: Product of reaction 4.1; *ca.* 5 mg pure compound isolated(appx B.4.1).

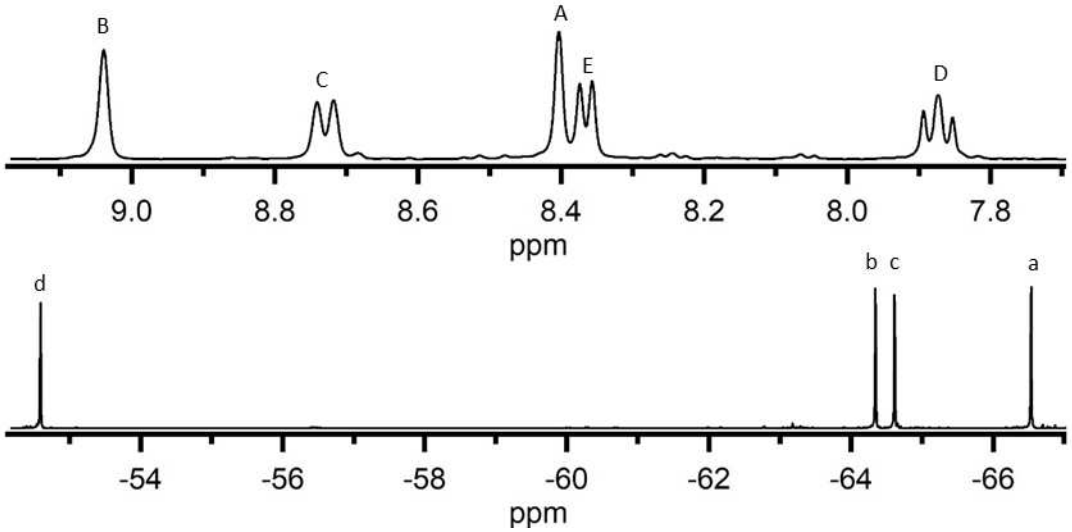

Figure C-102. NMR spectra of 2,4,5,9-ACRD(CF_3)$_4$. Product > 95% pure. ^{1}H NMR spectrum (top) referenced to $CHCl_3$ (δ = 7.26, not shown). ^{19}F NMR spectrum (bottom) referenced to perfluorobenzene (δ = −164.9, not shown). See figure below for probable peak assignments.

1H NMR ($CDCl_3$, 400 MHz): δ 9.04 (s, 1H), 8.73 (d, J=9.6 Hz, 1H), 8.40 (s, 1H), 8.36 (d, J=7.3 Hz, 1H), 7.87 (m, 1H).
19F NMR ($CDCl_3$ with C_6F_6, 376 MHz): δ −52.6(s, 1CF_3), −64.3(s, 1CF_3), −64.6(s, 1CF_3), −66.5(s, 1CF_3).

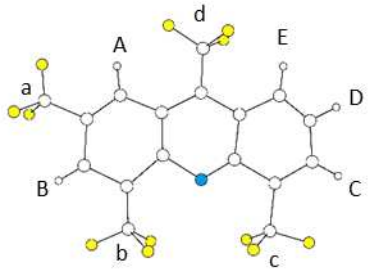

Figure C-103. Preliminary single crystal x-ray structure of 2,4,5,9-ACRD(CF_3)$_4$.

C.4.3. CHARACTERIZATION OF 2,4,6,9-ACRD(CF_3)$_4$

2,4,6,9-tetrakis(trifluoromethyl)acridine

HPLC method: Multi-stage isolation; Stages 1, 2, and 3 on COSMOSIL Buckyprep semi-preparative column Flow rate 5 mL min^{-1} in indicated eluent.; Stage 4 on Fluroflash analytical column, 1 mL min^{-1} (Figure 4-2/B-45). Stage 1: acetonitrile, 7.0 min (F3). Stage 2: 1:3 toluene:heptane, 4.5 min (F3F1). Stage 3: heptane, 8.0 min. Stage 4: acetonitrile, 6.1 min (pure compound), (appx B Figure B-42).
Yield information: Product of reaction 4.1; <5 mg pure compound isolated(appx B.4.1).

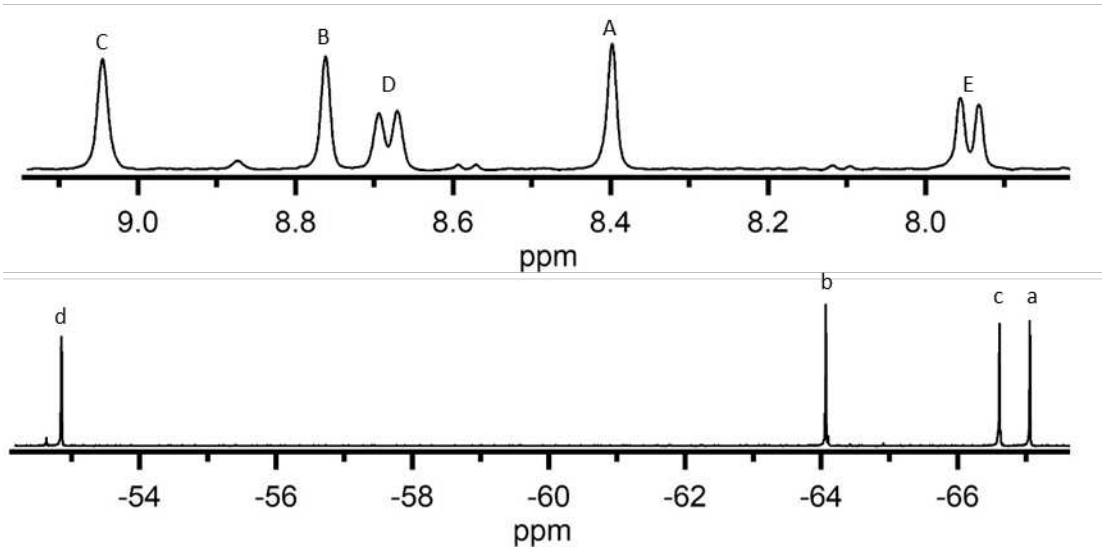

Figure C-104. NMR spectra of 2,4,6,9-ACRD(CF_3)$_4$. Product > 95% pure. ^{1}H NMR spectrum (top) referenced to $CHCl_3$ (δ = 7.26, not shown). ^{19}F NMR spectrum (bottom) referenced to perfluorobenzene (δ = –164.9, not shown). See figure below for probable peak assignments.

1H NMR ($CDCl_3$, 400 MHz): δ 9.04(s, 1H), 8.76(s, 1H), 8.67(d, J=10.3 Hz, 1H), 8.40(s, 1H), 7.95(d, J=10.3 Hz, 1H).
19F NMR ($CDCl_3$ with C_6F_6, 376 MHz): δ −52.8(s, 1CF_3), −64.1(s, 1CF_3), −66.6(s, 1CF_3), −67.1(s, 1CF_3).

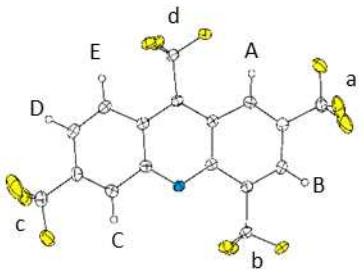

Figure C-105. Single crystal x-ray structure of 2,4,6,9-ACRD(CF_3)$_4$. Thermal ellipsoids shown at the 50% probability level.

C.4.4. CHARACTERIZATION OF 1,4,5,7-ACRD(CF_3)$_4$

1,4,5,7-tetrakis(trifluoromethyl)acridine

HPLC method: Multi-stage isolation on COSMOSIL Buckyprep semi-preparative column (Figure 4-2/B-45). Flow rate 5 mL min^{-1} in indicated eluent. Stage 1: acetonitrile, 5.0 min (F1). Stage 2: 1:3 toluene:heptane, 7.0 min (pure compound), (appx B Figure B-42).
Yield information: Product of reaction 4.1; *ca.* 5 mg pure compound isolated(appx B.4.1).

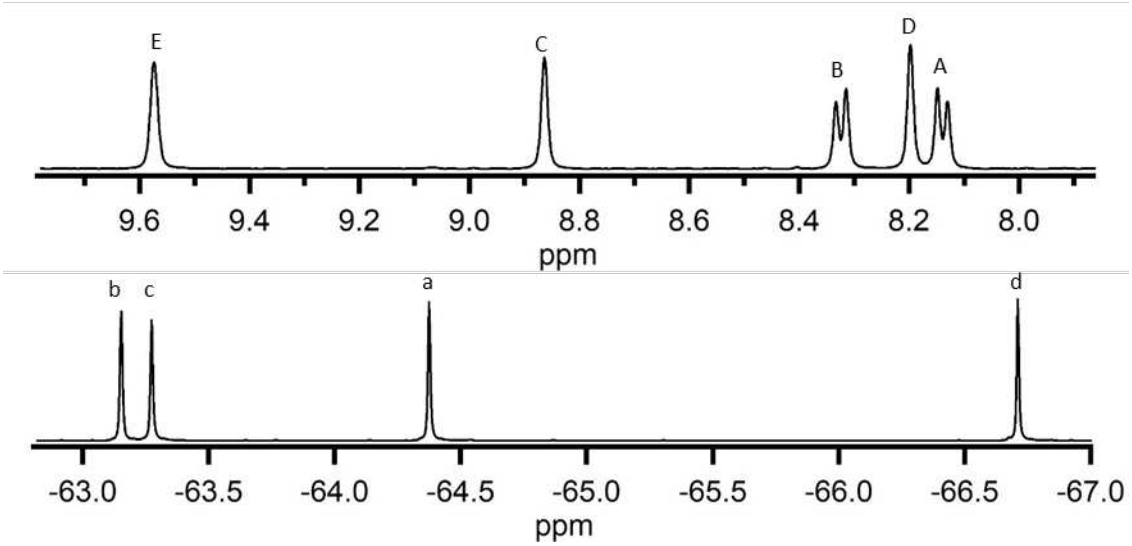

Figure C-106. NMR spectra of 1,4,5,7-ACRD(CF_3)$_4$. Product > 98% pure. ^{1}H NMR spectrum (top) referenced to $CHCl_3$ (δ = 7.26, not shown). ^{19}F NMR spectrum (bottom) referenced to perfluorobenzene (δ = −164.9, not shown). See figure below for probable peak assignments.

1H NMR ($CDCl_3$, 400 MHz): δ 9.36(s, 1H), 8.65(s, 1H), 8.40(s, 1H), 8.34(d, J=7.0 Hz, 1H), 8.12 (d, J=7.0 Hz, 1H).
19F NMR ($CDCl_3$ with C_6F_6, 376 MHz): **δ** −63.1(s, 1CF_3), −64.8(s, 1CF_3), −64.9(s, 1CF_3), −66.3(s, 1CF_3).

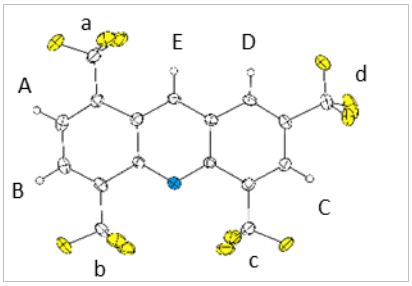

Figure C-107. Single crystal x-ray structure of 1,4,5,7-ACRD(CF_3)$_4$. Thermal ellipsoids shown at the 50% probability level.

C.4.5. CHARACTERIZATION OF 1,4,5,8-ACRD(CF_3)$_4$

1,4,5,8-tetrakis(trifluoromethyl)acridine

HPLC method: Isolated on COSMOSIL Buckyprep semi-preparative column (Figure 4-2/B-45). Flow rate 5 mL min^{-1} in acetonitrile, 7.0 min (F3). Pure compound did not dissolve when F3 was placed in 3:1 toluene:heptane and was collected by filtration, (appx B Figure B-42).
Yield information: Product of reaction 4.1; <5 mg pure compound isolated(appx B.4.1).

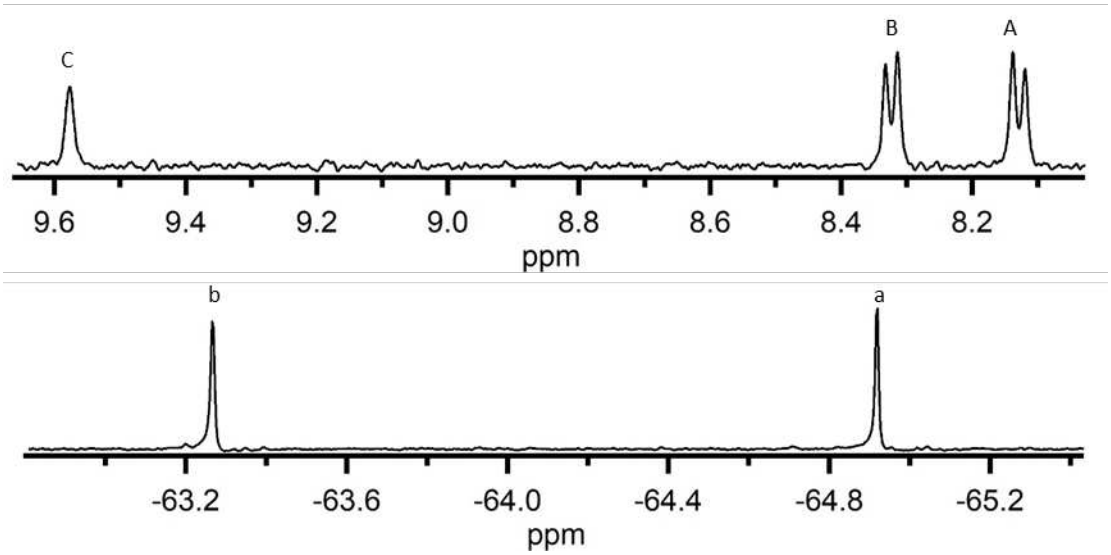

Figure C-108. NMR spectra of 1,4,6,9-ACRD(CF_3)$_4$. Product > 98% pure. ^{1}H NMR spectrum (top) referenced to $CHCl_3$ (δ = 7.26, not shown). ^{19}F NMR spectrum (bottom) referenced to perfluorobenzene (δ = −164.9, not shown). See figure below for probable peak assignments.

1H NMR ($CDCl_3$, 400 MHz): δ 9.58 (s, 1H), 8.32 (d, J=7.3 Hz, 2H), 8.13 (d, J=7.3 Hz, 2H).
19F NMR ($CDCl_3$ with C_6F_6, 376 MHz): δ −63.2 (s, 2CF_3), −64.9 (s, 2CF_3).

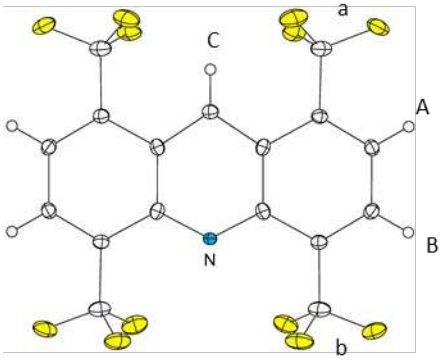

Figure C-109. Single crystal structure of 1,4,5,8-ACRD(CF_3)$_4$. Thermal ellipsoids shown at the 50% probability level.

C.4.6. CHARACTERIZATION OF 1,3,5,8-ACRD(CF_3)$_4$

1,3,5,8-tetrakis(trifluoromethyl)acridine

HPLC method: Multi-stage isolation on COSMOSIL Buckyprep semi-preparative column (Figure 4-2/B-45). Flow rate 5 mL min^{-1} in indicated eluent. Stage 1: acetonitrile, 7.0 min (F3). Stage 2: 1:3 toluene:heptane, 5.0 min (F3F2). Stage 3: heptane, 9.8 min (pure compound), (appx B Figure B-42).
Yield information: Product of reaction 4.1; *ca.* 5 mg pure compound isolated(appx B.4.1).

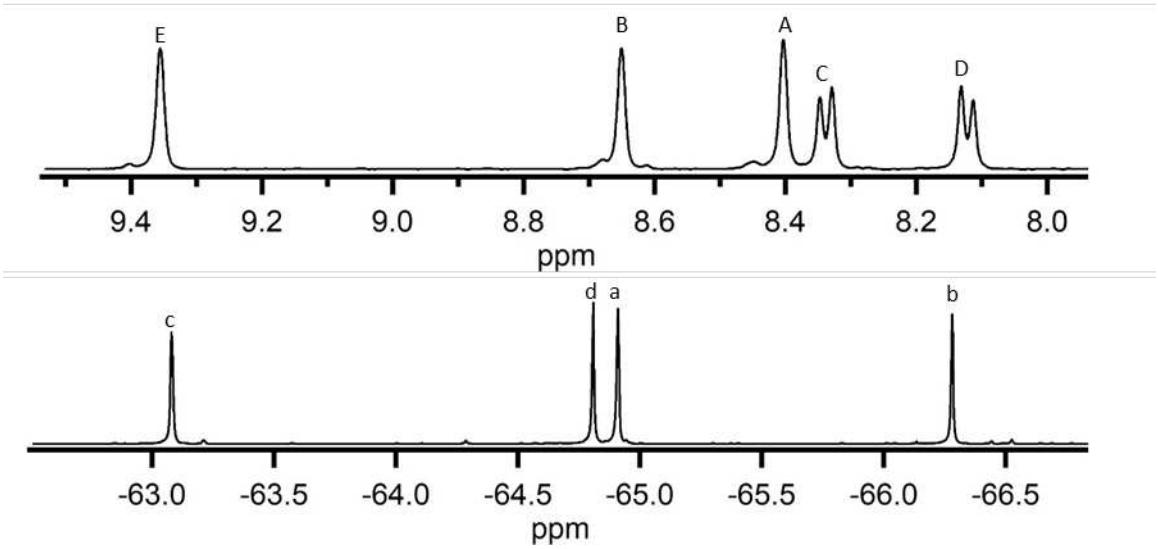

Figure C-110. NMR spectra of 1,3,5,8-ACRD(CF_3)$_4$. Product > 95% pure. ^{1}H NMR spectrum (top) referenced to $CHCl_3$ (δ = 7.26, not shown). ^{19}F NMR spectrum (bottom) referenced to perfluorobenzene (δ = −164.9, not shown). See figure below for probable peak assignments.

1H NMR ($CDCl_3$, 400 MHz): δ 9.57(s, 1H), 8.86(s, 1H), 8.32(d, J=7.3 Hz, 1H), 8.20(s, 1H), 8.14(d, J=7.3 Hz, 1H).
19F NMR ($CDCl_3$ with C_6F_6, 376 MHz): δ −63.2(s, 1CF_3), −63.3(s, 1CF_3), −64.4(s, 1CF_3), −66.7(s, 1CF_3).

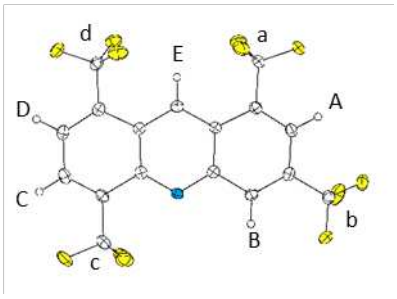

Figure C-111. Single crystal x-ray structure of 1,3,5,8-ACRD(CF_3)$_4$. Thermal ellipsoids shown at the 50% probability level.

C.4.7. CHARACTERIZATION OF 2,4,5,7,9-ACRD(CF_3)$_5$

2,4,5,7,9-pentakis(trifluoromethyl)acridine

HPLC method: Multi-stage isolation on COSMOSIL Buckyprep semi-preparative column (Figure 4-2/B-45). Flow rate 5 mL min^{-1} in indicated eluent. Stage 1: acetonitrile, 6.0 min (F2). Stage 2: 1:3 toluene:heptane, 5.0 min (pure compound), (appx B Figure B-42).
Yield information: Product of reaction 4.1; *ca.* 10 mg pure compound isolated(appx B.4.1).

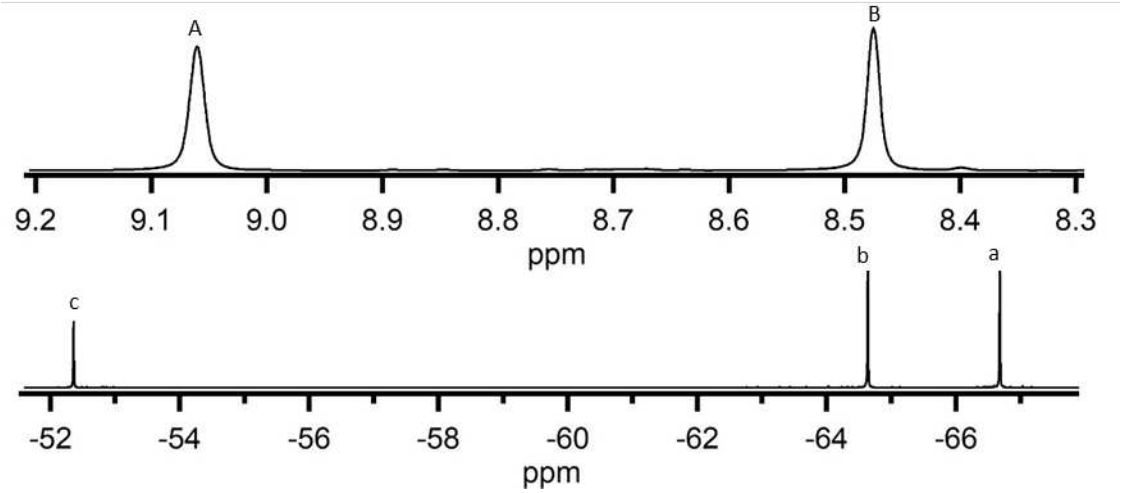

Figure C-112. NMR spectra of 2,4,5,7,9 -ACRD(CF_3)$_4$. Product > 95% pure. ^{1}H NMR spectrum (top) referenced to $CHCl_3$ (δ = 7.26, not shown). ^{19}F NMR spectrum (bottom) referenced to perfluorobenzene (δ = −164.9, not shown). See figure below for probable peak assignments.

1H NMR ($CDCl_3$, 400 MHz): δ 9.06(s, 2H), 8.48(s, 2H).
19F NMR ($CDCl_3$ with C_6F_6, 376 MHz): δ −52.4 (s, 1CF_3), −64.6 (s, 2CF_3), −66.7 (s, 2CF_3).

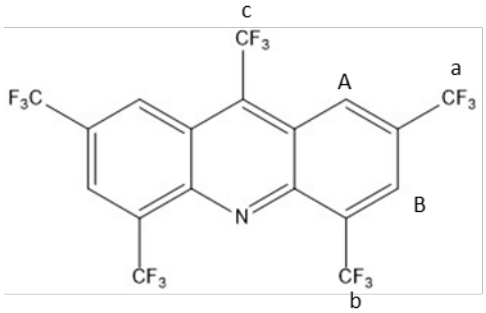

Figure C-113. Drawing of structure of 2,4,5,7,9 -ACRD(CF_3)$_4$, elucidated from NMR spectra.

C.4.8. CHARACTERIZATION OF 2,3,5,7,9-ACRD(CF_3)$_5$

1,3,5,7,9-pentakis(trifluoromethyl)acridine

HPLC method: Multi-stage isolation on COSMOSIL Buckyprep semi-preparative column (Figure 4-2/B-45). Flow rate 5 mL min^{-1} in indicated eluent. Stage 1: acetonitrile, 7.6 min (F4). Stage 2: 1:3 toluene:heptane, 5.3 min (pure compound), (appx B Figure B-42).
Yield information: Product of reaction 4.1; >5 mg pure compound isolated(appx B.4.1).

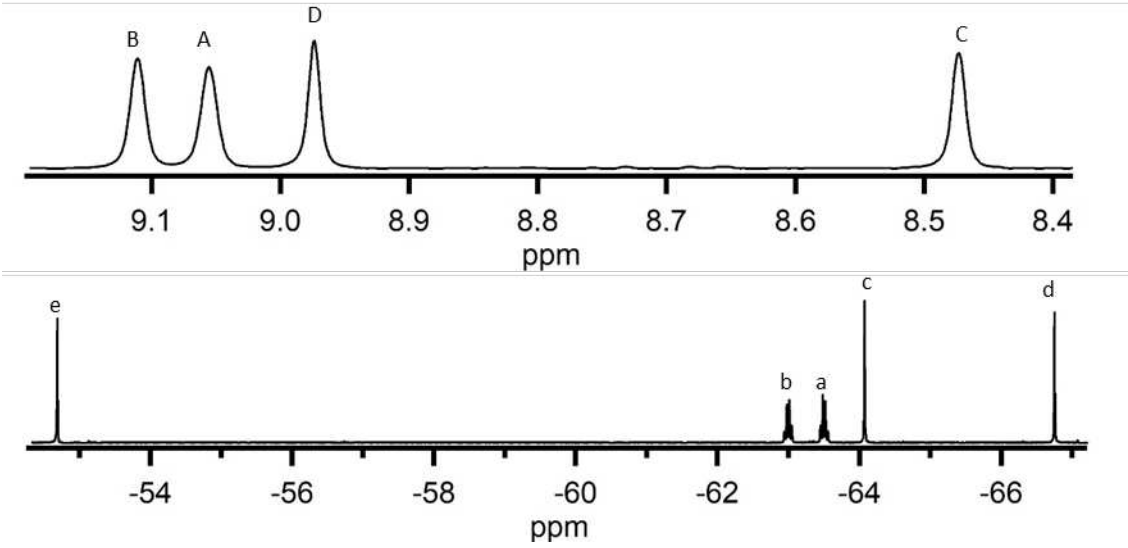

Figure C-114. NMR spectra of 2,3,5,7,9-ACRD(CF_3)$_5$. Product > 98% pure. ^{1}H NMR spectrum (top) referenced to $CHCl_3$ (δ = 7.26, not shown). ^{19}F NMR spectrum (bottom) referenced to perfluorobenzene (δ = −164.9, not shown). See figure below for probable peak assignments.

1H NMR ($CDCl_3$, 400 MHz): δ 9.11 (s, 1H); 9.06 (s, 1H); 8.97 (s, 1H); 8.47 (s, 1H).
19F NMR ($CDCl_3$ with C_6F_6, 376 MHz): δ −52.7 (s, 1CF_3); −63.0 (d, J=13 Hz, 1CF_3); −63.5 (d, J=13 Hz, 1CF_3); −64.1 (s, 1CF_3); −66.8 (s, 1CF_3).

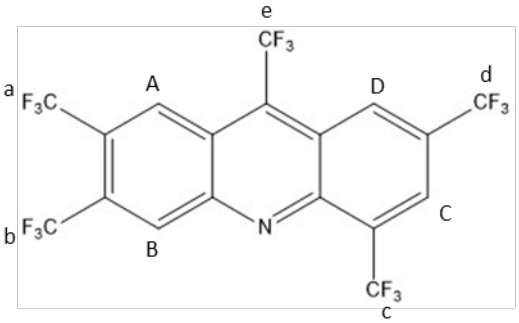

Figure C-115. Drawing of structure of 2,3,5,7,9-ACRD(CF_3)$_5$, elucidated from NMR spectra.

C.4.9. CHARACTERIZATION OF 3,4,5,6,9-ACRD(CF_3)$_5$

3,4,5,6,9-pentakis(trifluoromethyl)acridine

HPLC method: Multi-stage isolation on COSMOSIL Buckyprep semi-preparative column (Figure 4-2/B-45). Flow rate 5 mL min^{-1} in indicated eluent. Stage 1: acetonitrile, 7.6 min (F4). Stage 2: 1:3 toluene:heptane, 8.6 min (pure compound), (appx B Figure B-42).
Yield information: Product of reaction 4.1; >5 mg pure compound isolated(appx B.4.1).

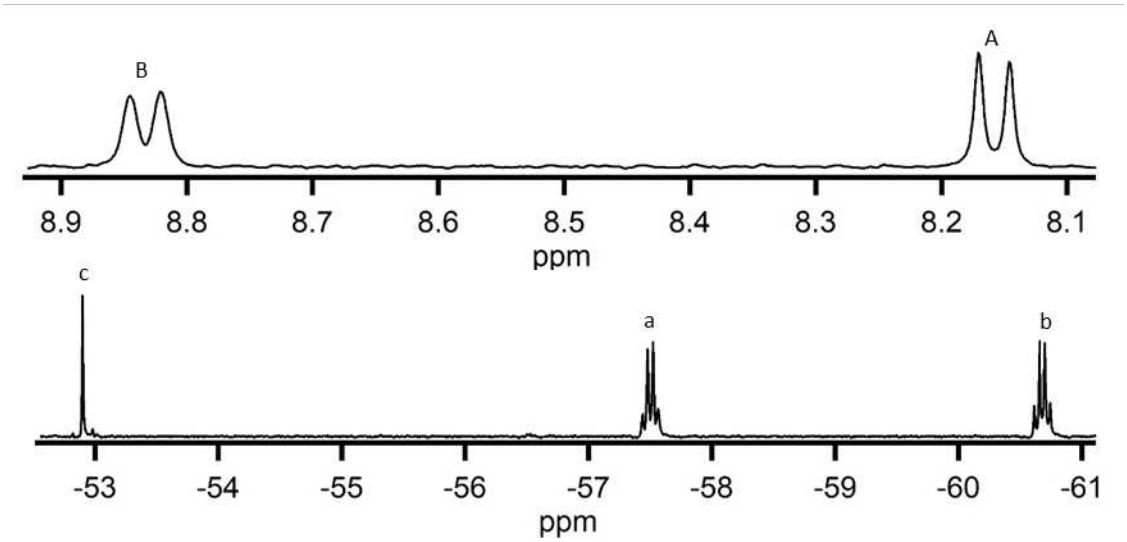

Figure C-116. NMR spectra of 3,4,5,6,9-ACRD(CF_3)$_5$. Product > 98% pure. ^{1}H NMR spectrum (top) referenced to $CHCl_3$ (δ = 7.26, not shown). ^{19}F NMR spectrum (bottom) referenced to perfluorobenzene (δ = −164.9, not shown). See figure below for probable peak assignments.

1H NMR ($CDCl_3$, 400 MHz): δ 9.06 (s, 2H), 8.48 (s, 2H).
19F NMR ($CDCl_3$ with C_6F_6, 376 MHz): δ −52.4 (s, 1CF_3), −64.6 (m, 2CF_3), −66.7 (m, 2CF_3).

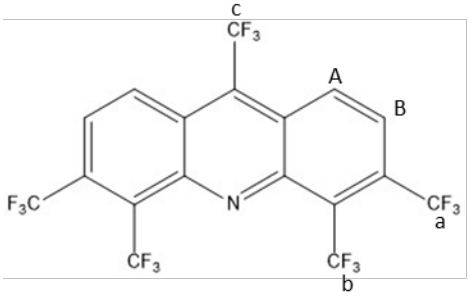

Figure C-117. Drawing of structure of 3,4,5,6,9-ACRD(CF_3)$_5$, elucidated from NMR spectra.

C.4.10. CHARACTERIZATION OF 1,2,4,5,8-ACRD(CF_3)$_5$

1,2,4,5,8-pentakis(trifluoromethyl)acridine

HPLC method: Multi-stage isolation on COSMOSIL Buckyprep semi-preparative column (Figure 4-2/B-45). Flow rate 5 mL min^{-1} in indicated eluent. Stage 1: acetonitrile, 7.0 min (F3). Stage 2: 1:3 toluene:heptane, 6.0 min (F3F3). Stage 3: heptane, 19.0 min (pure compound), (appx B Figure B-42).
Yield information: Product of reaction 4.1; > 5 mg pure compound isolated(appx B.4.1).

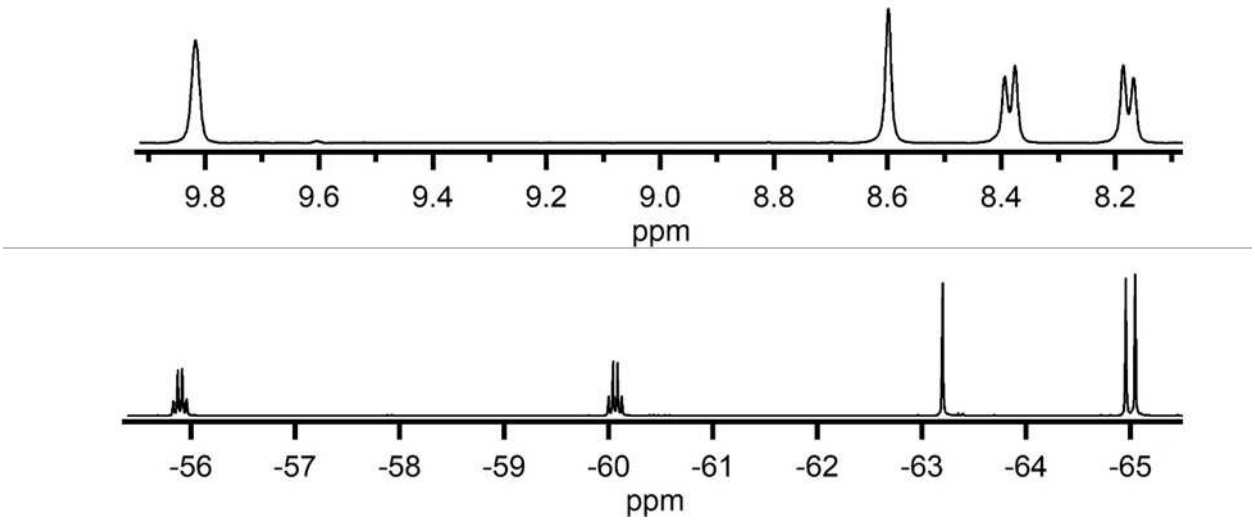

Figure C-118. NMR spectra of 1,2,4,5,8-ACRD(CF_3)$_5$. Product > 98% pure. ^{1}H NMR spectrum (top) referenced to $CHCl_3$ (δ = 7.26, not shown). ^{19}F NMR spectrum (bottom) referenced to perfluorobenzene (δ = −164.9, not shown). See figure below for probable peak assignments.

1H NMR ($CDCl_3$, 400 MHz): δ 9.82(s, 1H), 8.60(s, 1H), 8.38(d, J=8.0 Hz, 1H), 8.18(d, J=8.0 Hz, 1H).
19F NMR ($CDCl_3$ with C_6F_6, 376 MHz): δ −55.9(m, 1CF_3), −60.1(m, 1CF_3), −63.2(s, 1CF_3), −64.9(s, 1CF_3), −65.0(s, 1CF_3).

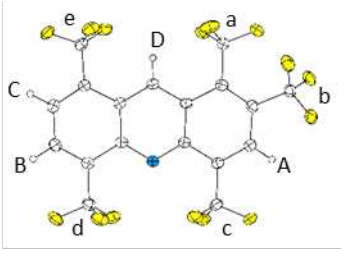

Figure C-119. Single crystal x-ray structure of 1,2,4,5,8-ACRD(CF_3)$_5$. Thermal ellipsoids shown at the 50% probability level.

C.4.11. CHARACTERIZATION OF 2,4,5,6,9-ACRD(CF_3)$_5$

2,4,5,6,9-pentakis(trifluoromethyl)acridine

HPLC method: Multi-stage isolation on COSMOSIL Buckyprep semi-preparative column (Figure 4-2/B-45). Flow rate 5 mL min^{-1} in indicated eluent. Stage 1: acetonitrile, 7.0 min (F3). Stage 2: 1:3 toluene:heptane, 7.0 min (pure compound), (appx B Figure B-42).
Yield information: Product of reaction 4.1; *ca.* 5 mg isolated(appx B.4.1).

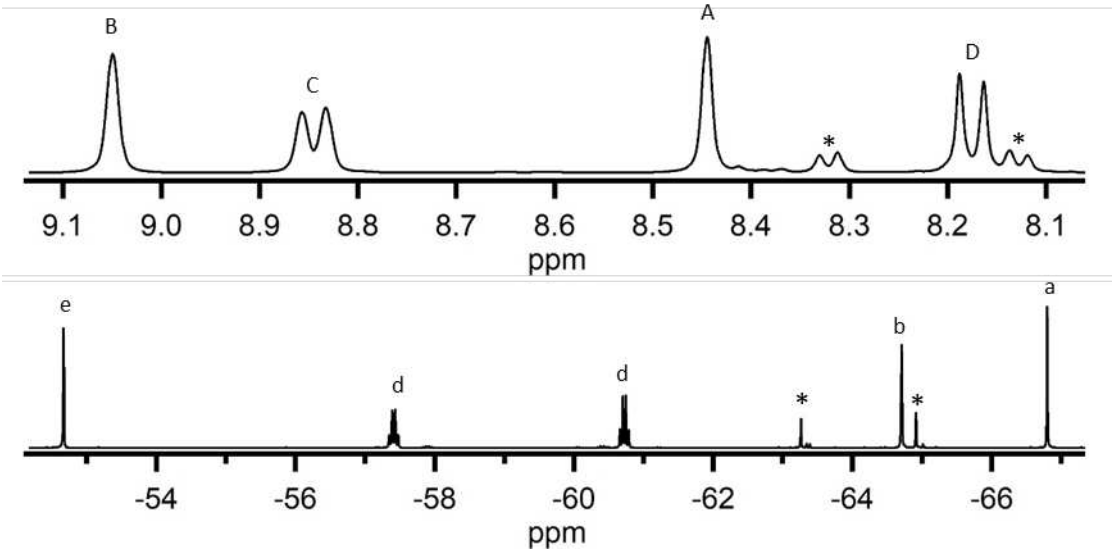

Figure C-120. NMR spectra of 2,4,5,6,9-ACRD(CF_3)$_5$. Product *ca.* 80% pure (impurity deonoted *). ^{1}H NMR spectrum (top) referenced to $CHCl_3$ (δ = 7.26, not shown). ^{19}F NMR spectrum (bottom) referenced to perfluorobenzene (δ = −164.9, not shown). See figure below for probable peak assignments.

1H NMR ($CDCl_3$, 400 MHz): δ 9.05(s, 1H), 8.85(d, J=9.5 Hz, 1H), 8.44(s, 1H), 8.17(d, J=9.5 Hz, 1H).
19F NMR ($CDCl_3$ with C_6F_6, 376 MHz): δ −52.7(s, 1CF_3), −57.4(m, 1CF_3), −60.7(m, 1CF_3), −64.7 (s, 1CF_3), −66.8(s, 1CF_3).

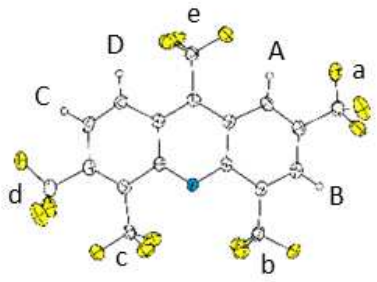

Figure C-121. Single crystal x-ray structure of 2,4,5,6,9-ACRD(CF_3)$_5$. Thermal ellipsoids shown at the 50% probability level.

C.4.12. CHARACTERIZATION OF 1,4,5,8,9-(H_2-ACRD)(CF_3)$_5$

1,4,5,8,9-pentakis(trifluoromethyl)-4a,9,9a,10-tetrahydroacridine

HPLC method: Multi-stage isolation on COSMOSIL Buckyprep semi-preparative column (Figure 4-2/B-45). Flow rate 5 mL min^{-1}in indicated eluent. Stage 1: acetonitrile, 5.0 min (F1). Stage 2: 1:3 toluene:heptane, 4.2 min (F1F1). Stage 3: heptane, 5.5 min (Pure compound), (appx B Figure B-42).
Yield information: Product of reaction 4.1; *ca.* 5 mg pure compound isolated(appx B.4.1).

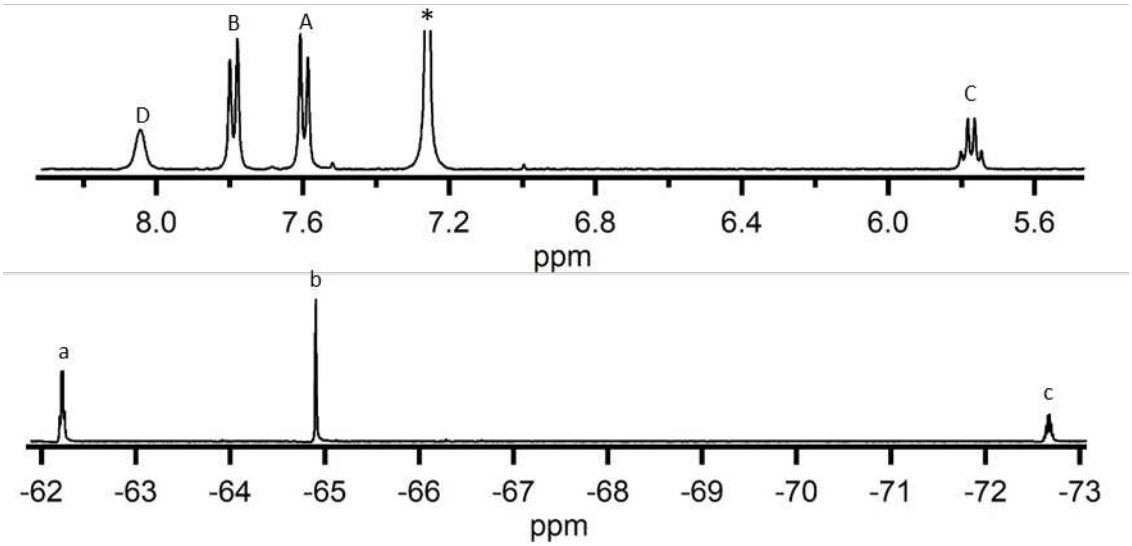

Figure C-122. NMR spectra of 1,4,5,8,9-(H_2-ACRD)(CF_3)$_5$. Product > 98% pure. ^{1}H NMR spectrum (top) referenced to $CHCl_3$ (δ = 7.26, denoted *). ^{19}F NMR spectrum (bottom) referenced to perfluorobenzene (δ = –164.9, not shown). See figure below for probable peak assignments.

1H NMR ($CDCl_3$, 400 MHz): δ 8.05 (m, 1H), 7.79 (d, J=8.0 Hz, 1H), 7.60 (d, J=8.0 Hz, 1H), 5.77 (m, 1H).
19F NMR ($CDCl_3$ with C_6F_6, 376 MHz): δ −62.2 (m, 2CF_3), −64.9(s, 2CF_3), −72.7 (m, 1CF_3).

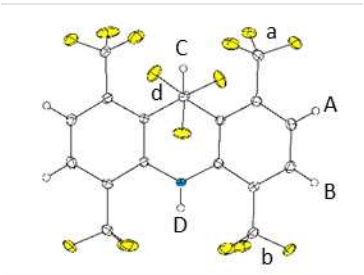

Figure C-123. Single crystal x-ray structure of 1,4,5,8,9-(H_2-ACRD)(CF_3)$_5$. Thermal ellipsoids shown at the 50% probability level.

C.4.13. CHARACTERIZATION OF 4-C_2F_5-2,5,7,9-ACRD(CF_3)$_4$

4-(perfluoroethyl)-2,5,7,9-tetrakis(trifluoromethyl)acridine

HPLC method: Multi-stage isolation on COSMOSIL Buckyprep semi-preparative column (Figure 4-2/B-45). Flow rate 5 mL min^{-1}in indicated eluent. Stage 1: acetonitrile, 5.0 min (F1). Stage 2: 1:3 toluene:heptane, 4.2 min (F1F1). Stage 3: heptane, 8.1 min (Pure compound), (appx B Figure B-42).
Yield information: Product of reaction 4.1; *ca.* 5 mg pure compound isolated(appx B.4.1).

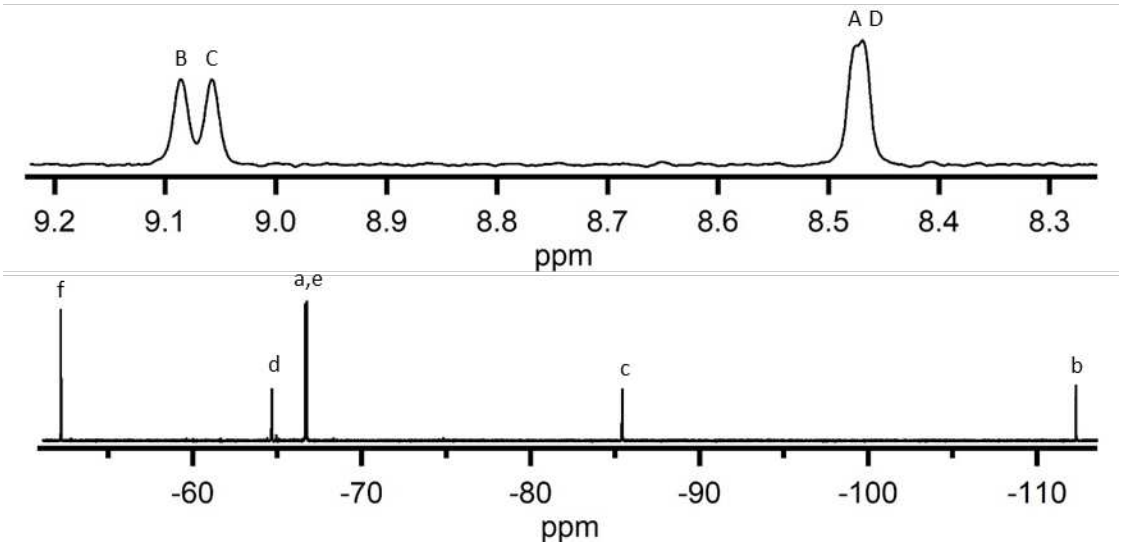

Figure C-124. NMR spectra of 4-C_2F_5-2,5,7,9-ACRD(CF_3)$_4$. Product > 98% pure. ^{1}H NMR spectrum (top) referenced to $CHCl_3$ (δ = 7.26, not shown). ^{19}F NMR spectrum (bottom) referenced to perfluorobenzene (δ = –164.9, not shown). See figure below for probable peak assignments.

1H NMR ($CDCl_3$, 400 MHz): δ 9.09(s, 1H), 9.06(s, 1H), 8.48 (s, 1H), 8.47 (s, 1H).
19F NMR ($CDCl_3$ with C_6F_6, 376 MHz): δ −52.2 (s, 1CF_3), −64.7(s, 1CF_3), −66.7(s, 1CF_3), 66.8(s, 1CF3), −85.4(s, 1CF_3), −112.3(s, 1CF_2).

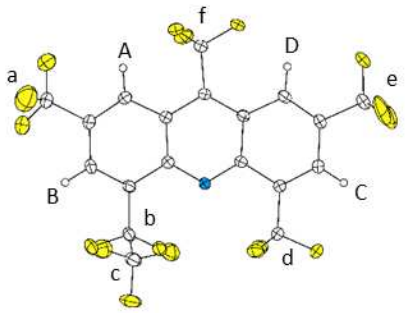

Figure C-125. Single crystal x-ray structure of 4-C_2F_5-2,5,7,9-ACRD(CF_3)$_4$. Thermal ellipsoids shown at the 50% probability level.

APPENDIX D

MISCELLANEOUS SUPPORING INFORMATION FOR CHAPTERS 1-4

D.i. INTRODUCTION MISCELLANEOUS SUPPORTING INFORMATION

D.i.1. Applications of organic electron acceptor materials

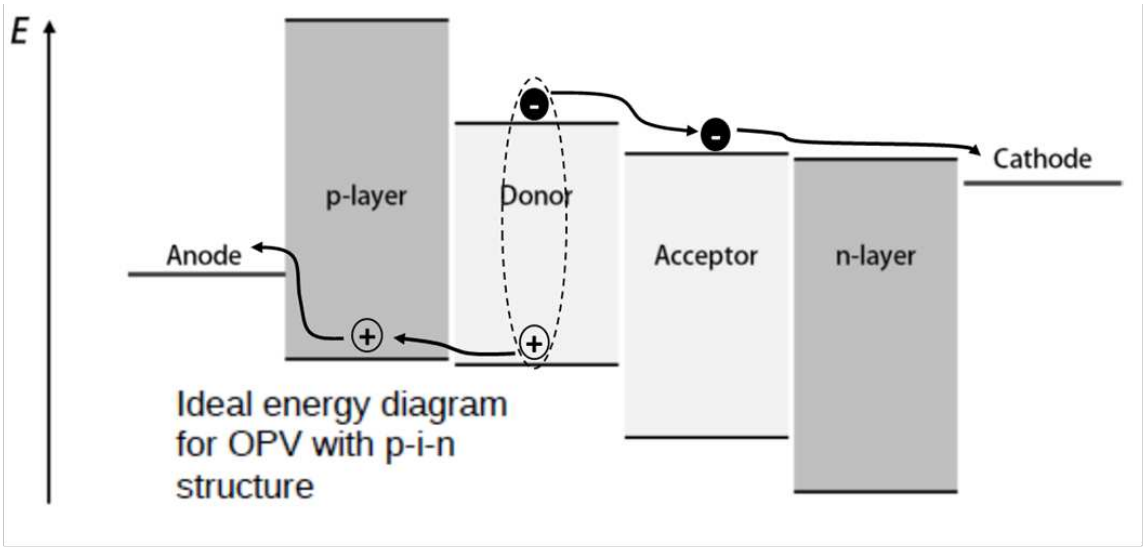

Figure D-1. A simplified schematic of the function of a OPV illustrating the necessity of electron acceptor materials in organic electronic devices. Upon excitation, electron-hole pairs are created in the form of a bound exciton, illustrated above by an oval with a dotted line. For inorganic materials, the exciton binding strength is comparable to thermal energies, and therefore, is easily overcome. However, for organic semiconductor materials, in which excitons are localized within the orbitals of individual molecules, the binding energy is significant. Therefore, driving force is required to separate the exciton in free carriers. This driving force is supplied by the transfer the electron to the LUMO of an electron acceptor material, which must be slightly lower in energy than the LUMO of the electron donor material.

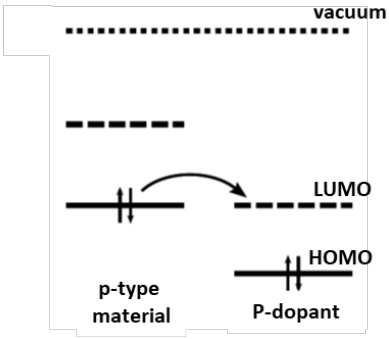

Figure D-2. A second use of organic electron acceptor materials is as dopants in p-type, or hole transport, materials. They are useful for this application because the filling of their LUMO levels creates holes in p-type materials. Use of organic dopants in p-type materials is not limited to organic electronics. Many different types of semiconductor material can be doped with organic electron acceptors.

D.1. CHAPTER 1 MISCELLANEOUS SUPPORTING INFORMATION

D.1.1. Other attempts to form C_4F_4 groups

Reductive defluorination by sodium napthalenide was attempted.[1] Reduction of triphenylene derivatives with napthalenide was expected to yield fully aromatic reductive defluorination derivatives of triphenylene (products bearing C_4F_4 groups), naphthalene, and sodium fluoride. Napthenalide has a formal potential of ca. -3.0 V vs $Fe(Cp_2)^{+/-}$. Triphenylene has an $E_{1/2}$ of -3.01 V vs $Fe(Cp_2)^{+/-}$ [2] While the reduction of the perfluorannulated triphenylenes reported here were not reversible, both the irreversible event observed during cyclic voltammetry attempts, and extrapolation from gas phase EA data indicate that the reduction potential of perfluorannulated triphenylenes increases with each C_4F_8 group added. This is consistent with previous reports that perfluoralkylation of PAHs results in stepwise increases in $E_{1/2}$ values, dependent upon the number of perfluoralkyl groups present. Therefore, sodium napthalenide should be sufficient to reduce any of the family of products reported here. Reduction of 2,3-C_4F_8 and 2,3;6,7;10,11-$(C_4F_8)_3$ were both attempted, as 2,3-C_4F_8 was expected to yield the simplest product mixture, and 2,3;6,7;10,11-$(C_4F_8)_3$ was expected to be the easiest to reduce. However, reductive defluorination was not successful in either case. Upon quenching and workup of the reaction, only 2,3-C_4F_8 and 2,3;6,7;10,11-$(C_4F_8)_3$, and naphthalene were observed by ^{1}H NMR, and only 2,3-C_4F_8 and 2,3;6,7;10,11-$(C_4F_8)_3$ was observed by ^{19}F NMR.

While the reduction potential of napthalenide was likely sufficient for reductive defluorination, kinetics of this process may be significantly different than reduction upon a copper surface. For example, kinetics of a multi-electron process would be slow, in this case involving interaction with multiple napthelenide ions, whereas reductive defluorination of a triphenylene derivative bound to copper surface could in theory proceed much more rapidly. Therefore, reduction of triphenylene derivatives in solution by sodium metal was attempted, as it is possible that this reaction could occur upon the surface of solid sodium metal. Sodium metal, with a reaction -3.11 vs $Fe(Cp_2)^{+/-}$[3] should be sufficient to reduce perfluorannulated triphenylenes. However, reduction of 2,3-C_4F_8 by stirring in THF with sodium metal overnight produced no evidence of reaction by ^{1}H and ^{19}F NMR. Starting material was intact.

In addition to sodium metal, bulk electrolysis on the surface of a platinum electrode in acetonitrile held at a potential of -2.9 V vs $Fe(Cp_2)^{+/-}$, the lowest potential available within the solvent window, was attempted. However, as was observed when cyclic voltammetry was attempted, an opaque white film was observed depositing on the platinum electrode, and no reductive defluorination products were recovered from solution.

As reported by Chen et al.,[2] in the presence of a mixture of sodium diothionate/sodium bicarbonate and zinc acetate in DMSO, perfluoroalkylation of porphyrins with $(CF_2)_nI_2$ is followed by reductive defluorination to give products bearing fused aromatic rings. This method was attempted with triphenylene and 1,4-$C_4F_8I_2$, but yielded no product.

Reaction of 2,3;6,7;10,11-$(C_4F_8)_3$ and calcium hydride in dry DMSO was attempted.[3, 4] Expected products included reductive defluorination product, hydrogen gas, and calcium fluoride, was attempted. However, no reaction was observed by ^1H and ^{19}F NMR.

Reductive defluorination of 2,3;6,7;10,11-$(C_4F_8)_3$ via a Birch reduction was attempted.[5] The Birch reduction is a metal-ammonia reduction of aromatic compounds by alkali metal in liquid ammonia in the presence of alcohol The Birch reduction uses the ammonia-solvated electrons arising from alkali metals as the reducing agent. Analysis by ^1H and ^{19}F NMR showed decomposition of 2,3;6,7;10,11-$(C_4F_8)_3$, leaving no observable starting material or product.

D.1.2. Reactions in Monel autoclave

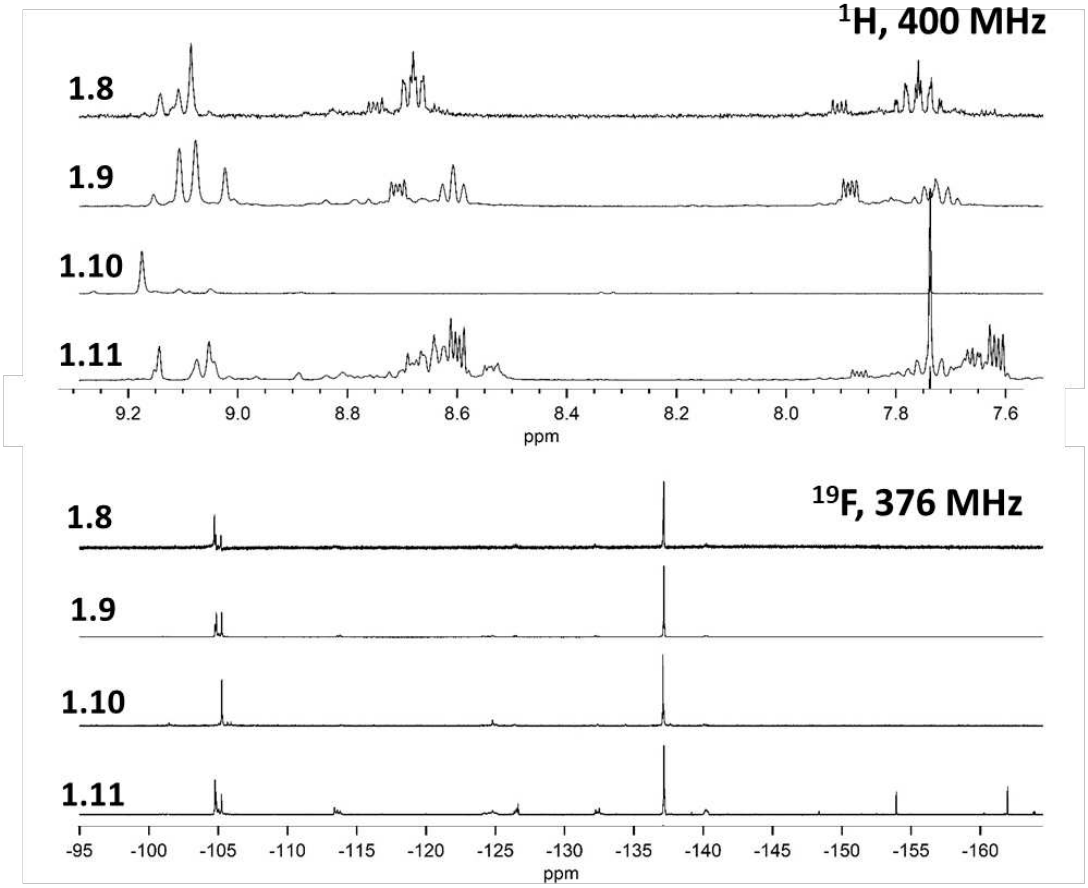

Figure D-3. NMR spectra of products of optimized reactions 1.8-1.11, which were conducted in Monel vessels under conditions analogous to reactions 1.1-1.4. Product distribution appears to be unaffected by vessel type.

D.1.3. Reactions with CF_3I and C_2F_5

Table D-1. Table summarizing reaction details for all reactions conducted with TRPH and perfluroalkyl iodides other than 1,4-$C_4F_8I_2$.

Reaction Number	Starting Materials	Temp (°C)	Duration (h)	Product Recovered (mg)	Products
1R	85 mg TRPH, 6 equiv CF_3I	360	24	-	**Many products with 5 and 6 CF_3 groups, including TRPH(CF3)$_6$-1 and TRPH(CF3)$_6$-3**
2R	25 mg TRPH, 12 equiv CF_3I, 0.5 g Cu	300	6	24	**Many products with up to 5 CF_3 groups, including TRPH(CF3)$_6$-1**
3R	82 mg TRPH, 24 equiv CF_3I	360	30	220	**Many products with 5 and 6 CF_3 groups, including TRPH(CF3)$_6$-1**
4R	14 mg TRPH, 3 equiv CF_3I	300	14	28	**Many products**
5R	50 mg TRPH, 18 equiv C_2F_5I	300	24	140	**Many products including TRPH(C_2F_5)$_4$-1**

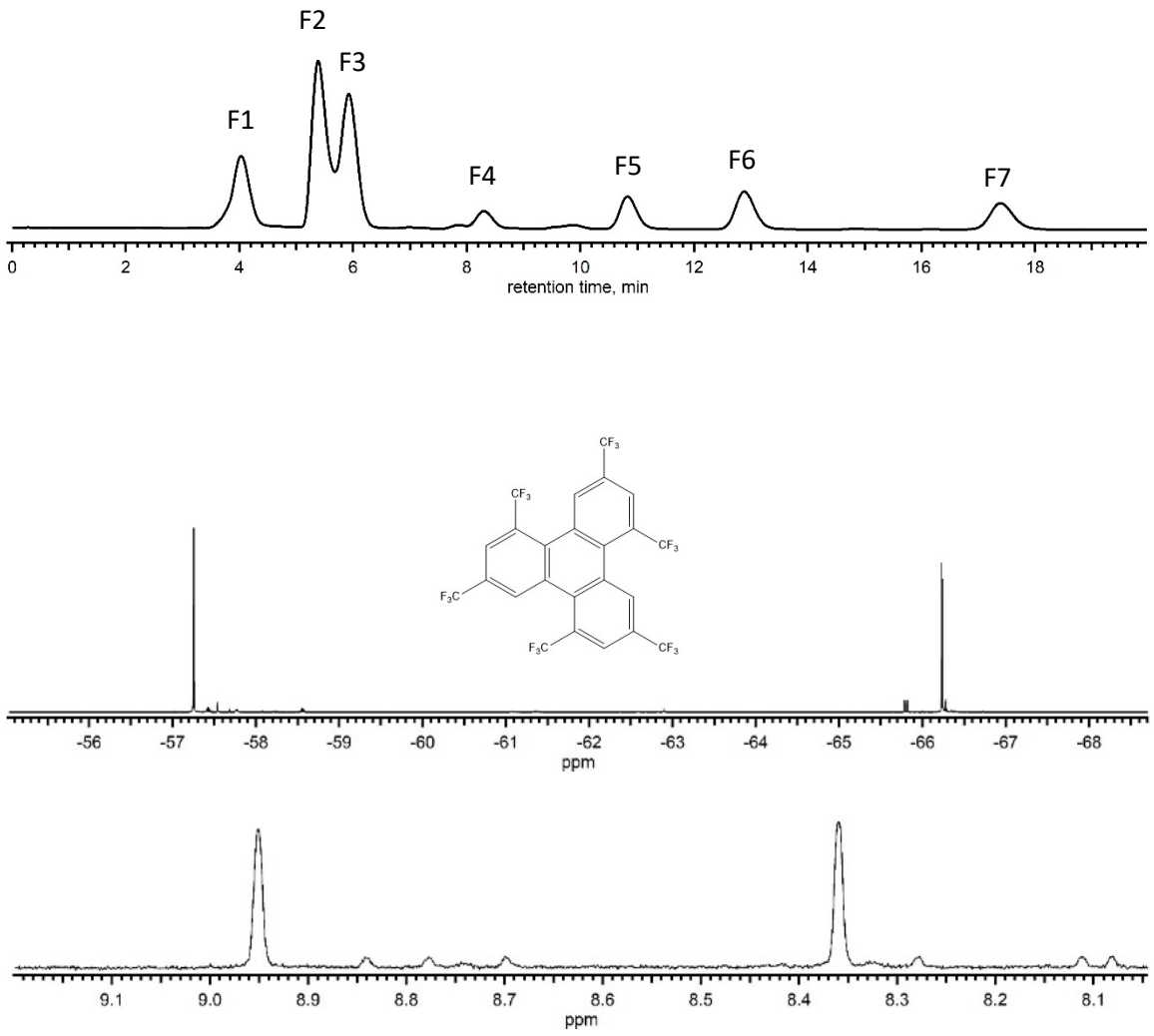

Figure D-4. (top) Representative HPLC trace showing the separation of reaction 1R. HPLC performed on BuckyPrep – Semi-preparative Column, 10.0 x 250 mm, flow rate 5 ml min^{-1}. Detection wavelength 300 nm. (bottom) ^{1}H and ^{19}F NMR spectra for fraction 1 from reaction 1R, with a retention time of 3 minutes in acetonitrile. This fraction predominantly contains TRPH-6-2, a high symmetry isomer with 6 CF_3's. We propose that the short retention time can be attributed to the fact that the TRPH core is likely quite twisted, and the high symmetry makes this molecule nonpolar.

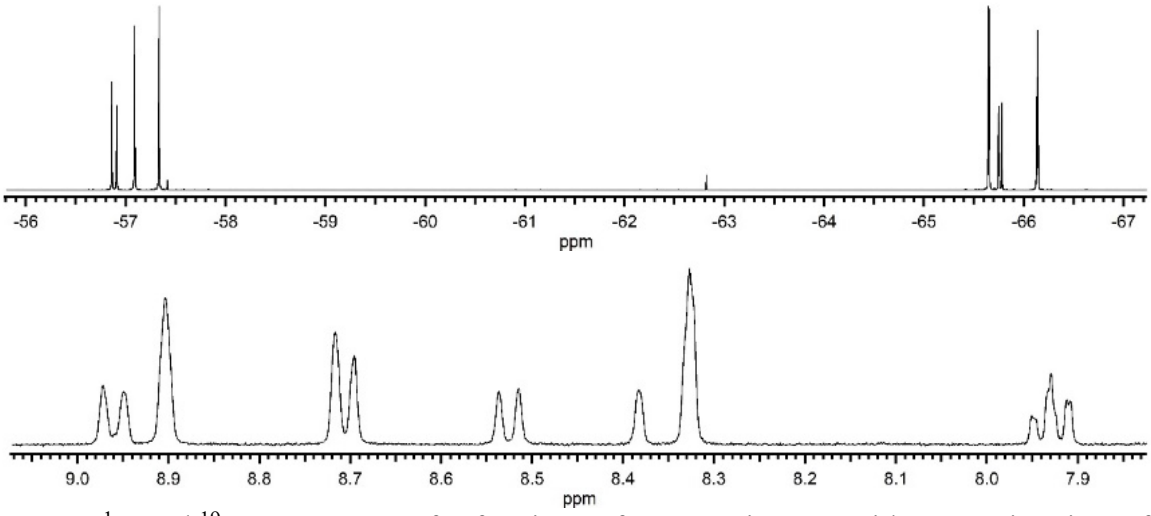

Figure D-5. ^{1}H and ^{19}F NMR spectra for fraction 2 from reaction 1R, with a retention time of 5 minutes in acetonitrile. This fraction contains a mixture of two products, likely TRPH$(CF_3)_5$-A and TRPH$(CF_3)_5$-B in an approximately 2:1 ratio.

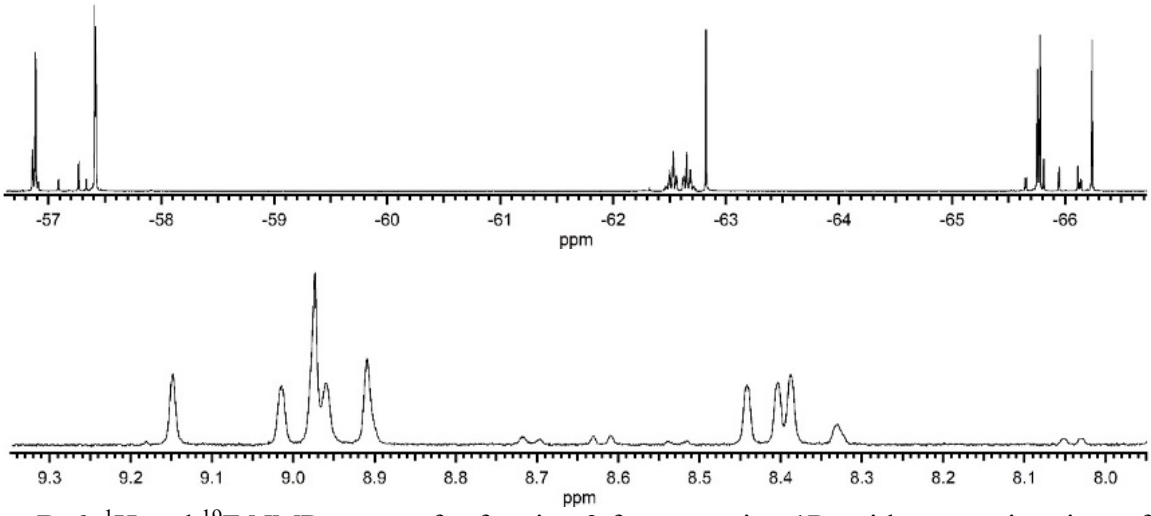

Figure D-6. ^{1}H and ^{19}F NMR spectra for fraction 3 from reaction 1R, with a retention time of 6 minutes in acetonitrile. This fraction contains a mixture of two products, likely TRPH$(CF_3)_5$-C, TRPH$(CF_3)_4$-A, other unidentified isomers of TRPH$(CF_3)_n$.

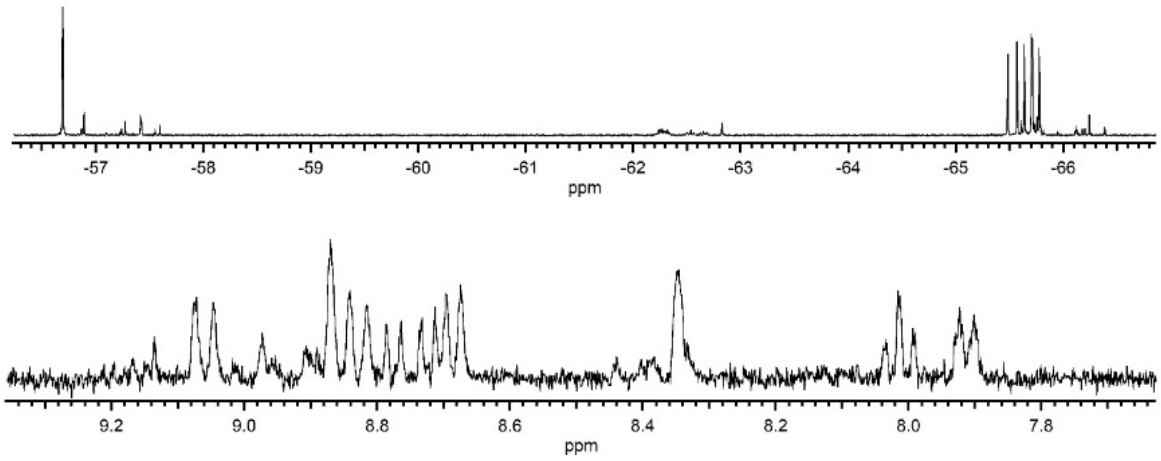

Figure D-7 ^{1}H and ^{19}F NMR spectra for fraction 4 from reaction 1R, with a retention time of 8.2 minutes in acetonitrile. This fraction contains a mixture of two products, likely TRPH$(CF_3)_5$-D and TRPH$(CF_3)_5$-E in an approximately 1:1 ratio.

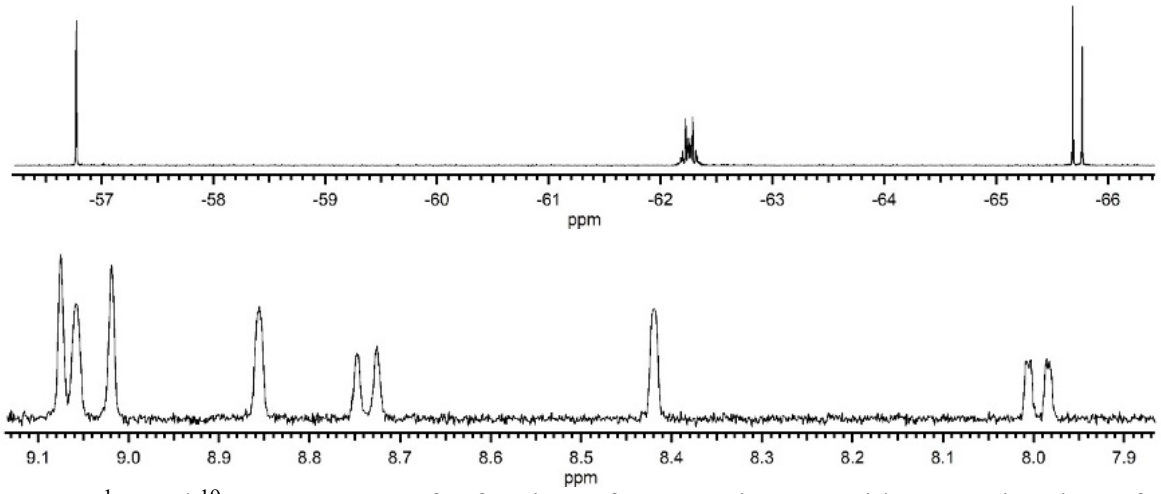

Figure D-8 ^{1}H and ^{19}F NMR spectra for fraction 5 from reaction 1R, with a retention time of 11 minutes in acetonitrile. This fraction is a 98% pure isomer of TRPH$(CF_3)_5$-F.

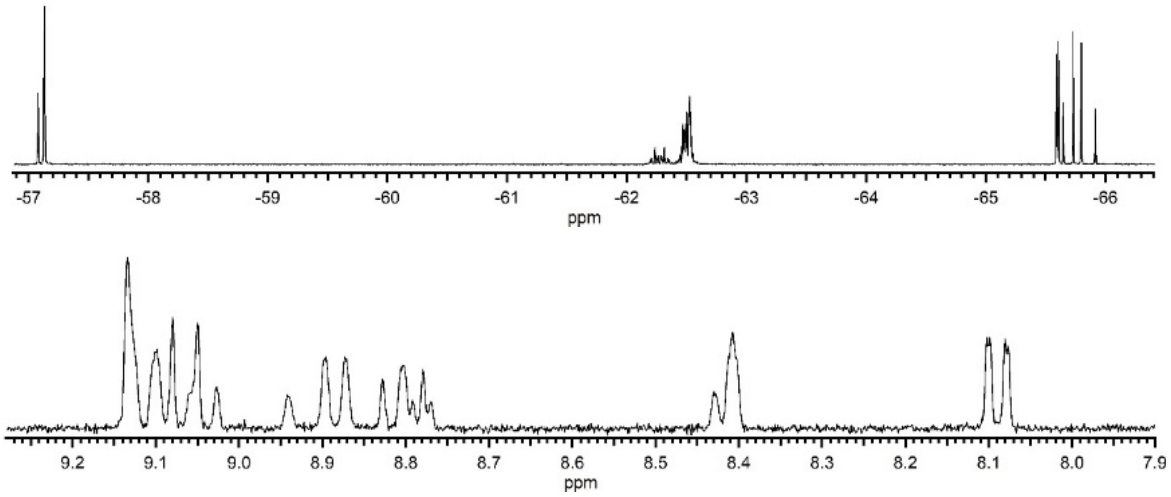

Figure D-9. ^{1}H and ^{19}F NMR spectra for fraction 6 from reaction 1R, with a retention time of 12.5 minutes in acetonitrile. This fraction is a a 4:1 mixture of two products, likely TRPH$(CF_3)_5$-G and TRPH$(CF_3)_5$-H.

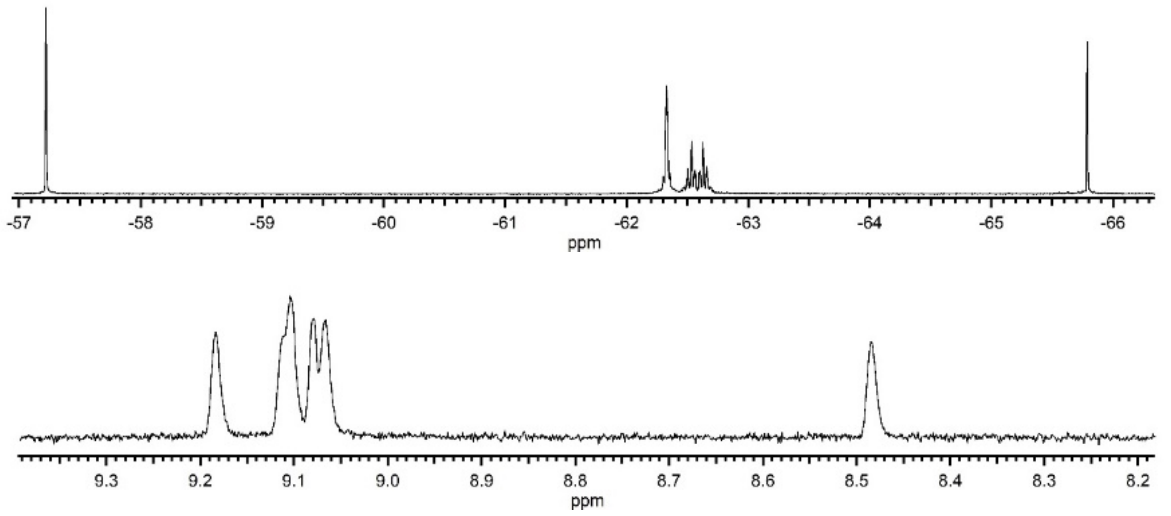

Figure D-10. ^{1}H and ^{19}F NMR spectra for fraction 7 from reaction 1R, with a retention time of 17 minutes in acetonitrile. This fraction is the previously reported compound TRPH-6-1.

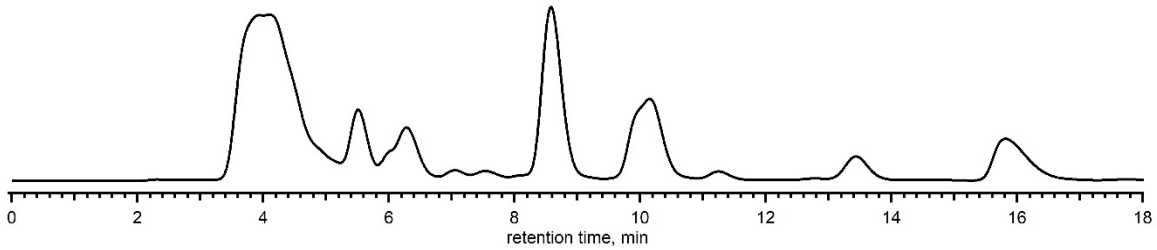

Figure D-11. Representative HPLC trace showing the separation of reaction 2R. HPLC performed on BuckyPrep – Semi-preparative Column, 10.0 x 250 mm, flow rate 5 ml min^{-1}. Detection wavelength 300 nm. Note that there are peaks with similar retention times to reaction 1R. The products contained within these peaks were similar to the products of reaction 1R. However, additional products were produced, including the product which eluted at 15 minutes, shown in figure S28.

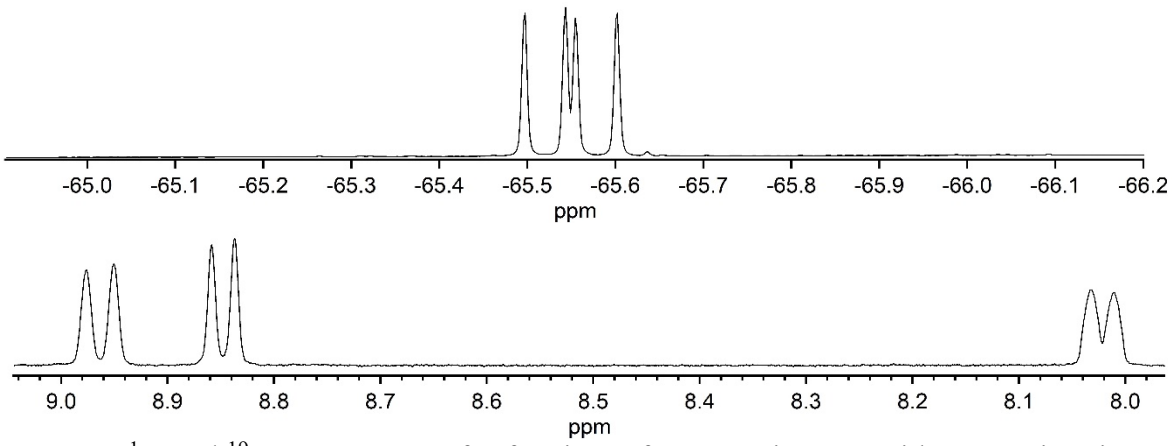

Figure D-12. ^{1}H and ^{19}F NMR spectra for fraction 1 from reaction 2R, with a retention time of 15 minutes in acetonitrile.

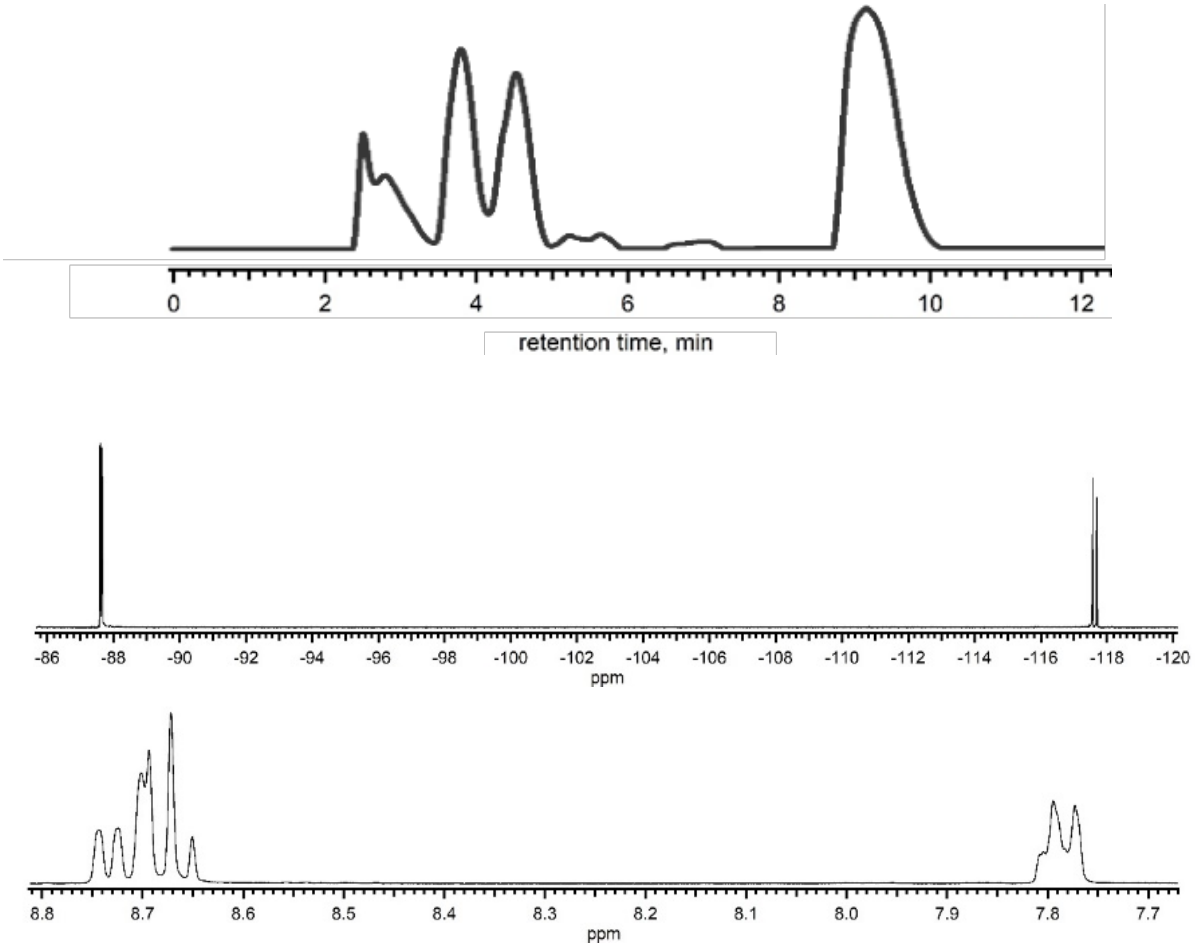

Figure D-13. (top) Representative HPLC trace showing the separation of reaction 5R. HPLC performed on BuckyPrep – Semi-preparative Column, 10.0 x 250 mm, flow rate 5 ml min^{-1}. Detection wavelength 300 nm. (bottom) ^{1}H and ^{19}F NMR spectra for fraction 1 from reaction 5R, with a retention time of 8.3 minutes in acetonitrile. This fraction predominantly contains the pure compound $TRPH(C_2F_5)_4$-1.

D.1.4. uv-Vis absorption of TRPH derivatives

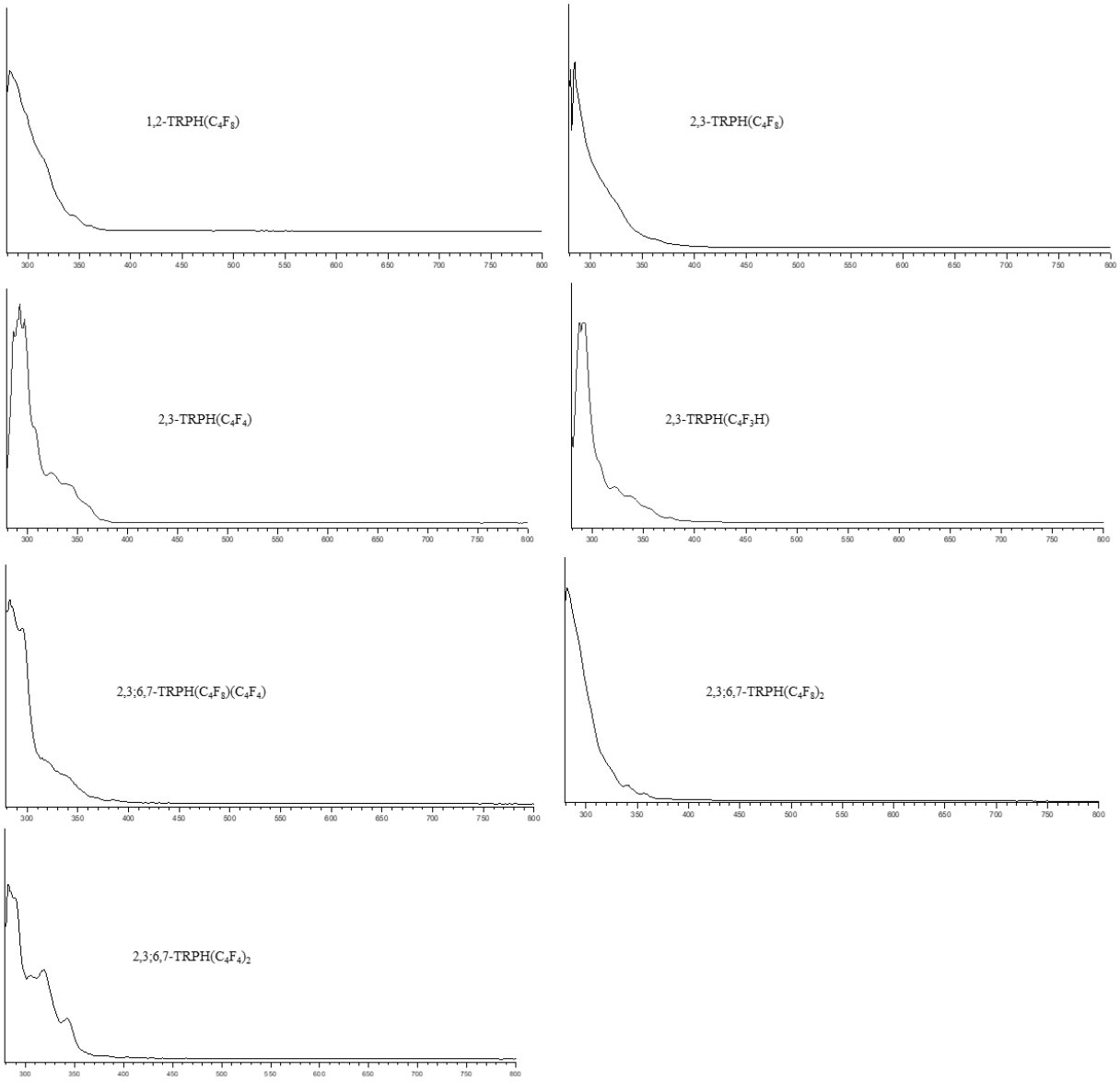

Figure D-14. UV-vis absorption spectra of select compounds reported in chapter 1.

D.1.5. Table D-1 Crystal Data and Refinement Parameters

Table D-2. Crystal data and final refinement parameters for X-ray diffraction structure from chapter 1 part 1.

compound[a]	2,3-C_4HF_3	2,3:6,7	1,2:10,11	1,2:5,6:10,11	2,3:6,7:10,11	2,3:6	2,3:6,7:10
formula	$C_{22}H_{11}F_3$	$C_{26}H_8F_{16}$	$C_{26}H_8F_{16}$	$C_{30}H_6F_{24}$	$C_{30}H_6F_{24}$	$C_{28}H_{10}F_{16}$	$C_{30}H_8F_{24}$
formula wt., g mol^{-1}	332.31	624.32	624.32	822.35	822.35	626.34	824.36
crystal system	triclinic	triclinic	orthorhombic	monoclinic	monoclinic	monoclinic	triclinic
space group, Z	$P\bar{1}$, 2	$P\bar{1}$, 8	*Pbca*, 8	*C*2/*c*, 8	$P2_1/c$, 4	*C*2/*c*, 8	$P\bar{1}$, 2
a, Å	8.1974)	11.9461(4)	7.7168(5)	24.3848(9)	18.380(3)	25.230(4)	10.0616(5)
b, Å	9.048(4)	14.9947(5)	23.5655(16)	9.1813(4)	6.973(1)	7.2354(11)	12.7315(6)
c, Å	10.934(5)	25.3203(9)	23.6738(16)	23.8772(10)	22.650(4)	26.920(4)	13.4600(6)
α, deg	75.007(10)	79.901(1)	90	90	90	90	68.286(1)
β, deg	85.151(9)	85.823(1)	90	93.241(1)	104.046(3)	115.750(3)	71.170(1)
γ, deg	70.053(10)	79.146(1)	90	90	90	90	88.304(1)
V, Å^3	736.3(6)	4381.7(3)	4305.1(5)	5337.2(4)	2816.1(8)	4426.2(12)	1508.21(12)
ρ_{calc} g cm^{-3}	1.499	1.893	1.926	2.047	1.940	1.880	1.815
T, K	100(2)	100(1)	100(2)	100(2)	100(2)	100(2)	100(2)
$R(F)$ ($I > 2\sigma(I)$)[b]	0.1179	0.0403	0.0584	0.0372	0.0650	0.0638	0.0464
$wR(F^2)$ [all data][b]	0.3932[c]	0.1127	0.1423	0.0977	0.2008	0.1781	0.1250
GOF	1.006	1.041	1.005	1.018	1.008	1.096	1.052

[a] Abbreviations: 2,3-C_4HF_3 = 2,3-TRPH(C_4HF_3); 2,3:6,7 = 2,3:6,7-TRPH(C_4F_8)$_2$; 1,2:10,11 = 1,2:10,11-TRPH(C_4F_8)$_2$; 1,2:5,6:10,11 = 1,2:5,6:10,11-TRPH(C_4F_8)$_2$; 2,3:6,7:10,11 = 2,3:6,7:10,11-TRPH(C_4F_8)$_2$; 2,3:6 = 2,3:6-TRPH(C_4F_8)(ω-C_4F_8H); 2,3:6,7:10 = 2,3:6,7:10-TRPH(C_4F_8)$_2$(ω-C_4F_8H). [b] $R(F) = \Sigma||F_o| - |F_c|| \,/\, \Sigma|F_o|$; $wR(F^2) = (\Sigma[w(F_o^2 - F_c^2)^2] \,/\, \Sigma[w(F_o^2)^2])^{1/2}$. [c] The high wR value is probably because the structure appears to be twinned. See CheckCIF file.

Table D-3. Crystal data and final refinement parameters for X-ray diffraction structure from chapter 1 part 2.

	2,3-TRPH(C_4F_8)	1,2-TRPH(C_4F_8)	2,3-TRPH(C_4F_4)
empirical formula, g mol^{-1}	$C_{22}H_{10}F_8$	$C_{22}H_{10}F_8$	$C_{22}H_{10}F_4$
formula weight	426.30	426.30	350.32
habit, color	rod, colorless	needle, colorless	needle, colorless
crystal size, mm			0.88 × 0.053 × 0.020
space group	*C*2/c	$P\bar{1}$	$P\bar{1}$
a (Å)	14.7137(9)	11.5700(4)	6.823(3)
b (Å)	16.5769(9)	12.5953(5)	9.388(4)
c (Å)	7.1777(4)	13.6440(5)	12.374(5)
α (°)	90.00	66.2175(8)	108.987(12)
β (°)	107.2763(16)	69.3626(7)	93.214(12)
γ (°)	90.00	77.8561(7)	102.002(13)
V(Å^3)	1671.71(16)	1697.30(11)	726.5(5)
Z	4	4	2
T(K)	100(2)	100(2)	120(2)
ρ_{calc} (g cm^{-3})	1.694	1.668	1.601
$R(F)$ ($I > 2\sigma(I)$)[a]	0.0481	0.0414	0.0512
$wR(F^2)$ [all data][a]	0.1379	0.1081	0.1193
residual e$^-$ density: max, min (Å^3)	0.54, −0.26	0.39, −0.27	0.25, −0.25

[a] $R(F) = \Sigma[||F_o|-|F_c||]/\Sigma[|F_o|]$; $wR(F^2) = [\Sigma[w(F_o^2 - F_c^2)^2]/\Sigma[w(F_o^2)^2]]^{1/2}$

D.1.6. Additional analysis of single crystal X-ray structures

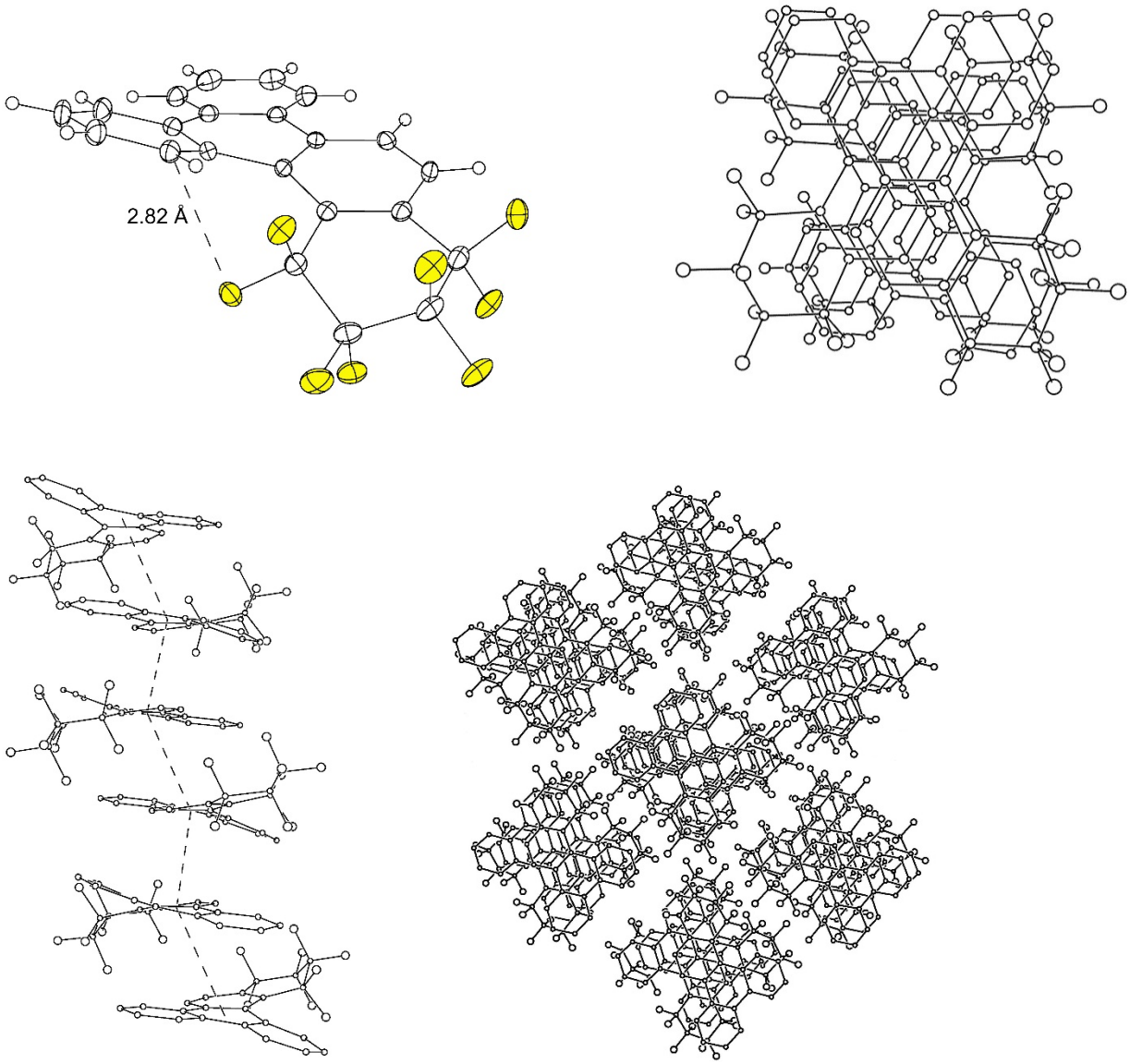

Figure D-15. Several drawings of the previously published structure of 1,2-TRPH(C_4F_8) (50% ellipsoids except for H atoms in the upper left drawing; H atoms omitted for clarity in the other drawings).[6] The central pentagon centroid···centroid distances shown in the lower left drawing are 4.08 and 5.20 Å. The perpendicular distance of some of the TRPH core C atoms from the plane of the π system in neighboring molecules in the stack with which they overlap are 3.4–3.6 Å.

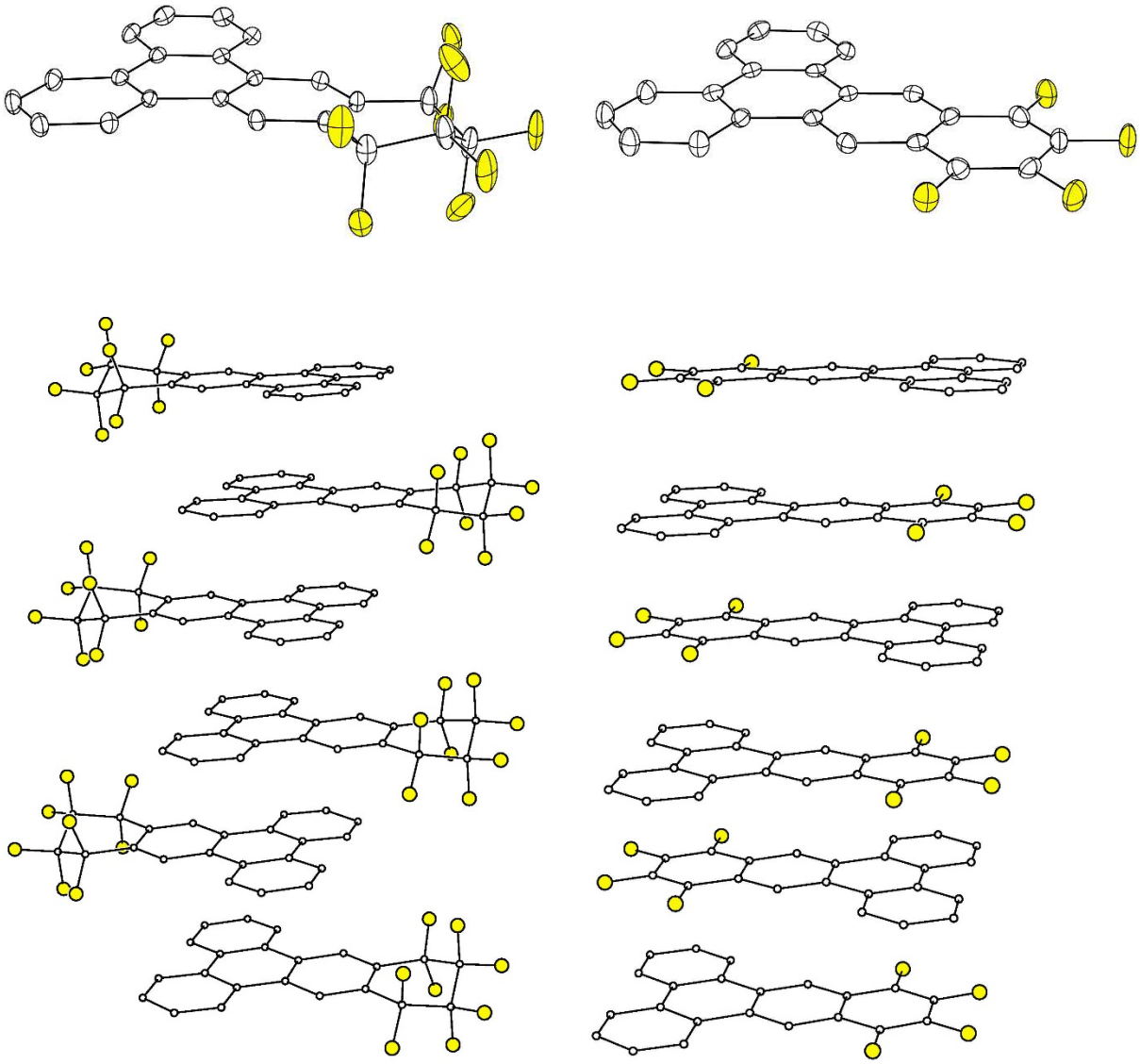

Figure D-16. The previously published structures of 2,3-TRPH(C_4F_8) and 2,3-TRPH(C_4F_4) (50% ellipsoids in the drawings at the top; H atoms omitted for clarity from all four drawings).[6] Unlike the structure of 1,2-TRPH(C_4F_8), the π systems of these two molecules are planar: the average out-of-plane displacement of the TRPH core C(sp^2) atoms in 2,3-TRPH(C_4F_8) from their least-squares plane is 0.034 Å, and the average out-of-plane displacement of all of the C(sp^2) atoms in 2,3-TRPH(C_4F_4) from their least-squares plane is 0.019 Å. Both molecules form hexagonal arrays of stacks of rigorously parallel molecules, with perpendicular distances between overlapped C(sp^2) atoms to the least-squares planes of neighboring molecules in the stacks of 3.30 to 3.40 Å (av. 3.34 Å) in 2,3-TRPH(C_4F_8) and from 3.38 to 3.42 Å (av. 3.40 Å) in 2,3-TRPH(C_4F_4).

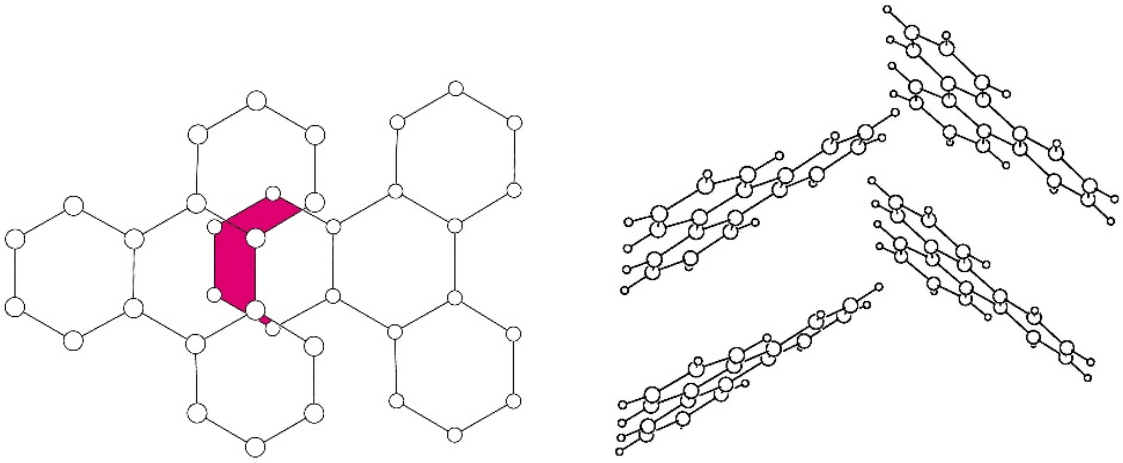

Figure D-17. The herringbone structure of tetragonal TRPH.[7] The range and average value of the perpendicular distances between the four C(sp^2) atoms in one molecule and the least-square planes of neighboring molecules in the slipped stacks with which they overlap are 3.32–3.34 Å and 3.32 Å. Hydrogen atoms have been omitted for clarity in the drawing on the left.

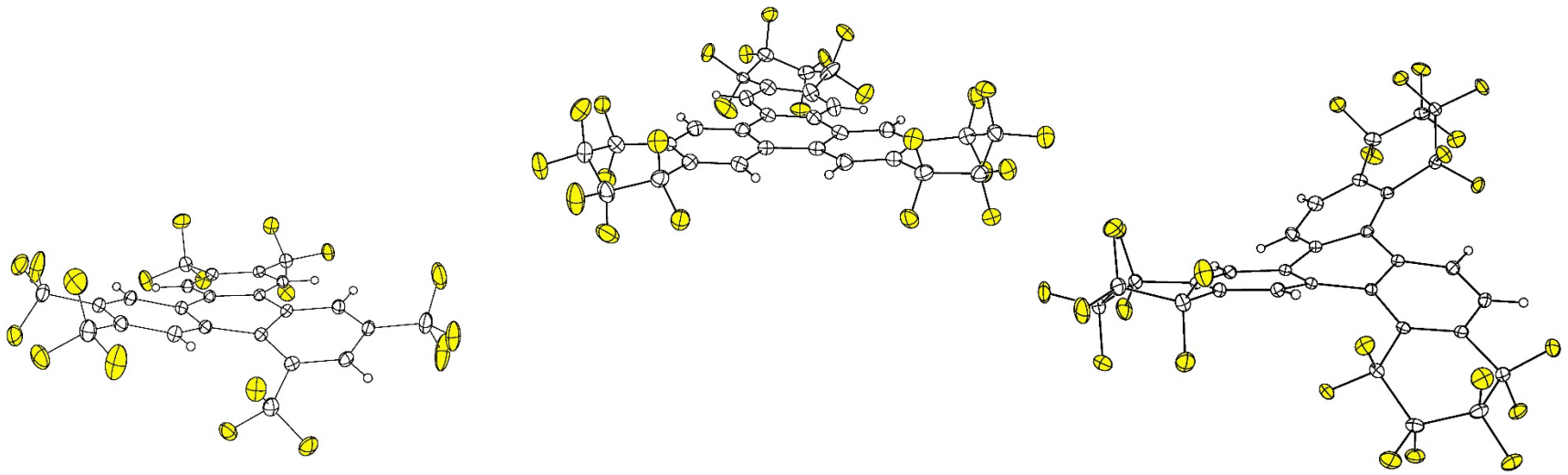

Figure D-18. Comparison of the degrees of planarity of three TRPH derivatives with six perfluorocarbyl substituents, 2,3:6,7:10,11-TRPH(C_4F_8)$_3$ (left, no bay C(sp^2) substituents; this work), 1,3,6,7,10,11-TRPH(CF_3)$_6$ (middle, one bay C(sp^2) substituent; ref. [8]), and 1,2:5,6:10,11- TRPH(C_4F_8)$_3$ (right, two bay C(sp^2) substituents; this work).

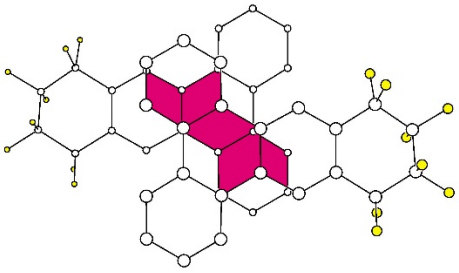

2,3-TRPH(C_4F_8): 3.30–3.40 Å; av. 3.34 Å

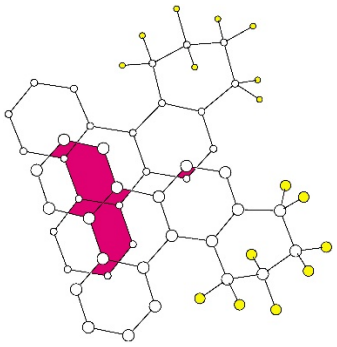

1,2-TRPH(C_4F_8): 3.47–3.63 Å; av. 3.55 Å

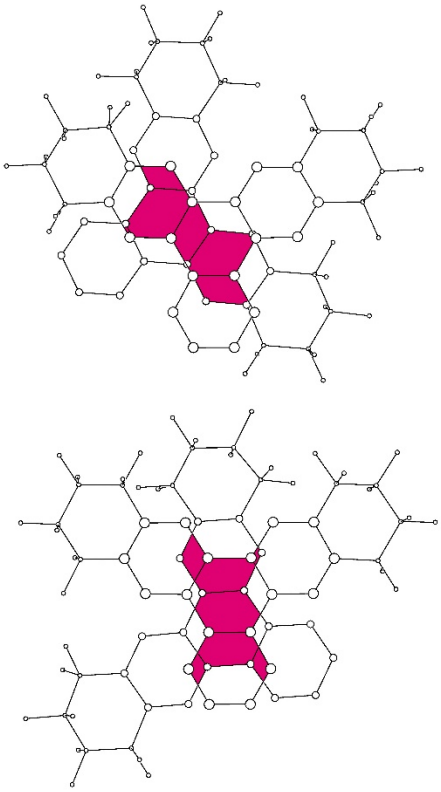

2,3:6,7-TRPH(C_4F_8)$_2$: 3.38–3.62 Å; av. 3.51 Å

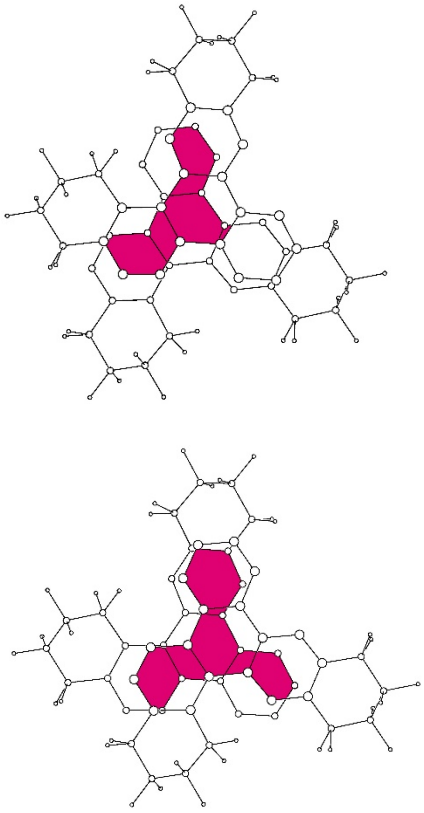

1,2:10,11-TRPH(C_4F_8)$_2$: 3.48–3.74 Å; av. 3.62 Å

Figure D-19. Parallel projections of neighboring molecules in the structures of 2,3-TRPH(C_4F_8), 1,2-TRPH(C_4F_8), 2,3:6,7-TRPH(C_4F_8)$_2$, and 1,2:10,11-TRPH(C_4F_8)$_2$. The ranges and average values of perpendicular distances between C(sp^2) atoms and the least-square planes of neighboring molecules with which they overlap are shown.

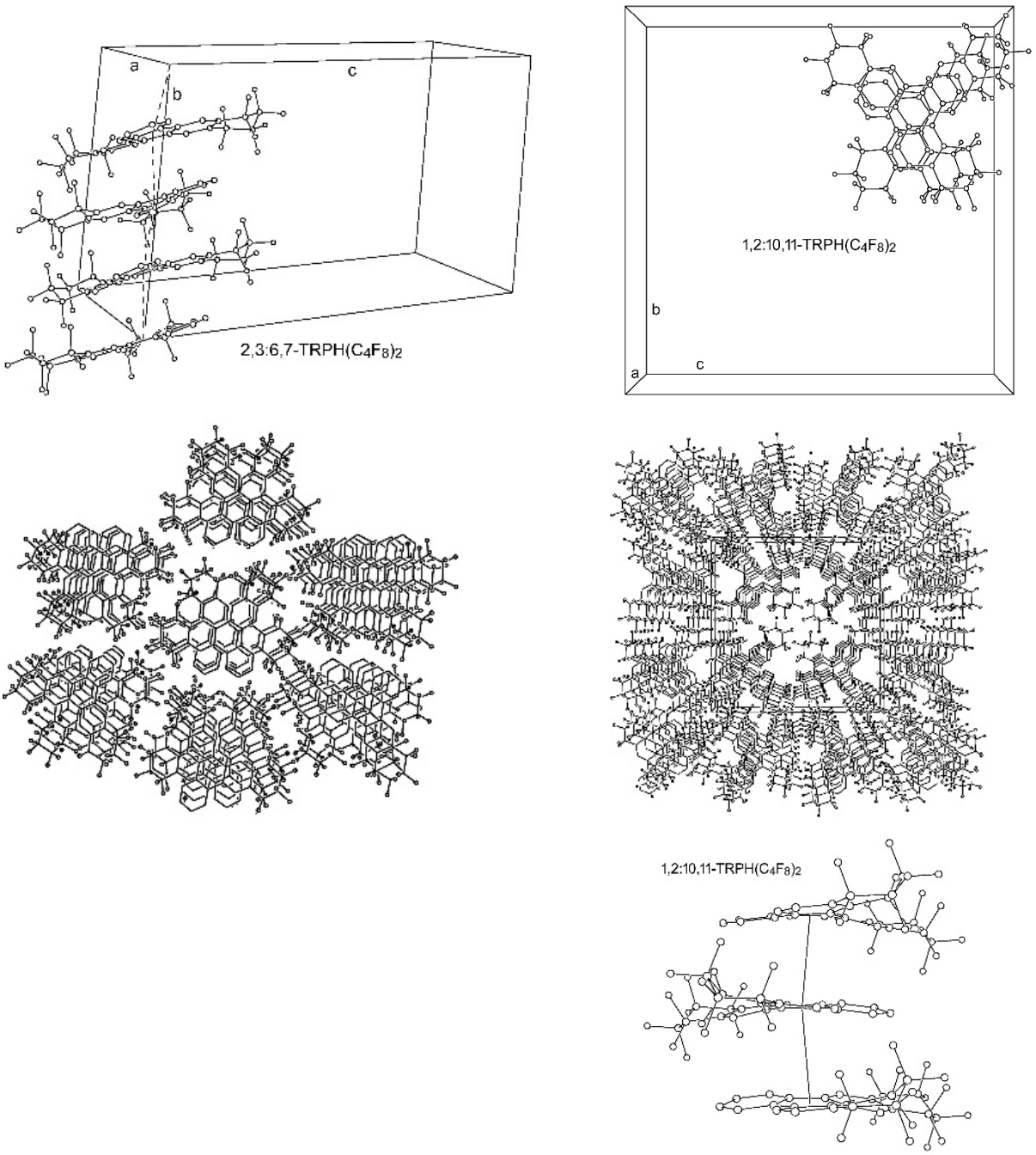

2,3:6,7-TRPH(C_4F_8)$_2$ 1,2:10,11-TRPH(C_4F_8)$_2$

Figure D-20. Comparison of the packing of molecules in the structures of 2,3:6,7-TRPH(C_4F_8)$_2$ (left) and 1,2:10,11-TRPH(C_4F_8)$_2$ (right). The central hexagon centroid···centroid (⊙···⊙) distances in the 2,3:6,7 isomer (dashed lines) are 3.63, 3.64, 3.86, and 4.00 Å. The ⊙···⊙ distances in the 1,2:10,11 isomer (jagged lines) are both 3.87 Å.

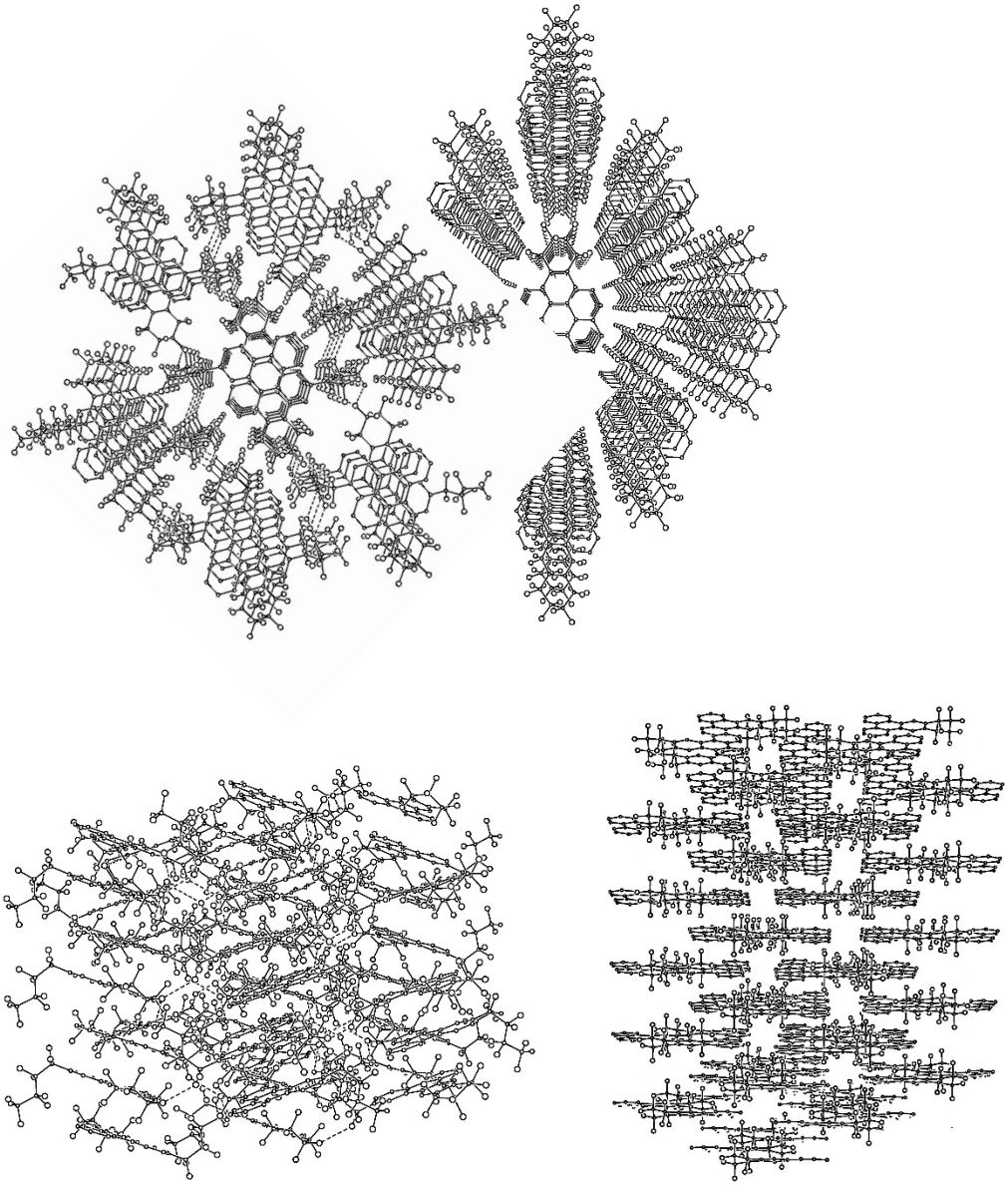

2,3:6-TRPH(C_4F_8)(ω-C_4F_8H) 2,3-TRPH(C_4F_8)

Figure D-21 Comparison of the hexagonal arrays of stacks of molecules in the structures of 2,3:6-TRPH(C_4F_8)(ω-C_4F_8H) (left) and 2,3-TRPH(C_4F_8) (right).

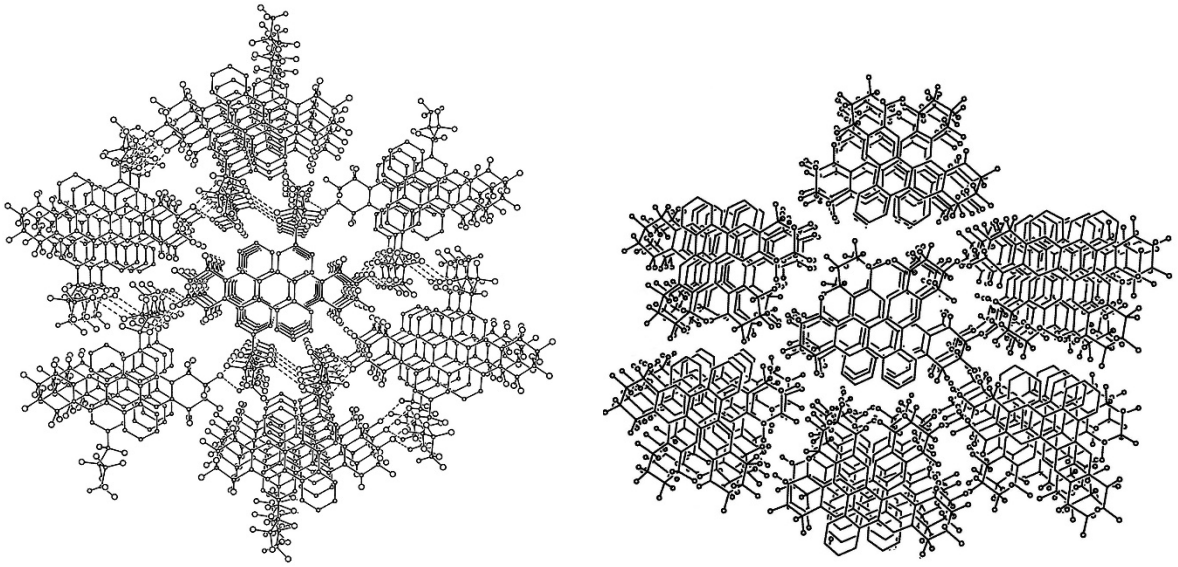

2,3:6-TRPH(C_4F_8)(ω-C_4F_8H)　　2,3:6,7-TRPH(C_4F_8)$_2$

Figure D-22. Comparison of the hexagonal arrays of stacks of molecules in the structures of 2,3:6-TRPH(C_4F_8)(ω-C_4F_8H) (left) and 2,3:6,7-TRPH(C_4F_8)$_2$ (right), the molecular formulas for which differ only by 2 H atoms.

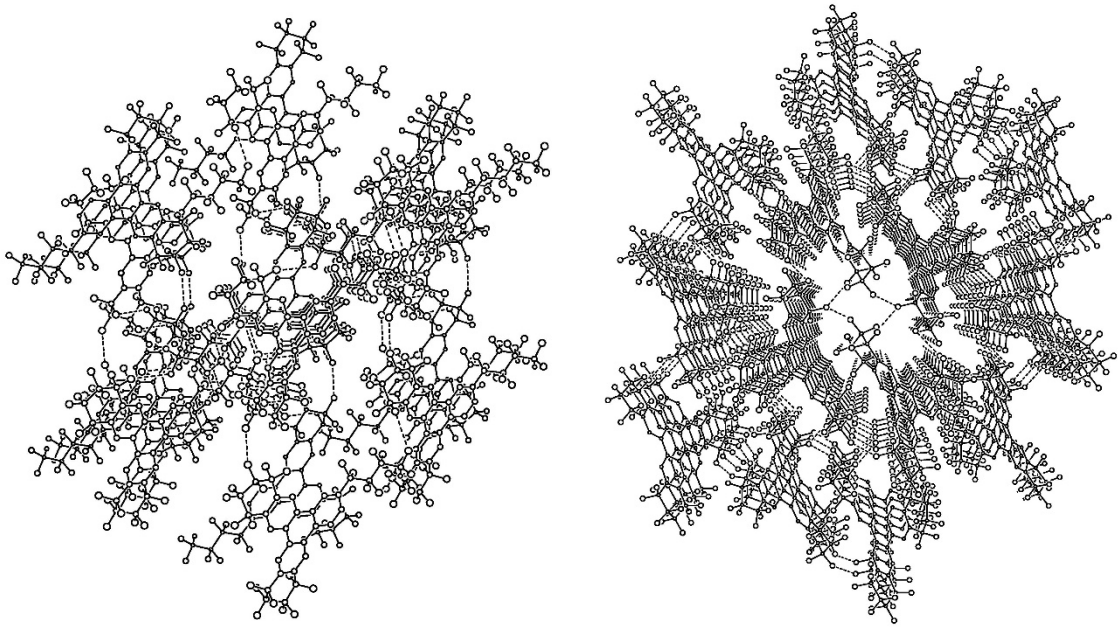

2,3:6,7:10-TRPH(C_4F_8)$_2$(ω-C_4F_8H) 2,3:6,7:10,11-TRPH(C_4F_8)$_3$

Figure D-23. Comparison of the hexagonal arrays of stacks of molecules in the structures of 2,3:6,7:10-TRPH(C_4F_8)$_2$(ω-C_4F_8H) (left) and 2,3:6,7:10,11-TRPH(C_4F_8)$_3$ (right), the molecular formulas for which differ only by 2 H atoms.

Comparison of the structures of 2,3-TRPH(C_4F_3H) and 2,3-TRPH(C_4F_4)

Notes: 1. technically these are tetrafluoro and trifluoro derivatives of benzo[b]triphenylene;

they are referred to as triphenylene (TRPH) derivatives for convenience.

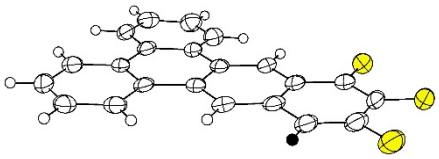

2,3-TRPH(C_4F_3H)

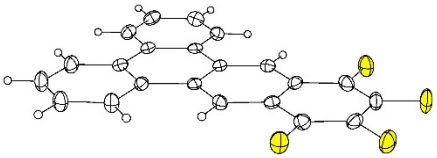

2,3-TRPH(C_4F_4)

The figures above are 50% thermal ellipsoid plots of the crystallographically unique molecule in the structures of 2,3-TRPH(C_4F_3H) and 2,3-TRPH(C_4F_4). The H atom on the fluorinated ring in 2,3-TRPH(C_4F_3H) is shaded black for emphasis; 2,3-TRPH(C_4F_3H) molecule is 68:32 disordered with respect to that H atom and the F atom that is *para* to it. Both structures are triclinic.

Both molecules are essentially planar, although 2,3-TRPH(C_4F_3H) is slightly less so, as shown in the figures below. The average perpendicular displacements of C and F atoms from the least-squares plane of the C and F atoms in the structure of 2,3-TRPH(C_4F_3H) range from −0.11 (for F1) to 0.12 Å (C11, C12) and average 0.05 Å. The average perpendicular displacements of C and F atoms from the least-squares plane of the C and F atoms in the structure of 2,3-TRPH(C_4F_4) range from −0.05 to 0.05 Å and average 0.02 Å (neither extreme is an F atoms).

2,3-TRPH(C_4F_3H)

2,3-TRPH(C_4F_4)

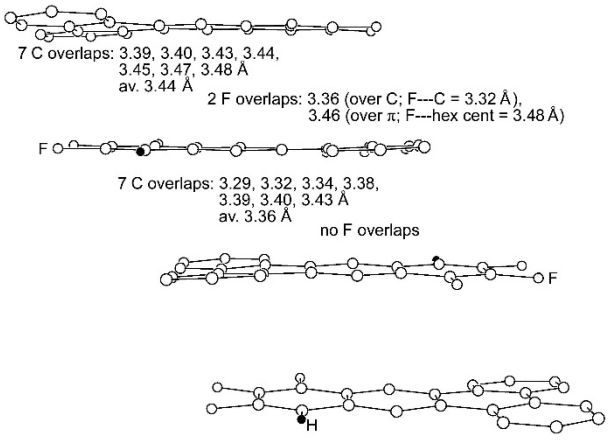

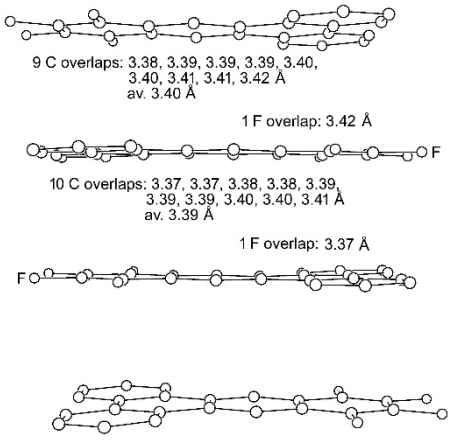

In the figures above, the perpendicular distances between the least-squares plane of the π system of a single molecule and the C and F atoms that overlap that π system in the neighboring molecules (above and below) within a given stack are given. The perpendicular distances between the least-squares planes of every other molecule are essentially the same in both structures, 6.80 Å for 2,3-TRPH(C_4F_3H) and 6.79 Å for 2,3-TRPH(C_4F_4).

Two views of the stacks of molecules in the two structures are shown below. The lower drawing is rotated relative to the upper drawing in both cases. In both upper drawings the view is approximately looking down the crystallographic *a* axis, which is also the shortest unit cell axis. In both structures each stack is surrounded by six other stacks in a pseudo-hexagonal array. All of the molecules in all of the stacks in each structure are rigorously parallel to one another (i.e., the least-squares planes of the C atoms are rigorously parallel to one another). Therefore, in both struc-tures the Desiraju-Gavezzotti interplanar angle θ is 0.0°. See related drawings on the next page.

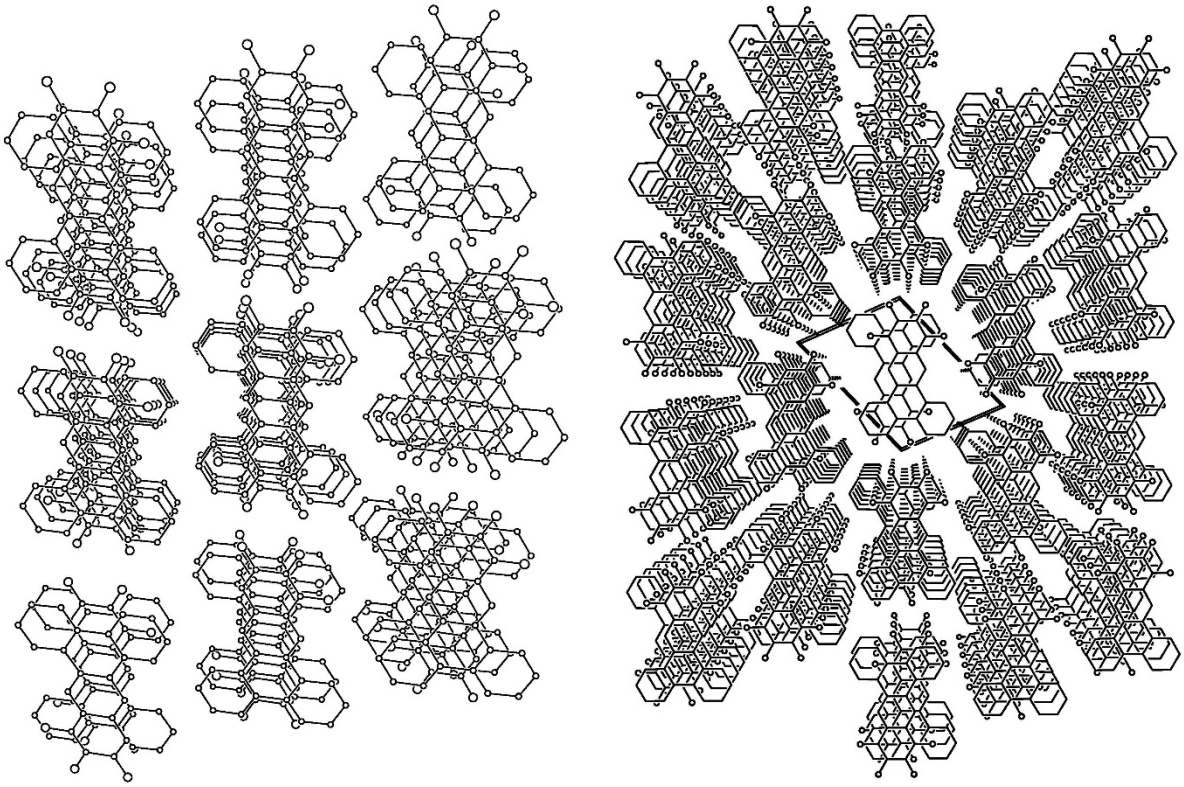

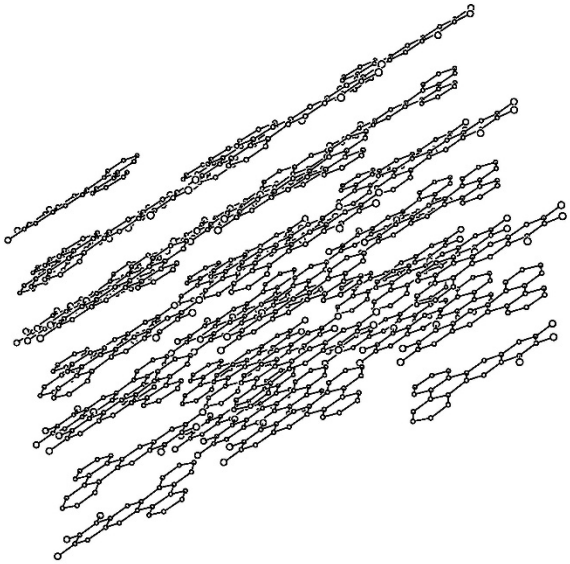

2,3-TRPH(C_4F_3H)

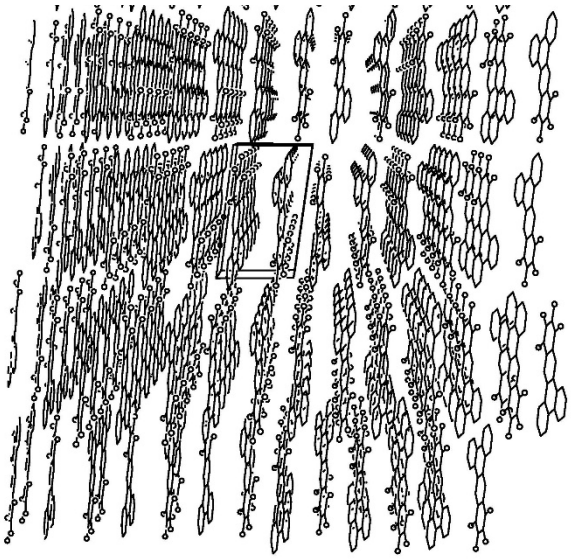

2,3-TRPH(C_4F_4)

In the two drawings below, showing three neighboring molecules in each of three neighboring infinite stacks of molecules, the view is rigorously looking down the crystallogrphic *a* axis. The least-squares planes of the molecules are not in the plane of the page in these drawings.

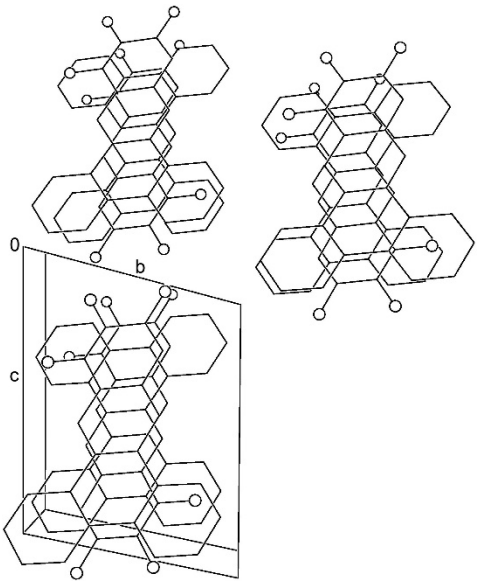

2,3-TRPH(C_4F_3H)

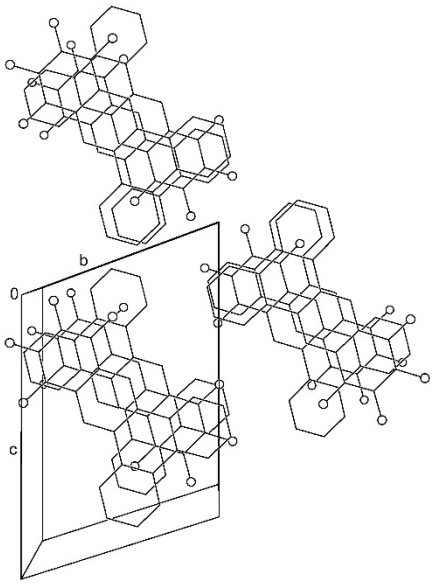

2,3-TRPH(C_4F_4)

The drawings below show overlap of the π systems in the two types of neighboring molecules in each stack. Note the large lateral shift, highlighted by the double-headed arrow, along the long molecular axis in every other pair of molecules in the stacks in the structure of 2,3-TRPH(C_4F_3H).

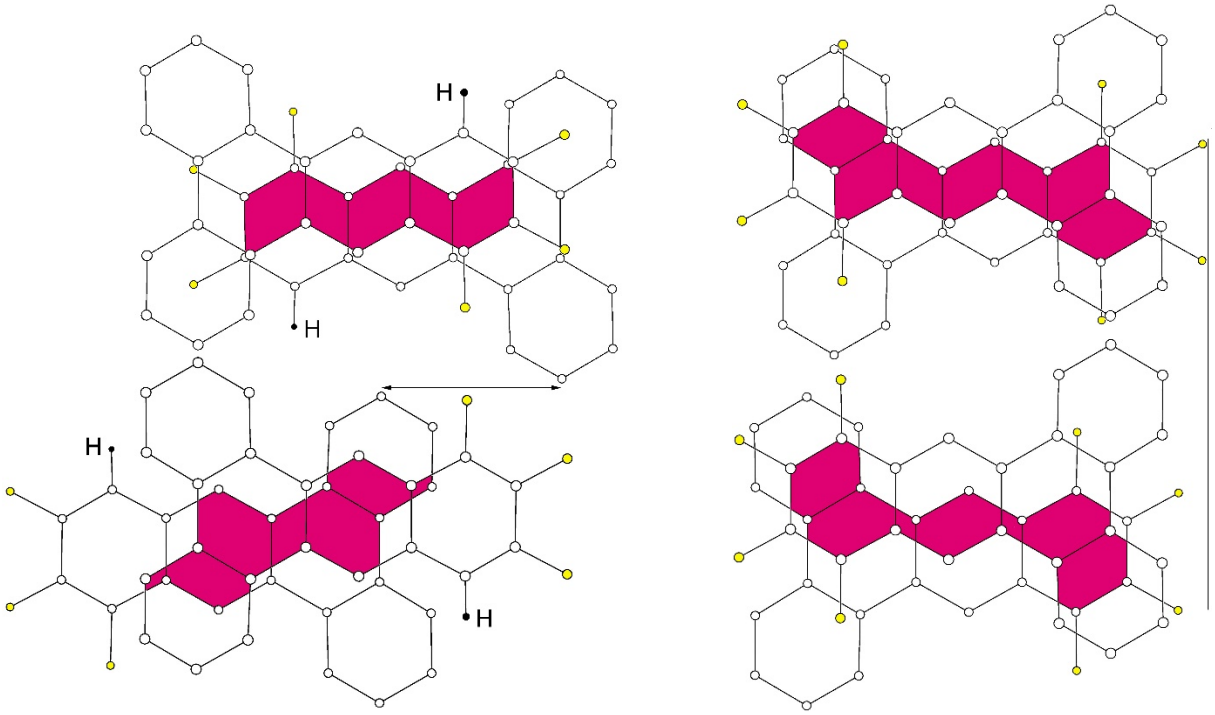

2,3-TRPH(C_4F_3H) 2,3-TRPH(C_4F_4)

The drawings below show two views of six molecules in the stacks in the structures of 2,3-TRPH(C_4F_3H) and 2,3-TRPH(C_4F_4). The least-squares planes of the molecules in the lower drawings are in the plane of the page. The dramatic difference in the long-axis lateral shift and the smaller but still significant difference in the short-axis lateral shift is readily apparent. The differences are the reason that the areas of π overlap are ca. 30% smaller in 2,3-TRPH(C_4F_3H) than in 2,3-TRPH(C_4F_4).

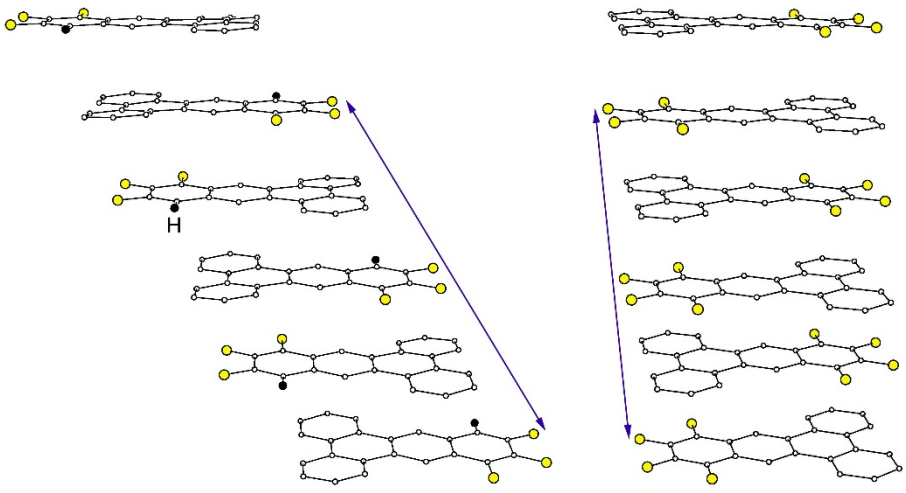

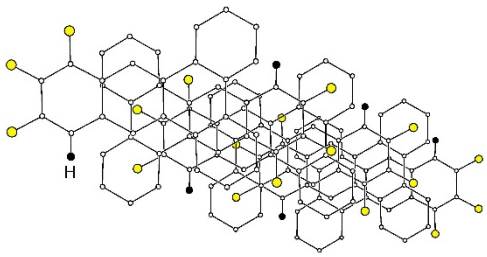

2,3-TRPH(C_4F_3H)

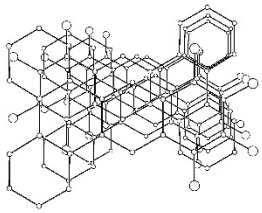

2,3-TRPH(C_4F_4)

It is not clear at this time why two such similar molecules form stacks with such different amounts of π–π overlap between neighboring molecules in the stacks when they crystallize. It may be related to the number and strength of CH···FH interactions (see figures below), or the different magnitudes and directions of the molecular dipole moments, or differences in the electrostatic potential distributions, or differences in molecular quandrupole interactions, or a combination of some or all of these factors.

The drawings below are an attempt to compare the number and strength (distances) of CH···FH "hydrogen bonds". The are three triplets of molecules for 2,3-TRPH(C_4F_3H), with 16 interactions ranging from 2.51 to 2.92 Å and averaging 2.76 Å. There are three pairs of molecules for 2,3-TRPH(C_4F_4), with 13 interactions ranging from 2.63 to 2.80 Å and averaging 2.73 Å).

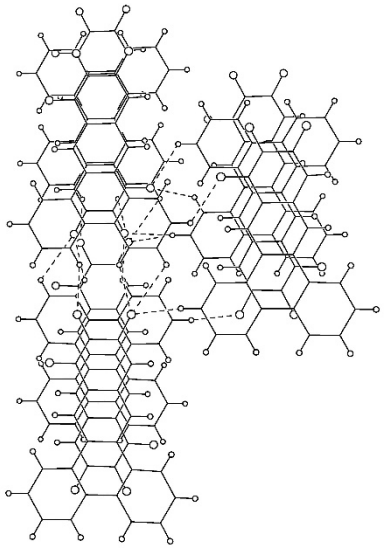

2,3-TRPH(C_4F_3H)

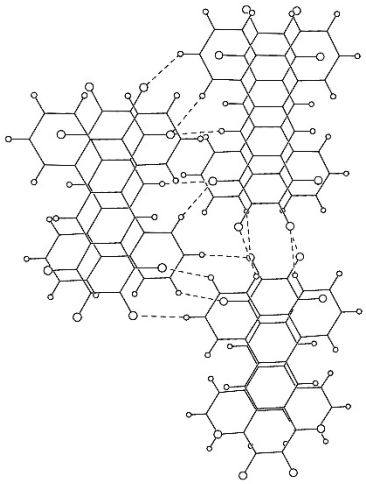

2,3-TRPH(C_4F_4)

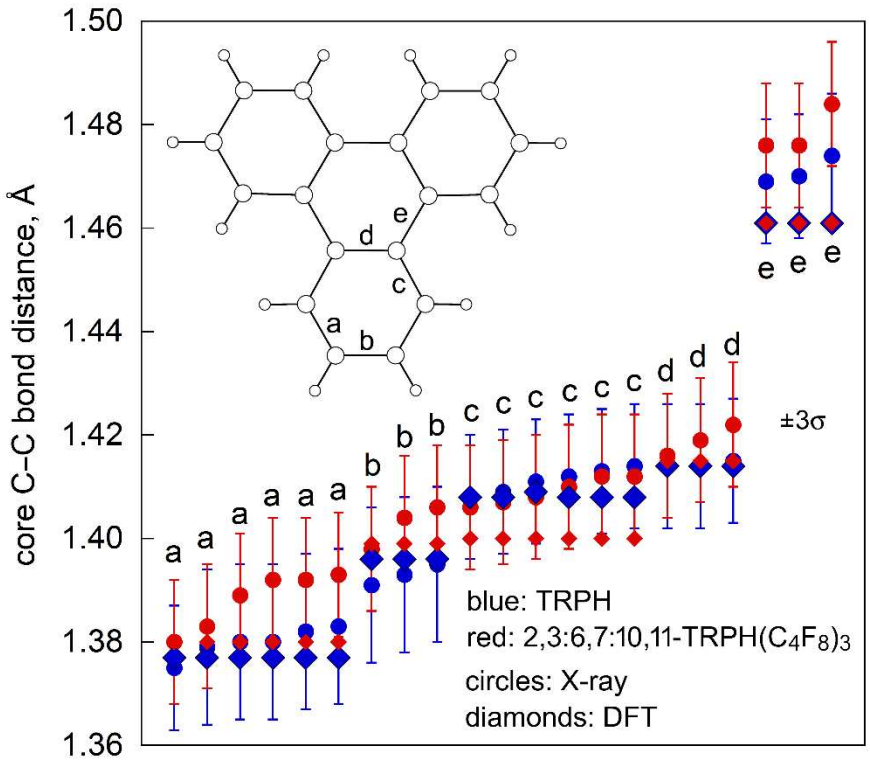

Figure D-24. Plots of X-ray and DFT-predicted core C–C bond distances in TRPH (blue data points) and 2,3:6,7:10,11-TRPH(C_4F_8)$_3$ (red data points). The data for the X-ray structure of TRPH were taken from ref. [7]. The data for the X-ray structure of 2,3:6,7:10,11-TRPH(C_4F_8)$_3$ and both DFT optimized structures (with enforced symmetry) are from this work.

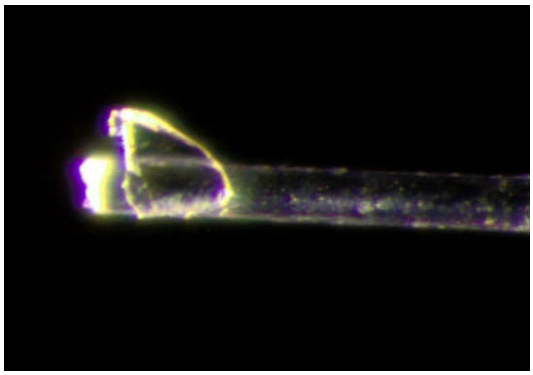

Figure D-25. Enlarged image of crystal on the tip of a glass fiber, studied at APS. Dimension are approximately 100 by 200 by 50 microns. In many cases, crystals were needles, with short dimensions of tens of microns.

D.1.6. PES spectra of selected compounds

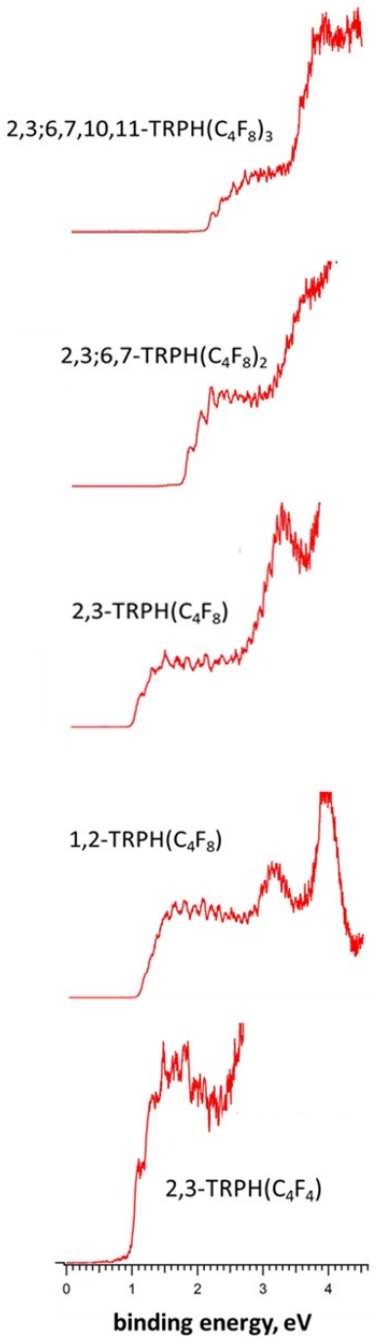

Figure D-26. Low-temperature photoelectron spectrum (20 K, 266 nm) of select compounds showing incremental increase on EA for each additional fluorous moiety. Note that the C_4F_4 derivatized compound has a lower EA than the mono-substituted C_4F_8 derivatives.

D.1.8. Attempted CV studies

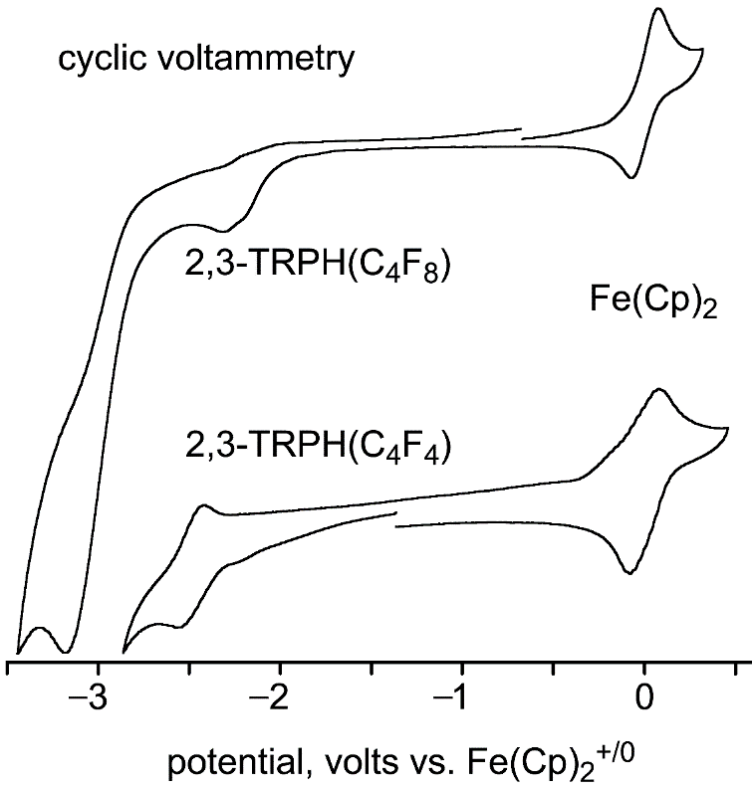

Figure D-27. Cyclic voltammograms of 2,3-C_4F_8 and 2,3-C_4F_4 dissolved in dimethoxyethane containing 0.1 M N(n-Bu)4ClO4 (0.2 mm platinum wire working and counter electrodes; silver wire quasi-reference electrode). The scan rate was 500 mV s−1. The irreversibility of the reduction may be due to *in situ* reductive defluorination.

D.1.9. DFT data for chapter 1

DFT Calculations. DFT calculations were performed at the B3LYP-D3/def2-TZVPP level as implemented in version 6.5 of the NWCHEM package (Valiev, M.; Bylaska, E. J.; Govind, N.; Kowalski, K.; Straatsma, T. P.; Van Dam, H. J. J.; Wang, D.; Nieplocha, J.; Apra, E.; Windus, T. L.; de Jong, W. A., "NWChem: A comprehensive and scalable open-source solution for large scale molecular simulations," *Comput. Phys. Commun.* **2010**, *181*, 1477-1489).

Table D-4. DFT-predicted relative energies

compound	relative energy, kJ mol^{-1}
2,3-TRPH(C_4F_8)	0.0
1,2-TRPH(C_4F_8)	53.3
2,3-TRPH(C_4F_4)	0.0
1,2-TRPH(C_4F_4)	32.7
2-TRPH(C_4F_8I)·	0.0
1-TRPH(C_4F_8I)·	65.4

Table D-5. DFT-predicted and experimental gas phase EAs

2,3-TRPH(C_4F_8)	1.003 eV (exp. value 1.13(3) eV)
2,3-TRPH(C_4F_4)	1.032 eV (exp. value 1.10(3) eV)
1,2-TRPH(C_4F_8)	1.107 eV (exp. value 1.20(5) eV)
1,2-TRPH(C_4F_4)	0.921 eV (no exp. value at this time)
2,3;6,7-TRPH(C_4F_8)$_2$	1.771 eV (exp. value 1.80(2) eV)
2,3;6,7;10,11-TRPH(C_4F_8)$_3$	2.233 eV (exp. value 2.25(2) eV)

Table D-6. DFT orthogonal coordinates for 1,2-TRPH(C_4F_8), 2,3-TRPH(C_4F_4), and 1,2-TRPH(C_4F_8).

F	-0.597575670	2.680451710	0.476087920
F	-2.141045170	3.133728720	-1.590101480
F	-2.146473180	1.029439900	-2.199387030
F	0.241579880	1.850624430	-1.379208700
F	-3.211147690	2.433442490	0.847661030
F	-3.760610430	-0.684504490	-0.591200530
F	-3.889540960	0.032398190	1.466388960
F	-4.412828720	1.769981720	-0.852127280
C	-0.705832240	1.651475910	-0.427524590
C	0.684968830	-1.756565460	0.670430240
C	-2.068960640	1.868042150	-1.138128880
C	2.008059680	0.295093560	0.347860460
C	3.081660580	-1.933195850	0.038536120
C	4.419096930	0.166848730	0.054547900
H	5.313413530	-0.411436380	-0.119403840
C	1.884510660	-2.562057950	0.442368430
C	0.695303600	-0.361874660	0.406522870
C	2.178649060	1.660066550	0.641848680
H	1.336815240	2.251419410	0.946228630
C	-3.251124710	1.578735010	-0.198027020
C	-1.746116120	-0.382064130	0.565653030
C	-1.698804470	-1.681872320	1.076378180
H	-2.613479310	-2.165444200	1.386123730
C	-0.570509430	0.288712020	0.231110680
C	4.105436560	-4.109871430	-0.304054780
H	4.955435550	-4.702143420	-0.615445530
C	-0.512979180	-2.363481460	1.082199260
H	-0.516608400	-3.395041850	1.396017290
C	1.849798090	-3.968796970	0.502000530
H	0.948338400	-4.479953210	0.801967540
C	3.414412940	2.268805680	0.598229570
H	3.501154810	3.320221190	0.836511360
C	4.169023160	-2.734175150	-0.354671080
H	5.075677600	-2.271204420	-0.713340350
C	3.171843400	-0.480021180	0.112592330
C	2.939497300	-4.733254860	0.145247880
H	2.879773670	-5.812199210	0.192050210
C	4.544777900	1.521774850	0.271243090
H	5.519687750	1.988837860	0.230488570
C	-3.149628990	0.126280950	0.324608940

F	-0.000050870	2.733614830	3.026584850
F	-0.000014570	1.346198080	5.363032940
F	0.000045910	-1.346325990	5.362996520
F	0.000056570	-2.733719640	3.026425450
C	-0.000027770	1.390986270	3.009087600
C	-0.000009160	0.707955250	4.190591940
C	0.000023460	-0.708011890	4.190607770
C	0.000028310	-1.390991340	3.009016320
C	0.000004620	-0.712876920	1.766807300
C	-0.000005330	-1.386948170	0.540843300
H	-0.000013110	-2.463608950	0.576808600
C	0.000001740	-0.716914120	-0.674446390
C	-0.000005270	-1.444990250	-1.947697600
C	0.000000260	-2.851680800	-1.987753700
H	0.000007890	-3.419368570	-1.070280130
C	-0.000003990	-3.546364300	-3.178060880
H	-0.000002800	-4.628002990	-3.172668080
C	-0.000006370	-2.845214730	-4.383700900
H	-0.000011200	-3.376377770	-5.326088980
C	-0.000010620	-1.466848010	-4.370635740
H	-0.000004770	-0.951114320	-5.317852060
C	-0.000008760	-0.733461550	-3.169371990
C	-0.000009570	0.733491060	-3.169312730
C	-0.000011930	1.466810060	-4.370631070
H	-0.000024340	0.951108220	-5.317887760
C	0.000006290	2.845200610	-4.383734120
H	0.000002740	3.376331970	-5.326166780
C	0.000035040	3.546366230	-3.178068240
H	0.000062530	4.627998540	-3.172729880
C	0.000034200	2.851696230	-1.987803590
H	0.000070820	3.419334670	-1.070410800
C	0.000000230	1.445043530	-1.947682560
C	-0.000022680	0.717077000	-0.674393140
C	-0.000050490	1.387007630	0.540853760
H	-0.000110350	2.463518430	0.576763430
C	-0.000024200	0.713077220	1.766792260

C	2.609430940	-1.270367540	-0.569816180
C	1.332063750	-0.625201070	-0.275117840
C	0.111671600	-1.269277730	-0.525748080
C	3.819302860	-0.591828230	-0.290527640
C	5.032861650	-1.241139250	-0.588420780
C	-2.356632980	-1.476530510	-0.488383480
C	2.669936330	-2.559321530	-1.133386130
C	-1.103890930	-0.672534100	-0.263502500
C	3.871087590	-3.171050620	-1.415051350
F	-4.734060650	-1.389053060	-0.466283180
C	-3.640057850	-0.610670060	-0.560992060
C	5.065679340	-2.503722860	-1.138412970
F	-2.516062930	-2.383967220	0.521488260
F	-3.664420320	0.019917430	-1.759411780
F	-2.278437580	-2.199801920	-1.640612910
C	2.554191490	1.377939400	0.571301980
C	1.304700020	0.678946680	0.279333070
C	0.058142620	1.270358310	0.531474980
C	3.791305100	0.750358700	0.291657900
C	4.976891230	1.450323900	0.587477000
C	-2.416623890	1.374908850	0.490152290
C	2.561267970	2.669778940	1.131535180
C	-1.131233220	0.623131870	0.268289380
C	3.736112360	3.331890670	1.410537420
F	-4.788516990	1.192128100	0.453149240
C	-3.664851320	0.458134600	0.554915050
C	4.957345480	2.714321900	1.134760660
F	-2.608004500	2.277718000	-0.518370070
F	-3.671563680	-0.172931100	1.753247340
F	-2.372635940	2.097912590	1.644352690
H	0.096542810	-2.265557940	-0.936244260
H	0.000835220	2.264694750	0.943084990
H	1.631567200	3.168956460	1.356318950
H	3.708586190	4.323573310	1.841344510
H	5.887388540	3.223433220	1.349380640
H	5.935313960	0.998194500	0.386746980
H	5.971720680	-0.749711920	-0.387590640
H	6.015996400	-2.973017990	-1.354961040
H	3.884369340	-4.161720980	-1.848865490
H	1.761714310	-3.095999210	-1.359424250

Table D-7. DFT orthogonal coordinates for 2-TRPH(C_4F_8I), 1,2-TRPH(C_4F_4), and 1-TRPH(C_4F_8I).

C	0.615110730	-2.671477140	-2.494698760
C	1.071053370	-1.977365570	-1.291694230
C	1.427715730	-2.713175840	-0.137326840
C	0.076264180	-4.721329360	-3.673387170
H	-0.004902120	-5.796479720	-3.705886570
C	1.330677300	-4.170922420	-0.141811540
C	-0.166374750	-2.617726760	-4.799284740
H	-0.427794450	-2.048097650	-5.680951750
C	1.161481480	-0.574982090	-1.249861250
H	0.887534710	0.012027210	-2.109580260
C	1.951305890	-0.633805230	1.018652710
H	2.293485820	-0.118737560	1.904077880
C	1.125639100	-6.973165560	-0.145375030
H	1.042103420	-8.051784760	-0.153275640
C	0.519285410	-4.083199400	-2.498355000
C	1.673550240	-4.935294120	0.990810250
H	2.022730380	-4.446683910	1.886991750
C	0.264288790	-1.968440030	-3.663661140
H	0.329587410	-0.891812910	-3.688665300
C	0.877964820	-4.844079150	-1.301919800
C	1.868322250	-2.005329020	0.998717540
H	2.153337990	-2.539313580	1.891123910
C	0.785998780	-6.249258560	-1.266882890
H	0.440276030	-6.788849040	-2.134571630
C	-0.261481120	-4.010608940	-4.803819890
H	-0.597637870	-4.532706690	-5.689686710
C	1.590267550	0.090099200	-0.122375020
C	1.576258290	-6.308929200	0.997089630
H	1.846736530	-6.866446230	1.883803130
C	-0.976748620	1.868902420	0.138056980
C	1.641386860	1.591960020	-0.096839920
C	0.443833630	2.282676950	0.644011020
C	-2.160367560	2.841567690	0.465261590
I	-2.493502440	3.214649760	2.584179280
F	-0.945920130	1.770802930	-1.215222040
F	-1.970267460	4.004885660	-0.172925030
F	1.704264240	2.117726220	-1.349000110
F	-1.282089250	0.656343510	0.640129400
F	0.537995280	1.960782200	1.955776390
F	2.754338200	2.020074690	0.571449720
F	-3.270729330	2.271891190	-0.040633540
F	0.581933020	3.621418330	0.527259730

C	2.664530050	-0.218774200	0.124085890
C	2.621936070	-1.659368530	-0.081529720
C	3.774238110	-2.410196060	-0.378185790
C	1.452665450	0.508862320	0.232175130
C	1.518177270	1.855500240	0.642520070
C	3.881271720	0.464167720	0.306102560
C	3.733927190	-3.783963750	-0.477052640
C	3.916813110	1.800917770	0.637537930
C	2.721023290	2.495351620	0.837293170
C	0.158820940	-1.575752130	0.240500570
C	1.390561690	-2.338373510	0.080918770
C	1.378454010	-3.744187440	-0.014181800
C	0.179264440	-0.182848610	0.082063250
C	-1.080242100	0.495776730	-0.128980850
C	-1.072645980	-2.218672330	0.552745390
C	2.525635810	-4.458459320	-0.282668860
C	-2.243749950	-1.533038150	0.626116700
C	-2.291625950	-0.173481030	0.226238960
H	4.714466920	-1.905997400	-0.543889960
H	0.450149950	-4.285200030	0.088394870
H	-1.077032950	-3.271178210	0.789814880
H	-3.157470230	-2.024366370	0.925130140
H	0.606973580	2.394797390	0.846979770
H	2.735619420	3.527538550	1.160509490
H	4.867217780	2.297097980	0.782274050
H	4.814025740	-0.073709580	0.228326390
H	4.634432070	-4.335936310	-0.711156710
H	2.483793940	-5.536413220	-0.363066400
C	-3.524308860	0.490374970	0.096207860
C	-1.222818410	1.747899100	-0.769820400
C	-3.612048870	1.746734620	-0.441826490
C	-2.443849010	2.366232740	-0.904733610
F	-0.183251840	2.353844930	-1.363892090
F	-2.539569730	3.546830250	-1.520850010
F	-4.785656830	2.364359110	-0.585981180
F	-4.653222280	-0.135707890	0.466521970

C	-1.969534340	-1.343522120	0.352591130
C	-1.535450150	-0.527017470	1.487799110
C	-1.154678040	-1.220086600	2.666926140
C	-1.960801700	-3.446548840	-0.860265500
H	-1.645788530	-4.474631930	-0.955499660
C	-0.729177640	-2.619820720	2.579773050
C	-3.325980460	-1.641121840	-1.645174920
H	-4.057294700	-1.247694140	-2.338407380
C	-1.488689520	0.903643010	1.524094220
C	-1.293836180	0.836224040	3.936978900
H	-1.275085960	1.359058310	4.883036380
C	0.381245610	-5.188860350	2.314870170
H	0.827992840	-6.167684530	2.202245670
C	-1.546346540	-2.690963560	0.249969000
C	-0.134808360	-3.277600340	3.673053140
H	-0.060612350	-2.783438590	4.629519940
C	-2.913441540	-0.873318600	-0.576799460
H	-3.354726710	0.095356600	-0.435230560
C	-0.796937860	-3.299134220	1.343257360
C	-1.104838280	-0.524219850	3.885112480
H	-0.907972380	-1.056613240	4.802584930
C	-0.210788220	-4.572399920	1.233424380
H	-0.213866290	-5.083858690	0.282564220
C	-2.816547240	-2.928568790	-1.809944970
H	-3.127645390	-3.538526370	-2.647640570
C	-1.400068210	1.551400000	2.749118960
C	0.404228330	-4.540989670	3.551306750
H	0.863703230	-5.015318260	4.408102600
C	-1.272232130	1.809746060	0.311134670
C	1.317871040	1.251614350	0.199738050
C	-0.023954440	1.454291960	-0.582725020
C	2.644507300	1.416367860	-0.618250520
I	2.864591230	0.056564900	-2.305022260
F	1.386573670	2.161516510	1.201109650
F	2.757006040	2.683267730	-1.040864150
F	-1.069175630	3.097554700	0.710469270
F	1.325541250	0.020048290	0.748688430
F	-0.283894390	0.328672870	-1.277559180
F	-2.325724990	1.886862700	-0.556029500
F	3.652686260	1.180781550	0.243583960
F	0.139630350	2.460800120	-1.471728880
H	-1.371078490	2.627772910	2.783922890

D.2. CHAPTER 2 MISCELLANEOUS SUPPORTING INFORMATION

D.2.1. NMR spectra of 1,4-$C_4F_8I_2$

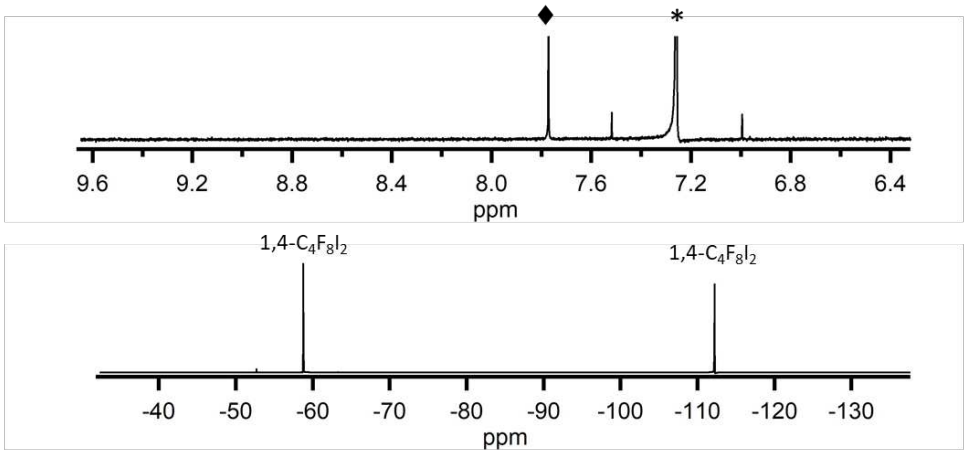

Figure D-28. NMR spectra of 1,4-$C_4F_8I_2$, showing that starting material is not containing. ^{19}F NMR spectrum (bottom) shows only expected peaks. ^{1}H NMR spectrum, top, shows only $CDCl_3$ (denoted *), $CDCl_3$ ^{13}C satellite peaks, and 1,4-bistrifluromethylbenzene (reference, denoted ♦).

D.2.2. Absorption spectrum of 1,10-PHEN based Cu Complex

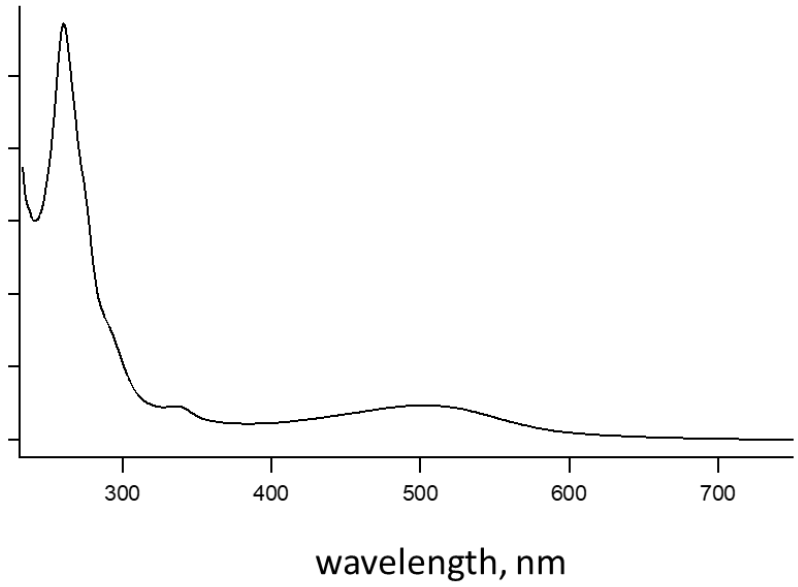

Figure D-29. UV-vis absorption spectrum of possible Cu-(2,3;5,6-(1,10-PHEN)$(C_4F_8)_2)_2$ complex, showing absorption band centered around 500 nm. This absorption is much more red-shifted than the absorption of the pure ligand or copper(I) triflate toluene starting material.

D.2.3. Reactions with substrates which did not produce isolable products

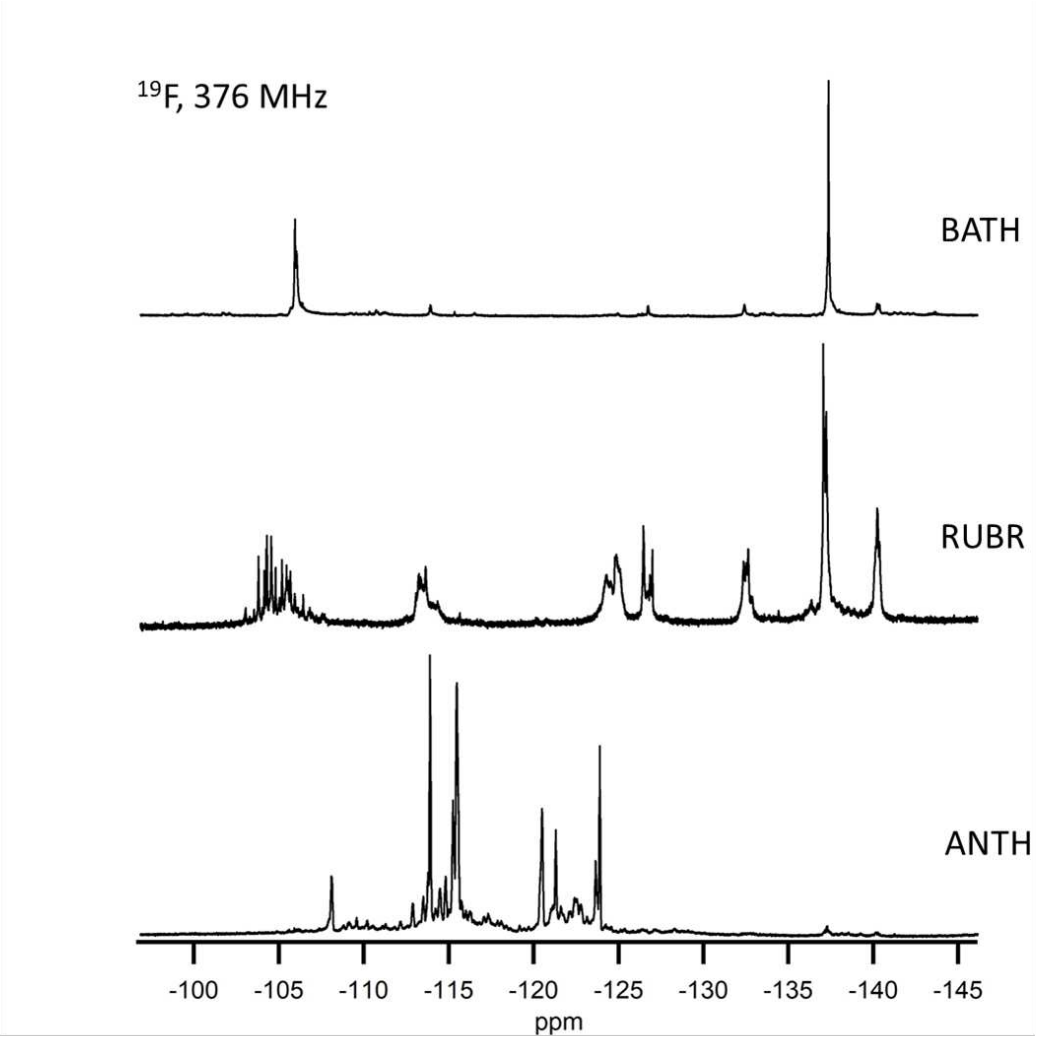

Figure D-30. NMR spectra of crude reaction mixtures recovered from reactions of substrates BATH, RUBR, and ANTH with 1,4-$C_4F_8I_2$. Reactions have occurred, but separations methods have not been developed to isolate pure products. In the case of BATH, the reactions appears to have been selective, but attempts to further purfy the sample by HPLC and crystallization were unsuccessful.

D.2.4. Crystal Data and Refinement Parameters

Table D-8. Crystal data and final refinement parameters for structures reported in chapter 2

Compound	3,4:9,10-PERY(*cyclo*-C4F8)$_2$	2,3-(1,10-PHEN)(*cyclo*-C_4F_8)	2,3:5,6-(1,10-PHEN)(*cyclo*-C_4F_8)$_2$	4,5-PYRN(*cyclo*-C_4F_8)	1,2-ACRD(*cyclo*-C_4F_3H)	7,8-(PHRD)(*cyclo*-C_4F_8)	6,7-(4,7-PHEN)(*cyclo*-C_4F_7H)
Empirical formula	$C_{28}H_8F_{16}$	$C_{16}H_6F_8N_2$	$C_{20}H_4F_{16}N_2$	$C_{20}H_8F_8$	$C_{17}H_8F_3N$	$C_{17}H_7F_8N$	$C_{16}H_7F_7N_2$
Common name	3,4:9,10-(C4F8)-PERY	2,3-(C4F8)-1,10-PHEN	2,3:5,6-(C4F8)-1,10-PHEN	4,5-(C4F8)-PYRN	1,2-(C4F3H)-ACRD	7,8-(C4F8)-PHRD	6,7-(C4F7H)-4,7-PHEN
Formula weight	648.34	378.23	576.25	400.26	283.24	377.24	361.90
Habit, color	needle, clear yellow	needle, clear yellow	rhombohedral, clear colorless	needle, clear colorless	needle, clear colorless	plate, clear colorless	needle, clear colorless
Crystal size, mm	0.35 × 0.01 × 0.01	0.202 × 0.05 × 0.038	0.529 × 0.309 × 0.099	0.23 × 0.084 × 0.061	0.15 × 0.035 × 0.021	0.189 × 0.044 × 0.037	0.112 × 0.032 × 0.023
Space group	$P3_121$	$P2_1/n$	P-1	Pbca	P-1	Pbcm	
a (Å)	13.5206(8)	7.7504(15)	6.9649(5)	9.0467(4)	7.241(3)	8.644(2)	
b (Å)	13.5206(8)	7.1252(14)	11.0540(7)	15.2147(7)	9.260(4)	24.376(6)	
c (Å)	10.5293(9)	25.503(5)	13.1094(8)	21.2263(10)	9.564(4)	6.8248(16)	
α (°)	90	90	79.223(2)	90	87.761(8)	90	
β (°)	90	98.402(3)	80.866(2)	90	68.907(9)	90	
γ (°)	120	90	88.3680(10)	90	84.609(9)	90	
V (Å^3)	1666.9(2)	1393.2(5)	978.92(11)	2921.6	595.7(4)	1438.0(6)	
Z	3	4	2	8	2	4	
T (K)	150	150	100	100	100	100	100
ρ_{calc} (g cm^{-3})	1.938	1.803	1.955	1.802	1.579	1.742	
GooF [all data]	0.848	1.087	1.076	1.029	1.09	1.032	
R(F) (*I*>2σ(*I*))[a]	0.0372	0.0368	0.0572	0.0426	0.0735	0.0697	
wR(F^2) [all data][a]	0.0781	0.1045	0.1692	0.1165	0.2194	0.1862	
C–C bond precision (Å)	0.0064	0.0019	0.0031	0.0022	0.0047	0.0062	
min., max. e– dens., (e Å^{-3})	−0.177, 0.207	−0.211, 0.351	−0.464, 0.749	−0.382, 0.528	−0.35, 0.09	−0.48, 0.641	
source	synchrotron	synchrotron	synchrotron	synchrotron	synchrotron	synchrotron	synchrotron

D.2.5. Additional LT-PES data

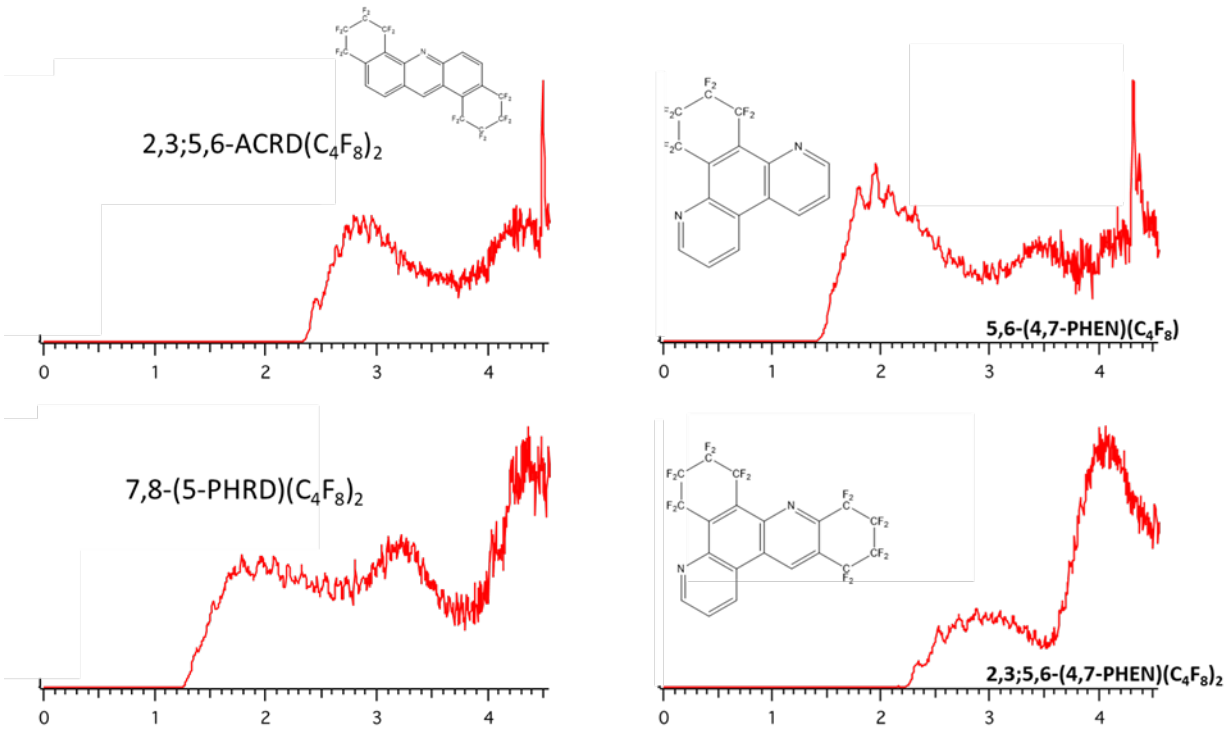

Figure D-31. Additional LT-PES spectra of compounds reported in chapter 2.

D.3. CHAPTER 3 MISCELLANEOUS SUPPORTING INFORMATION

D.3.1 Crystal Refinement Parameters

Table D-9. Crystal data collection and final refinement parameters for the PHNZ derivative X-ray diffraction structures

compound[a]	1,2-PHNZ(C_4HF_3)	1,2-PHNZ(C_4F_4)	1,2-PHNZ(C_4F_8)	2,3-PHNZ(C_4F_8)	ANTH/[1,2:8,9-PHNZ(C_4F_8)$_2$]$_2$
formula unit	$C_{16}H_7F_3N_2$	$C_{16}H_6F_4N_2$	$C_{16}H_6F_8N_2$	$C_{16}H_6F_8N_2$	$C_{27}H_9F_{16}N_2$
formula wt., g mol^{-1}	284.24	302.23	378.23	378.23	665.36
habit, color	needle, yellow	needle, yellow	needle, colorless	needle, light yellow	needle, dark green
crystal system	monoclinic	triclinic	triclinic	orthorhombic	triclinic
space group, Z	*Cc*, 4	$P\bar{1}$, 2	$P\bar{1}$, 2	*Pnma*, 4	$P\bar{1}$, 2
a, Å	7.212(2)	7.2459(14)	7.1430(15)	28.331(5)	9.718(4)
b, Å	24.349(6)	7.7265(15)	7.5836(15)	6.7839(13)	10.499(5)
c, Å	6.8759(19)	11.668(2)	13.357(3)	7.3082(14)	12.460(6)
α, deg	90	99.520(4)	89.843(4)	90	91.508(7)
β, deg	108.403(7)	98.324(4)	80.734(4)	90	100.877(7)
γ, deg	90	108.622(4)	86.167(5)	90	102.415(7)
V, Å^3	1145.6(5)	596.7(2)	704.4(3)	1404.6(5)	1216.3(9)
ρ_{calc}, g cm^{-3}	1.648	1.682	1.764	1.789	1.817
T, K	150(1)	100(1)	100(1)	100(1)	100(1)
$R(F)$ ($I > 2\sigma(I)$)[b]	0.0475	0.0570	0.0649	0.0508	0.0669
$wR(F^2)$ [all data][b]	0.1122	0.1710	0.1860	0.1469	0.1814
GOF	0.983	1.048	0.988	1.059	1.000

[a] Abbreviations: ANTH = anthracene; PHNZ = phenazine; [b] $R(F) = \Sigma||F_o| - |F_c||/\Sigma|F_o|$; $wR(F^2) = (\Sigma[w(F_o^2 - F_c^2)^2]/\Sigma[w(F_o^2)^2])^1$

D.3.2 Additional analysis of single crystal X-ray structures

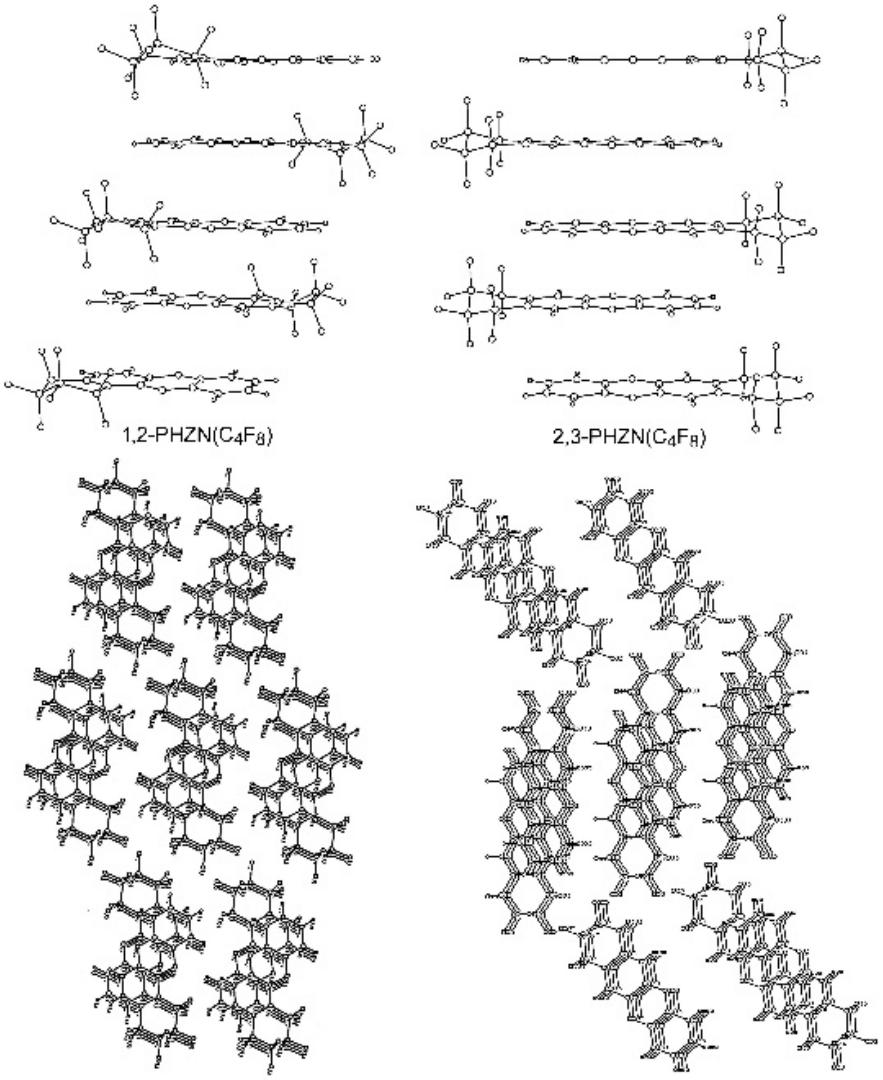

Figure D-32. Stacks of molecules in the structures of 1,2-PHNZ(C_4F_8) (left) and 1,2-PHNZ(C_4F_8) (right; H atoms omitted for clarity). The drawings on the bottom are not precisely to scale.

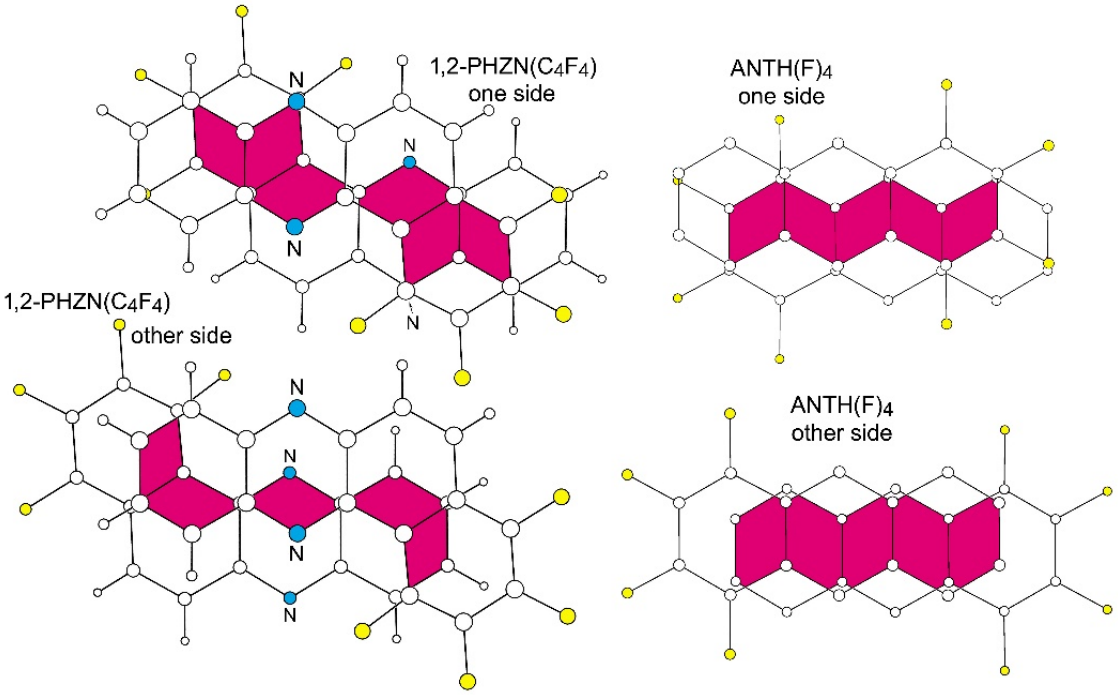

Figure D-33. Overlap drawings of adjacent molecules in stacks in the structures of 1,2-PHNZ(C_4F_4) (left) and 1,2-PHNZ(C_4F_8) (right; ref. [9]).

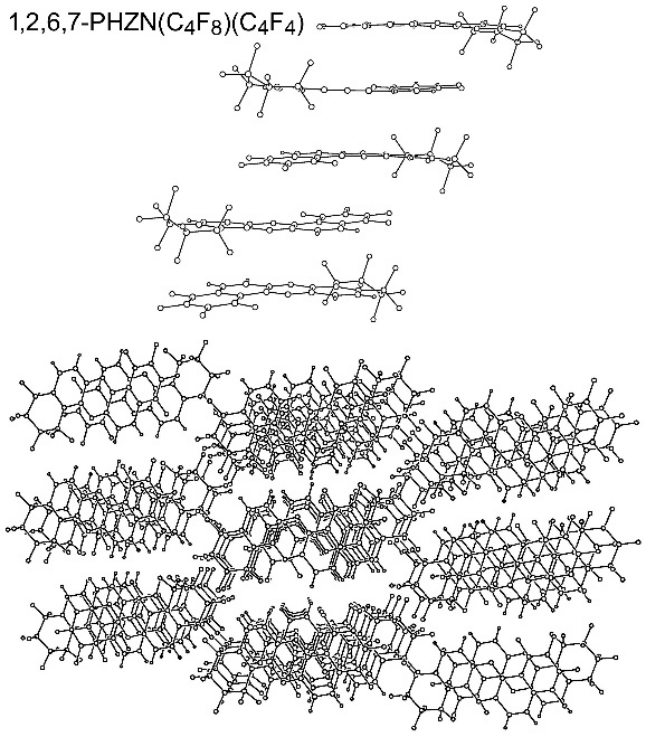

Figure D-34. The head-to-tail parallel stacking of molecules (top) and the hexagonal array of stacks (bottom) in the structure of 1,2:6,7-PHNZ(C_4F_8)(C_4F_4).

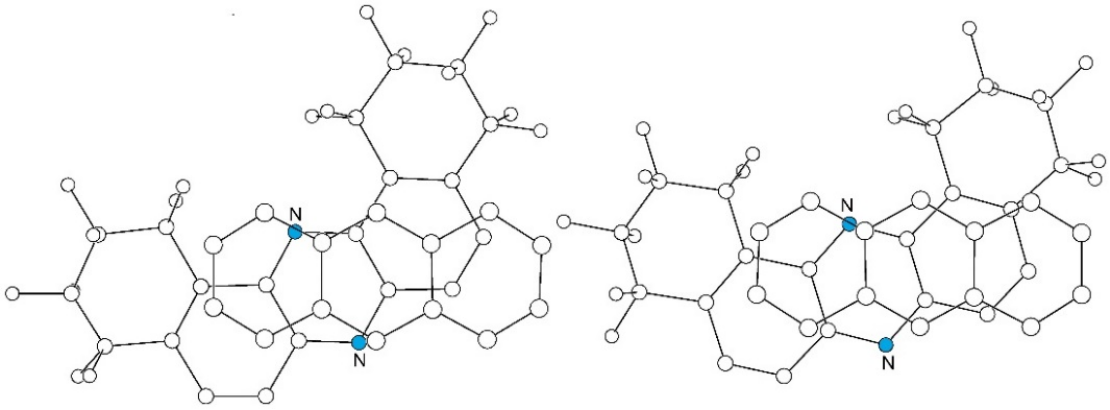

Figure D-35. Donor/acceptor overlaps in the structure of ANTH/1,2:8,9-PHNZ(C_4F_8)$_2$ (N atoms shaded; H atoms omitted for clarity). In each drawing the ANTH C(sp^2) least-squares plane is in the plane of the page and is above the 1,2:8,9-PHNZ(C_4F_8)$_2$ acceptor.

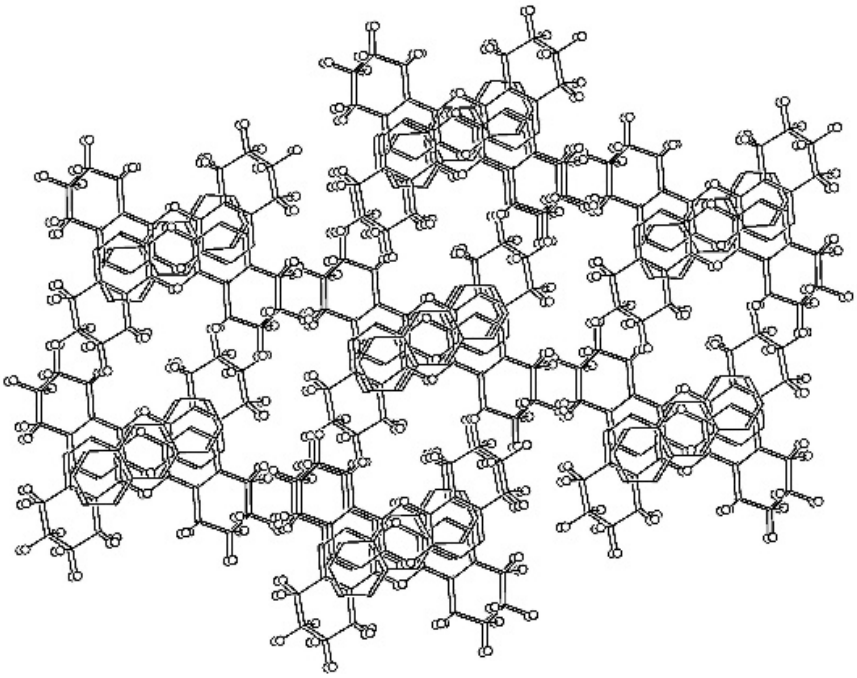

Figure D-36. Distorted hexagonal array of D/A/A/D/A/A stacks in the structure of ANTH/[1,2:8,9-PHNZ(C_4F_8)$_2$]$_2$ (N and F atoms are larger spheres than C atoms).

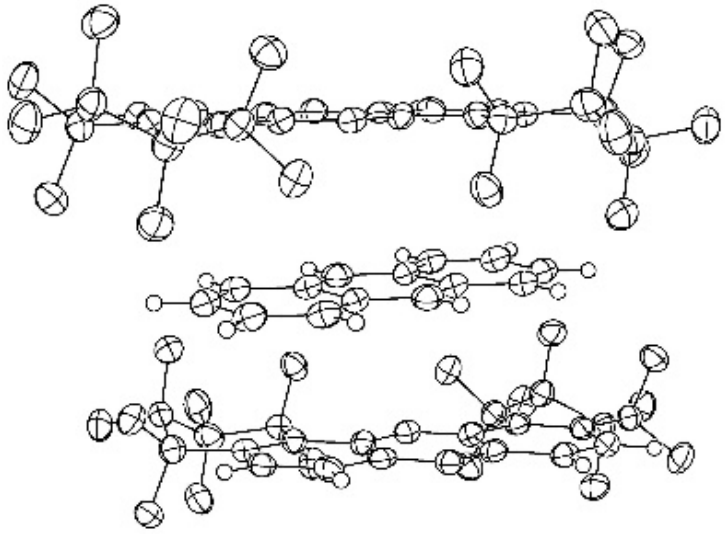

Figure D-37. Drawing of the structure of ANTH/[1,2:8,9-PHNZ(C_4F_8)]$_2$ (40% thermal ellipsoids except for H atoms).

D.3.3. Reference information for EA data

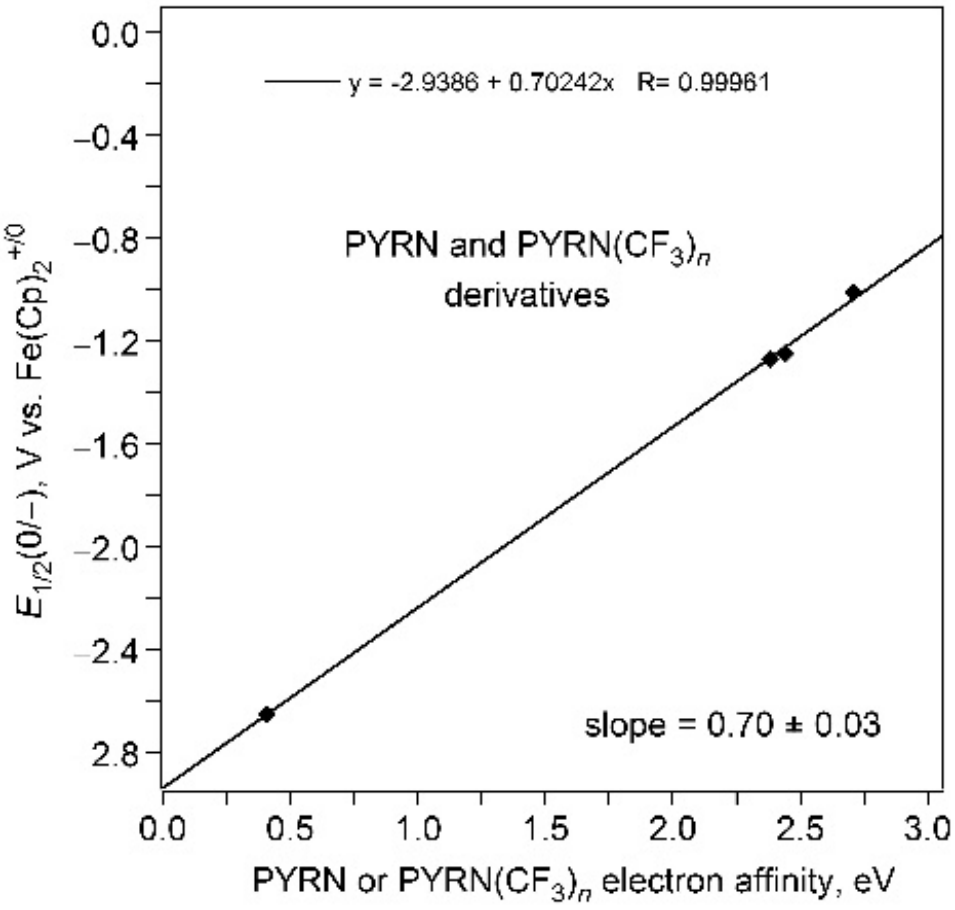

Figure D-38. Plot of $E_{1/2}(0/-)$ values vs electron affinities for pyrene (PYRN) and three PYRN$(CF_3)_{5,6}$ derivatives. The data are from ref. [10]. Note that the lengths and ranges of values on both axes are equal (i.e., these are square plots), to show unambiguously that the slope of the linear least-squares fit to the data is significantly less than unity.

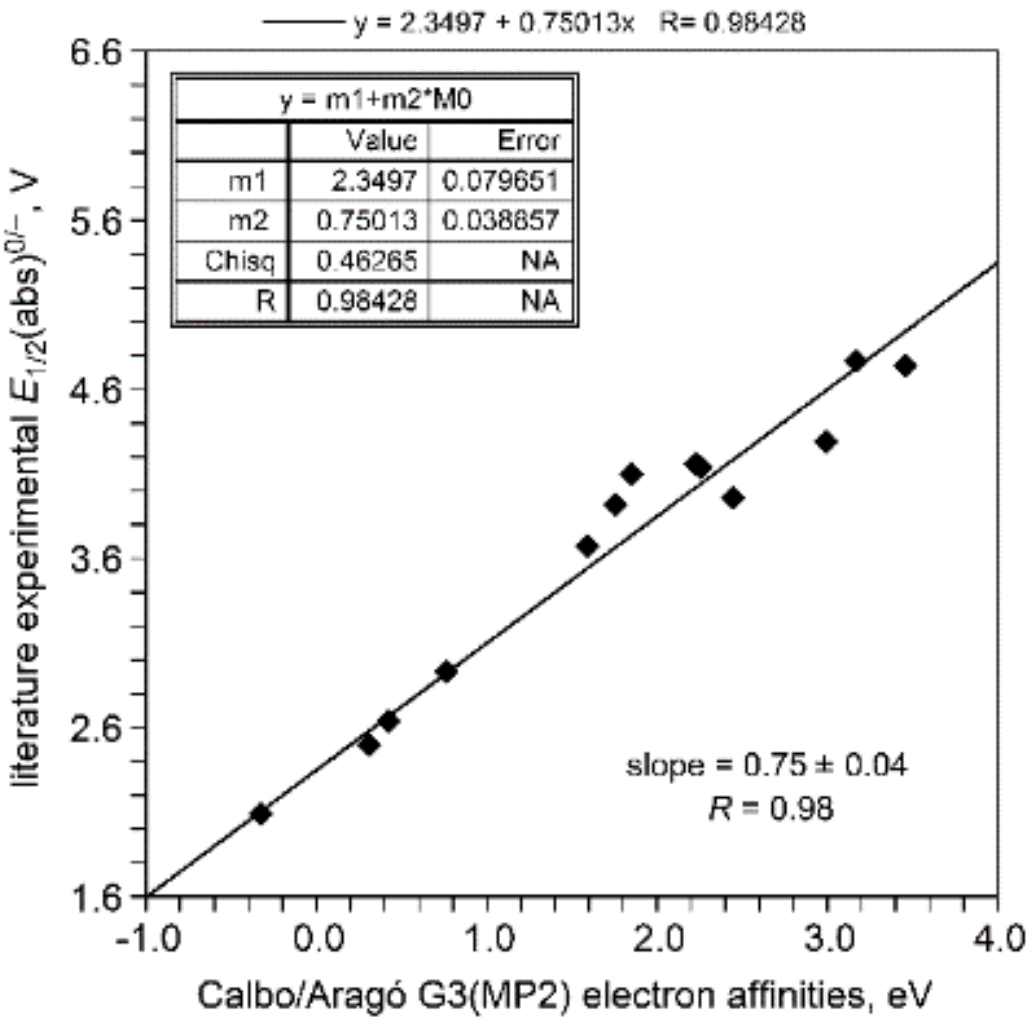

Figure D-39. G3(MP2) predicted electron affinities vs. electrochemical $E_{1/2}(0/-)$ values for aromatic compounds and other strong electron acceptors, including C_6H_6, NAPH, ANTH, PYRN, PERY, benzoquinone, 1.2.4.5.-$C_6H_2(CN)_4$, TCNE, and TCNQ, among others (ref. [11]). Note that the lengths and ranges of values on both axes are equal (i.e., this is a square plot), to show unequivocally that the slope is less than unity).

D.3.4. Supplementary spectroelectrochemical data

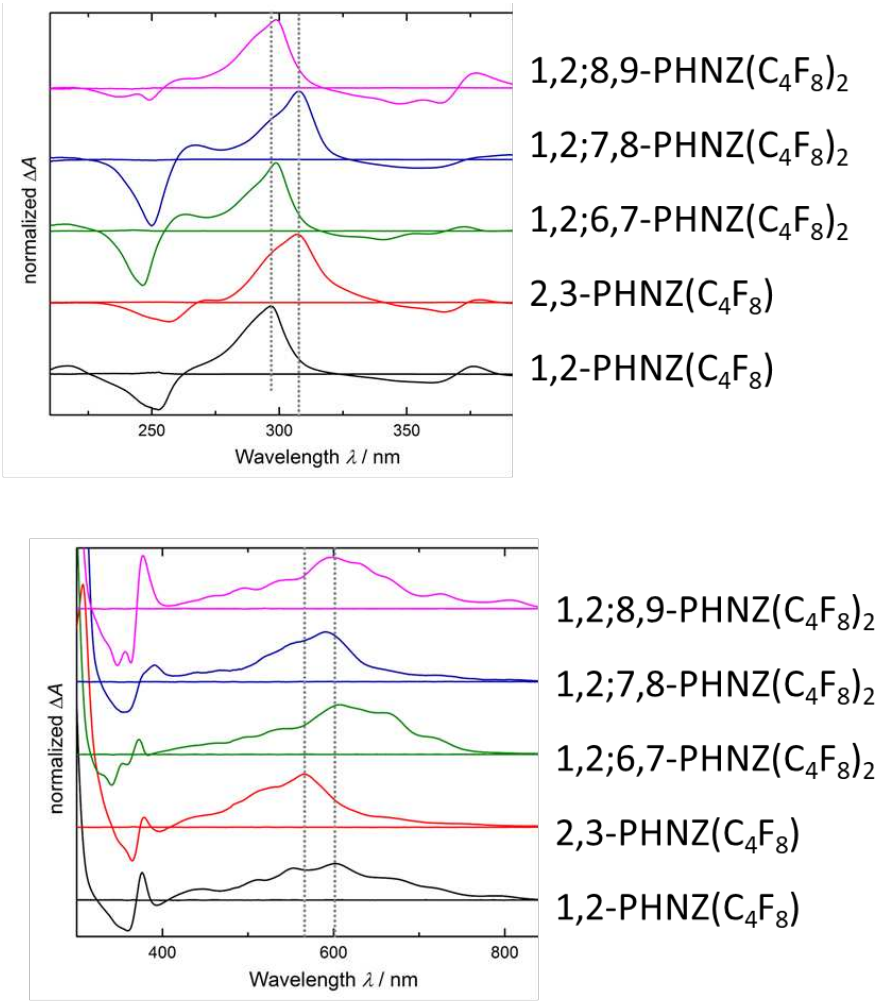

Figure D-40 Absorption of the reduced form of substituted phenazines relative to their neutralform in the UV-range (top) and the visible range (bottom). Reduced forms absorb so much more strongly that the neutral absorption peaks are not visible. Note the different maxima for peninsular-substituted compounds.

D.3.5. Supplementary TRMC data

Table D-10. *Details of films for TRMC and PL measurements*

compound	I_0 photons/cm^2/pulse	film composition % PHNZ compound/ % P3HT
1,2-PHNZ(C_4F_8)	3.06574e+15	9/91
2,3-PHNZ(C_4F_8)	2.91202e+15	7/93
1,2;6,7-PHNZ(C_4F_8)$_2$	2.91202e+15	8/92
1,2;7,8-PHNZ(C_4F_8)$_2$	2.91202e+15	9/91
1,2-PHNZ(C_4F_4)	3.20237e+15	8/92
1,2;6,7-PHNZ(C_4F_8)(C_4F_8)	3.20237e+15	8/92

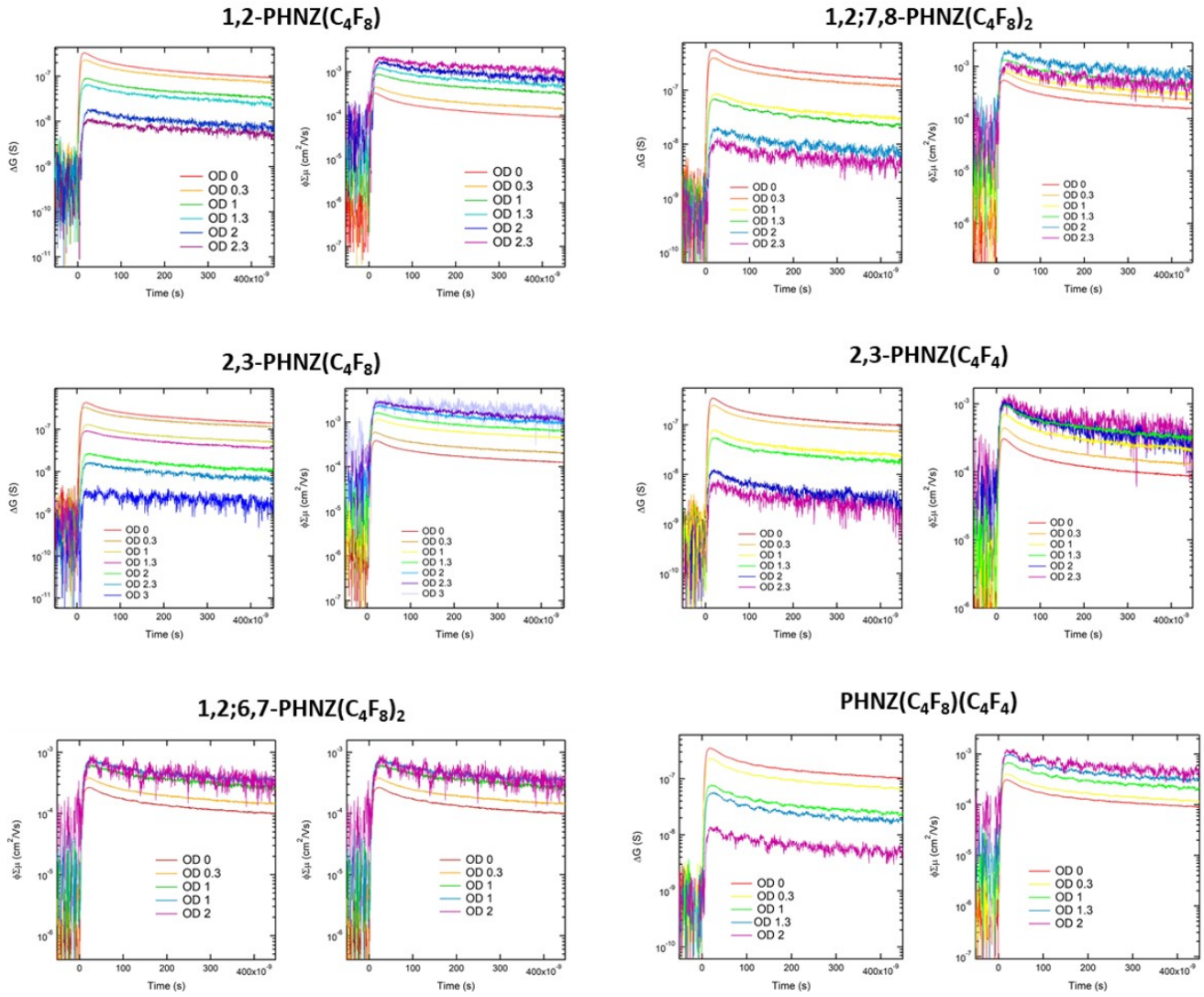

Figure D-41. Plots TRMC series for each film studied with OD from 0 to maximum possible OD for which signal was observed. Maximum OD possible for any of these films was 3.

D.4. CHAPTER 4 MISCELLANEOUS SUPPORTING INFORMATION

D.4.1 Crystal Refinement Parameters

Table D-11. Crystal Data and Final Refinement Parameters for ACRD(CF_3)$_{4,5}$, ACRD(C_2F_5)(CF_3)$_4$, and H_2ACRD(CF_3)$_5$ X-ray Diffraction Structures

compd abbreviation[a]	1,4,5,7	1,3,5,8	2,4,6,9	1,2,4,5,8	2,4,5,6,9	4-C_2F_5-2,5,7,9	H_2-1,4,5,8,9
formula	$C_{17}H_5F_{12}N$	$C_{17}H_5F_{12}N$	$C_{17}H_5F_{12}N$	$C_{18}H_4F_{15}N$	$C_{18}H_4F_{15}N$	$C_{19}H_4F_{17}N$	$C_{18}H_6F_{15}N$
formula wt., g mol^{-1}	451.22	451.22	451.22	519.22	519.22	569.23	521.24
crystal size, μm	50 × 20 × 10	126 × 50 × 50	500 × 250 × 250	110 × 20 × 10	40 × 10 × 10	200 × 50 × 50	250 × 50 × 50
color	colorless	colorless	yellow	colorless	yellow	yellow	colorless
crystal system	monoclinic	orthorhombic	monoclinic	monoclinic	monoclinic	monoclinic	monoclinic
space group, Z	Cc, 4	$Pca2_1$, 8	$P2_1$, 4	$P2_1/n$, 4	$P2_1/c$, 4	$P2_1/c$, 8	$C2/c$, 8
a, Å	10.5254(8)	13.1440(5)	7.4910(2)	6.7751(5)	9.2906(5)	9.9248(6)	22.9638(7)
b, Å	16.6117(12)	16.2662(7)	16.4412(5)	11.9516(9)	18.3703(11)	16.4516(10)	8.7438(2)
c, Å	9.1211(6)	14.8610(6)	12.7791(4)	21.3706(16)	10.6488(6)	23.6753(15)	19.3617(6)
α, deg	90	90	90	90	90	90	90
β, deg	97.403(4)	90	96.4930(10)	92.695(2)	103.503(2)	107.200 (2)	114.5550(10)
γ, deg	90	90	90	90	90	90	90
V, Å^3	1581.5(2)	3177.3(2)	1563.79(8)	1728.5(2)	1333.52(8)	3864.4 (4)	3536.06(18)
ρ_{calc}, g cm^{-3}	1.895	1.887	1.917	1.995	1.952	1.957	1.958
T, K	100(1)	100(1)	100(1)	100(1)	100(1)	100(1)	100(1)
min/max e$^-$ dens., e Å^{-3}	−0.242/0.306	−0.168/0.266	−0.219/0.289	−0.393/0.345	−0.484/0.634	−0.972/0.852	−0.367/0.493
$R(F)$ ($I > 2\sigma(I)$)[b]	0.0322	0.0250	0.0371	0.0454	0.0551	0.0558	0.0349
$wR(F^2)$ [all data][b]	0.0832	0.0682	0.0840	0.1217	0.1461	0.1512	0.0909
GOF	1.033	1.040	1.035	1.019	1.033	1.025	1.041

[a] Abbreviations: 1,4,5,7 = 1,4,5,7-ACRD(CF_3)$_4$; 1,3,5,8 = 1,3,5,8-ACRD(CF_3)$_4$; 2,4,6,9 = 2,4,6,9-ACRD(CF_3)$_4$; 1,2,4,5,8 = 1,2,4,5,8-ACRD(CF_3)$_5$; 2,4,5,6,9 = 2,4,5,6,9-ACRD(CF_3)$_5$; 4-C_2F_5-2,5,7,9 = 4-C_2F_5-2,5,7,9-ACRD(CF_3)$_5$; H_2-1,4,5,8,9 = 1,4,5,8,9-(9,10-H_2ACRD)(CF_3)$_5$; dens. = density.

[b] $R(F) = \Sigma||F_o| - |F_c||/\Sigma|F_o|$; $wR(F^2) = (\Sigma[w(F_o^2 - F_c^2)^2]/\Sigma[w(F_o^2)^2])^{1/2}$.

D.4.2. Example mass spectrum of failed LT-PES sample

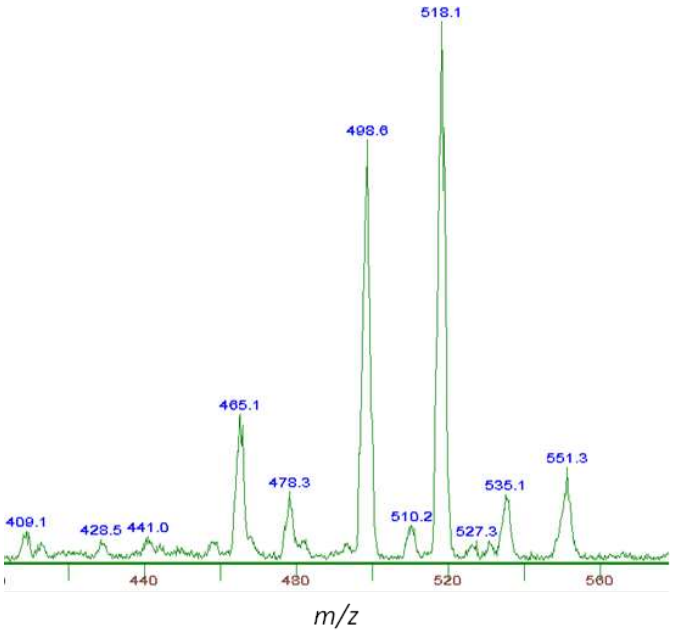

Figure D-42. As an example of the observed decomposition a mass spectrum of 1,3,5,8-ACRD$(CF_3)_4$ upon reduction for PES analysis is shown. The expected peak at an *m/z* of 451 is not present. This was the case for the entire family of ACRD$(CF_3)_n$ compounds when EA experiments were obtained.

REFERENCES

1. Garst, J. F.; Barbas, J. T.; Barton, F. E., Radical mechanism of alkylation of sodium naphthalenide. *J. Am. Chem. Soc.* **1968,** *90* (25), 7159-7160.
2. Zeng, Z.; Liu, C.; Jin, L.-M.; Guo, C.-C.; Chen, Q.-Y., Unexpected Intramolecular Cyclization of 2-(Perfluoroalkyl)tetraarylporphyrin Radicals: Approaches for the Intramolecular Cyclization of 2-(Perfluoroalkyl)tetraarylporphyrin Radicals. *Eur. J. Org. Chem.* **2005**, 306-316.
3. Amli, H.; Uneyama, K., C-F Bond Activation in Organic Synthesis. *Chem. Rev.* **2009,** *109*, 2119-2183.
4. Utsumi, S.; Katagiri, T.; Uneyama, K., Defluorination–silylation of alkyl trifluoroacetates to 2,2-difluoro-2-(trimethylsilyl)acetates by copper-deposited magnesium and trimethylsilyl chloride. *Tetrahedron* **2012,** *68* (2), 580-583.
5. Birch, A. J., 117. Reduction by dissolving metals. Part I. *Journal of the Chemical Society (Resumed)* **1944,** (0), 430-436.
6. Rippy, K. C.; Bukovsky, E. V.; Clikeman, T. T.; Chen, Y.-S.; Hou, G.-L.; Wang, X.-B.; Popov, A. A.; Boltalina, O. V.; Strauss, S. H., Copper Causes Regiospecific Formation of C_4F_8-Containing Six-Membered Rings and their Defluorination/Aromatization to C_4F_4-Containing Rings in Triphenylene/1,4-$C_4F_8I_2$ Reactions. *Chem. Eur. J.* **2016,** *22*, 874–877.
7. Collings, J. C.; Roscoe, K. P.; Thomas, R. L.; Batsanov, A. S.; Stimson, L. M.; Howard, J. A. K.; Marder, T. B., Arene-Perfluoroarene Interactions in Crystal Engineering. Part 3. Single-Crystal Structures of 1:1 Complexes of Octafluoronaphthalene with Fused-Ring Polyaromatic Hydrocarbons. *New J. Chem.* **2001,** *25* (11), 1410–1417.
8. Kuvychko, I. V.; Castro, K. P.; Deng, S. H. M.; Wang, X.-B.; Strauss, S. H.; Boltalina, O. V., Taming Hot CF_3 Radicals: Incrementally Tuned Families of Polyarene Electron Acceptors for Air-Stable Molecular Optoelectronics. *Angew. Chem. Int. Ed.* **2013,** *52*, 4871-4874.
9. Cozzi, F.; Bacchi, S.; Filippini, G.; Pilati, T.; Gavezzotti, A., Synthesis, X-ray Diffraction and Computational Study of the Crystal Packing of Polycyclic Hydrocarbons Featuring Aromatic and Perfluoroaromatic Rings Condensed in the Same Molecule: 1,2,3,4-Tetrafluoronaphthalene, -anthracene and -phenanthrene. *Chem. Eur. J.* **2007,** *13*, 7177–7184.
10. Kuvychko, I. V.; Castro, K. P.; Deng, S. H. M.; Wang, X.-B.; Strauss, S. H.; Boltalina, O. B., Taming Hot CF_3 Radicals: Incrementally Tuned Families of Polyarene Electron Acceptors for Air-Stable Molecular Optoelectronics. *Angew. Chem. Int. Ed.* **2013,** *52*, 4871–4874.
11. Calbo, J.; Viruela, R.; Ortí, E.; Aragó, J., Relationship between Electron Affinity and Half-Wave Reduction Potential: A Theoretical Study on Cyclic Electron-Acceptor Compounds. *ChemPhysChem* **2016,** *17*, 3881–3890.

ALPHABETIZED LIST OF COMMONLY USED ABBREVIATIONS

Abbreviation	**Full Terminology**
ANTH	anthracene
appx	appendix
APS	Advance Photon Source at Argonne National Laboratory, Lemont, IL
$CDCl_3$	deuterated chloroform
CSU	Colorado State University
CV	cyclic voltammetry
DFT	density functional theorem
$E_{1/2}$	reduction potential in solution
EA	electron affinity
ESR	electron spin resonance spectroscopy
h	hours
H_2-ACRD	9,10-dihydroacridine
HPLC	high pressure liquid chromatography
HOMO	highest occupied molecular orbital
IFW	Leibniz Institute for Solid State and Materials Research, Dresden, DE
LUMO	lowest unoccupied molecular orbital
n-type	electron (negative charge) transport material
NMR	nuclear magnetic resonance spectroscopy
o-DCB	*ortho*-dichlorobenzene
OOP_{av}	average displacement of PAH core atoms from their least-squares plane
OOP_{max}	maximum displacement of PAH core atoms from their least-squares plane
P3HT	poly(3-hexylthiophene-2,5-diyl)
PERY	perylene

p-type	hole (positive charge) transport material
PES	photoelectron spectroscopy
PHNZ	phenazine
PHRD	phenanthridine
PL	photoluminescence
PNNL	Pacific Northwest National Laboratory, Richland, WA
PNTZ	phenothiazine
PYRN	pyrene
RD/Z	reductive defluorination/aromatization
R_F group	perfluoroalkyl group
RUBR	rubrene
T	temperature
$TBAPF_6$	tetrabutylammonium hexafluorophosphate
TRMC	time resolved microwave conductivity measurement
TRPH	triphenylene
UV-vis	ultraviolet-visible spectroscopy
vis-NIR	visible-near infrared spectroscopy
1,10-PHEN	1,10-phenanthroline
1,4-$C_4F_8I_2$	1,4-diiodooctaflurobutane
CF_3I	trifluoromethyl iodide
4,7-PHEN	4,7-phenanthroline
9,10-ANTH$(Me)_2$	9,10-dimethylanthracene
9,10-ANTH$(Ph)_2$	9,10-diphenylanthracene
π system	aromatic system of π bonds